

UNCLASSIFIED

AD NUMBER

**AD848983**

NEW LIMITATION CHANGE

TO

**Approved for public release, distribution  
unlimited**

FROM

**Distribution authorized to U.S. Gov't.  
agencies only; Administrative/Operational  
Use; 22 FEB 1969. Other requests shall be  
referred to Air Force Aero Propulsion  
Laboratory, Wright-Patterson AFB, OH  
45433.**

AUTHORITY

**AFRPL ltr, 30 Jun 1975**

THIS PAGE IS UNCLASSIFIED

THIS REPORT HAS BEEN DELIMITED  
AND CLEARED FOR PUBLIC RELEASE  
UNDER DOD DIRECTIVE 5200.20 AND  
NO RESTRICTIONS ARE IMPOSED UPON  
ITS USE AND DISCLOSURE.

DISTRIBUTION STATEMENT A

APPROVED FOR PUBLIC RELEASE;  
DISTRIBUTION UNLIMITED.

AD848983

AFAPL-TR-69-7  
Volume II

(UNCLASSIFIED TITLE)

AIR FORCE ADVANCED LIFT FAN AND LIFT/CRUISE  
FAN DEMONSTRATOR PROGRAM

Walter A. Fasching  
General Electric Company

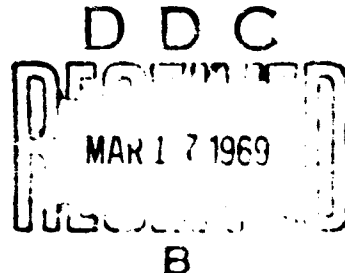
TECHNICAL REPORT AFAPL-TR-69-7, VOLUME II  
February 22, 1969

SPECIAL HANDLING REQUIRED  
NOT RELEASABLE TO FOREIGN NATIONALS

The information in this document will not  
be disclosed to foreign nationals or their  
representatives.

Each transmittal of this document outside  
the agencies of the U.S. Government must  
have prior approval of the Air Force, Aero  
Propulsion Laboratory. *3/27/69*

Air Force Aero Propulsion Laboratory  
Air Force Systems Command  
Wright-Patterson Air Force Base, Ohio



NOTICE

When Government drawings, specifications, or other data are used for any purpose other than in connection with a definitely related Government procurement operation, the United States Government thereby incurs no responsibility nor any obligation whatsoever; and the fact that the Government may have formulated, furnished, or in any way supplied the said drawings, specifications, or other data, is not to be regarded by implication or otherwise as in any manner licensing the holder or any other person or corporation, or conveying any rights or permission to manufacture, use, or sell any patented invention that may in any way be related thereto.

Accessed by	WIRE BUREAU
CRSTI	BUFF SECTION
DDC	
DDC-HANFORD	<input type="checkbox"/>
DDC-LA	
DDC-NS	
DDC-R	
DDC-S	
DDC-T	
DDC-V	
DDC-W	
DDC-X	
DDC-Y	
DDC-Z	
DDC-A	
DDC-B	
DDC-C	
DDC-D	
DDC-E	
DDC-F	
DDC-G	
DDC-H	
DDC-I	
DDC-J	
DDC-K	
DDC-L	
DDC-M	
DDC-N	
DDC-O	
DDC-P	
DDC-Q	
DDC-R	
DDC-S	
DDC-T	
DDC-U	
DDC-V	
DDC-W	
DDC-X	
DDC-Y	
DDC-Z	
DDC-A	
DDC-B	
DDC-C	
DDC-D	
DDC-E	
DDC-F	
DDC-G	
DDC-H	
DDC-I	
DDC-J	
DDC-K	
DDC-L	
DDC-M	
DDC-N	
DDC-O	
DDC-P	
DDC-Q	
DDC-R	
DDC-S	
DDC-T	
DDC-U	
DDC-V	
DDC-W	
DDC-X	
DDC-Y	
DDC-Z	
DDC-A	
DDC-B	
DDC-C	
DDC-D	
DDC-E	
DDC-F	
DDC-G	
DDC-H	
DDC-I	
DDC-J	
DDC-K	
DDC-L	
DDC-M	
DDC-N	
DDC-O	
DDC-P	
DDC-Q	
DDC-R	
DDC-S	
DDC-T	
DDC-U	
DDC-V	
DDC-W	
DDC-X	
DDC-Y	
DDC-Z	
DDC-A	
DDC-B	
DDC-C	
DDC-D	
DDC-E	
DDC-F	
DDC-G	
DDC-H	
DDC-I	
DDC-J	
DDC-K	
DDC-L	
DDC-M	
DDC-N	
DDC-O	
DDC-P	
DDC-Q	
DDC-R	
DDC-S	
DDC-T	
DDC-U	
DDC-V	
DDC-W	
DDC-X	
DDC-Y	
DDC-Z	
DDC-A	
DDC-B	
DDC-C	
DDC-D	
DDC-E	
DDC-F	
DDC-G	
DDC-H	
DDC-I	
DDC-J	
DDC-K	
DDC-L	
DDC-M	
DDC-N	
DDC-O	
DDC-P	
DDC-Q	
DDC-R	
DDC-S	
DDC-T	
DDC-U	
DDC-V	
DDC-W	
DDC-X	
DDC-Y	
DDC-Z	
DDC-A	
DDC-B	
DDC-C	
DDC-D	
DDC-E	
DDC-F	
DDC-G	
DDC-H	
DDC-I	
DDC-J	
DDC-K	
DDC-L	
DDC-M	
DDC-N	
DDC-O	
DDC-P	
DDC-Q	
DDC-R	
DDC-S	
DDC-T	
DDC-U	
DDC-V	
DDC-W	
DDC-X	
DDC-Y	
DDC-Z	
DDC-A	
DDC-B	
DDC-C	
DDC-D	
DDC-E	
DDC-F	
DDC-G	
DDC-H	
DDC-I	
DDC-J	
DDC-K	
DDC-L	
DDC-M	
DDC-N	
DDC-O	
DDC-P	
DDC-Q	
DDC-R	
DDC-S	
DDC-T	
DDC-U	
DDC-V	
DDC-W	
DDC-X	
DDC-Y	
DDC-Z	
DDC-A	
DDC-B	
DDC-C	
DDC-D	
DDC-E	
DDC-F	
DDC-G	
DDC-H	
DDC-I	
DDC-J	
DDC-K	
DDC-L	
DDC-M	
DDC-N	
DDC-O	
DDC-P	
DDC-Q	
DDC-R	
DDC-S	
DDC-T	
DDC-U	
DDC-V	
DDC-W	
DDC-X	
DDC-Y	
DDC-Z	
DDC-A	
DDC-B	
DDC-C	
DDC-D	
DDC-E	
DDC-F	
DDC-G	
DDC-H	
DDC-I	
DDC-J	
DDC-K	
DDC-L	
DDC-M	
DDC-N	
DDC-O	
DDC-P	
DDC-Q	
DDC-R	
DDC-S	
DDC-T	
DDC-U	
DDC-V	
DDC-W	
DDC-X	
DDC-Y	
DDC-Z	
DDC-A	
DDC-B	
DDC-C	
DDC-D	
DDC-E	
DDC-F	
DDC-G	
DDC-H	
DDC-I	
DDC-J	
DDC-K	
DDC-L	
DDC-M	
DDC-N	
DDC-O	
DDC-P	
DDC-Q	
DDC-R	
DDC-S	
DDC-T	
DDC-U	
DDC-V	
DDC-W	
DDC-X	
DDC-Y	
DDC-Z	
DDC-A	
DDC-B	
DDC-C	
DDC-D	
DDC-E	
DDC-F	
DDC-G	
DDC-H	
DDC-I	
DDC-J	
DDC-K	
DDC-L	
DDC-M	
DDC-N	
DDC-O	
DDC-P	
DDC-Q	
DDC-R	
DDC-S	
DDC-T	
DDC-U	
DDC-V	
DDC-W	
DDC-X	
DDC-Y	
DDC-Z	
DDC-A	
DDC-B	
DDC-C	
DDC-D	
DDC-E	
DDC-F	
DDC-G	
DDC-H	
DDC-I	
DDC-J	
DDC-K	
DDC-L	
DDC-M	
DDC-N	
DDC-O	
DDC-P	
DDC-Q	
DDC-R	
DDC-S	
DDC-T	
DDC-U	
DDC-V	
DDC-W	
DDC-X	
DDC-Y	
DDC-Z	
DDC-A	
DDC-B	
DDC-C	
DDC-D	
DDC-E	
DDC-F	
DDC-G	
DDC-H	
DDC-I	
DDC-J	
DDC-K	
DDC-L	
DDC-M	
DDC-N	
DDC-O	
DDC-P	
DDC-Q	
DDC-R	
DDC-S	
DDC-T	
DDC-U	
DDC-V	
DDC-W	
DDC-X	
DDC-Y	
DDC-Z	
DDC-A	
DDC-B	
DDC-C	
DDC-D	
DDC-E	
DDC-F	
DDC-G	
DDC-H	
DDC-I	
DDC-J	
DDC-K	
DDC-L	
DDC-M	
DDC-N	
DDC-O	
DDC-P	
DDC-Q	
DDC-R	
DDC-S	
DDC-T	
DDC-U	
DDC-V	
DDC-W	
DDC-X	
DDC-Y	
DDC-Z	
DDC-A	
DDC-B	
DDC-C	
DDC-D	
DDC-E	
DDC-F	
DDC-G	
DDC-H	
DDC-I	
DDC-J	
DDC-K	
DDC-L	
DDC-M	
DDC-N	
DDC-O	
DDC-P	
DDC-Q	
DDC-R	
DDC-S	
DDC-T	
DDC-U	
DDC-V	
DDC-W	
DDC-X	
DDC-Y	
DDC-Z	
DDC-A	
DDC-B	
DDC-C	
DDC-D	
DDC-E	
DDC-F	
DDC-G	
DDC-H	
DDC-I	
DDC-J	
DDC-K	
DDC-L	
DDC-M	
DDC-N	
DDC-O	
DDC-P	
DDC-Q	
DDC-R	
DDC-S	
DDC-T	
DDC-U	
DDC-V	
DDC-W	
DDC-X	
DDC-Y	
DDC-Z	
DDC-A	
DDC-B	
DDC-C	
DDC-D	
DDC-E	
DDC-F	
DDC-G	
DDC-H	
DDC-I	
DDC-J	
DDC-K	
DDC-L	
DDC-M	
DDC-N	
DDC-O	
DDC-P	
DDC-Q	
DDC-R	
DDC-S	
DDC-T	
DDC-U	
DDC-V	
DDC-W	
DDC-X	
DDC-Y	
DDC-Z	
DDC-A	
DDC-B	
DDC-C	
DDC-D	
DDC-E	
DDC-F	
DDC-G	
DDC-H	
DDC-I	
DDC-J	
DDC-K	
DDC-L	
DDC-M	
DDC-N	
DDC-O	
DDC-P	
DDC-Q	
DDC-R	
DDC-S	
DDC-T	
DDC-U	
DDC-V	
DDC-W	
DDC-X	
DDC-Y	
DDC-Z	
DDC-A	
DDC-B	
DDC-C	
DDC-D	
DDC-E	
DDC-F	
DDC-G	
DDC-H	
DDC-I	
DDC-J	
DDC-K	
DDC-L	
DDC-M	
DDC-N	
DDC-O	
DDC-P	
DDC-Q	
DDC-R	
DDC-S	
DDC-T	
DDC-U	
DDC-V	
DDC-W	
DDC-X	
DDC-Y	
DDC-Z	
DDC-A	
DDC-B	
DDC-C	
DDC-D	
DDC-E	
DDC-F	
DDC-G	
DDC-H	
DDC-I	
DDC-J	
DDC-K	
DDC-L	
DDC-M	
DDC-N	
DDC-O	
DDC-P	
DDC-Q	
DDC-R	
DDC-S	
DDC-T	
DDC-U	
DDC-V	
DDC-W	
DDC-X	
DDC-Y	
DDC-Z	
DDC-A	
DDC-B	
DDC-C	
DDC-D	
DDC-E	
DDC-F	
DDC-G	
DDC-H	
DDC-I	
DDC-J	
DDC-K	
DDC-L	
DDC-M	
DDC-N	
DDC-O	
DDC-P	
DDC-Q	
DDC-R	
DDC-S	
DDC-T	
DDC-U	
DDC-V	
DDC-W	
DDC-X	
DDC-Y	
DDC-Z	
DDC-A	
DDC-B	
DDC-C	
DDC-D	
DDC-E	
DDC-F	
DDC-G	
DDC-H	
DDC-I	
DDC-J	
DDC-K	
DDC-L	
DDC-M	
DDC-N	
DDC-O	
DDC-P	
DDC-Q	
DDC-R	
DDC-S	
DDC-T	
DDC-U	
DDC-V	
DDC-W	
DDC-X	
DDC-Y	
DDC-Z	
DDC-A	
DDC-B	
DDC-C	
DDC-D	
DDC-E	
DDC-F	
DDC-G	
DDC-H	
DDC-I	
DDC-J	
DDC-K	
DDC-L	
DDC-M	
DDC-N	
DDC-O	
DDC-P	
DDC-Q	
DDC-R	
DDC-S	
DDC-T	
DDC-U	
DDC-V	
DDC-W	
DDC-X	
DDC-Y	
DDC-Z	
DDC-A	
DDC-B	
DDC-C	
DDC-D	
DDC-E	
DDC-F	
DDC-G	
DDC-H	
DDC-I	
DDC-J	
DDC-K	
DDC-L	
DDC-M	
DDC-N	
DDC-O	
DDC-P	
DDC-Q	
DDC-R	
DDC-S	
DDC-T	
DDC-U	
DDC-V	
DDC-W	
DDC-X	
DDC-Y	
DDC-Z	
DDC-A	
DDC-B	
DDC-C	
DDC-D	
DDC-E	
DDC-F	
DDC-G	
DDC-H	
DDC-I	
DDC-J	
DDC-K	
DDC-L	
DDC-M	
DDC-N	
DDC-O	
DDC-P	
DDC-Q	
DDC-R	
DDC-S	
DDC-T	
DDC-U	
DDC-V</td	

(UNCLASSIFIED TITLE)

AIR FORCE ADVANCED LIFT FAN AND LIFT/CRUISE  
FAN DEMONSTRATOR PROGRAM

Walter A. Fasching

SPECIAL HANDLING REQUIRED  
NOT RELEASABLE TO FOREIGN NATIONALS

The information in this document will not  
be disclosed to foreign nationals or their  
representatives.

Each transmittal of this document outside  
the agencies of the U.S. Government must  
have prior approval of the Air Force Base  
Propulsion Laboratory.

FOREWORD

(U) The Air Force Advanced Lift Fan and Lift/Cruise Fan Demonstrator Program was conducted by the VTOL Propulsion Systems Operation of the General Electric Company's Advanced Engine Technical Division, Cincinnati, Ohio. The program was conducted for the United States Air Force Aero Propulsion Laboratory, Wright Patterson Air Force Base, Ohio, under Contract Number F33657-67-C-0812. The Air Force Project Engineer for this contract is R.J. Krabal, APTP. The program was initiated January 1, 1967, and the final report was submitted on December 15, 1968.

(U) This technical report has been reviewed and is approved.

## SECTION V

### COMPONENT TECHNOLOGY PROGRAM

#### FAN PROGRAMS

##### Blade-Turbine Seals

###### Introduction

(U) All tip turbine lift and and lift/cruise fans employ radial labyrinth type rubbing seals to reduce or restrict the flow of hot turbine gas into the compressor air stream.

(U) Experience gained during design and construction of four generations of fan designs have shown certain liabilities associated with this type of seal in tip turbine lift fans.

1. Hot gas leakage has first order effects on blade tip performance and failure to do an adequate seal design reduces installed performance.

2. Optimum seal gaps have only been achieved in practice by grinding seals in position.

3. Mounting of seals on large diameter relatively flexible static parts causes problems in predicting and achieving design radial clearances in the fan assembly.

(U) The technology defined in the advanced fan demonstrator program has added a new dimension to the blade tip seal design problem. The design has been deliberately aimed at reducing the fan diameter through smaller radial gaps required to effect a blade-turbine tip attachment and seal in the fan. To realize technology improvements in overall fan design and performance, we must take a fresh look at the problem and ascertain the acceptability of radial rubbing seals as the best type to do the job.

(U) Two-dimensional bench testing does not effectively reproduce the hot gas leakage associated with this type of rotating seal. Full scale and scale model fan tests were performed for evaluating seal leakage effects.

###### Summary

(U) Component tests on a scale model, low pressure ratio fan were made to evaluate the effects of hot gas leakage on blade tip performance. The results of these investigations are inconclusive. A full scale LF-2 fan test showed no pronounced effect of hot gas leakage on the blade tip performance.

(U) A third series of tests, employing a 15 inch scale model high pressure ratio fan, were also used to investigate the effects of seal leakage. This fan system more closely approximated the aerodynamic design of advanced lift fans. The results of these tests verified the conclusion that seal leakage effects are not detrimental to fan performance as long as fan tip aerodynamic design is not marginal to begin with.

(U) As a closing comment, tests of a 36 inch fan with a design pressure ratio of 1.3 were recently completed, November 1968, and indicated that indeed a fan tip can perform satisfactorily with the simple seal system recommended for use in the LF475 and shown in Figure 189.

#### Present Seal Design

(U) The present state-of-the-art design for tip seals on large diameter fans is the radial labyrinth type honeycomb rubbing seal. The present design of lift fans require a segmented shroud at the fan blade tip to provide an aerodynamic flow path through the rotor (See Figure 190). The edge of the shroud is turned radially outward to provide the rotating tooth of the seal. The stationary portion of the seal, made up in circumferential segments to allow for thermal growth, is bolted to the stationary supporting structure. This portion of the seal is made from a strip of honeycomb brazed to a support. The brazing materials used is P9F filler material P50T9N. To assure optimum clearance, the stationary portion of the seal is bolted into position and then ground to the required diameter. The seal is ground to a calculated zero clearance, see Figure 191, at 100% fan speed to prevent axial wiping of the honeycomb seal surface by the rotating seal lip during axial excursions of the rotor. These axial excursions are caused by the gyroscopic precession of the rotor during airframe maneuvers. The honeycomb used is A.I.S.I. 30321 foil, .002 to .004 inches thick and with .125 inch square or hexagonal cells. The thickness is dependent on the specific fan the seal is to be used on.

(U) The advantages of this type of seal are: 1. light weight, 2. simple, 3. ease of assembly, 4. low cost, and 5. productivity. The lips of the segmented shroud form a light-weight rotating tooth. This portion must be kept light since a one pound increase in weight at the tip area of the rotor increases the overall weight of the rotor and supporting structure by approximately three pounds to provide sufficient strength to carry the additional tip weight.

(U) The disadvantages are: 1. seal tip flow leakage, 2. high local temperatures in the fan tip area, and 3. counter flow direction of leakage into fan stream. The rotating seal lip is less than .020 inches thick and is not capable of carrying large axial loads. At maximum RPM, the lip should just touch the

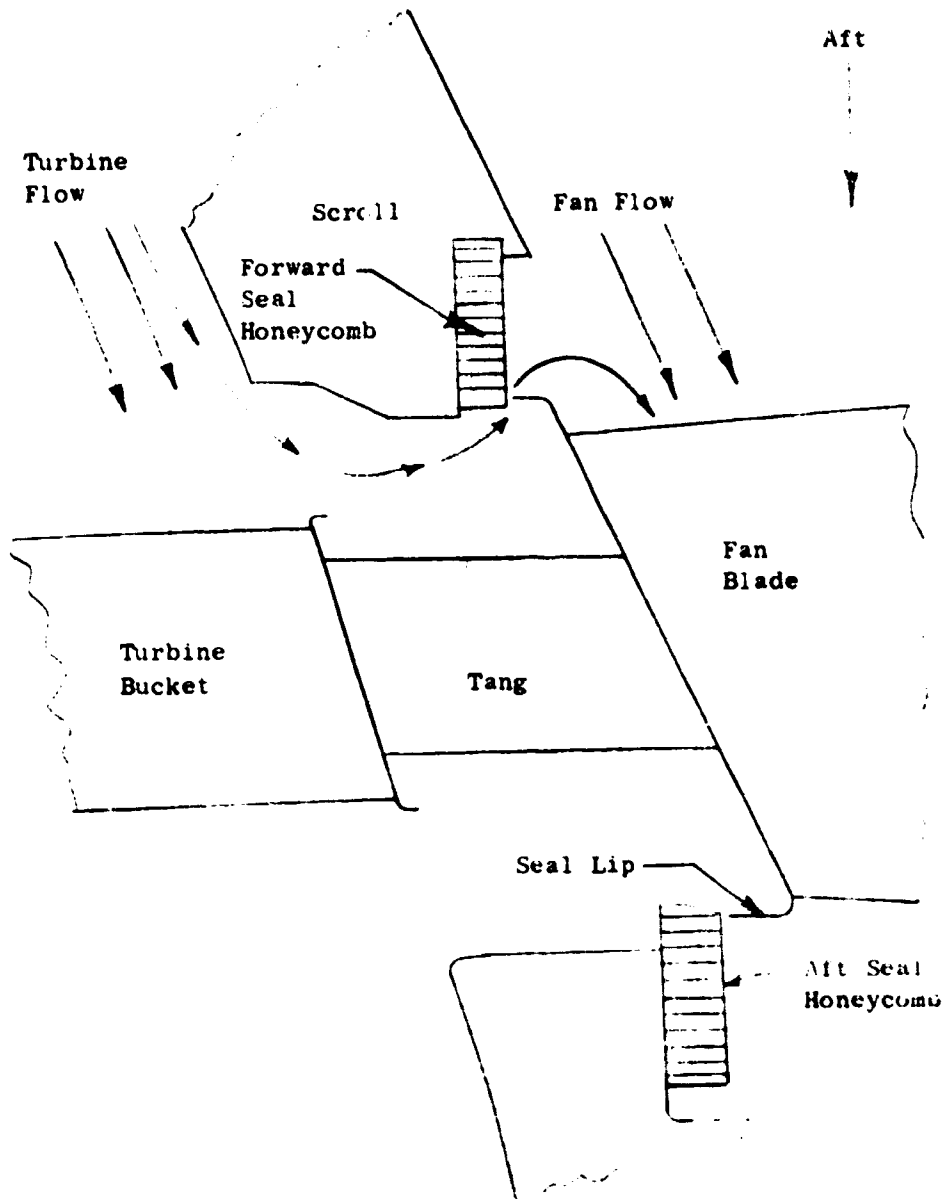


Figure 189 Tip Seal - L.F. 475

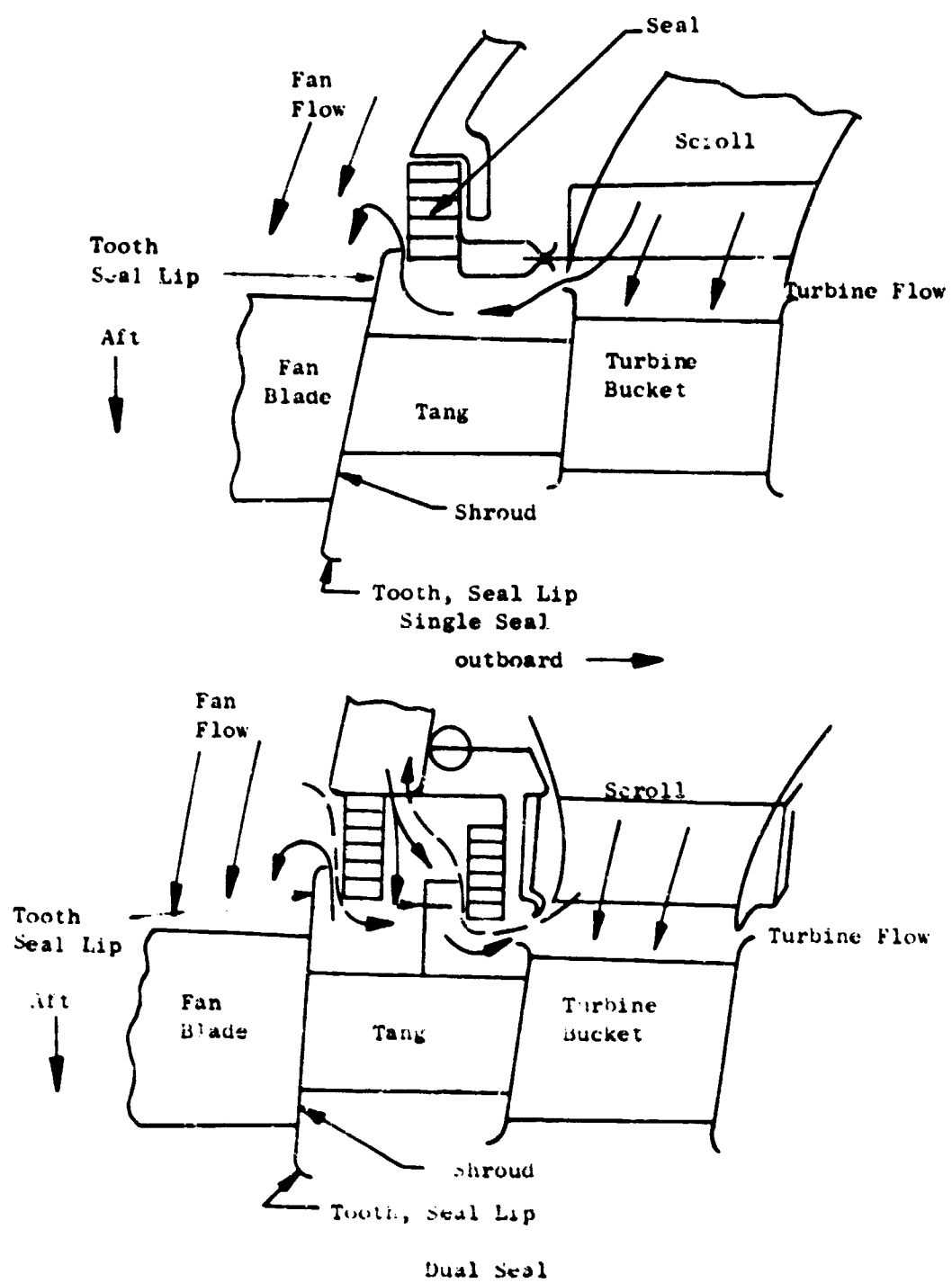


Figure 100 - Single and Dual Tip Seal ~ Flow Pattern

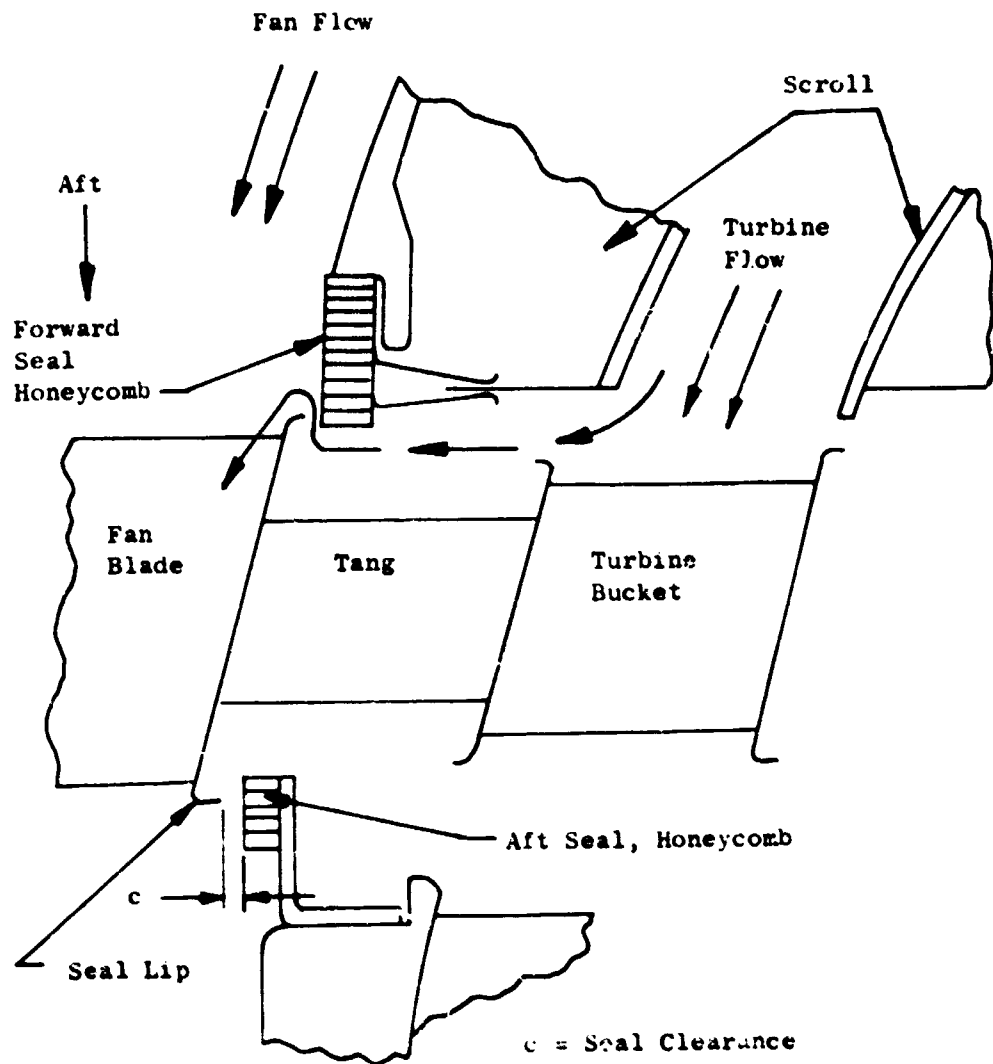


Figure 191 Single Tip Seal ~ Flow Pattern

stationary seal. If the seal lip is allowed to cut into the honeycomb, axial excursion of the rotor could fail the lip and cause large flow leakage. At fan speeds less than maximum, the clearance between the lip and the seal increases. Even at maximum RPM some clearance exists due to fabricated out-of-roundness of the rotating shroud lip and distortion of the stationary seal supporting structure from aerodynamic and inertia loading.

#### Proposed Designs

(U) The following seal designs are discussed with respect to their apparent advantages and disadvantages. The designs are:

- 1) Redirected Leakage Flow Seal
- 2) Axial Seal
- 3) Pumping Seal
  - a) Axial
  - b) Radial
- 4) Negative Reaction Turbine

#### Redirected leakage flow seal. -

(U) The redirected leakage flow seal arrangement (shown in Figure 192) will have the same basic design as present seals with the addition of a redirection lip from the bellmouth over the leading edge of the segmented shroud. The advantages of this type of seal are:

- 1) Hot gas penetration from the turbine to the fan is directed downward, reducing the possibility of boundary layer separation.
- 2) The boundary layer thickness is held to a minimum.
- 3) The fan flow path (fan tip shroud) can be moved radially outward to allow flow space for the fan leakage.

(U) Again, as with the present design, the seal clearance varies with speed and is only the optimum at 100% speed. Also, the fan stream moving over the redirection lip could cause ejector type action that might increase the leakage flow into the fan area. Relatively large radial clearances are required to accommodate thermal and steady state deflections and large axial clearances are required to allow for rotor gyroscopic excursions. Due to the redirected flow path there could be high local temperatures in the fan tip region. This concept was evaluated during check-out of the LF336/A fans.

#### Axial seal. -

(U) The axial seal (shown in Figure 193) could be manufactured in the same way as the present design, but would be mounted differently. Also, it would incorporate either a multi-toothed, or single tooth lip. The seal clearance would be held to zero under

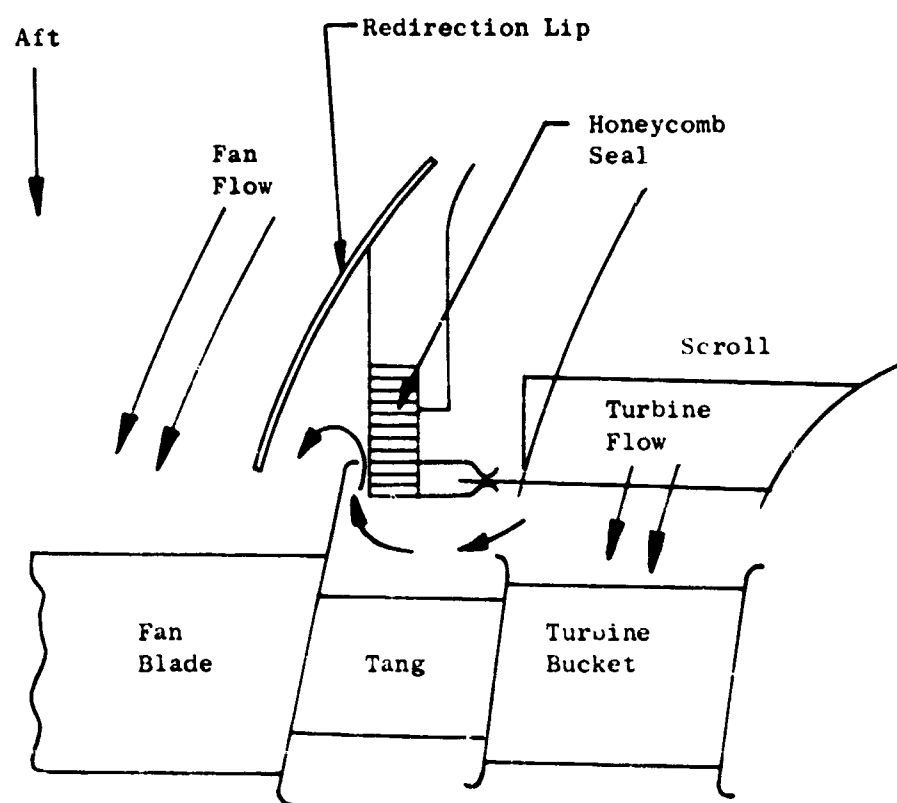


Figure 192 Redirected Tip Seal ~ Flow Pattern

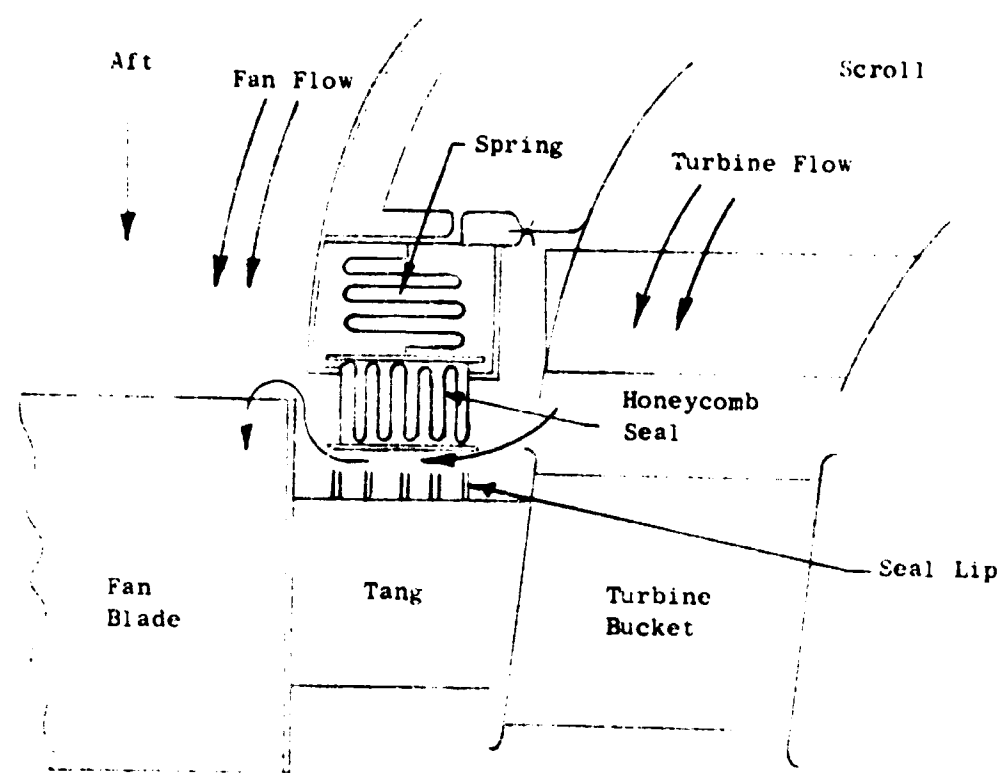


Figure 193 Axial Tip Seal - Flow Pattern

the spring loaded action of the seal attachment. Under ideal working conditions this type of seal would reduce the leakage to zero. Under transient, steady state, and gyroscopic movement of the rotor there could be the possibility of seizure between the seal and lip or, worse yet, the loss of a lip. At high RPM the loss of one or more of the seal lips could be very destructive to the fan. Also, the proper design of the spring would be a difficult problem in itself.

Pumping seal - axial. -

(U) Another seal configuration incorporates a "pumping" seal to be used in conjunction with the present rubbing seal (See Figures 194 and 195). The type of seal would have "pumping" vanes built into the fan tip shroud of the rotor. The seal could, if properly designed, reduce the leakage from turbine to fan to zero. Also, relatively cool air is drawn off the fan which tends to cool the rotor tang area. Any increase in weight due to the pumping vanes would increase the weight of the backup structure for strength purposes. Also, this is primarily an aerodynamic design with variable geometry in the boundary layer area. With present technology, it is felt that a design could not be adequately analyzed without a large testing program.

Pumping seal - radial. -

(U) The radial pumping seal, like the axial design, would have pumping vanes built into the fan-end position of the rotor (See Figures 196 and 197). Again, this design would have basically the same advantages and disadvantages of the axial pumping seal. In addition the aerodynamics of this flow pattern are more involved than the axial flow type.

Negative reaction turbine. -

(U) A theoretical investigation into the feasibility of using a negative reaction turbine on the LF475 fan has been completed. This study is presented in Section III. With this concept the pressure forward of the turbine can be adjusted to just equal or slightly lower than the pressure forward of the fan. This not only allows removal of the forward air seal but provides a means of extracting the bellmouth boundary layer and cooling the forward side of the turbine carrier for improved aerodynamic inlet characteristics and reduced bucket carrier temperatures. The increased solidity and the pressure loading across the turbine bucket dictates heavier bucket carriers with a proportionate increase in disc and rotor blade weight. Because of the pressure drop across the turbine, an additional seal would be required between the bucket tip and the outer casing. Being at a larger diameter and experiencing turbine inlet temperatures, the sealing problem would be aggravated.

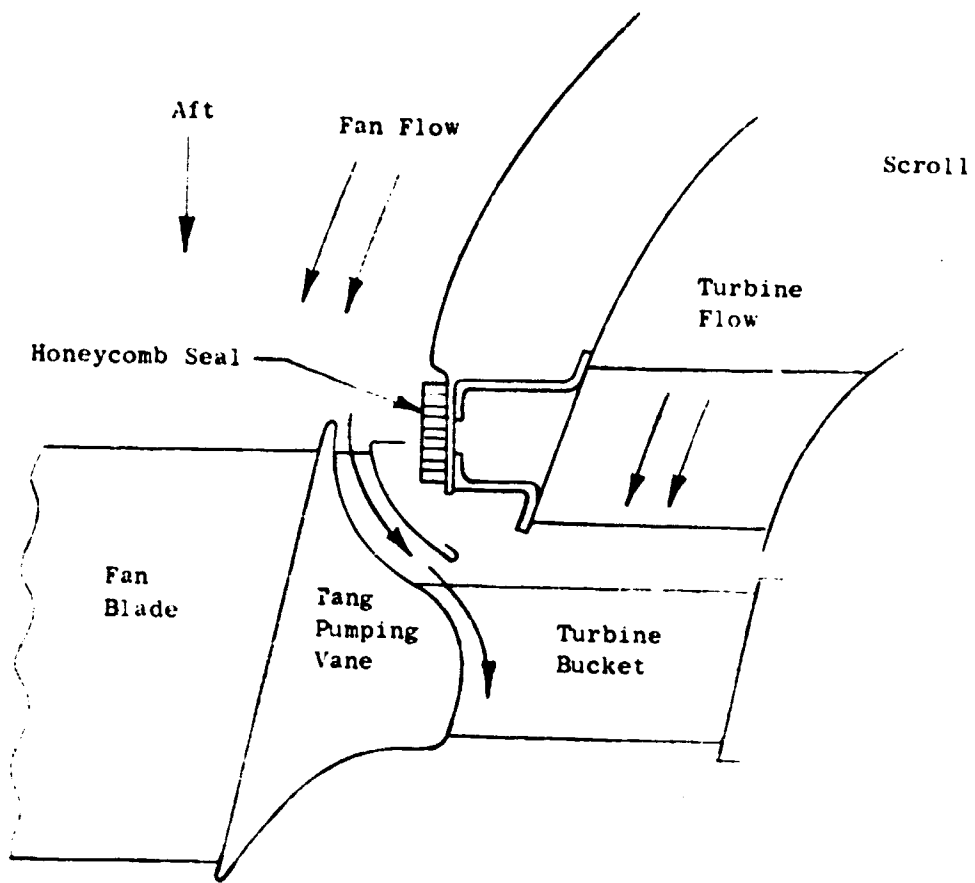


Figure 194 Axial Pumping Tip Seal Flow Pattern

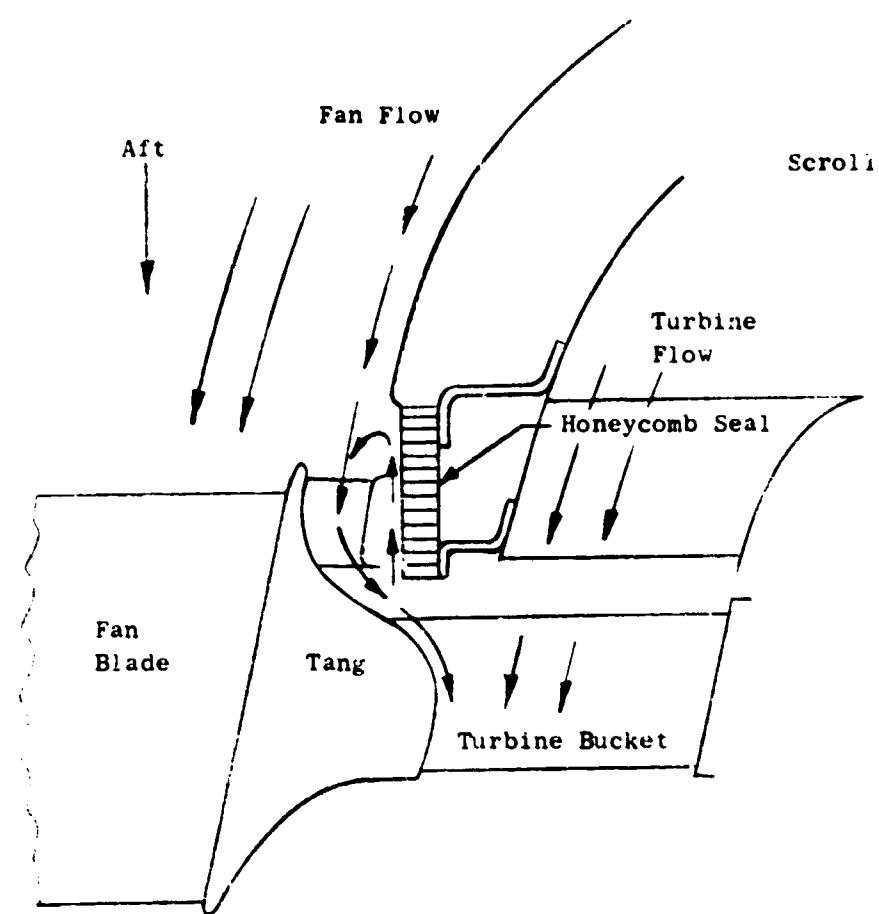


Figure 195 Axial Pumping Tip Seal ~ Flow Pattern

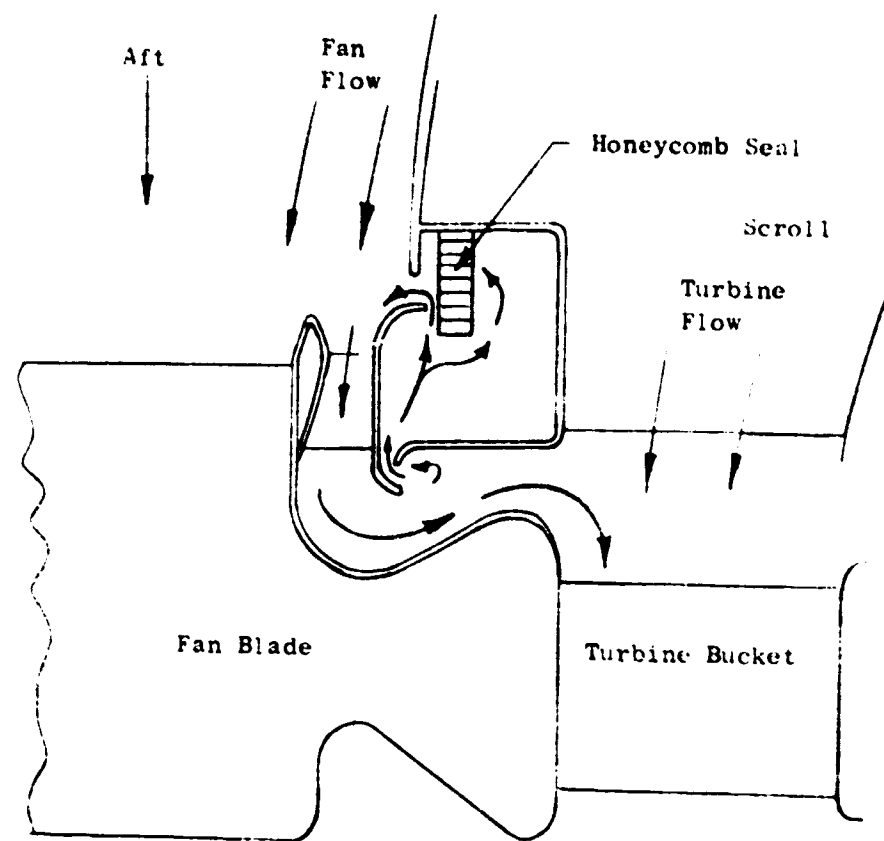


Figure 196 Radial Pumping Tip Seal Flow Pattern

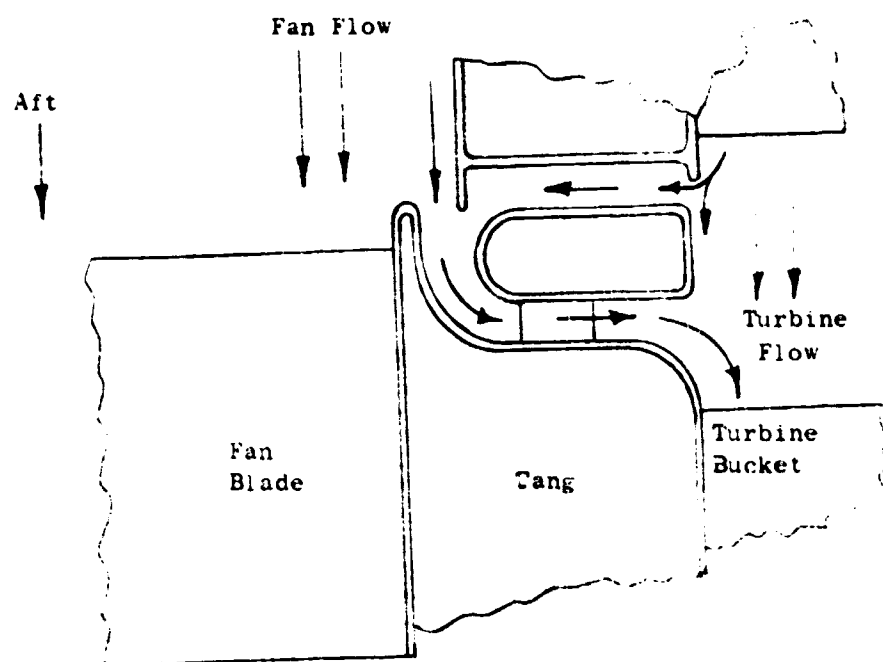
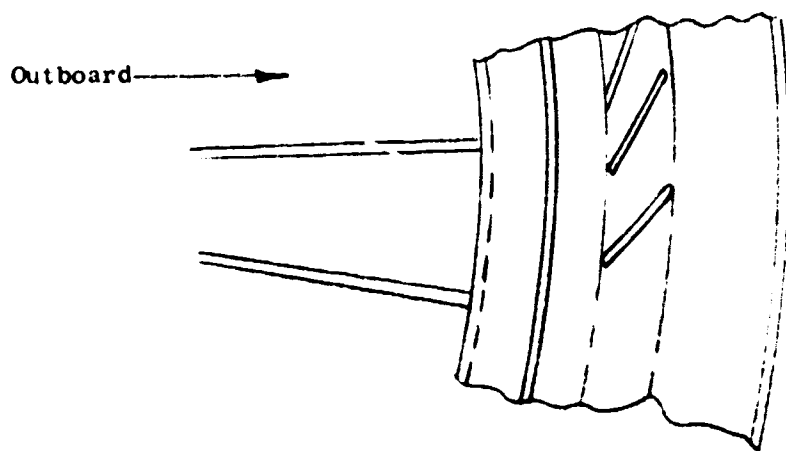


Figure 197 Radial Pumping Tip Seal Flow Pattern

This concept retains the sealing problem (moves seal from fan tip to turbine tip) and in addition increases rotor weight.

Conclusions and Recommendations:

(U) To date, on existing fan hardware, the effect of forward air seal leakage from the turbine to the fan flow path has not been significant. Because of this apparent small performance effect and the added cost, weight and complexity of pumping seals, the LF475 seals will utilize the simple, low cost, single tooth rotating seal as originally proposed. The fan flow path through the rotor will be moved radially outward to allow a flow path for the hot gas leakage at the rotor tip. Also if testing of the LF336A with a deflector installed, Figure 192, provides the anticipated improvement, this concept will also be incorporated. Figure 189 shows the proposed tip seal design for the LF475.

MF415 Tests

Introduction

(U) Test were performed on the 15 inch scale model high pressure ratio fan (MF415) to determine the effects of seal leakage on fan performance characteristics. Test configurations were selected to investigate both greater and lesser amounts of leakage flow into the fan rotor inlet relative to the base configuration. Leakage air temperatures were limited to near ambient levels.

Test Vehicle

(U) The MF415 is a shaft driven fan that approximates the LF475 aerodynamic design. The design included a leakage manifold arrangement as shown by the sketch in Figure 198. With the manifold closed, some leakage air is present flowing from the discharge to the inlet side of the rotor. The leakage flow to the inlet side of the rotor was increased by venting the manifold to the atmosphere. It was decreased by pumping (sucking) it through the leakage manifold. An ejector type flow nozzle was used to provide the pumping action. An orifice was used to measure leakage flow out of the manifold.

Test Procedure

(U) Seal leakage tests were performed on two fan test configurations. The first configuration had the fan discharge measuring section installed as well as the ejector type nozzle for pumping leakage flow out of the manifold. The following three test runs were made.

1. Base configuration with leakage manifold closed.
2. Pumping leakage flow out of the manifold.
3. Manifold open to atmosphere through same flow path used for pumping.

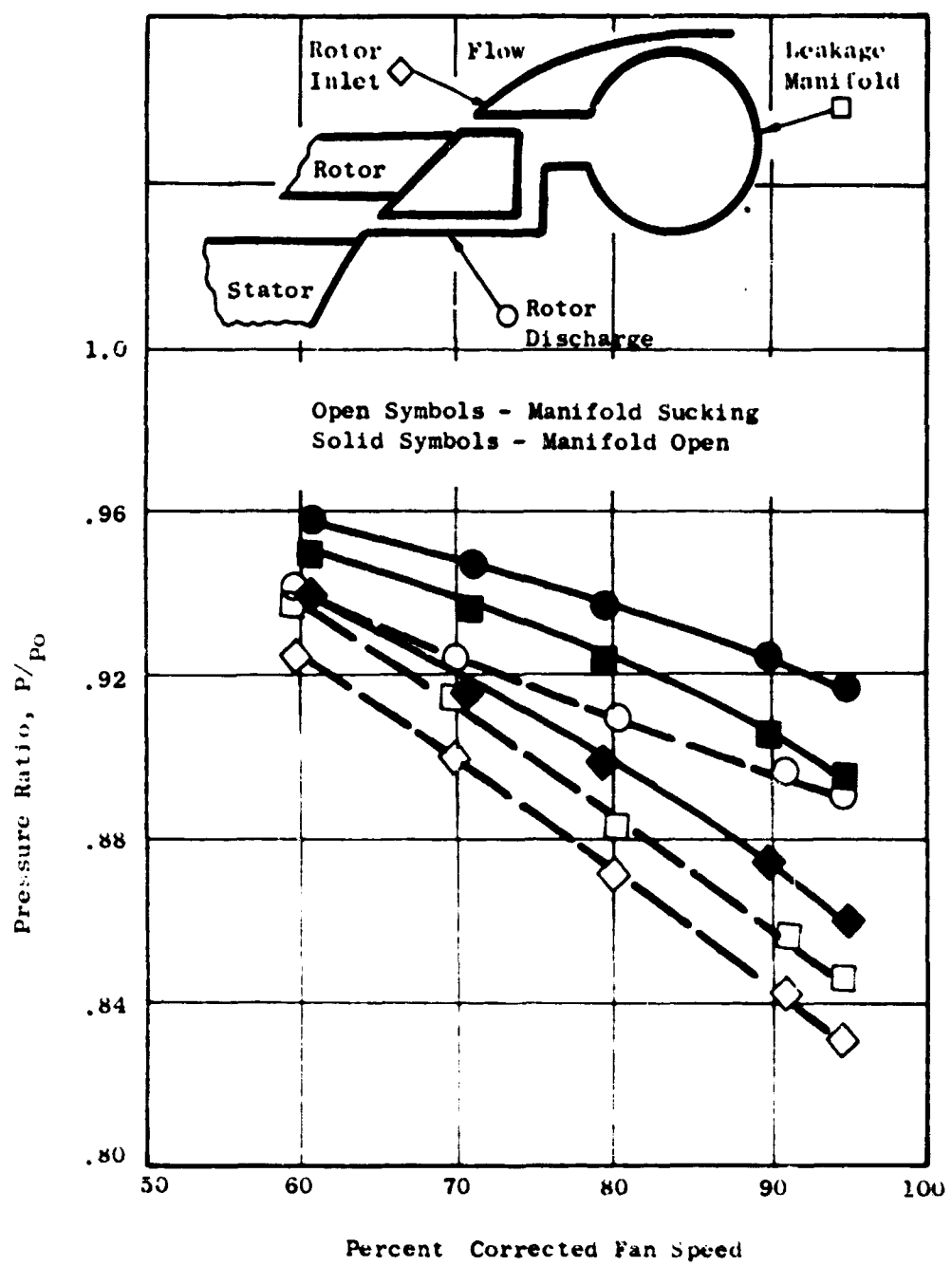


Figure 198 Seal Pressures as a Function of Speed and Manifold Conditions

(U) The second test configuration had the fan discharge measuring section removed and the exit louvers installed in the dropped position (1/2 louver chord aft of the fan discharge). Provisions were made to open the manifold directly to ambient. Test runs were made at the following conditions.

1. Base configuration with leakage manifold closed and exit louvers at 0°.
2. Leakage manifold open with exit louvers at 0°.
3. Leakage manifold open with exit louvers at 40°.

(U) For both configurations, data was recorded at 60, 70, 80, 90 and 95 percent corrected fan speeds.

#### Results

(U) The test results for the fan configurations with exit measuring section on are presented in Figures 198 through 210. The base configuration with manifold closed has a leakage flow path from the discharge to the inlet side of the rotor. Since there is no flow into or out of the manifold, the bleed flow is indicated as 0 percent in Figure 199. The relative static pressure levels of the rotor inlet, the manifold and the rotor discharge are presented in Figures 198 and 200 through 202. Manifold to rotor discharge and manifold to rotor inlet pressure ratios are shown in Figures 200 and 201 respectively. Figure 202 gives the effects of seal leakage on bellmouth pressure distribution and Figure 198 indicates the relative level of all three seal leakage pressures. Seal leakage effects on fan performance characteristics are described in Figures 203 through 209.

(U) Comparable data for the fan configuration with exit louvers installed are included in Figures 211 through 222. Figures 211 through 214 describe seal leakage pressure relations and Figures 215 through 222 present resulting fan performance characteristics. Two methods were developed for determining fan airflow characteristics with the discharge measuring section removed. Figures 215 and 216 show these characteristics as determined by the turbine energy method and Figures 217 and 218 give comparable results using bell-mouth static pressures.

#### Discussion

##### Measuring section on. -

(U) For purposes of comparison, the seal leakage configuration with manifold closed is used as a base. Some leakage is present and flows from the rotor discharge to the rotor inlet as indicated by the relative pressure levels of Figures 198 and 200 through 202.

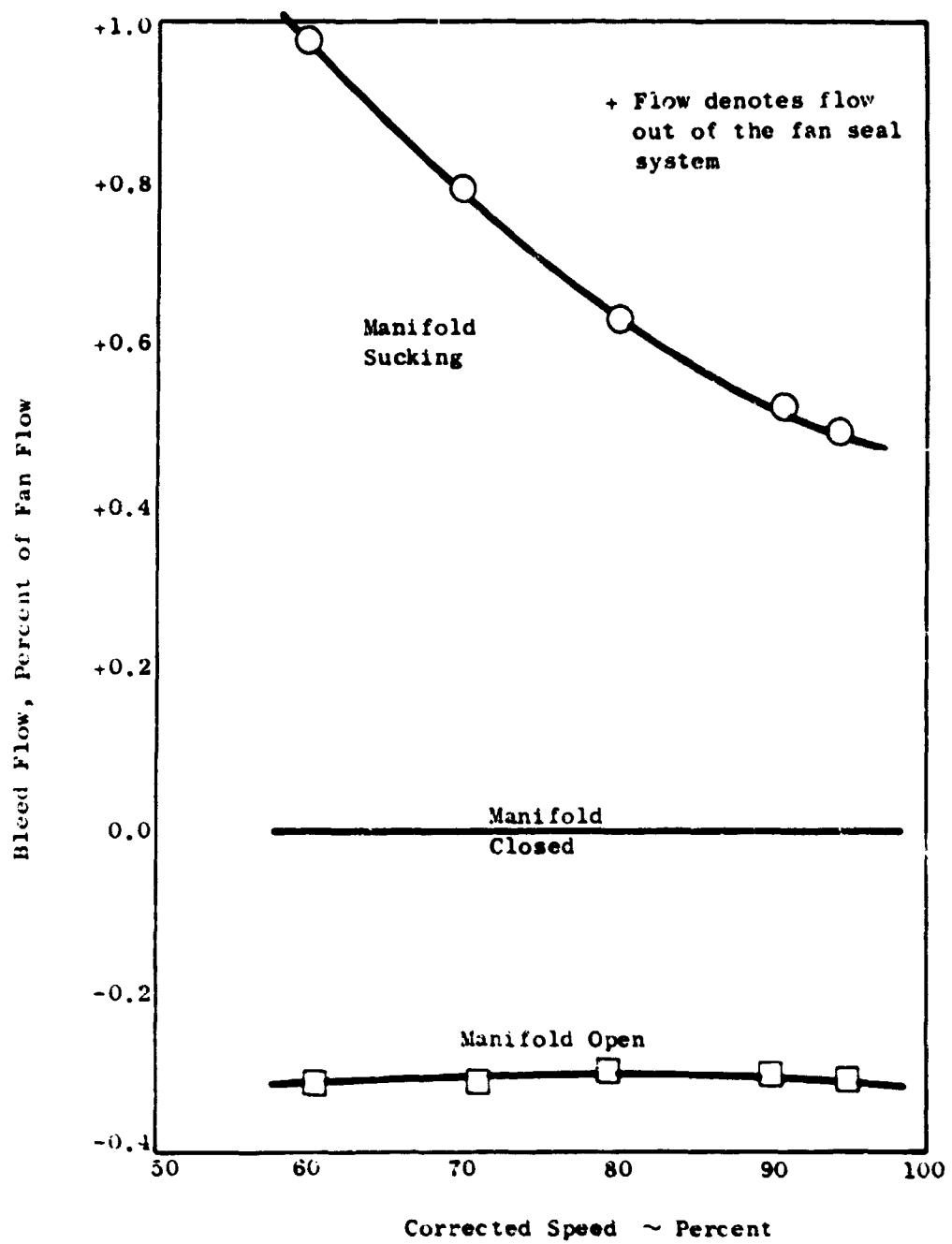


Figure 199 Bleed Flow Versus Corrected Speed

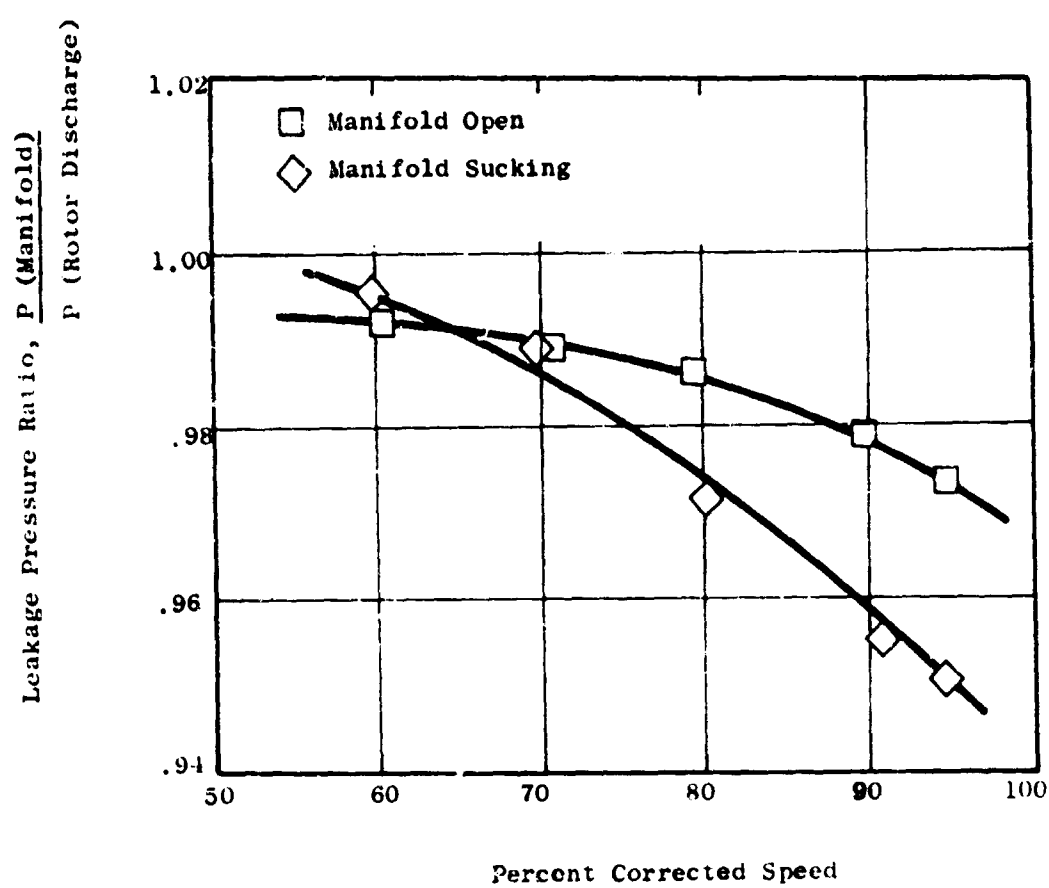


Figure 200 Rotor Discharge Seal Pressure Ratio

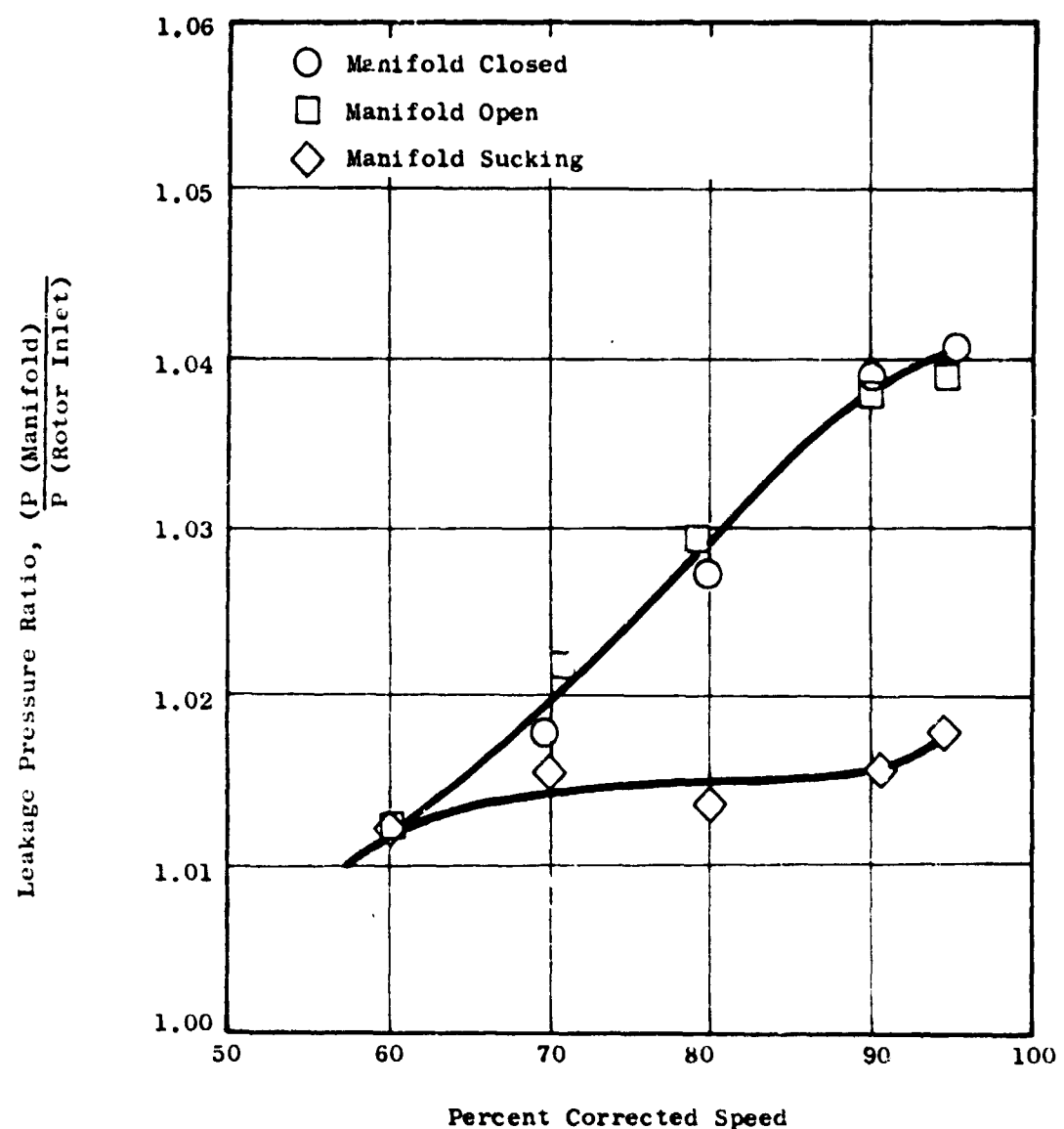


Figure 201 Rotor Inlet Seal Pressure Ratio

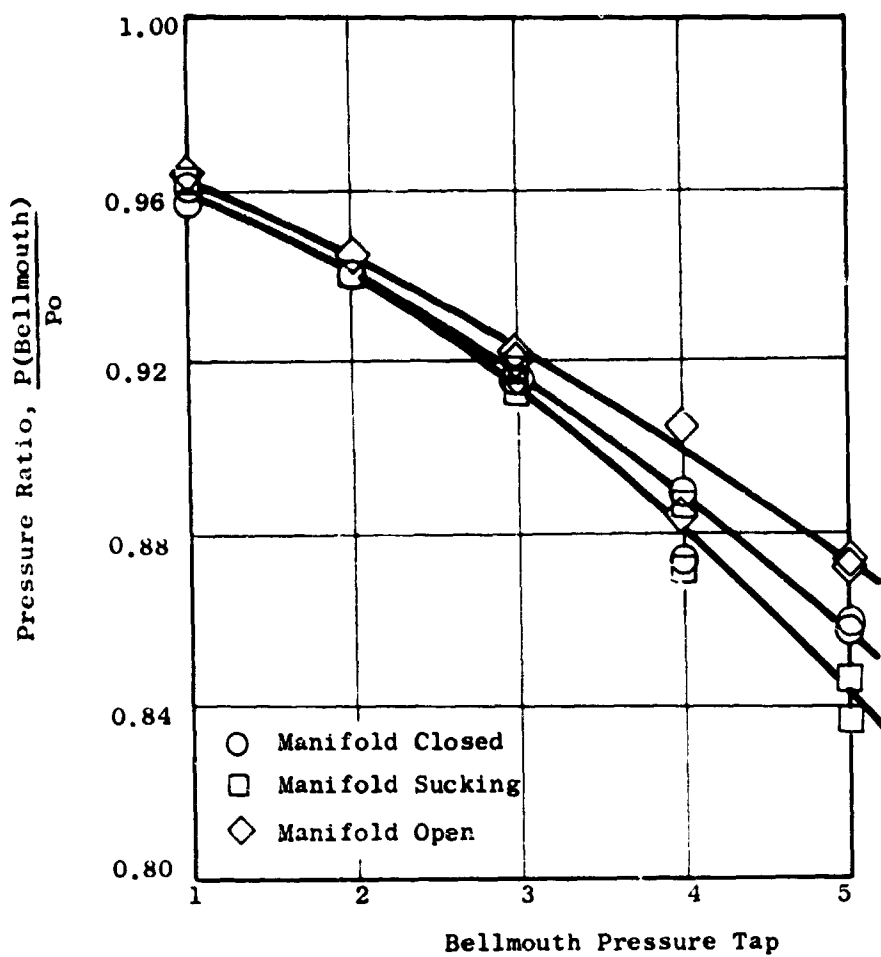


Figure 202 Effects of Seal Leakage on Bellmouth Pressure Distribution  $\sim 90\%$  Speed

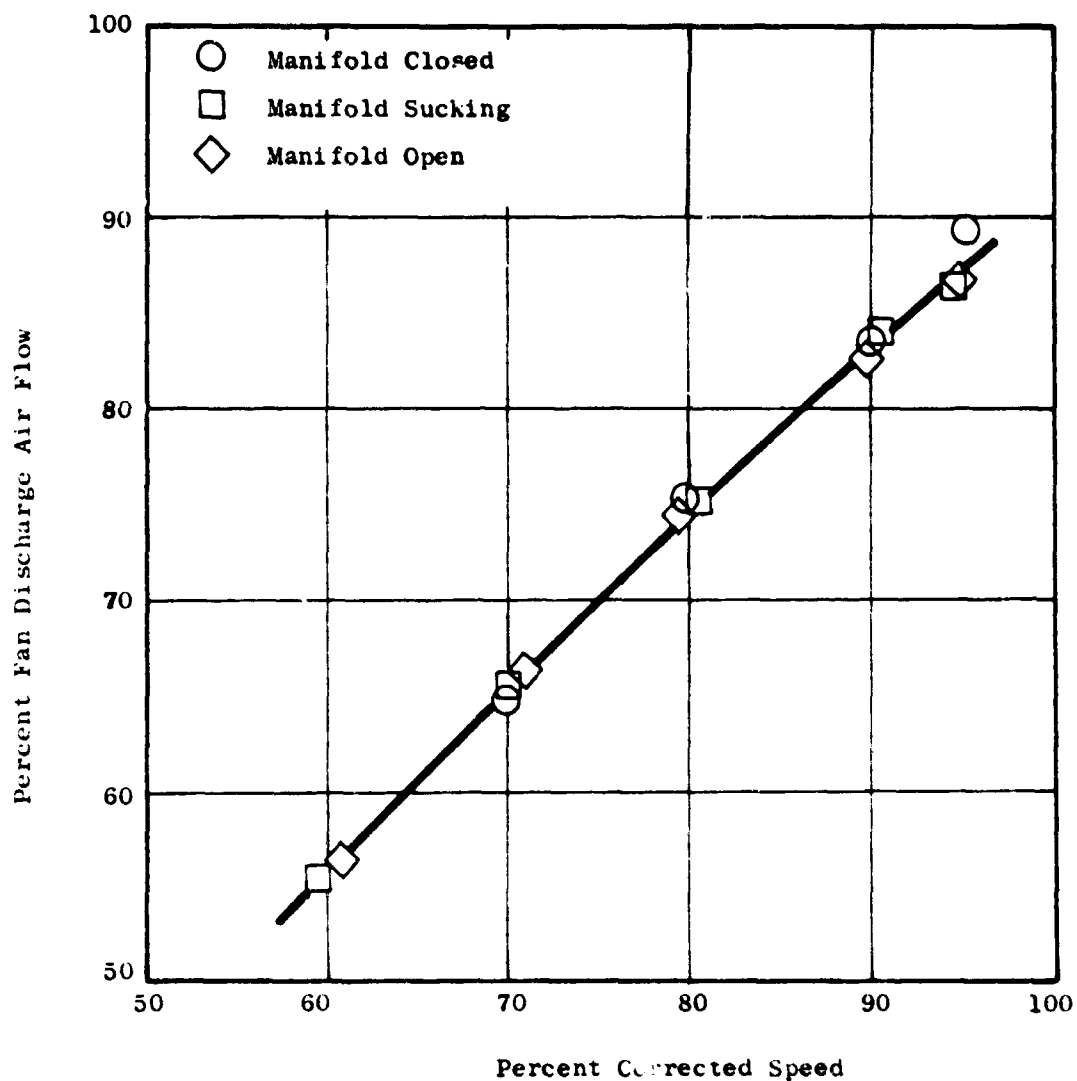


Figure 203 Fan Discharge Air Flow Versus Percent Corrected Speed

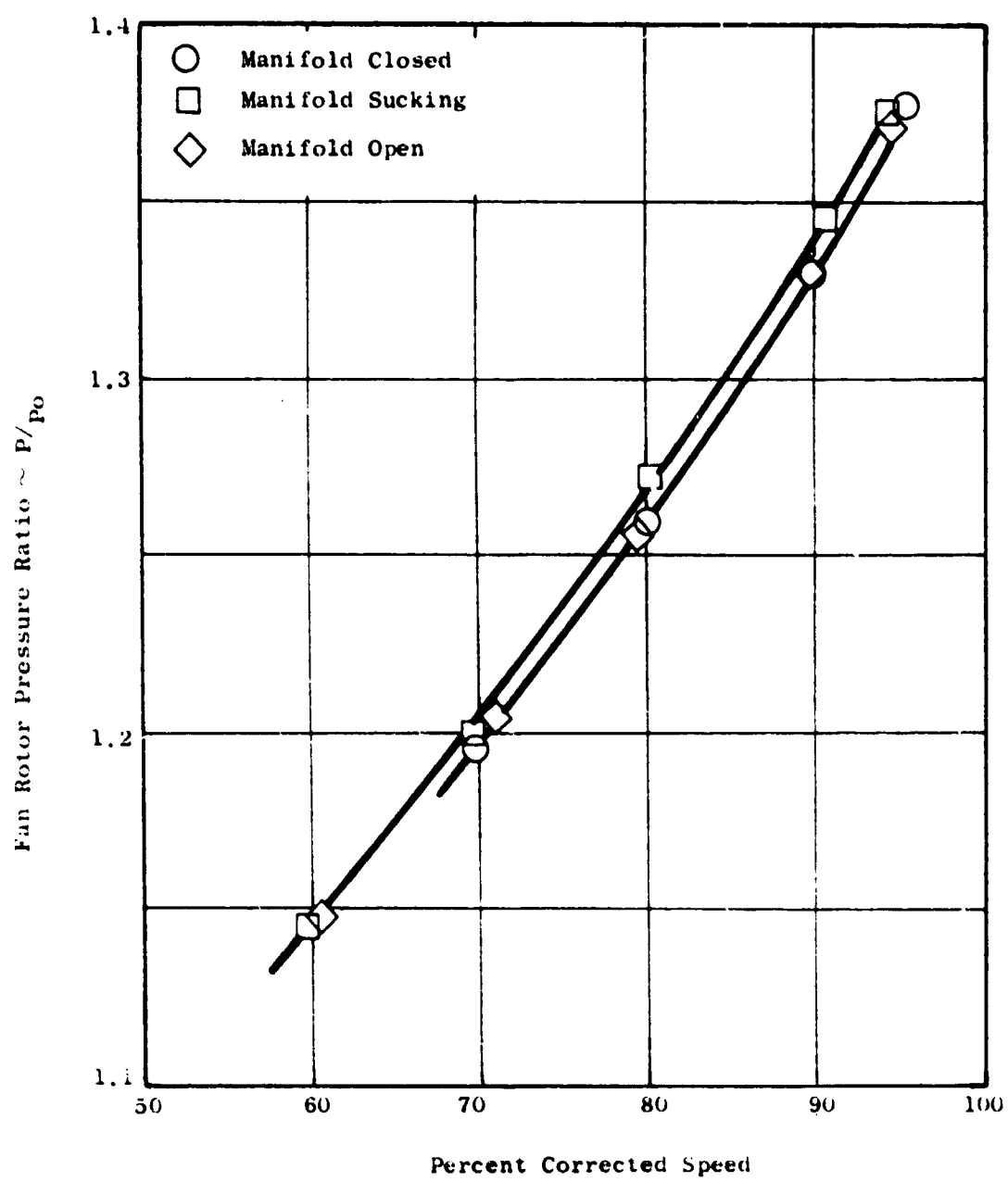


Figure 204 Fan Rotor Pressure Ratio ~  $P/P_o$  Versus Percent Corrected Speed

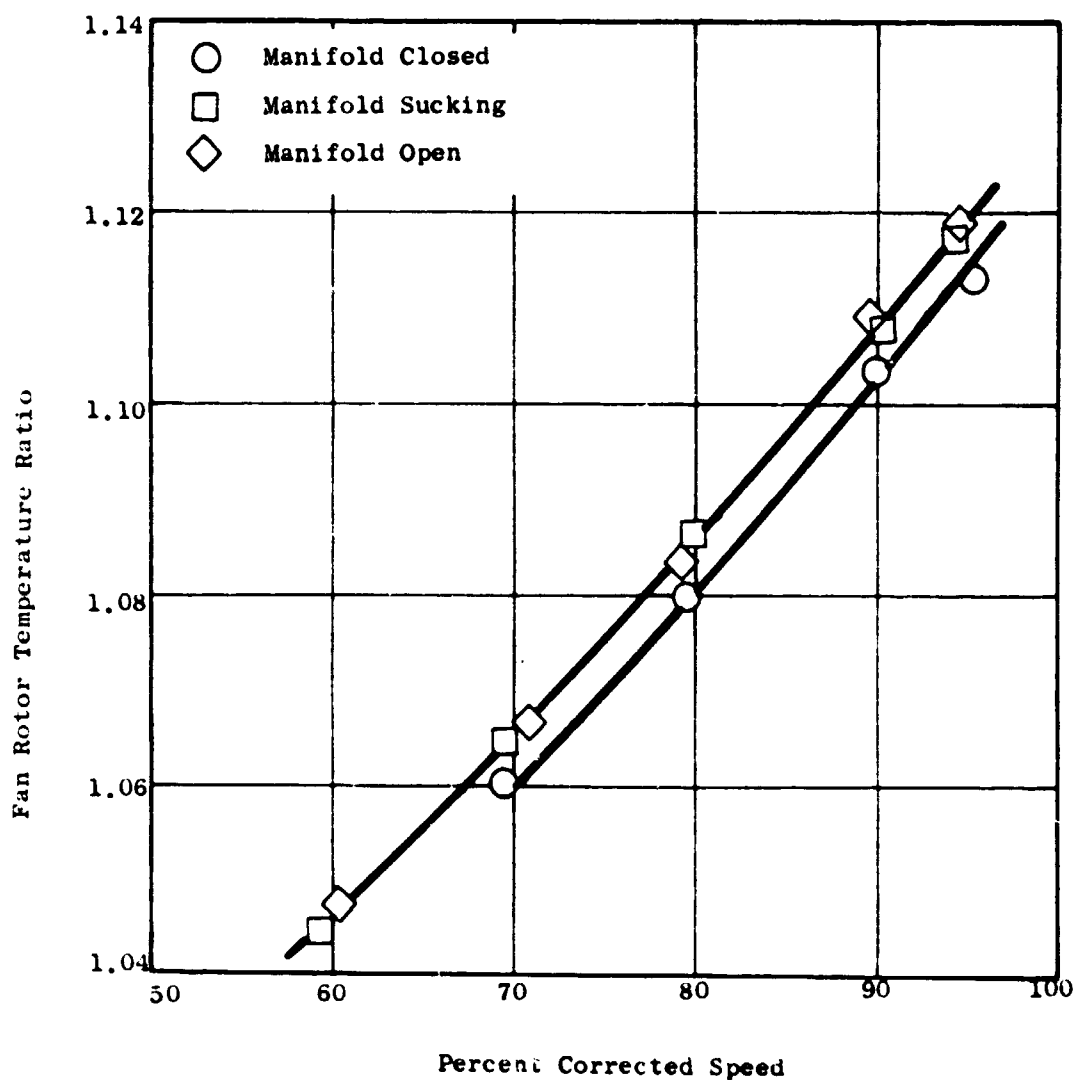


Figure 205 Fan Rotor Temperature Ratio Versus Corrected Speed

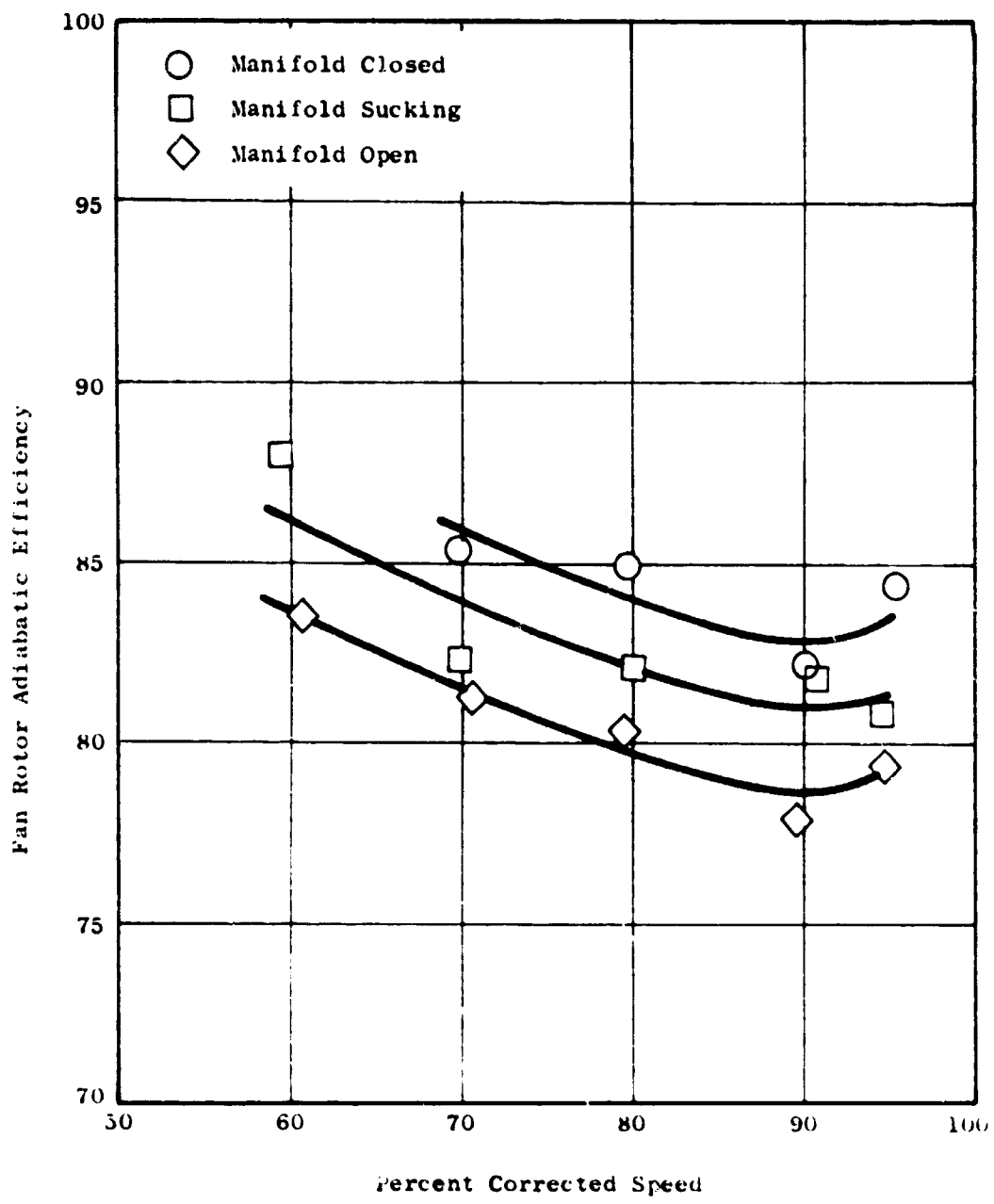


Figure 206 Fan Rotor Adiabatic Efficiency  
Versus Corrected Speed

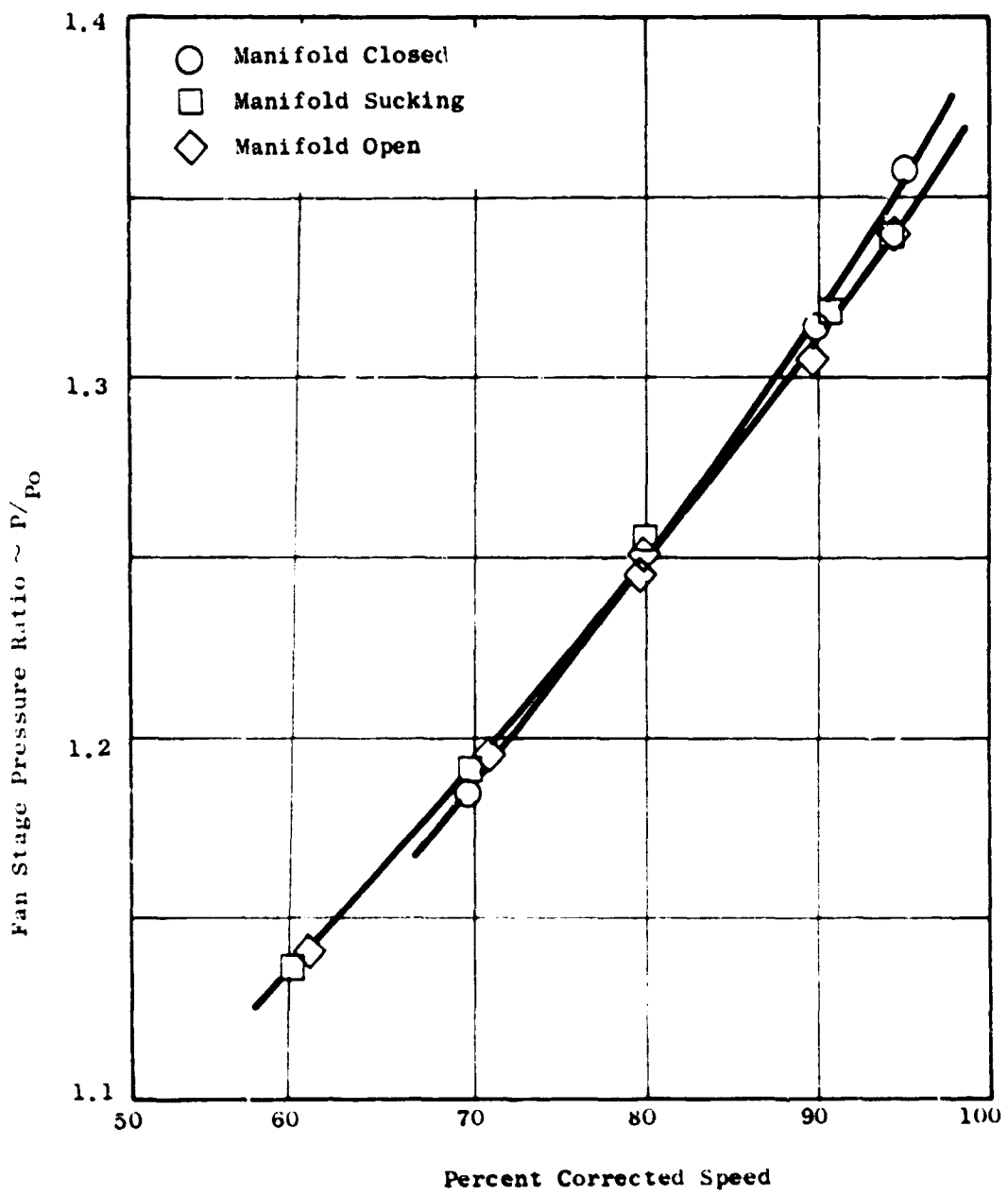


Figure 207    Fan Stage Pressure Ratio  
Versus Corrected Speed

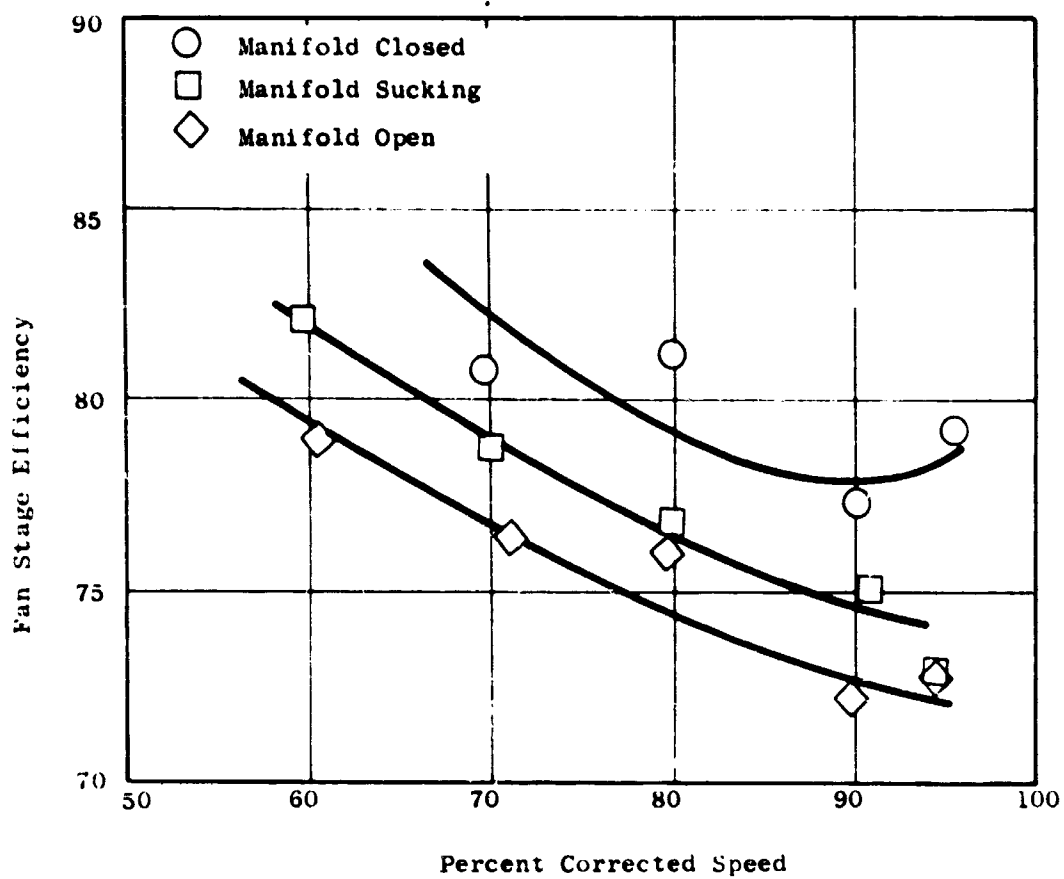


Figure 208 Fan Stage Efficiency Versus Corrected Speed

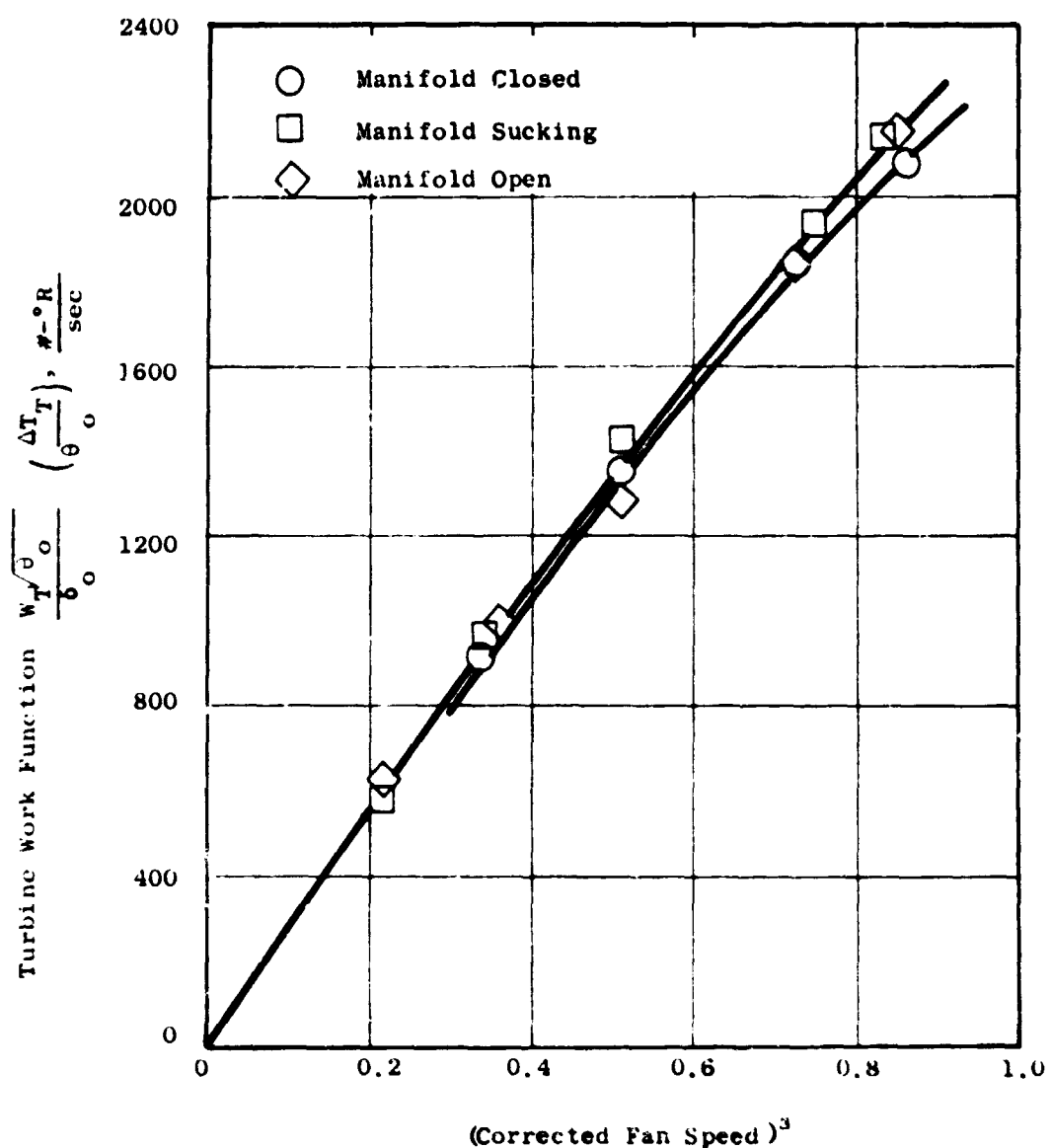


Figure 209 Effects of Seal Leakage on Turbine Work

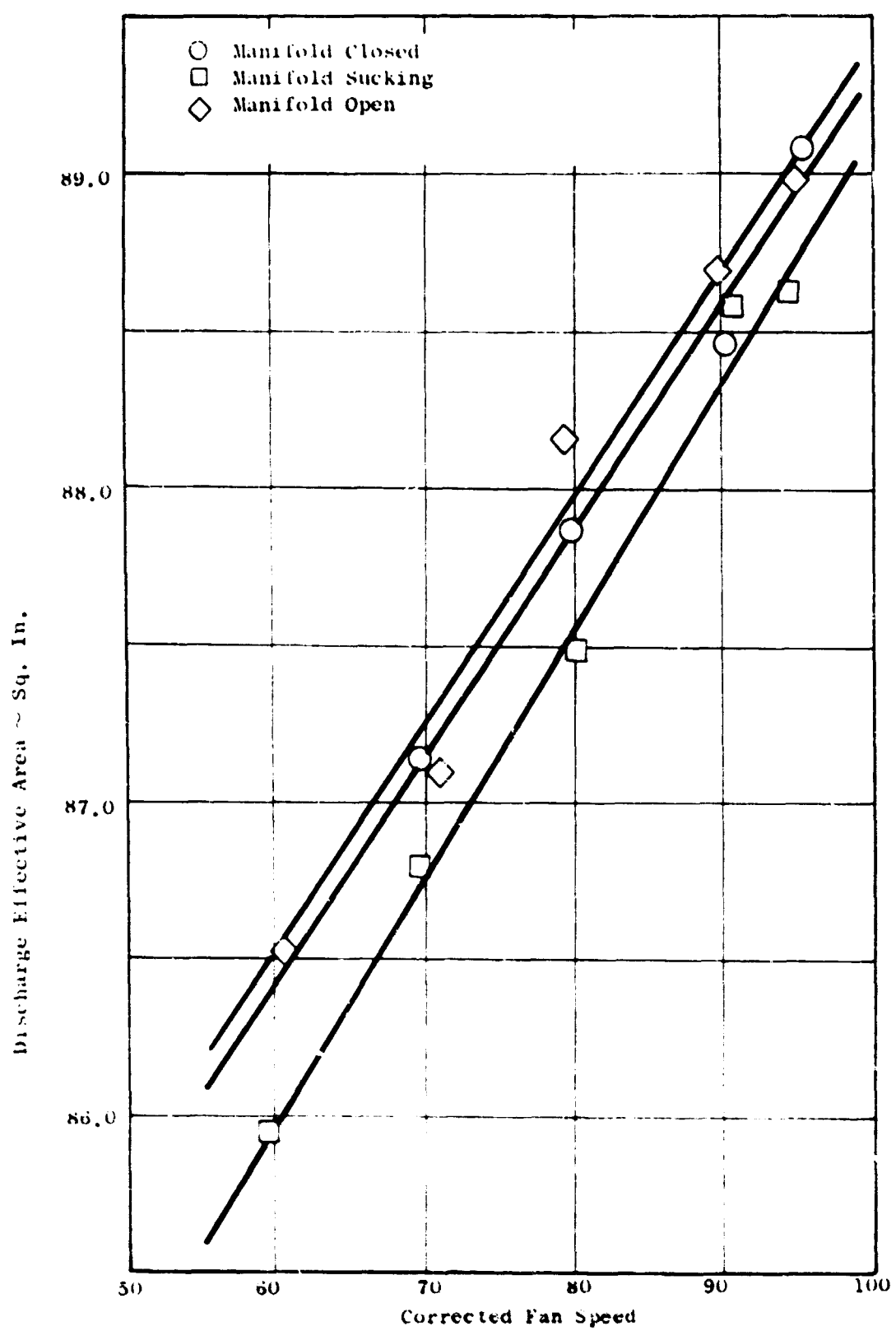


Figure 210 Effects of Seal Leakage on Fan Discharge Effective Area

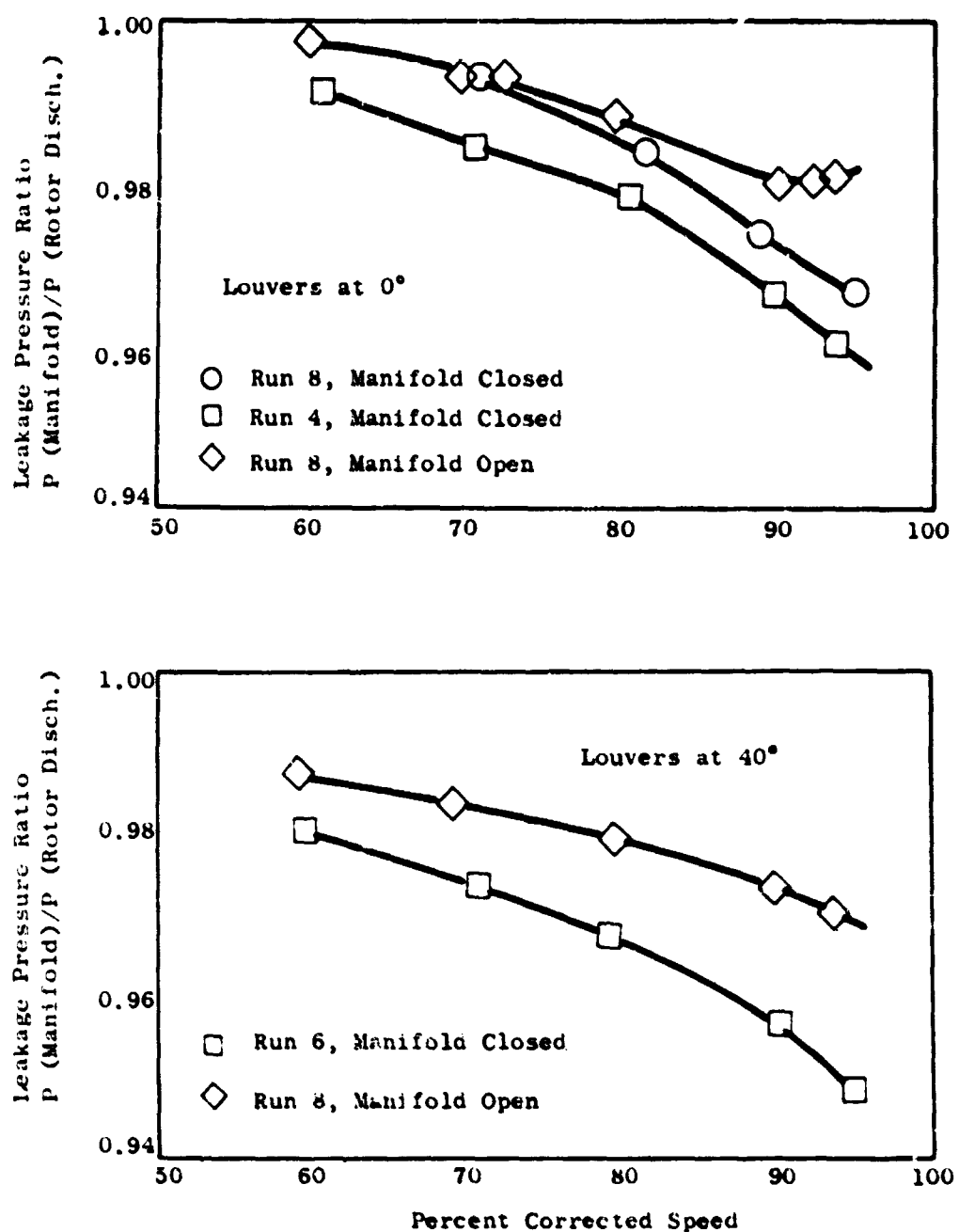


Figure 211 Rotor Discharge Seal Pressure Ratio  
Louvers in Dropped Position

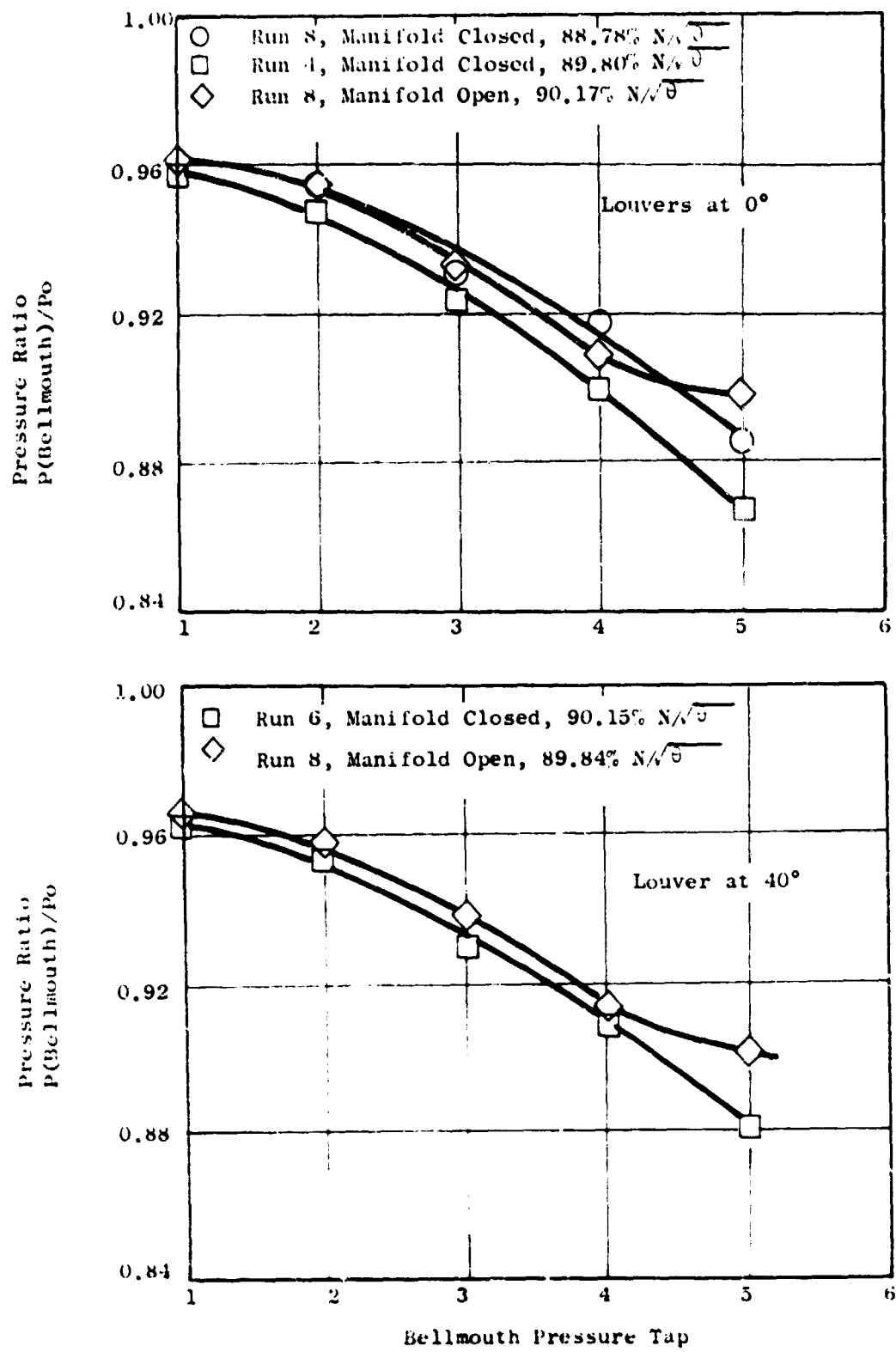


Figure 212 Bellmouth Pressure Distribution as Function of Seal Leakage Louvers in Dropped Position

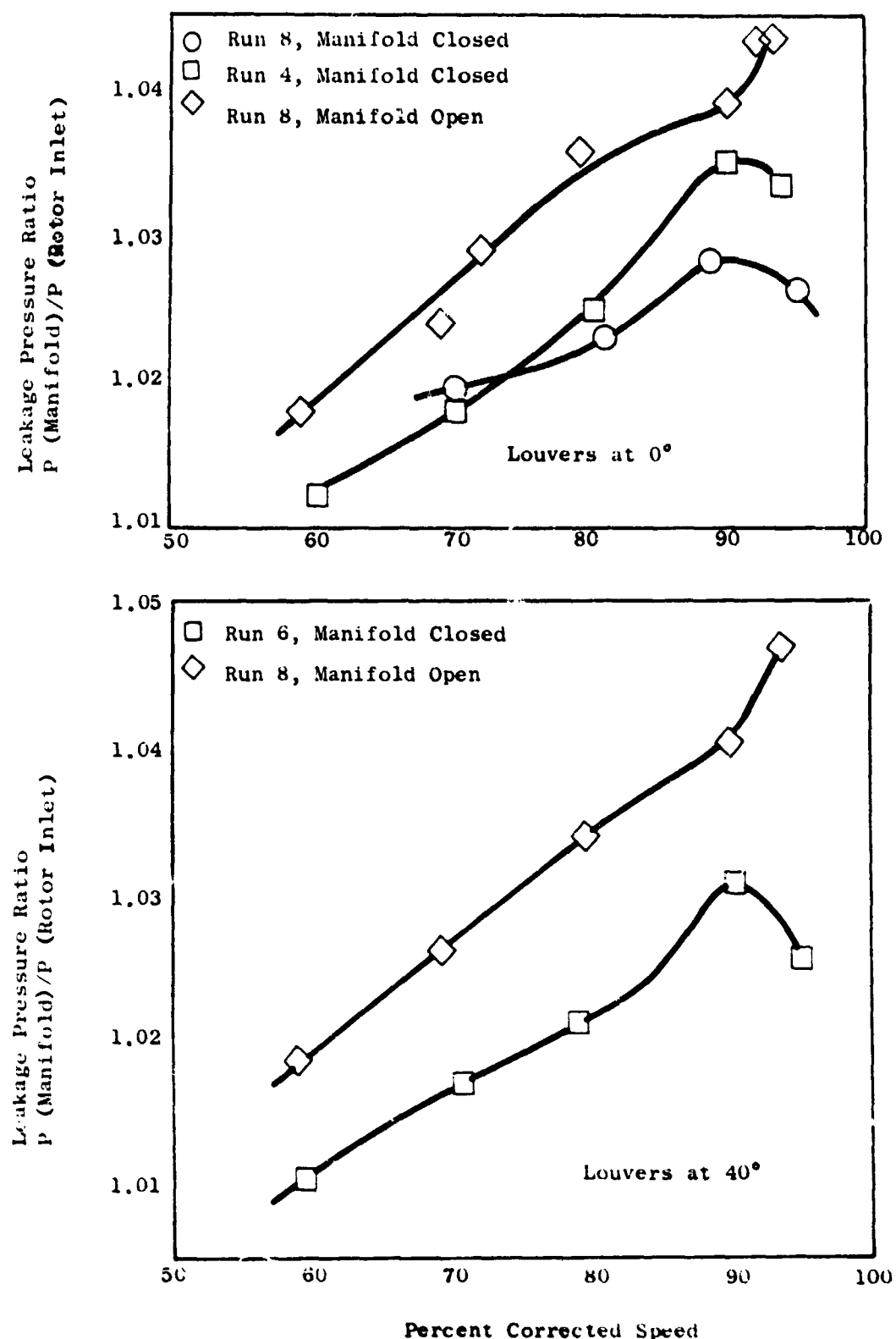


Figure 213 Rotor Inlet Seal Pressure Ratio  
Dropped Louvers

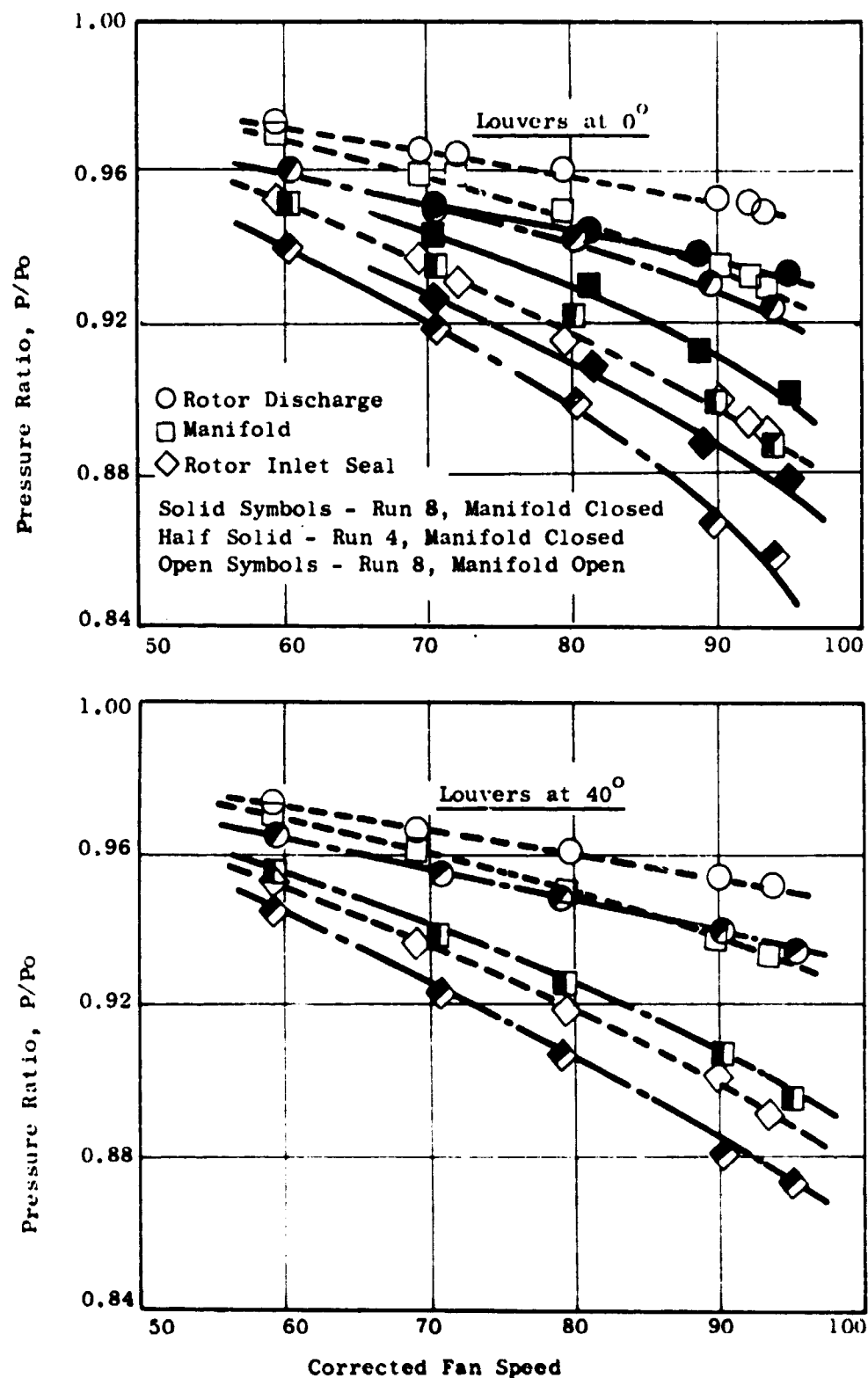


Figure 214 Seal Pressures as a Function of Speed and Manifold Conditions Louvers in Dropped Position

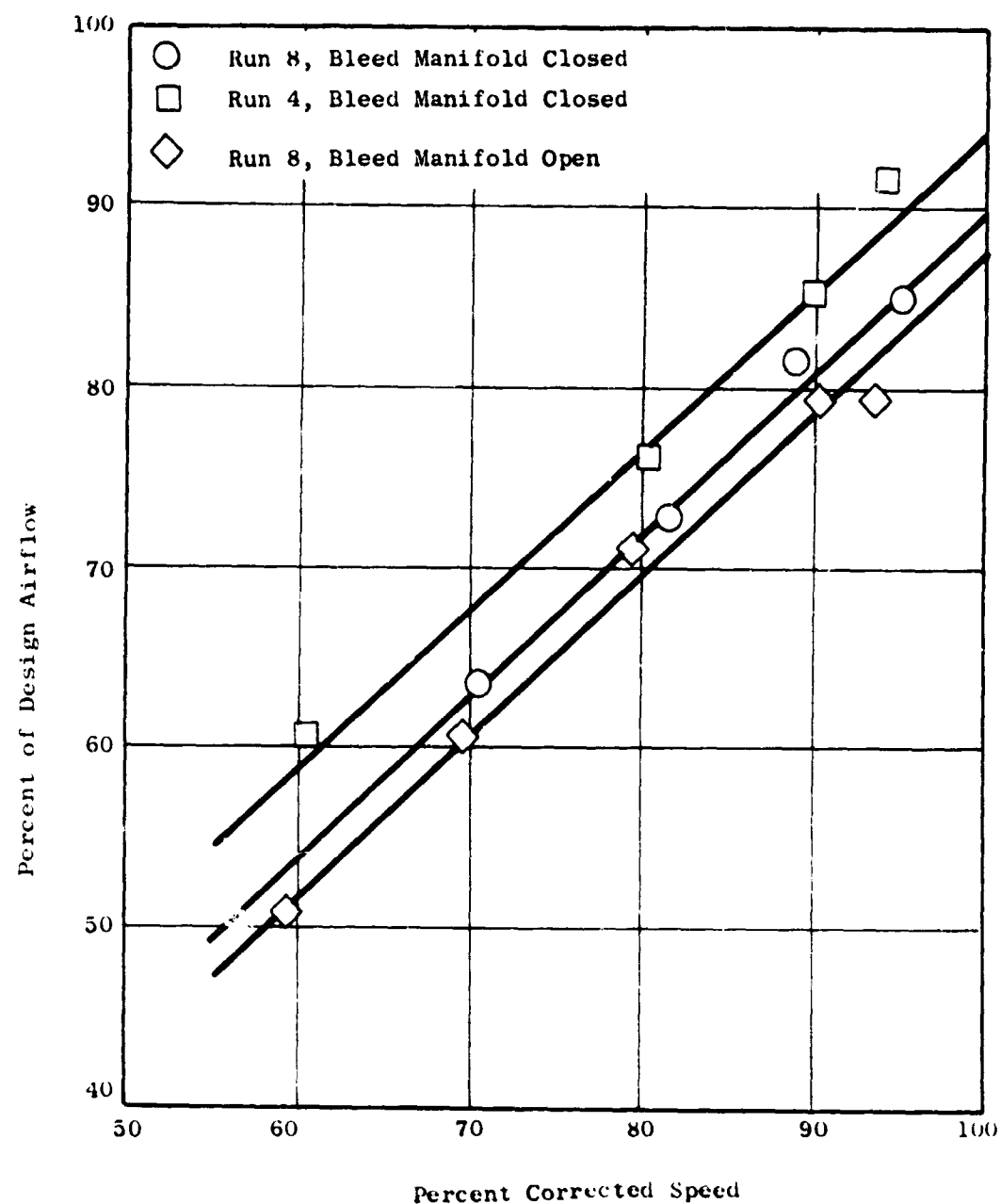


Figure 215 Fan Airflow Characteristics Louvers at 0°,  
Dropped Position, Energy Method

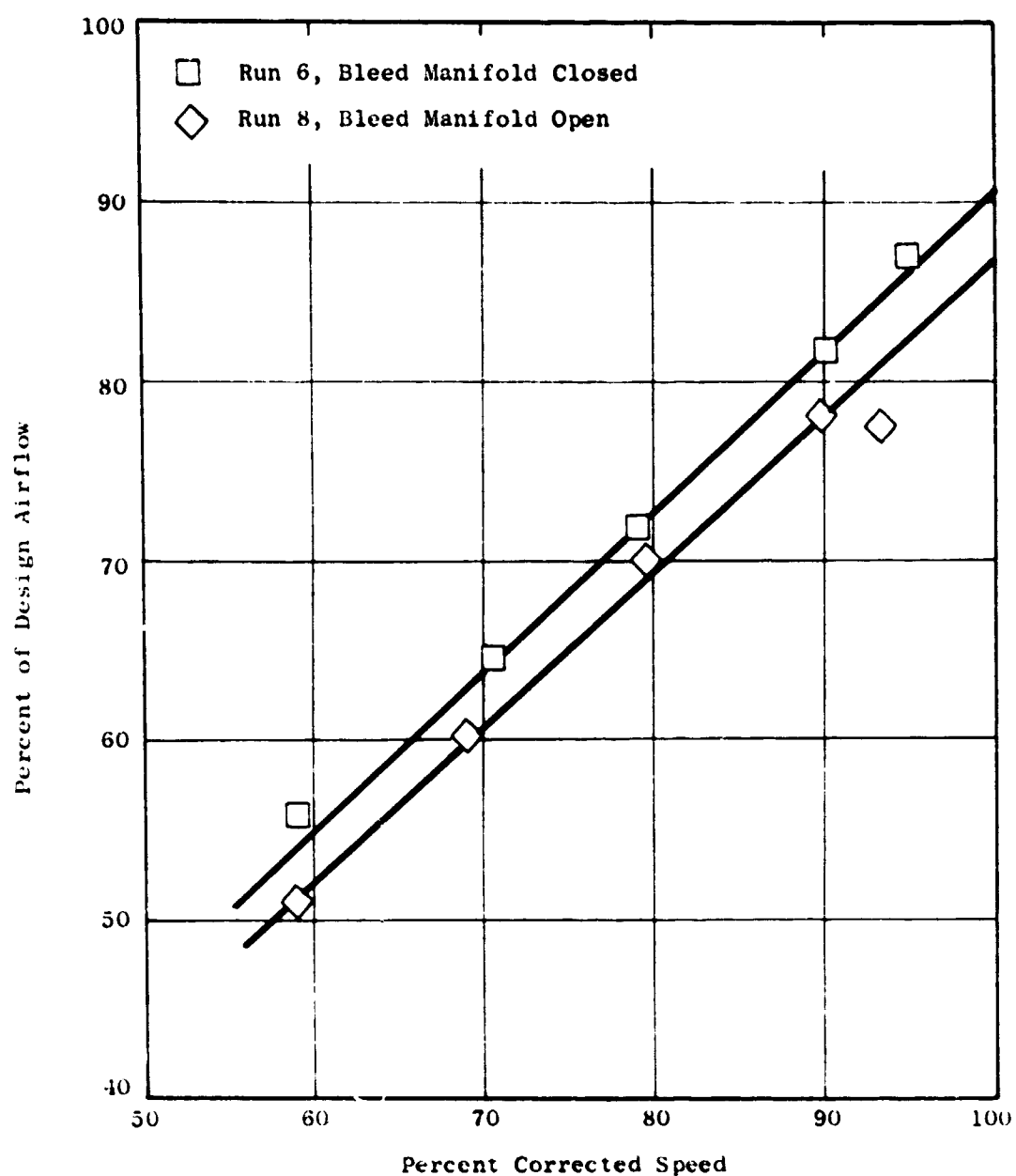


Figure 216 Fan Airflow Characteristics Louvers at 40°, Dropped Position, Energy Method

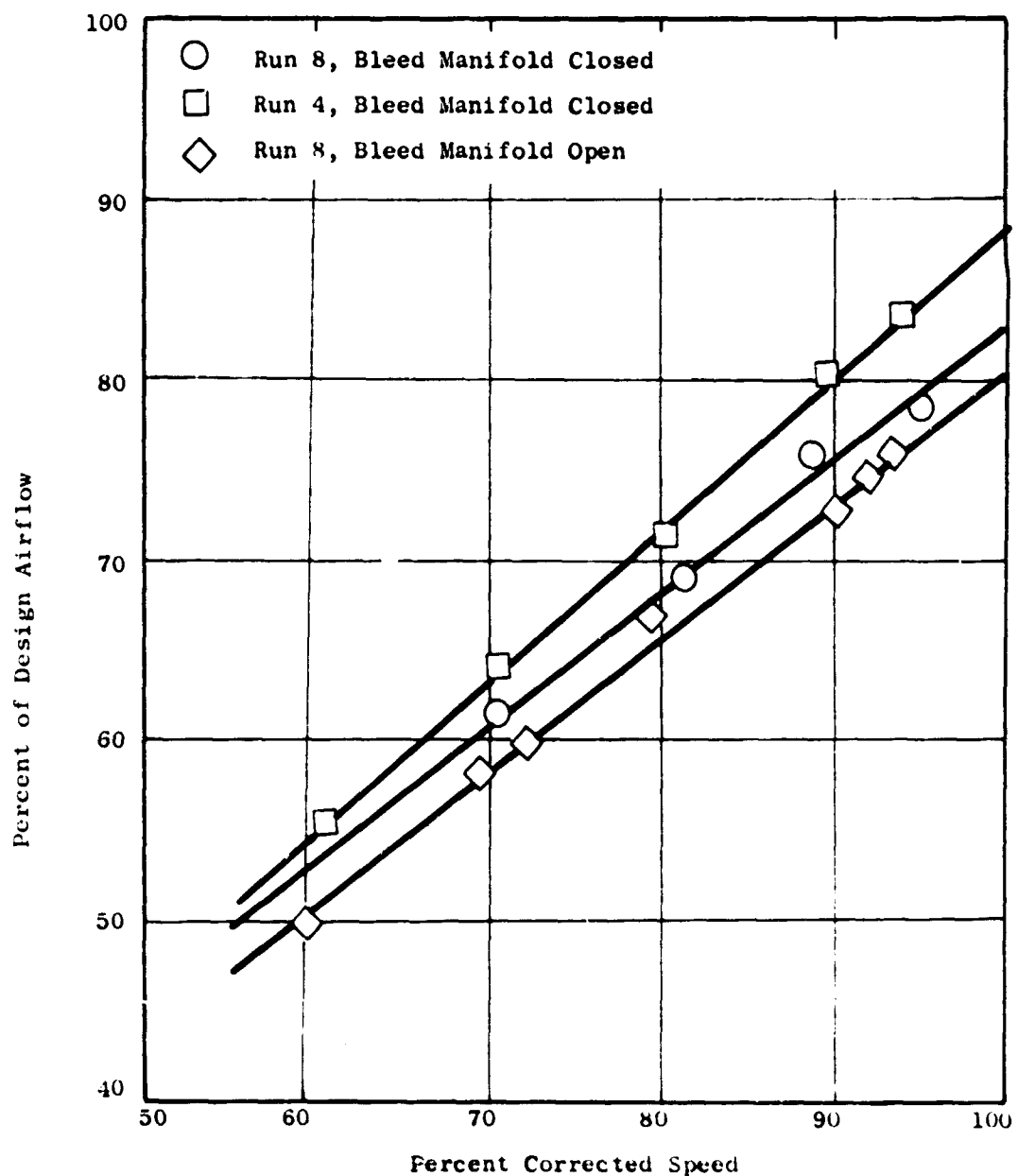


Figure 217 Fan Airflow Characteristics Louvers at 0°, Dropped Position, Based on Bellmouth Statics

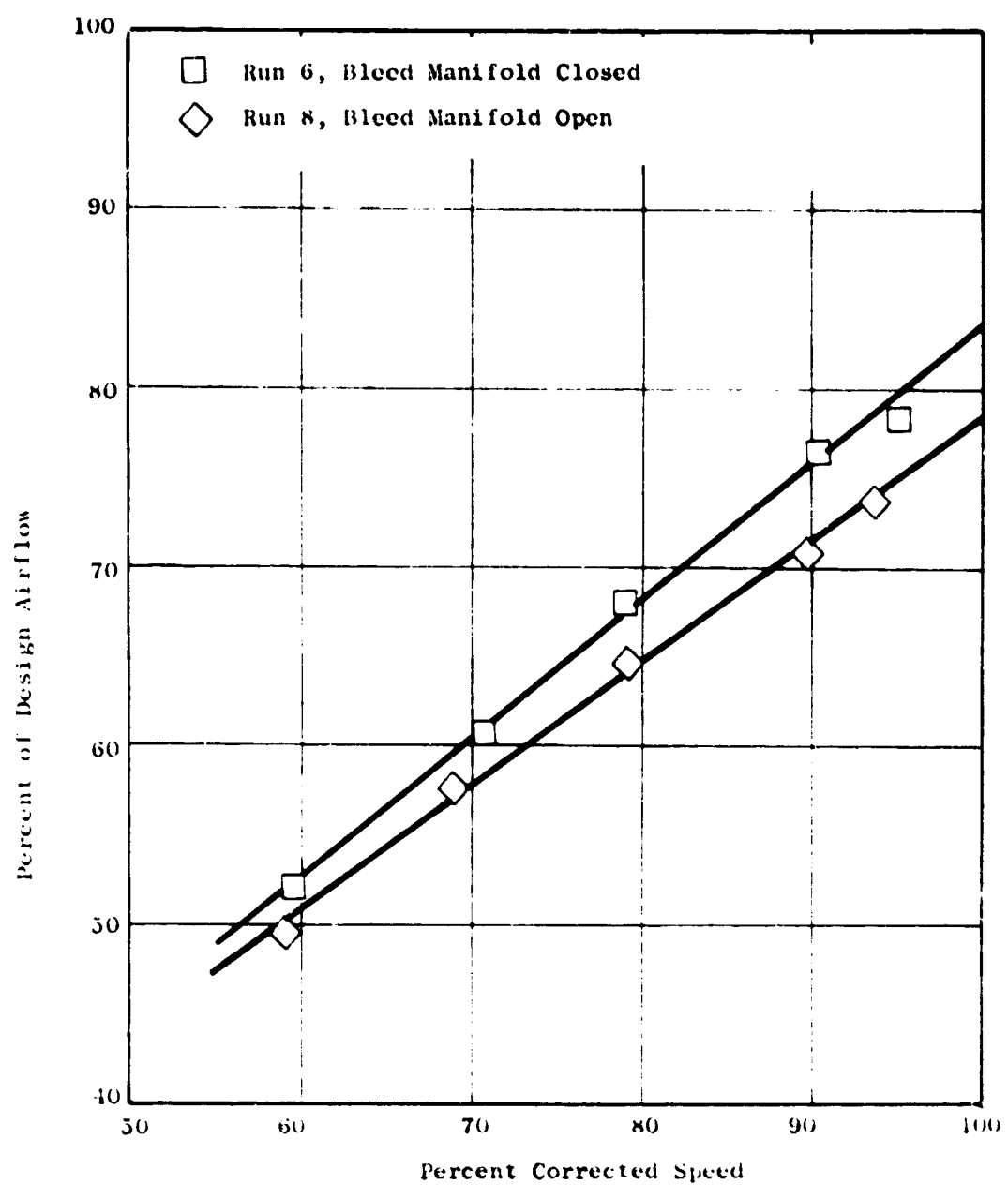


Figure 218 Fan Airflow Characteristics Louvers at 10°, Dropped Position, Based on Bellmouth Statics

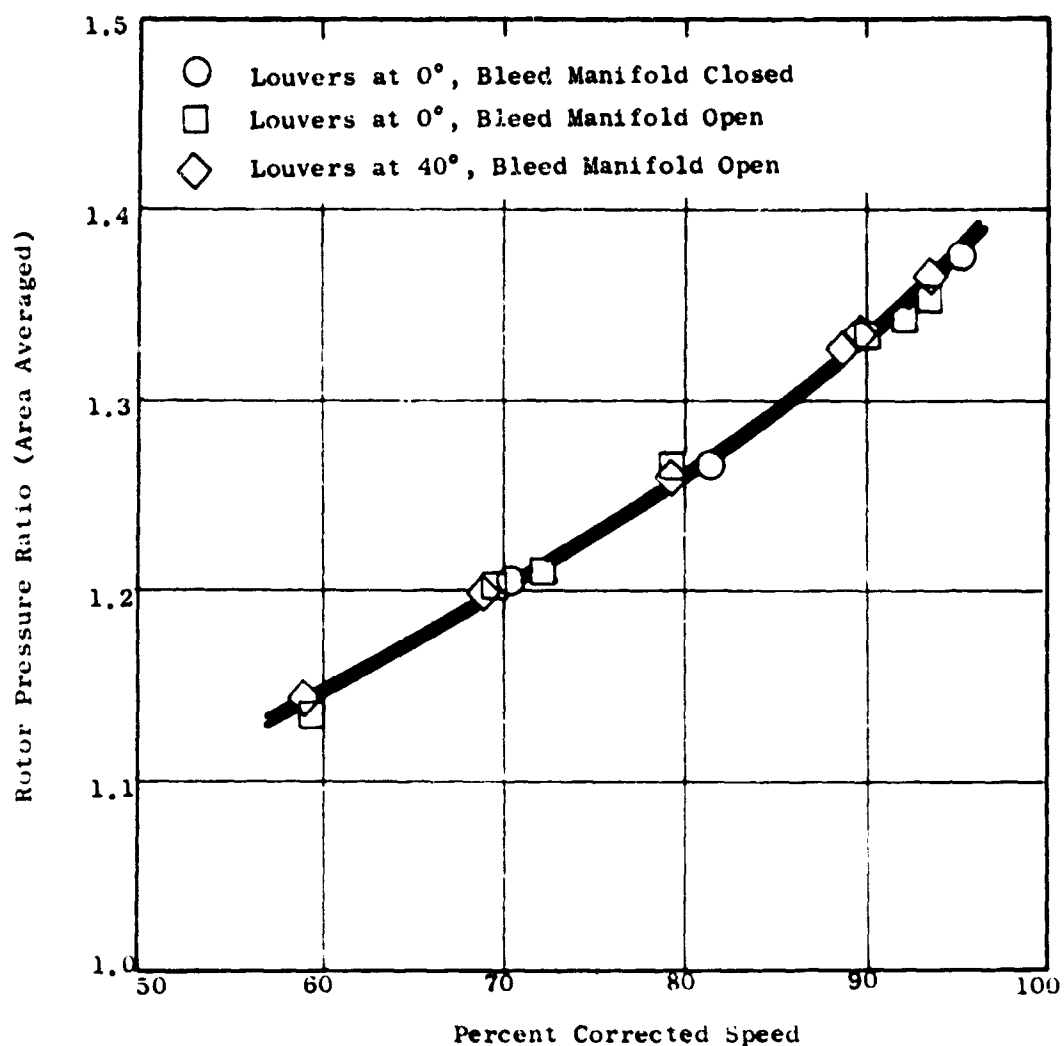


Figure 219 Fan Rotor Pressure Ratio Run 8,  
Louvers in Dropped Position

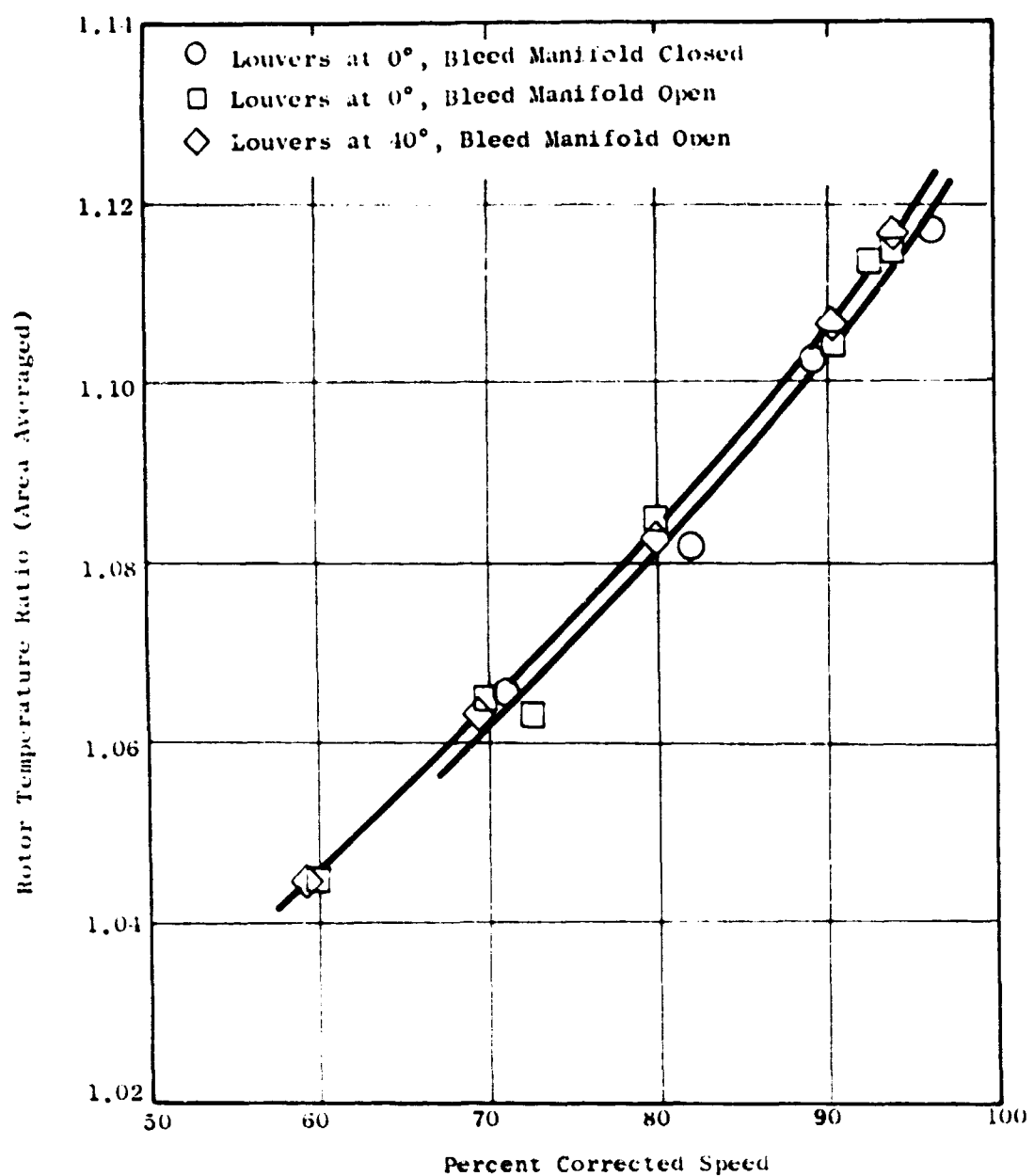


Figure 220 Rotor Temperature Ratio Run 8,  
Louvers in Dropped Position

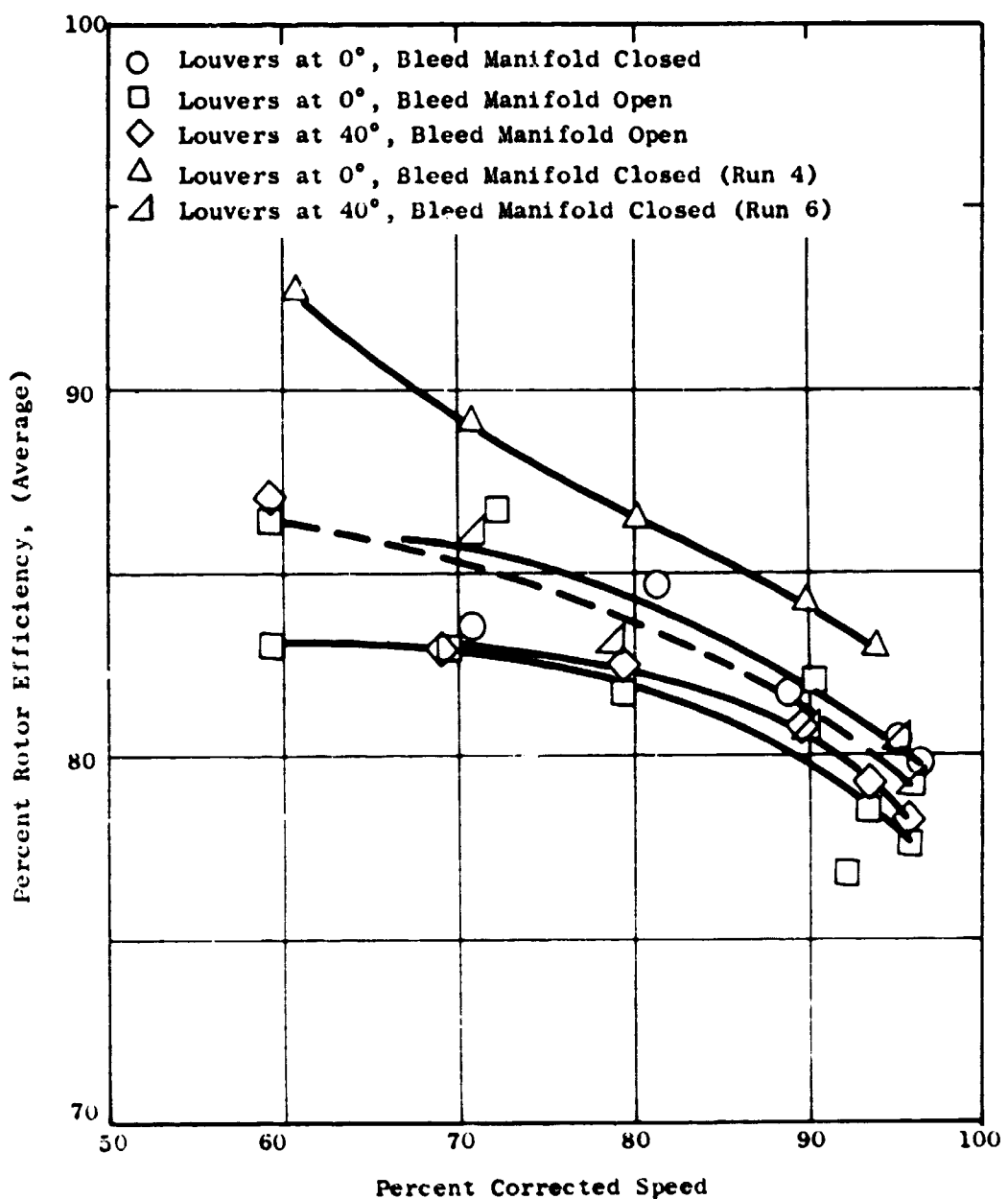


Figure 221 Fan Rotor Efficiency Run 8,  
Louvers in Dropped Position

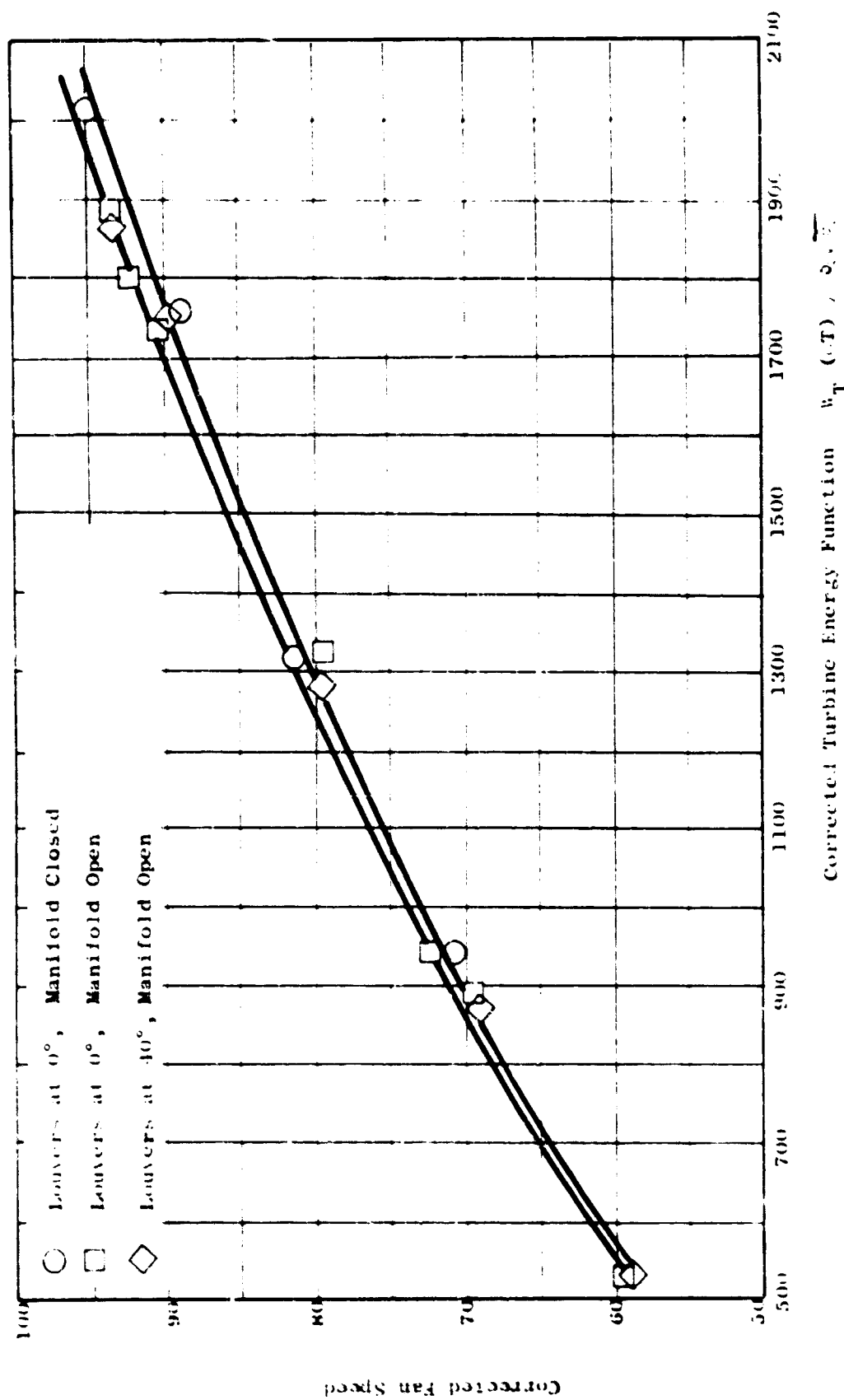


Figure 22: Fan Speed Versus Turbine Energy Function Run S,  
Louvers in Dropped Position

(U) The reduced leakage configuration pumped air from the manifold through an ejector type nozzle. All three of the seal pressure levels were reduced with the manifold pressure coming closer to the rotor inlet pressure. Seal leakage flow into the rotor inlet is greatly reduced, but as indicated by the manifold to rotor inlet pressure ratio (Figure 201) some leakage into the inlet is still present.

(U) The increased leakage configuration permitted flow from ambient through the manifold as well as from rotor discharge. The three seal pressures increased with the manifold pressure coming closer to rotor discharge pressure. The manifold to rotor inlet pressure ratio shown in Figure 201 indicates approximately the same levels for both the manifold closed and open configuration.

(U) Fan performance characteristics for the three leakage configurations are shown in Figures 203 through 210. For comparison purposes, a tabulation of fan performance parameters at 90 percent fan speed are presented in Table 45. Measured fan airflow did not change as a function of leakage. Decreasing leakage (sucking) provided a higher rotor pressure rise and temperature rise resulting in a lower rotor efficiency. Even though rotor pressure rise is higher, stage pressure rise is slightly lower and stage efficiency is correspondingly lower.

(U) Increasing leakage (manifold open) gave the same fan flow and rotor pressure rise along with a higher temperature rise and lower efficiency. Stage pressure ratio and efficiency were also lower.

(U) All three leakage configurations were run with the same physical discharge area and the calculated effective areas are very close. More turbine work (higher power) is required to drive the fan at 90% speed for both decreasing or increasing leakage.

Exit louvers on. -

(U) Manifold closed and manifold open were the only two leakage configurations investigated with this test setup. The manifold open configuration represents a greater increase in leakage than the corresponding configuration with measuring section on. In this case, all the manifold bleed ports were opened directly to ambient providing greater flow area with less losses.

(U) Base run data at 0 degree louver setting was made with manifold closed prior to taking data at 0 and 40 degree louver settings with manifold open. Data at both louver settings with manifold closed was available from previous tests and are included for comparison purposes.

TABLE 45  
LEAKAGE PERFORMANCE SUMMARY

90% SPEED - EXIT MEASURING SECTION INSTALLED

Parameter	Performance Levels			Leakage Effects	
	Base	Sucking	Open	Sucking	Open
Airflow, Percent	83.4	83.4	83.4	0	0
Rotor Pressure Ratio	1.332	1.341	1.332	+0.65	0
Rotor Temperature Ratio	1.1035	1.108	1.108	+0.41	+0.41
Rotor Efficiency	0.827	0.809	0.785	-2.18	-5.08
Stage Pressure Ratio	1.317	1.314	1.308	-0.23	-0.68
Stage Efficiency	0.778	0.745	0.727	-4.24	-6.56
Turbine Work	1840	1895	1865	+2.99	+1.36
Effective Area	88.6	88.35	88.71	-0.28	+0.12

(U) The relative level of the seal leakage pressures are indicated in Figures 211 through 214. As shown in Figure 214, increased leakage flow as provided by the manifold open configuration, results in higher leakage pressure levels with manifold pressure approaching, but still less than, rotor discharge pressure. This observation is further supported by the significant increase in manifold to rotor inlet pressure ratio as given in Figure 213. Rotor inlet pressure does increase some (Figure 214) and the bellmouth static pressure profile begins to show some deviation from its normal shape near the rotor inlet station in Figure 212.

(U) Fan performance characteristics are presented in Figure 215 through 222. The leakage test base run performance at 0° louver setting with manifold closed is significantly lower than the previous data from Run 4 for the same configuration. This deterioration may have been caused by the accumulation of an oil-carbon mixture on the fan rotor blades which was present during the Run 8 leakage test series. Although the previous data at 0 and 40 degree louver settings do not provide a direct comparison for the effects of leakage, they are included to show louver effects with manifold closed.

(U) Table 46 presents a summary of the results at 90 percent fan speed. At 0 degree louver setting, increased leakage resulted in a 2.6 percent reduction in fan airflow, a small increase in rotor pressure and temperature ratios, and a 2.5 percent penalty in fan efficiency. Turbine work function was 3.9 percent lower to drive the fan at the same speed.

(U) Changing louver angle setting from 0 to 40 degrees had much less effect on fan performance with manifold open compared to manifold closed. Airflow was decreased only 0.9 percent and efficiency increased 0.9 percent for manifold open compared to an airflow and efficiency decrease of 4.33 and 3.45 percent, respectively, for manifold closed.

#### Conclusions and Recommendations

(U) The MF415 fan with measuring section installed produced its best performance levels with some nominal amount of seal leakage present; increasing or decreasing the amount of seal leakage from this point resulted in poorer performance levels.

(U) With exit louvers installed, the fan was operated with the largest amounts of seal leakage producing significant performance penalties in both airflow and efficiency at 0° louver setting. Increasing louver angle setting from 0 to 40 degrees produced less change in fan performance characteristics during operation with the larger amounts of seal leakage.

TABLE 46

LEAKAGE PERFORMANCE SUMMARY  
90% SPEED - EXIT LOUVERS INSTALLED

Parameter	Performance Levels				Effects of Leakage	Effects of Louvers	Effects of Louvers
	8	8	8	4			
Run	8	8	8	6	8	8	4 and 6
Manifold	Closed	Open	Open	Closed	Closed vs. 0°	Open	Closed
Louver Angle	0°	0°	10°	0°	40°	0 to 40°	0 to 40°
Airflow (Energy Method)	80.8	78.7	78.0	85.5	81.8	-2.6	-0.9
Airflow (B.M. Statics)	75.3	72.8	71.6	80.2	75.8	-3.3	-1.65
Rotor Pressure Ratio	1.329	1.337	1.337	1.338	1.338	+0.6	+0.6
Rotor Temperature Ratio	1.1045	1.108	1.108	1.103	1.107	+0.3	+0.3
Rotor Efficiency	0.818	0.798	0.805	0.841	0.812	-2.5	+0.9
Turbine Work	1775	1705	1775				-3.45

(U) These tests have demonstrated that the MF415 fan can tolerate large amounts of seal leakage accompanied by some expected nominal penalties in performance. No regions of rapid or radical performance deterioration were observed. Effects, such as inlet bellmouth separation and rotor tip performance deterioration, observed on other previous fan designs were not present.

#### LF2 Tests

(U) The LF2 "Fan Inlet Investigation" is reported in Section V of the Component Technology Program Section. This lift fan is equipped with the present design, radial labyrinth seal and has a front seal only. The test results showed only small changes in fan performance. These were not attributed to seal leakage but were probably caused by cross wind variations and test accuracy.

### 26 Inch Fan Tip Recamber Test

#### Introduction

(U) Past experience with tip driven lift fans has shown that the flow in the tip region is generally weak due to the combined effects of bellmouth curvature, turbine hot gas leakage and normal blade end losses. Since the tip region will stall prematurely because of these factors when the fan is throttled, the overall fan stall margin is impaired. One possible solution to this problem may be to load up the rotor tip sections so that they produce a pressure rise equivalent to the rest of the fan in spite of their higher losses. In order to evaluate this idea the 26 inch LSSM fan has been run in two configurations, identical except for 10 degrees difference in rotor tip camber angle.

#### Tests

(U) The 26 inch LSSM fan is a low speed scale model of the 62.5 inch X353-5 lift fan. The flow path, blades, and vanes are in exact scale. The fan is mounted in a wing and driven at 1783 RPM by an electric motor through a forward shaft. The wing is mounted in a thrust stand in a cross flow tunnel which produces an average cross flow velocity of 45 FPS. In this test the fan exhaust was equipped with a set of conventional thrust vectoring louvers in a close up position. It is also possible, in the model, to simulate turbine tip leakage effects by blowing cold air through the rotor tip seals.

(U) After the original rotor blade configuration was tested the rotor blades were removed and recambered at their tips. The amount of increased camber was 10 degrees at the tip, and reduced gradually to 0 degrees at a point about 2 inches in from the tip. The remainder of the blade was unchanged. In the recambering process the orientation angle remained unchanged.

(U) Each fan configuration was tested over a range of exit louver setting angles, with the cross flow tunnel on and off, and with the tip leakage air on and off. At each test point net lift and thrust were measured, and a three element pressure probe was traversed radially at several locations in the fan. The traverse probe measured total pressure, static pressure, and flow angle. Also the drive motor torque was measured in order to determine the fan power consumption.

(U) Figures 223 and 224 show the results of the lift and thrust measurements. Figure 223 is with the cross flow tunnel off and Figure 224 is with crossflow. The drag of the wing, measured with the fan off, has been added to the horizontal thrust measurements in Figure 224. The lift of the wing, measured with the fan off, was found to be essentially zero. The magnitudes of all the thrust vectors shown in these figures are ratioed to a base point vertical lift of 96.25 pounds, and have also been corrected to a constant horsepower. Thus, although the test was actually run at essentially constant fan speed, the results presented here have been adjusted by the ideal fan laws to a constant fan horsepower. The adjusted speed corresponding to each data point then varies somewhat.

#### Conclusions & Recommendations

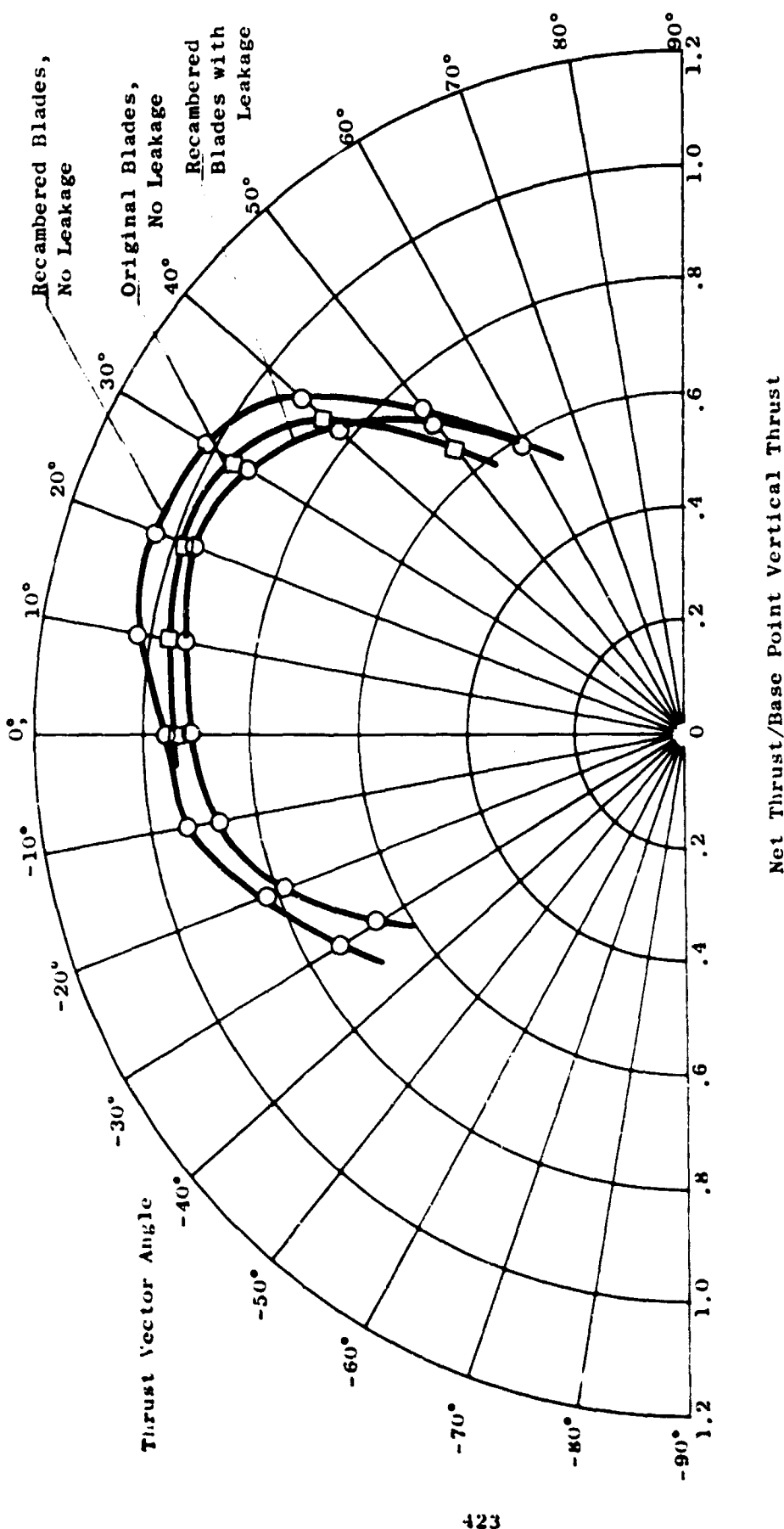
(U) From Figures 223 and 224 it can be seen that the original rotor configuration produces 2 to 5 percent less resultant thrust at any vector angle than the rotor with the recambered blades. This is true with or without cross flow. Since this comparison is made on the basis of constant power we may conclude that the recambered rotor blade configuration has a significantly higher efficiency than the original configuration.

(U) In comparing the recambered configuration with and without seal leakage simulation, it is apparent that the leakage has a dramatic effect on performance, with up to 10 percent thrust loss without crossflow and up to 15 percent with crossflow. The actual quantity of leakage air used in these tests was quite high, however, it does show that seal leakage can be very important.

#### Straight Versus Circular Arc Dovetail

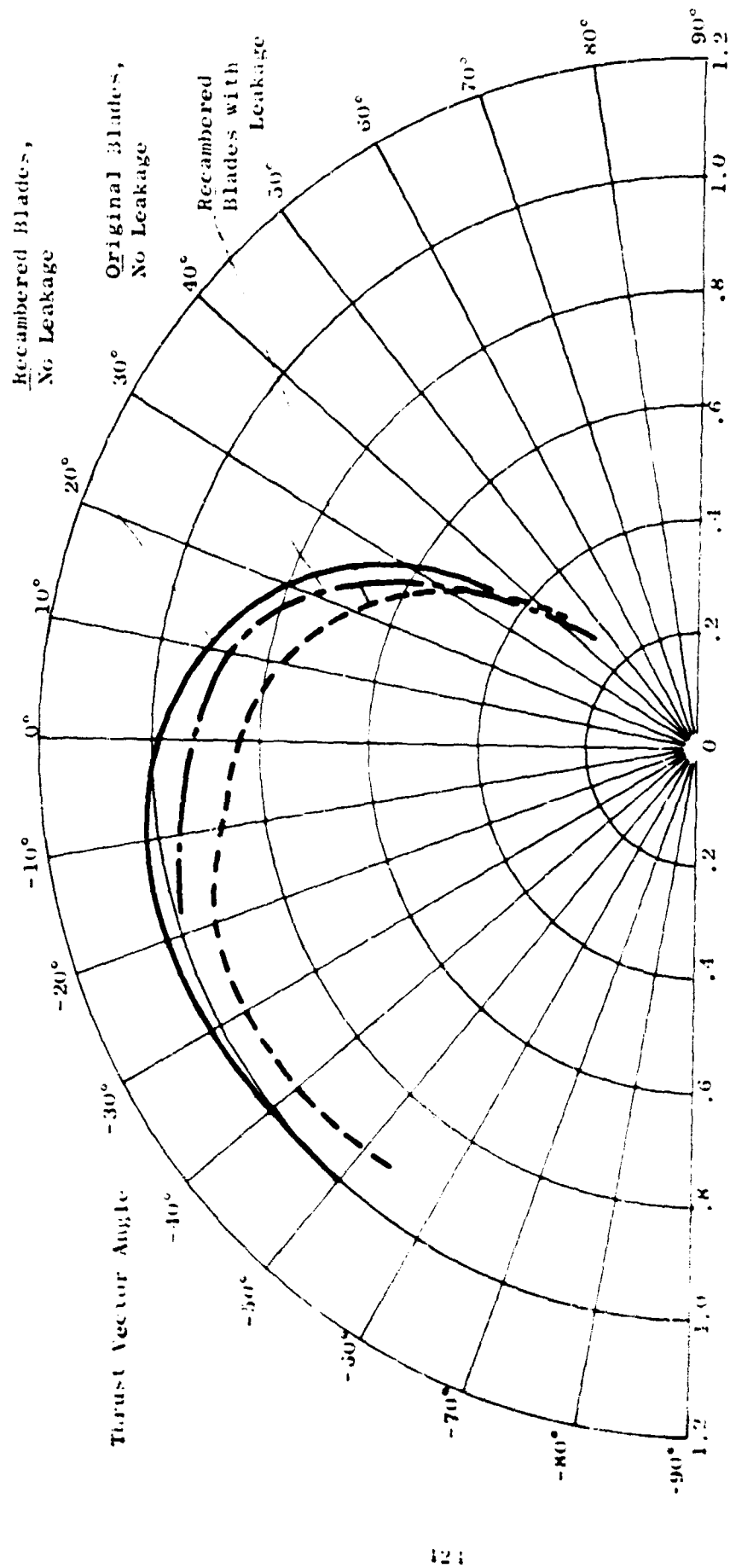
##### Introduction

(U) Advanced fans operating at high tip speeds to produce high pressure ratios result in high blade root camber and solidity. As camber and solidity increase, a point is reached where the mechanical integrity of the blade and shank and the ease of assembly of the rotor may be improved through the use of circular arc rather than straight dovetails. Less data are available on the design characteristics and bench test correlation of the



Net Thrust/Base Point Vertical Thrust

Figure 223 26 Inch LSSM Fan Resultant Thrust Polars with no Cross Flow and with Conventional Louvers



Net Thrust/Base Point Vertical Thrust

Figure 224 2.6 Inch LSSM Fan Resultant Thrust Polars with Cross Flow and Conventional Louvers

curved form than on the rectangular form of dovetail. Therefore, it is necessary to study the application in depth as part of the fan optimization program.

(U) The objectives of this program were to analytically determine minimum weight configurations for the LF475 lift fan and to select the optimum configuration considering weight, ease of assembly, and rotor stress. A test program for verification of the optimum dovetail was initially planned.

#### Discussion

(U) Design and test experience from all available sources was collected and correlated to accelerate the application and understanding of circular arc dovetails as applied to large, advanced fans.

(U) A test program was also planned with the objective of comparing a curved versus straight dovetail. The program was redirected in September 1968, which changed the program scope and omitted the testing program. The new scope was: 1) analytically determine the minimum weight of straight and circular arc dovetail configuration, and 2) select a dovetail configuration based on lightest weight, ease of assembly and forgiveness for misalignment and dimensional contour errors.

#### Analysis

(U) The stress analysis approach was to optimize a straight dovetail design to produce the lightest dovetail and disc rim weight which would support the LF475 blade and turbine loads. Once the straight dovetail geometry was frozen, the same cross section configuration would be used to design the lightest circular arc dovetail to optimize the fit of dovetail geometry to blade shank. A weight and stress comparison would then be made of the resulting designs.

#### Basic dimensions. -

(U) The outer rim radius was set at 16.6 inches, the dovetail face angle at 55°. All analyses were based on procedures reported in references 1 through 4. To minimize the quantity of calculations required it was assumed that the worst stresses occur with a friction angle of 21.8° and a maximum tang stress location ( $\lambda$ ) of 35° for both the dovetail and the post. The first of these assumptions was conservative, the second was true for all cases checked and should not cause significant errors within the range of geometry variation contemplated. These studies also neglected dimensional tolerances.

Loads. -

(U) The dovetail geometric parameter studies were run with two sets of loads. The first set consisted of: 1) the design point steady state loads and 2) the vibratory loads in the first flexural mode of an amplitude to make the worst point on the airfoil fall on the stress range diagram limit line. That is, the vibratory loads from a Twisted Blade Analysis of the airfoil were scaled to cause the worst point on the airfoil to be at the maximum allowable combined stress level.

(U) The second set of loads consisted of the worst combination of centrifugal, aerodynamic and maneuver loads the fan was expected to see. As these loads only occur instantaneously, the resulting stresses were evaluated in terms of tensile properties rather than stress range properties.

(U) These two sets of loads were as follows:

	<u>M<sub>X</sub></u>	<u>M<sub>Y</sub></u>	<u>M<sub>Z</sub></u>	<u>V<sub>X</sub></u>	<u>V<sub>Y</sub></u>	<u>V<sub>Z</sub></u>
steady state design point:	-2565	1690	-931	460	171	25630
first flex vibratory:	-16610	3681	6.6	-213	1524	-
worst maneuver:	12865	-2690	-612	-73	499	25806

Materials. -

(U) Preliminary materials selection for the LF475 include use of 6Al-2Sn-4Zr-2Mo (6-2-4-2) titanium for the blades and 6Al-6V-2Sn (6-6-2) titanium for the disk. Either or both of these choices could change in the light of detail design requirements. In view of this possibility the stresses calculated for the various configurations in this study were compared against the lower properties of the 6-2-4-2 titanium alloy. The minimum combined stress properties are as shown in Figure 225. The tensile properties used were as follows:

Minimum .2% yield strength - 106.1 ksi  
80% of minimum ultimate strength - 99.3 ksi

Criteria. -

(U) Dovetail post combined stresses should be lower than blade dovetail combined stresses on the pertinent Goodman diagram. Combined dovetail stresses should in turn be lower than combined airfoil stresses. Stresses due to the worst combination of aero, centrifugal, crossflow and maneuver loads should not exceed minimum .2% yield strength or 80% of the minimum material ultimate strength. Blade neck tensile stress due to centrifugal loads should not exceed 40,000 psi. Post neck tensile stress due to centrifugal loads should

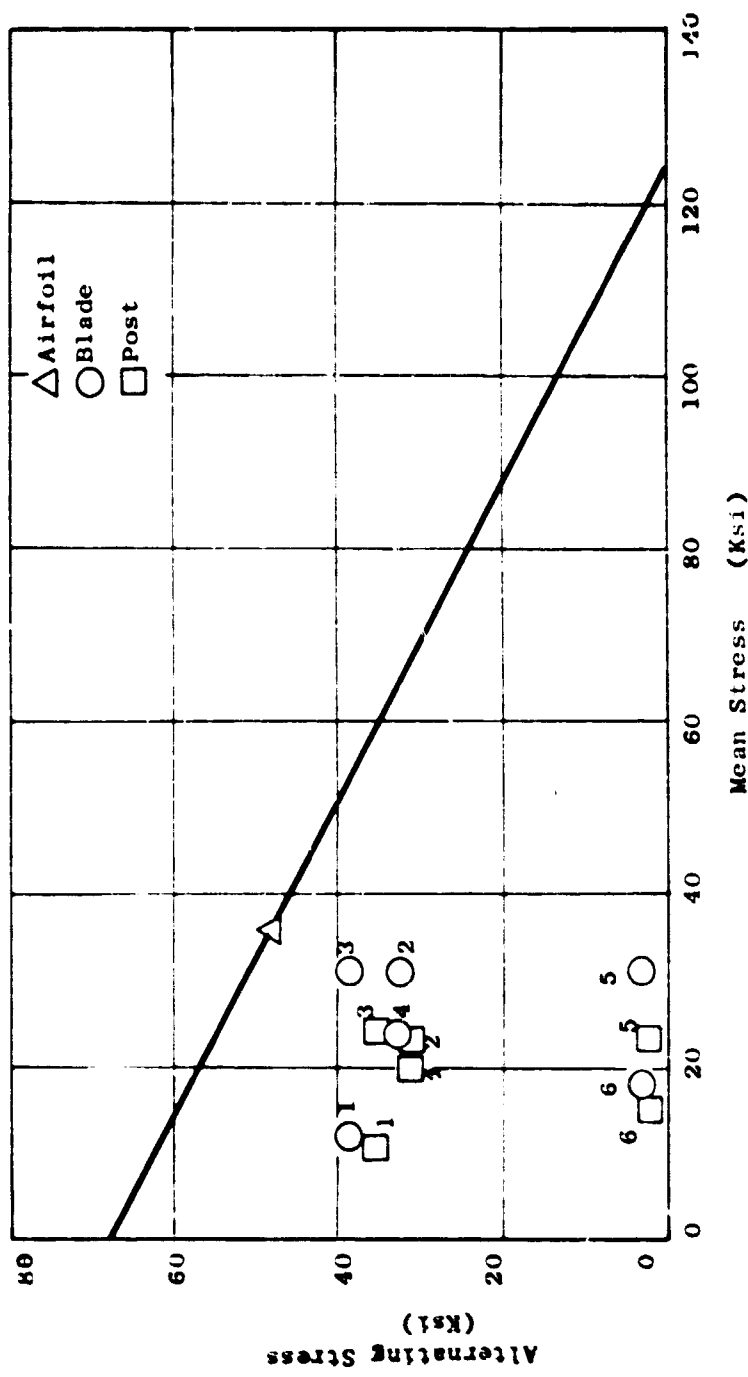


Figure 225 6-2-4-2 Titanium Combined Stress Diagram Showing Worst Airfoil, Blade Dovetail and Disk Post Combined Stresses Under Corresponding Loads

not exceed 30,000 psi. Bearing stress on the contact face due to centrifugal loads should not exceed 25,000 psi.

Geometry. -

(U) The conservative philosophy of successful design is to avoid changing a design or design approach that works successfully until it fails to meet the new requirements made of it. With this philosophy in mind, the range of geometric parameters used in previous Lift Fan dovetails were collected to be used as a guide in selecting the range of variables to be studied in optimizing the LF475 dovetail configuration. The following table lists geometric characteristics of previous Lift Fan dovetails:

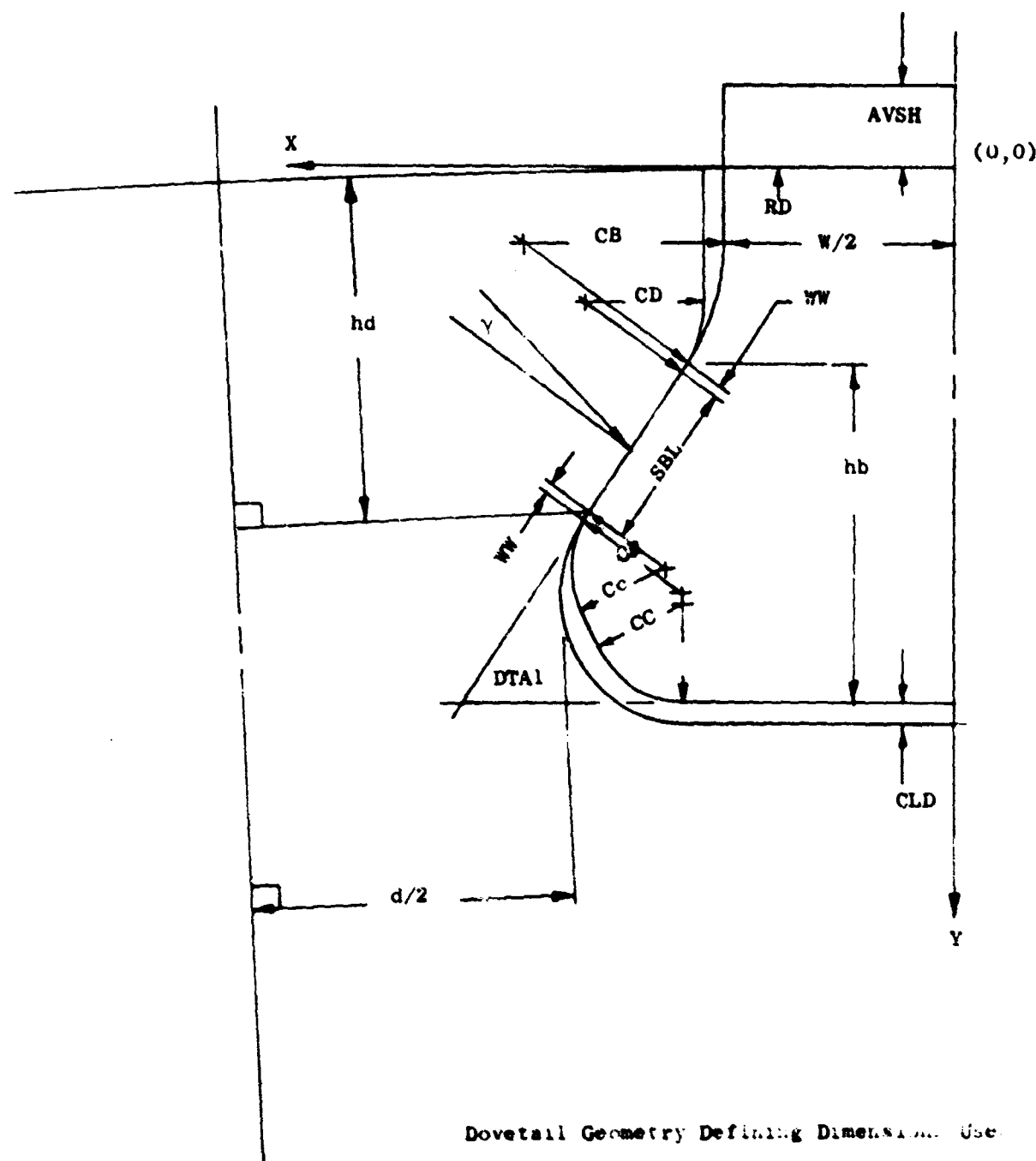
Lift Fan	Dimensions							
	hd	hb	CB	CR	W	d	Zt	$\alpha$
LF336	.4462	.4115	.218	.100	.316	.432	2.535	10°45'
LCF380	.65	.460	.680	.130	.500	1.248	4.75	8°
LF262	.375	.288	.150	.093	.750	1.015	3.2	9°24'
X-353	.382	.297	.672	.09	.290	1.135	2.25	9°24'
X-376	.285	.138	.120	.039	.458	.730	1.85	15°

Straight Dovetail

(U) Twenty-five configurations were analyzed to determine the effect of eight geometric variables on rim weight and dovetail stresses. Figure 226 presents the set dimensions used. This particular set comes from a time sharing computer program developed for preliminary sizing of Lift Fan rotors. The base case geometry used in all studies is presented in Table 47 and illustrated in Figures 227 and 228.

(U) A dovetail by nature has face angles. Because of this it was difficult to change any radial or circumferential dimensions without causing secondary changes. An attempt was made to minimize this effect in selecting the dimensional variations made. Table 48 presents the variations from the base case geometry for each of the other configurations studied.

(U) The first geometric variable studied was the ratio of shank to post neck width, W/d. The geometry for each of the configurations in this study was determined by changing the value of W from the base case to each of three new values to cover the desired range of study. All other dimensions remained constant.



Dovetail Geometry Defining Dimensions Use

Figure 226

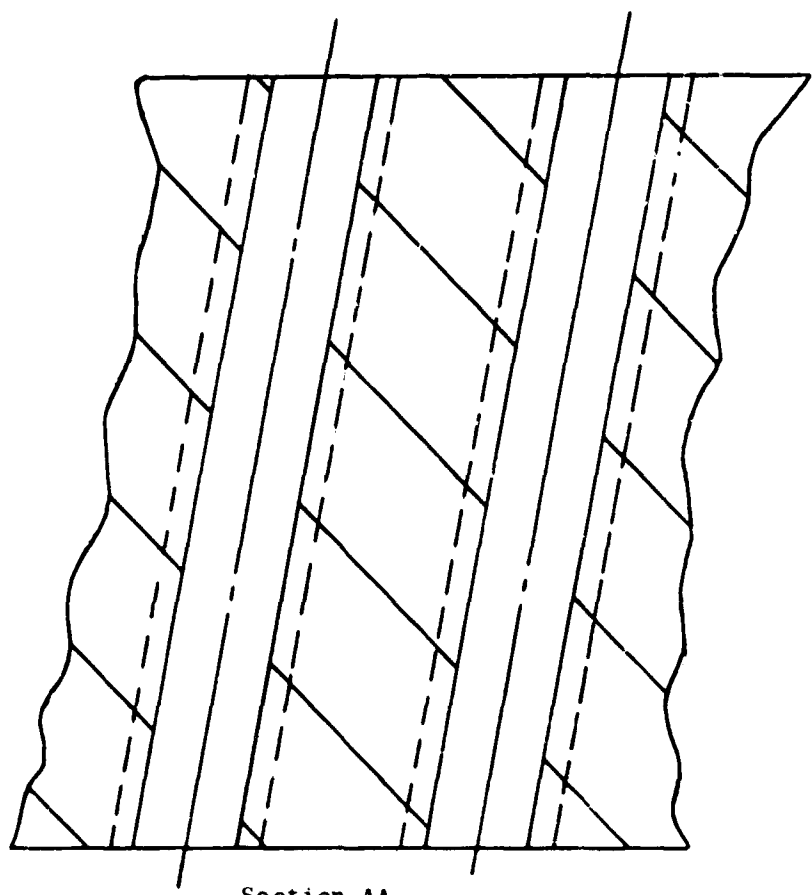
TABLE 47

Base Case Dovetail Dimensions

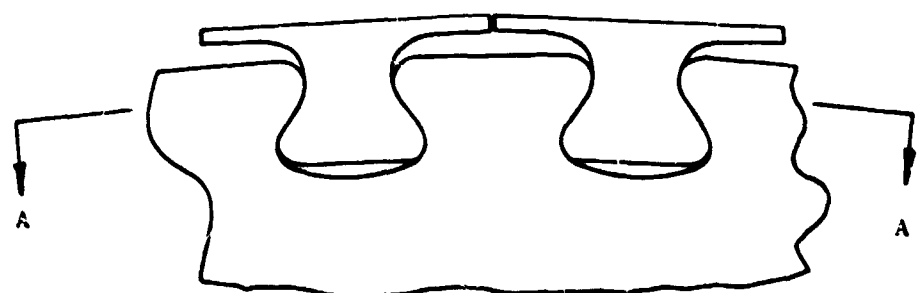
<u>Symbol</u>	<u>Dimension</u>	<u>Limits</u>	<u>Base Case</u>	<u>Constant Values</u>
RD	rim radius	set by a separate study	---	16.6
YA	also hd		.35	--
SBL	face length	P/A=35 Ksi Crush	.175	--
DTA1	face angle	(experience)	----	55°
CR	disk slot		.13	--
W	bld. neck width	P/A 40000 Psi	.492	--
γ	friction angle	(conservative)	----	21.8
WW	tangent pt. Clear	(detail)	----	0
CB	bld. neck curve	>CD	.215	-
CC	bld. tang corners	(doesn't effect calculations)	----	.1
CLD	bld.-slot base	(minimize)	----	.0265
RHOB	density bld.	(titanium)	----	.162
AVSH	shank height	(set in load table)	----	0
NOB	No. of Blades	(separate study)	----	66
RHOD	density dsk	(titanium)	----	.162
CD	dsk tang tip rad	<CB	----	.13

Variables for this study:

YA, SBL, CR, W, CB,

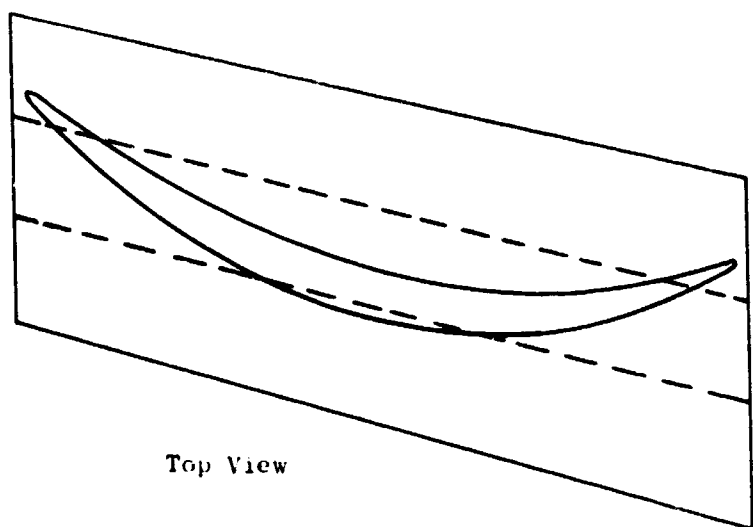


Section AA

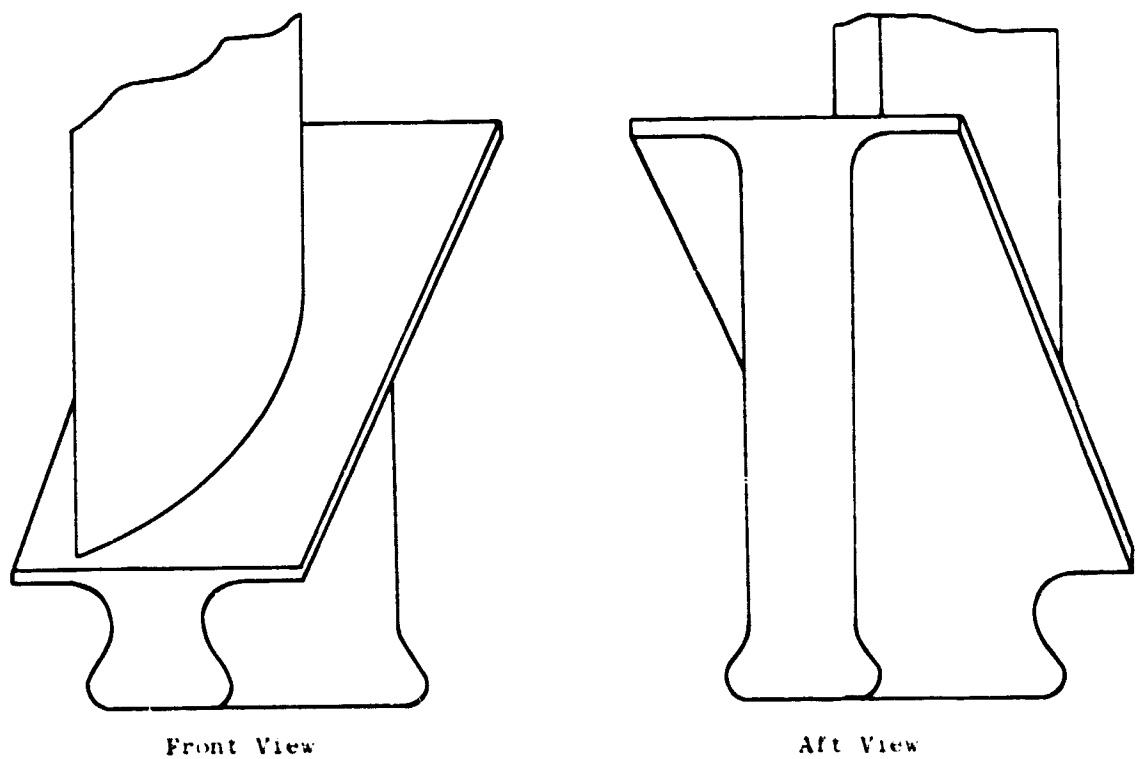


Base Case Dovetail Configuration

Figure 227



Top View



Front View

Aft View

Base Case Dovetail With Shank, Platform and Blade Root

Figure 228

TABLE 48

## Geometry Variation

YA	W	CR	CB	Zt	SBL	$\alpha$
<u>Base Case</u>						
.35	.492	.13	.215	4.693	.175	11
<u>Neck Thickness, W/D</u>						
.35	.532	.13	.215	4.693	.175	11
.35	.418	.13	.215	4.693	.175	11
.35	.345	.13	.215	4.693	.175	11
<u>Blade Fillet-Shank, CB/W</u>						
.35	.577	.13	.13	4.693	.175	11
.35	.457	.13	.25	4.693	.175	11
.35	.345	.13	.362	4.693	.175	11
<u>Tang Thickness Ratio, hd/hb</u>						
.45	.492	.13	.215	4.693	.175	11
.55	.492	.13	.215	4.693	.175	11
.6428	.492	.13	.215	4.693	.175	11
<u>Blade vs Slot Fillet, CB vs CR</u>						
.35	.492	.1725	.1725	4.693	.175	11
.35	.492	.150	.195	4.693	.175	11
.35	.492	.115	.23	4.693	.175	11
<u>Contact Length, SBL</u>						
.3705	.5064	.13	.215	4.693	.200	11
.3296	.4778	.13	.215	4.693	.150	11
.3091	.4634	.13	.215	4.693	.125	11
<u>Rim Thickness</u>						
.32	.4926	.1124	.215	4.693	.175	11
.37	.4914	.1416	.215	4.693	.175	11
.41	.4908	.1649	.215	4.693	.175	11
<u>Rim Width</u>						
.35	.492	.13	.215	4.00	.174	11
.35	.492	.13	.215	3.25	.175	11
.35	.492	.13	.215	2.50	.175	11
<u>Slot Angle</u>						
.35	.492	.13	.215	4.693	.175	18
.35	.492	.13	.215	4.693	.175	6
.35	.492	.13	.215	4.693	.175	0

(U) The second geometric variable studied was the ratio of blade shank fillet radius to blade shank width, CB/W. This study was made keeping the sum of shank width and fillet radius constant, thus it is not independent of the effect of blade to post neck width. It was assumed that the resulting post stress changes could be tolerated.

(U) The study of post-to-blade tang height ratio (hd/hb) was run by varying the post tang radial height, hd, while maintaining all other dimensions constant. This ratio is of interest because it defines the point of load application on the pressure face of the dovetail section as discussed in reference 5.

(U) The ratio of blade shank fillet radius to disk slot fillet radius CB/CR was studied by varying CB and CR in such a manner that their sum was always constant. By also maintaining post and shank neck widths and pressure face length constant, the post secondary effect is to move the circumferential location of the pressure face with respect to the dovetail centerline.

(U) The fifth variable studied was the contact face length, SBL. As changing this dimension by itself changes the relative size of blade and post portions of the dovetail, compensatory adjustments were made in tang height and shank width to maintain the relationships between the center of the contact face and the dovetail and post center lines.

(U) In varying the rim thickness adjustments were made in shank width and post slot fillet radius to maintain tang height and neck width ratios. The last two geometric variables (rim width, Zt and dovetail slot angle,  $\alpha$ ) were varied with no change in the base case dovetail section geometry.

(U) Using design point steady state and vibratory loads as discussed under Requirements, stress analyses were run for the twenty-five configurations described. The resulting stresses were plotted on a stress range diagram for 6-2-4-2 titanium and the ratio of the worst corner vibratory stress to the allowable vibratory stress at that steady stress was determined. This ratio is plotted as a function of each of the eight geometric variables in Figures 229 through 236.

(U) Using the worst maneuver loads as defined in the Requirements and the same analytical tools, peak short time stresses were calculated. These stresses are plotted as functions of the eight geometric variables in Figures 237 through 244 where they are also compared with minimum material tensile properties. (80% of minimum ultimate strength).

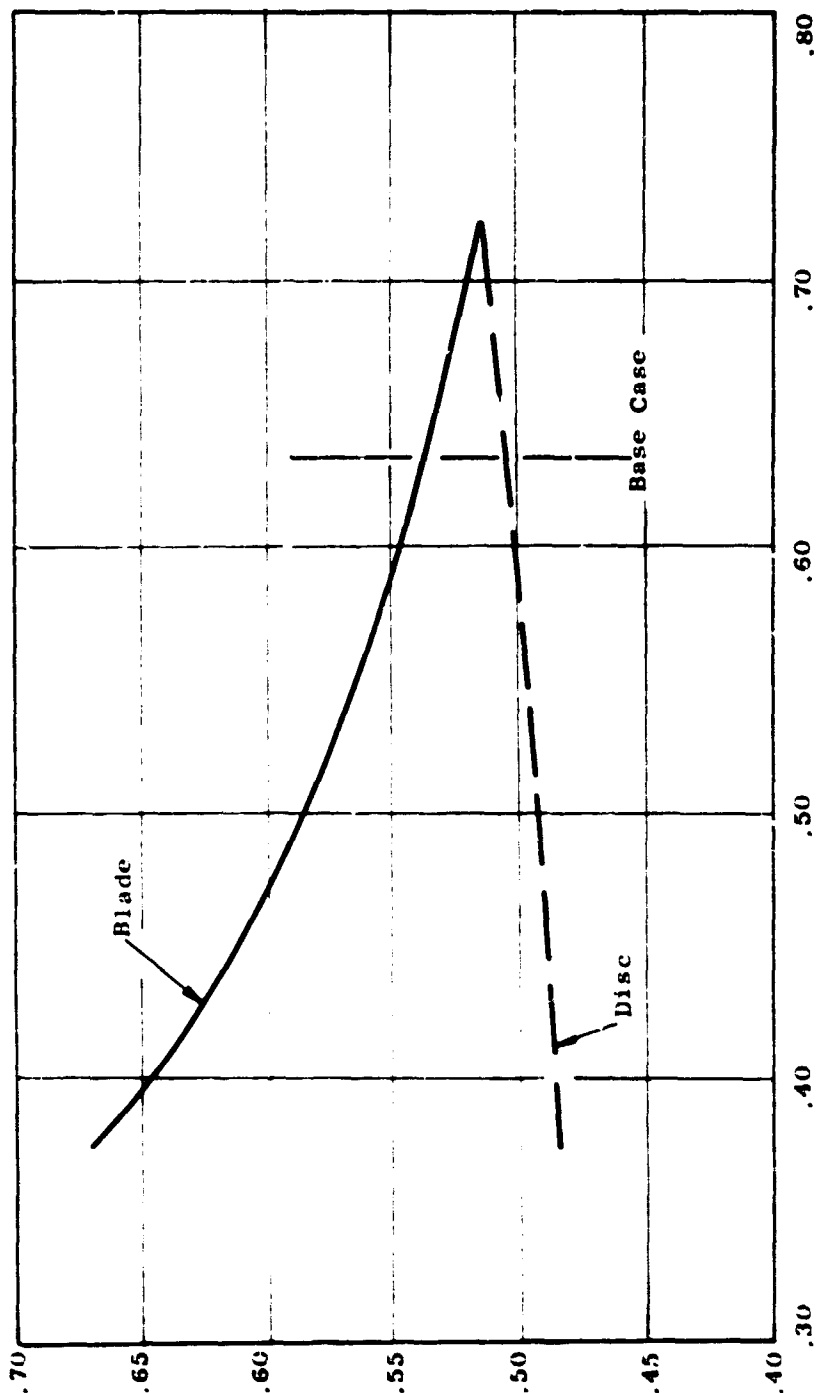


Figure 229 Percent of Dovetail Alternating Stress to Cause Simultaneous Failure of Dovetail and Airfoil Versus Ratio of Blade to Post Neck Width

Allowable Dovetail to Airfoil Alternating Stress Ratio (Dimensionless)

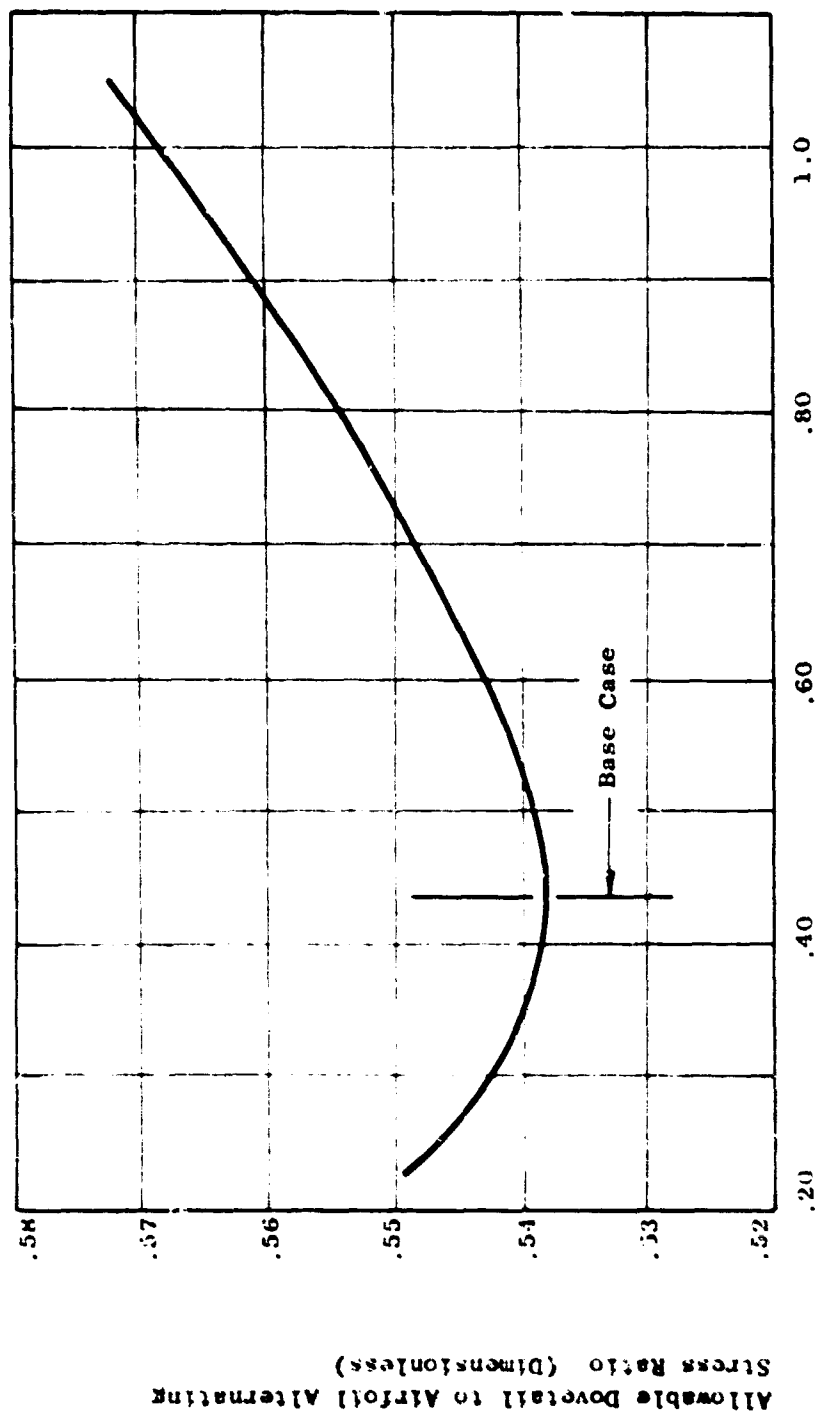


Figure 230 Percent of Dovetail Alternating Stress to Cause Simultaneous Failure of Dovetail and Airfoil Versus Ratio of Blade Shank Fillet Radius to Blade Dovetail Neck Width

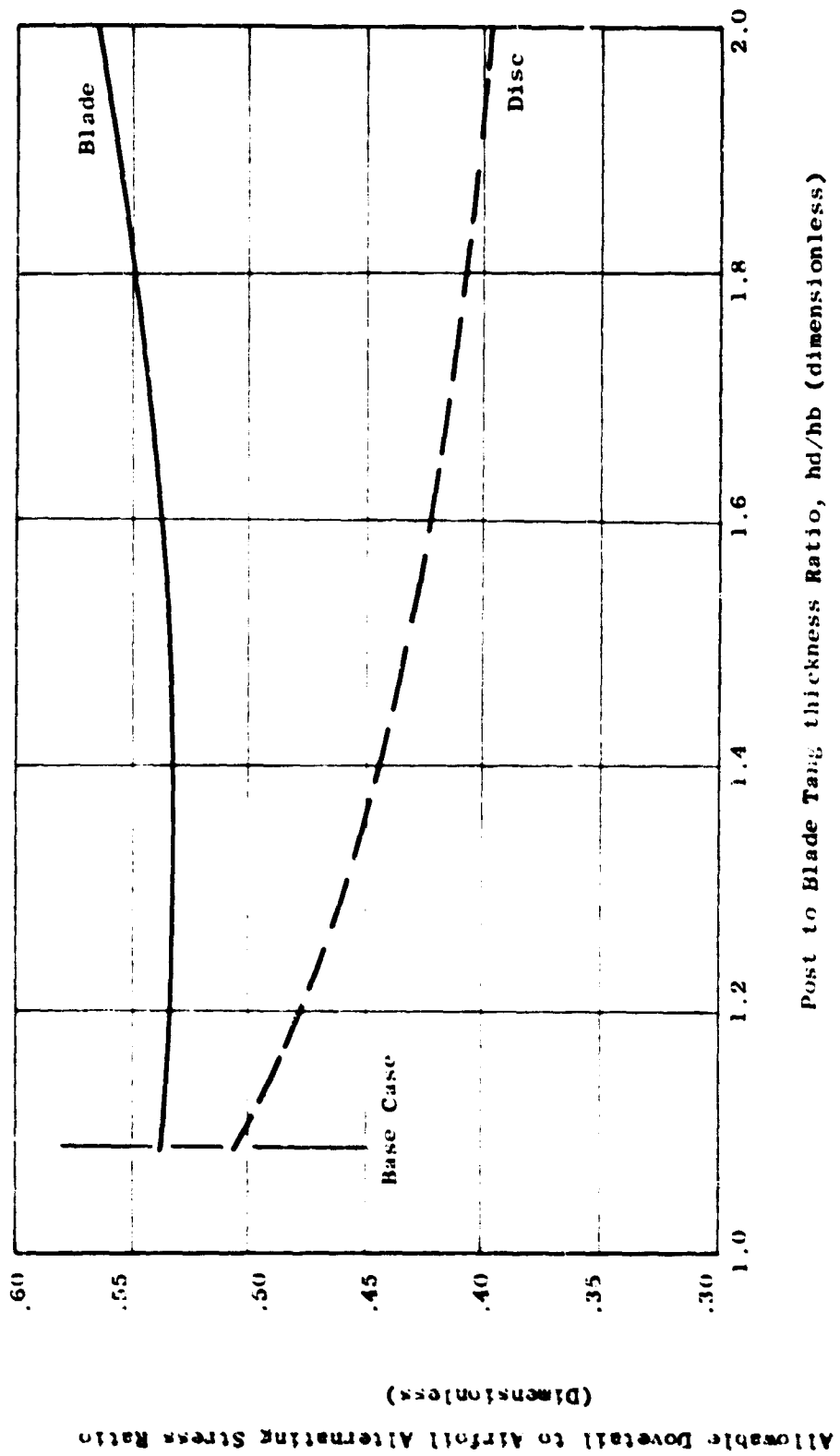


Figure 231 Percent of Dovetail Alternating Stress to Cause Simultaneous Failure of Dovetail and Airfoil Versus Ratio of Post Tang to Blade Tang Thickness

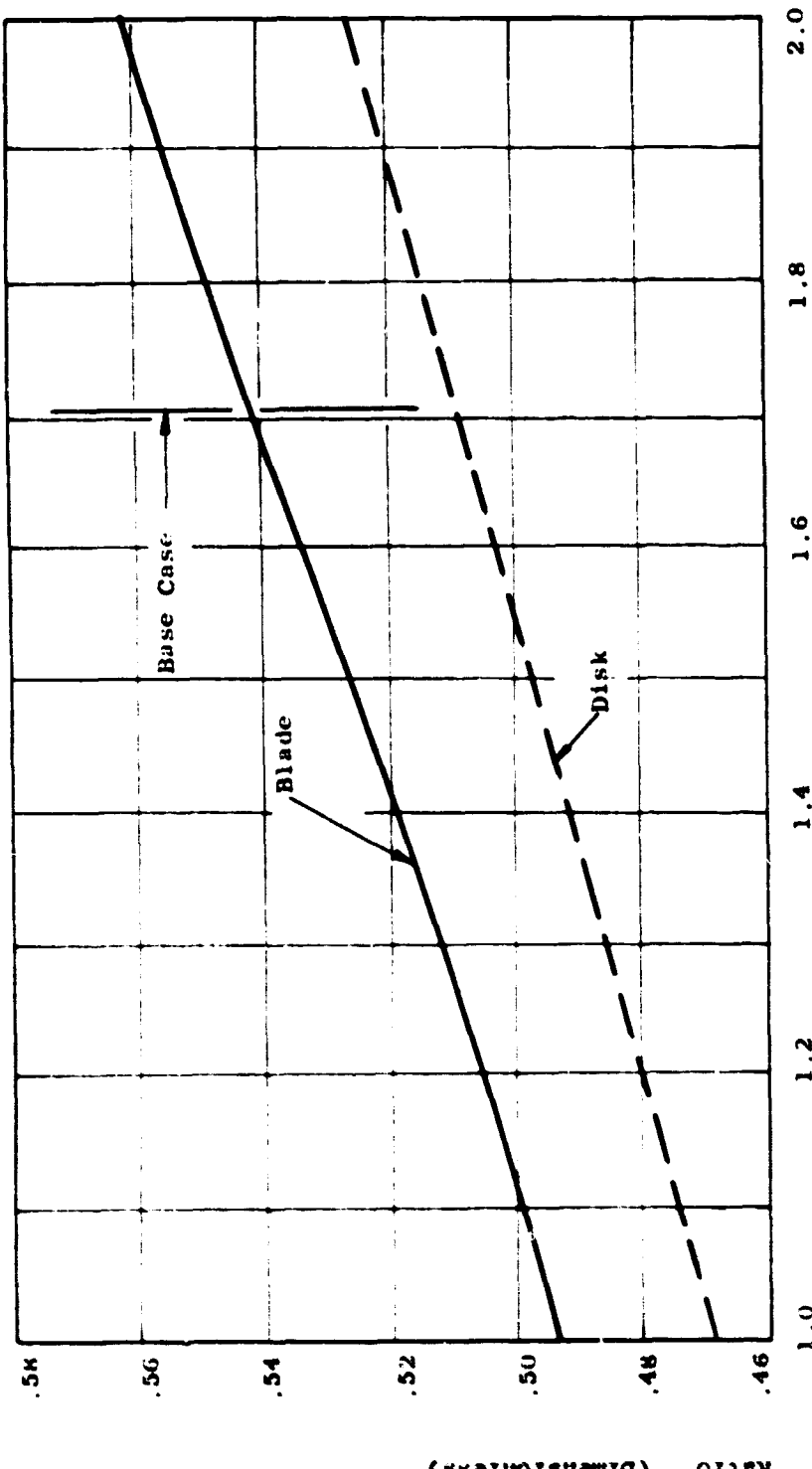


Figure 232 Percent of Dovetail Alternating Stress to Cause Simultaneous Failure of Dovetail and Airfoil Versus Ratio of Blade Shank Fillet Radius to Disk Slot Fillet Radius

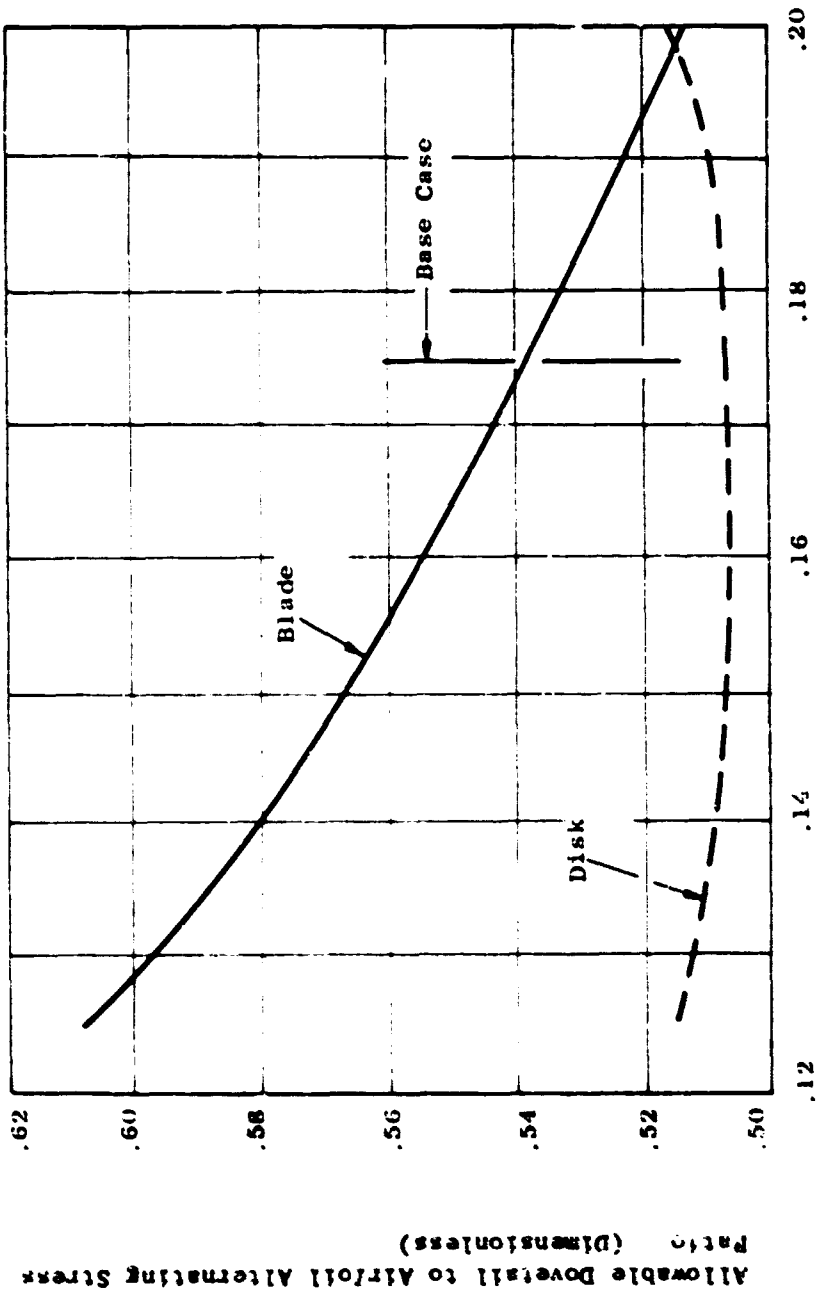
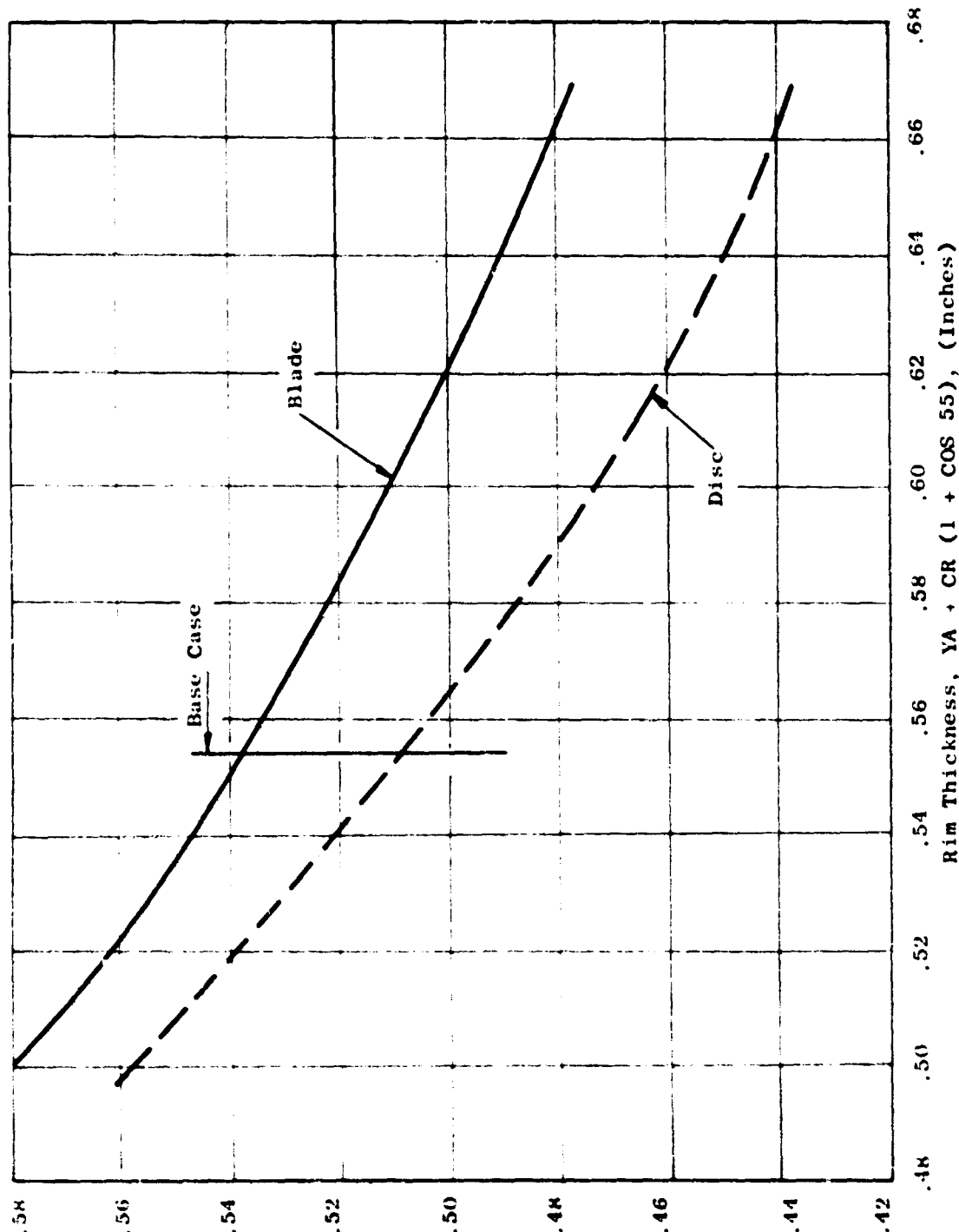


Figure 233 Percent of Dovetail Alternating Stress to Cause Simultaneous Failure of Dovetail and Airfoil Versus Contact Face Length



Allowable Dovetail to Airfoil Alternating Stress Ratio  
(Dimensionsless)

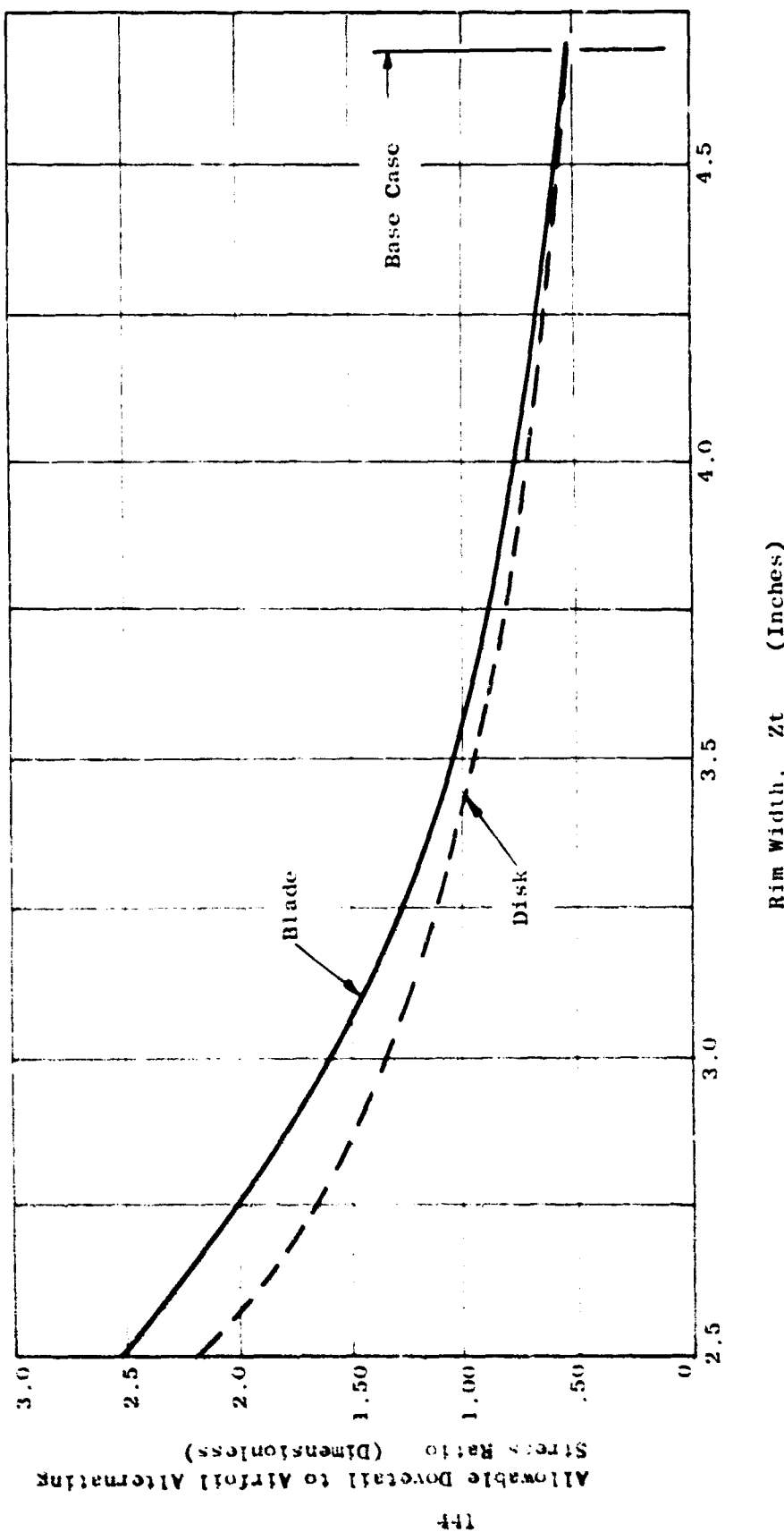


Figure 235 Percent of Dovetail Alternating Stress to Cause Simultaneous Failure of Dovetail and Airfoil Versus Rim Width

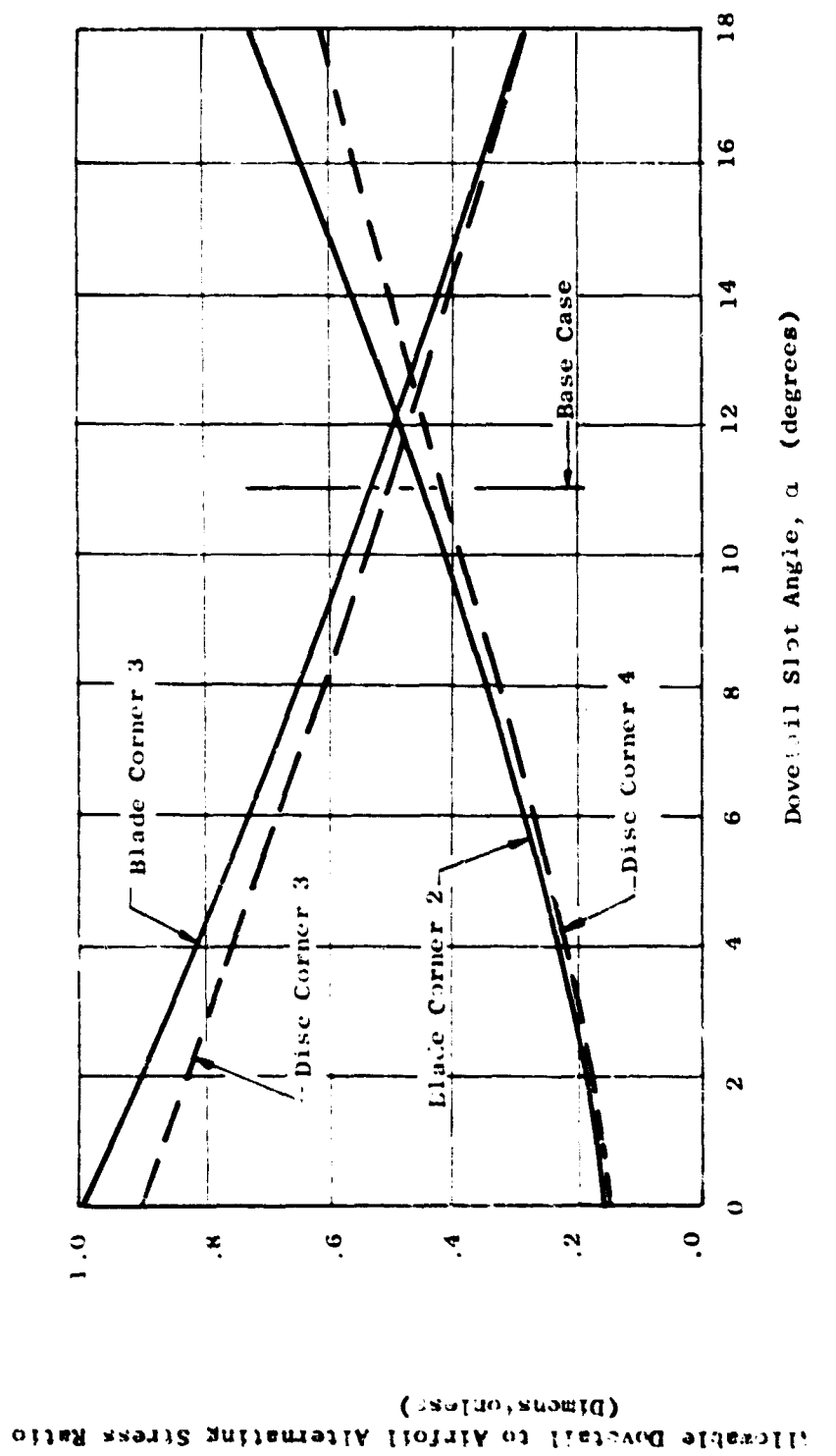


Figure 236 Percent of Dovetail Alternating Stress to Cause Simultaneous Failure of Dovetail and Airfoil Versus Dovetail Slot Angle

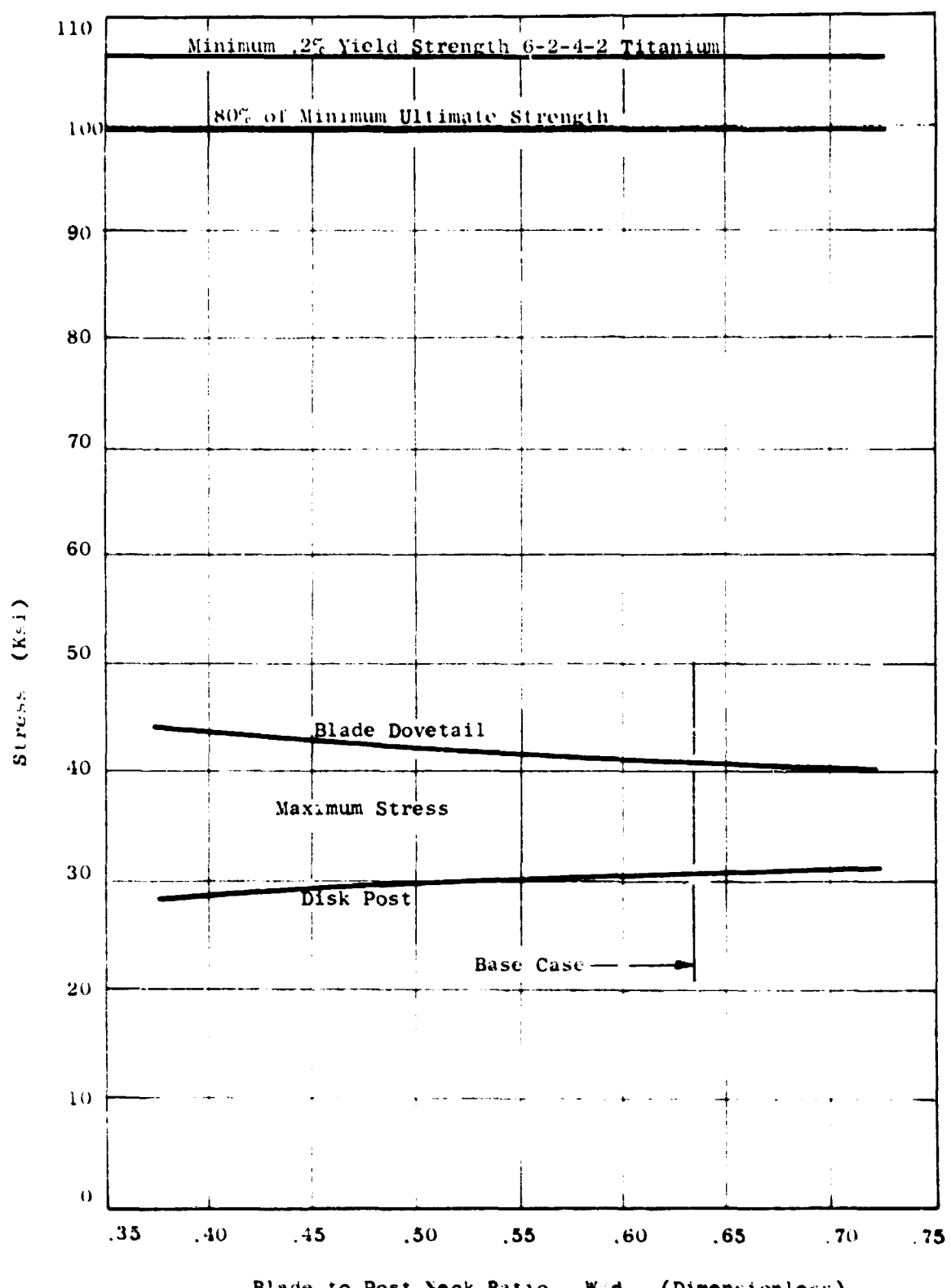


Figure 237 Max Dovetail Stresses Under Worst Maneuver Load Versus Blade to Post Neck Ratio Compared with Minimum Allowable 6-2-4-2 Titanium Properties

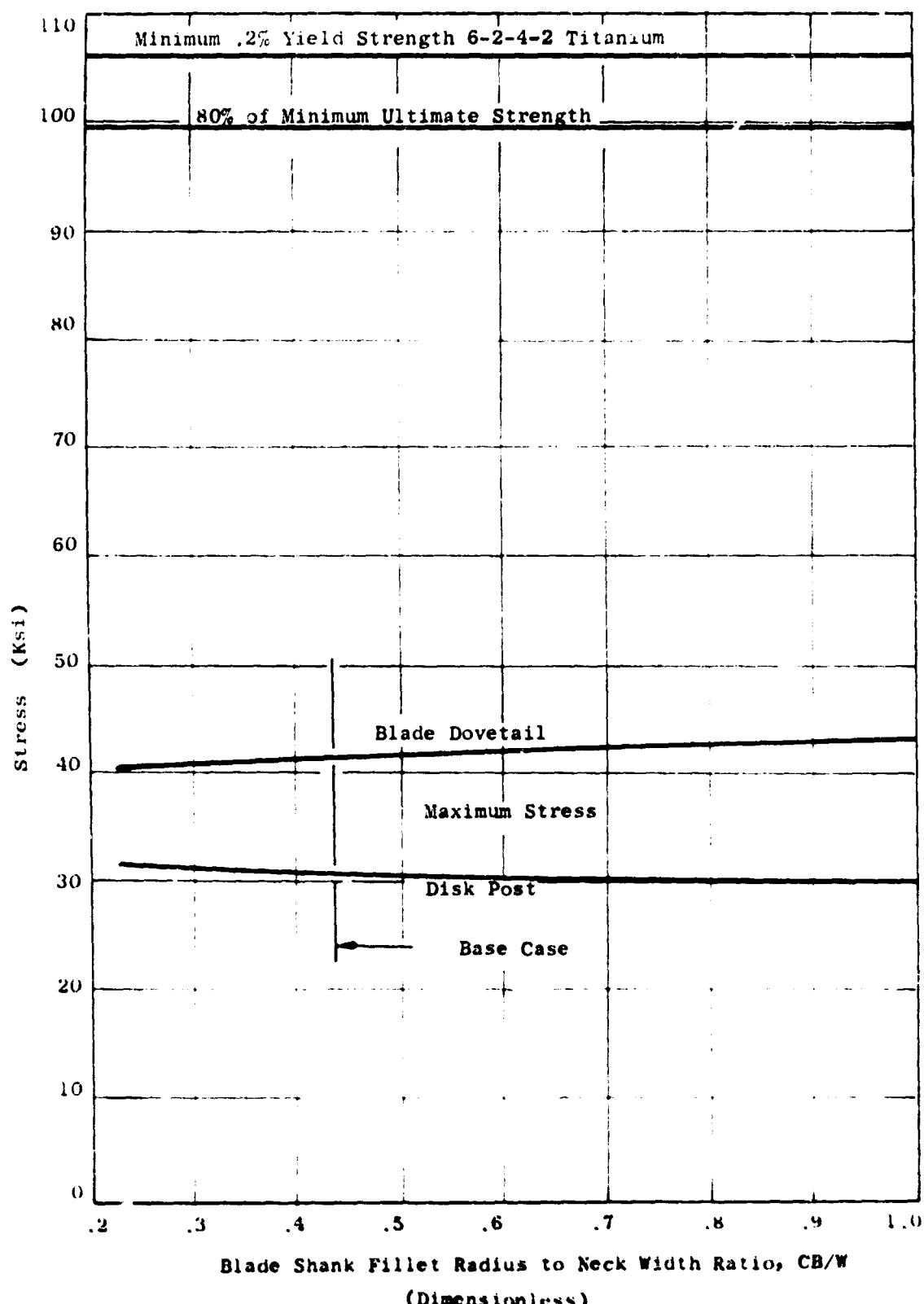
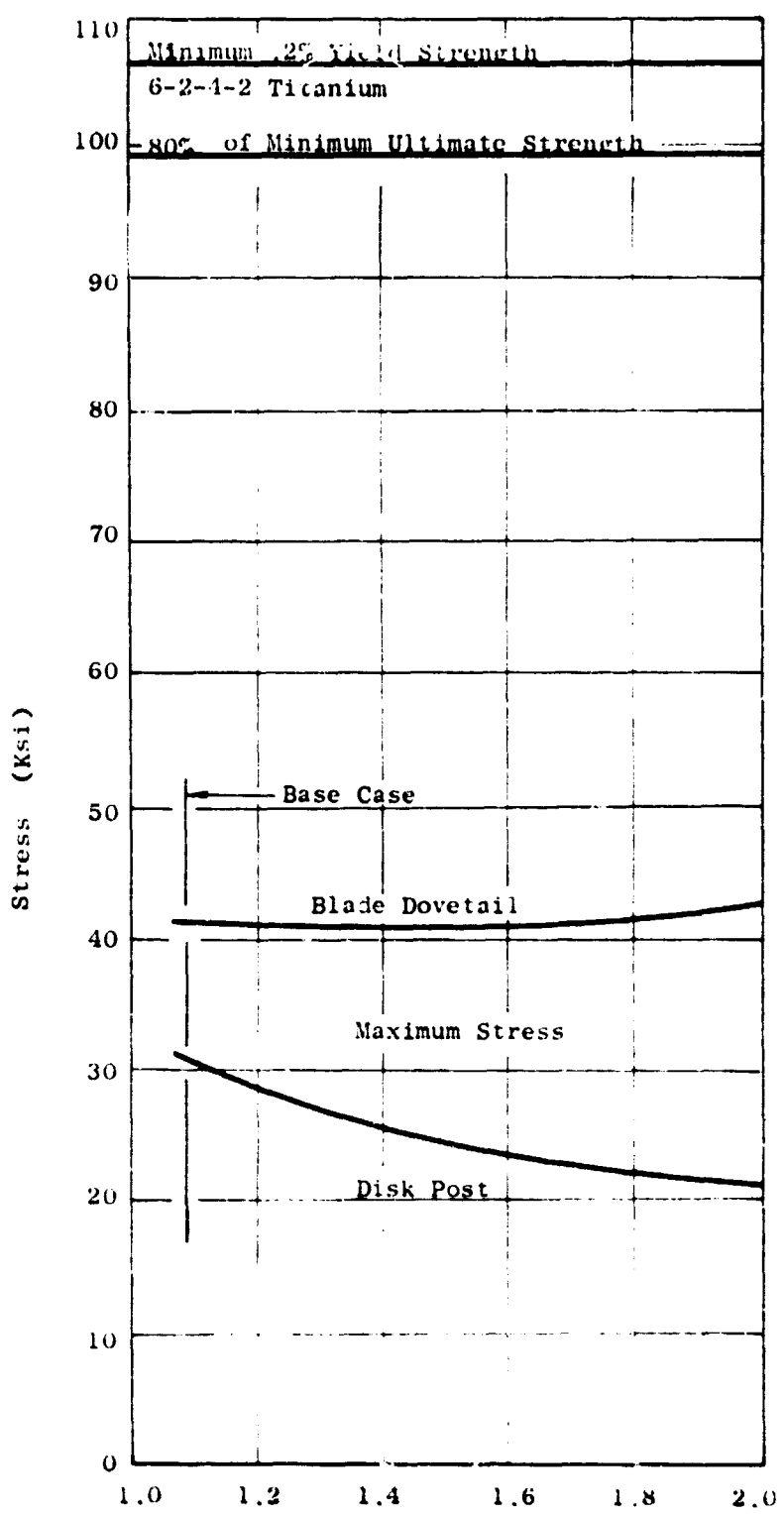


Figure 238 Max Dovetail Stresses Under Worst Maneuver Load Versus Blade Shank Fillet Radius to Neck Width Ratio Compared with Minimum Allowable 6-2-4-2 Titanium Properties



Post to Blade Tang Thickness Ratio,  $h_d / h_b$   
(Dimensionless)

Figure 239 Max Dovetail Stresses Under Worst Maneuver Load versus Post to Blade Tang Thickness Ratio Compared with Minimum Allowable 6-2-4-2 Titanium Properties

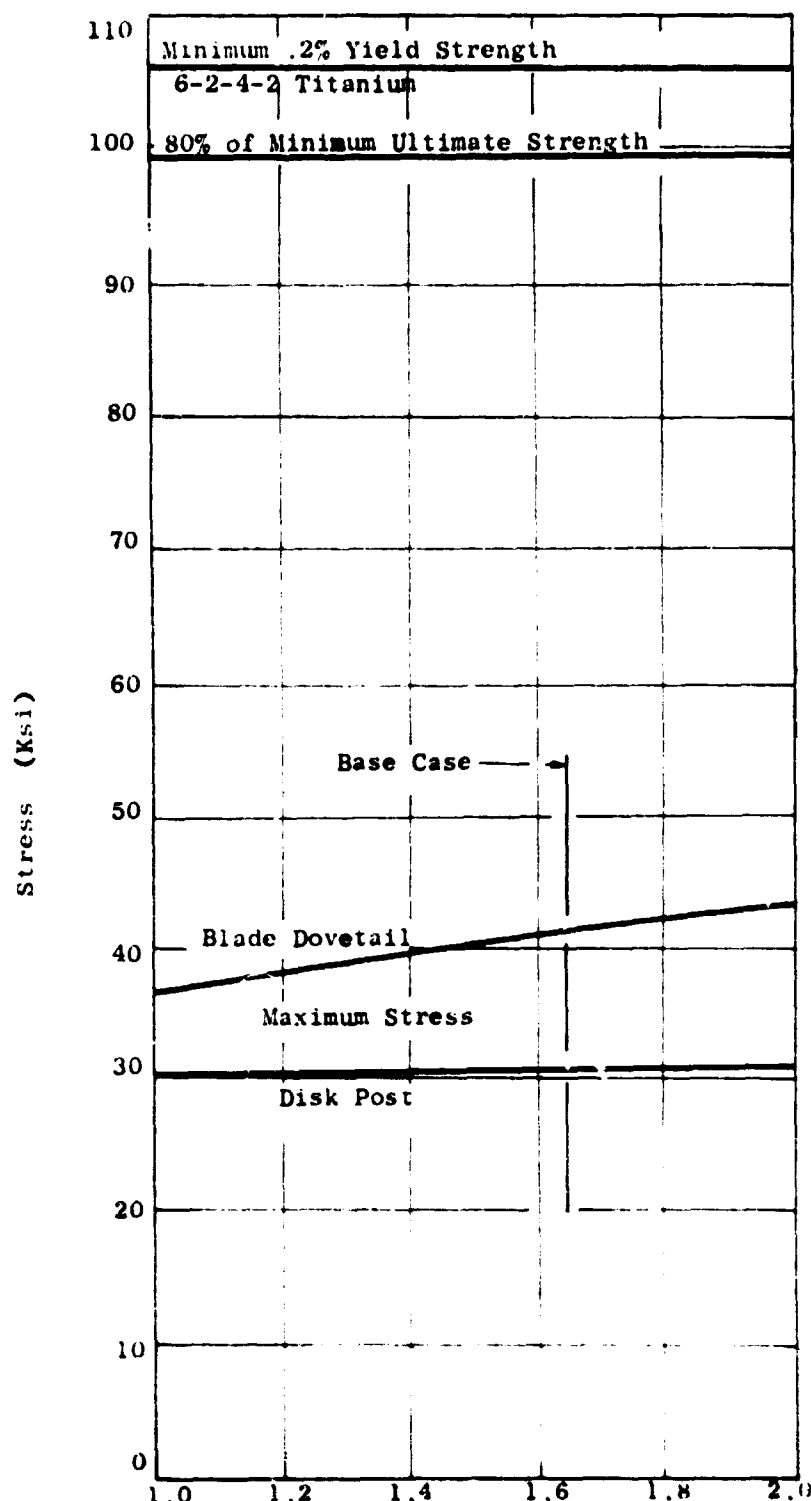
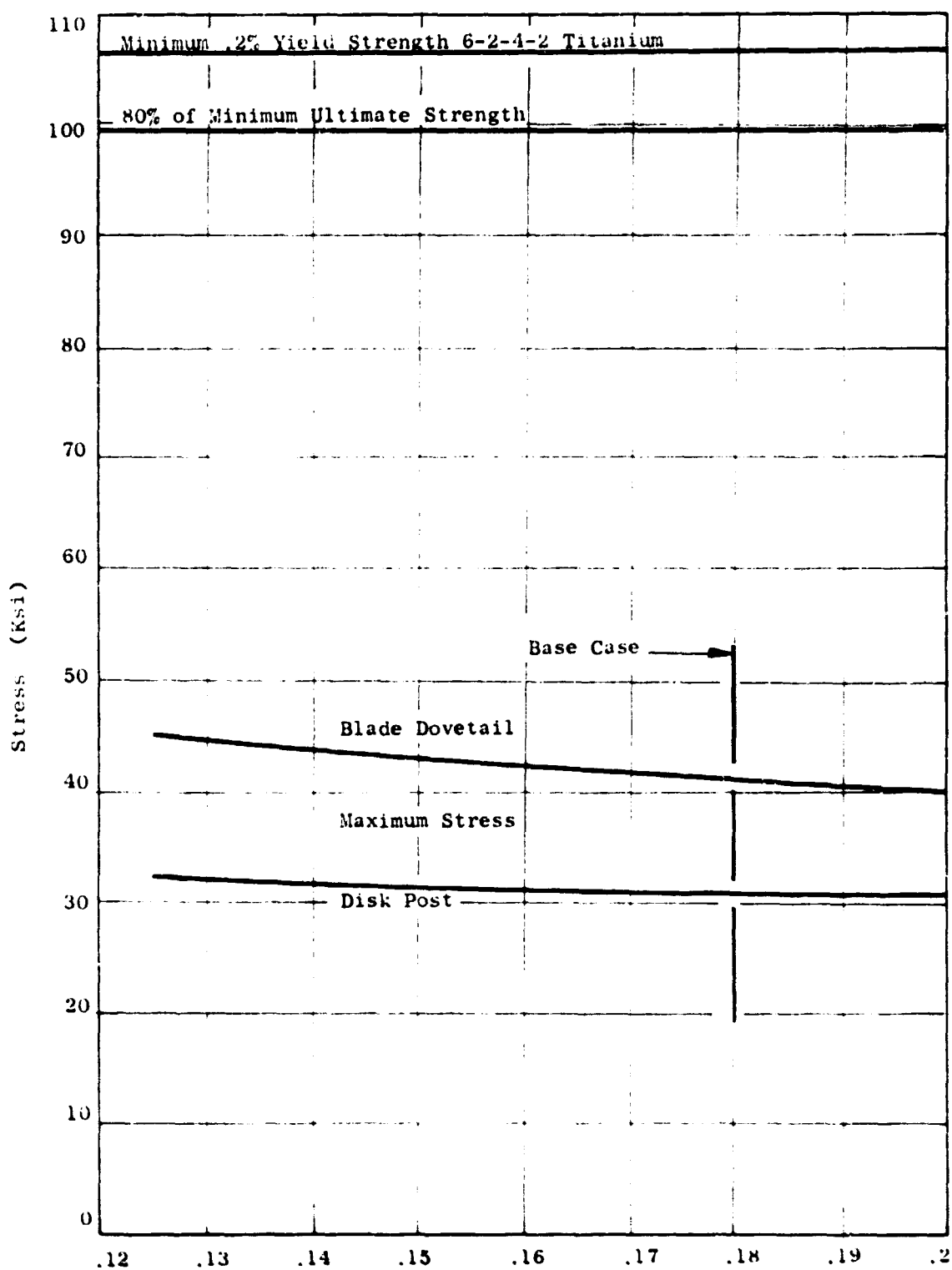


Figure 240  
 (Dimensionless)  
 Max Dovetail Stresses Under Worst Maneuver Load Versus Blade Shank to Disk Slot, Fillet Radius Ratio, Compared with Minimum Allowable 6-2-4-2 Titanium Properties



Contact Face Length, SBL (Inches)

Figure 241 Max Dovetail Stresses Under Worst Maneuver Load Versus Contact Face Length Compared with Minimum Allowable 6-2-4-2 Titanium Properties

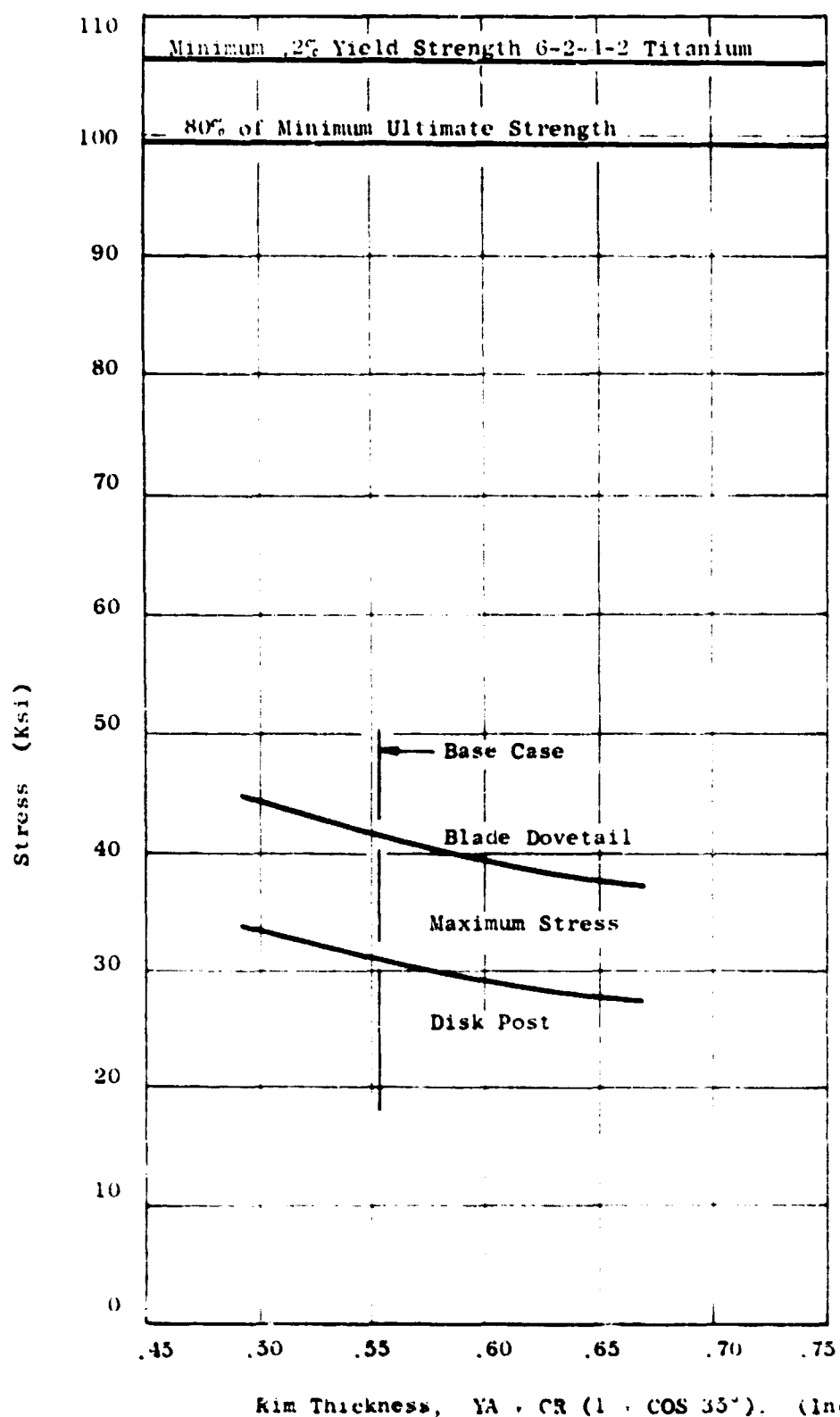


Figure 242 Max Dovetail Stresses Under Worst Maneuver Load Versus Rim Thickness Compared with Minimum Allowable 6-2-4-2 Titanium Properties

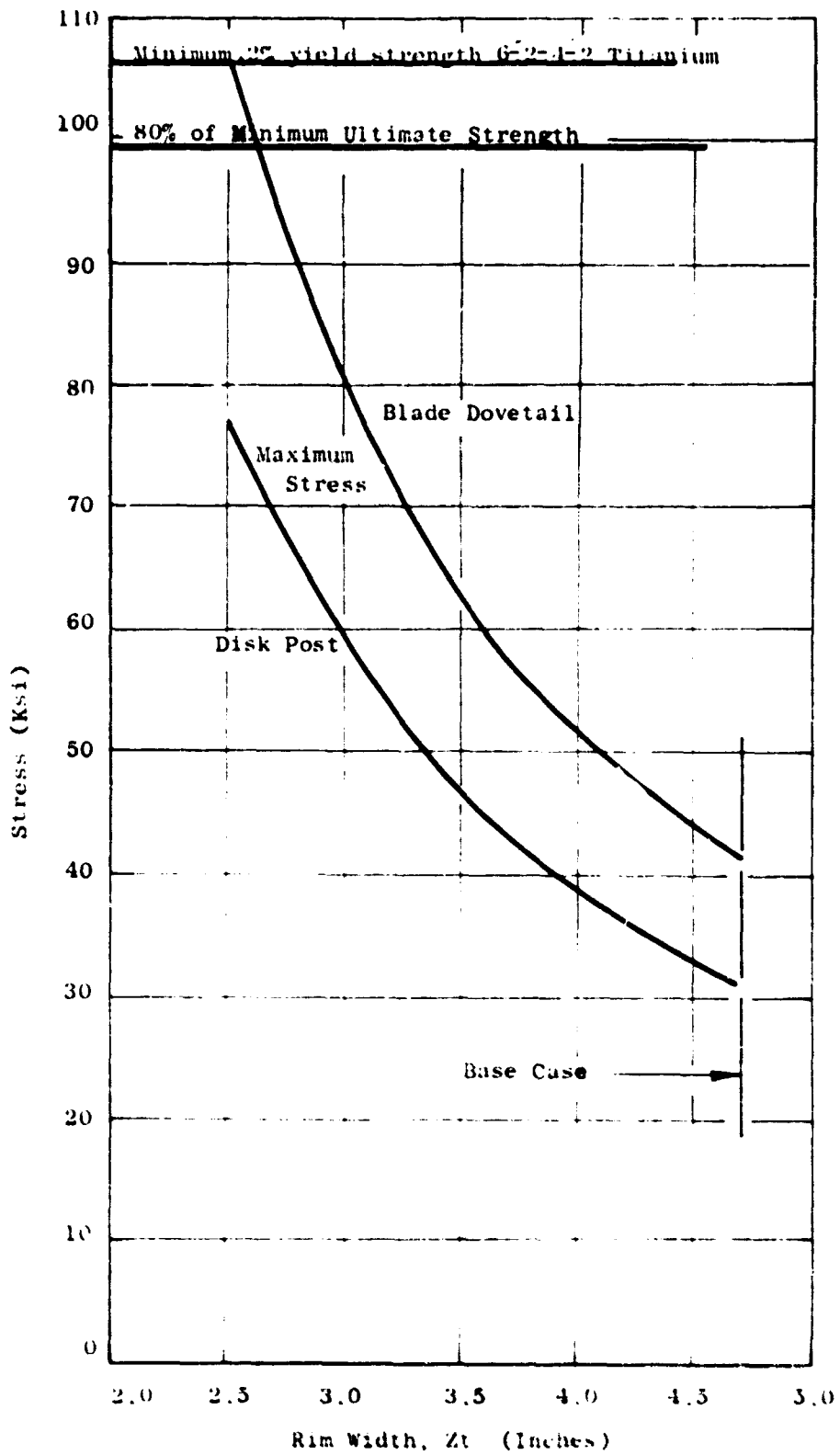


Figure 243 Max Dovetail Stresses Under Worst Maneuver Load Versus Rim Width Compared with Minimum Allowable 6-2-4-2 Titanium Properties

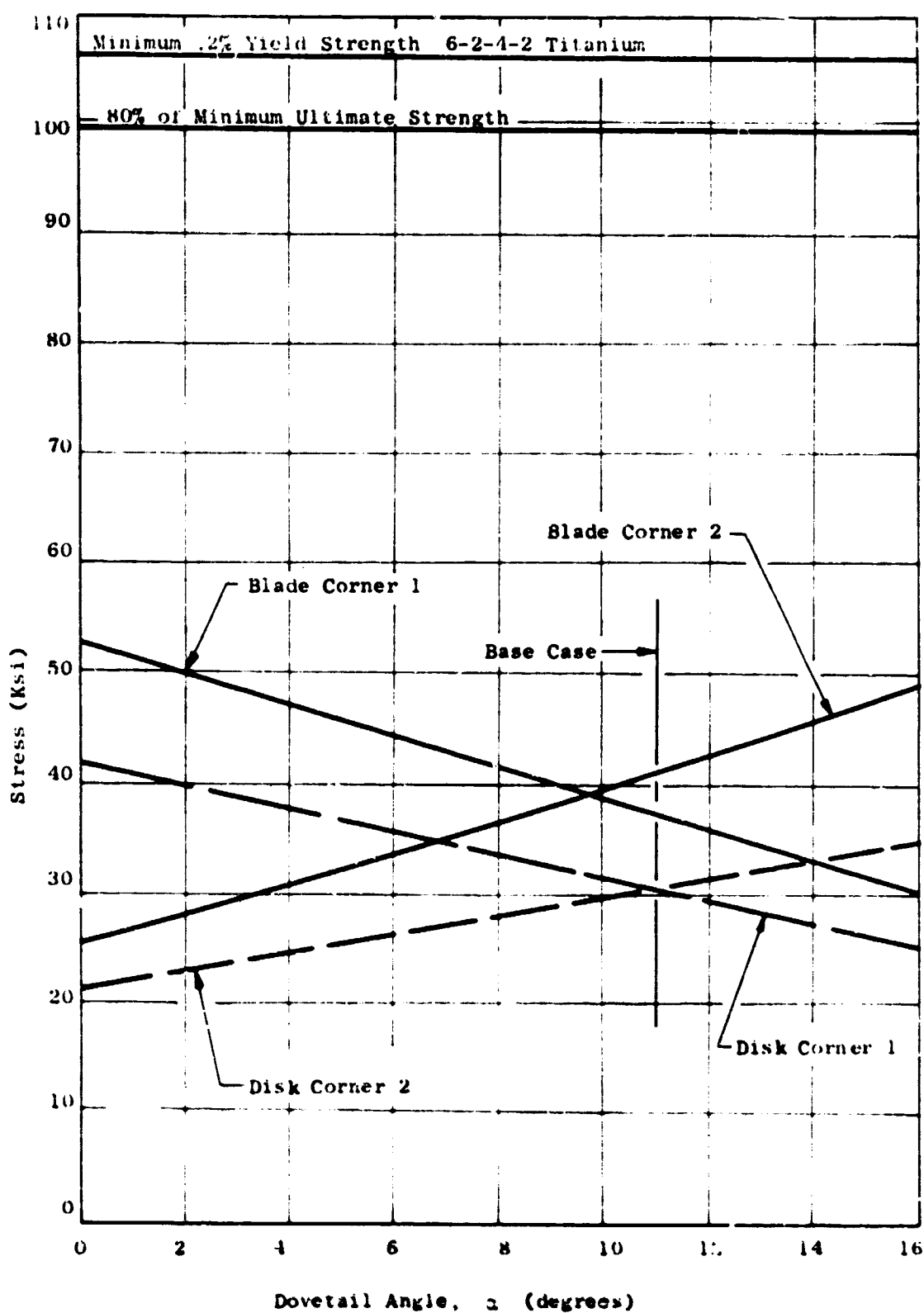


Figure 2-4 Max Dovetail Stresses Under Worst Maneuver Load Versus Dovetail Slot Angle Compared with Minimum Allowable 6-2-4-2 Titanium Properties.

### Circular Arc Dovetail Analysis

(U) The circular arc dovetail analyzed had a cross section identical to the cross section of the base case straight dovetail. The blade section at the top of the rim found by smoothly extrapolating the blade coordinates to this radius has a meanline camber, stagger and chord of  $60^\circ$ ,  $13^\circ$  and 4 inches respectively. These numbers and the section as discussed above define the circular arc dovetail analyzed. Figure 245 shows fore, aft, and top views of this dovetail with shank, platform and the root portion of the blade.

(U) The effects of the changes in section studied under straight dovetails apply also to changes in section for circular arc dovetails. The only variable peculiar to circular arc dovetails is the radius of curvature. The only value used was that which corresponds to the blade shape at the top of the shank. No other radius of curvature is of particular interest as the purpose of the circular arc dovetail is to make the dovetail and shank conform smoothly to the shape of the blade.

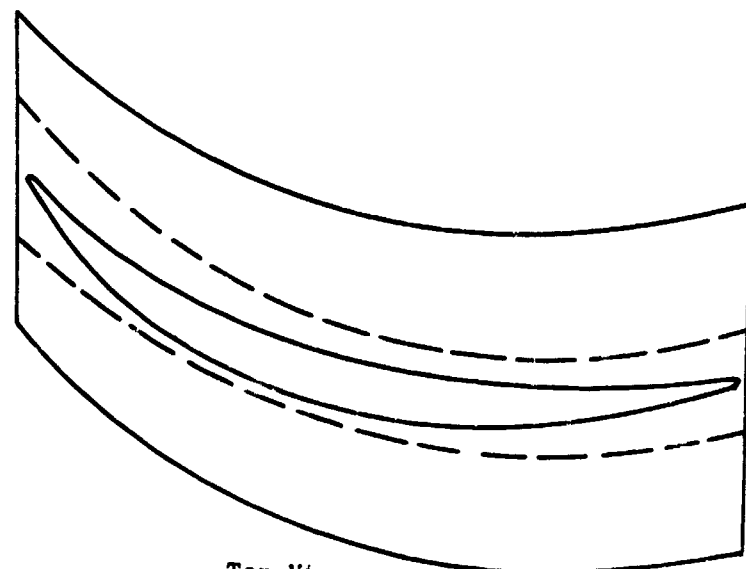
(U) Stress analysis of this dovetail was done using the procedures developed for circular arc dovetails as reported in Reference 5 through 8.

### Results

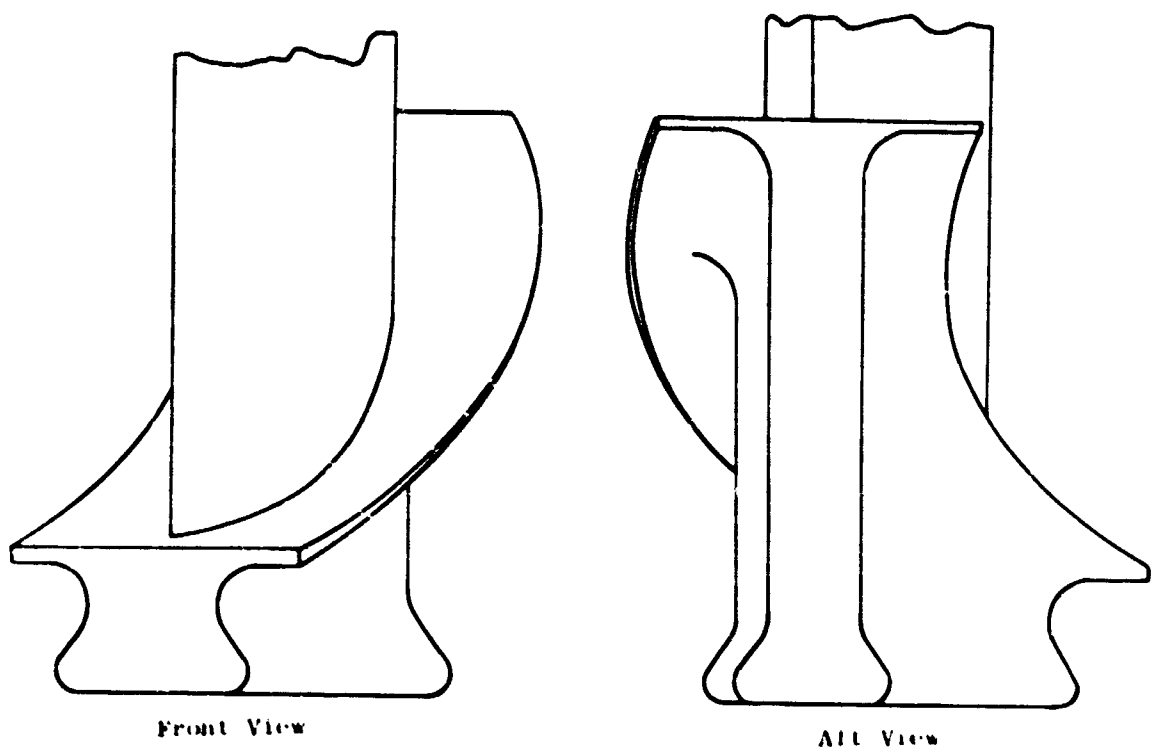
(U) Figure 225 shows the base case dovetail and post corner stresses plotted on the 6-2-4-2 Titanium stress range diagram. The worst corner for both the blade and the post is corner 3. At each corner the blade dovetail stress is closer to the material limit than the post stress. The loads used in the dovetail analysis were those that made the airfoil stress fall on the material limit line as shown. The base case is shown to have considerable margin in this figure. The results of the geometric studies will show how to best reduce dovetail weight in exchange for this excess margin.

(U) The next eight figures present the results of geometric configuration studies in terms of the ratio of alternating stress to allowable alternating stress. In Figure 225 the worst corner of the post and dovetail is corner 3, as in the base case except as noted.

(U) Figure 229 presents the effect of blade neck to post neck width ratio on allowable vibratory stress. As the ratio of blade neck to post neck width increases from a low value, the percentage of allowable alternating strength required by the blade decreases and that required by the post increases. The curves cross at a  $W/d$  ratio of less than unity because the post neck has to carry the centrifugal load due to the post as well as the load applied by the airfoil. The base case has a post about 3% stronger than the blade dovetail which is consistent with the design criteria of making the post stronger than the blade.



Top View



Front View

Alt View

Circular Arc Dovetail with Shank, Platform, and Blade Root

Figure 245

(U) Figure 230 shows the effect on allowable alternating strength of the ratio of blade shank fillet radius to blade shank (neck) width. Decreasing the neck thickness increases the neck tensile stress while decreasing the fillet radius increases the stress concentration factor. The base case geometry appears to have a nearly optimum trade between these two dimensions. This study was not run on the post.

(U) The effect of increasing the ratio of post to blade tang thickness is presented in Figure 231. As this ratio is increased, the point of load transfer from blade tang to post tang moves closer to the root of the blade tang. This decreases the bending moment in the blade tang, but it also decreases the load carrying section of this tang. The figure indicates the optimum ratio is in the vicinity of 1.3 to 1.35 for the configuration under study which is a little higher than the base case.

(U) Looking at a dovetail it appears evident that the stress levels in the two portions must depend to some extent upon the relationship between their tang fillet radii. To investigate this question a study was made varying the ratio of blade shank fillet to disk slot fillet keeping all other defining dimensions and the sum of the two fillet radii constant. The results of this study are shown in Figure 232. It is interesting that as the ratio of blade to disk fillet radius is increased the worst corner stresses of both the blade and the disk dovetails increase. It is logical that the post stress increases as its fillet becomes smaller. A smaller fillet not only increases the stress concentration factor, but it also reduces the post neck width a little with the geometry defined as it was.

(U) It is less obvious why the blade stress goes up with increasing blade shank fillet radius. Two factors influence this trend. One factor is the rapid reduction in blade tang height with a reduction in post fillet radius. The second factor is the relative insensitivity of blade stress concentration factor to fillet radius when the blade to post fillet radius ratio is greater than one. This relative insensitivity is not too surprising when you recognize the loads are greater on the post as it must carry its own weight as well as that of the blade; that the blade has a shoulder fillet while the post has a notch fillet; and that the relative sizes of the two dovetail portions are not very different for the case under study.

(U) Previous Lift Fan dovetails have had CB/CR ratios of between 1.5 and 5.2. For the loads and basic geometry of this study the optimum CB/CR is about .85. The factors mentioned above which tend to reduce the optimum level of this ratio are enhanced by having more blades. This fan has more blades than any previous Lift Fan so it is not surprising that its optimum falls outside previous design experience.

(U) In Figure 233 are displayed the results of varying the length of the pressure face. As would be expected with a fixed number of dovetails in a rim of fixed diameter an increase in the length of the pressure face decreases the stress in the face of the dovetail, but by reducing the neck thickness the post stresses are increased. For this study the post neck (and therefore post stress) was kept at a relatively constant level by adjusting the geometry so an increase in face length reduced blade neck width more than post neck width. This figure shows that increasing face length could reduce stress levels, however, it would be done at the expense of increased weight.

(U) Increasing rim thickness reduces stresses as shown in Figure 234 by allowing both tangs to get stronger. As rim weight is directly proportional to rim thickness, the derivative of worst corner stress with weight for a change in rim thickness can be determined directly from this figure.

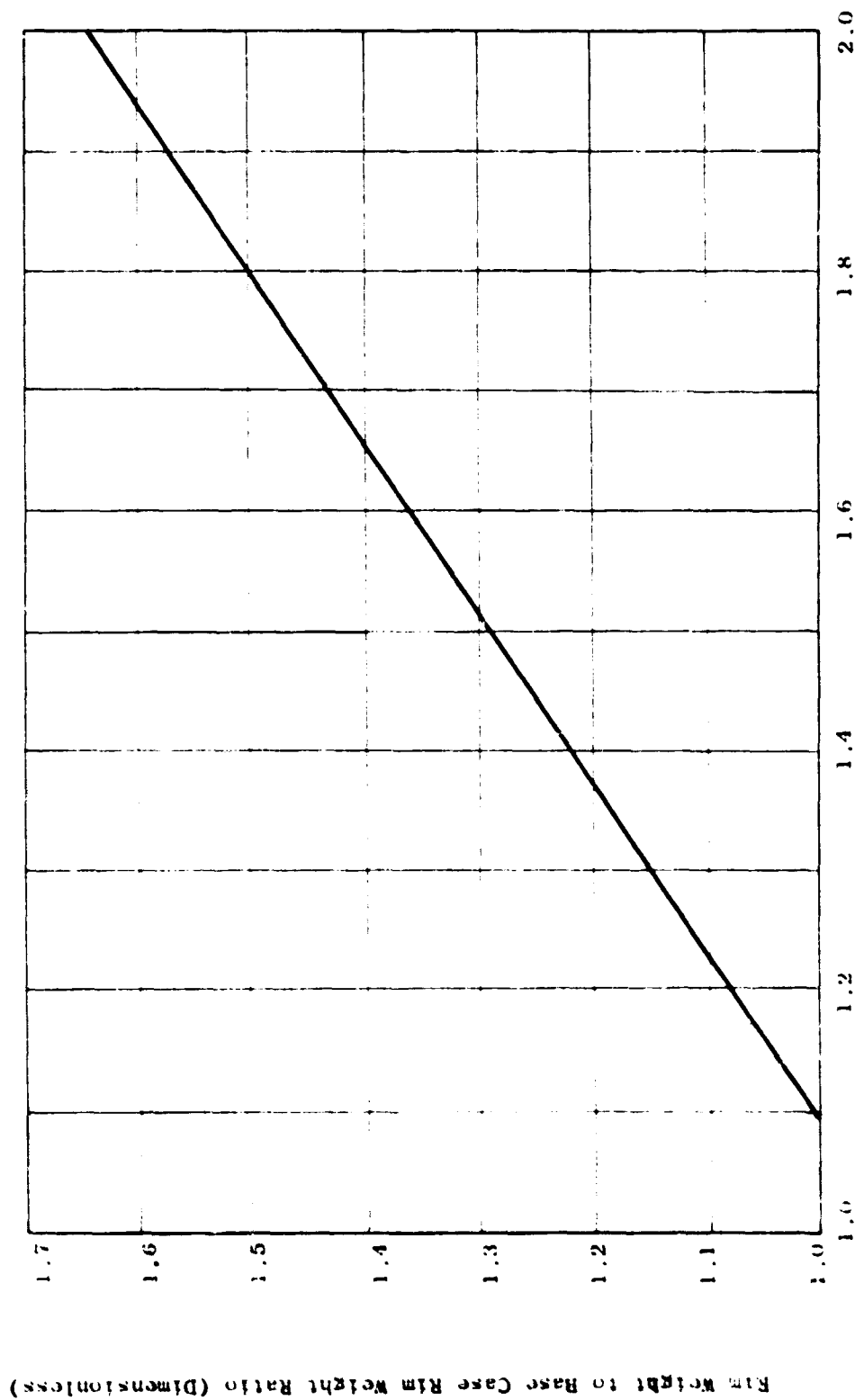
(U) The relationship between stress and rim width is shown in Figure 235. Again rim weight is directly proportional to the abscissa. This figure points out that with the base case section, a rim width of less than 3.6 inches would result in a blade dovetail with less strength than the airfoil which would violate one of the design criteria.

(U) Figure 236 shows that corner 2 becomes the corner with highest stress at a slot angle greater than about 12 degrees. Thus the base case angle is within a few degrees of an optimum distribution of stresses between the two worst corners.

(U) The next eight figures 237 through 244 compare the effects of the same geometric variables (in the same order) under the worst combined aero, centrifugal and maneuver loads with the allowable short time properties of 6-2-4-2 titanium. The trends are similar to those just discussed. In all cases we have greater combined stress strength in the dovetail than in the airfoil, the worst short time peak stresses are less than 60% of minimum material allowables.

(U) Three of the eight dimensional parameters being studied have no significant effect on rim weight. A change in the ratio of blade shank to post neck width,  $w/d$ , just transfers weight between the two parts of the dovetail. Changes in the ratio of blade shank fillet radius to shank neck width,  $CB/W$ , has only a very slight effect on rim weight though it does effect the weight of the shank portion of the blade a little. Dovetail slot angle, has no effect on rim weight for a given dovetail section configuration.

(U) The study of the effects of post to blade tang height,  $hd/hb$ , was done keeping the blade tang height constant and increasing the post tang height. The rim weight increased linearly with the increase in tang height ratio. This is illustrated in Figure 246.



Post to Blade Tang Thickness Ratio,  $hd/hb$  (Dimensionless)

Figure 2-16 Change in Rim Weight with Post to Blade Tang Thickness Ratio

(U) An increase in the ratio of blade shank to disk slot fillet radius ratio caused a gradual decrease in rim weight as shown in Figure 247. This is logical as the study was run in a way that maintained post tang height and decreased blade tang height with increasing blade shank fillet radius. Thus rim thickness decreased as blade shank to disk slot fillet radius ratio increased.

(U) An increase in contact face length, SBL, directly increased rim thickness and therefore rim weight as shown in Figure 248. Linear relationships between rim weight and both rim thickness and rim width were found as expected and are portrayed in Figures 249 and 250.

(U) In Reference 1, the author points out that, "it appears that the best curved dovetail will always have higher peak stresses than the best straight dovetail for the same profile and same axial width". This statement is born out in our case by Figure 251 which compares corner stresses for the circular arc dovetail with those for a straight dovetail with the same section, rim width and stagger angle. Five of the six corner stresses are higher for the circular arc configuration. Four of these corners have higher stresses than the worst corner on the straight dovetail.

(U) Preliminary test results from other projects have indicated that for rims supported by a single web disk, these peak stresses at dovetail ends are relieved due to deflections to a greater extent than for straight dovetails. However, lift fan rotors are designed with two webs which result in a much stiffer rim, so there is less deflection and the ends of curved dovetails will be required to carry the higher loads and stresses.

(U) Circular arc dovetails have been used in demonstrator jet engines to facilitate assembly in highly cambered, high solidity, unshrouded blade rows where they make it possible to assemble a single blade at a time.

(U) In a shrouded rotor such as the LF475, however, design studies showed that no ease of assembly advantage can be gained by using curved dovetails. This is because the LF475 blade has an integral midspan shroud and turbine sector both designed to prevent blade twist. If the blade had a circular arc dovetail on it there is only one possible assembly procedure. The dovetail slot would have to be deep enough so that each blade in turn could be rotated along the curve of the dovetail into the plane of the rotor, but at a lower radial position so that the midspan shroud and the turbine carrier can clear those of the next blade. Once the blade is in the plane of the rotor it could then be moved radially outward into position with the dovetail faces in contact. A spacer would then have to be inserted between the base of the blade and the bottom of the slot. The depth of the slots in the rim required to do this would double the weight of the rim. Even with a mechanical

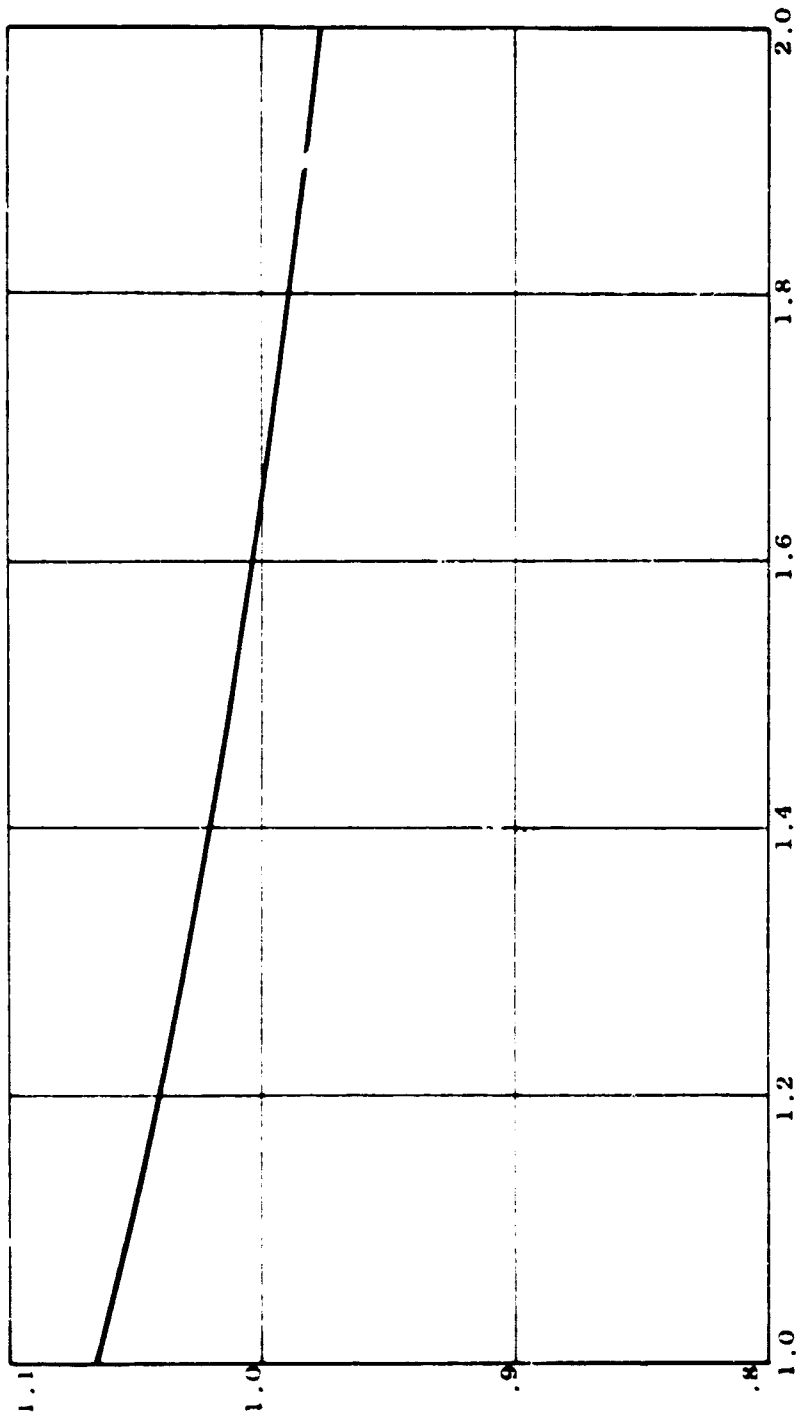


Figure 2-47 Change in Rim Weight with Change in Blade Shank to Disk Slot Fillet Radius Ratio

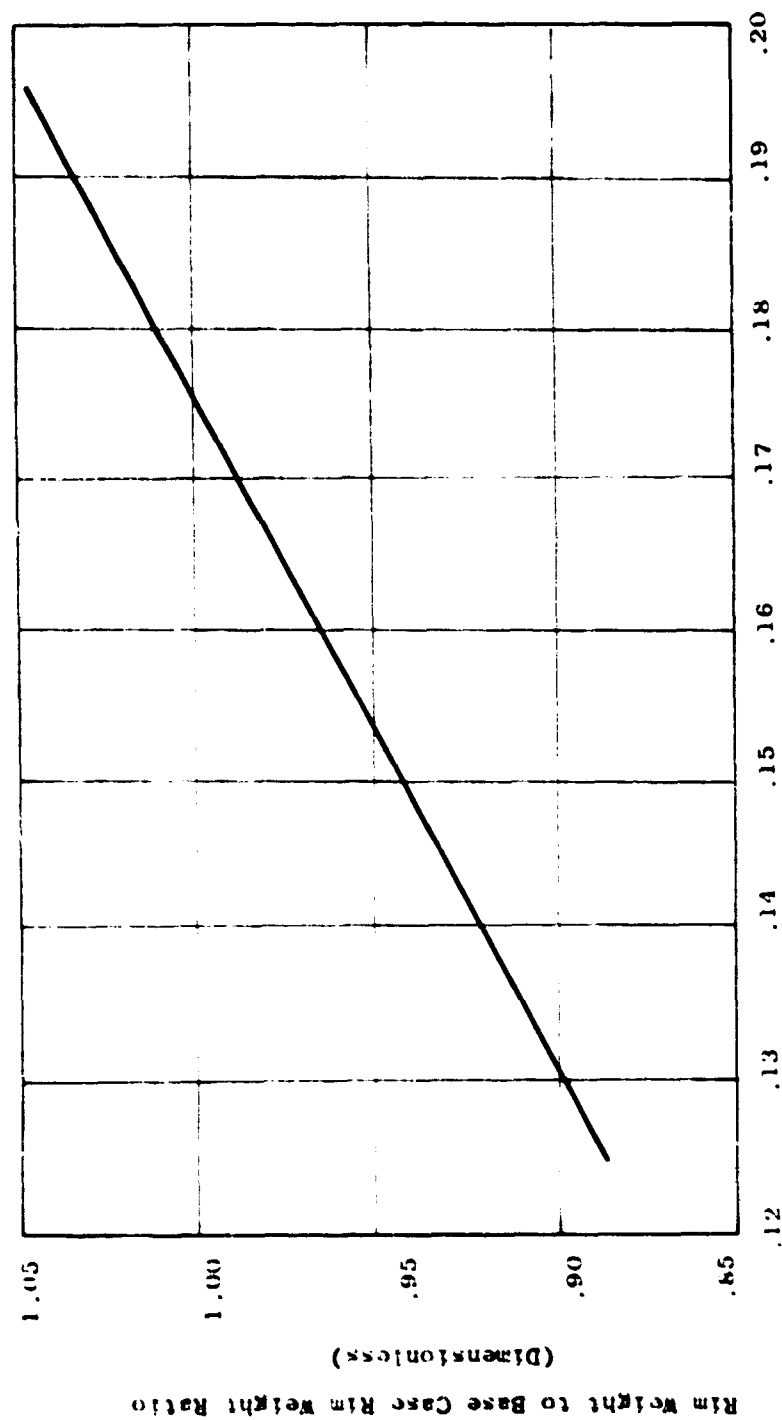


Figure 248 Change in Rim Weight with Contact Face Length

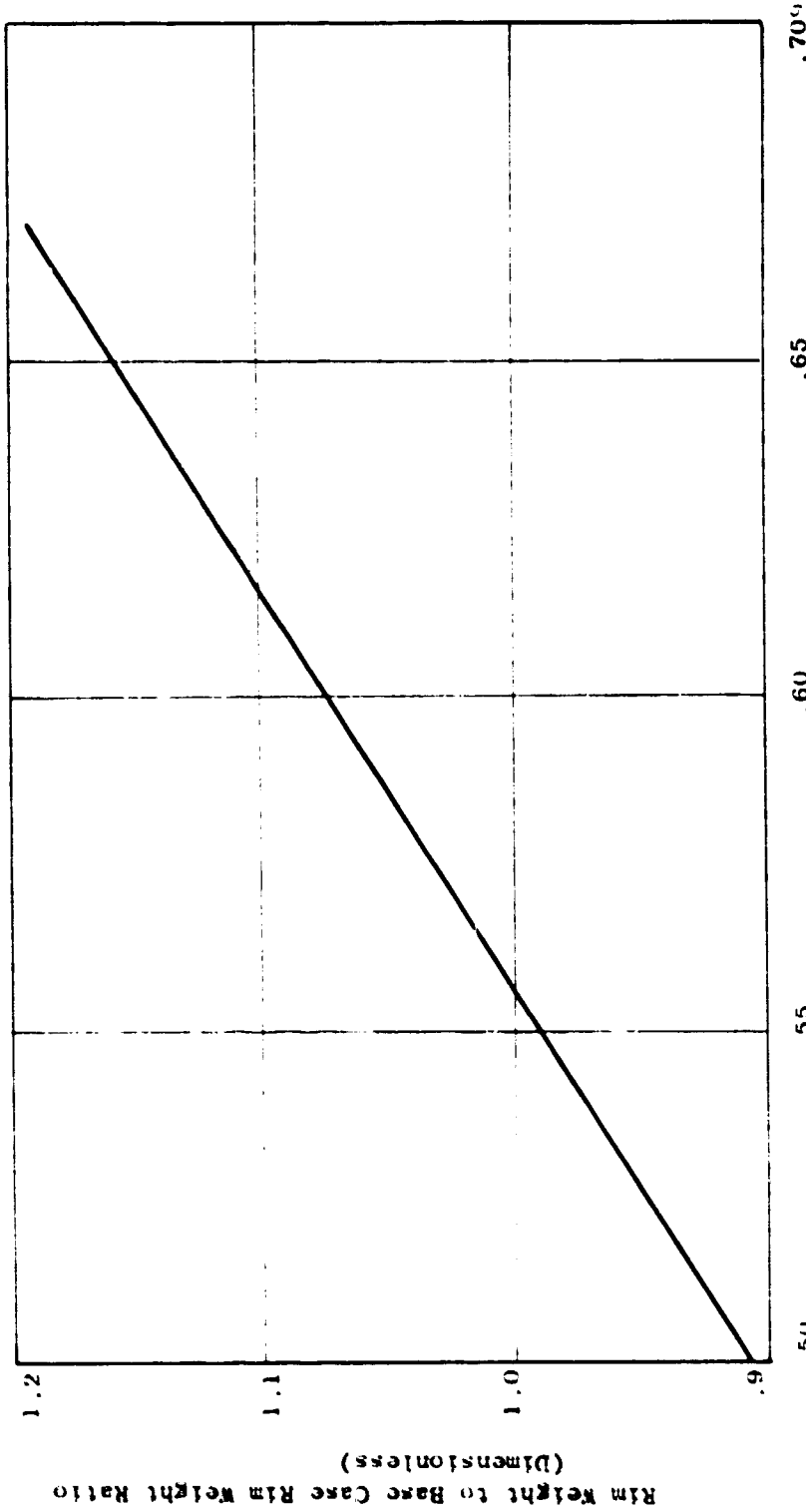


Figure 249 Change in Rim Weight with Rim Thickness  
Rim Thickness,  $Y_A + CR (1 + \cos 55^\circ)$ , (inches)

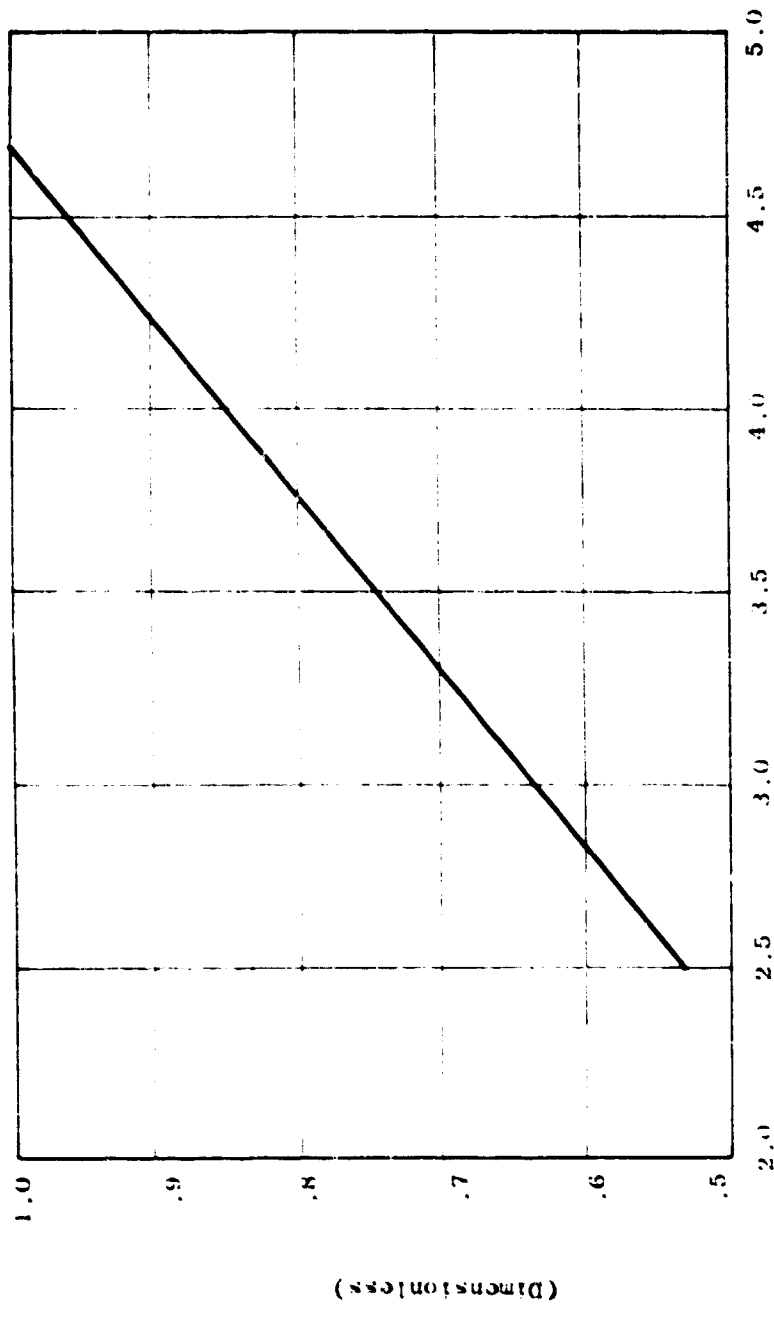


Figure 250 Change in Rim Weight with Rim Width

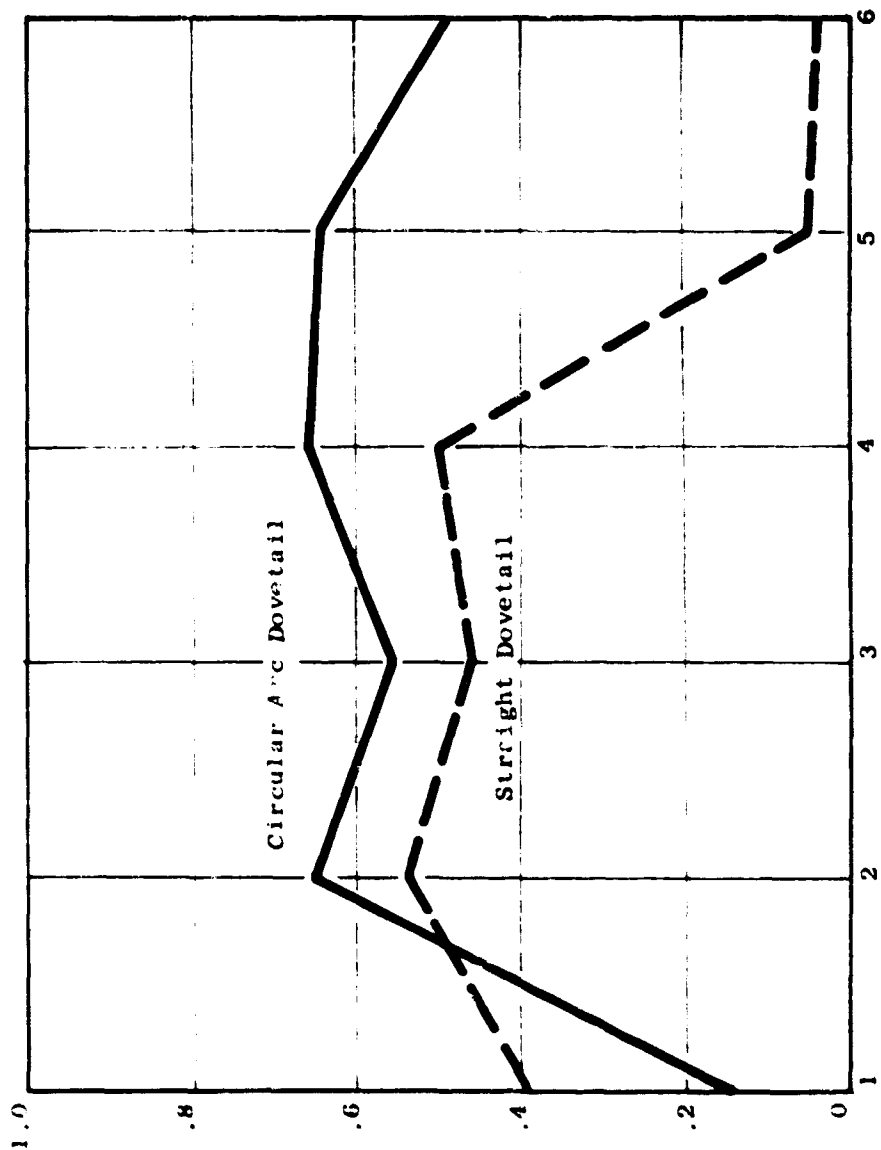


Figure 251  
Comparison of Percent of Dovetail Alternating Stress to Cause Simultaneous Failure of Dovetail and Airfoil as a Function of Dovetail Corner for Straight and Circular Arc Dovetails of Identical Section, Rim Width and Stagger Angle

joint in the blade inside the midspan shroud radius, the outer portion of the blades and the turbine would have to be assembled as a unit prior to being attached to the inner portion.

### Summary

(U) The variation in geometry resulted in similar trends under both combined stress and worst maneuver loading. The level at which optimum strength or weight occurred, however, did change some. In evaluating the results, allowances must therefore be made for the fact that final design loads may be different from those used here. Also final analyses must at least consider the effect of combined stress under several different modes of vibration.

(U) The effect of increasing the blade to disk neck width ratio from the base case was to reduce the stresses in the blade dovetail and the margin of post strength over blade dovetail strength. For the loading used in the study the base case value of  $W/d$  appears to be a little low but within a few percent of optimum.

(U) For the loading used, the ratio of blade shank fillet radius to shank or neck width in the base case yields the minimum combined stress in the blade dovetail.

(U) Post to blade tang height ratio change produced very little change in blade dovetail stress over the range of study. Post stresses dropped as this ratio increased. The margin of post to blade dovetail strength is adequate with the base case geometry. An increase in  $h_d/h_b$  could be counter balanced by an increase in blade to post neck width  $W/d$  to produce a net reduction in stress levels. Increasing  $h_d/h_b$ , however, also increases weight so it is doubtful that this approach would improve the design significantly.

(U) Lengthening the contact face length reduces stresses in the blade dovetail without effecting post stresses much, however, it also increases weight. Keeping a reasonable post to blade dovetail strength relationship the optimum contact face length appears to be very little greater than the base case value.

(U) Increasing either rim thickness or rim width reduces stress levels, but also increases weight. These variables can be used for "tuning" the final design to the desired stress level.

(U) The optimum dovetail slot angle varies somewhat with loading condition and between blade dovetail and post. The optimum range, however, appears to be between ten and twelve degrees which includes the base case point.

(U) The base case geometry is seen to be very nearly optimum. An optimum configuration could be found by reducing the blade shank

to post fillet radius ratio and then adjusting the rim width and thickness to achieve the desired stress level.

#### Comparison of Concepts

##### Stress. -

(U) The circular arc dovetail was found to have higher "worst corner" stresses than the straight dovetail with an identical section, stagger angle and rim width as was expected from other experience with curved dovetails. From strength considerations the straight configurations are better.

##### Ease of Assembly. -

(U) Blades with circular arc dovetails can be assembled one at a time only by making the dovetail slots deep enough so that the shroud segments clear each other while the blade is slid into position. It also requires a lower rim diameter to allow post-to-platform clearance. This in turn requires a longer blade shank. All of these factors increase the weight of the rim for a circular arc dovetail design.

(U) The same rim height and assembly procedure would be required with a straight dovetail if it was necessary to assemble the blades one at a time, however, with straight dovetails the entire set of blades can be assembled to the disk at once. This design approach saves several pounds of rotor weight.

(U) Straight dovetails rather than circular arc are required to minimize weight which is a primary design consideration for the LF475.

#### Conclusions and Recommendations

(U) The results show the base case dovetail section configuration is close to the optimum straight dovetail configuration for the conditions studied. It can be improved somewhat by reducing the ratio of blade shank fillet radius to disk slot fillet radius to less than unity. The data generated in this study and presented in this report will insure the rapid selection of an optimum dovetail configuration.

(U) A straight dovetail configuration was found to be better than the circular arc for this application because it has lower peak stresses, has significantly lower rim weight and makes it easier to assemble the shrouded blades to the disk.

(U) The proposed dovetail hardware program is not required.

## Hollow Blade Program

### Introduction

(U) The purpose of this program was to provide design engineering and evaluation support for the development of a manufacturing process for fabricated diffusion bonded hollow blades. This effort was divided into two phases number I and III to correspond with the phases of the MDLO Prime Program. Phase I effort would consist of design fabrication and test of specific flat panel airfoil simulated test specifications to define airfoil cross section design and establish process parameters. Phase III would consist of manufacture and component test of six full size LF475 hollow blades. Component testing and final evaluation of Phase III would be conducted by ACDO.

### Discussion

(U) The advanced fan design weight objectives were based on use of hollow titanium blade airfoils. Studies showed that the weight advantage for hollow titanium blades compared to solid titanium blades in the LF473 and L/CF470 sizes were:

	Hollow	Solid
Airfoil Weight (lbs)	95	146
Rotor Weight (lbs)	300	373
Fan Weight (lbs)	982	1123

Thus hollow blades appeared mandatory if objective thrust/weight values were to be met.

(U) Application of hollow compressor blade airfoils as a key element of weight reduction in large diameter turbomachinery is not new. The introduction of the diffusion bonding joining process, however, is a step change in technology which would permit the type of joint efficiency with the application of titanium alloys that make the significant gains of hollow blading become a reality.

(U) Diffusion bonding is a joining process that does not require the use of a filler material or melting of the parent material as in brazing or welding. To join materials by diffusion bonding, the interface of the joint must be clean and free of oxides and foreign material, and intimate contact must be provided while the joint is held at bonding temperature for a period of time. The joint is accomplished as the atoms at the interface acquire increased energy from the heat and, as a function of time, migrate across the joint growing continuous grains and producing a solid state bond.

(U) Advantages of the diffusion bonded process are:

- No cast material in the joint.
- No heat affected zone.
- Inclusion, porosity, and contamination minimized.
- No dissimilar metal in the joint.
- Micro cracking is eliminated.
- Elimination of joint shrinkage.
- Joint strength approaching parent metal strength.

(U) Applicable technology from other GE-Aircraft Engine Group hollow blade and diffusion bonding programs was used for a guide in starting this program.

(U) Major activity at GE in development of hollow diffusion bonded compressor airfoils utilizes two precision airfoil shapes generated and bonded together to form a single light weight hollow airfoil. This process is inherently expensive by requiring two precision shapes to yield one final precision component and it will require significant development in manufacturing and processing technology to reduce the cost of these types of compressor blading in advanced light weight turbomachinery.

(U) Hollow titanium blades considered for other GE propulsion systems have blade configurations varying from 5-inch long airfoils with 4-inch chords to 18-inch long airfoils with 6-inch chords. These airfoils are being designed using 6AJ-4V Titanium alloy and an internal longitudinal rib construction (Figure 252).

(U) The development of diffusion bonding of hollow titanium airfoils in other programs has produced the following results:

Failures in simulated airfoil specimens occurred in the parent material and were not associated with the bonded joint.

Artificial defects in the bonded joint did not cause failures, and in most cases were not propagated during the tests.

Ultrasonic inspection methods have proven successful for identifying bonding defects.

Manufacturing tooling and processes have been developed for producing full-scale compressor airfoils.

(U) Testing of two full-scale hollow blade configurations in other programs has shown a need for more investigation to identify optimum designs and to clarify the preliminary test results.

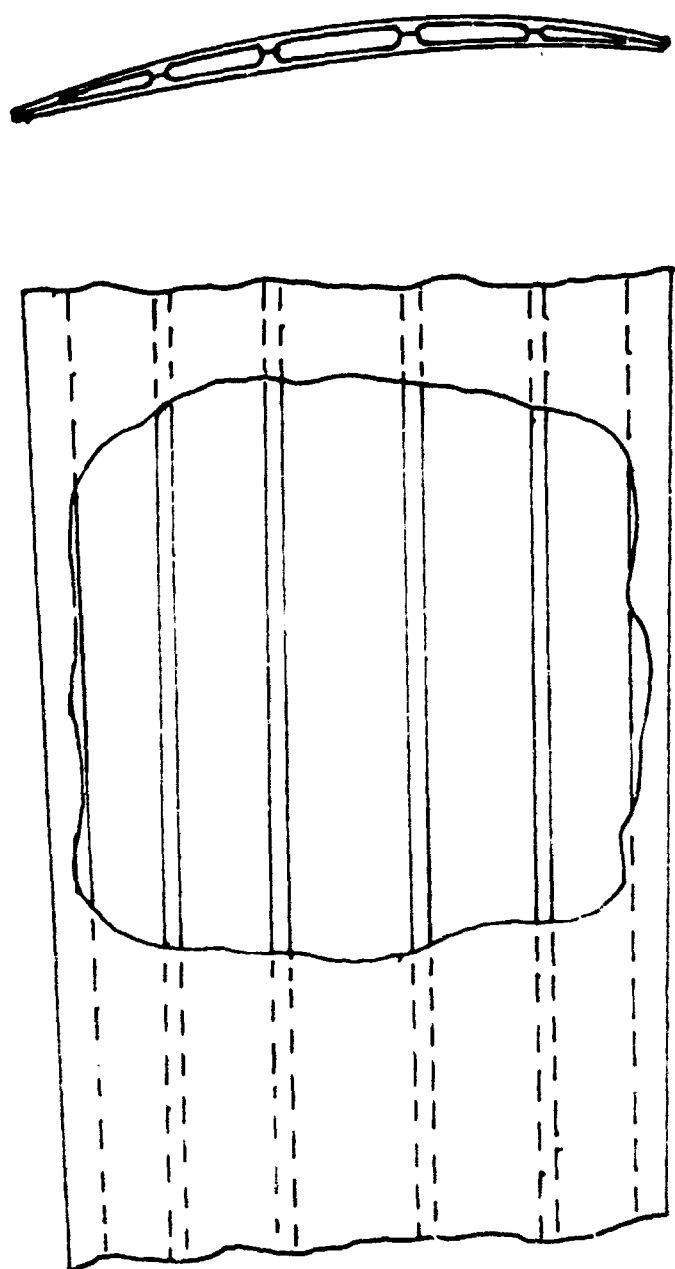


Figure 252 Waffle Type Hollow Blade Structure

Also, funding levels assigned to this component technology program were not sufficient by themselves to develop a completely new construction and process. The current component program had to deal with first order variables and attempt to maximize the application of current art, and work being conducted under other programs. Major program emphasis was placed on analysis and test of optimum state of the art geometry (Figure 252) in the LF475 size.

#### Analysis

(U) The complexity encountered in the analysis of these blades was due to difficulty in numerically describing the geometry of the airfoil and its internal configuration. The internal geometry was complicated not only by being contained in a twisted airfoil of varying camber and thickness, but also by the necessity of maintaining a smooth radial flow of section properties to avoid stress concentrations, particularly in the vicinity of the solid portions of the blade necessary for added stiffness, at the blade ends, and at the mid-span shroud.

(U) The mechanical design analysis of hollow airfoils was accomplished using the Twisted Blade program. A separate program was developed to calculate section properties for use in hollow blade design. It calculated the required input data for the Twisted Blade program for a blade with any number of arbitrarily shaped holes. Data predicted for the GE4 hollow blades by use of this program has been confirmed by test. Calculated vibrational frequencies were very close to the actual test values, with the exception of a 10 percent error in the first torsional mode. Calculations of stress versus tip deflection were within 10 percent of test results.

(U) In support of Phase I of the Hollow, Diffusion Bonded Titanium Blade process program being carried out by the Process Development group in the Materials Lab, two test specimens were designed. One of these was a simulated hollow blade panel (Figure 253) and one was a bending shear specimen (Figure 254).

(U) The simulated hollow blade panel specimen was designed to have approximately the same values as the LF475 hollow titanium blade for such parameters as  $tm/c$ ,  $te/c$  and hollow to solid section properties. It was also designed to have similar geometry in the transition areas between the hollow panel sections and the solid ends. Program cost limits dictated that these specimens be made from existing, partially machined blanks.

(U) The design intent behind this specimen was to determine the effects of this geometry on the assumptions in the pertinent analytical programs. This information would either confirm the validity of the analytical tools or provide correction factors to apply to the analysis of the LF475 Blade.

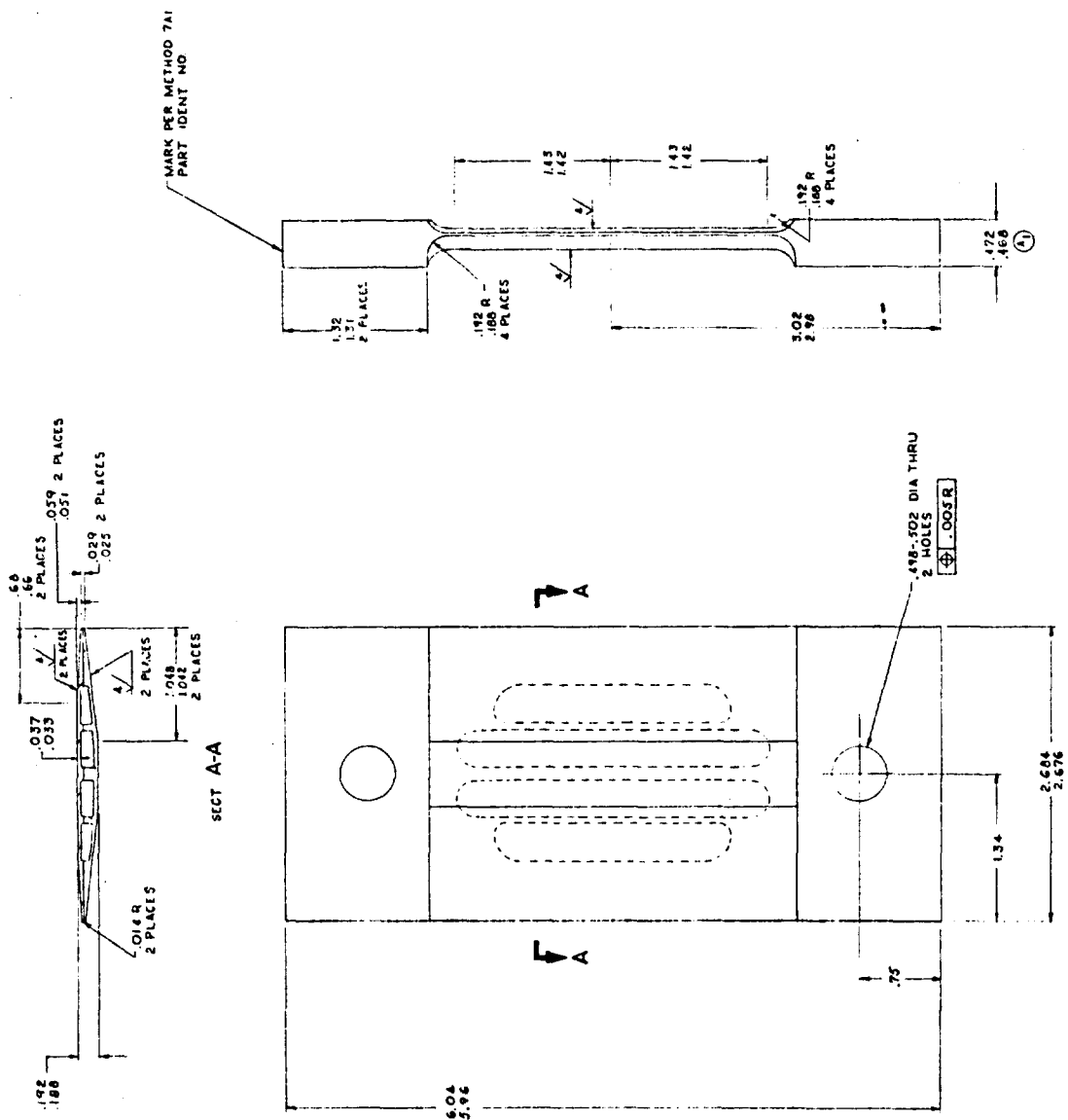


Figure 253 Hollow Blade Specimen

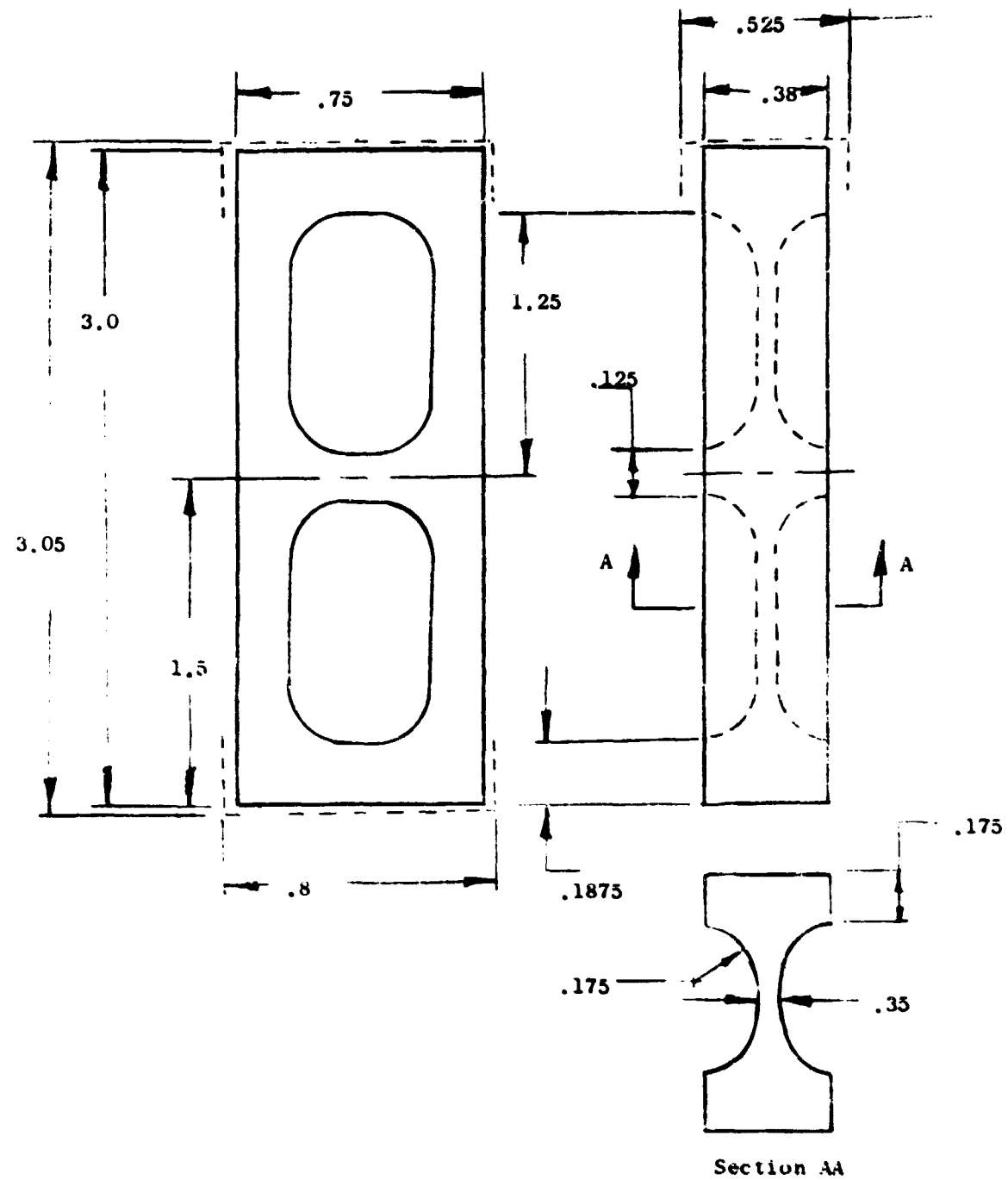


Figure 254 Bending - Shear Test Specimen

(U) The bending shear specimen was designed to force a shear fatigue failure at a diffusion bond line to determine if diffusion bonding effects this material property. This design was scaled to two different sizes to fit the loading capabilities of existing high and low cycle fatigue machines.

(U) Responsibility for this program was then switched from V/STOL Propulsion to SST Engineering, under Air Force contract F33 615 - 68 - C - 1215 in early 1968.

#### Results and Conclusions

(U) Preliminary results from the bending shear specimen have shown bond strengths equal to parent metal strength, confirming the integrity of the proposed hollow blade design. Future tests results will be reported under the above contract.

### Fan Blade Turbine Joint

#### Introduction

(U) Gas generator temperatures and optimization of fan diameters and component technology require new-novel approaches to design and construction of the blade/turbine attachment. Advanced fan designs propose the use of mechanical and/or metallurgical joints between hollow titanium compressor blades and hollow nickel base alloy blade stubs.

(U) This program defines acceptable mechanical design technology in the blade/turbine joint and is supplemented by material/process studies which provide basic metallurgical data needed for the selection of materials and joint strength parameters. (See Material Processing Section).

(U) Models of proposed blade/turbine attachment shall be built employing designs, materials, and processes judged to assure realization of component technology objectives. Tests will be directed towards evaluation of joint construction in terms of mechanical design parameters; i.e., steady state design loads, fatigue tests, endurance limits, and stress distribution.

#### Discussion

(U) Both tip turbine fans in this report have high gas temperatures which make the use of titanium in the joint impractical. This attachment problem has been compounded by reduced radial spacing between the fan and turbine air streams, and as a result it is impractical to use a conventional bolted attachment between the fan blade and the tip turbine components. The desire for common technology in the fans results in the selection of a bi-metal fan blade in order to realize optimum material utilization without requiring impractical cooling techniques on the rotating components.

A possible location of the bi-metal joint would be at the blade mid-span (required to meet vibration criteria on high aspect ratio fan airfoils).

(U) The lightest weight blade-to-turbine attachment would be a metallurgical or adhesive bonded joint between the two radically dissimilar materials (Rene' 41 and Titanium). However, potential problems of a bonded joint in maintainability, serviceability, and assembly of parts in three critical areas (dovetail, mid-span, and tip-turbine) suggested concurrent investigation of a mechanical joint.

(U) The results from the turbine cooling program heat transfer studies (Section V) were integrated into the joint analysis because of operational and soak-back temperature levels which affect the final joint configuration.

(U) Various attachment schemes were analyzed to optimize: a) strength and margin of safety considerations and, b) weight in an effort to achieve the rotor weight objective. The actual joint designs were closely dovetailed with the basic metallurgical material process definition programs being conducted by the Materials Development Laboratory Operation and required their basic inputs to add assurance to the end results.

(U) The several "best" joint designs under consideration (Figures 255, 256, 257 & 258) were taken from the "idea" stage to detailed drawing layouts. This allowed detailed study of joint construction and component fit-up. The major portion of the drawing work was in the pinned, the transverse dovetail, the piano hinge, and the brazed joints.

(U) The pinned joint (Figure 255) would be a mechanical assembly of the upper and lower finished blade sections. Its strong points were: no metallurgical or heat treat problems and good repairability.

(U) The piano hinge (Figure 256) was another mechanical assembly technique. Its advantages were the same as the pinned joint plus greater strength potential.

(U) Another attachment scheme was the dovetail joint shown in Figure 257. This configuration employed a dovetail on the R41 outer blade tip (attached to an integral turbine) mating with a dovetail slot in the inner titanium blade section. The inner blade would be made in convex and concave halves which, once the dovetail was put into position, would be bonded together around the dovetail. Manufacture of blade half sections would be required for fabricating hollow airfoils. Thus the dovetail joint would be only a minor added operation to the blade manufacturing process.

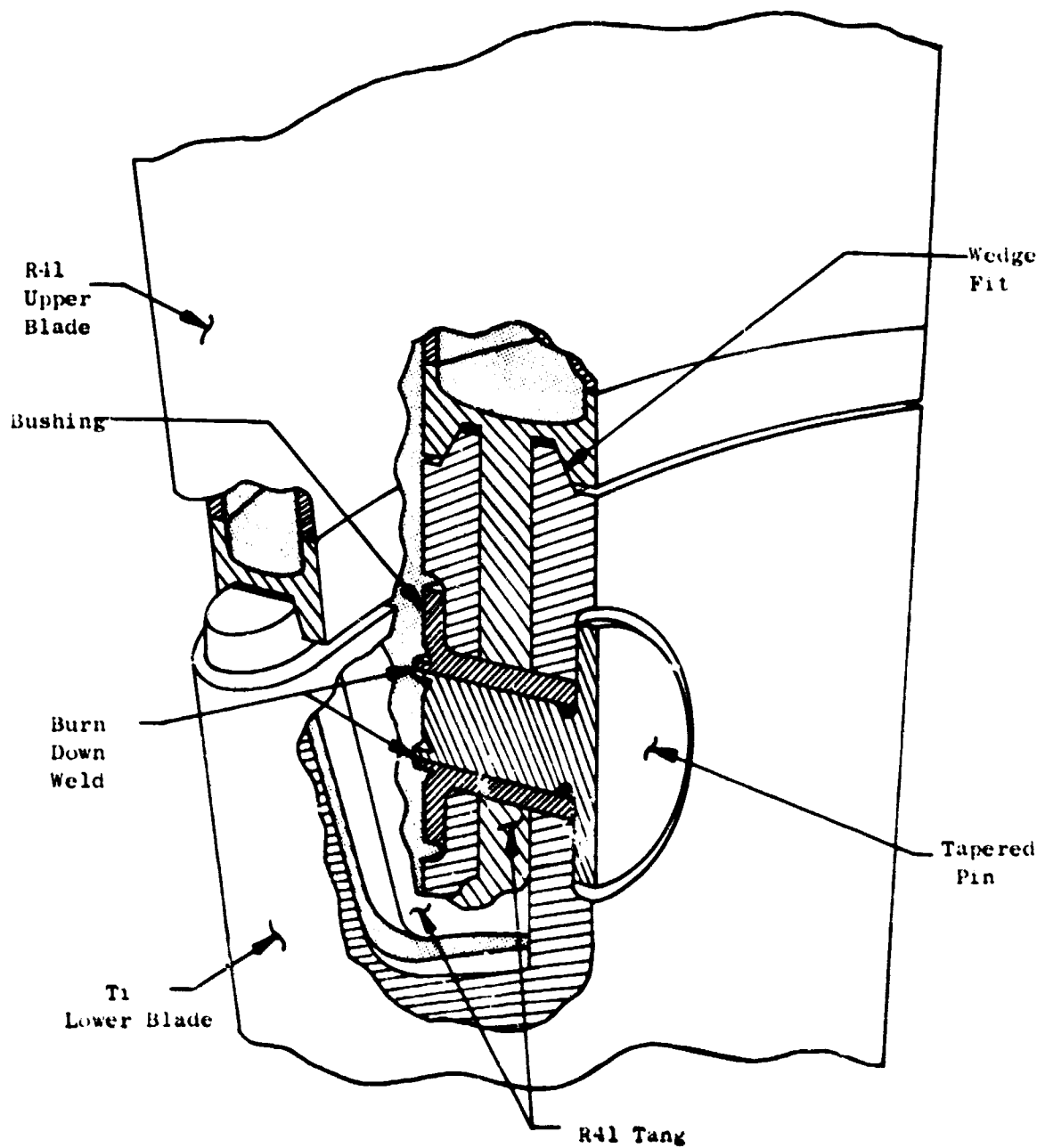


Figure 253 Pin Attachment

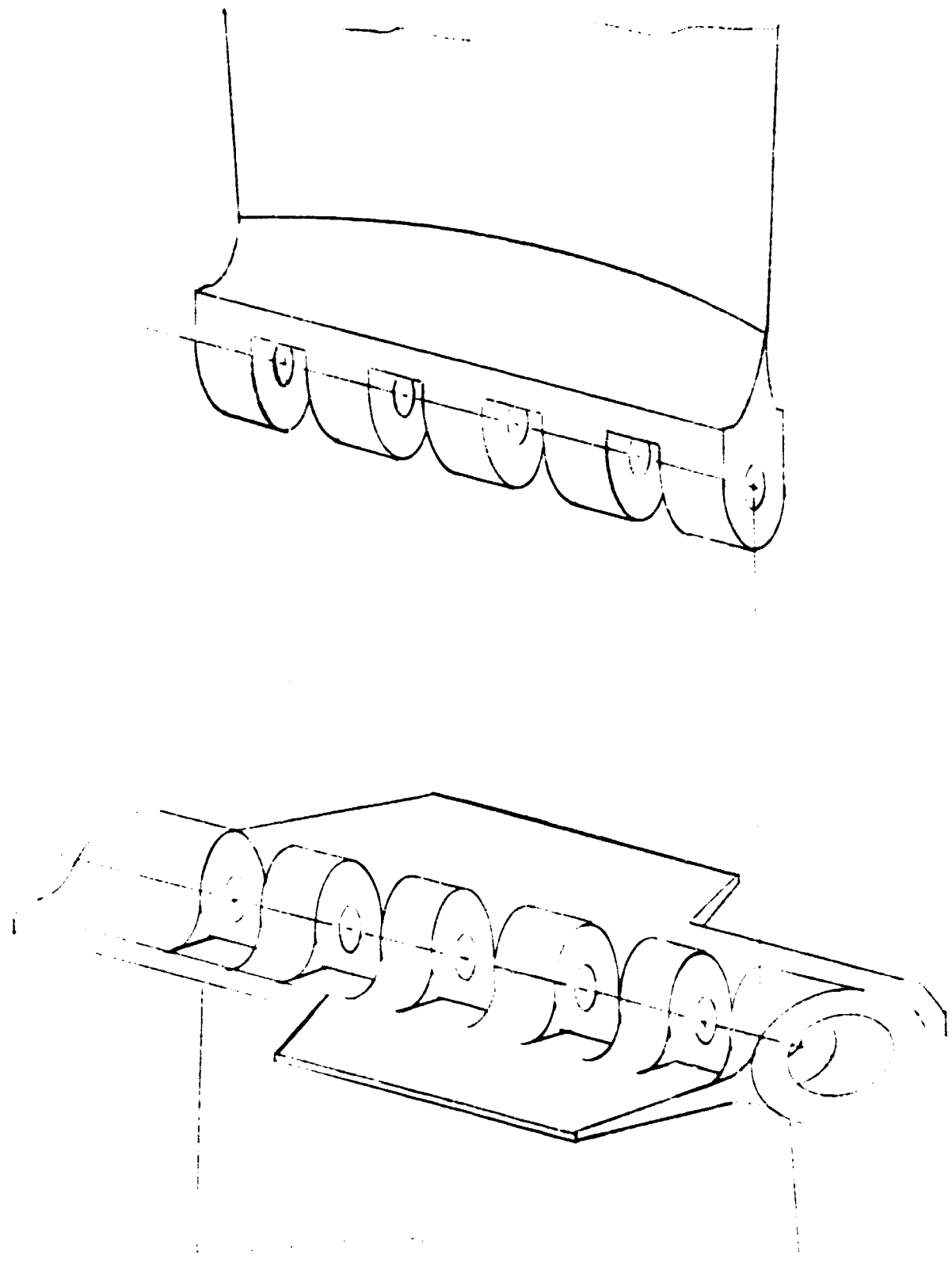


Figure 256 Piano Hinge Blade Attachment Between Inner and Outer Span

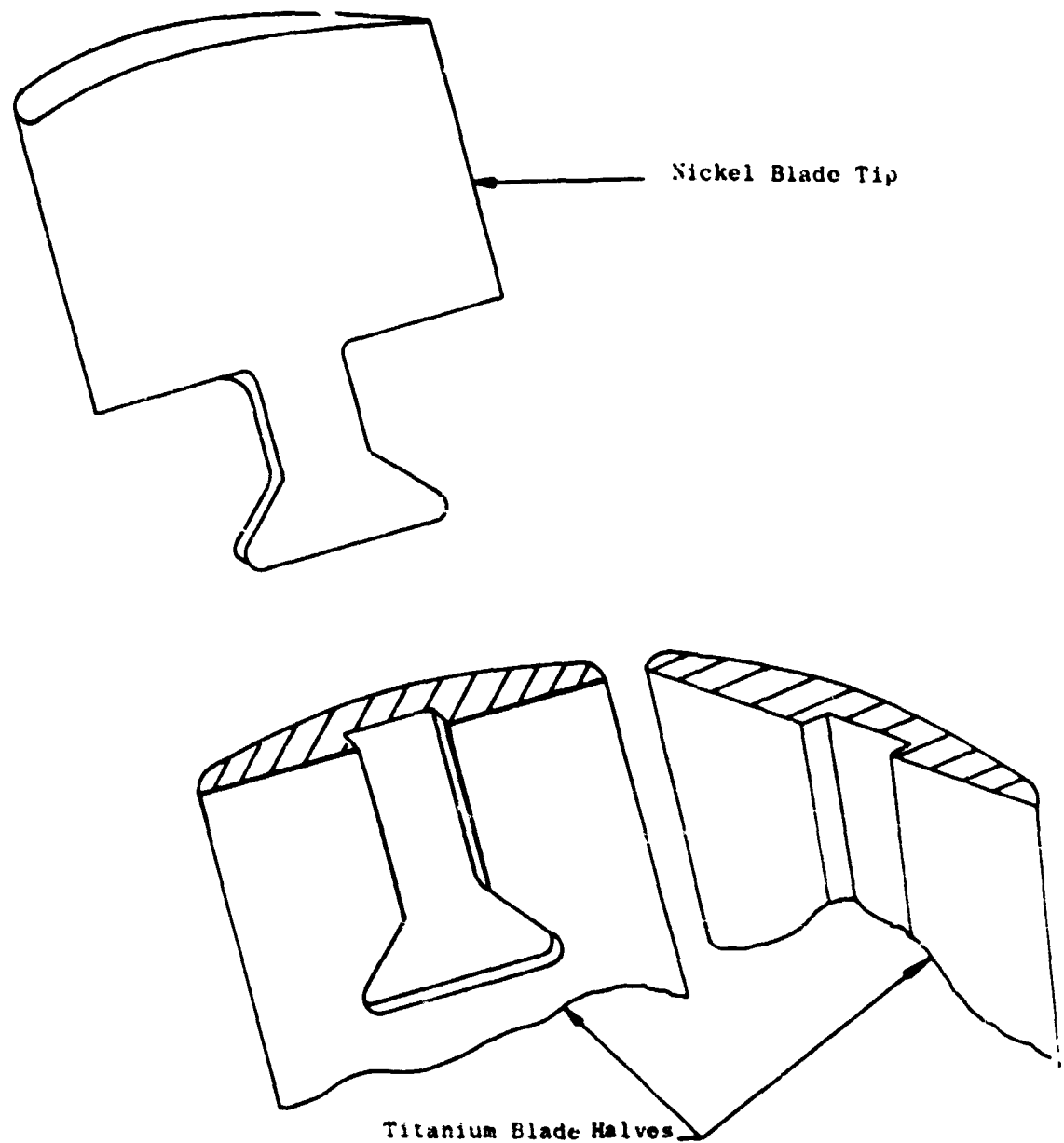


Figure 257 Bonded Dovetail Blade, Turbine Joint

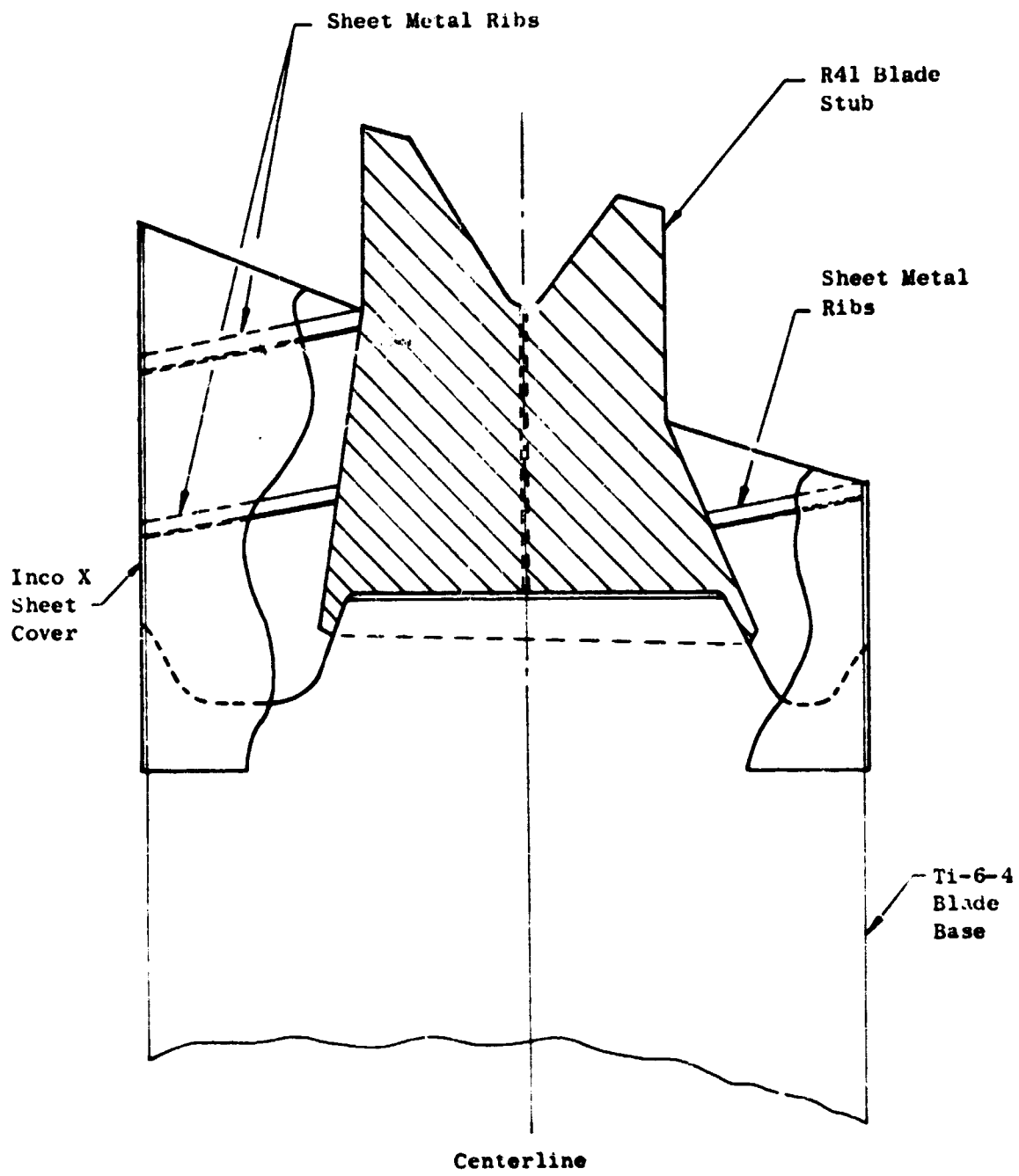


Figure 258 Blade/Turbine Joint Construction

(U) The dovetail was found to be satisfactory for transfer of the primary radial load but weak in blade bending and twisting, as well as subject to fretting in blade vibratory modes. The pins offered adequate strength only if adequate bearing area, dimensional tolerances and a method for positive retention could be provided. The piano hinge was too bulky if located away from the mid span shroud and added too much heavy R41 if brought down to the mid span. Drafting studies made of a brazed joint confirmed its advantages, which were: larger capacity for transferring high radial loads; low tip weight due to thin skin construction; more "rugged" construction for substantial vibratory loads.

(U) Information received from the metallurgical program investigating coextrusion of bi-metal joints was disappointing. Although material properties of the test piece joints (see Section V for actual data) appeared adequate, extension of this program from the successful bar material pieces to actual airfoil parts required development timing and funding beyond the scope of this program. Instead, redirection of the program toward a brazed joint appeared a much better utilization of time, funds, and metallurgical effort. The brazed joint also appeared much more promising for obtaining a process directly applicable to actual hardware. Thus the braze joint was chosen to be continued into detail design.

(U) Detail design of a brazed joint attachment was begun with the major effort directed toward joint geometry rather than sizing for particular loads or braze strengths.

(U) This geometry design effort was directed to: 1) improving the joint load-carrying efficiency and 2) reduction of stress concentrations in order to approach maximum material vibratory capabilities.

(U) The preliminary braze joint design is shown in Figures 258 and 259. It consisted of the lower titanium blade stub brazed to a structural Rene' 41 tip which tapers as it leads to the turbine above. This structure was covered by a non-load-carrying Inconel X shell that formed the required airfoil shape at the blade tip. This design channels the turbine tip load into the full titanium blade while saving weight by using sheet metal edges at the blade tip.

(U) All braze joints were designed as lap or scarf (tapered) joints (Section V, Figure 259) to allow the best possible load transfer through the braze alloy.

(U) Section properties through the joint had to be "tailored" to give smooth changes and prevent discontinuities which cause high local stresses. Figure 260 shows a preliminary distribution of properties in the joint area. All of the parameters peaked between sections 1 and 2, showing that all change from hollow blade to solid joint region needed careful design attention to stress concentration factors.

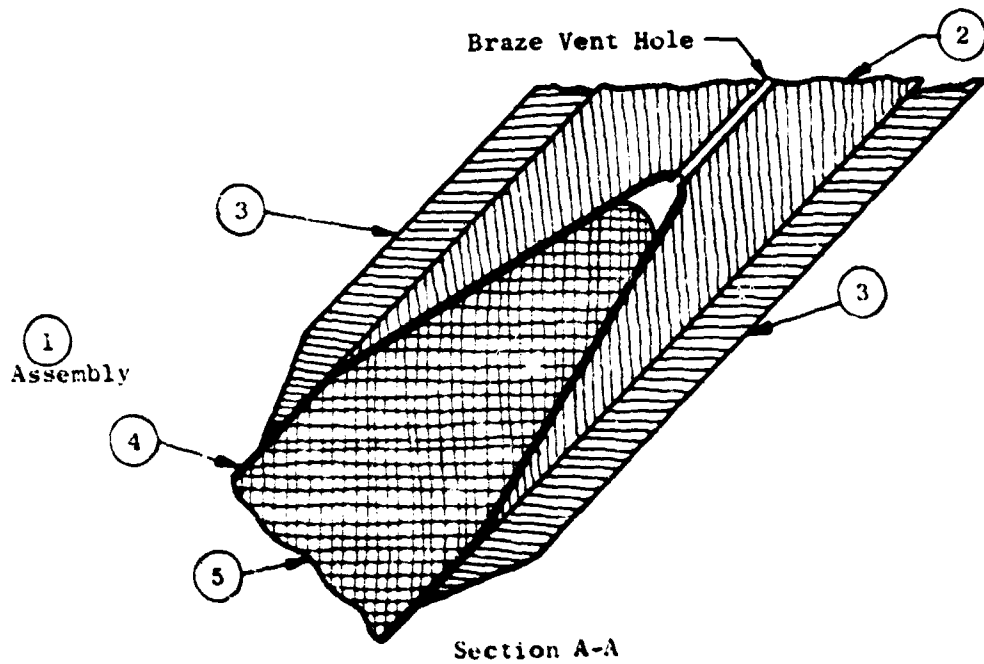
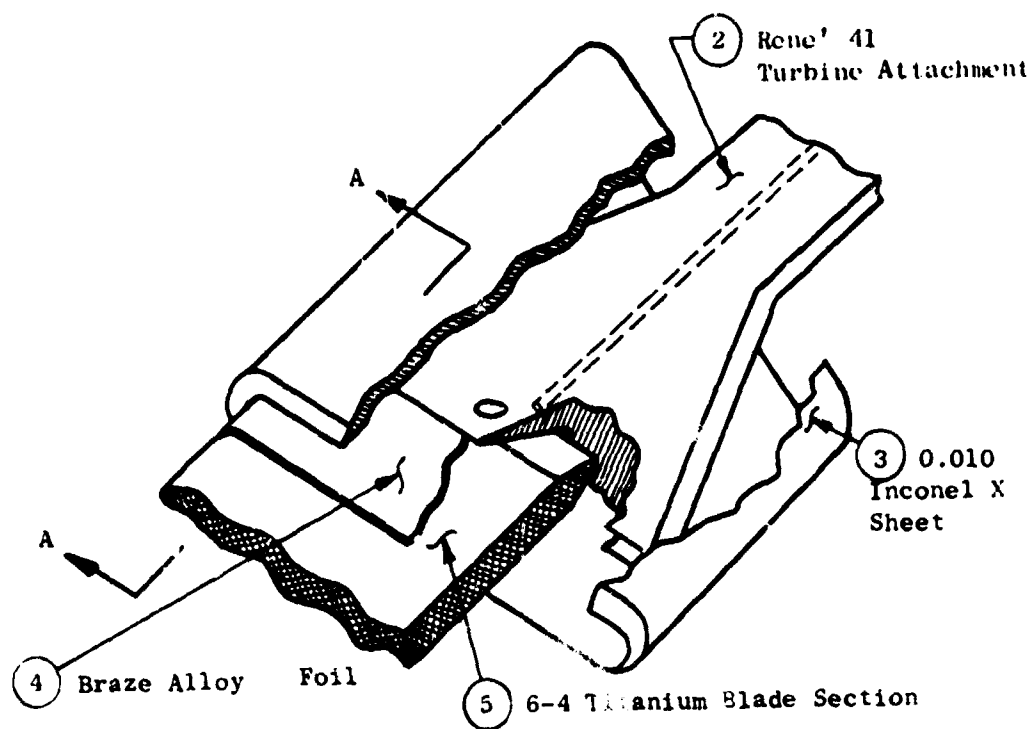


Figure 239 Original Brazed Design - Blade/Turbine Joint

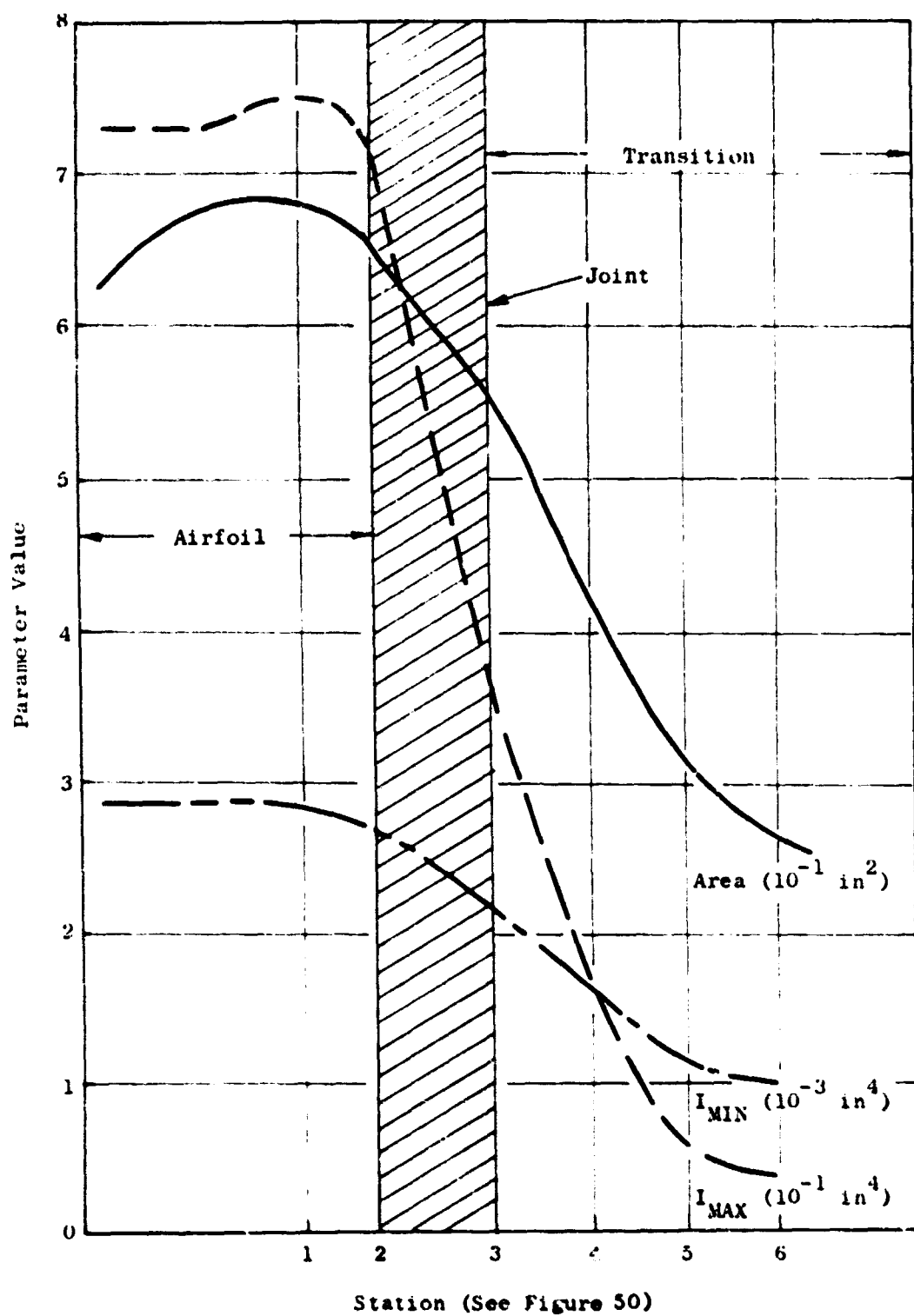


Figure 260 Preliminary Section Properties - Blade/Turbine Attachment

(U) Other than the joint region, the most critical stress areas were at Stations 5 and 6 (Figure 260). The required section properties there were set by the tip load. Section strength appeared adequate but properties could be improved by increasing the chord-wise width of the Rene '41 or by making a fillet blend in part thickness as the Rene' 41 piece passes through the seal.

(U) Joint strength requirements were defined as follows:

1. Radial load = 10,000 lb
2. Braze joint allowable shear stress = 13,000 psi
3. Effective braze area = 80%
4. Load factor applied = 2.0

(U) These requirements, when applied to the preliminary braze joint geometry found the steady state load strength as:

1. Joint design margin = 1.3
2. Ultimate margin of safety = 3.8

(U) A proof test of the calculated joint strength was planned. A test specimen (Figure 261) simulating the actual joint would be instrumented and tested in a modified tensile test machine as follows:

1. Pull to design load
2. Twist to design load
3. Pull to ultimate load

The specimen would be checked for any defective areas or stress concentration regions, and modifications made accordingly in the final joint design.

(U) Joint fatigue strength would be investigated through bench tests. Simplified test specimens (Figure 262) would be subjected to vibratory loads to determine their endurance limit. This information would then be factored into the detail design of the blade joint.

(U) At this point increasing difficulties were encountered with braze development due to: 1) excessive scatter in tensile strengths, 2) apparent requirement for a braze barrier material which complicated joint manufacture, and 3) excessively thin joint geometry due to the low tm/c of the blade.

(U) An alternative approach using electron beam (E.B.) welding was begun as a replacement for the braze joint approach, should braze drawbacks prove too formidable. The welds would be butt welds across the full blade thickness, greatly simplifying the joint geometry (Figure 263). The Inconel X tip cover sheet would only be used if weight limits required it. Instead the solid tip would be relieved with lightening holes.

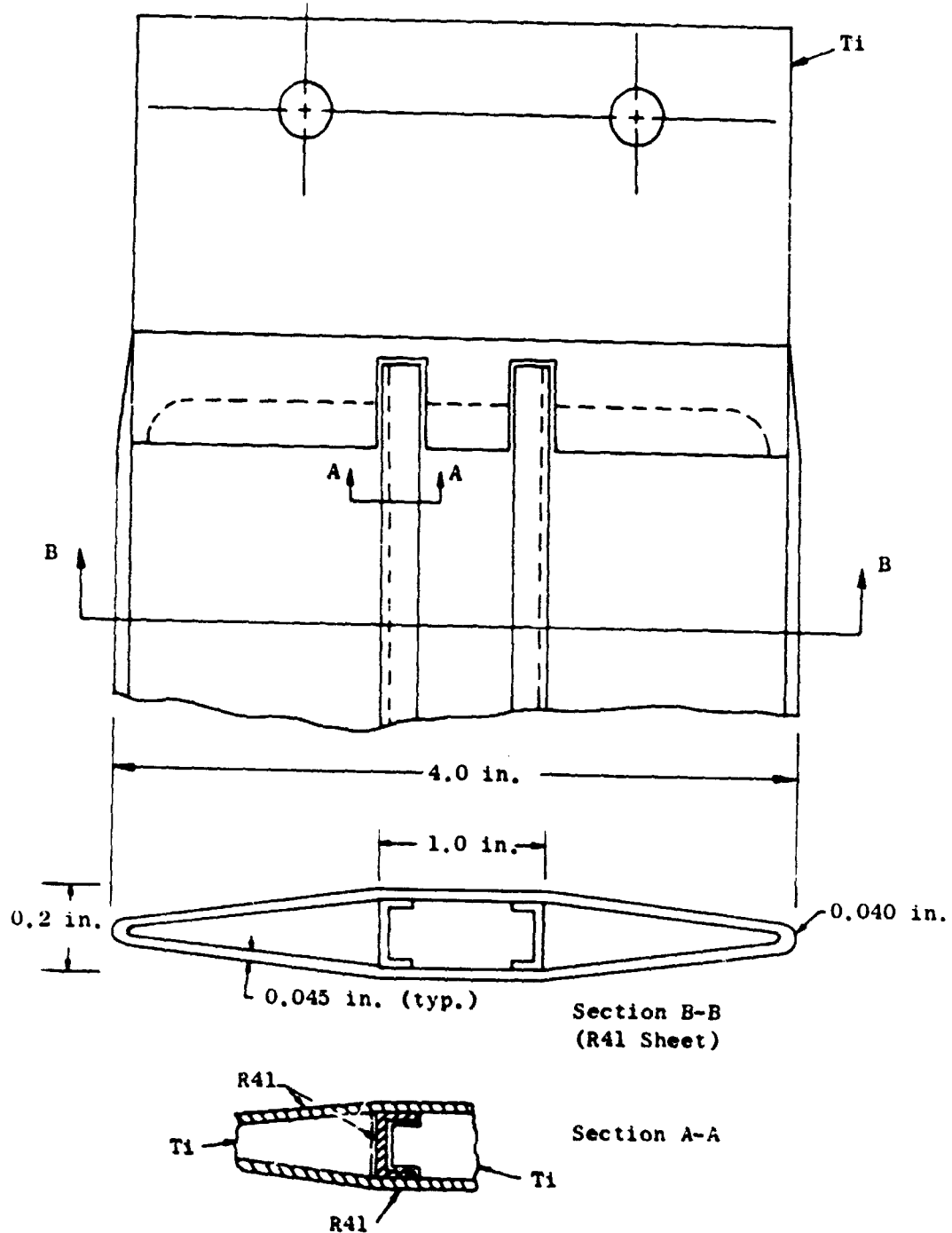
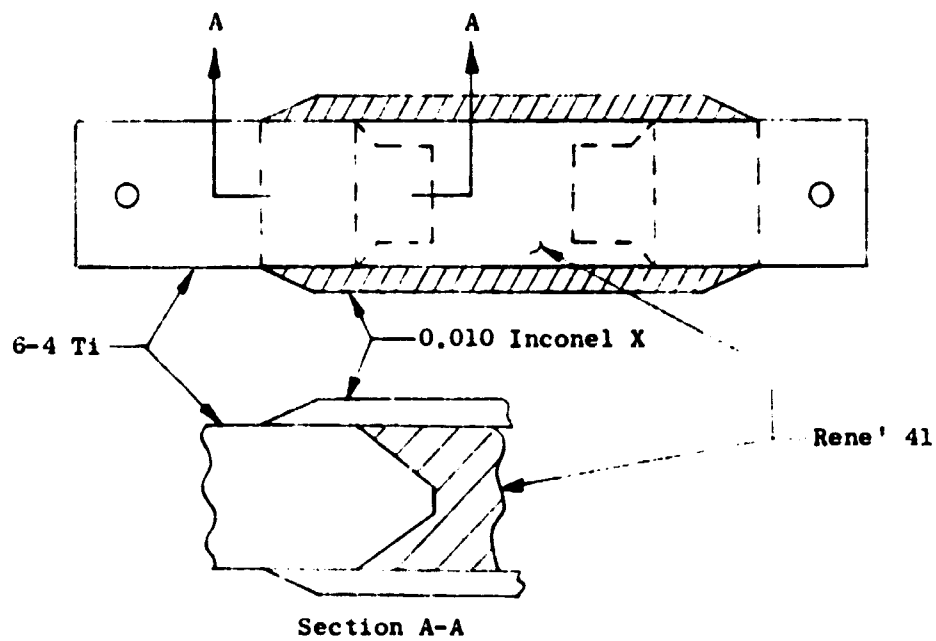


Figure 261 Blade Attachment Braze Test Sample



Tensile Test Model

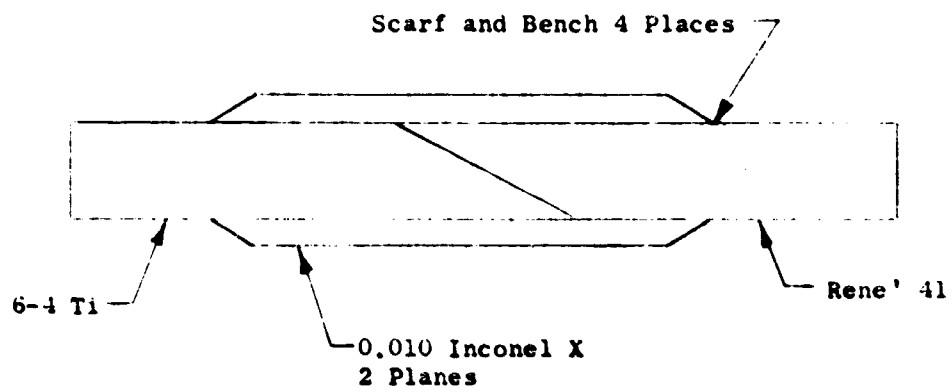


Figure 262 Fatigue Test Specimen

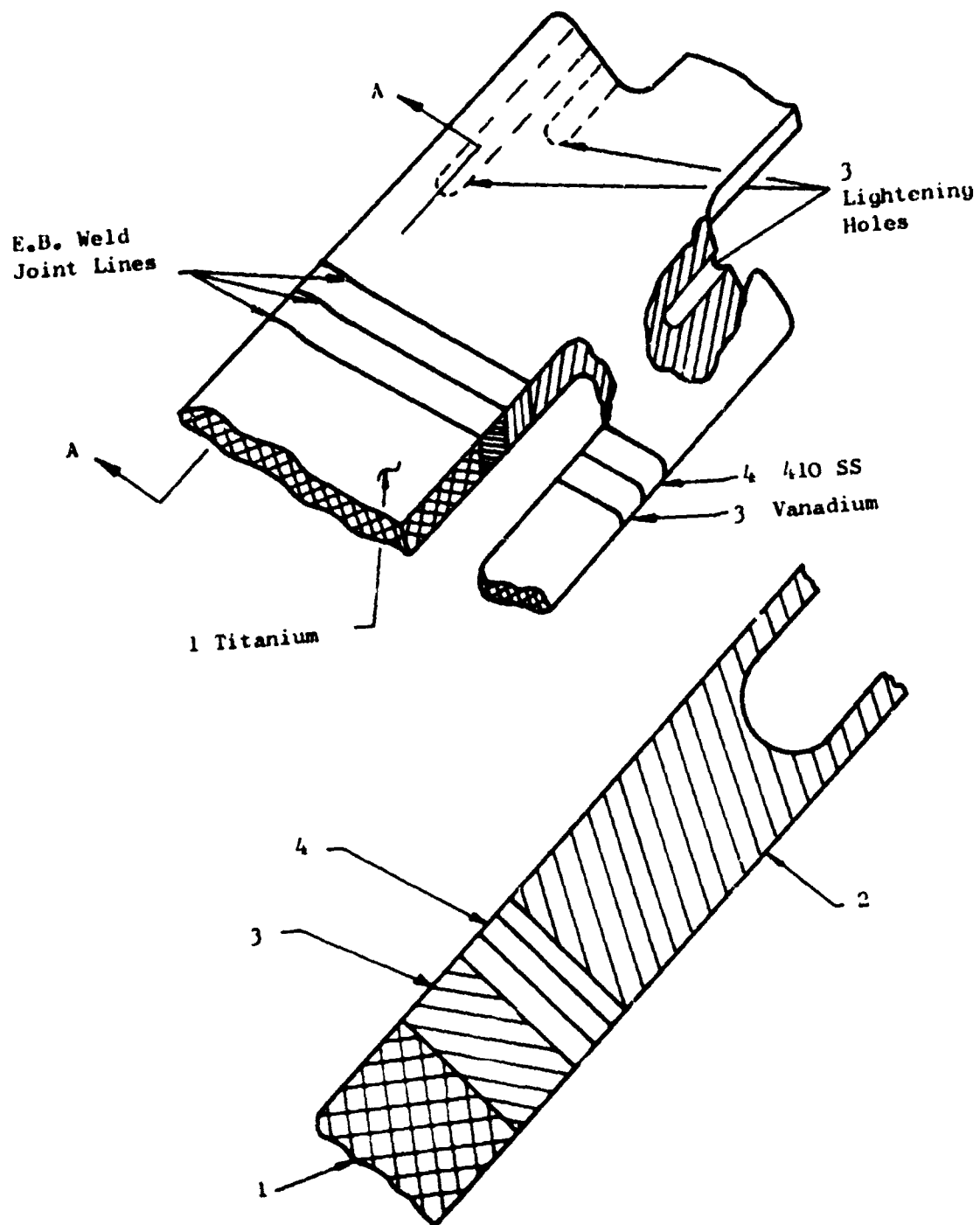


Figure 263 Dissimilar Metal - Blade/Turbine Joint Electron Beam  
Welded Design

(U) Work was also begun to solve the braze joint problems. Scatter was combatted by 1) greater concentration on making braze parameters uniform on all samples, 2) using lower braze temperatures and 3) using shorter braze time. Elimination of the Cb carrier was investigated by running tests with Au - Cu and Ag - Cu braze alloys. These alloys would hopefully be compatible with both R41 and Ti without requiring a Cb carrier.

(U) New geometry studies showed that a single scarf joint rather than an "arrow head" scarf joint (see Figures 259 & 264) could be used. This "simple" joint was not self aligning but would be simpler to manufacture. Tolerances would be easier to hold and braze fit up between parts would be easier to obtain.

(U) Joint test results on both E.B. welded and modified braze joints proved very encouraging. The 80 Au - 20 Cu braze alloy was found to give strong, consistent joints without the use of a Cb barrier. Ultimate joint strengths were about 150% of the minimum required. This alloy was chosen as the best R41-to-titanium joining braze.

(U) E.B. welding of R41 directly to titanium is unsatisfactory unless intermediate alloys are used to transition from Ti-base to Ni-base. Lab tests (see Section V) showed the most promising "chain" of E.B. welded materials to be: titanium - Vanadium - 410 S.S. - R41.

(U) Thus adequate tensile strengths were found in both the 80 Au - 20 Cu braze joint (about 20,000 psi) and the ti - Va - S.S. - R41 welded joint (about 50,000 psi). A choice of the single best joint depended in large measure on the fatigue properties of each. Tests were scheduled for fatigue tests of 15 braze joint samples and 15 E.B. welded joint samples.

(U) The "best" joint method will then be used to build 2 full size simulated blade joints.

(U) The detail drawing of the LF475 blade has been issued showing the double scarf (arrowhead) braze joint between R41 and titanium areas (same design as shown in Figure 259). Two alternative designs, an E.B. welded joint and a single scarf braze joint are shown in Figures 263 and 264 respectively.

#### Conclusions and Recommendations

(U) The blade/turbine joint can be designed to exceed required tensile strength.

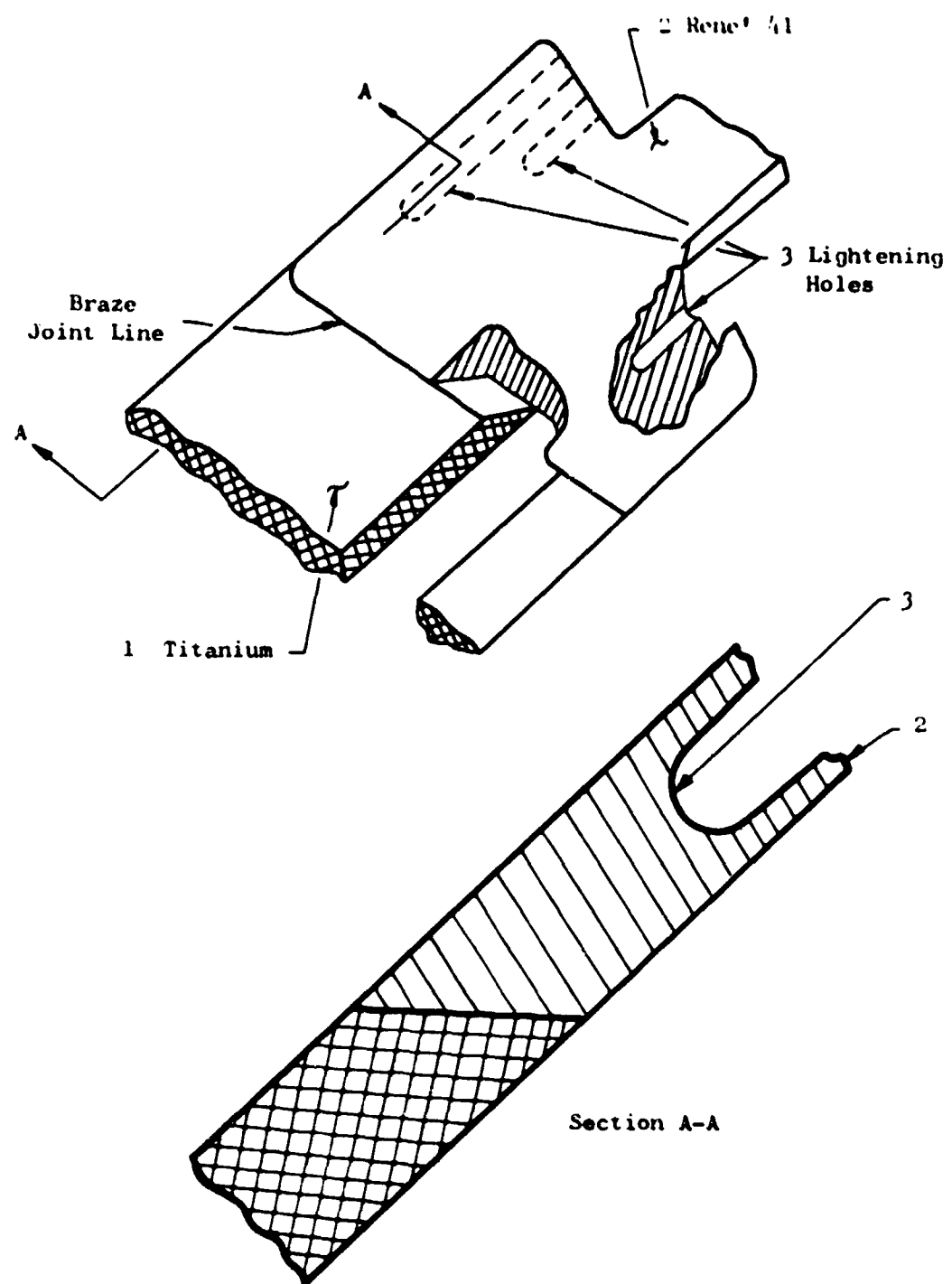


Figure 264 Dissimilar Metal - Blade/Turbine Joint Simplified Braze Design

(U) Three acceptable joint designs are presented:

- a) double scarf braze joint (Figure 259 )
- b) E.B. welded joint (Figure 263)
- c) Single scarf braze joint (Figure 264)

Each of the above can be made with a fabricated sheet metal tip or a one piece relieved tip.

(U) The "best" joint can be picked by considering:

- a) fatigue strengths of E.B. versus braze.
- b) manufacturing cost versus weight bogey.

## TURBINE PROGRAMS

### Aerodynamic Tests

#### Bucket Cascade Tests

##### Introduction. -

(U) The purpose of this program was to obtain specific aerodynamic design data on bucket airfoils representative of the LF475 and L/CP470 tip turbines. In particular it was intended to determine the effect of leading edge radius on aerodynamic performance over a range of inlet Mach numbers and flow angles.

##### Test. -

(U) Three turbine bucket airfoil sections were designed which closely represent the mid-span sections of both the proposed lift and lift/cruise fan tip turbines. These sections were designed with edge thicknesses ranging from 0.016 inch to 0.052 inch, and were designed as impulse sections, i.e. there is no change in static pressure across the cascades at their design inlet angle. Other pertinent design parameters were as follows:

Solidity . . . . . 1.85

Inlet angle (from axial) . . . . . 50°

Inlet Mach number . . . . . 1.00

(U) These sections are shown in Figure 265. It is seen that each of these sections is symmetrical about a centerline. The sections vary slightly in camber angle, the sections with thicker edges having less camber in order to maintain the same flow area and prevent choking.

(U) These airfoil sections were tested in the transonic cascade tunnel over a range of inlet angles and Mach numbers. Since the blade span in the tunnel is fixed at 4 inches, the blade sections were scaled up to a chord of 1.85 inches from the 1.39 inch full scale tip turbine size in order to maintain similarity of aspect ratio between the cascade test and the actual turbines.

(U) Figures 266 and 267 are photographs of an assembled cascade package installed in the wind tunnel. Also shown in these photographs is the downstream total pressure and angle measuring rake and traverse mechanism. In these photographs air enters the cascade test section from the left, is turned downward by the airfoils and exhausted into a large tank.

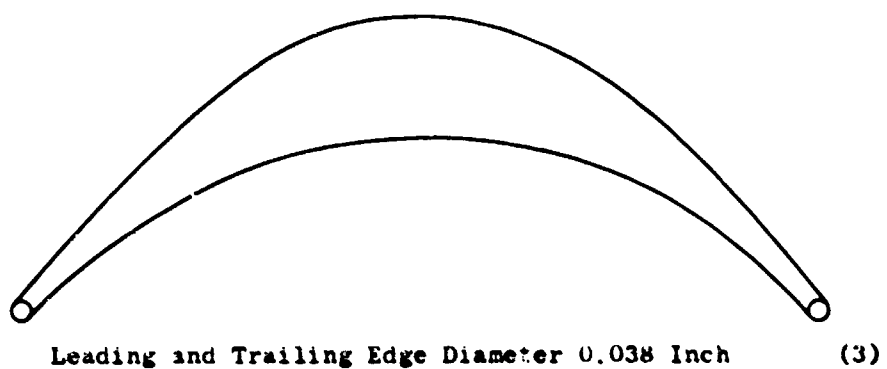
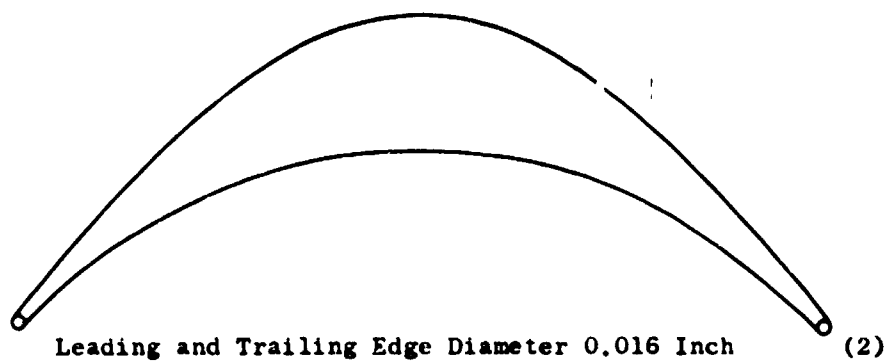
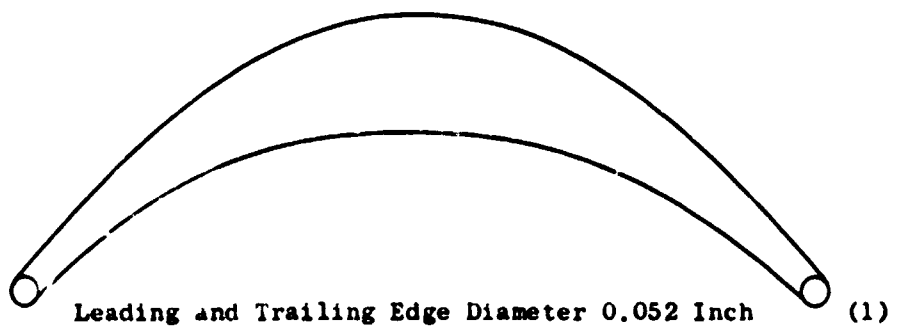
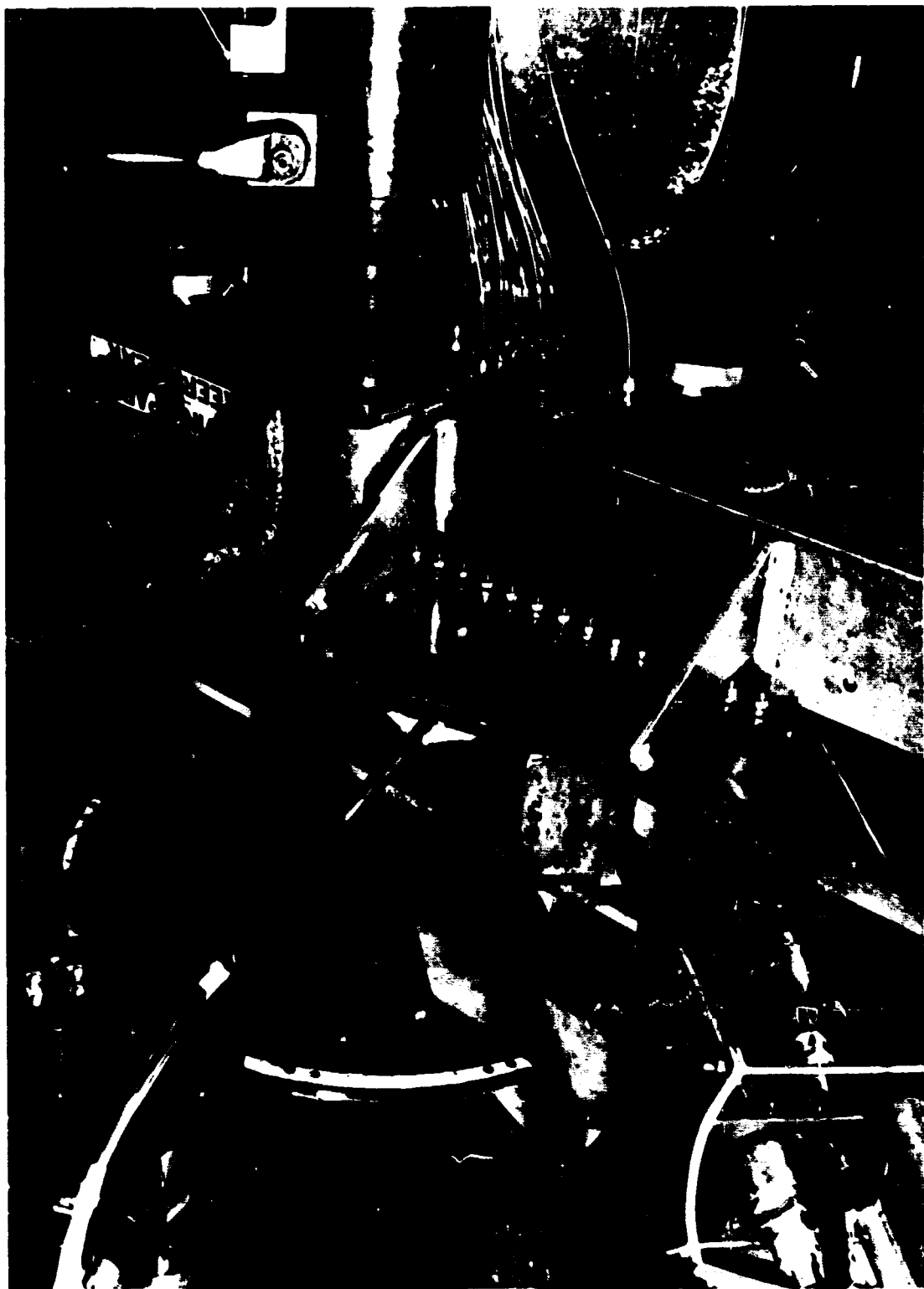


Figure 263 Tip Turbine Test Airfoil Sections



Figure 266. Bucket Airfoils - Transonic Cascade Tunnel

Figure 267 Bucket Airfoils - Transonic Cascade Tunnel



(U) Initially tests were run on all three sections over a range of inlet Mach numbers and inlet flow angles. Subsequently, however, it was found that the data taken on the medium and thinnest edge sections was invalid and needed to be rerun. It was decided not to rerun the thinnest edge section because 1) data from the other two configurations indicated less than expected losses with increased edge thickness and 2) the thinnest edged was considered to thin to be feasible mechanically.

(U) Results from these tests are presented in Figures 268 through 272. Figure 268 shows the total pressure loss through the cascades in terms of a total pressure loss coefficient based on upstream total minus static pressure difference. These values are averaged across the blade span and are corrected for the loss due to the inlet side walls. In the actual turbine these buckets will see an inlet Mach number of about .94. From Figure 268 this appears to be ideal since the loss goes through a minimum between an inlet Mach number of .9 and .96. For Mach numbers higher than this the loss rises very steeply and for lower Mach numbers there is also a substantial increase in loss. Figure 269 presents the losses in terms of a cascade efficiency but shows essentially the same trends. It is noted in both Figure 268 and Figure 269 that in the range of interest of losses for both configurations are nearly identical.

(U) Figure 270 compares the average exit angles for the two configurations. It can be seen that the thick edge configuration turns the flow several degrees less for all inlet Mach numbers. Figure 271 shows the average change of tangential velocity produced by each cascade. This is a measure of the torque and power output for the actual turbines. It can be seen that in the Mach number range of most interest, that the thick leading edge configuration compares favorably with the medium edge configuration. However, at higher or lower inlet Mach numbers it does not perform as well.

(U) Figure 272 shows the change in static pressure divided by the upstream dynamic pressure, positive values indicated a decrease in static pressure in the direction of flow. It will be recalled that all these cascades were designed for zero static pressure change. In the Mach number range of most interest, .94, both configurations are acceptably near zero, however it may be seen that the thickest edge configuration has much more variation.

Conclusions and recommendations. -

(U) For inlet Mach numbers lower than .96 at the design inlet angle of 30° there is no significant difference in the efficiencies of the medium and thick leading edge configurations. There is a difference, however, in the turning angles and static pressure ratios across the blades. The thick leading edge configuration

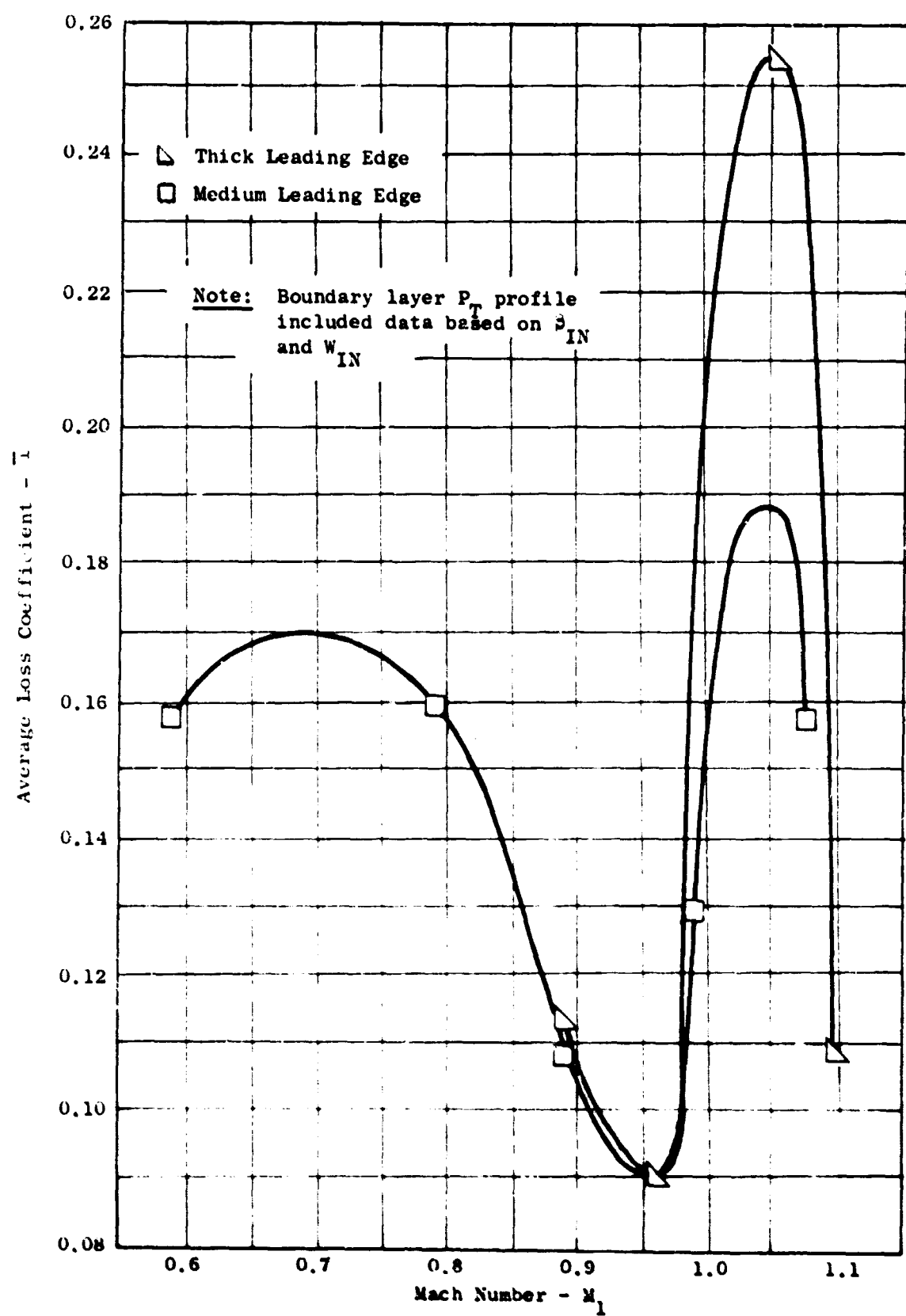


Figure 268 Average Loss Coefficient Versus Mach Number

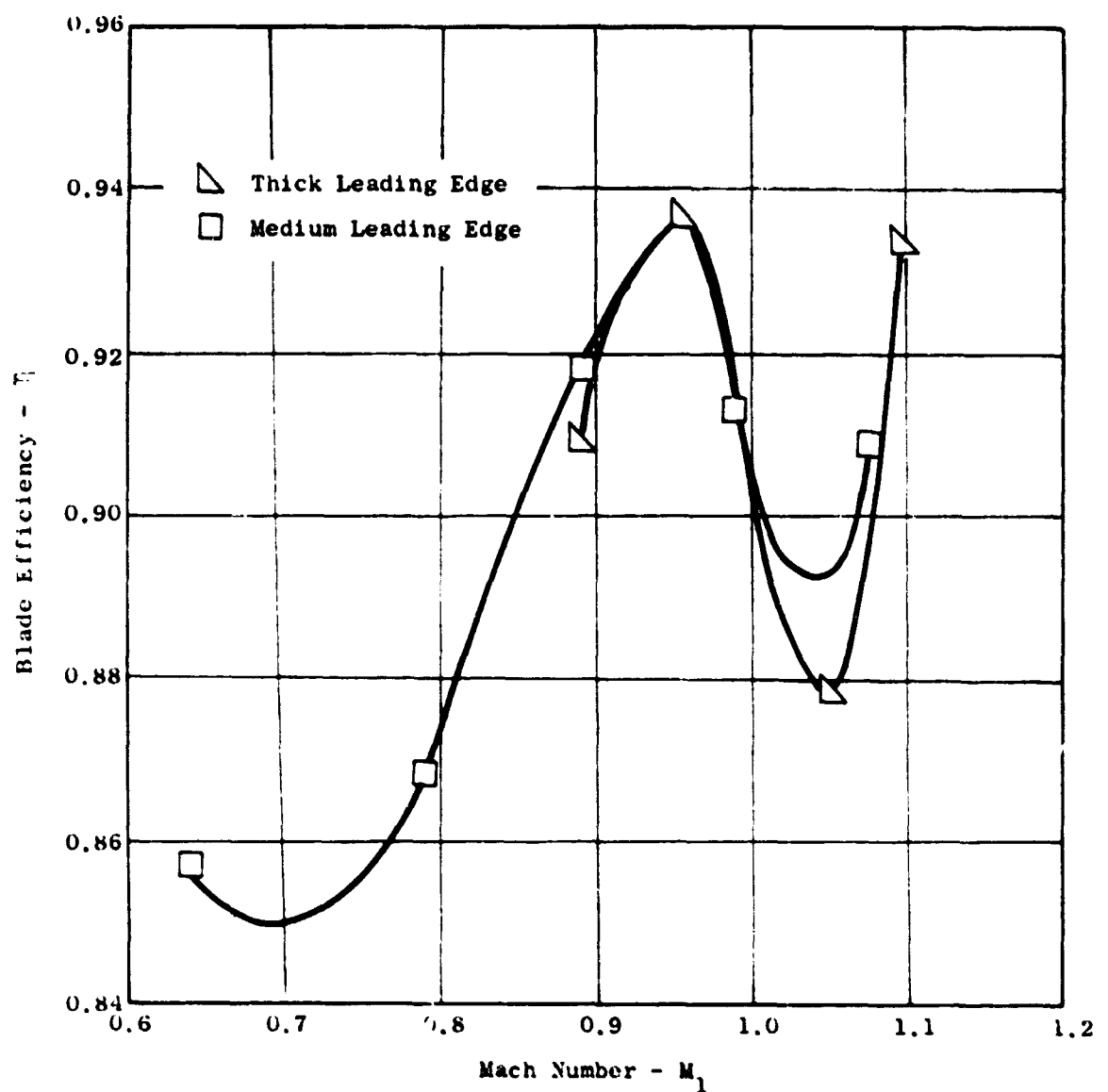


Figure 269 Blade Efficiency Versus Mach Number

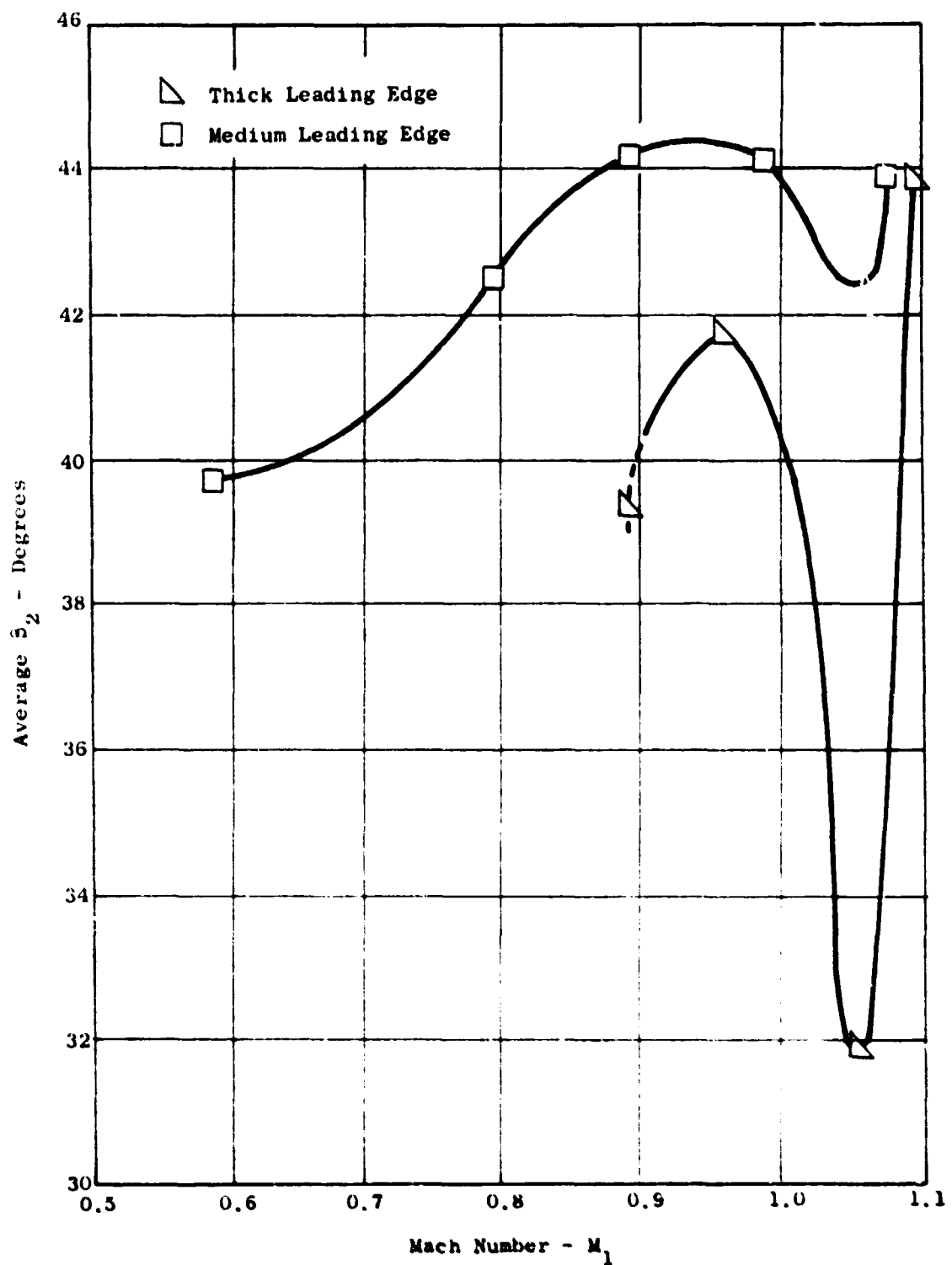


Figure 270 Average  $\beta_2$  Versus Mach Number

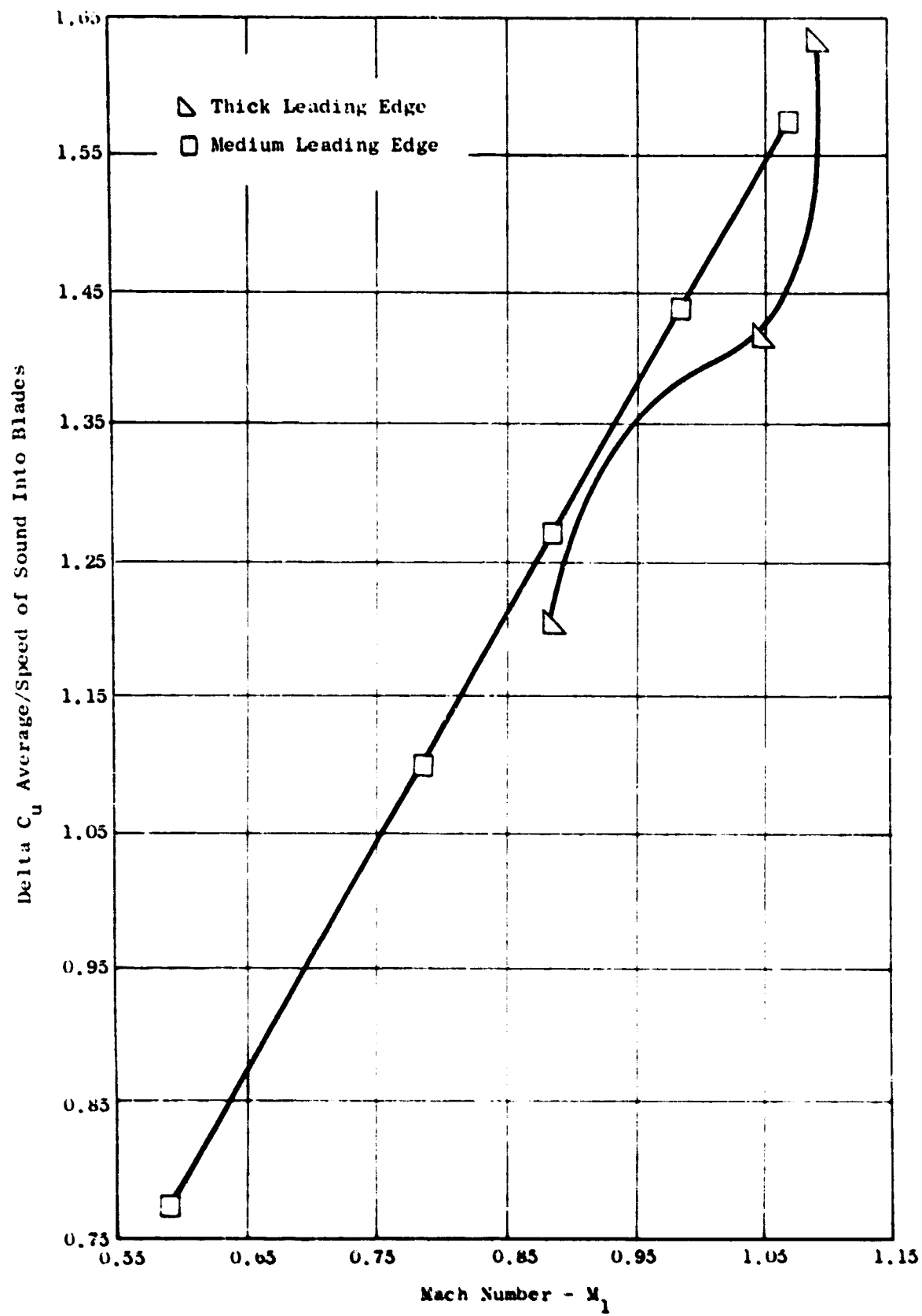


Figure 271  $\Delta C_u$  Average/Speed of Sound Into Blades Versus Mach Number

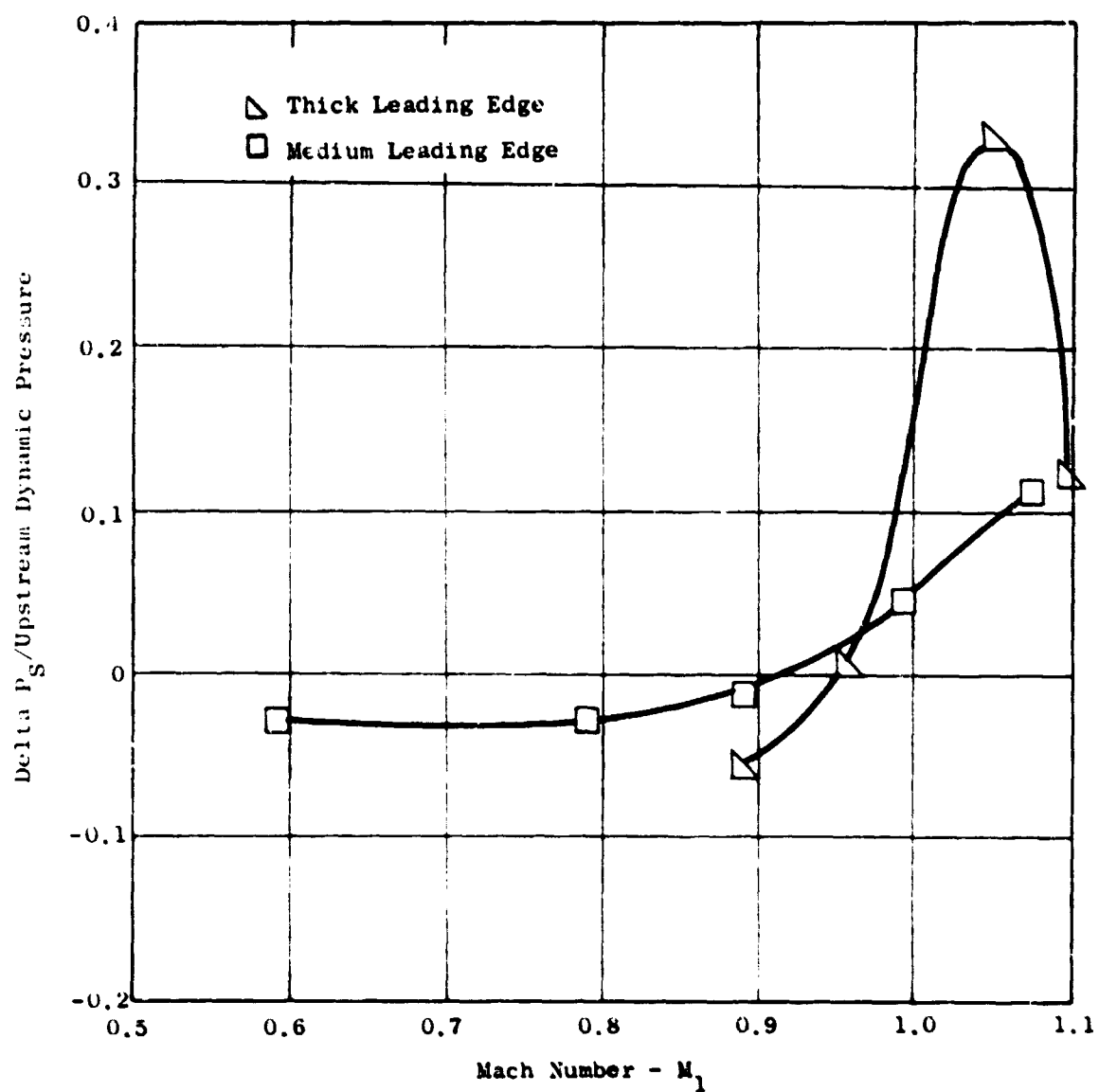


Figure 272 Delta  $P_S$  / Upstream Dynamic Pressure Versus Mach Number

turns about 3° less and also has a higher exit static pressure. This can be attributed in part to the slightly smaller camber of this configuration.

(U) For inlet Mach numbers higher than .96 at the design inlet angle of 50° both configurations show wide variations in efficiency with Mach number changes, with indications that the thick leading edge configuration may have substantially higher losses when the Mach number is between 1.0 and 1.1. Figures 270, 271 and 272 also support this conclusion showing that the turning angle and exit static pressure also drop sharply in this range for the thick leading edge configuration.

(U) From the data shown in Table 49 we may conclude that the comparison between the two configurations at  $\pm 5^\circ$  from the design inlet angle does not change greatly from the comparison at the design angle and Mach numbers of about .9. Thus the thick leading edges do not show significant off design superiority over the thinner edges as might have been expected.

(U) It is recommended then, that for inlet Mach numbers up to .96 edge thickness up to 10 or 11 percent of the inlet throat area may be used with no loss of performance. For inlet Mach numbers higher than .96 edge thicknesses must be kept below 8 percent of the inlet throat and preferably thinner.

TABLE 49

Tip Turbine Cascade Test  
Aerodynamic Performance Parameters

Inlet Velocity Angle	Configuration*	Mach No.	Total Pressure Loss Coef.	Efficiency	Static Pressure Rise Coef.	Exit Velocity Angle
45°	1	.78	.122	.920	.190	42.8
	2	.77	.138	.914	.240	44.1
50°	1	.89	.114	.909	-.057	39.3
	2	.89	.109	.918	-.014	44.1
55°	1	.88	.153	.848	-.221	41.1
	2	.89	.158	.857	-.151	42.4

\* "1" Indicates thick leading and trailing edges.

"2" Indicates medium leading the trailing edges.

## Exhaust Diffuser Tests

### Introduction. -

(U) The objective of this program was to verify the feasibility of diffusing the turbine exhaust flow under adverse conditions and to obtain specific aerodynamic design data with which to optimize the diffuser geometry. Testing was conducted to determine the effects of inlet Mach number, inlet swirl angle, inlet velocity profile, flow path misalignment, fan-to-turbine seal leakage, and diffusion angle.

### Test. -

(U) Figure 273 shows a cross section of the diffuser test model with the 12° diffuser angle. In this model the airflow entered a short rectangular duct, 2" x 22.26", from a large plenum. In this duct, the exit side of which is shown in Figure 274, are located eight adjustable swirl vanes used to turn the flow and simulate turbine swirl angles. Just downstream of the swirl vanes there was provision for mounting metal bars of various thicknesses and at varying distances from the surface. These bars, one of which is seen in Figure 274, were used to generate velocity profiles in the flow. As can be seen in Figure 273 the diffuser section was attached just downstream of this duct, with discontinuities in the flow path representative of a tip turbine. Provision is made on the fan side of the flow path to simulate seal leakage from the fan into the diffuser by means of adjustable seal clearance. The exit side of the diffuser section is shown in Figure 275. The diffusion angle can be changed to 0, 6 or 12 degrees by insertion of other flow path blocks between the stator vanes. The two ends of the model were formed by wooden blocks which conformed to the expected streamline shapes of the flow and were changed with each change in swirl vane setting.

(U) The diffuser section included eight stator vanes designed to remove the swirl from the flow. Their profile was composed of a NACA 65010 thickness distribution on a circular arc mean line. The circular arc mean line had 26.5 degrees of camber and a stagger angle of 10 degrees. The vane chord was 2.5 inches which gave a solidity of .79.

(U) Testing of the diffuser model was divided into two phases. The first phase was a series of calibration runs on the inlet bell-mouth and upstream swirl vanes without the diffuser to evaluate the diffuser entering conditions for a range of swirl angles, Mach numbers and velocity profiles. Swirl angles of 12, 17, and 23 degrees; Mach numbers of 0.3 and 0.6; and three velocity profiles were tested. The design point for all diffuser configurations was at a swirl angle of 17 degrees and a Mach number of 0.6. Table 50 list the combination of these variables tested. Velocity

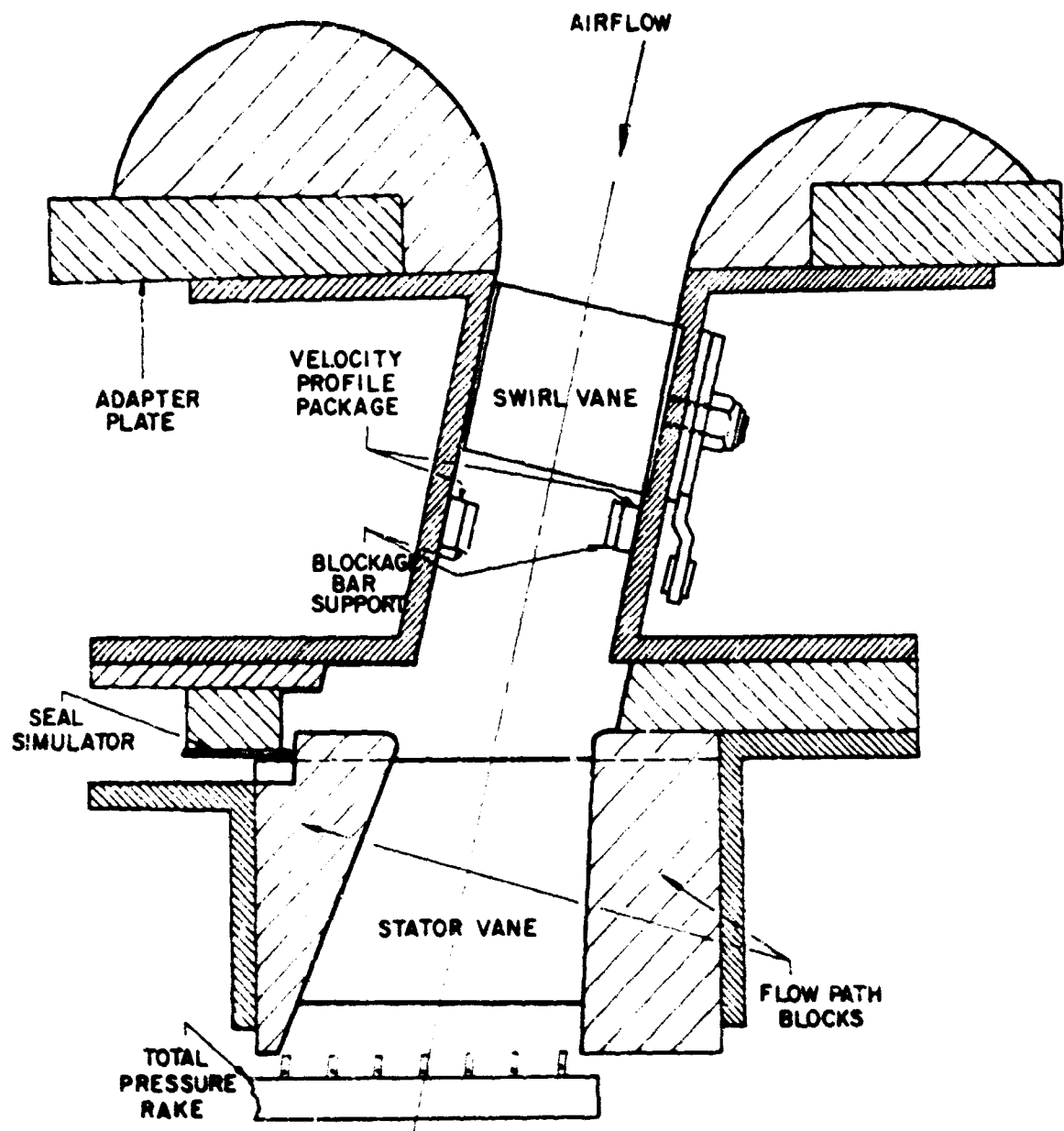


Figure 273 Tip Turbine Diffuser Test Model



Figure 274 Tip Turbine Diffuser Test Swirl Vanes - Without Diffuser

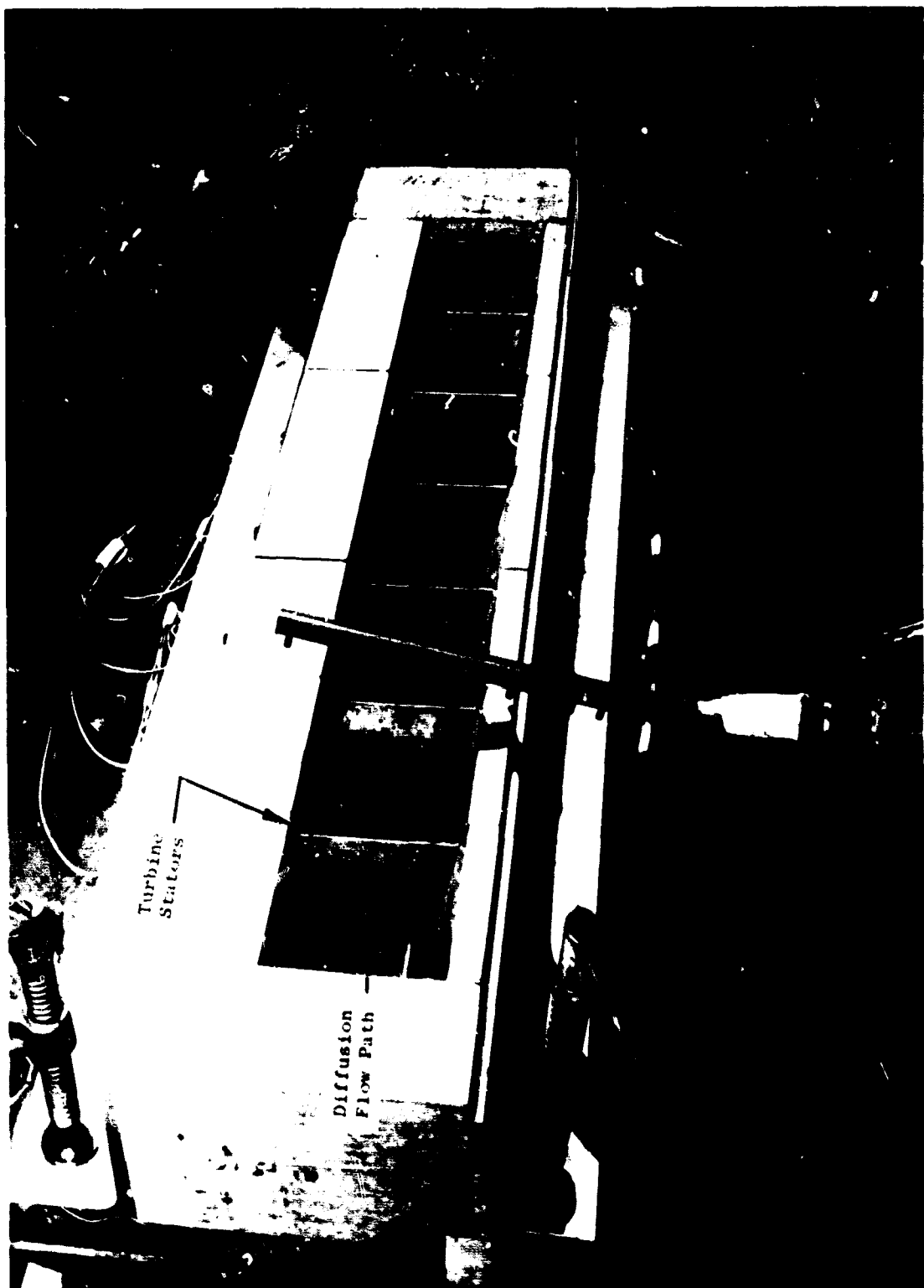


Figure 275 Tip Turbine Diffuser Test 12° diffuser Installed

profile "1" was with no boundary layer strips installed and can be described as rather uniform and representative of the best to be expected at the exit of an actual tip turbine. Velocity profile "2" had a 1/16 inch thick steel strip installed 1/4 inch from the tip wall and can be described as having a definite velocity deficiency near the tip. For velocity profile "3", the 1/16 inch strip was replaced by a 1/8 inch strip and the tip velocity deficiency was increased. It was felt that these velocity profiles covered the range of profiles to be expected from an actual tip turbine.

(U) The second phase of this test was the testing of three basic diffuser models which were attached to the inlet hardware previously described. The three diffuser models may be identified by the included diffusion angles between their side walls; these were 0, 6 and 12 degrees. All three had swirl straightening vanes designed for a 17-degree inlet swirl angle. Thus the diffusion in the 0-degree diffuser was due entirely to removal of the swirl velocity component. For this phase of testing, two additional test variables were introduced: the seal clearance at the hub and the radial alignment between the inlet and the diffuser.

(U) The 6-degree angle diffuser was tested first and Table 53 gives a summary of the test points taken. Seal clearances denoted as "out" in Table 51 indicate that the seal was completely removed, leaving about a 3/4-inch gap for leakage. The test point schedules for the 0 and 12-degree diffusers were similar except that all 0.5 Mach number points and all "seal-out" configurations were eliminated.

(U) At the end of this testing two other brief investigations were made. The first of these consisted of the removal of one of the end blocks from the 12-degree diffuser to simulate conditions at the end of the admission arc in a partial admission tip turbine. The second, also on the 12-degree diffuser, was a flow visualization study. Beads of black grease were placed at the leading edges of the diffuser vanes and walls and the air turned on for a short time. This study showed very graphically areas of flow separation.

(U) Figures 276 through 285 show the static pressure rise coefficient for the diffuser section as a function of the various test variables. The static pressure rise coefficient is defined as the static pressure rise across the diffuser divided by the diffuser inlet dynamic head.

(U) Figure 276 shows the effect of diffuser divergence angle with zero leakage, zero misalignment and a flat inlet velocity profile. This indicates that pressure rise coefficients of about 13 can be obtained for this rather idealized case and that divergence angles up to 12° are quite reasonable for swirl angles up to 23°.

TABLE 50  
TEST POINT SCHEDULE FOR CALIBRATION RUNS

Point Number	Swirl Angle (degrees)	Mach Number	Velocity Profile
1	12	0.6	1
2	12	0.5	
3	23	0.6	
4	23	0.5	
5	17	0.6	
6	17	0.5	
7	17	0.6	2
8	17	0.6	
9	17	0.6	
10	17	0.6	3
11	12	0.6	
12	23	0.6	

TABLE 51  
TEST POINT SCHEDULE FOR 6-DEGREE DIFFUSER

Point Number	Swirl Angle (deg)	Mach Number	Velocity Profile	Seal Clearance (in)	Radial Misalignment (in)
1	17	0.6	3	0	0
2	17	0.5	3	0	0
3	17	0.6	3	0.04	0
4	17	0.5	3	0.04	0
5	17	0.6	3	0.08	0
6	17	0.5	3	0.08	0
7	17	0.6	3	Out	0
8	17	0.6	3	Out	+ 1/4
9	17	0.6	3	0.08	+ 1/4
10	17	0.6	3	0.04	+ 1/4
11	17	0.6	3	0	+ 1/4
12	17	0.6	3	0	- 1/4
13	17	0.6	3	0.04	- 1/4
14	17	0.6	3	0.08	- 1/4
15	17	0.6	3	Out	- 1/4
16	17	0.6	1	0	0
17	17	0.5	1	0	0
18	17	0.6	1	0.04	0
19	17	0.5	1	0.04	0
20	17	0.6	1	0.08	0
21	17	0.5	1	0.08	0
22	17	0.6	1	Out	0
23	17	0.6	1	Out	+ 1/4
24	17	0.6	1	0.08	+ 1/4
25	17	0.6	1	0.04	+ 1/4
26	17	0.6	1	0	+ 1/4
27	17	0.6	1	0	- 1/4
28	17	0.6	1	0.04	- 1/4
29	17	0.6	1	0.08	- 1/4
30	17	0.6	1	Out	- 1/4
31	17	0.6	1	0.08	- 1/8
32	17	0.6	1	0.04	- 1/8
33	17	0.6	1	0	- 1/8
34	17	0.6	1	0	+ 1/8
35	17	0.6	1	0.04	+ 1/8
36	17	0.6	1	0.08	+ 1/8
37	12	0.6	1	0	0
38	12	0.6	1	0.04	0
39	12	0.6	1	0.08	0
40	12	0.6	3	0.08	0

TABLE 51 (Continued)  
TEST POINT SCHEDULE FOR 6-DEGREE DIFFUSER

Point Number	Swirl Angle (deg)	Mach Number	Velocity Profile	Seal Clearance (in)	Radial Misalignment (in)
41	12	0.6	3	0.04	0
42	12	0.6	3	0	0
43	23	0.6	3	0	0
44	23	0.6	3	0.04	0
45	23	0.6	3	0.08	0
46	23	0.6	1	0.08	0
47	23	0.6	1	0.04	0
48	23	0.6	1	0	0

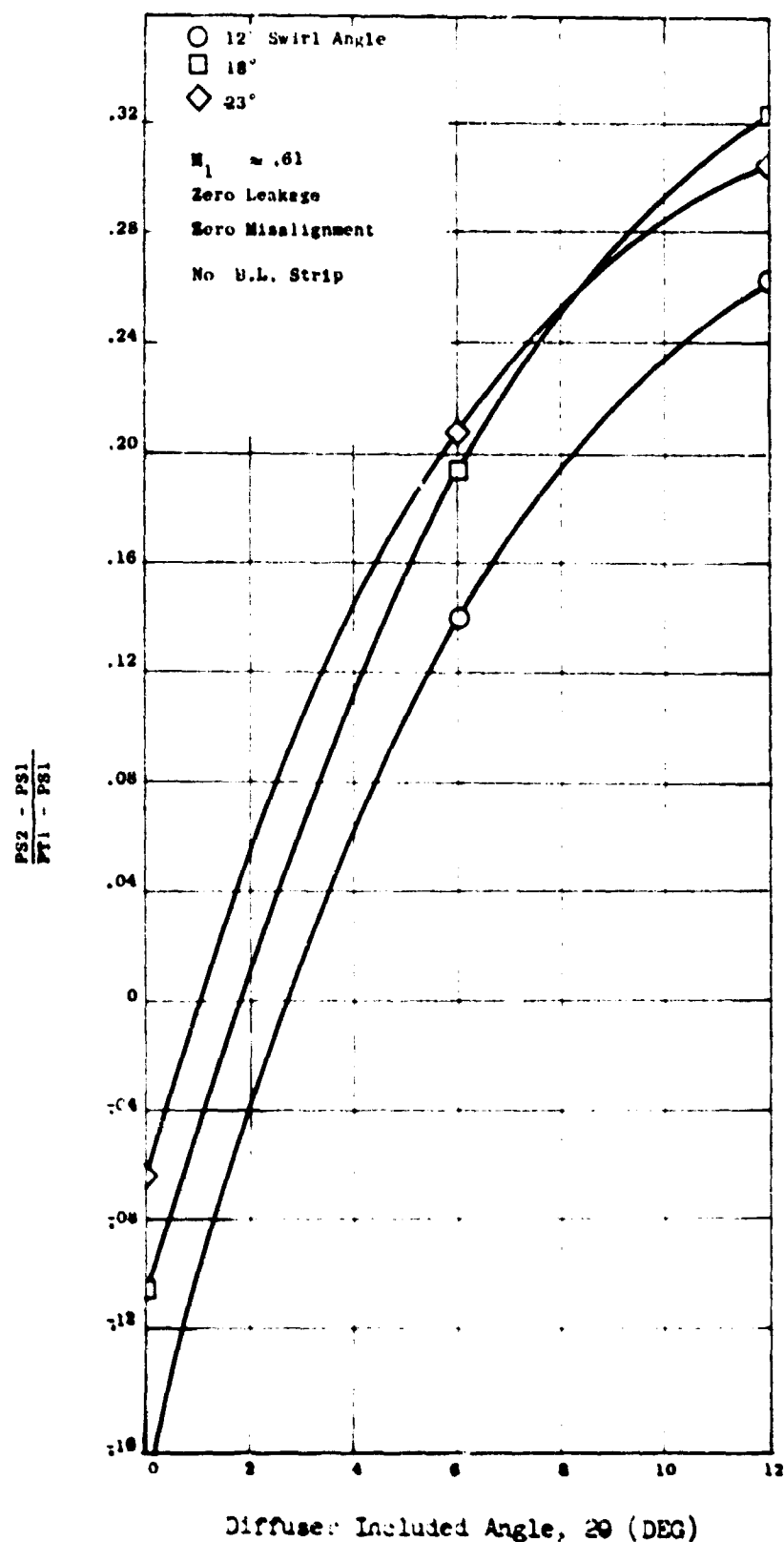


Figure 276 Tip Turbine Diffuser Investigations - Effect of Divergence Angle

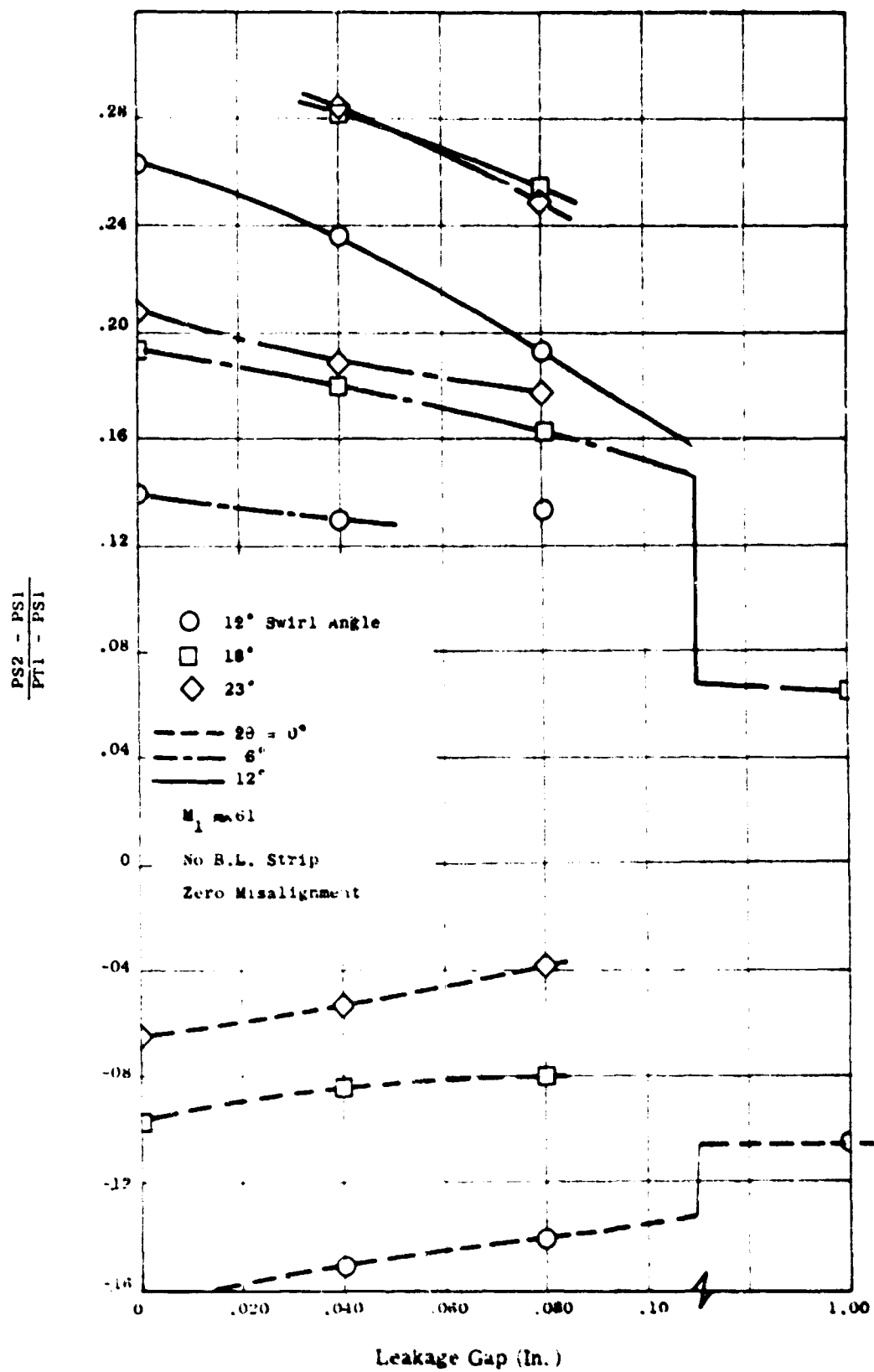


Figure 277 Tip Turbine Diffuser Investigation  
Effect of Leakage

(U) Figure 277 shows the effect of leakage at the diffuser inlet. The general effect is to reduce the pressure change across the diffuser as was expected.

(U) Figure 278 shows the effect of radial misalignment. This shows that any radial misalignment decreases the effectiveness of the diffuser but that a negative displacement is much worse than a positive displacement. With the leakage gap open this effect can be partially explained by a decrease in leakage for the positive displacement cases because of the higher static pressure which would exist on the hot side of the seal. However, the effect remains unexplained for the zero leakage case.

(U) Figures 279 and 280 show the effect of inlet Mach numbers. It can be seen that the effect of increasing the Mach number is to cause a small decrease in the static pressure rise coefficient while the theoretical value computed from inlet and exit areas shows a rise with Mach number. The reason for this difference is in all probability that the total pressure losses increase with increasing Mach number causing a decrease in effective exit area.

(U) Figure 281 shows the effect of inlet swirl angle with no leakage or misalignment. With the flat inlet velocity profile, i.e. (no B.L. Strip), the static pressure rise coefficient peaks at a swirl angle of about 20 degrees.

(U) Figures 282 through 286 are similar to figures 275 through 280 except that they have an inlet velocity profile generated by the thick 1/8 inch strip on the upper side of the flow path.

(U) Figure 287 is a photo of the inlet side of the diffuser section showing the results of the flow visualization test. The results of this test showed flow separations in several of the intersections between the stator vane convex side and the diffuser wall. These separated areas could also be detected on the total pressure traverses just downstream of the vanes and seemed to be related to rather small gaps between the vanes and the flow path which could have allowed some leakage flow or recirculation within the gap.

#### Conclusions and recommendations.-

- (U) Turbine diffusers with up to 12 degrees included wall angle and 23 degrees of inlet swirl will work well as long as the leakage and flowpath misalignment are carefully controlled. Static pressure rise coefficients up to .3 are obtainable under these good conditions.
- (U) Seal leakage causes a steady degradation of the pressure rise attainable through the diffuser but does not cause any sudden discontinuities in performance. The seal-out configurations were practically unable to function as diffusers.

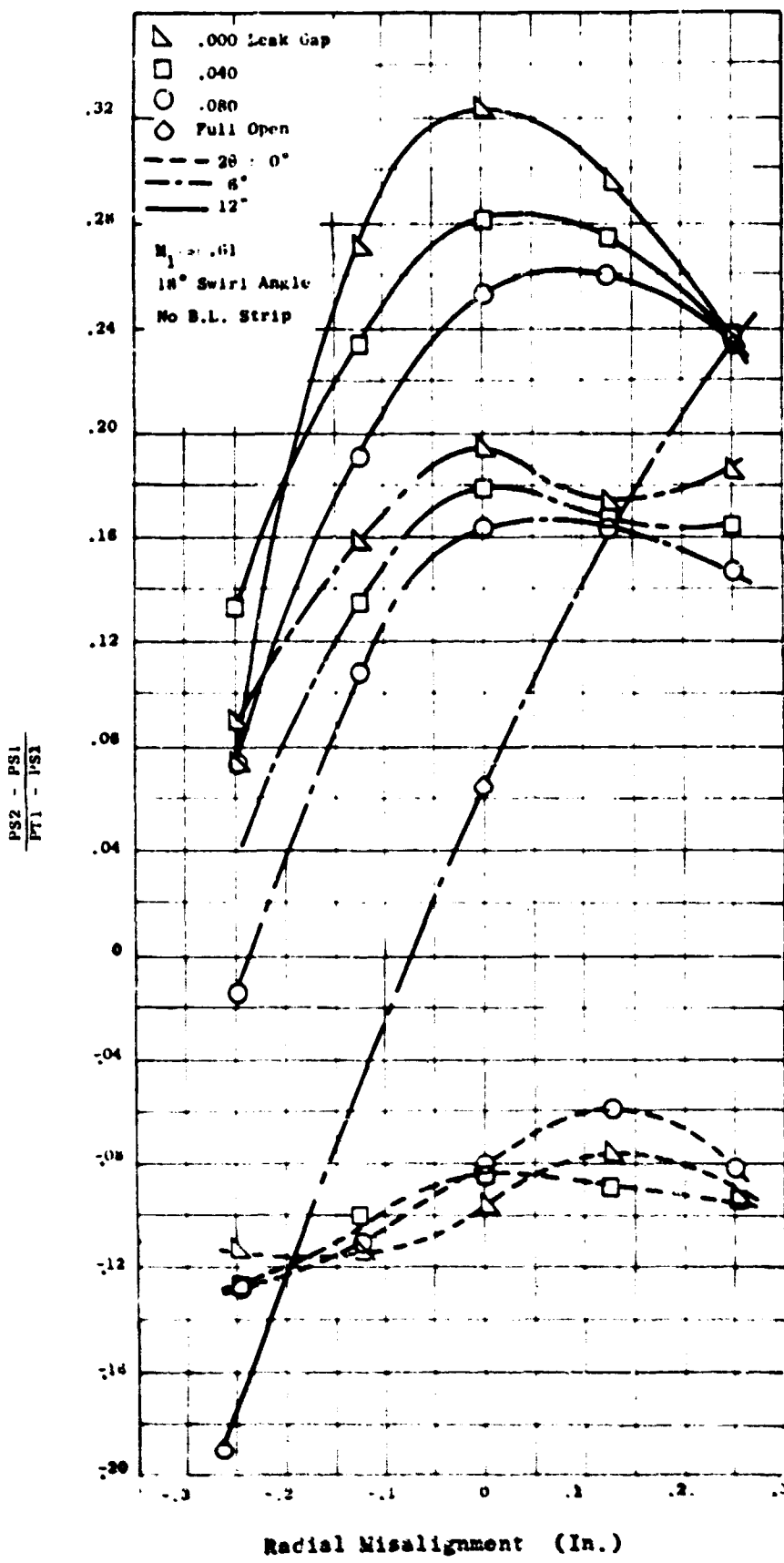


Figure 278 Tip Turbine Diffuser Investigation  
Effect of Radial Misalignment

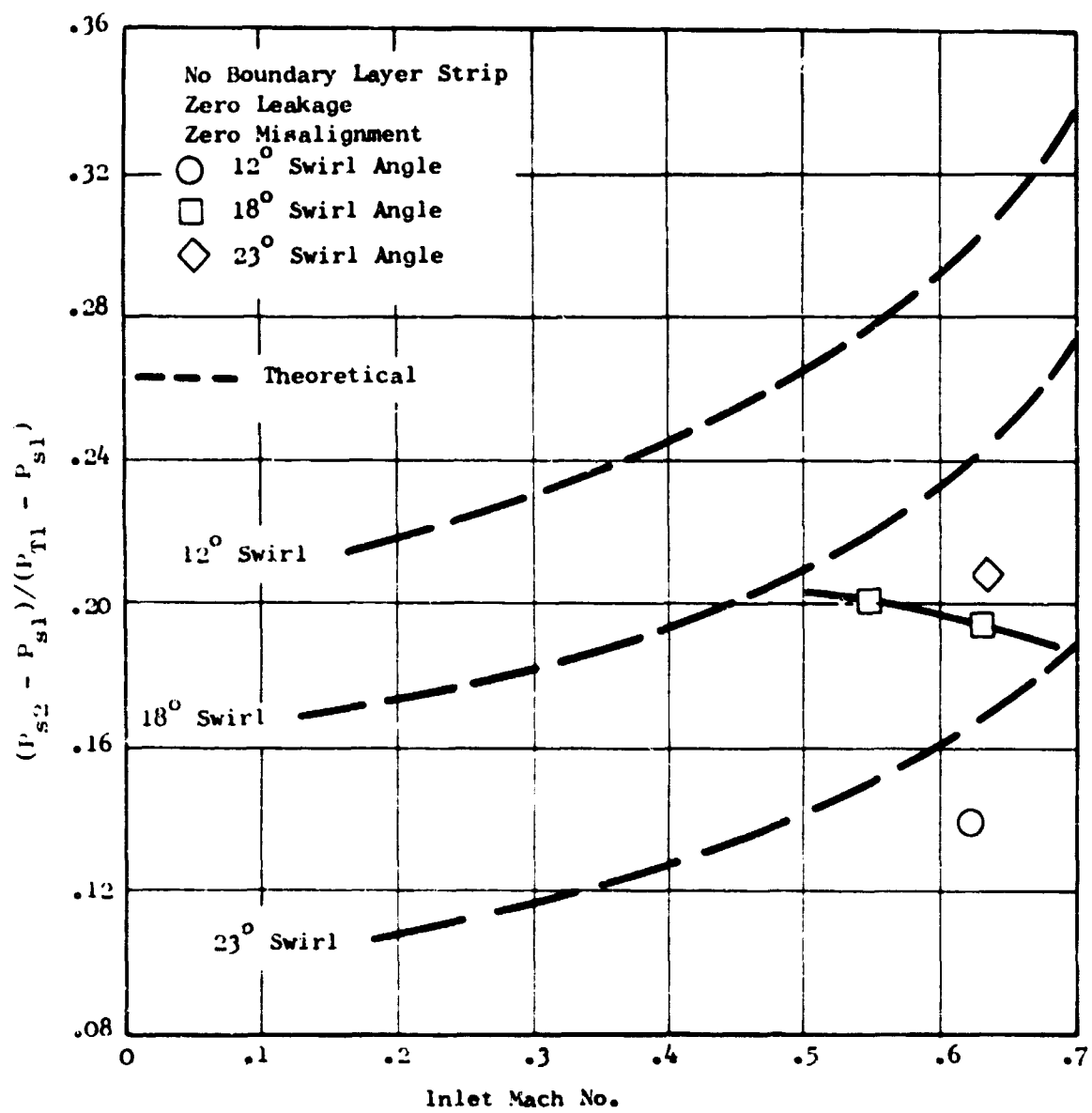


Figure 279 Tip Turbine Diffuser Investigation Effect of Inlet Mach No.;  $2\theta = 6^\circ$

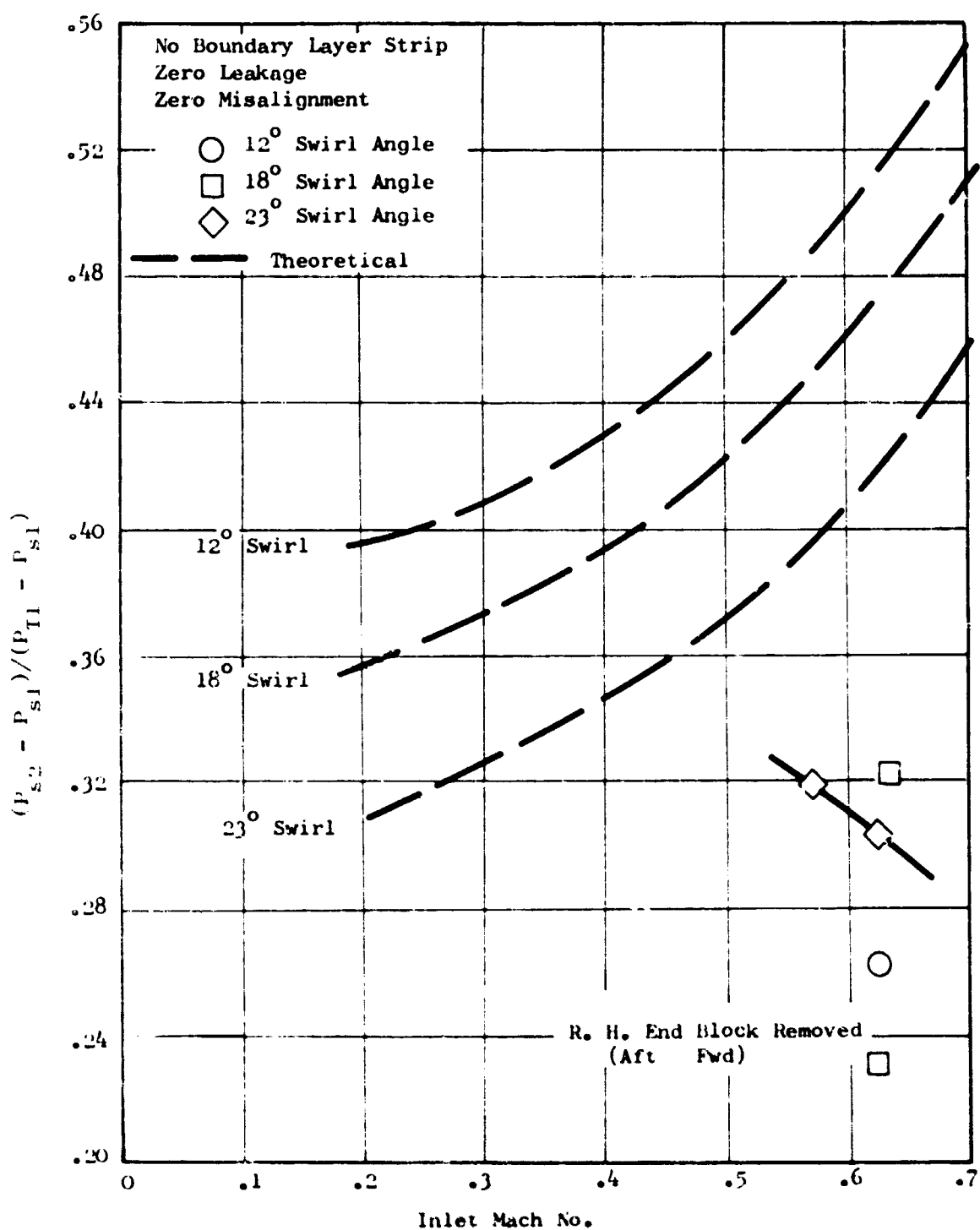


Figure 280 Tip Turbine Diffuser Investigation - Effect of Inlet Mach No.;  $2\theta = 12^\circ$

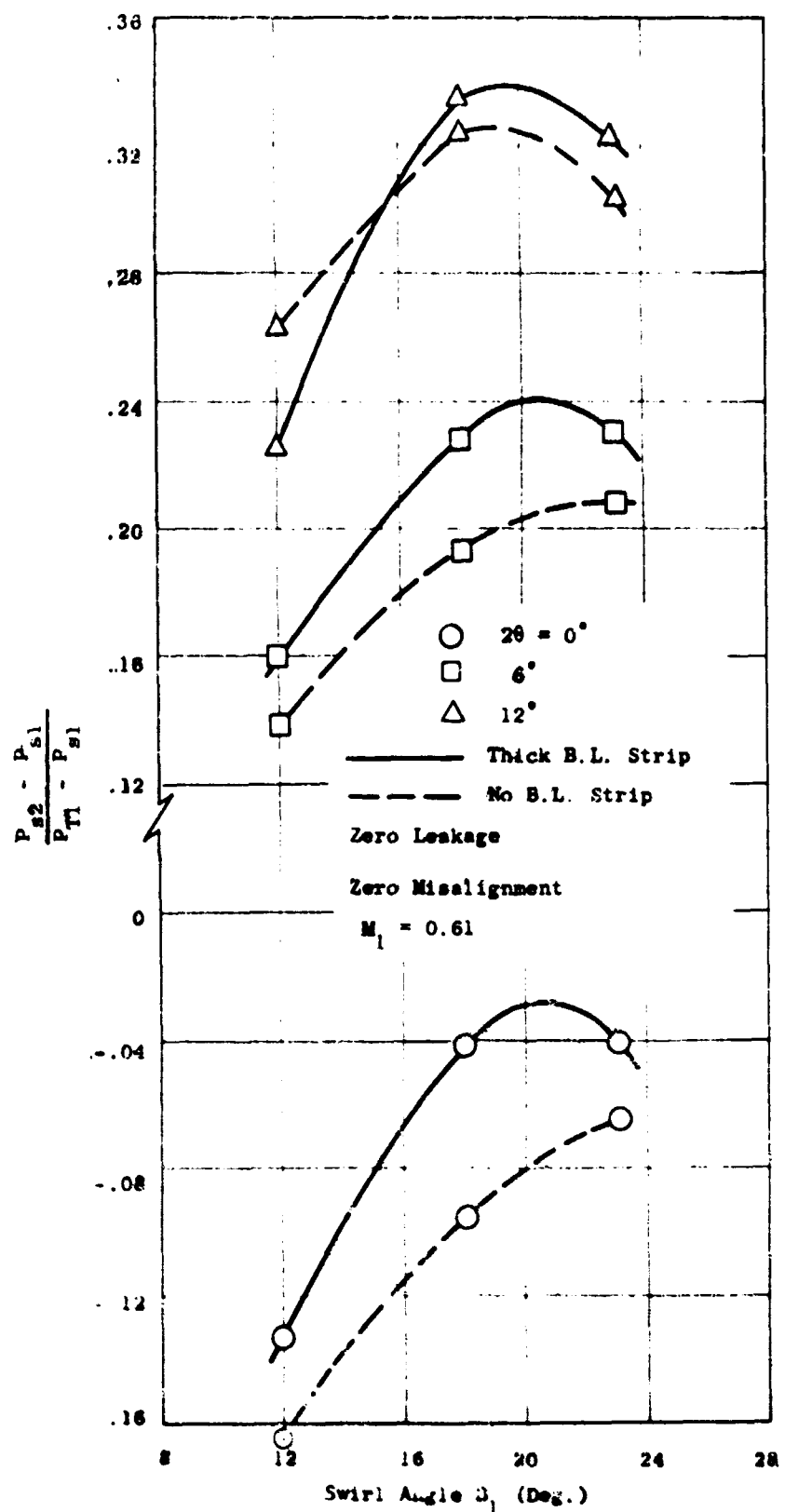


Figure 281 Tip Turbine Diffuser Investigation -  
Effect of Inlet Swirl Angle

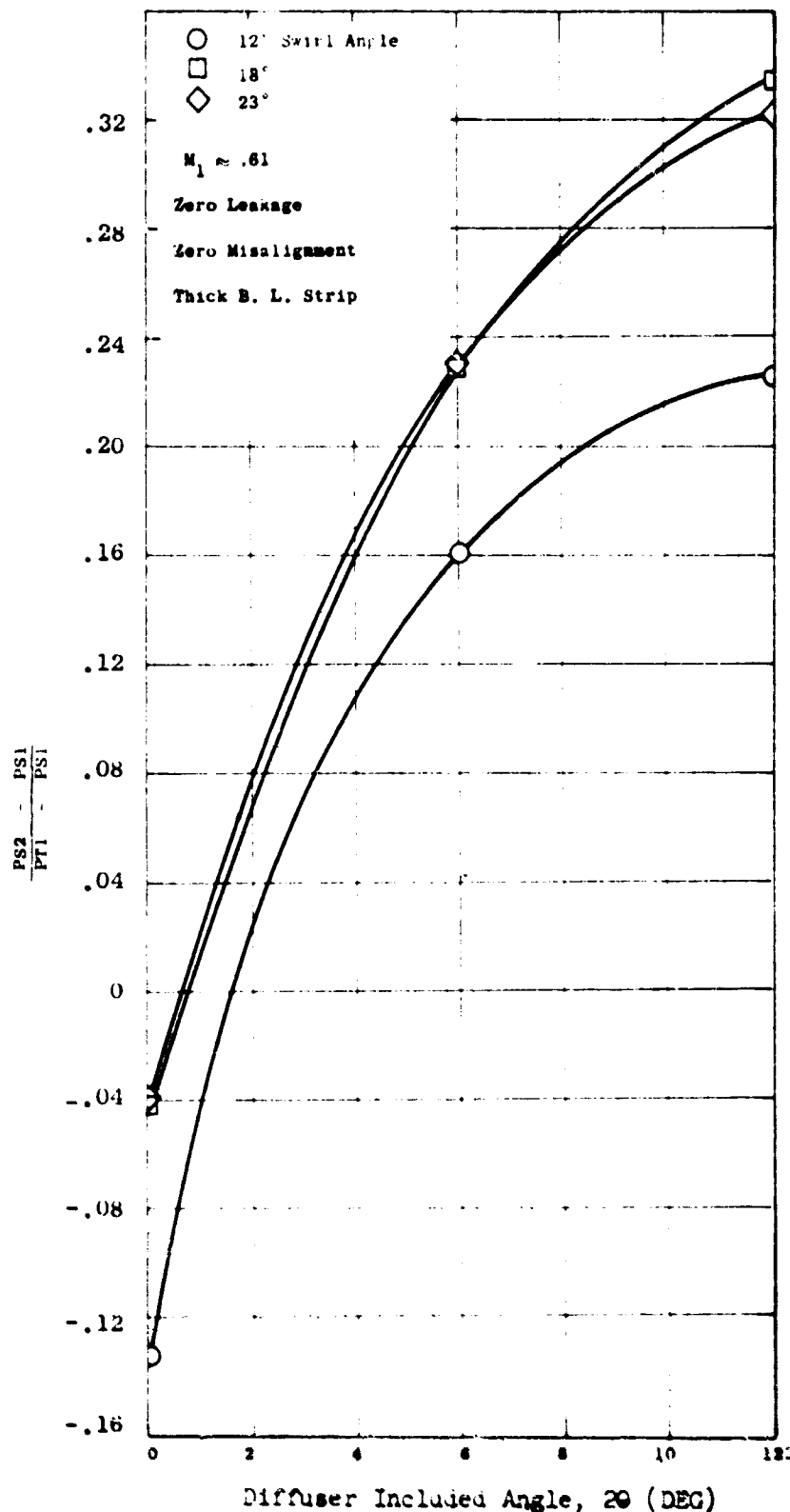


Figure 282 Tip Turbine Diffuser Investigations - Effect of Divergence Angle

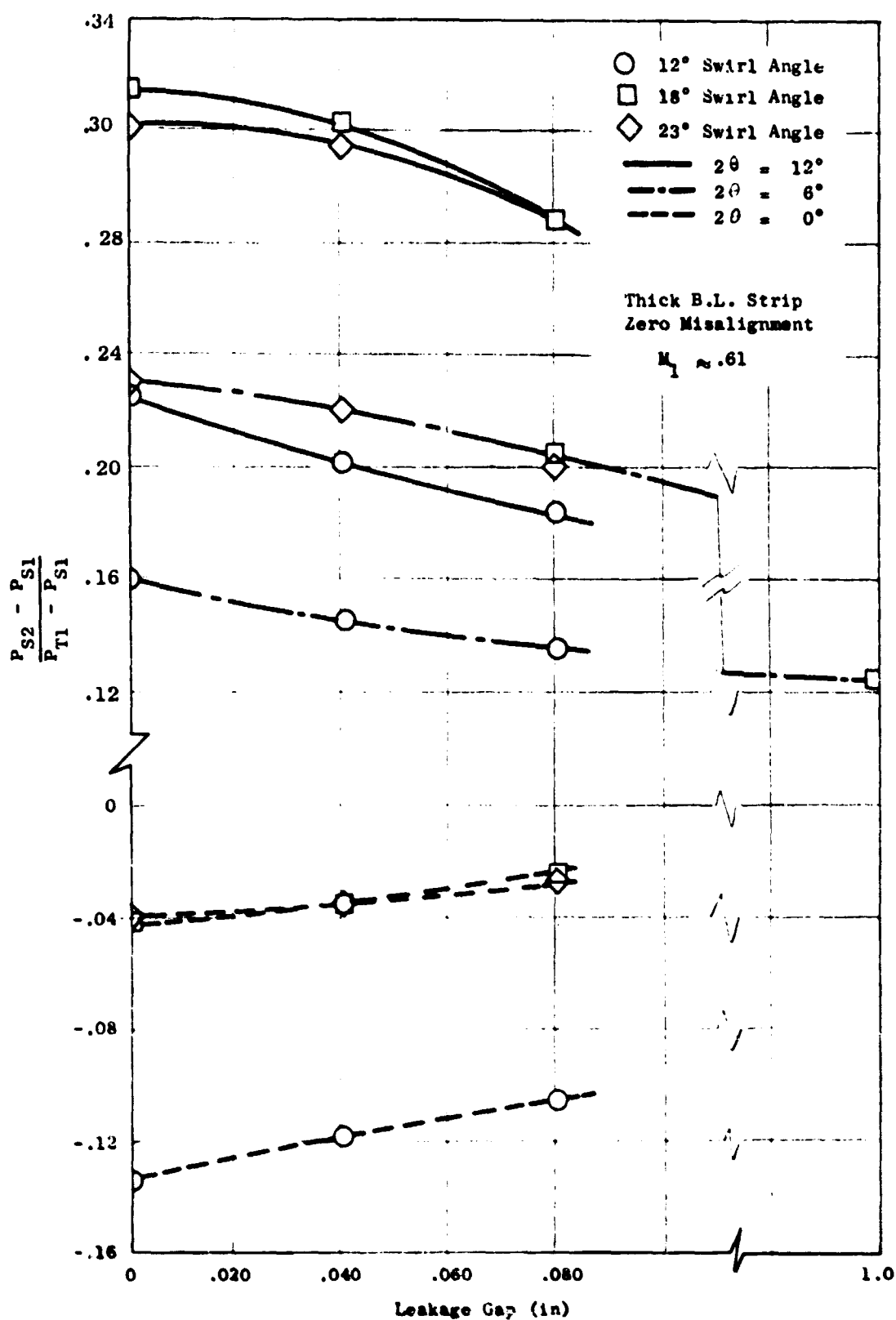


Figure 283 Tip Turbine Diffuser Investigation -  
Effect of Leakage

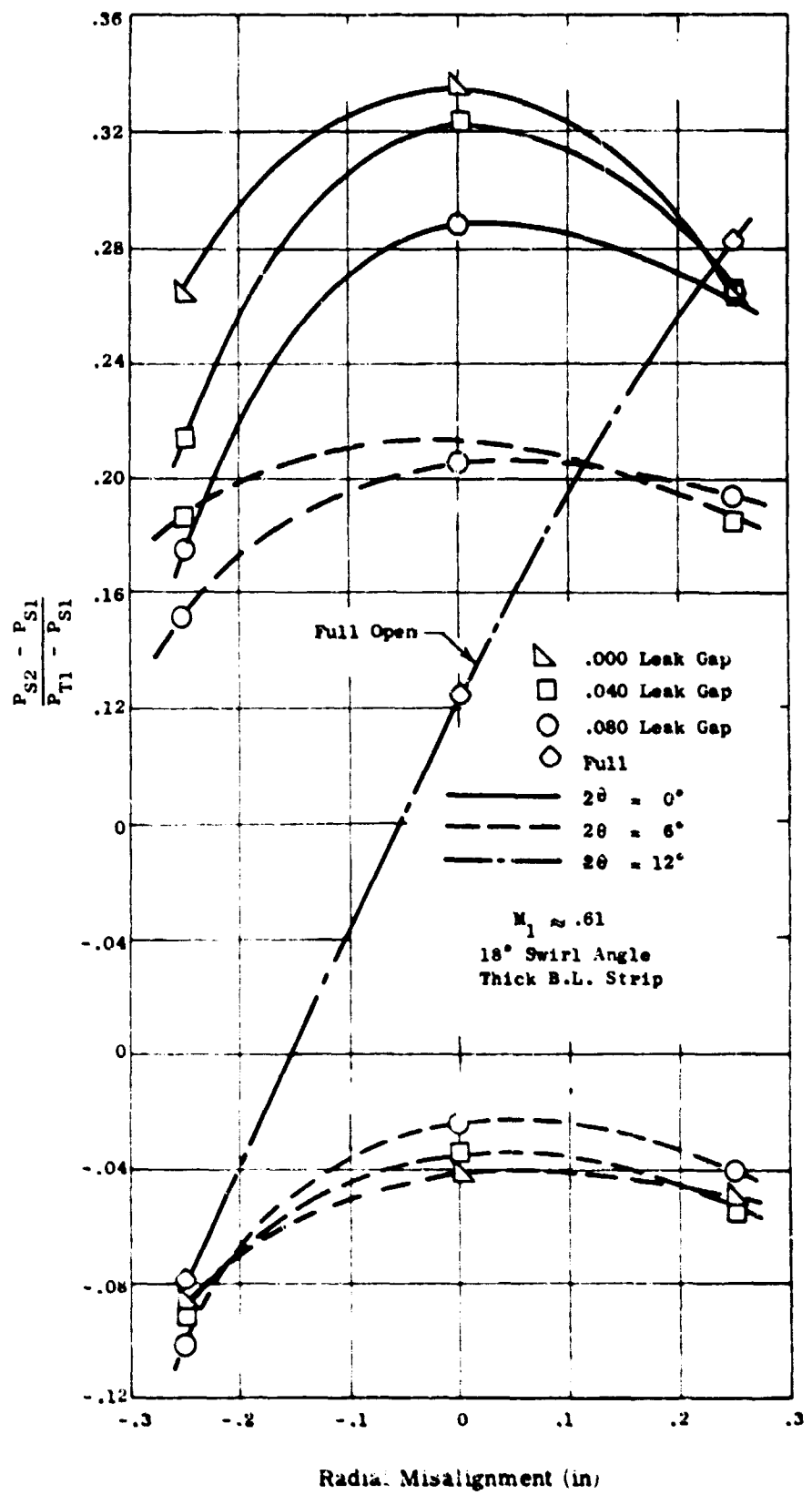


Figure 284 Tip Turbine Diffuser Investigation-  
Effect of Radial Misalignment

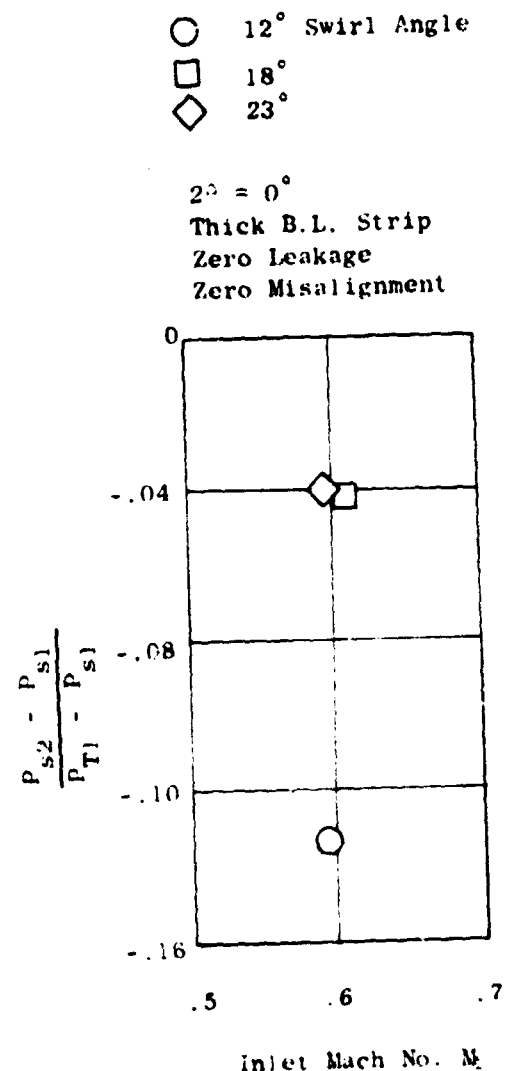


Figure 285 Tip Turbine Diffuser Investigation -  
Effect of Inlet Mach No.;  $2^\circ = 0^\circ$

$2^a = 6^\circ$

- $12^\circ$  Swirl Angle
- $18^\circ$
- ◇  $23^\circ$

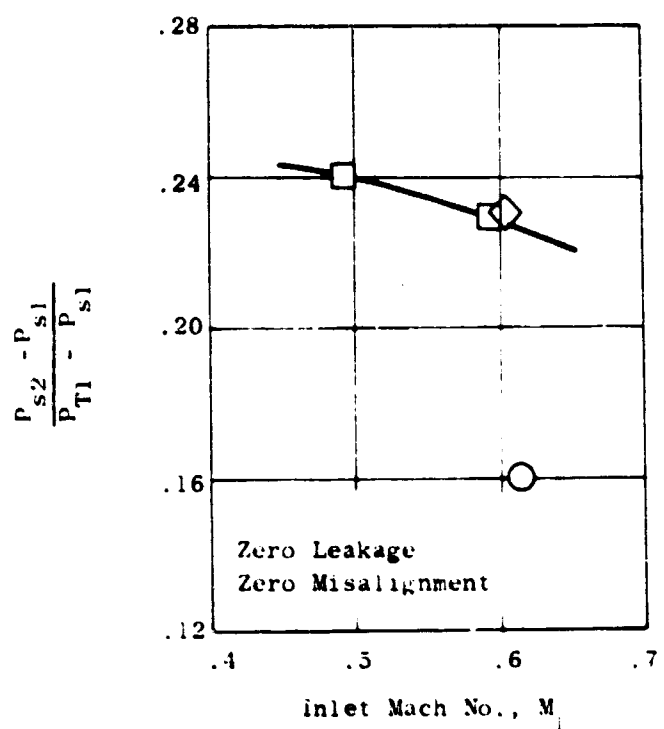


Figure 286 Tip Turbine Diffuser Investigation  
Effect of Inlet Mach No.;  $2^a = 6^\circ$



Figure 287 Tip Turbine Diffuser Test, Flow Visualization with Grease

(U) Radial misalignment of  $\pm 0.25$  inch in the flowpath has a severe effect on diffuser performance and may even cause a static pressure drop in some cases. Radial misalignment of  $\pm 1/8$  inch had much less severe effects but were still quite detrimental to the attainable static pressure rise.

(U) A radial velocity profile at the diffuser inlet representative of a typical tip turbine exit profile does not decrease the static pressure rise coefficient and even seems to be beneficial for large negative flowpath misalignments.

## Mechanical Programs

### Turbine Sector Cooling

#### Introduction.-

(U) Advanced lift fan and lift/cruise fans, in order to keep pace with advanced jet engine thermodynamic technology, are required to operate at hotter turbine inlet temperatures. This turbine design will be compatible with 1600°F inlet gas temperature as compared with the present fan operating inlet gas temperature of 1200±F. The present Inconel turbine carrier and 6Al-4Vn titanium blade attachment geometry is endurance and creep limited because of the allowable material properties at the metal operating temperatures. In order to comply with the 1600°F gas compatibility, new bucket and turbine carrier materials and/or turbine bucket and turbine carrier cooling may be required.

(U) In support of the preliminary design of the proposed fan configuration, this Program's fundamental objective was to evaluate the need for, and if required, to determine the configuration of, the turbine bucket and turbine bucket carrier cooling scheme which is directly applicable to the demonstrator fan rotor design. The evaluation shall be to analytically investigate the need for cooling through mechanical design to determine if weight and stress requirements can be achieved without the aid of cooling. This investigation shall be backed up by heat transfer analysis and bench test, to test the validity of the assumed part temperatures.

#### Discussion.-

(U) Preliminary heat transfer studies of the carrier system indicated the gross temperature levels associated with various heat transfer models of the carrier. They showed that significant (greater than 100°F) reductions in carrier side rail temperatures can be obtained by heat shields, forced convection cooling, or by relocation of the turbine flowpath seal. However, temperature levels were not as severe as some prior estimates. As a result the heat transfer testing program initially considered was omitted and the program concentrated on analytical determination of the need and configuration (if required) of the optimum cooling configuration.

(U) Turbine Preliminary Design Requirements were issued to better define the turbine to be studied for weight and cooling effectiveness. This insured that the recommendations of this program will be directly applicable to detail design of demonstrator hardware.

(U) Additional capability was brought into the program by sub-contracting a portion of the heat transfer analysis to the General Electric, Design Technology Operation group. By sub-contracting, the program will benefit from the best experience

available. This heat transfer analysis group has contributed to the success of Evendale jet engine products by predicting metal operating temperatures in very close agreement of actual test engine data, thus supporting advanced programs in the drafting and design phase, where the payoff is the greatest.

(U) Initial analysis was of the "base case" carrier having an integral blade attachment and no cooling or shielding. The temperature distribution in this carrier is shown in Figure 290.

(U) A review of strength-versus-temperature (Figure 286) for the turbine material showed the significance of the various turbine temperatures. For turbine components operating at 1100°F or below, any reduction in temperature does not improve material strength as noted by the flatness of the curve at temperatures below 1100°F.

(U) Since Figure 290 shows that only the upper carrier blades and shrouds operate above 1100°F, the only weight improvement through cooling lay in these areas. Furthermore, previous studies ruled out bucket and shroud cooling because they require such extreme cooling techniques.

(U) Weight penalties would be excessive for cooling these areas except where gas generator EGT is significantly above the present 1600°F design point. This leaves only the upper carrier as a fruitful area for cooling/weight trade-off studies.

(U) Work on cooling studies was concentrated on reduction of temperatures in the locally hot, upper carrier areas. This amounts to temperature reduction on the forward carrier from approximately 1400°F to approximately 1100°F (approximately 20% reduction) and on the aft carrier from approximately 1225°F to approximately 1100°F (only approximately 10% reduction).

(U) The most feasible scheme for cooling the side rails was to vent the turbine carrier interior to fan stream air. (Figure 289) This scheme allows fan air from the pressure side of the airfoil into the carrier through a cooling port. This vented air then circulates through the hot interior of the carrier and escapes through another cooling port into the fan stream on the suction side of the airfoil. Pressure differential across the airfoil is the driving force behind the vent air. The only geometry changes required to convert an uncooled carrier to this cooled configuration are bulkheads on the sector ends (to prevent leakage) and cooling ports.

(U) More detailed heat transfer calculations were made on an uncooled turbine with both vented and unvented carrier interiors. Steady state running conditions and soak back cases after fan shutdown were studied.

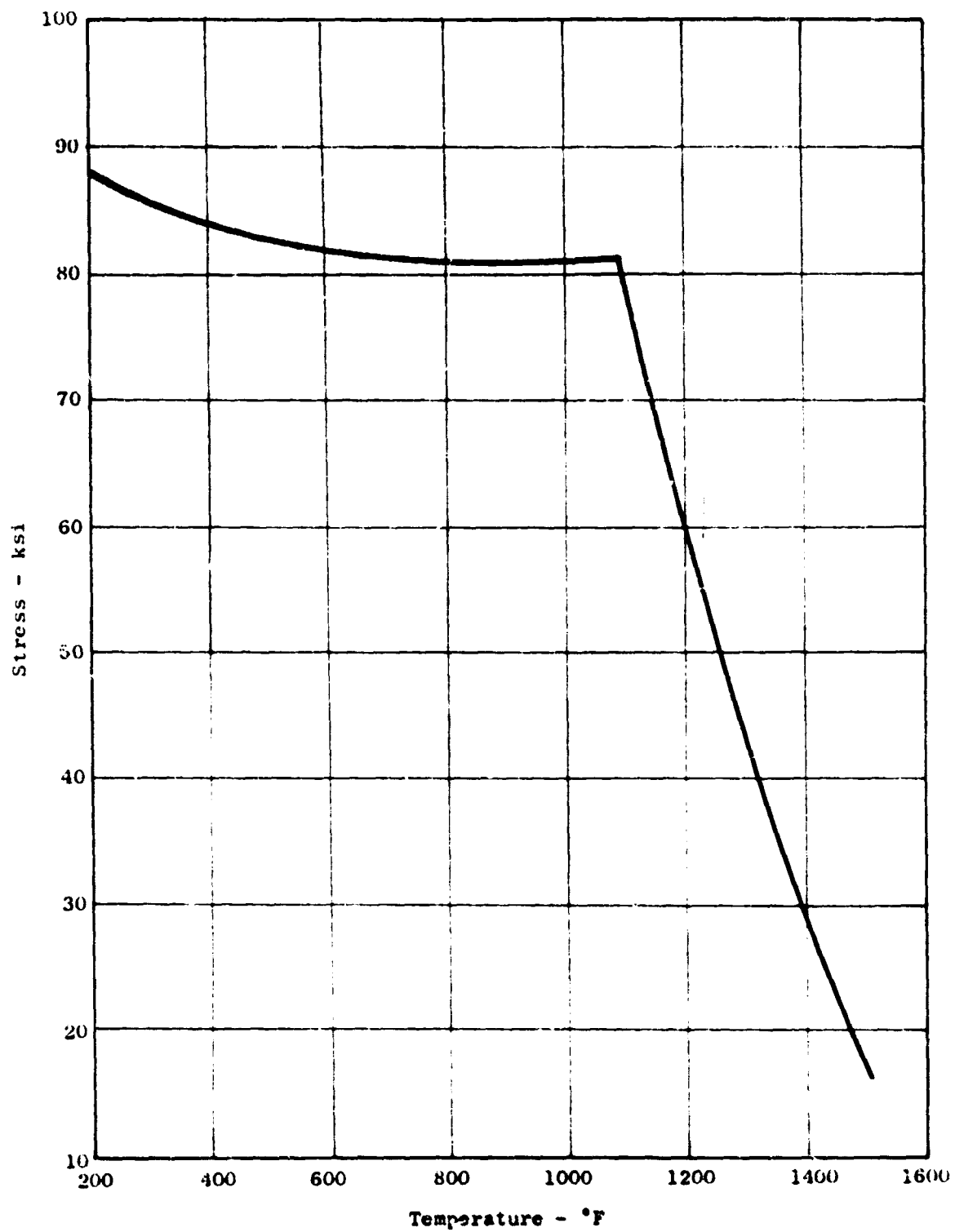


Figure 288 Minimum Properties of R41 Sheet

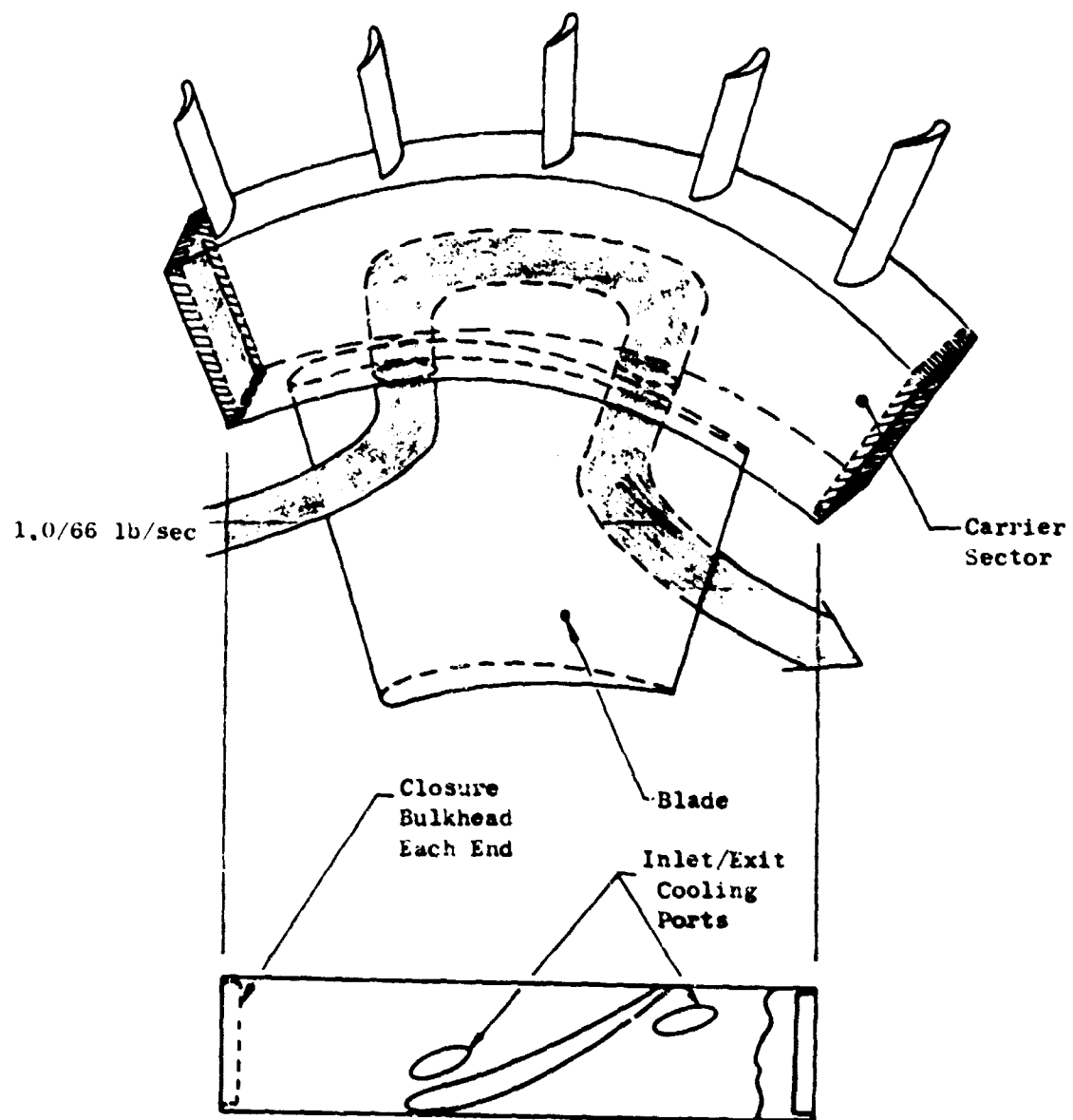


Figure 289 Turbine Cooled by Vented Fan Air

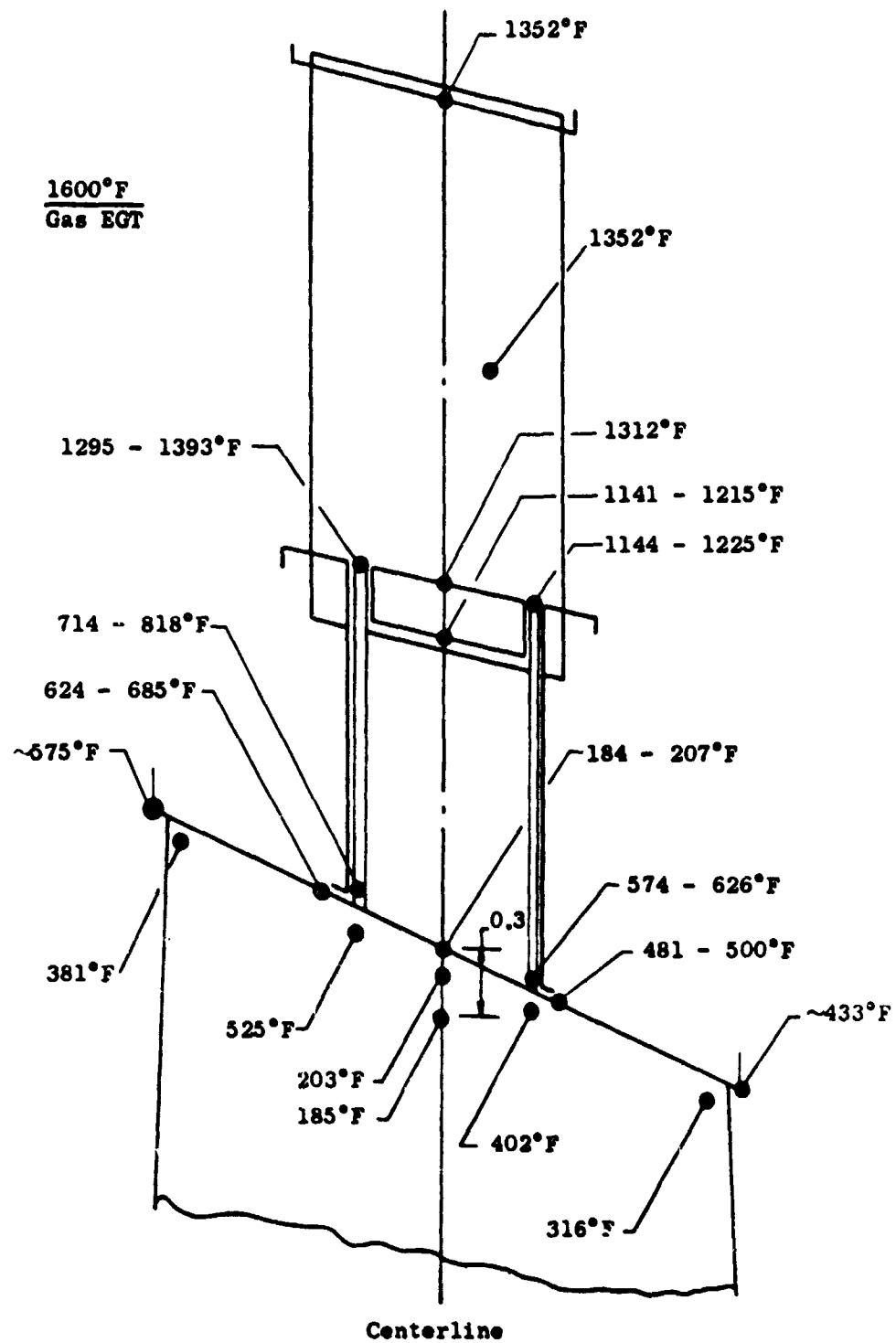


Figure 290 LF475 Rotor Tip Temperature Distribution - Steady State

(U) In weight tradeoff studies the configuration analyzed was a vented carrier identical to the base case uncooled carrier except for added cooling ports and end bulkheads. Upper regions of the vented carrier were also lightened to take advantage of the higher allowable stresses in these areas of reduced temperature.

(U) These weight studies showed that only marginal weight reductions were possible through the use of turbine cooling for the LF475 operating conditions.

Analysis.-

(U) Figure 291 shows the geometry assumptions for the heat transfer model.

(U) Heat Transfer Model: Figures 292 and 293 show the grid used to break the turbine geometry into small nodes or rectangular squares as required for computer analysis.

(U) Computer Program: The General Electric Transient Heat Transfer program, revision D, was used. This has been developed over the past several years as the best method available for detailed thermal analysis of complex geometry.

(U) Heat Transfer Assumptions:

Solid blade tip

Cycle conditions as defined in section III

Boundary conditions for adjacent gas:

<u>Location</u>	<u>Steady State</u>		<u>Soak Back</u>	
	T (°F)	h (BTU/hr-Ft <sup>2</sup> -°F)	T (°F)	h (BTU/hr-Ft <sup>2</sup> -°F)
Forward side rail	1675	34	130	5
Aft side rail	1266	39	130	5
Buckets & Carrier Top	1312	13-21	130	5-10
Blade Fwd 1/3 chord	130	75	130	5
Blade mid 1/3 chord	160	99	130	5
Blade aft 1/3 chord	192	123	130	5
Inner carrier(insulated)	1000	.01	130	.01
Inner carrier(.5 lb/sec cooling)	500	15	130	.01
Inner carrier(1.0 lb/sec cooling)	330	23.5	130	.01

Results.-

(U) Curves are grouped by cooling case: Figures 290 & 294 through 297 for no cooling, Figures 300 through 303 for .5 lb/sec bleed air, Figures 304 through 307 for 1.0 lb/sec bleed air.

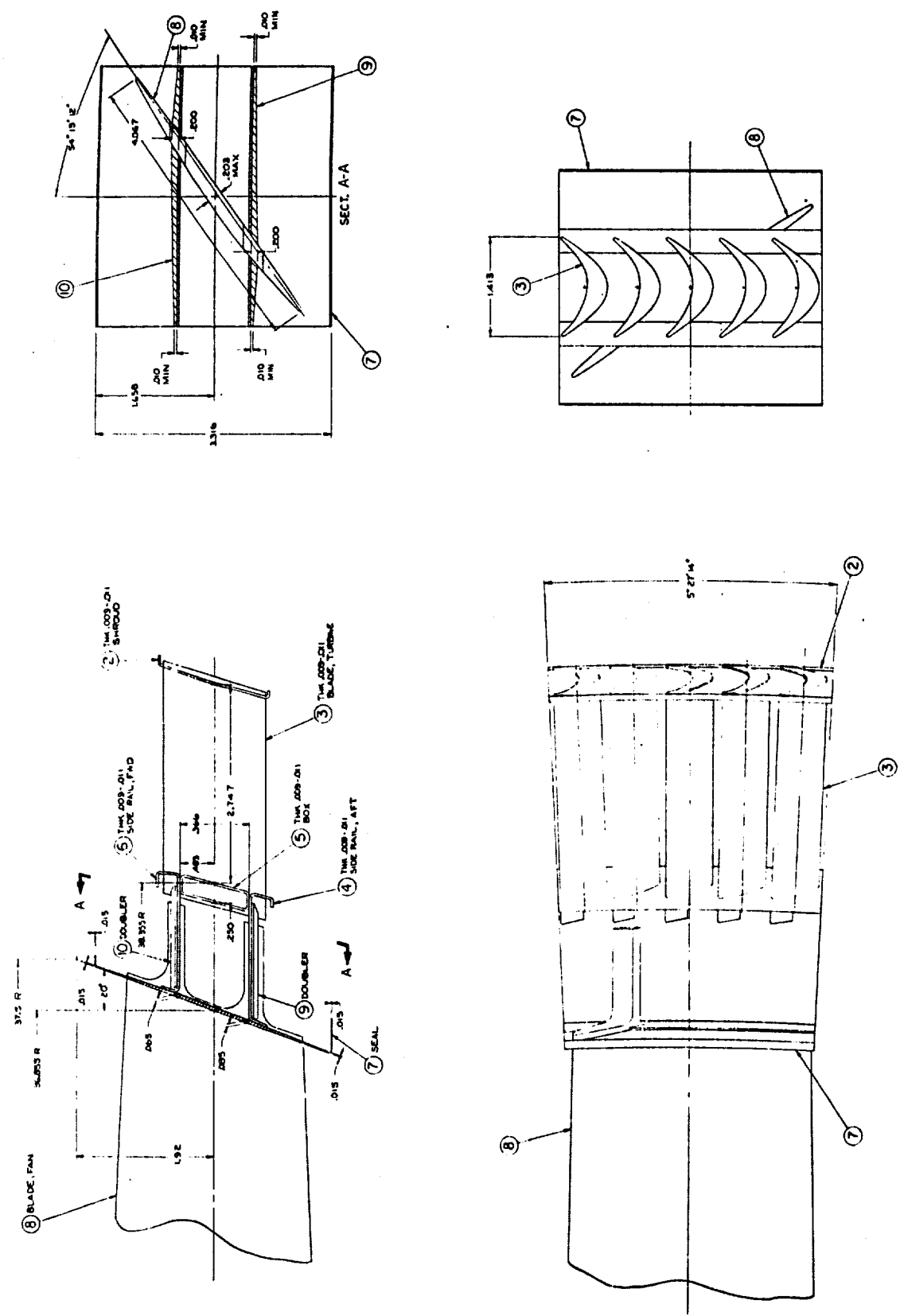


Figure 291 Carrier Assembly Preliminary Design

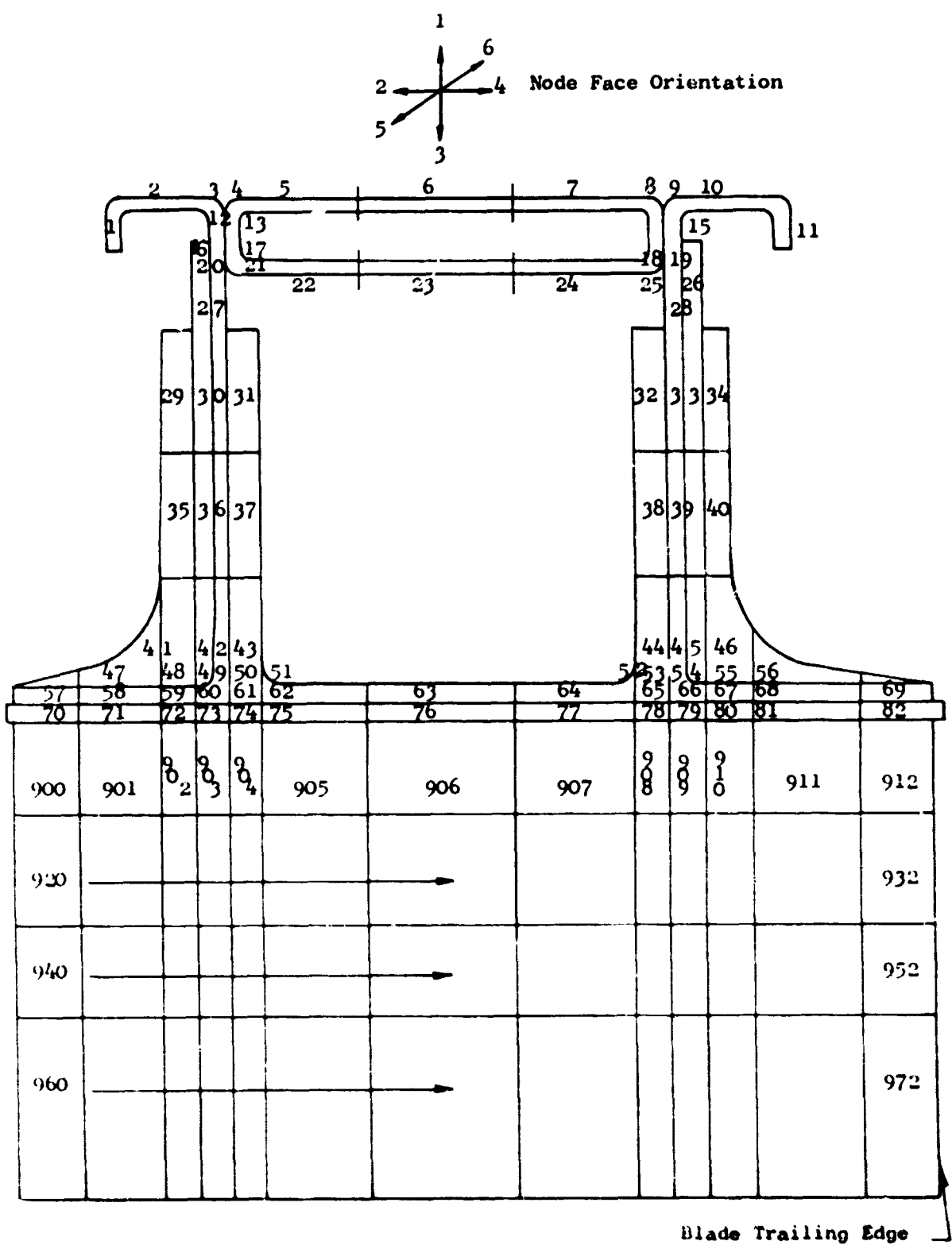


Figure 292 THTD Nodes - Turbine Cross Section

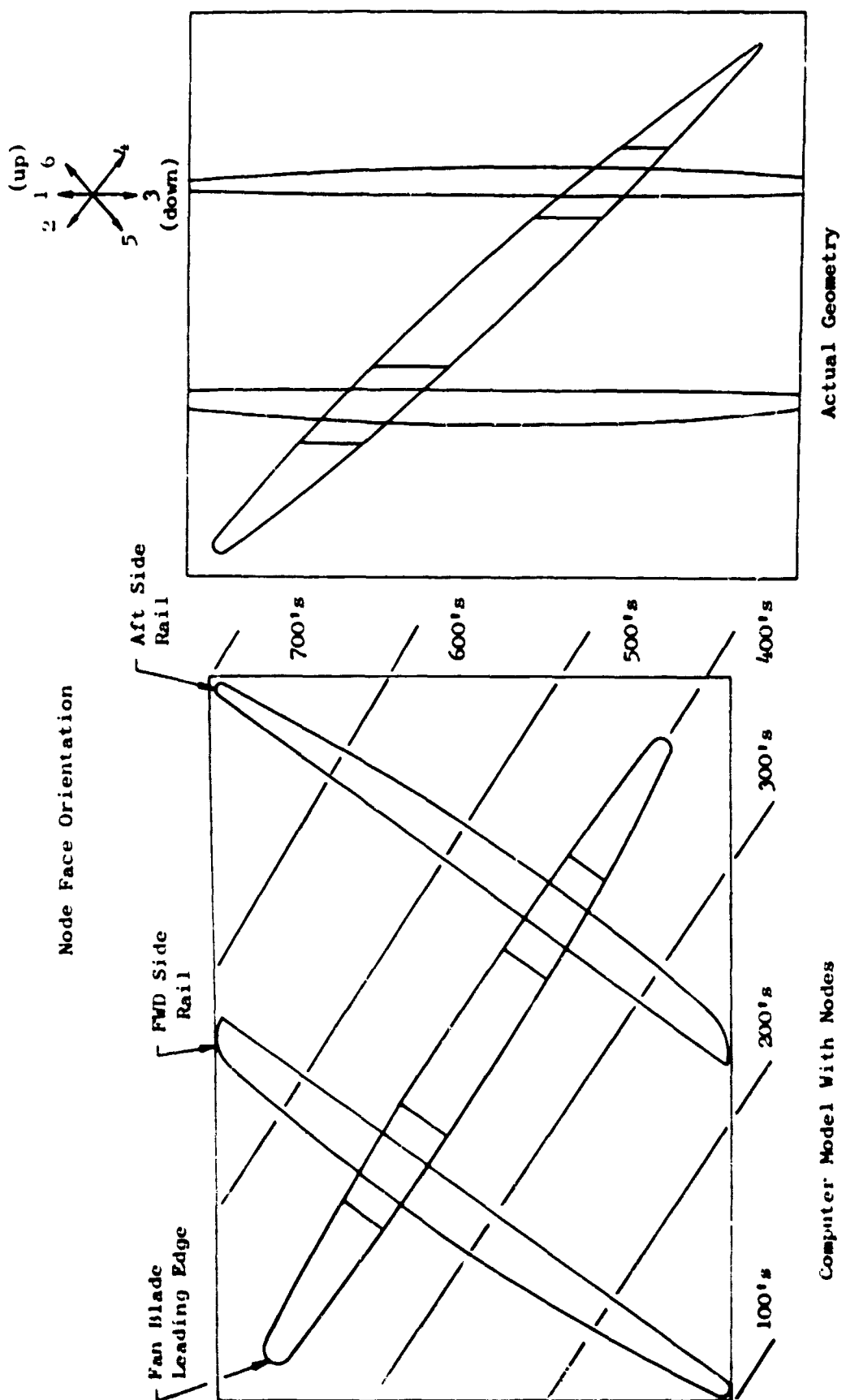


Figure 293 MHD Nodes - Turbine Top View

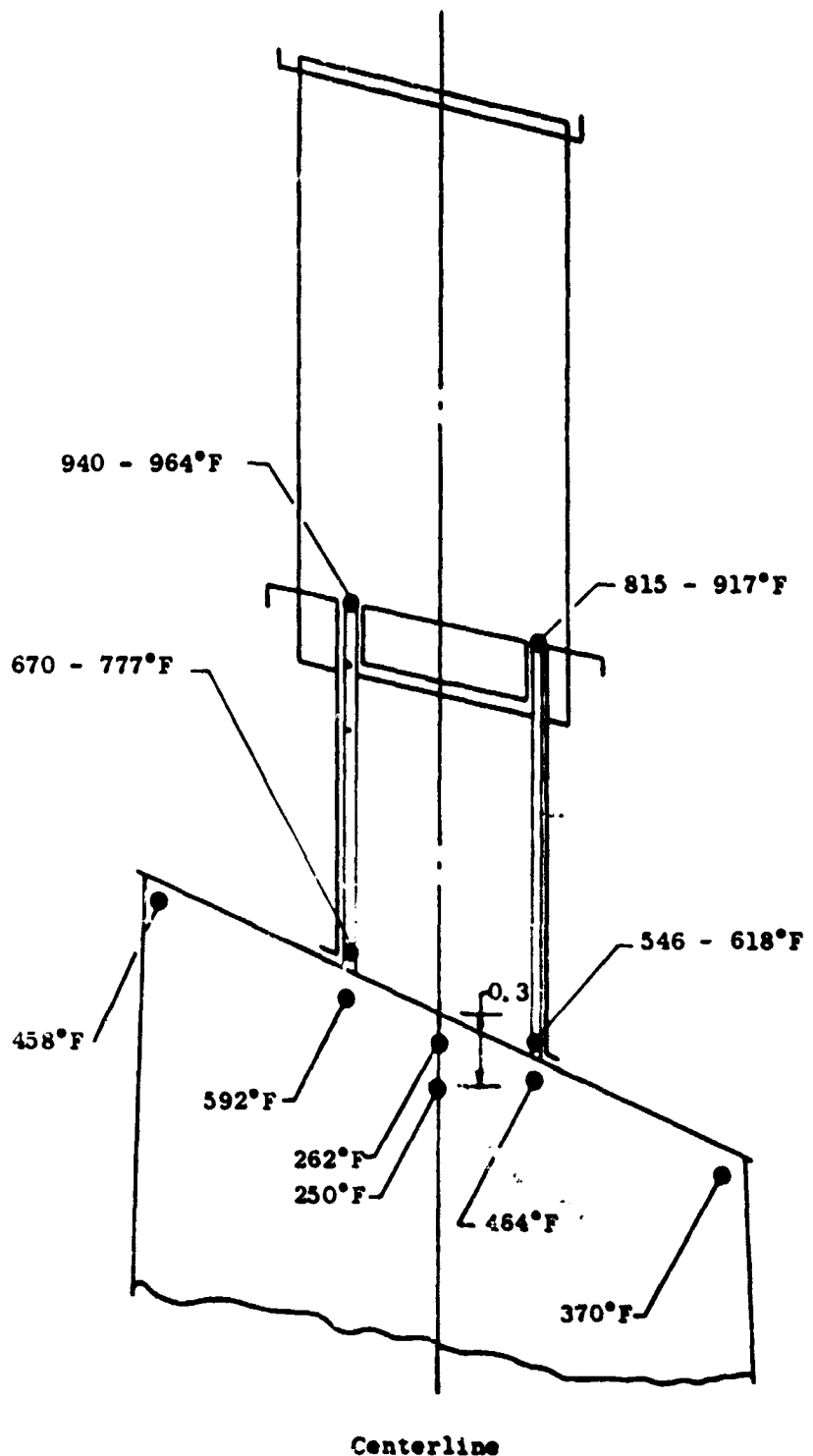


Figure 294 LP475 Rotor Tip Temperature Distribution - 20 Seconds Soak Back

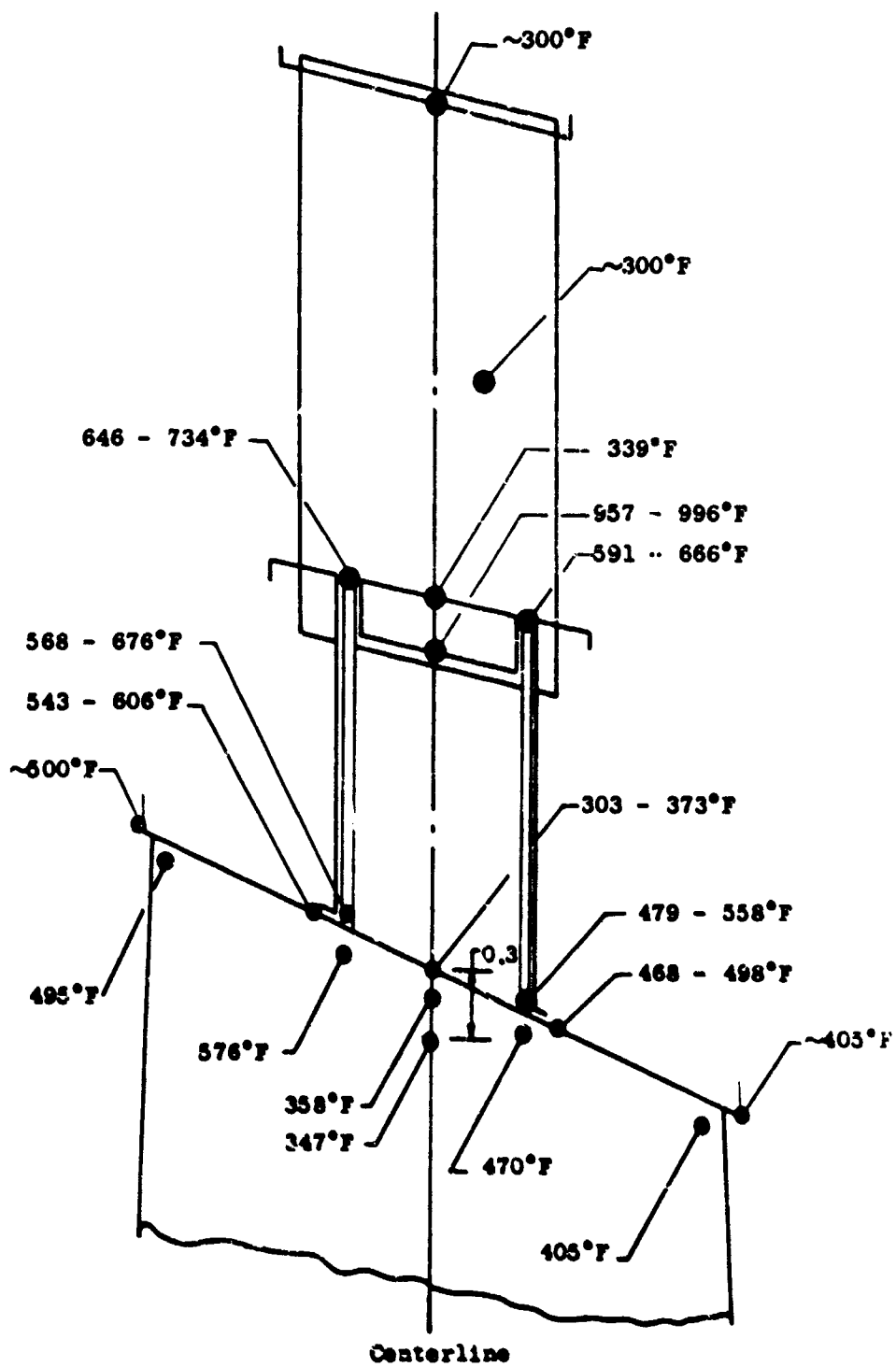


Figure 295 LP475 Rotor Tip Temperature Distribution - 50 Seconds Sod Back

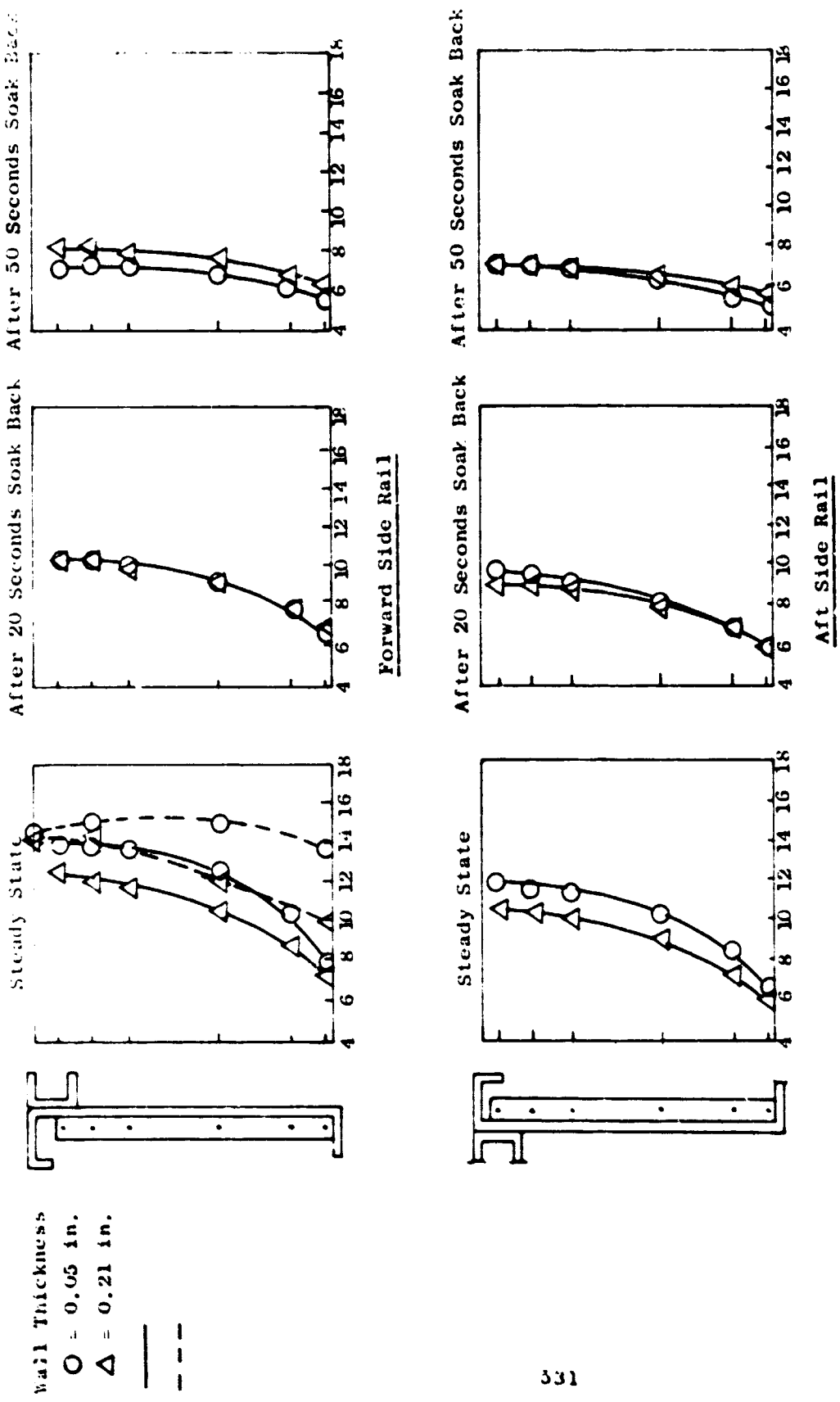


Figure 296 Turbine Side Rail Transient Temperatures

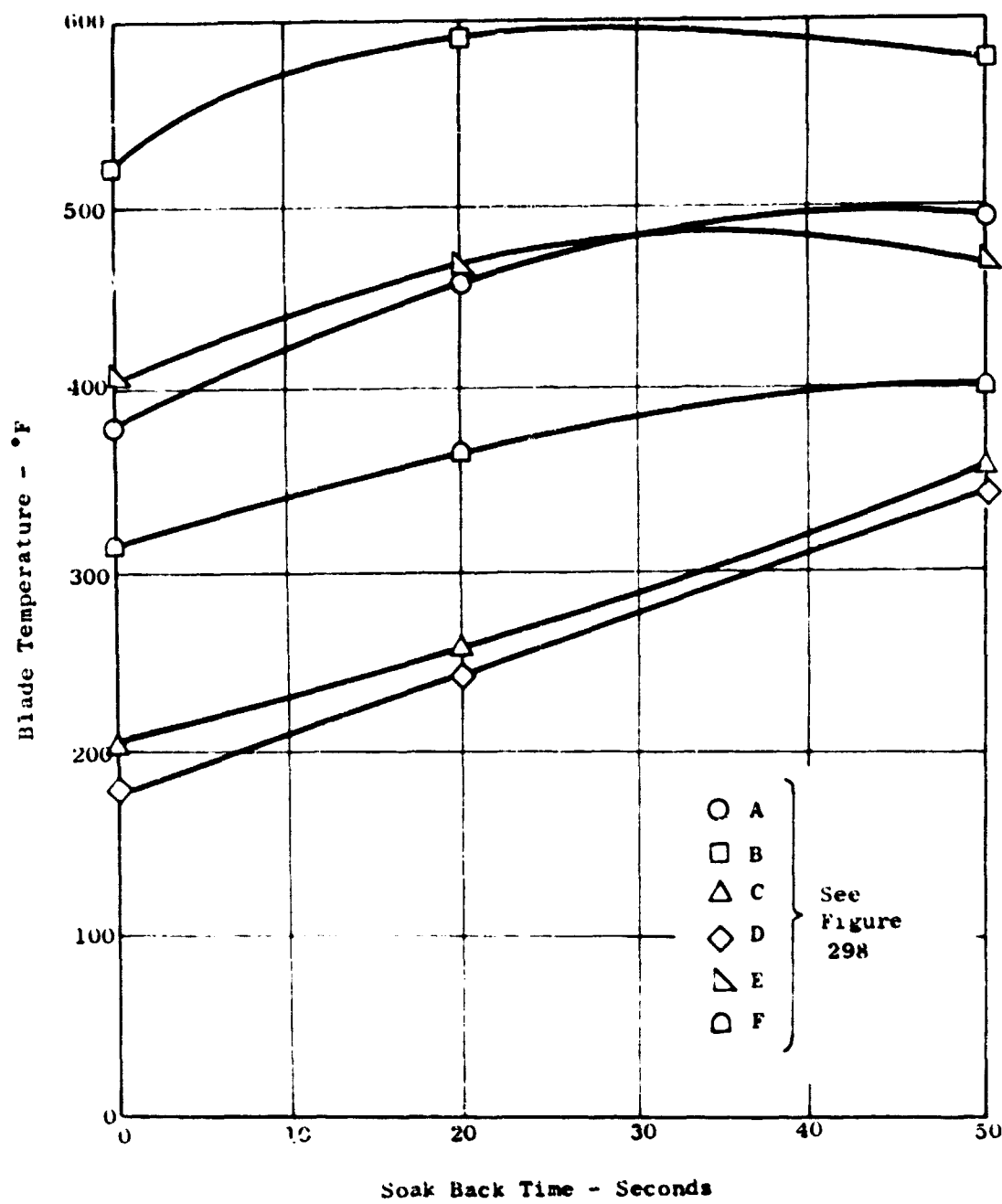


Figure 297 Blade Tip Soak Back - No Turbine Cooling

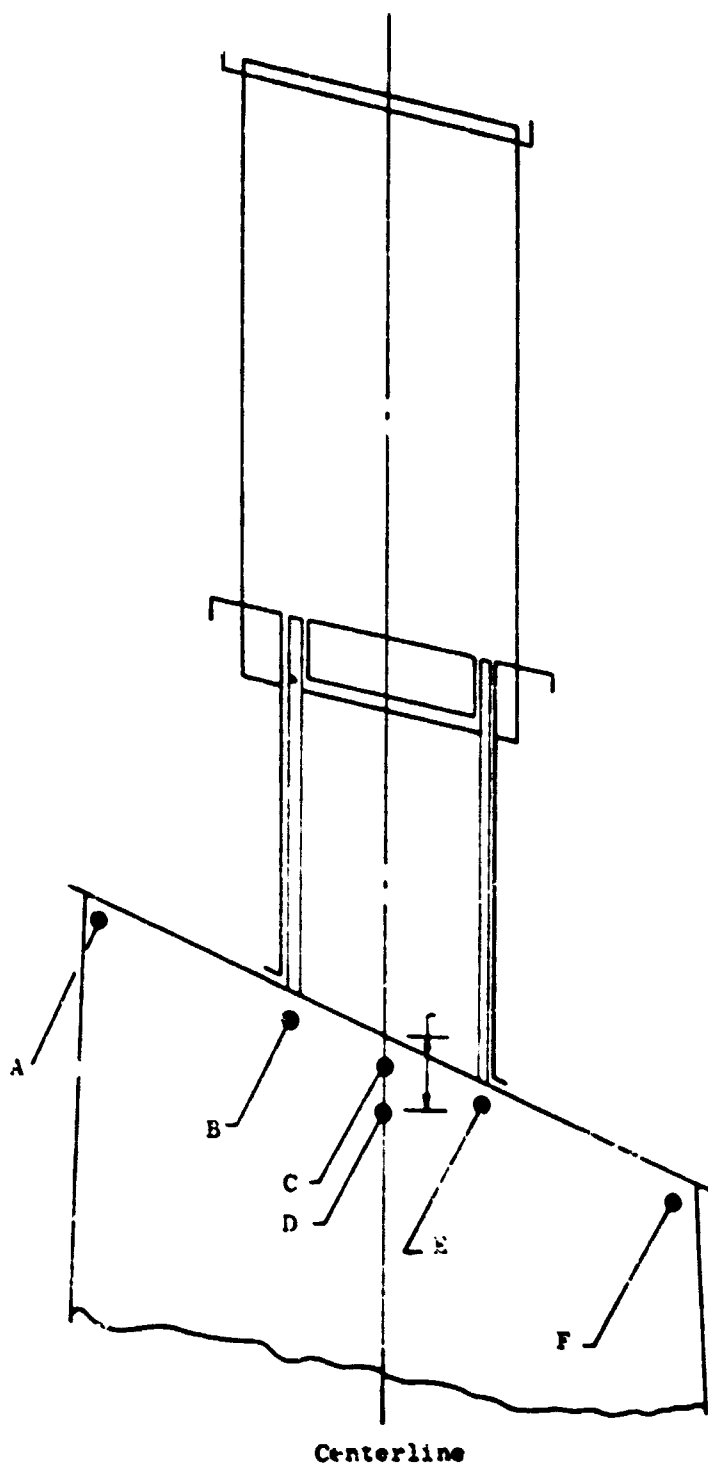


Figure 29F Temperature Distribution - LF475 Rotor Tip

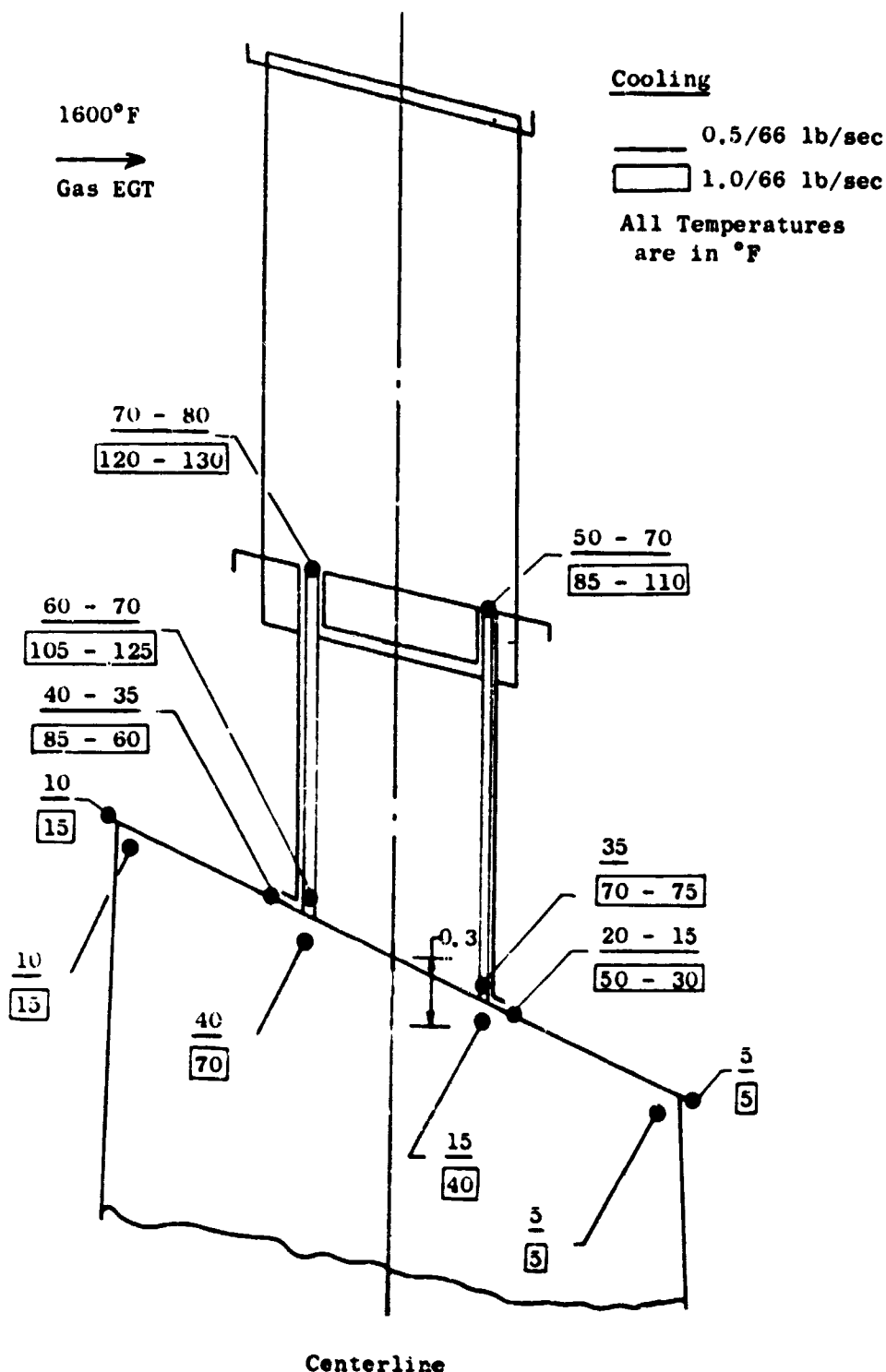


Figure 299 Drop in Steady State Temperatures Due to Carrier Cooling

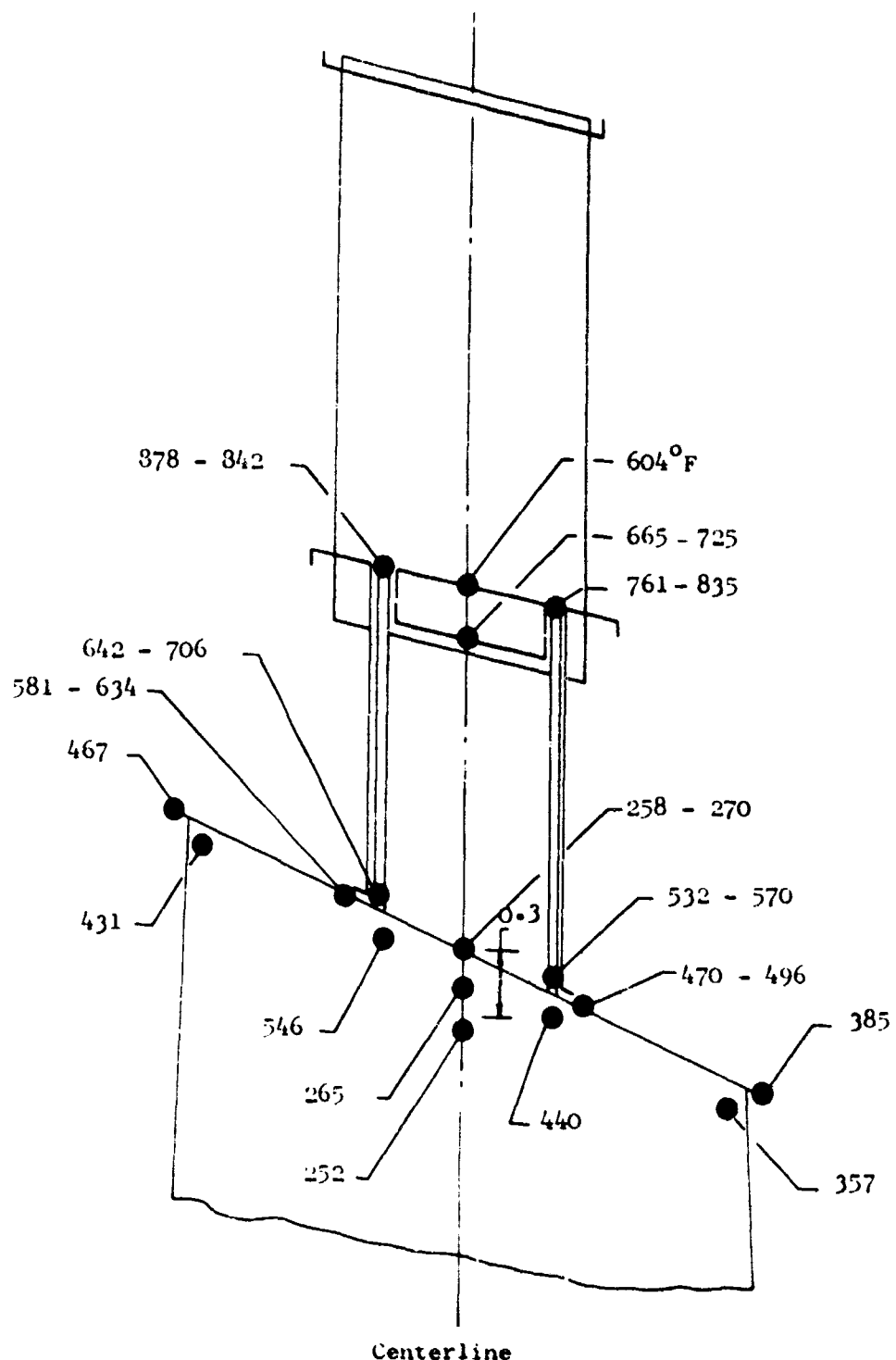


Figure 300 Temperatures After 30 Second Soak Back -  
.5 sec Carrier Cooling

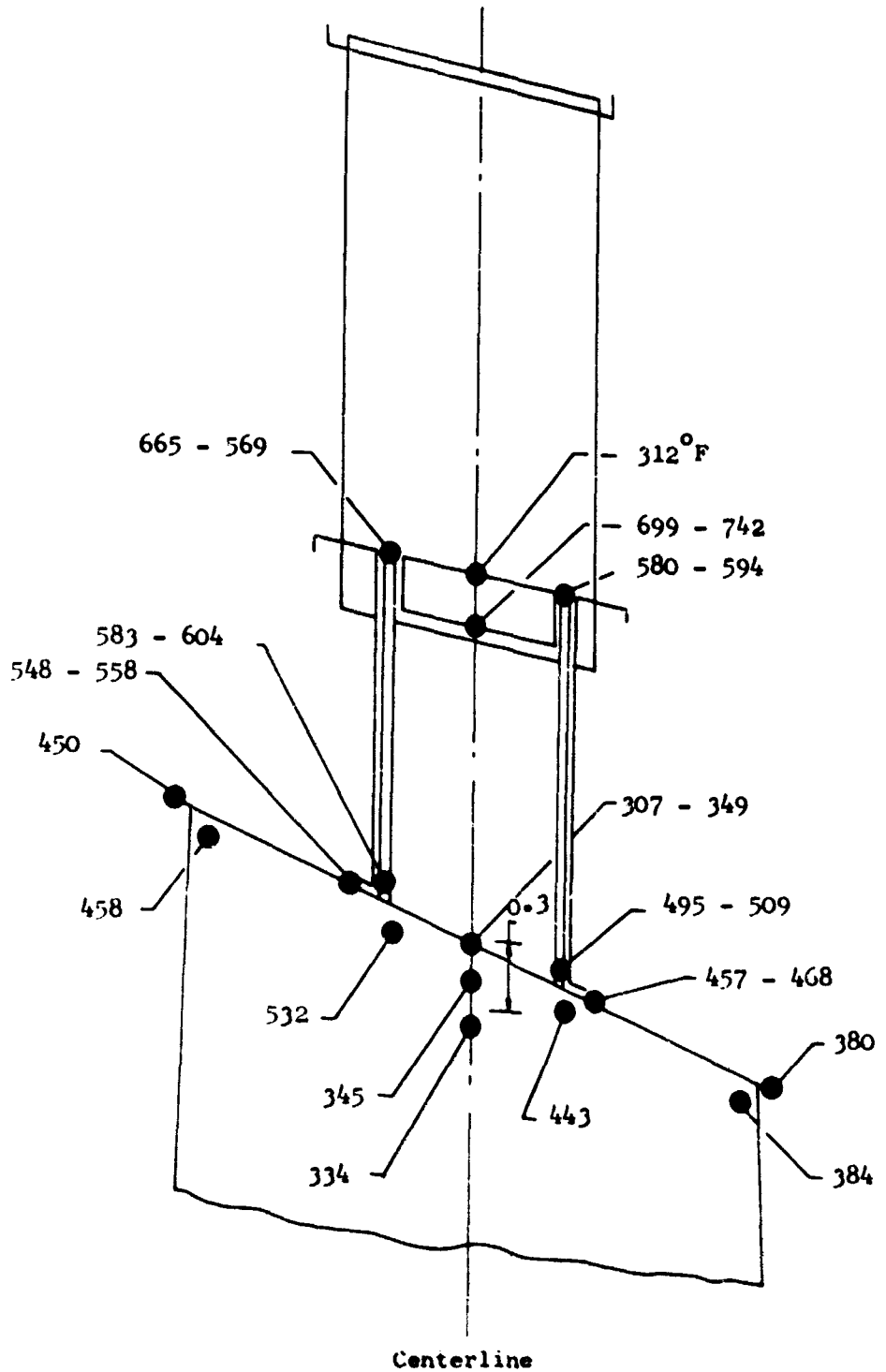


Figure 301 Temperatures After 50 Second Soak Back - .5  
lb/sq ft Carrier Cooling

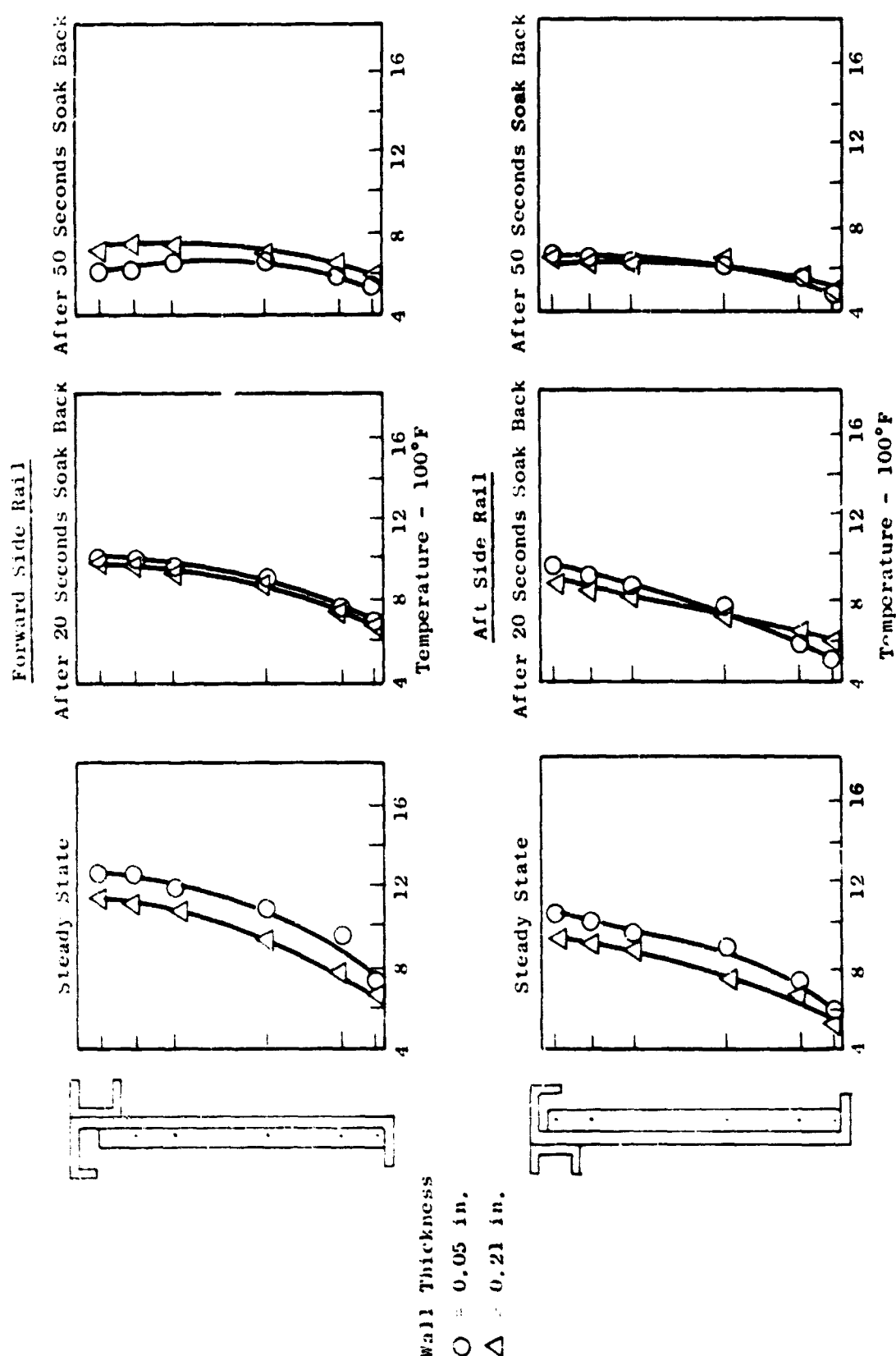


Figure 302 Turbine Side Rail Transient Temperatures - 0.5 lb/sec Bleed Air Cooling

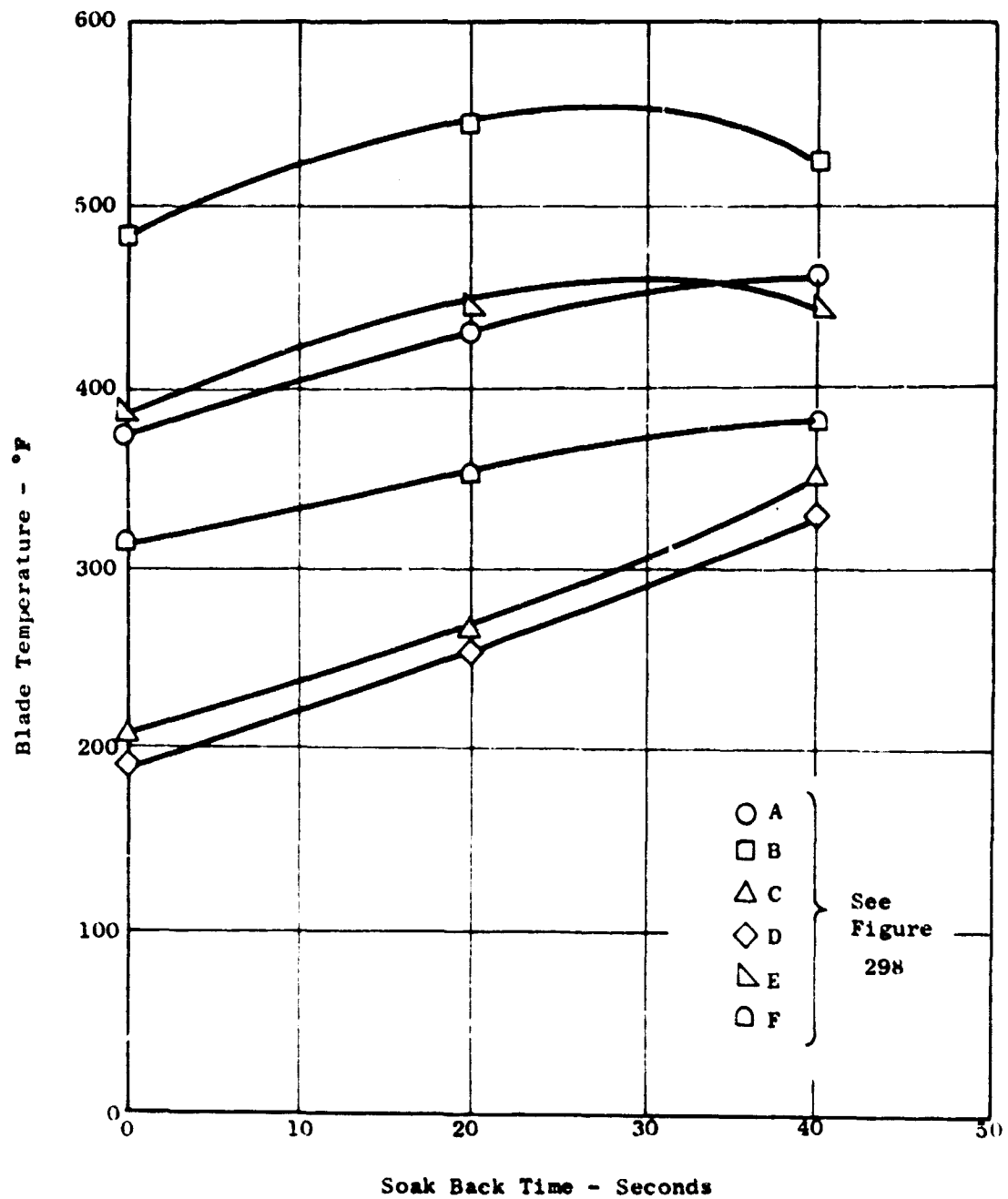


Figure 303 Blade Tip Soak Back - 0.5 lb/sec Bleed Air Cooling

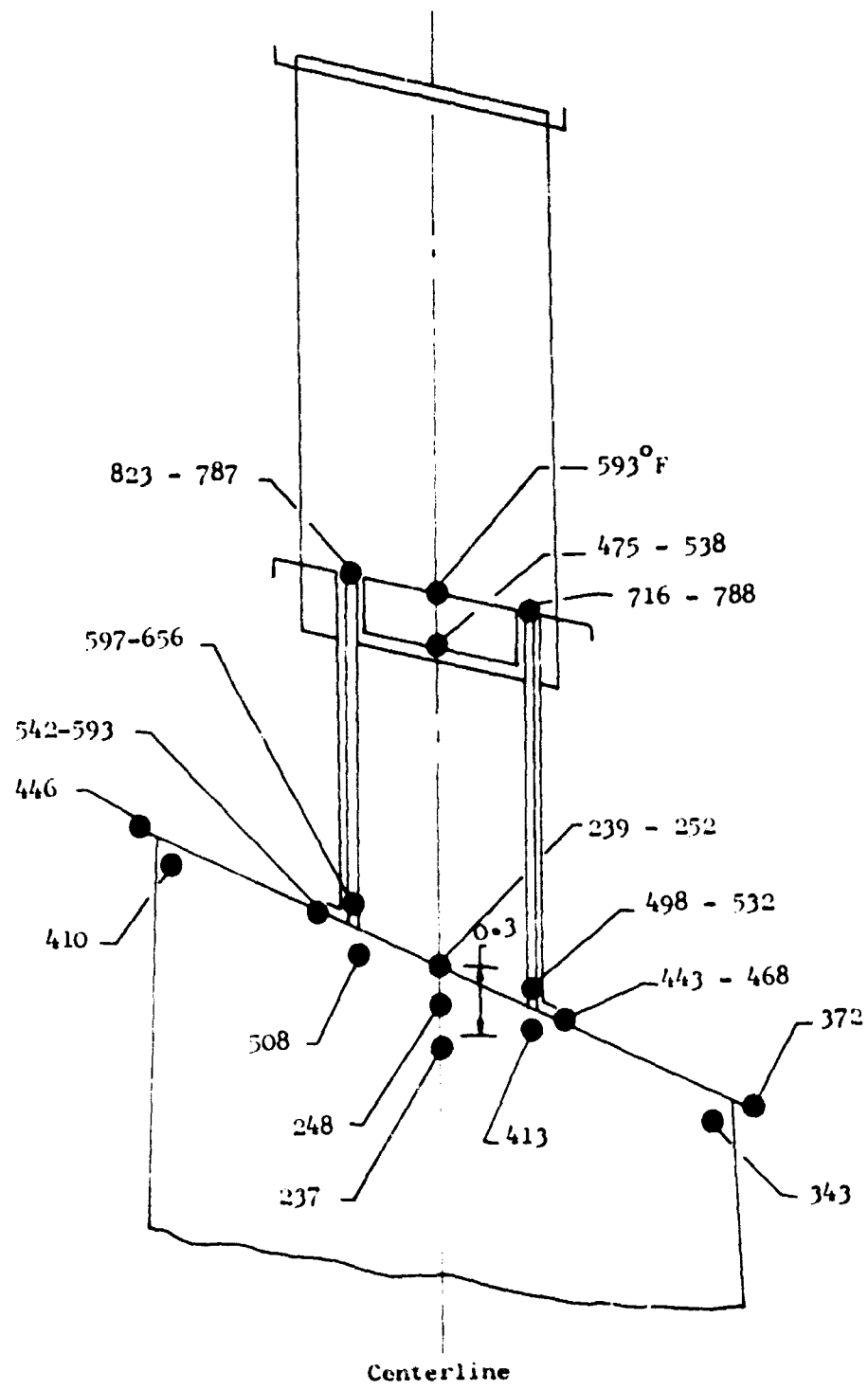


Figure 304 Temperatures After 30 Second Soak Back - 1.0  
lb/sec Carrier Cooling

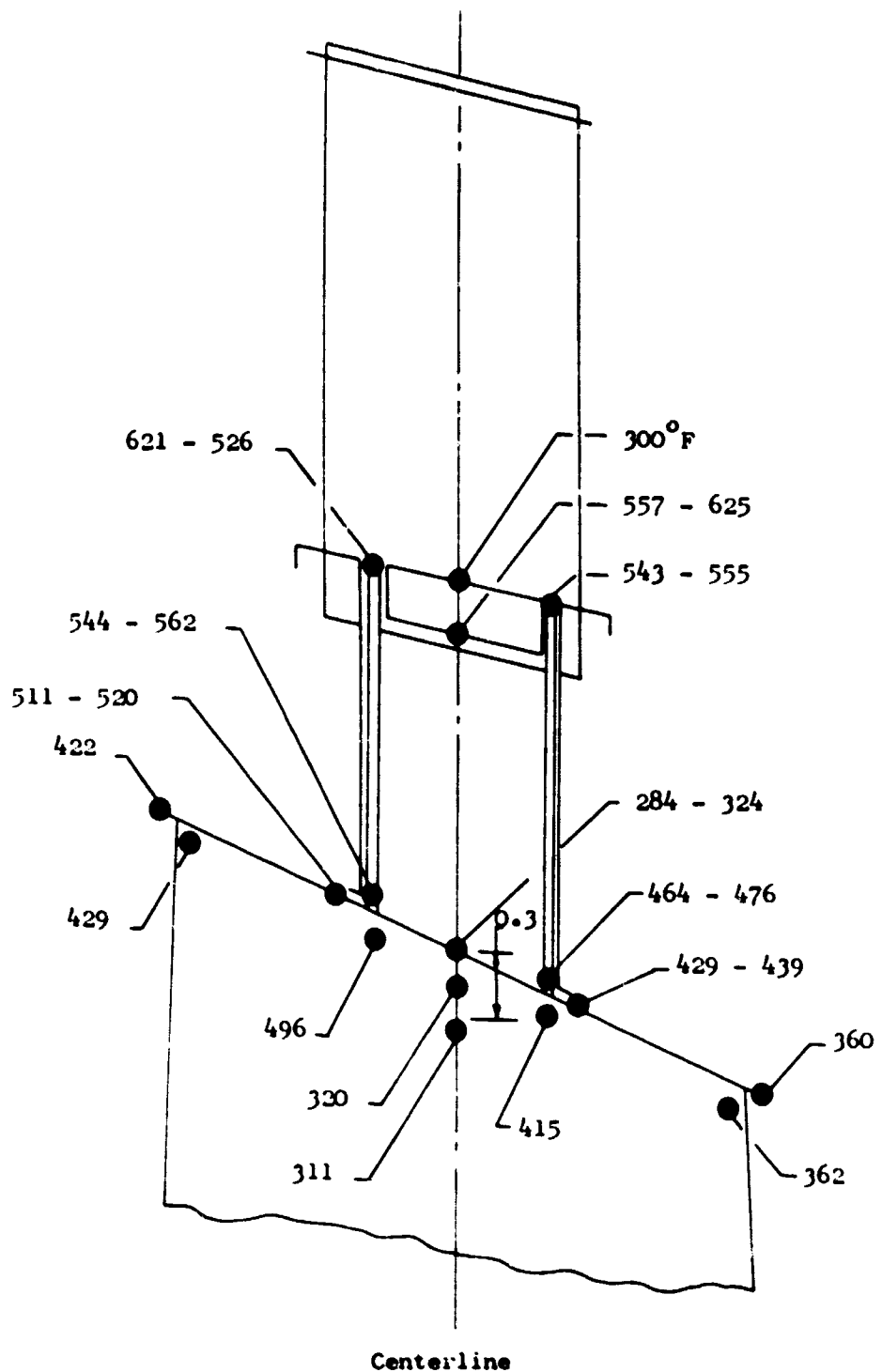
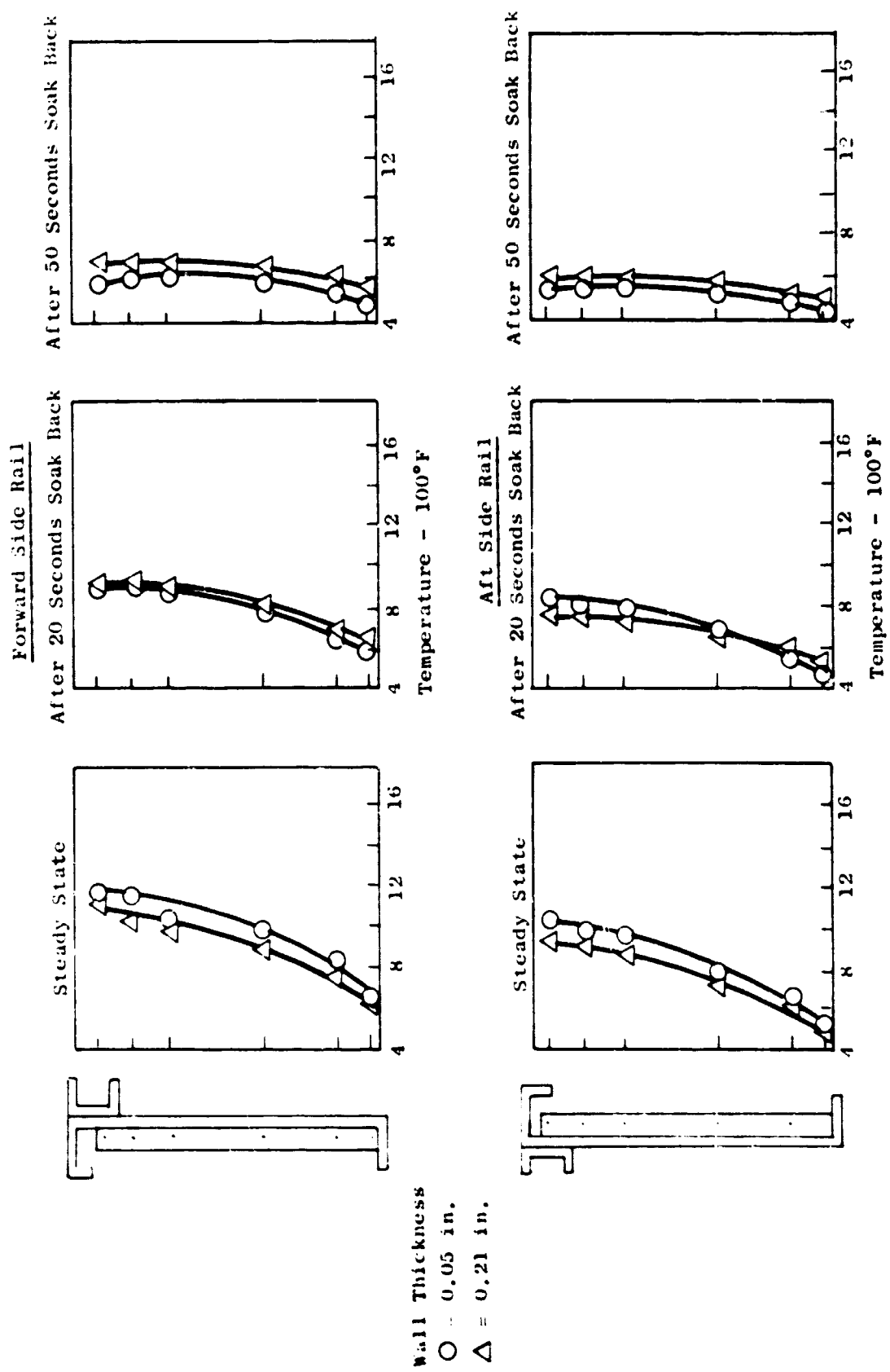


Figure 305 Temperatures After 50 Seconds Soak Back - 1.0  
lb/sec Carrier Cooling



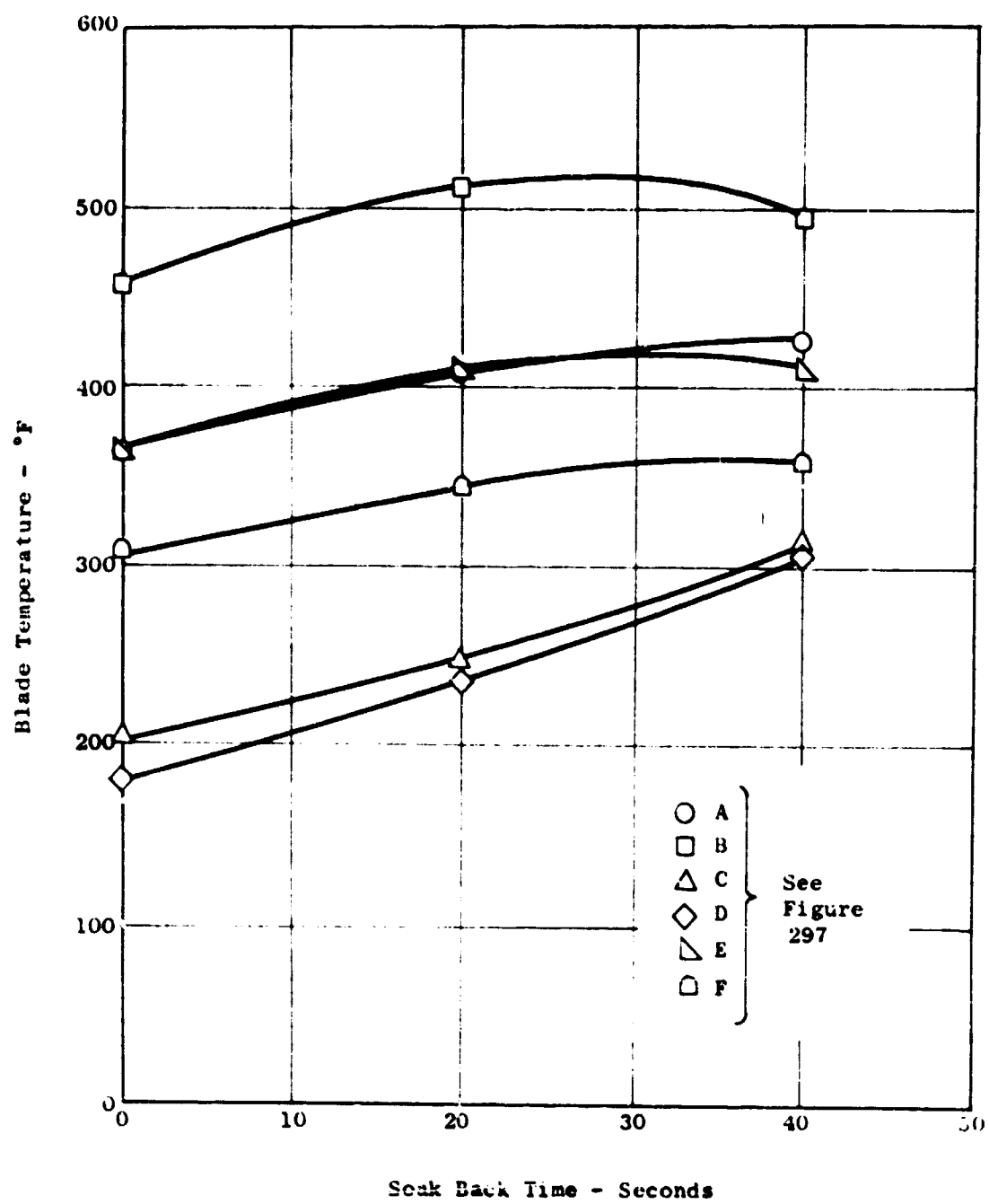


Figure 307 Blade Soak Back - 1.0 lb/sec Bleed Air Cooling

Steady State - Uncooled:

(U) Forward side rails are 140-190°F hotter than aft side rails in the uncooled case. Venting the carrier reduces this difference only at the top of the respective side rails.

(U) The temperature range at points on the side rails show the values at thin and thick side rail sections. The thin sections are hotter, primarily because they are far removed from the blade attachment "heat sink" but also because their thinness prevents a good conduction path to the blade attachment.

(U) Temperature distribution from top to bottom of each side rail is not linear. It is almost parabolic with the upper 2/3 of each side rail significantly hotter than the bottom point. This is due to the hot surroundings on three sides with only one cooling path at the bottom attachment to the blade. Venting the carrier tends to reduce this effect slightly.

(U) Blade temperature levels, as expected, are highest near the carrier attachment areas.

Steady State - Cooled:

(U) Venting the carrier with small amounts of bleed air (.5 lb/sec total for 66 carriers) decreases side rail temperatures by 4 - 8%. Doubling the cooling air (to 1.0 lb/sec total) reduces side rail temperatures by a lesser degree (2-7% more).

(U) Only the higher temperature blade tip areas at the leading edge and adjacent to the carrier side rails (points A,B,E in Figure 298) appear cooled to any degree by the vent carrier.

Soak Back-Uncooled:

(U) In the side rails (Figures 296, 302, 306) cool down is faster in the upper hot areas. In fact, the bottom temperature of each side rail remains fairly steady until the  $\Delta T$  from top-to-bottom drops to about 200°F. At this time the bottom temperature begins to drop, but at a slower rate than the top. A check of the vented carriers shows this same effect. Throughout soak back, no part of the side rails gets hotter than its steady state temperature.

(U) All blade tip areas heat up in the first 20 seconds of soak back. The "hot spot" below the forward rail (in Figure 298) levels out at this time, never exceeding 600°F. The aft "hot spot" (point E) follows the leveling out of the forward "hot spot". The other points are shown continuing their temperature rise after 30 seconds of soak back. These points should reach leveling out points in 20-30 additional seconds due to the depressing effects of the cooling "hot spots" and side rails.

**Soak Back-Cooled:**

(U) Side rail cooling rates do not appear affected to any degree by carrier cooling.

(U) Blade tip temperatures seem to level off quicker when the carrier is cooled. Doubling the amount of bleed cooling flow more than doubles the tip cooling rate.

**Weight:**

(U) Results of the weight tradeoff studies showed that the maximum flow of one pound/second total turbine cooling allowed a turbine weight reduction of about 2.5 pounds per fan. This value was not considered significant, however, in light of the overall accuracy of the weight analysis.

**Conclusions and recommendations.-**

(U) Low seal temperature may allow weight savings. Temperature in fan turbine seal is 435° - 820°F in the uncooled turbine and 430 - 695°F in the 1.0 lb/sec cooled turbine. This indicated that a material having higher strength than R41 in the 400 - 900°F temperature range might allow a seal weight reduction. Any new material must be compatible in joining to the upper turbine carrier, however, and joint weight should also be considered.

(U) There are no significant heating problems due to soak back. Maximum blade tip heating due to soak back is about 70°F, and maximum possible tip temperature is 525 to 600°F. All carrier temperatures decrease during soak back.

(U) Turbine cooling is not required for the LF475. The turbine should be designed to operate under uncooled conditions.

## INLETS

### LF475 Inlet Studies

(U) During the detail design of the LF475 fan a number of inlet configurations were analytically studied, however, because of the close interrelationship between inlet and fan in a lift fan configuration it is not realistic to study the inlet separately. A discussion of the various inlet modifications, design criteria, etc. is included in section IV, B., 1. with the LF475 detail fan design.

### L/CF470 Inlet Studies

#### Objective

(U) The objective of this study has to investigate the effect of rounding the inlet lip with regard to static and cruise performance.

#### Nacelle Coordinates

(U) The nacelle coordinates for the basic and modified LCF470 nacelle are shown in Tables 52 and 53. The cowl contour of the basic nacelle is a standard NACA series 1 contour. The modified contour features an increased lip outer radius of 1.25 inches. This is equivalent to a radius to high-light diameter ratio of .0197. The origin for the coordinate system is the intersection of the inlet lip plane with the inlet centerline.

#### Static

(U) Pressure coefficients and velocity ratios for the static operating condition were calculated by the incompressible flux plot computer program. The reference point was selected somewhat arbitrarily as there is no region of uniform flow. The selected reference point has the coordinates  $X = 10$ ,  $Y = 22.5$  and is located about 4 inches aft of the inlet throat near the cowl surface. Pressure coefficients are defined as:

$$C_p = \frac{P - P_{ref}}{\frac{1}{2} \rho v_{ref}^2} = 1 - \left( \frac{V}{V_{ref}} \right)^2$$

(U) Static to total pressure ratios under the assumption of low speed flow may be calculated by the relation:

$$\frac{P}{P_T} = \left( \frac{P}{P_T} \right)_{ref} + C_p \left( \frac{q}{P_T} \right)_{ref}$$

TABLE 52

L/CF470 NACELLE

<u>Cowl</u>	<u>Inlet</u>	<u>Spinner</u>			
<u>X</u>	<u>Y</u>	<u>X</u>	<u>Y</u>	<u>X</u>	<u>Y</u>
0	31.80	0	31.80	30.26	0
0.11	32.19	0.1	31.50	30.32	0.60
0.22	32.34	0.2	31.04	30.40	1.08
0.33	32.47	0.4	30.72	30.60	1.80
0.44	32.57	0.8	30.28	30.80	2.30
0.55	32.65	1.2	30.00	31.0	2.72
0.82	32.84	1.6	29.74	31.2	3.10
1.10	33.01	2.0	29.56	31.4	3.40
1.37	33.16	2.4	29.40	31.6	3.70
1.64	33.30	2.8	29.24	31.8	4.00
1.92	33.44	3.2	29.16	32.0	4.24
2.19	33.56	3.6	29.04	32.4	4.70
3.29	34.01	4.0	29.00	32.8	5.14
4.38	34.41	4.6	28.90	33.2	5.54
5.48	34.76	5.2	28.84	33.6	5.88
6.58	35.09	6.0	28.80	34.0	6.24
7.67	35.38	7.0	28.80	35.0	7.00
8.77	35.64	8.0	28.82	36.0	7.76
9.86	35.89	9	28.86	37.0	8.40
10.96	36.12	10	28.92	38.0	9.06
12.06	36.34	12	29.10	39.0	9.70
13.15	36.55	16	29.56	40	10.26
14.25	36.75	20	30.04	44	12.44
15.34	36.94	24	30.68	48	14.54
16.44	37.12	28	31.34	52	16.50
18.08	37.38	32	32.04	56	18.50
19.73	37.63	36	32.78	60	20.44
21.92	37.93	40	33.56	64	21.76
23.56	38.14	44	34.26	68	22.20
25.21	38.34	48	34.78	72	22.50
27.40	38.58	52	35.00		
29.59	38.81	56	34.56		
32.88	39.11	60	34.00		
38.36	39.50	64	33.90		
43.84	39.78	68	34.08		
49.32	39.95	72	34.30		
54.68	40.00				

TABLE 53

## MODIFIED CF 470 NACELLE

<u>COWL</u>			<u>INLET</u>		
<u>X</u>	<u>Y</u>	<u>CURVATURE</u>	<u>X</u>	<u>Y</u>	<u>CURVATURE</u>
%					
54.80	40.00	.003	54.80	35.00	—
51.15	39.98	.003	50.00	34.95	—
47.49	39.92	.003			
43.84	39.82	.003	40.00	33.54	
40.19	39.68	.003			NOT
36.53	39.50	.003	30.00	31.69	CALCULATED
32.88	39.27	.003			
29.23	39.00	.004	30.00	30.09	
25.57	38.68	.004			
21.92	38.31	.005	10.00	28.95	
18.27	37.68	.006			
14.61	37.34	.008			
10.96	36.70	.012	5.90	28.85	.063
7.31	35.88	.020	5.51	28.86	.067
5.80	35.47	.021	5.11	28.87	.073
4.60	35.09	.030	4.72	28.90	.079
3.65	34.75	.041	4.33	28.94	.086
3.29	34.61	.047	3.93	28.99	.094
2.92	34.45	.056	3.54	29.36	.104
2.56	34.29	.066	3.15	29.14	.115
2.19	34.11	.080	2.75	29.25	.130
1.80	33.91	.100	2.36	29.37	.148
1.46	33.69	.128	1.97	29.53	.171
1.10	33.44	.173	1.57	29.71	.202
0.73	33.15	.249	1.18	29.95	.245
0.37	32.75	.402	0.79	30.25	.309
0.00	31.80	.800	0.39	30.68	.412
		0.35	30.74	.426	
		0.31	30.79	.440	
		0.28	30.86	.456	
		0.24	30.92	.472	
		0.20	31.00	.490	
		0.16	31.08	.509	
		0.12	31.18	.529	
		0.08	31.29	.551	
		0.04	31.44	.575	
		0.00	31.80	.600	

where  $C_p$  is obtained from Figures 308 and 309. The radial velocity gradient at the fan inlet station is shown in Figure 310

#### Cruise

(U) The cruise condition of Mach 0.7 was calculated by the compressible flow flux plot program. Local surface Mach numbers are presented in Figure 311.

#### Lip Bluntness

(U) The rounding of the outer lip contour ( $R_e / D_{ML} = .0197$ ) has reduced the peak velocities at both the static and cruise conditions. The local Mach numbers at cruise were only slightly increased. More blunting of the lip resulted in a significant increase in the local Mach numbers.

#### Conclusions and Recommendations

(U) From the results of this analytical study it is concluded that some increase in the lip outer radius effectively reduces the local peak velocities.

(U) A fixed inlet with a blunted lip is recommended for the L/CF470 lift/cruise fan.

#### LF-2 Inlet Investigations

##### Introduction

(U) The LF2 Fan is a 1.12 pressure ratio turbotip lift fan demonstrator with a fan tip diameter of 62.5 inches. It is the same size and is aerodynamically similar to the LF1 series fans used to power the XV-5A aircraft. This fan was originally built and tested to demonstrate advanced lightweight fan components and the variable area scroll concept in conjunction with Army component development contracts and the Contribution Engineering Program.

(U) Early tests on the LF1 fan in a wing installation revealed a very drastic performance deficiency. But the same fan when operating with essentially the same radius bellmouth followed by a deep inlet, produced design performance. Leakage and flow control devices were investigated which led to the use of the inlet vane for fan-in-wing installations.

(U) Advancement in lift fan technology toward thinner and lighter-weight propulsion systems dictates the elimination of the inlet vane and dictates the development of aerodynamically compatible inlet, rotor, and stator components.

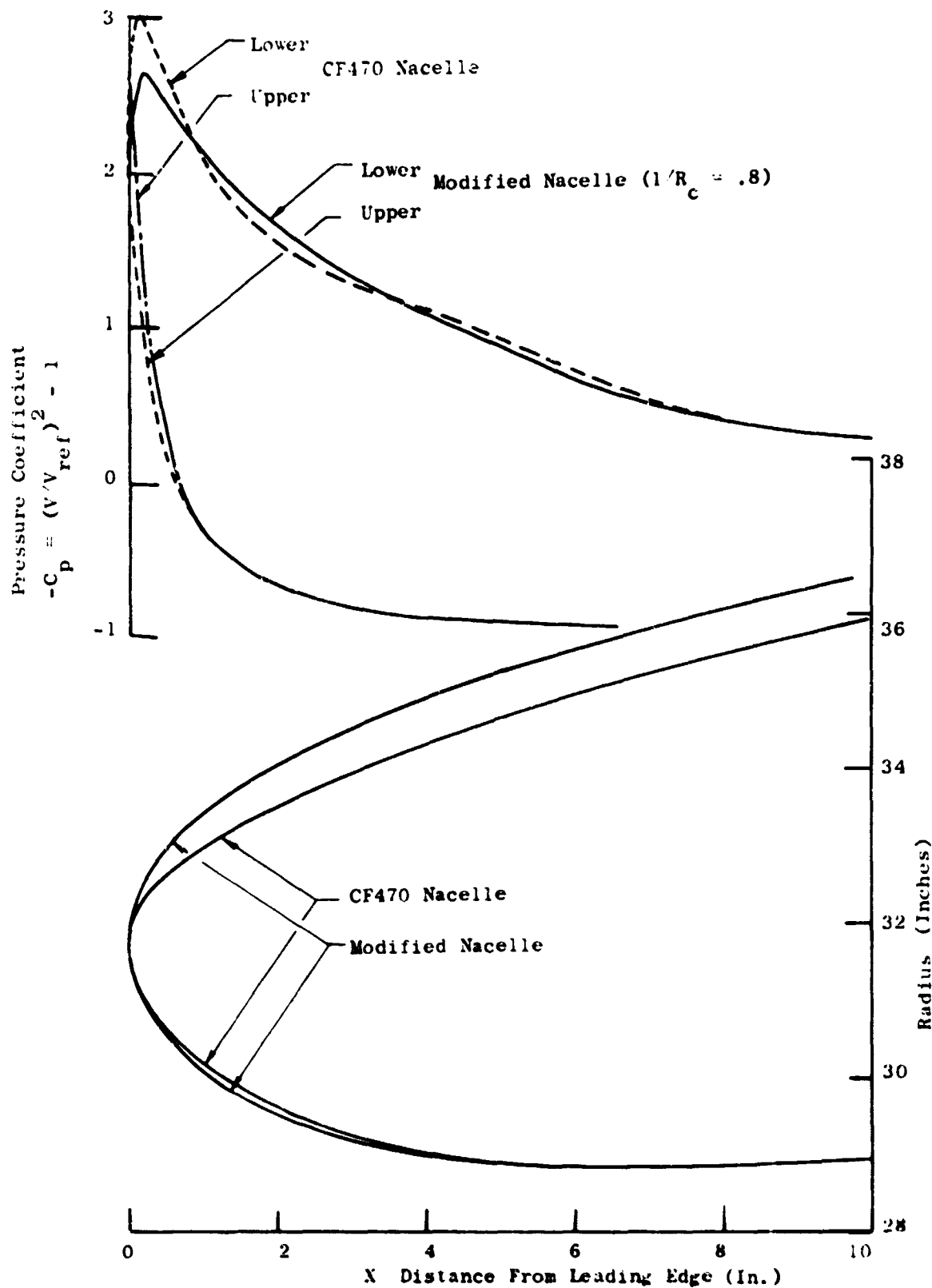


Figure 308 CF470 Nacelle Contour Pressure Coefficient Versus X

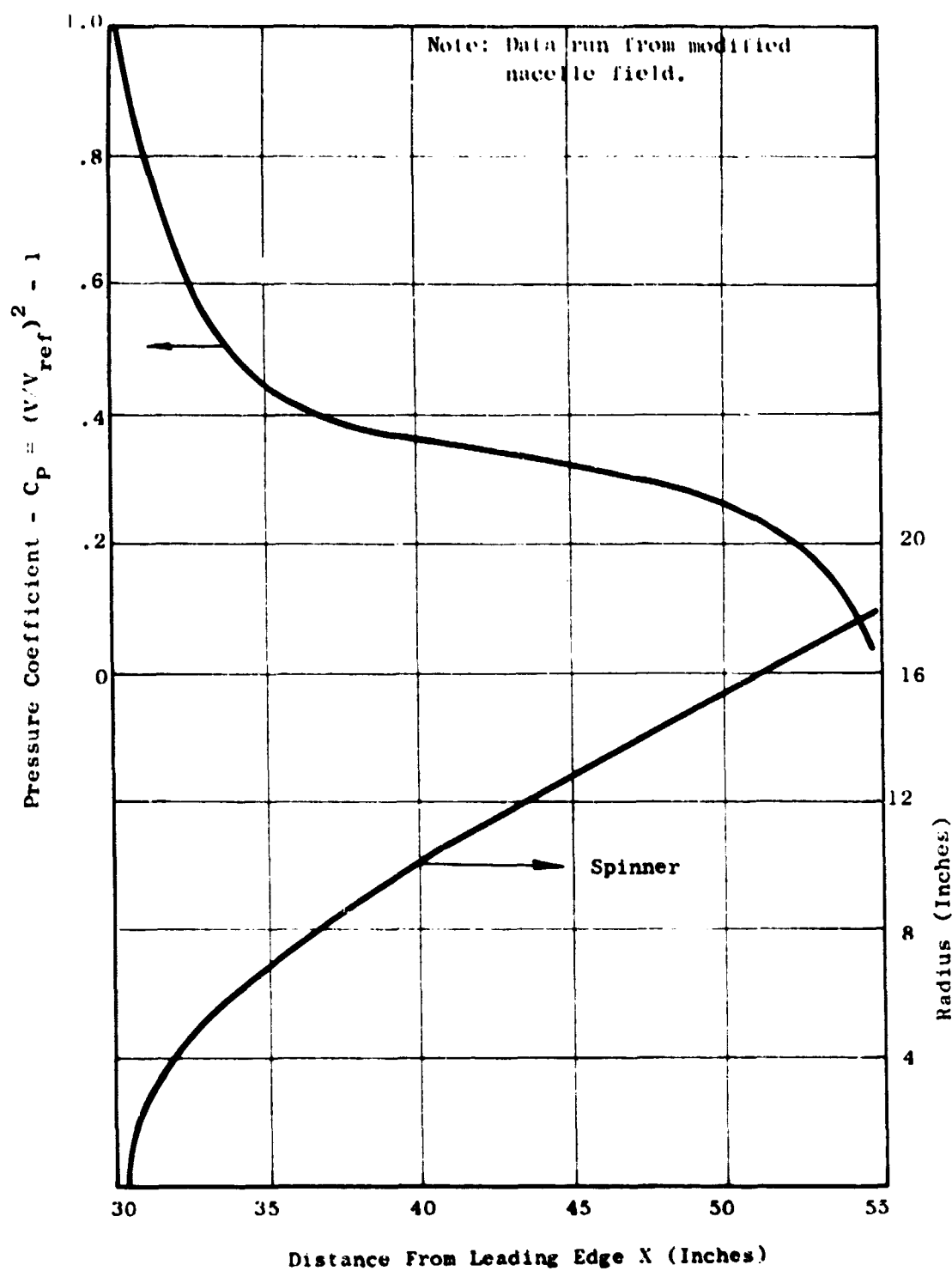


Figure 309 CF470 Spinner Pressure Coefficient Versus X

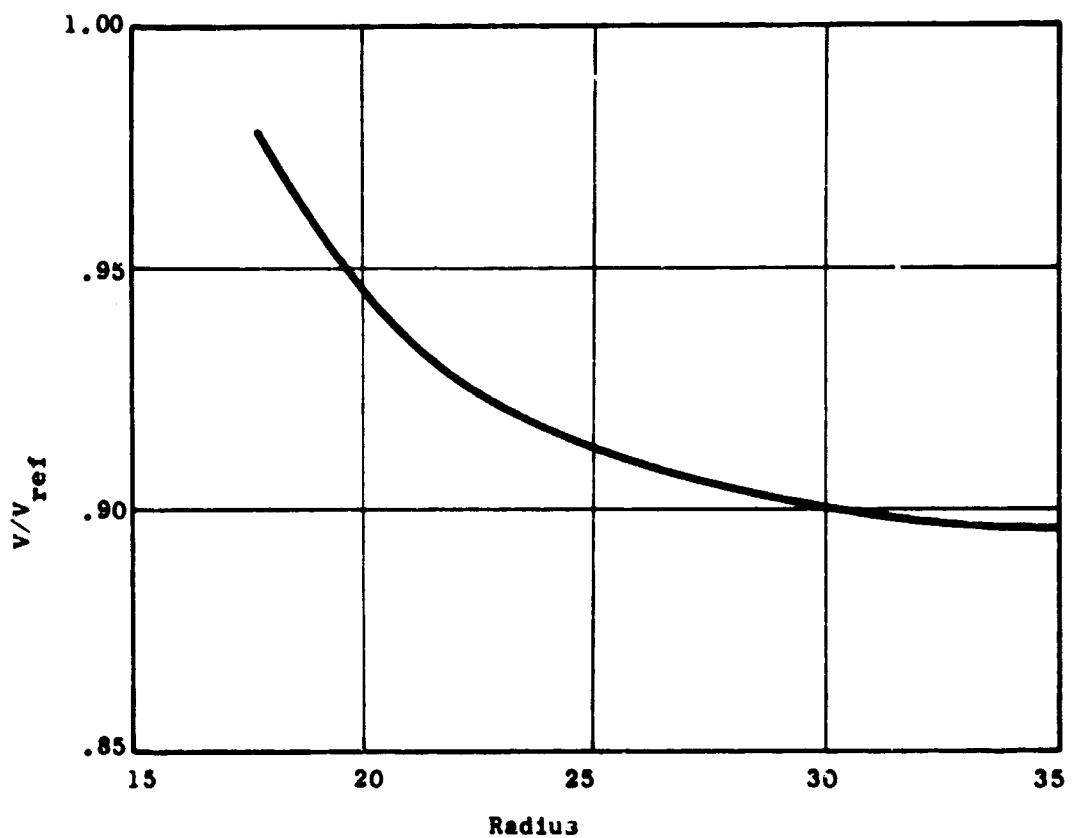


Figure 310 CF470 Fan Inlet Velocity Versus Radius

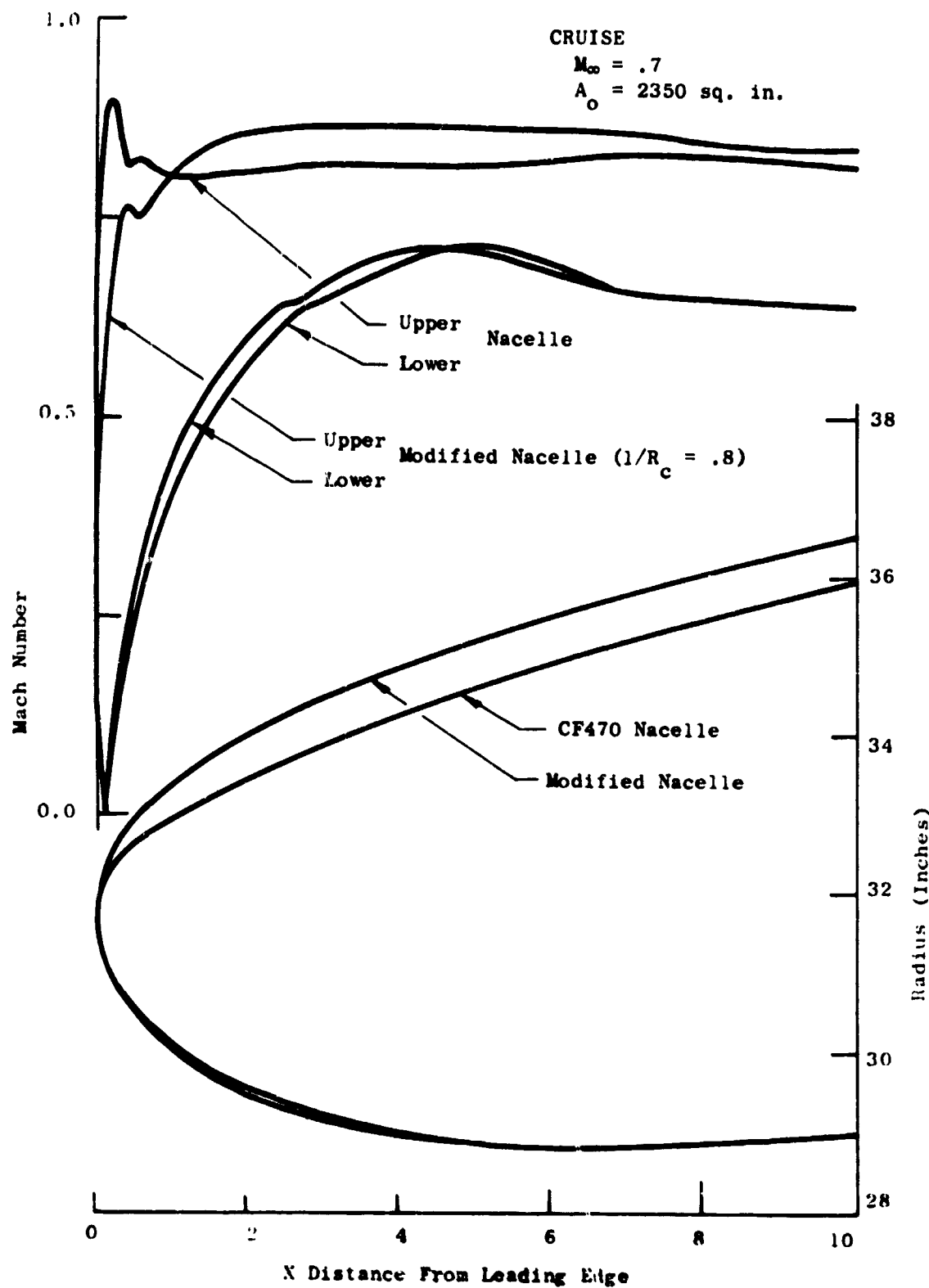


Figure 311 CF470 Nacelle Contour Mach Number Versus X

The objectives of the LF2 Inlet Investigation Program were:

1. To investigate the influence of a series of inlet configurations on rotor aerodynamic performance and fan system performance.
2. To provide inlet and rotor discharge flow characteristics data for use in inlet and stage tip design of the scale model LF475 fan test vehicle and other related programs.

The results of this test program are summarized in detail in Reference 11.

#### Test Vehicle and Installation

##### Fan assembly. -

(U) The complete fan assembly consists of four major sub-assemblies; namely, a modified X353-5A rear frame, a modified LF2 front frame, an LF2 rotor assembly and a variable area scroll assembly.

(U) The X353-5A rear frame is one of the components designed for the original X353 lift fan assembly. The rear frame component provides a supporting structure of the fan system and includes the exit stators of the fan and fan turbine exhaust. It is also a supporting structure for the fan exit louvers.

(U) The LF2 front frame is the major supporting component of the fan system. It provides a method of supporting the rotor assembly and the fan scroll. The inlet bellmouth is not included as an integral part of the front frame; it is a separate stainless steel component supported from the wing structure.

(U) The LF2 rotor assembly is a lightweight component using titanium fan blades and rotor disc. It was designed to be aerodynamically similar to the X353-5B fan system used in the XV-5A aircraft.

(U) The variable area scroll was basically a modified X353-5B scroll. It incorporated the variable area feature together with nozzle height and flow passage shape modifications for compatibility with the LF2 tip turbine.

(U) The configuration for the inlet investigation testing included the following:

1. Exit louvers were removed to permit installation of the rotor discharge traverse instrumentation.

2. Stiffener rings were installed on the fan stators to reduce the operating stress levels.
3. The variable area scroll was set at approximately 80 percent of maximum area and remained fixed throughout the complete test.
4. The inlet bellmouth was modified for the installation of additional inlet instrumentation and for provision for attachment of 88 stub vanes at two axial locations.

Bellmouth modification. -

(U) The bellmouth quadrants were removed from the facility to be reworked for provision to install 88 stub vanes at either of two axial locations. The stub vanes were made from scrap J79 third and fourth stage stator vanes as indicated in Figure 312. Holes were drilled perpendicular to the bellmouth skin at the two locations. (See Figure 313).

(U) The stub vanes were installed in the upper position as indicated in Figure 314 and in the lower position as shown in Figure 315. They were tightened securely and the flat washers and plate nuts were tack welded in place (See Figure 316). After the flat washers and nuts were permanently installed, the stub vanes could be removed or installed as desired while the bellmouth was installed in the test facility.

Test facility. -

(U) The Lift Fan Test Facility was previously used for flight-worthiness testing of the X353-5B propulsion system. The arrangement of the system components simulate the XV-5A aircraft type of installation (Figure 317). It includes two J85-GE-5 engines with diverter valves to direct the exhaust gas flow either to the two exhaust nozzles for conventional turbojet operation or to the two cross ducts for fan mode operation. Each XV-5A type cross duct distributes the flow from each engine to one scroll arm of each wing fan and one scroll arm of the pitch fan. The test installation has provision for one lift fan installed in a right wing position. The left wing fan is simulated by overboard ducts with nozzles sized for the proper flow area. The flow in each pitch fan leg was ducted overboard through properly sized nozzles.

Instrumentation and Test Equipment

(U) Aerodynamic and mechanical instrumentation of both core engines and the fan were provided to insure safe system operation and to acquire the desired aerodynamic performance of the fan system.

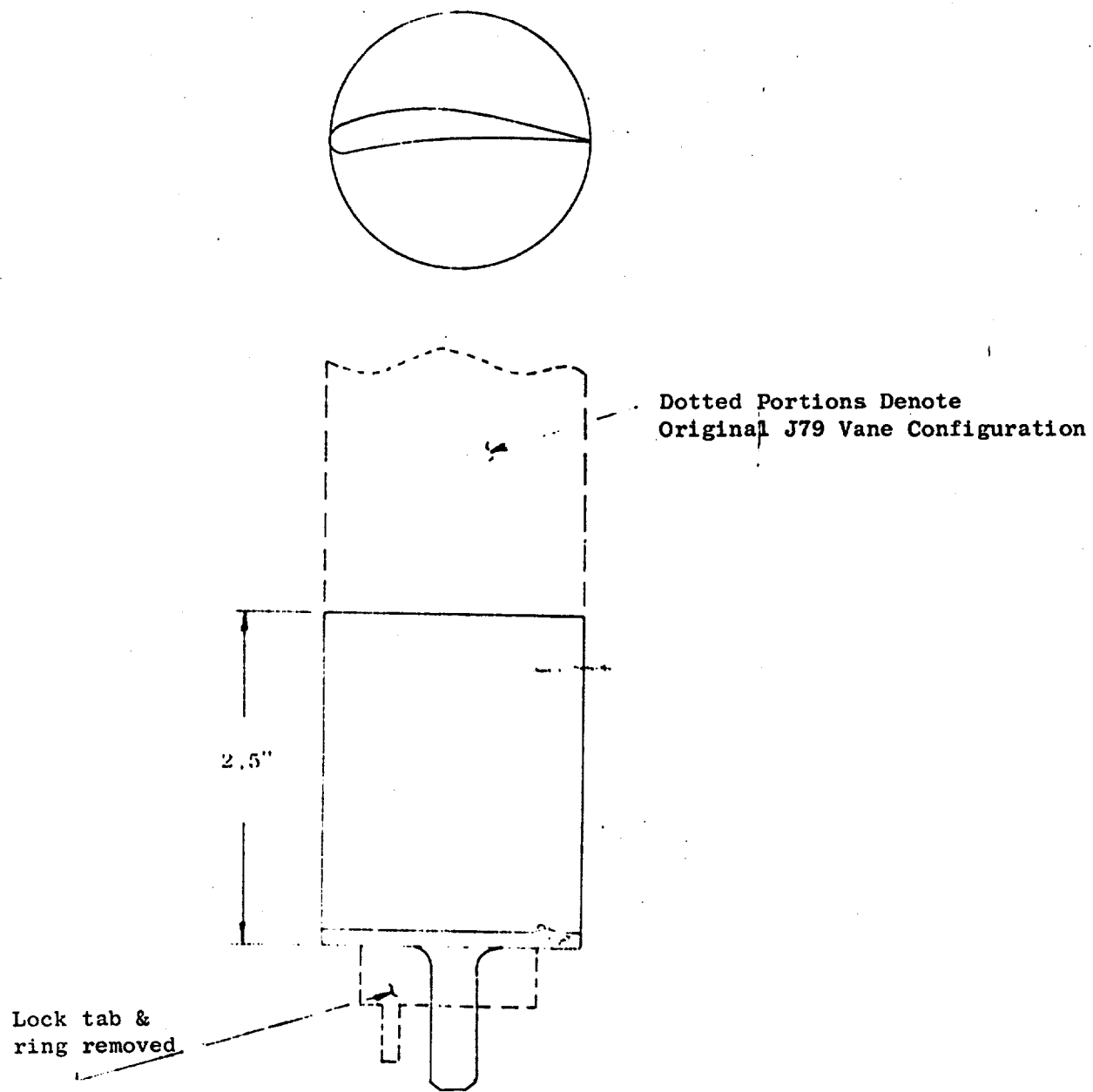


Figure 312 LF2 Inlet Stub Vane

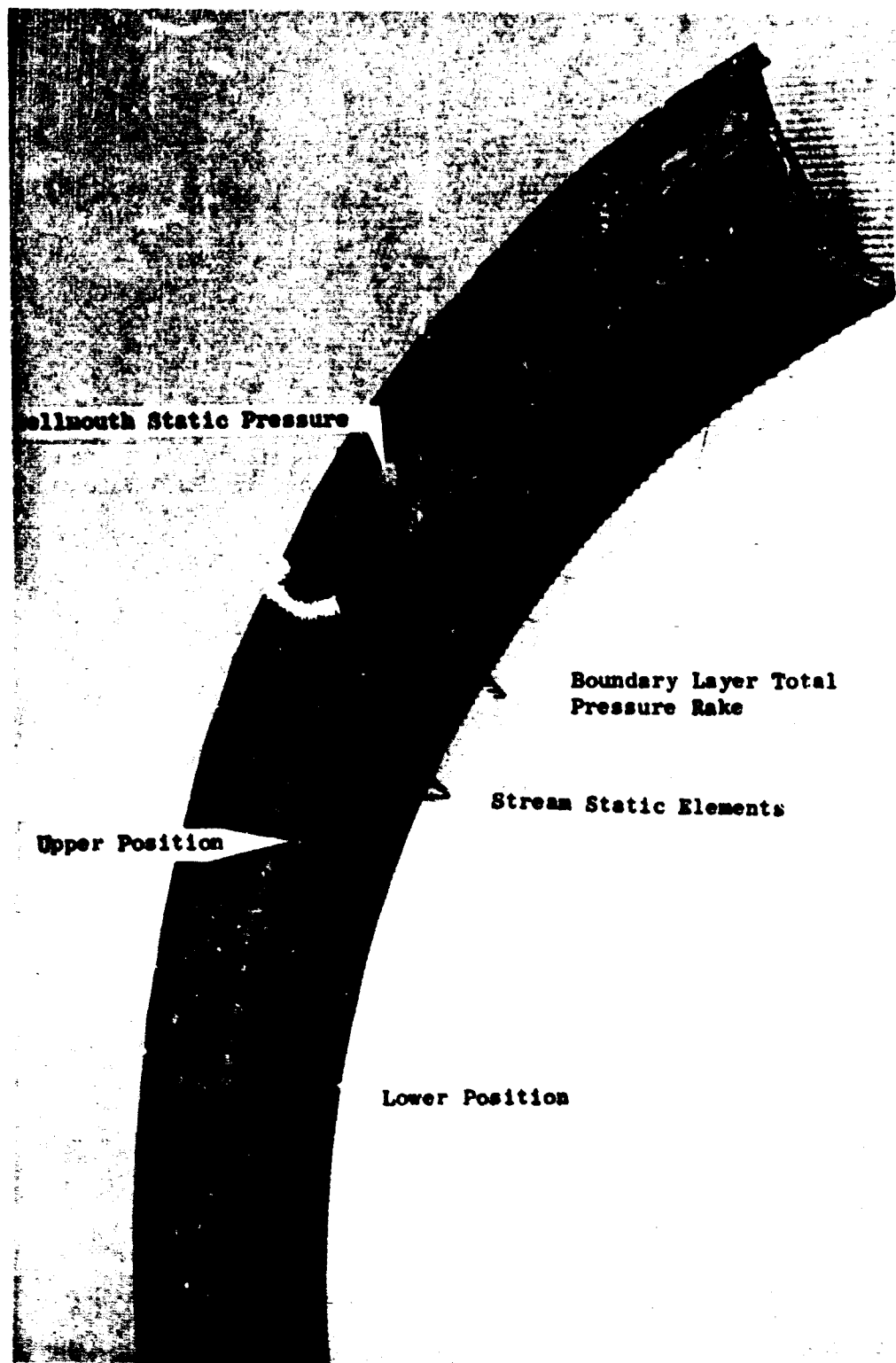
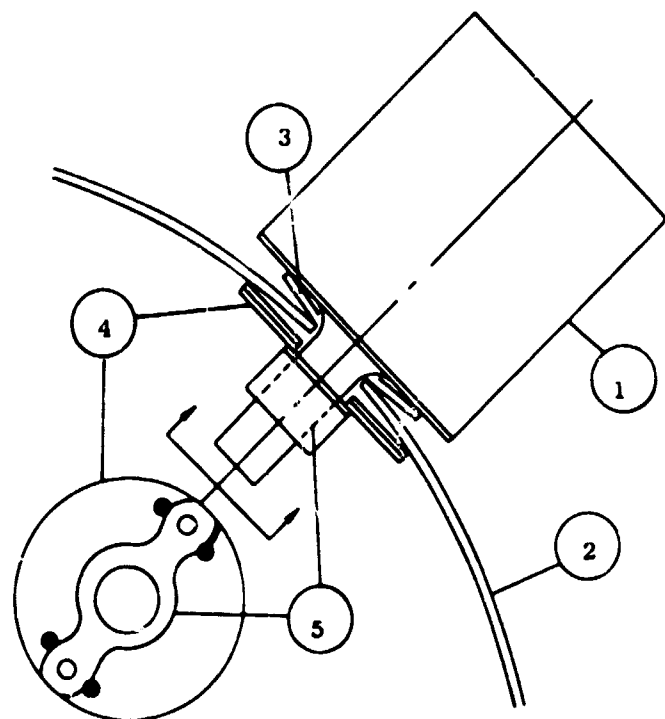


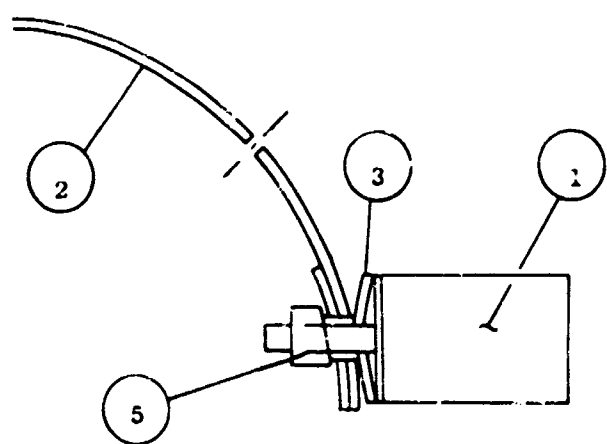
Figure 313 Bellmouth Quadrant with Hole Locations for Stub Vane Installation



Parts Identification

1. Stub Vane
2. Bellmouth Quadrant
3. Compression Washer
4. Flat Washer
5. Plate Nut

Figure 314 Stub Vane Assembly, Upper Position



Parts Identification

1. Stub Vane
2. Bellmouth Quadrant
3. Compression Washer
5. Plate Nut

Figure 315 Stub Vane Assembly, Lower Position



**Figure 316.** View of Underside of Bellmouth Quadrant Modified for Stub Valve Installation.

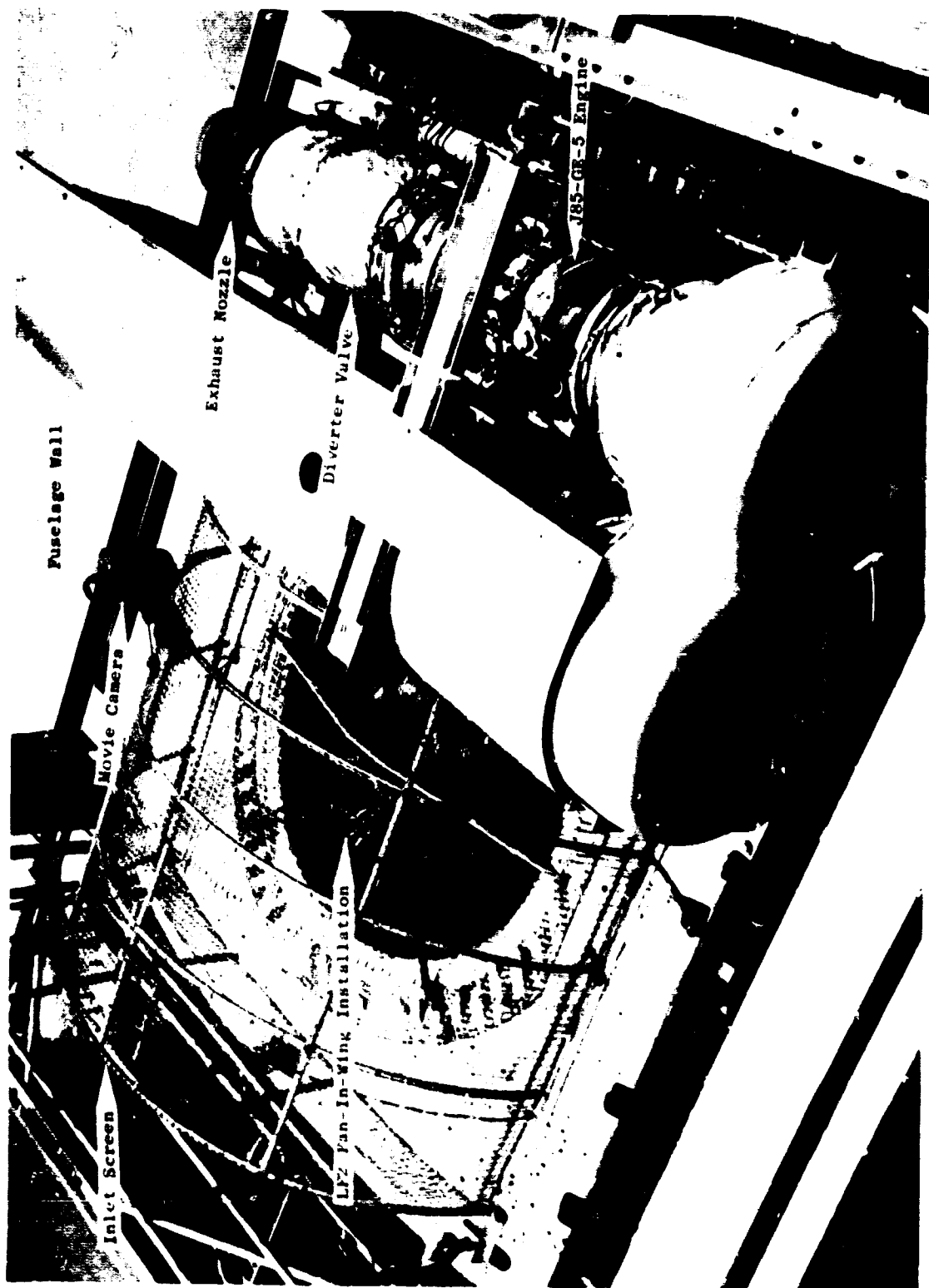


Figure 317 LF2 Fan Test Installation

(U) Performance instrumentation included:

Static pressure taps installed on the fan bellmouth.

Rotor inlet boundary layer total pressures

A rotor discharge traverse probe capable of measuring total pressure, velocity and flow angle in both the pitch and yaw quadrants. A photograph of the traverse probe installation is shown in Figure 318

#### Scope

(U) Five basic test configurations were defined for investigations to fulfill the test objective of this program. These are listed below in the order in which they were to be performed.

1. LF2 design configuration, inlet vane installed.
2. Inlet Vane removed.
3. Bellmouth stub vanes installed in position 1 (Figure 319).
4. Bellmouth stub vanes installed in position 2 (Figure 320).
5. Repeat configuration 4 with improved turbine seals.

(U) Configuration 2 is the reference or base configuration for comparison purposes. The effects of the circular vane on bellmouth flow separation and on fan blade performance are defined with configuration 1. The purpose of configuration 3 is to determine if stub vanes in this location acting as vortex generators can perform the circular vane function to maintain bellmouth flow attachment. Configuration 4 with stub vanes located in position 2 should be aerodynamically equivalent to changing the fan blade tip orientation angle and thereby permit investigation of reduced blade tip incidence and increased or decreased tip loading. The number of stub vane orientation angles to be investigated with configurations 3 and 4 are to be dependent on test results. A repeat of configuration 4 with inlet vane installed may also be warranted. Configuration 5 is planned as the last in the test series to assess the effect of reduced turbine seal leakage.

#### Test Run Summary

(U) The test runs and configurations investigated during the LF2 inlet program are summarized in chronological order in Table 54. The test series began on May 29, 1967, and was completed on August 17, 1967. Total accumulated operating time on the fan was 7.5 hours. Engine operating times were 12.3 hours on S/N 230-103 (Left Engine) and 11.3 hours on S/N 231-233 (Right Engine).

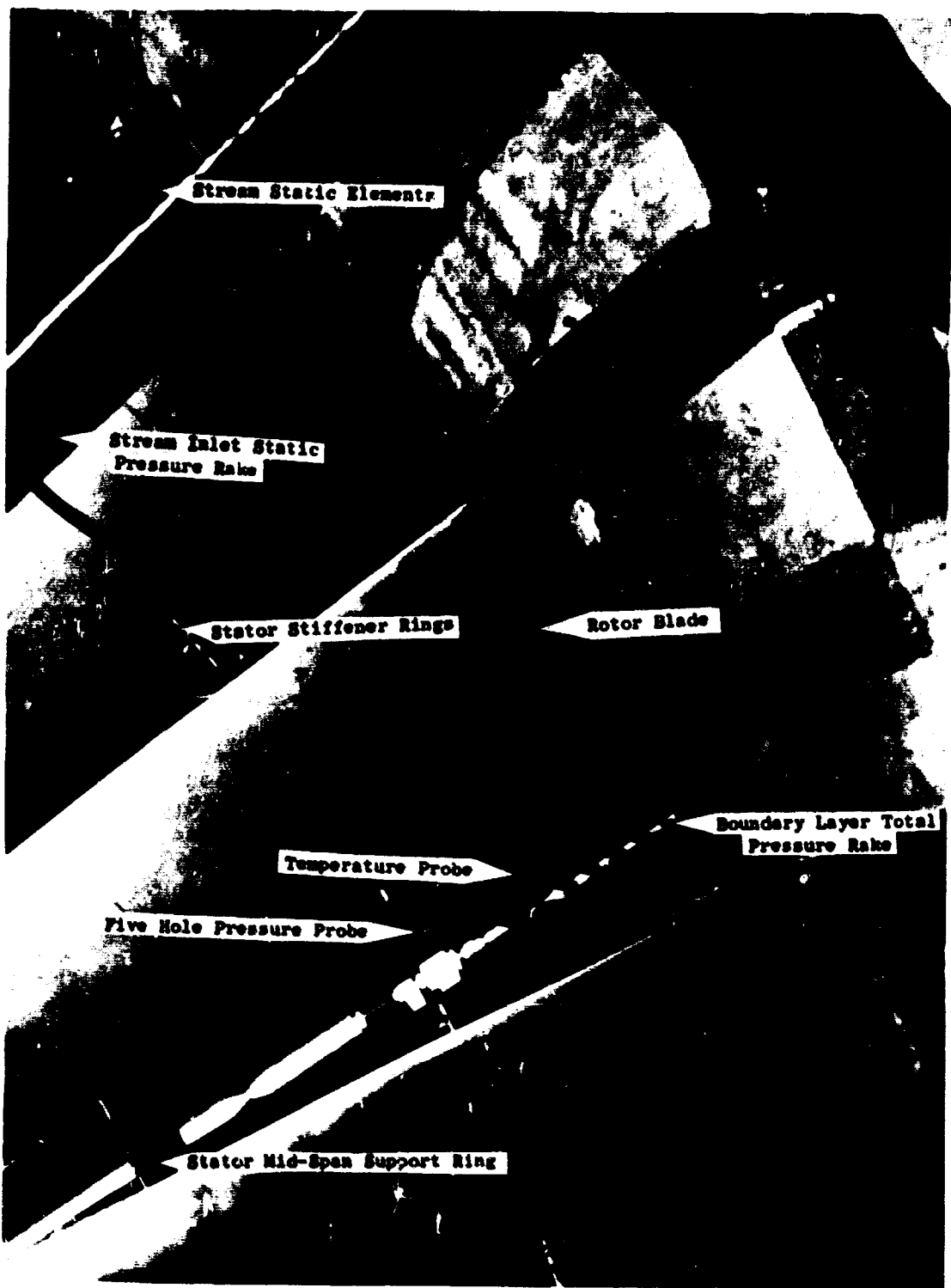


Figure 318 Top View of Traverse Probe Installation



Figure 319 Stub Vanes at 10° Stagger in Upper Position



Figure 320 Stub Vanes in Lower Position

TABLE 54

TEST RUN SUMMARY  
LF2 INLET INVESTIGATION

<u>Run</u>	<u>Rdg.</u>	<u>Date</u>	<u>Description</u>
1	1&2	5/29/67	Engine Checkout
2	3-7	5/31/67	Engine and Fan Checkout
3	8	6/1/67	Inlet Vane In, Traverse Tip Span
	9	6/1/67	Inlet Vane In, Traverse Hub Span
4	10	6/5/67	Inlet Vane Out, Traverse Hub Span
	11	6/5/67	Inlet Vane Out, Traverse Tip Span
5	12	6/12/67	Stub Vanes installed at +10° in High Position
6	13	6/13/67	Stub Vanes set at 10° Stagger in High Position
7	14	6/13/67	Stub Vanes set at -10° in High Position
8	15	6/16/67	Stub Vanes set at -10° in Low Position
9	16	6/20/67	Stub Vanes set at -20° in Low Position
10	17	6/20/67	Stub Vanes set at -15° in Low Position
11	18	6/27/67	Stub Vanes set at -30° in Low Position
12	19	6/27/67	Stub Vanes set at -25° in Low Position
13	20	7/6/67	Inlet Vane In, Stub Vanes at -10°
14	21	7/11/67	Inlet Vane In, Stub Vanes at -20°
	22	7/11/67	Inlet Vane In, Stub Vanes at -20°
15	23	7/11/67	Inlet Vane In, Stub Vanes at -30°
16	24	8/10/67	Inlet Vane In, Stub Vanes at -30°, Improved Seal
	25	8/10/67	Inlet Vane In, Stub Vanes at -30°, Improved Seal
17	26	8/17/67	Same as Run 16 with extensions on Temperature Probe
18	27	8/17/67	Same as Run 16 with extensions on Temperature Probe

Note: Stub Vane position relative to the bellmouth is illustrated in Figures 313 through 315 and 319 through 230. The upper or high position refers to position 1 and the low position refers to position 2.

### Test Results

(U) Measured test results are presented in Table 55 and in Figures 321 through 368. The "hot side" and "cold side" designation correspond to the quadrants being traversed with the rotor discharge traverse probe. Typical data are presented for each configuration and include the following:

- Fan Inlet Static Pressures.
- Bellmouth Static Pressure Profiles.
- Bellmouth Boundary Layer Total Pressure Profiles.
- Rotor Pressure Rise vs Probe Position.
- Rotor Pressure Rise Coefficient vs Probe Position.
- Yaw Angle vs Probe Position.
- Pitch Angle vs Probe Position.
- Rotor Discharge  $q$  (dynamic pressure).
- Rotor Discharge Temperature vs Probe Position.
- Corrected Lift at Same Fan Speed, Table 57

### Inlet vane in-versus-inlet vane out. -

(U) With inlet vane installed, the fan produces 21.4 percent higher lift at the same fan speed than with the inlet vane out. Fan inlet stream static pressures (Figure 321) indicate a very significant increase in flow with the inlet vane installed (Average values are noted on the curves). Bellmouth wall static pressure profiles, Figures 328 and 329, show a correspondingly lower static pressure at the fan rotor inlet (element 6). The profile shapes of both configurations are different between hot and cold sides in the region of elements 1 and 2 which are near the upper wing surface. This is attributed to the proximity of the fuselage wall on the hot side. Bellmouth boundary layer total pressure profiles, Figure 334, indicate very good recovery with inlet vane installed, with the cold side being a little better than the hot side. With the inlet vane out, the cold side becomes badly separated while the hot side shows much less effect. This is again attributed to the presence of the fuselage wall near the hot side.

(U) These results are further verified with traverse probe data. Figures 336 and 337 show rotor pressure rise in the tip region (from the mid-span stator support ring to the fan tip). Figures 338 and 339 show similar data for the hub region (from the mid-span to the hub). The addition of the inlet vane produced no significant change in rotor pressure rise coefficient in the hub region but showed much improvement over nearly the complete tip span.

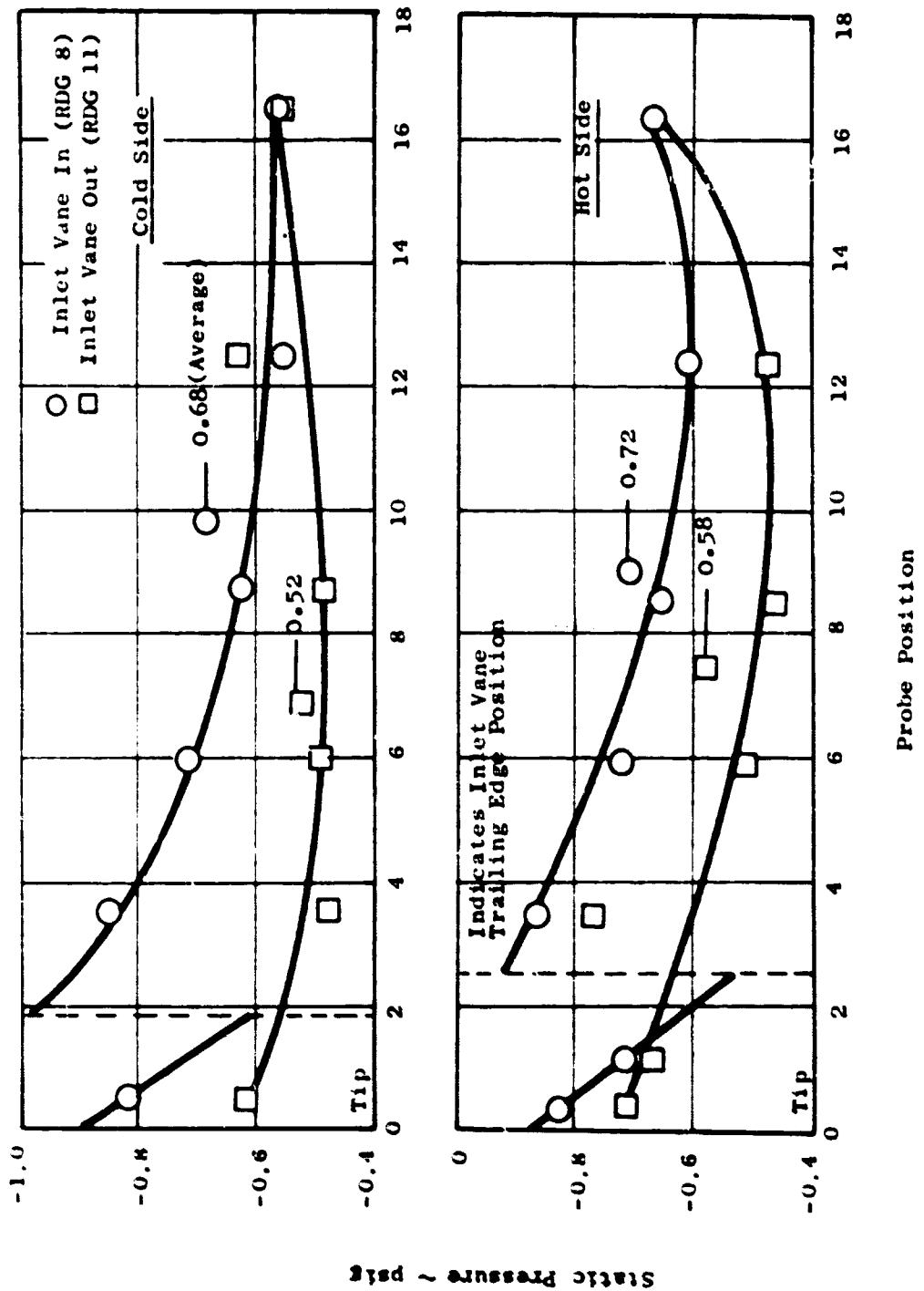


Figure 321 LF-2 Inlet Investigation  
Fan Inlet Static Pressures

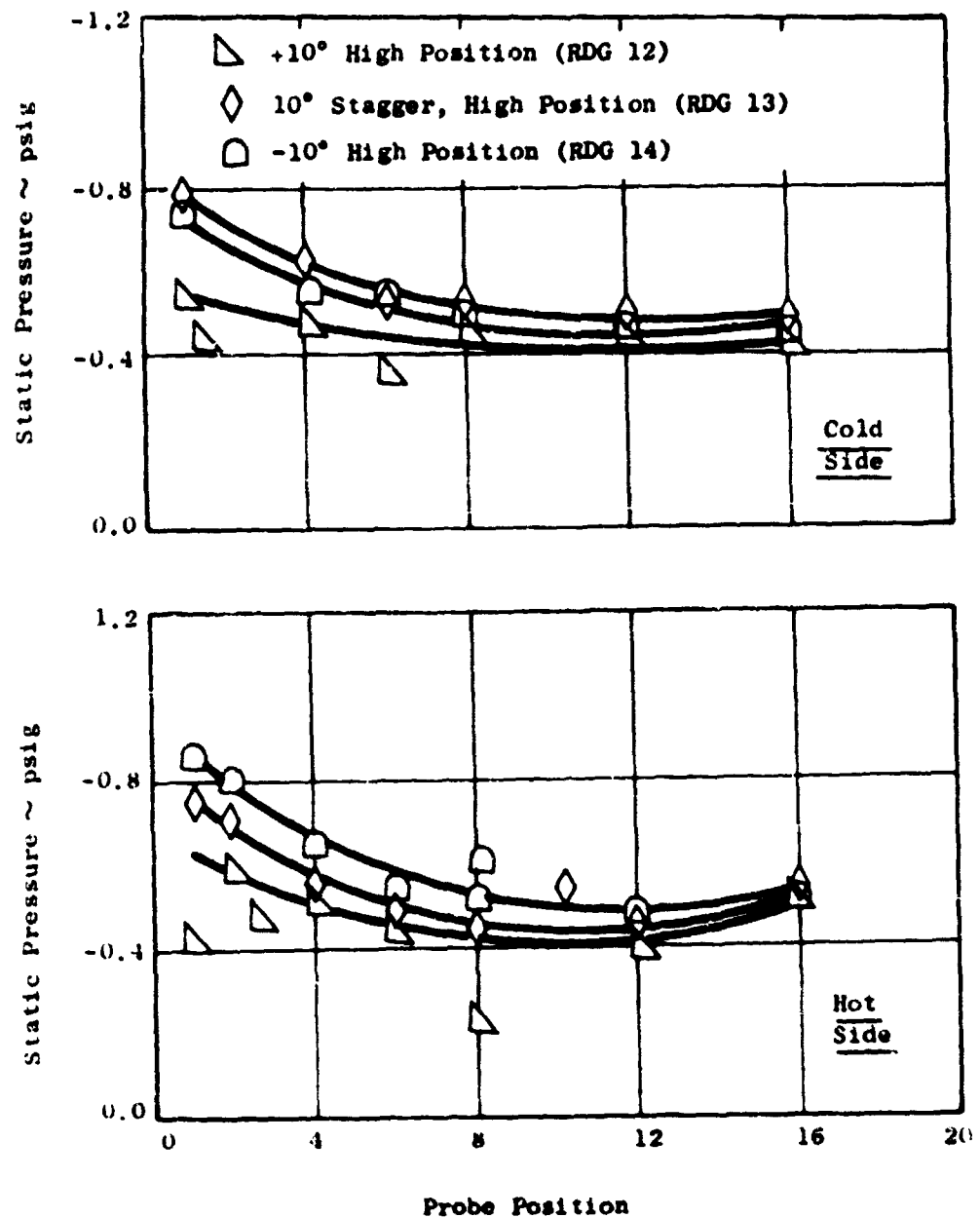


Figure 322 LF-2 Inlet Investigation  
Fan Inlet Static Pressures

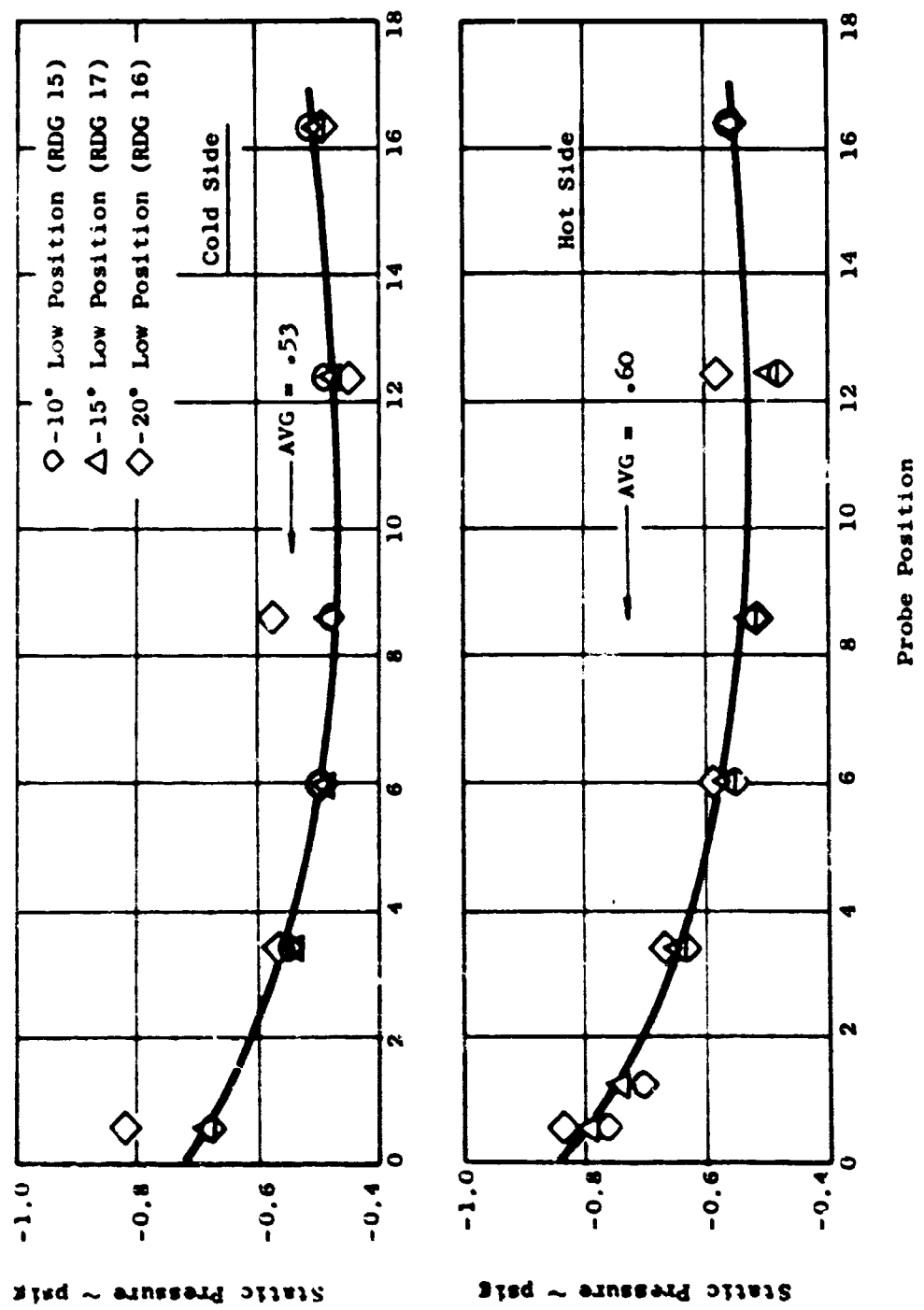


Figure 323 LP-2 Inlet Investigation  
Fan Inlet Static Pressures

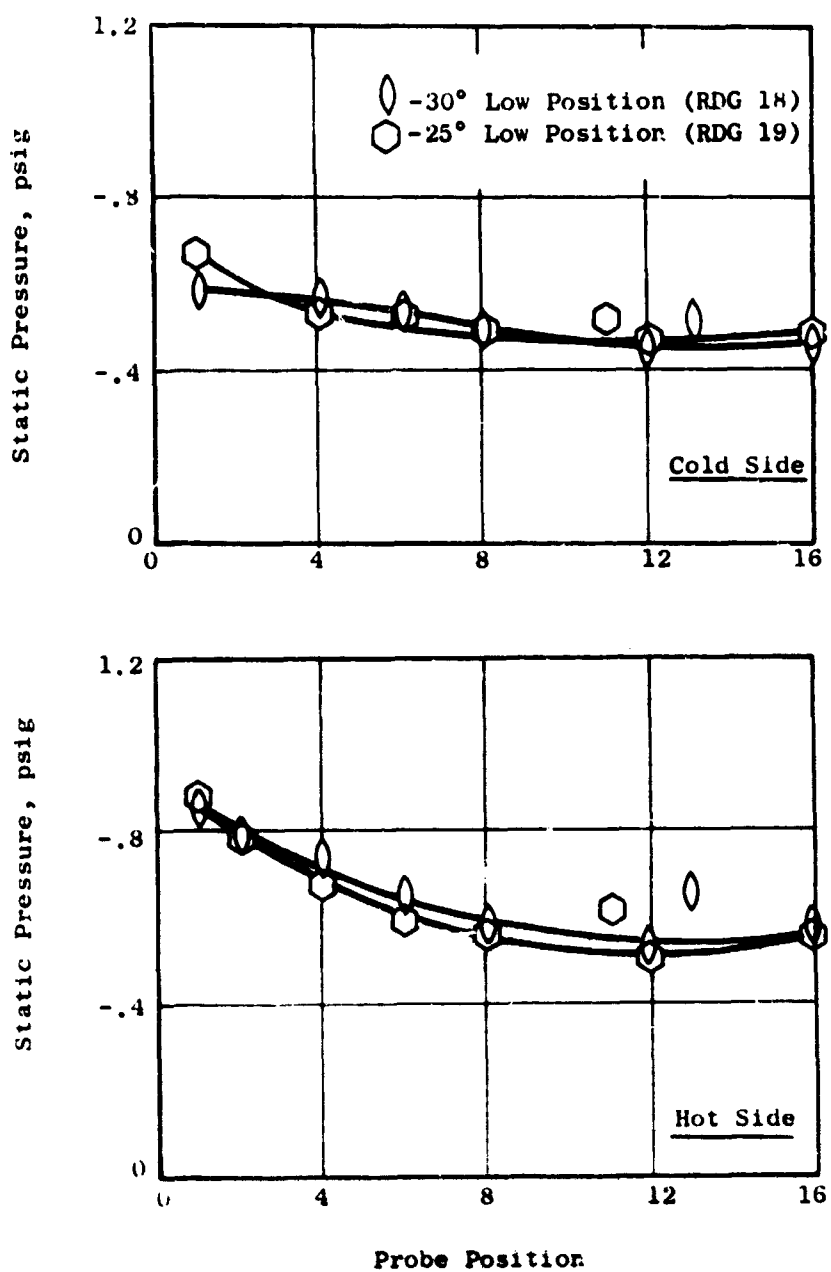


Figure 324 LF-2 Inlet Investigation  
Fan Inlet Static Pressures

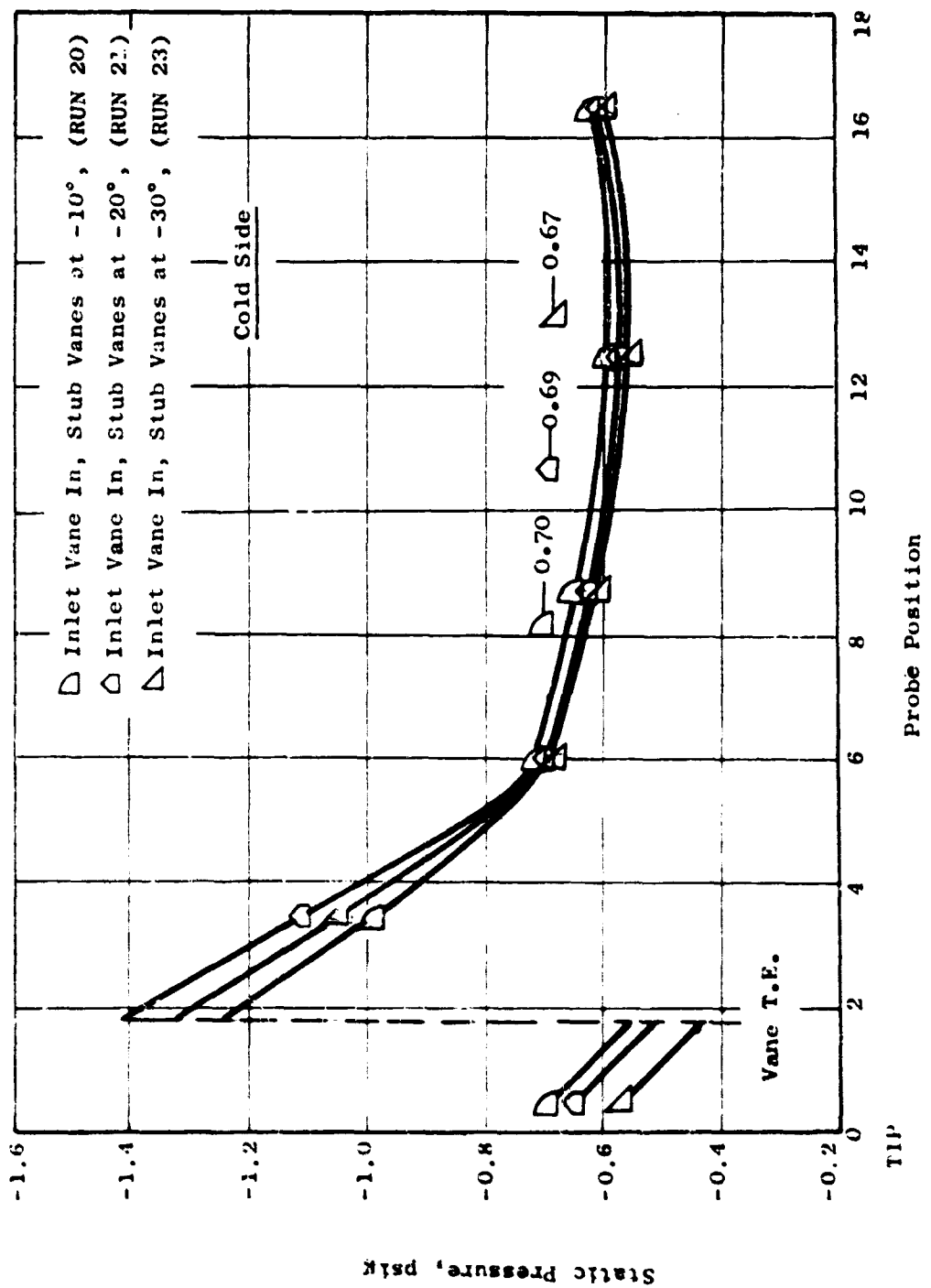


Figure 325 LF-2 Inlet Investigation  
Fan Inlet Static Pressures

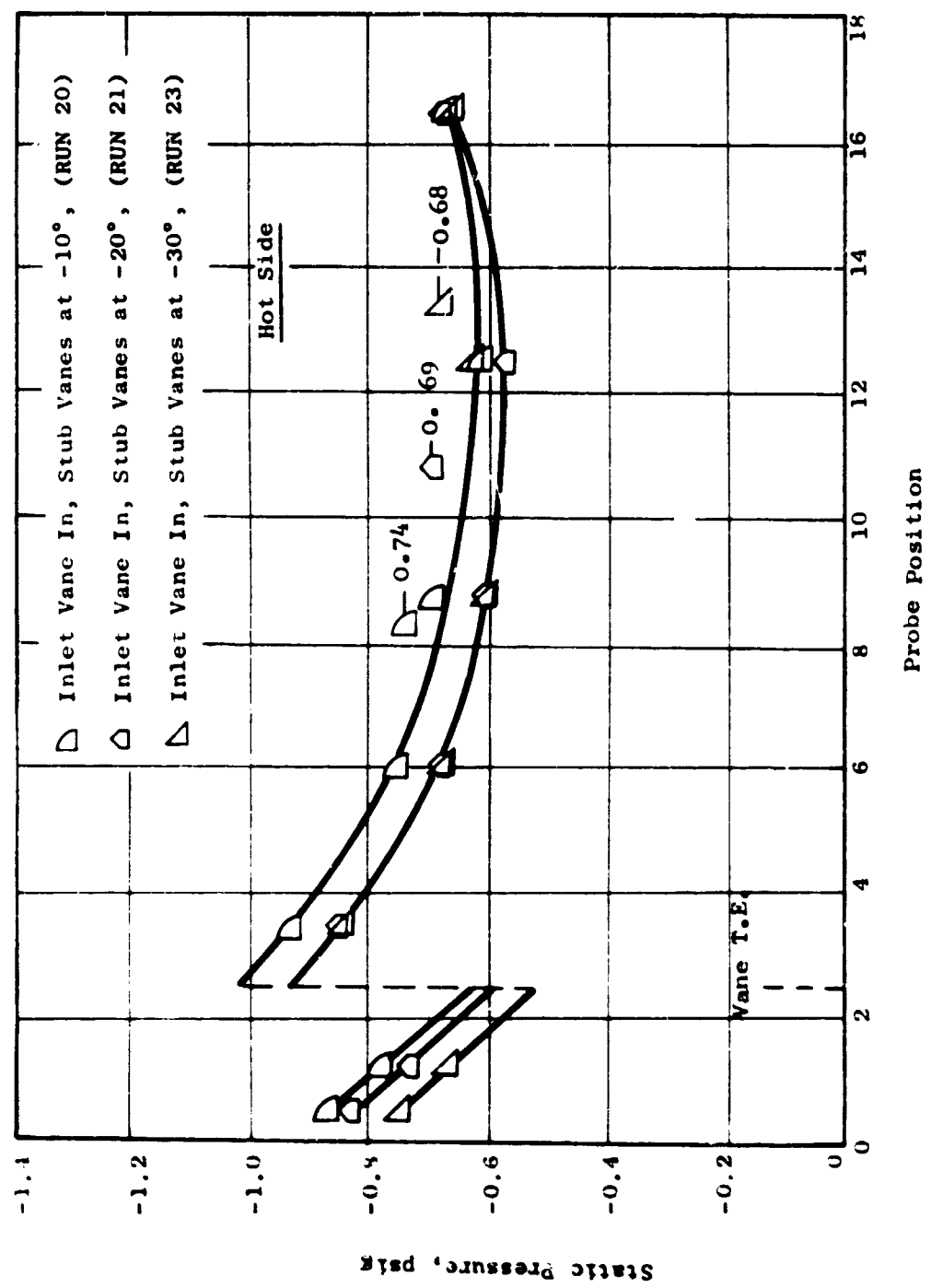


Figure 326 LF-2 Inlet Investigation  
Fan Inlet Static Pressures

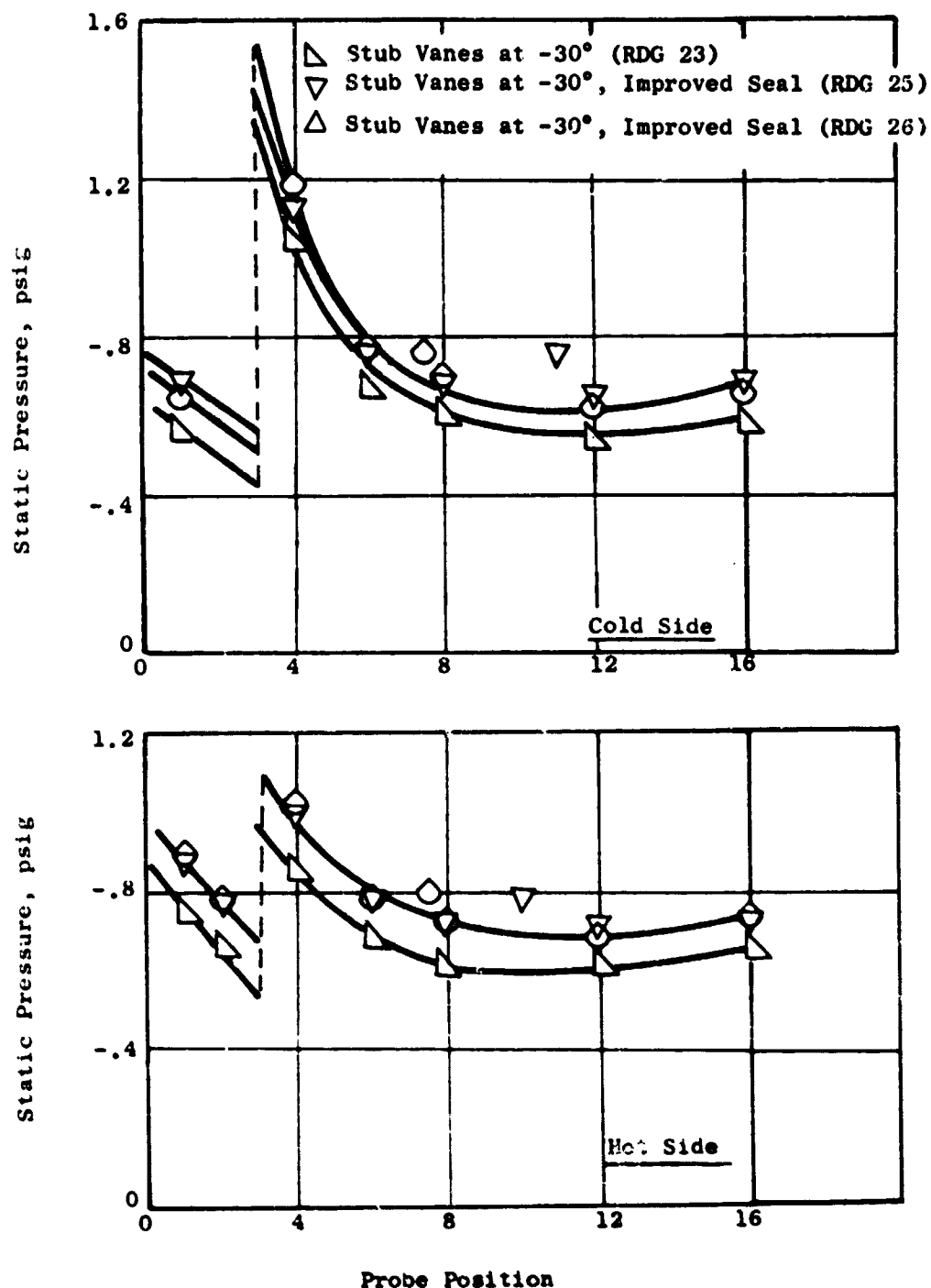
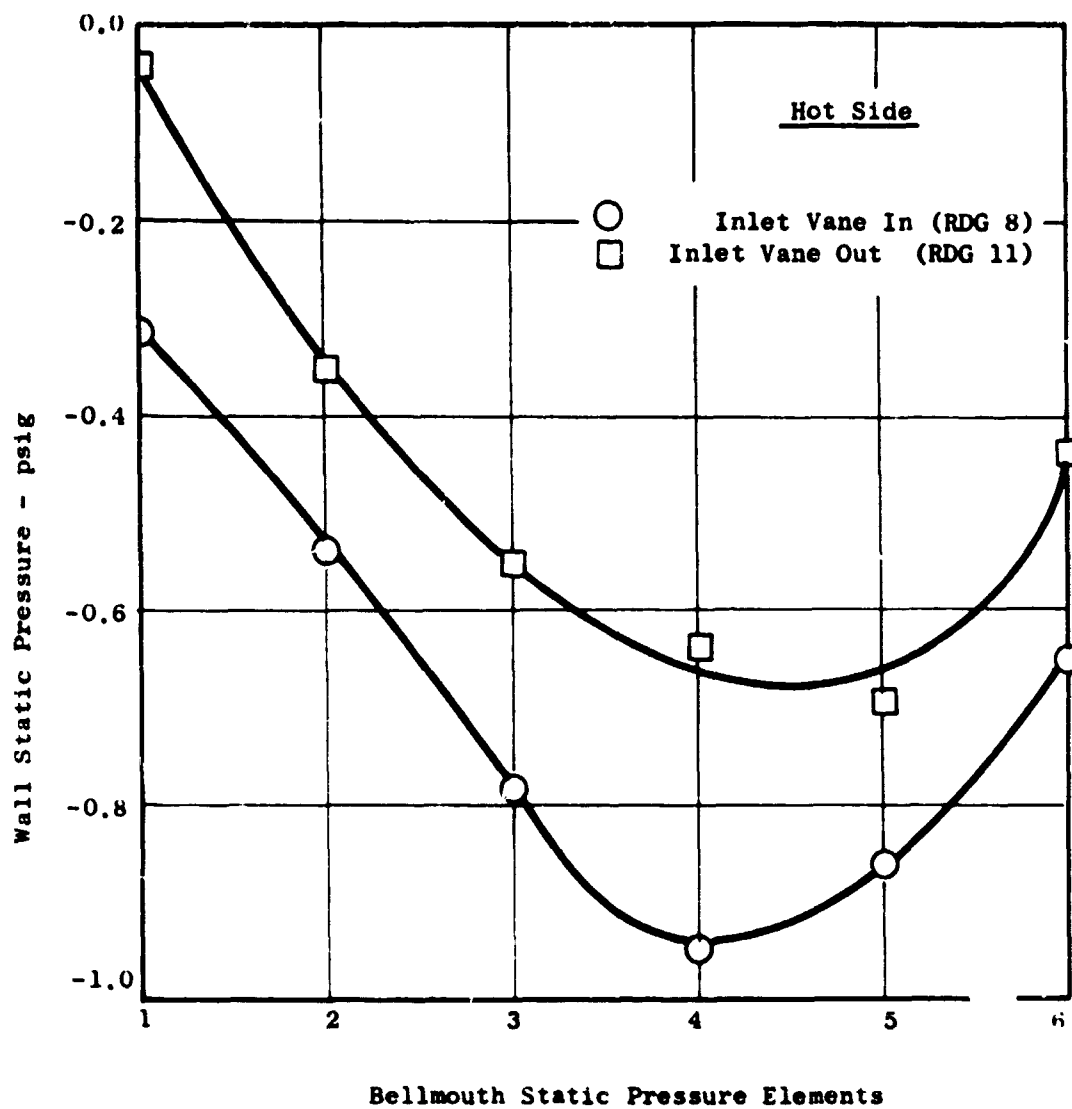


Figure 327 LF-2 Inlet Investigation  
Fan Inlet Static Pressures



**Figure 328 LF-2 Inlet Investigation**  
**Bellmouth Static Pressure Profile**

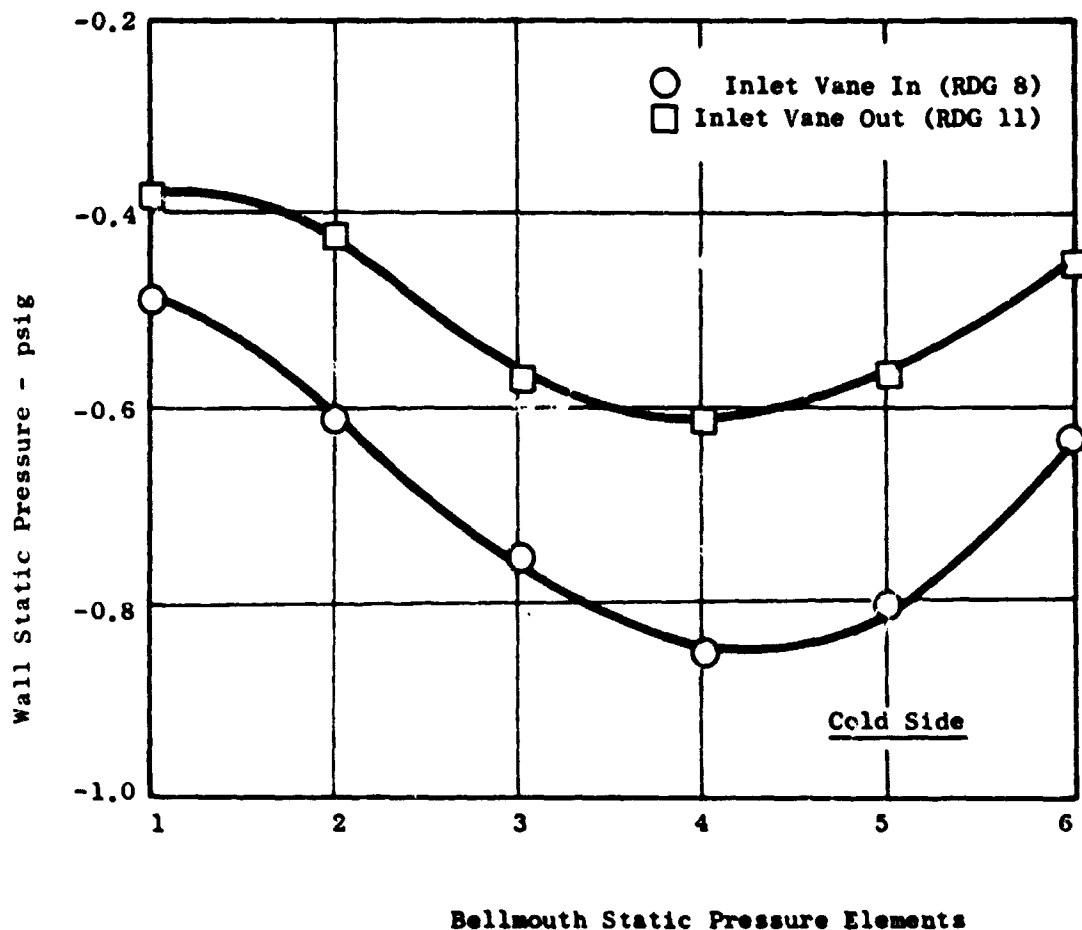


Figure 329 LF-2 Inlet Investigation  
Bellmouth Static Pressure Profile

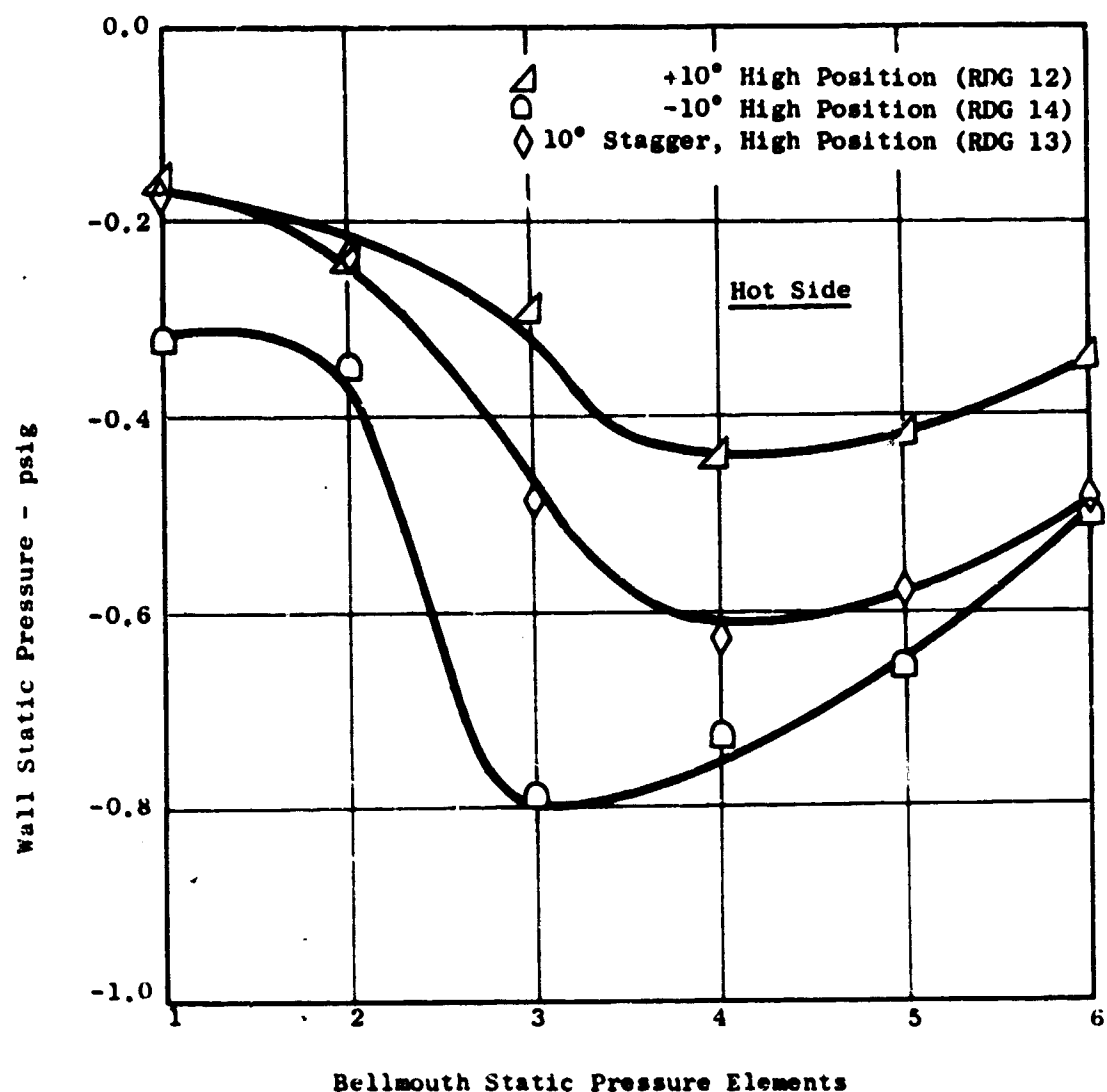


Figure 330 LF-2 Inlet Investigation  
Bellmouth Static Pressure Profile

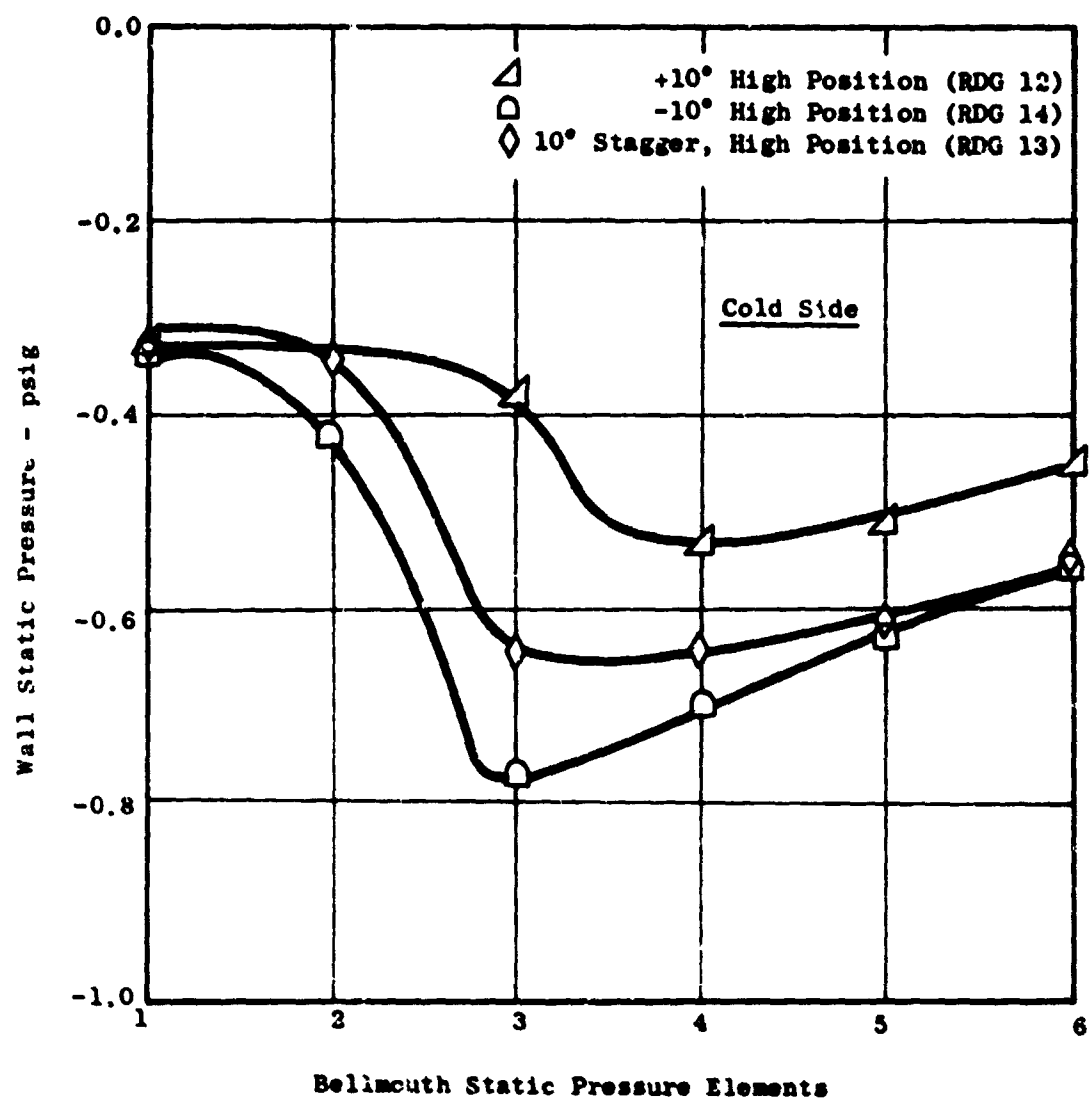


Figure 331 LF-2 Inlet Investigation  
Bellmouth Static Pressure Profile

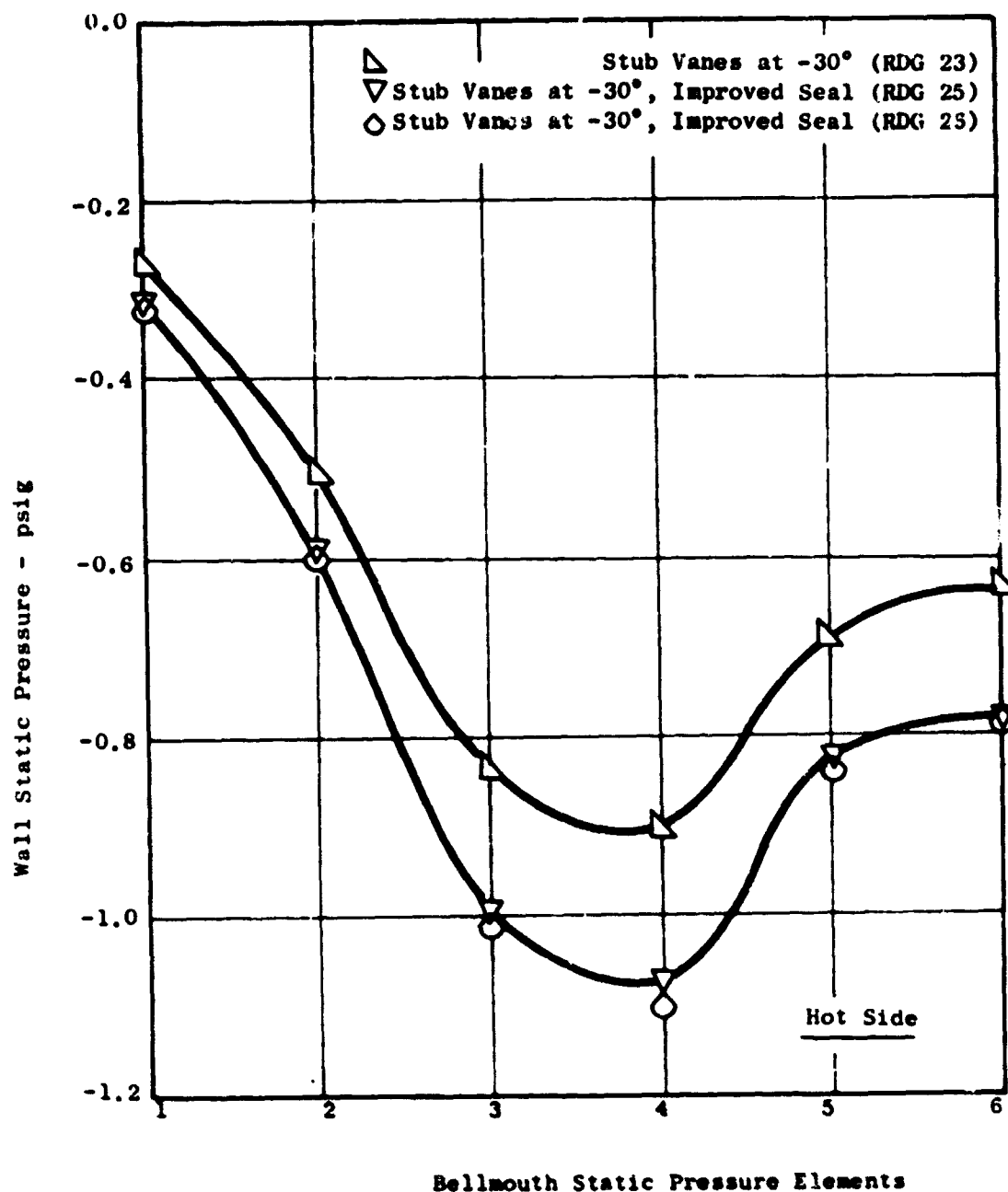


Figure 332 LF-2 Inlet Investigation  
Bellmouth Static Pressure Profile

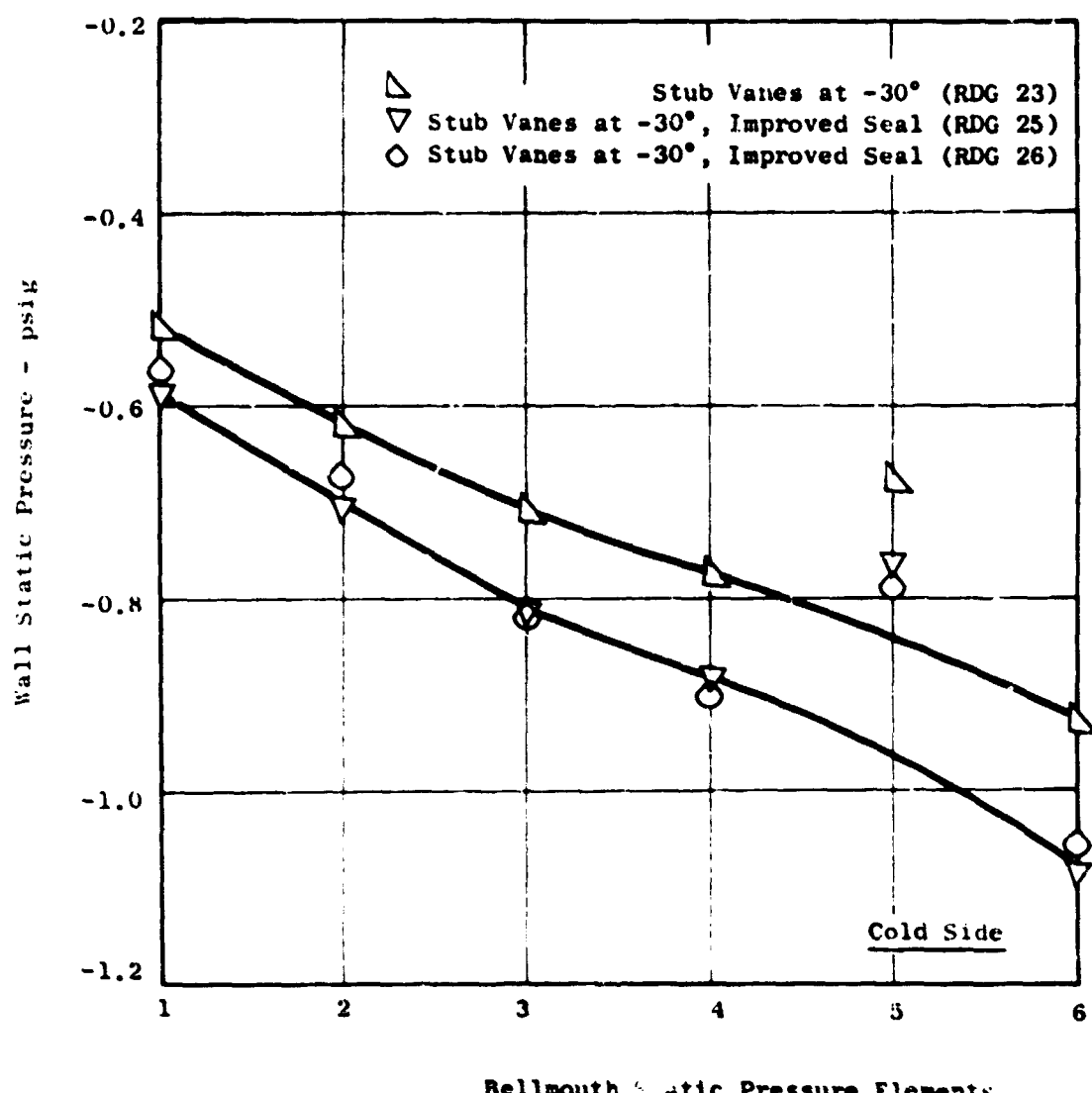


Figure 333 LF-2 Inlet Investigation  
Bellmouth Static Pressure Profiles

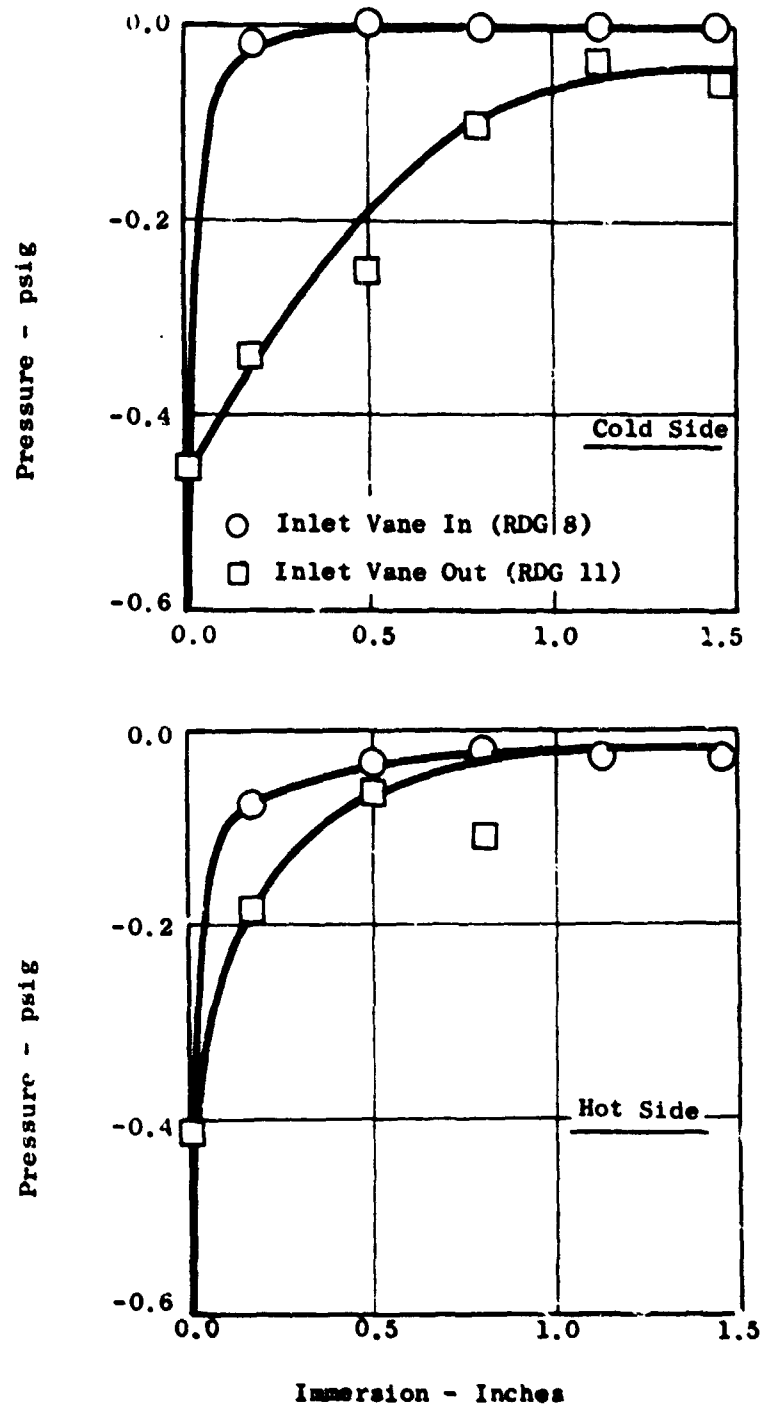


Figure 334 LF-2 Inlet Investigation  
Bellmouth Boundary Layer  
Total Pressure Profiles

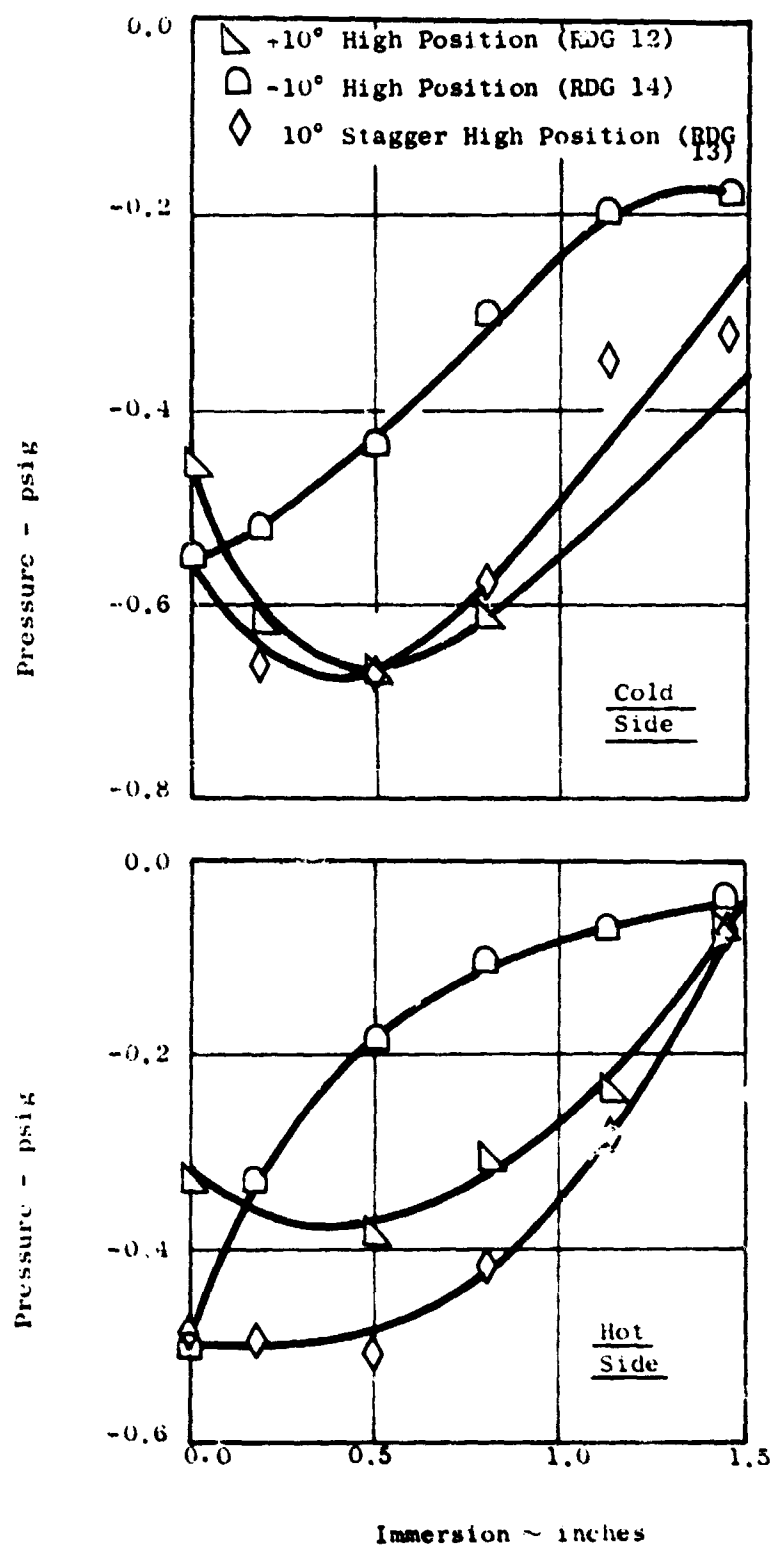


Figure 335 LF-2 Inlet Investigation  
Bellmouth Boundary Layer  
Total Pressure Profiles

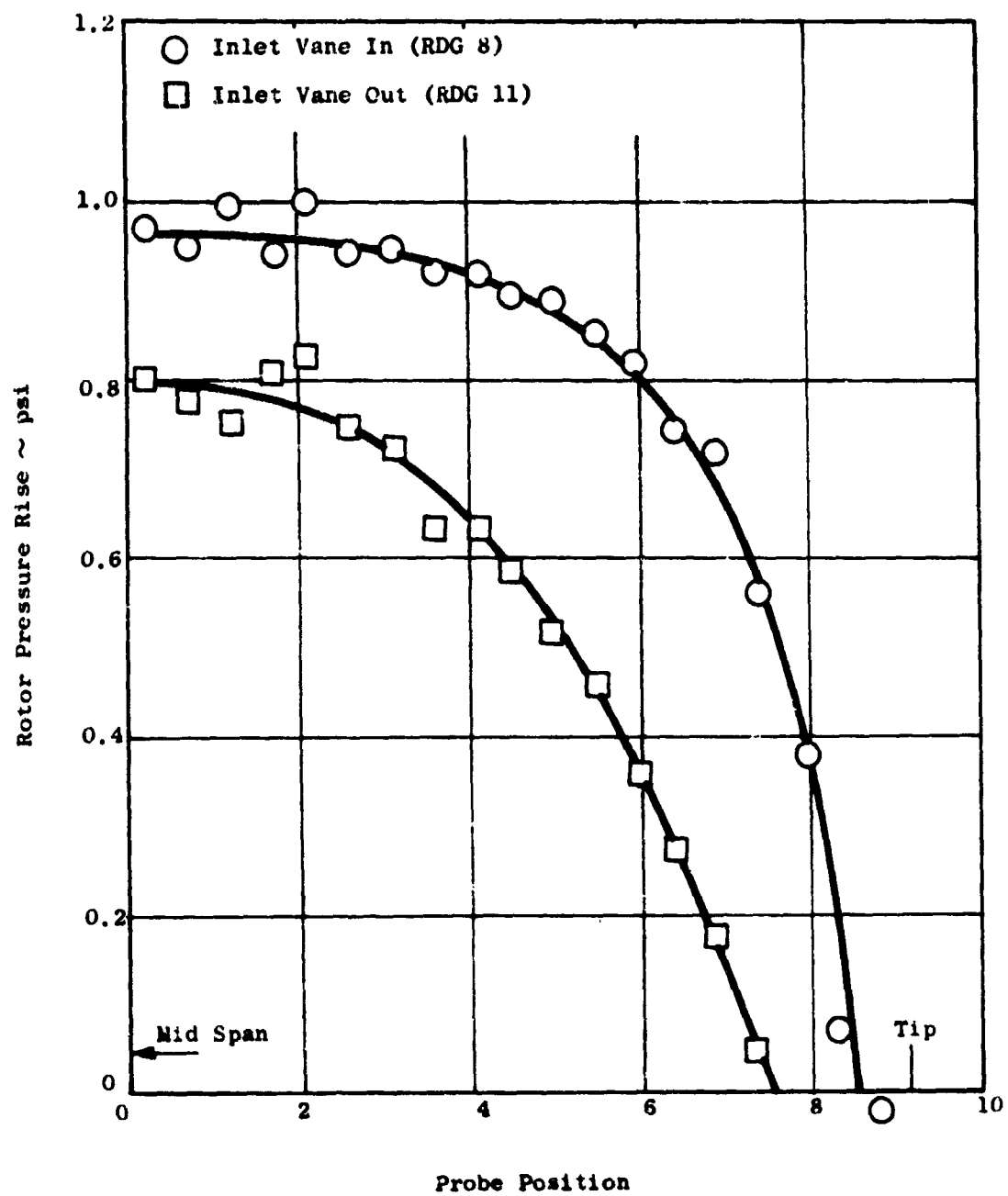


Figure 336 IF-2 Inlet investigation  
Traverse Data - Hot Side

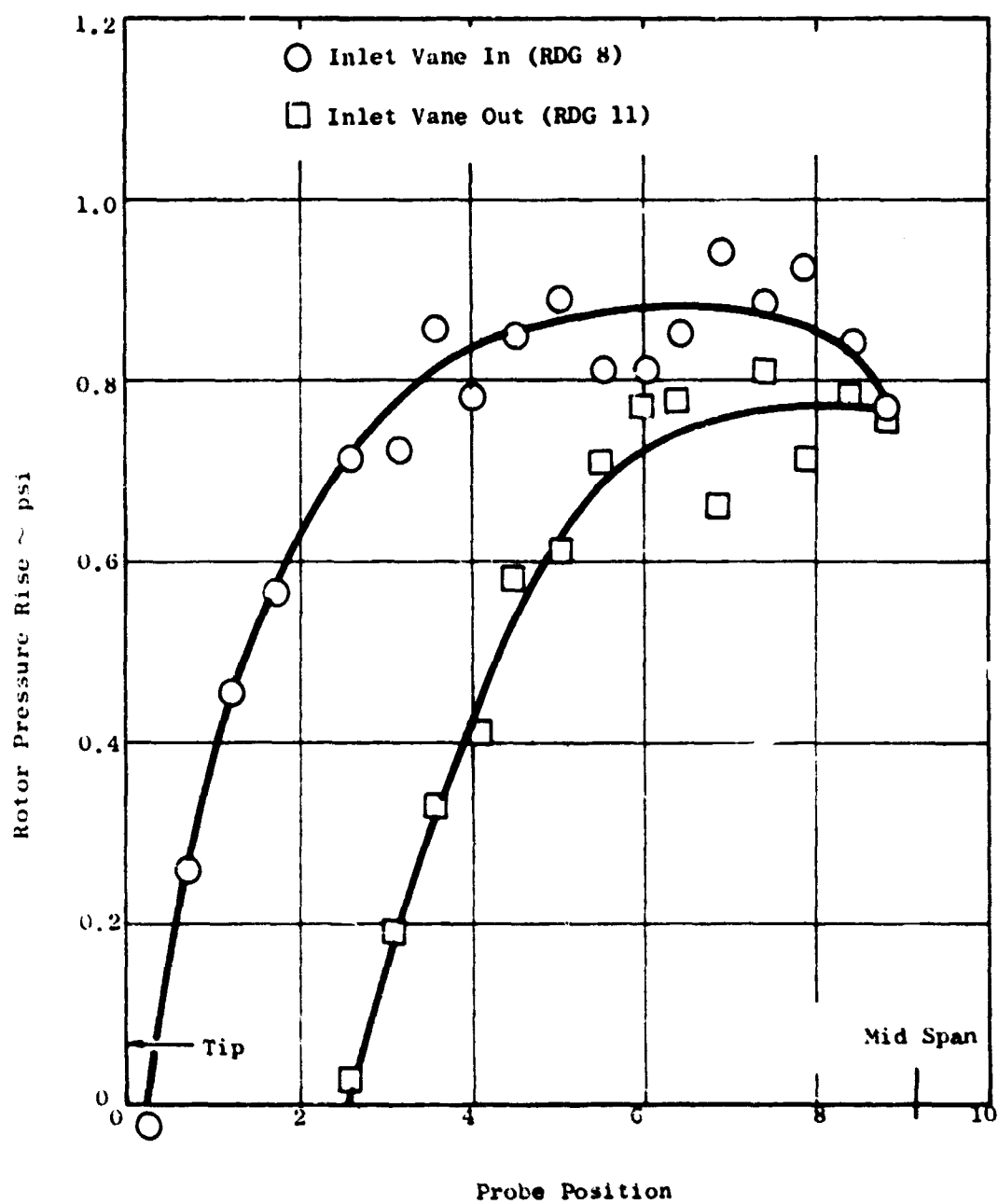


Figure 337 LF-2 Inlet Investigation  
Traverse Data - Cold Side

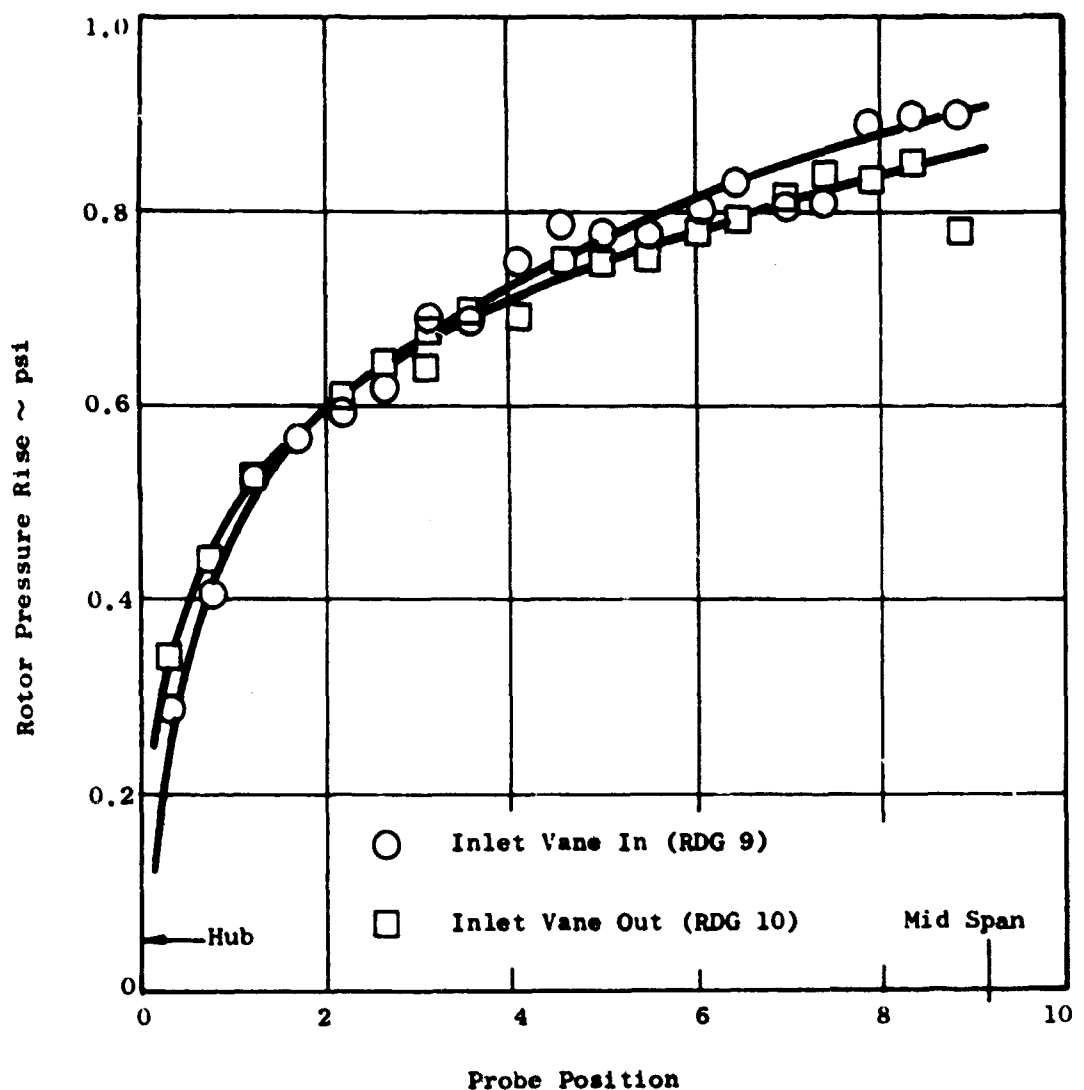


Figure 338 LF-2 Inlet Investigation  
Traverse Data ~ Hot Side

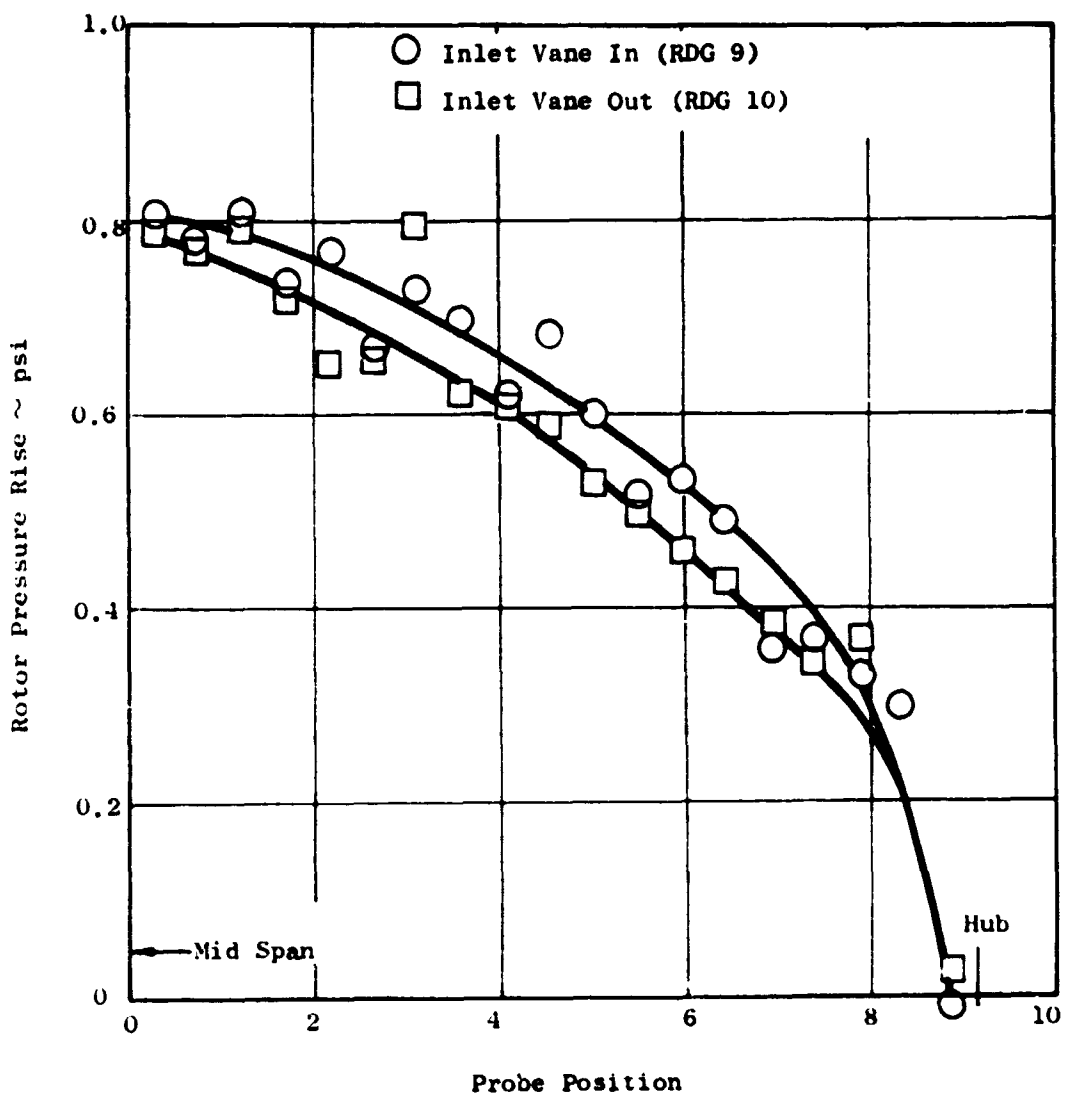


Figure 339 LF-2 Inlet Investigation  
Traverse Data ~ Cold Side

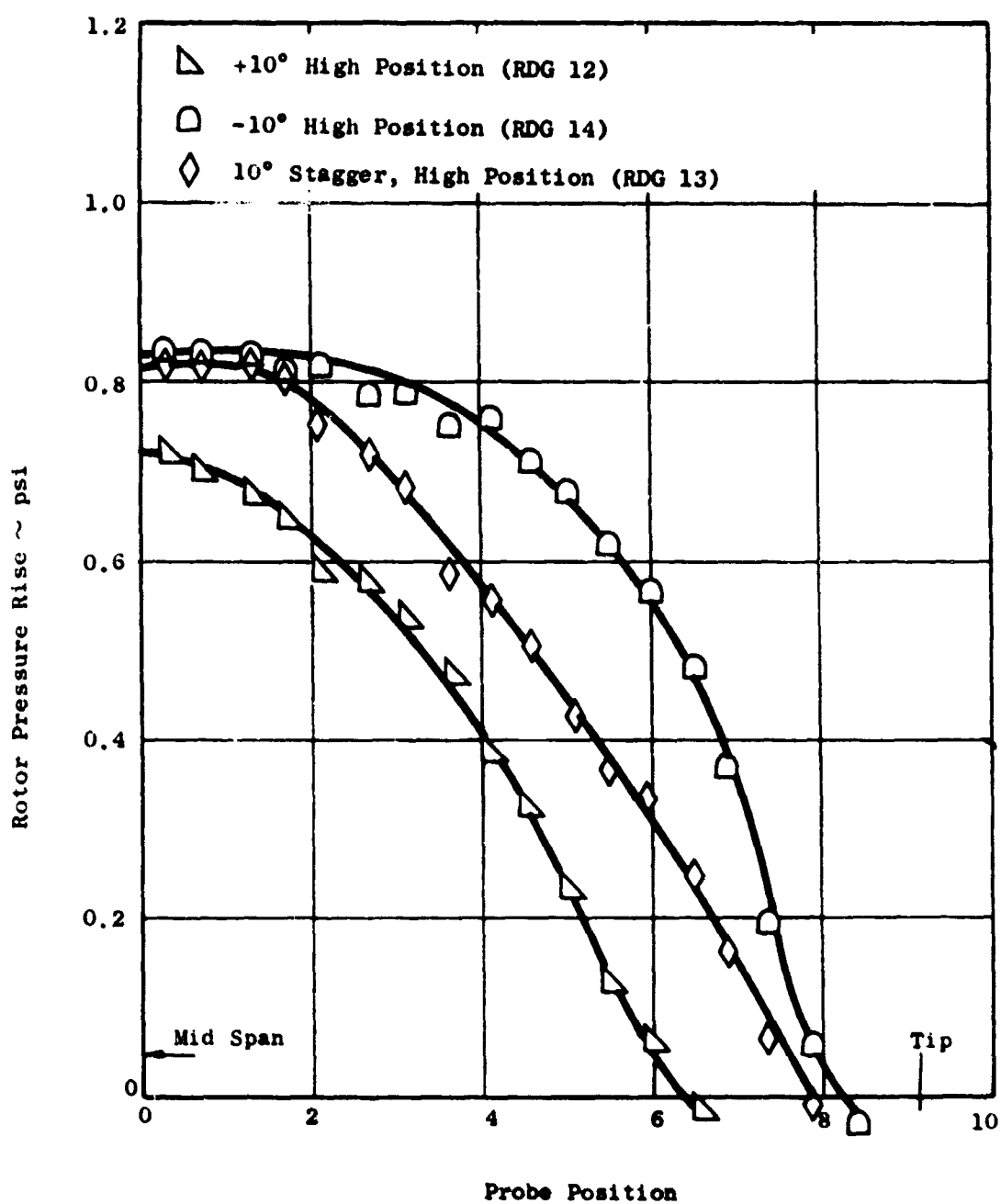


Figure 340 LF-2 Inlet Investigation  
Traverse Data ~ Hot Side

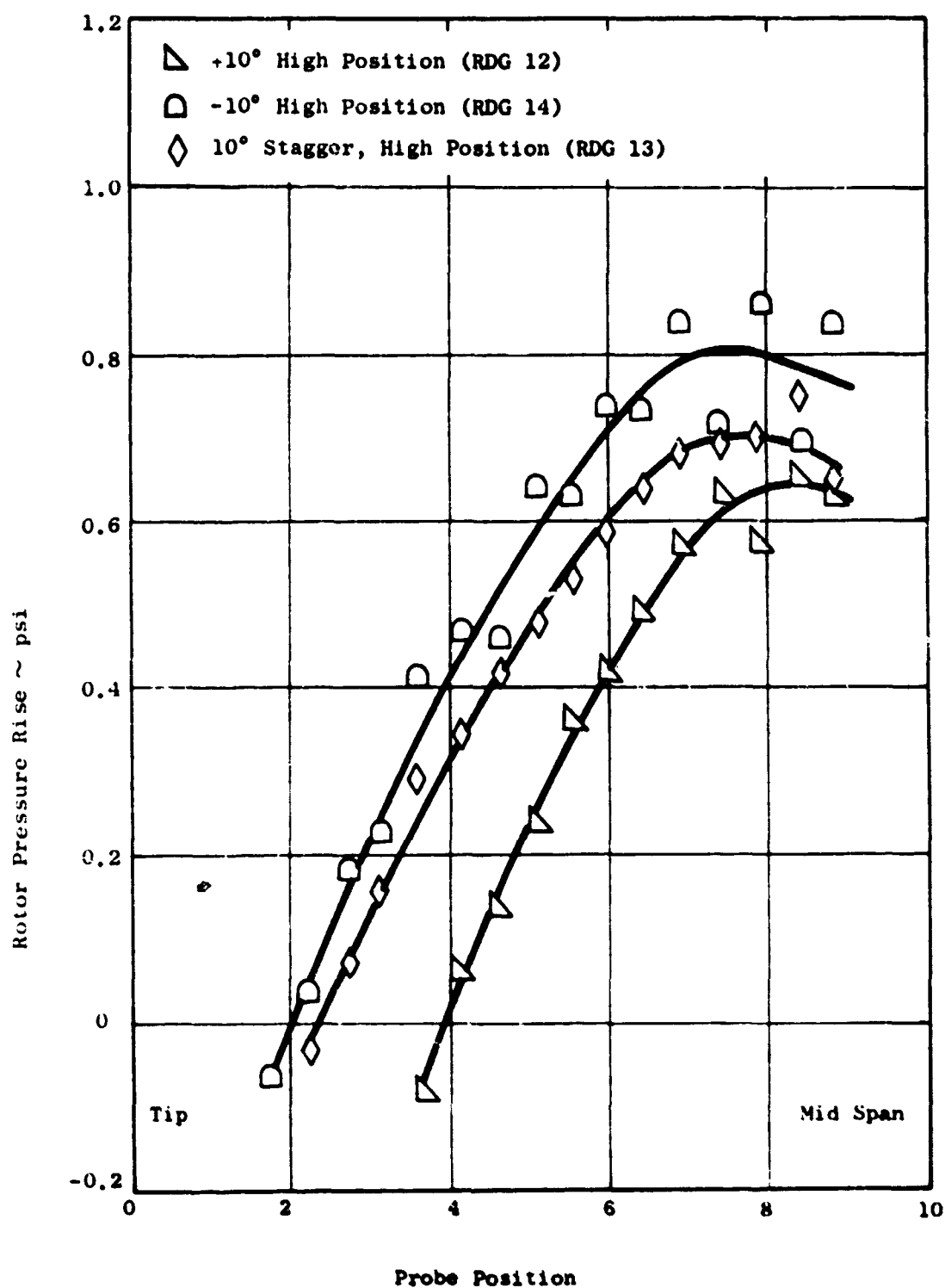


Figure 341 LF-2 Inlet Investigation  
Traverse Data ~ Cold Side

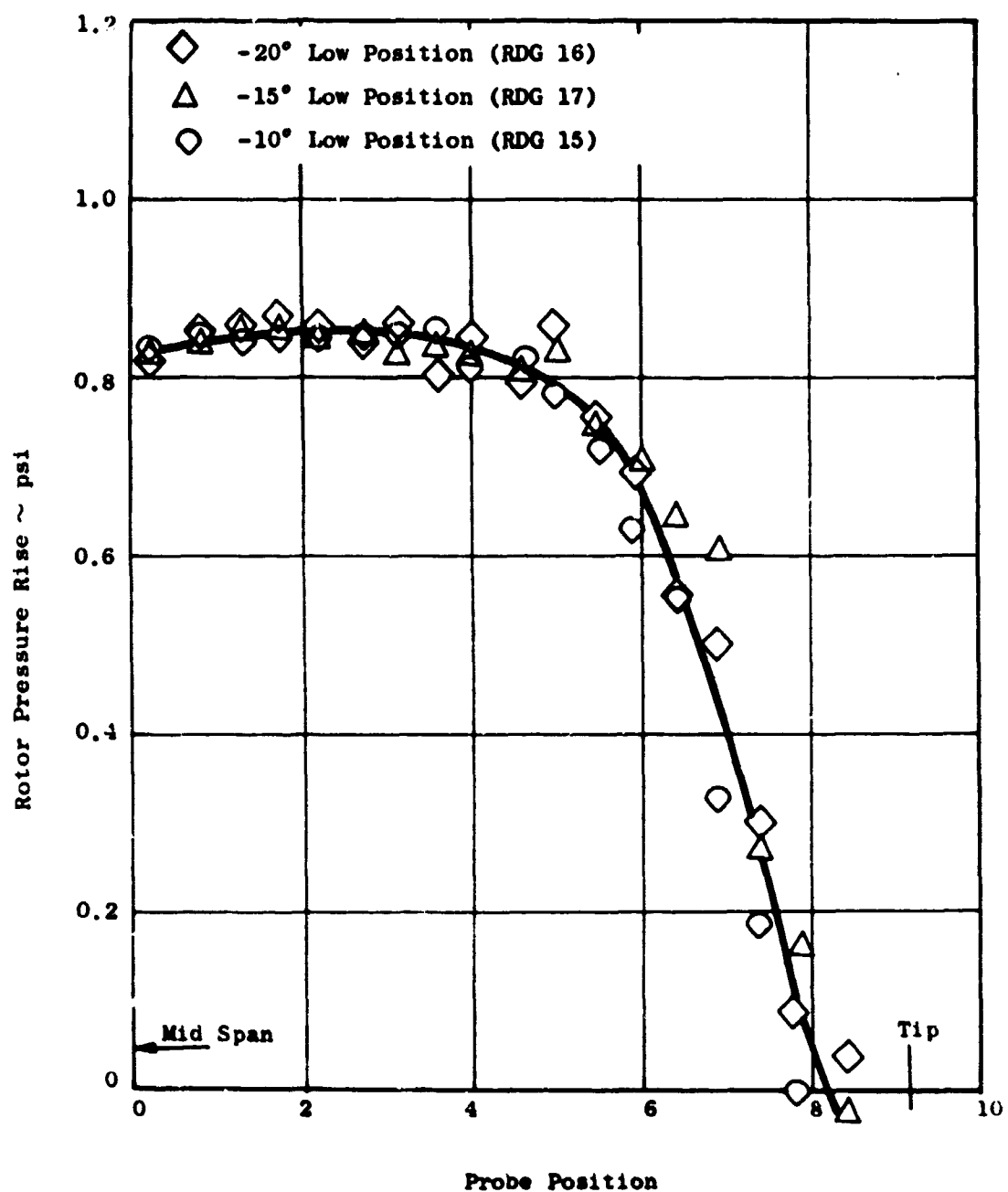


Figure 342 LF-2 Inlet Investigation  
Transverse Data ~ Hot Side

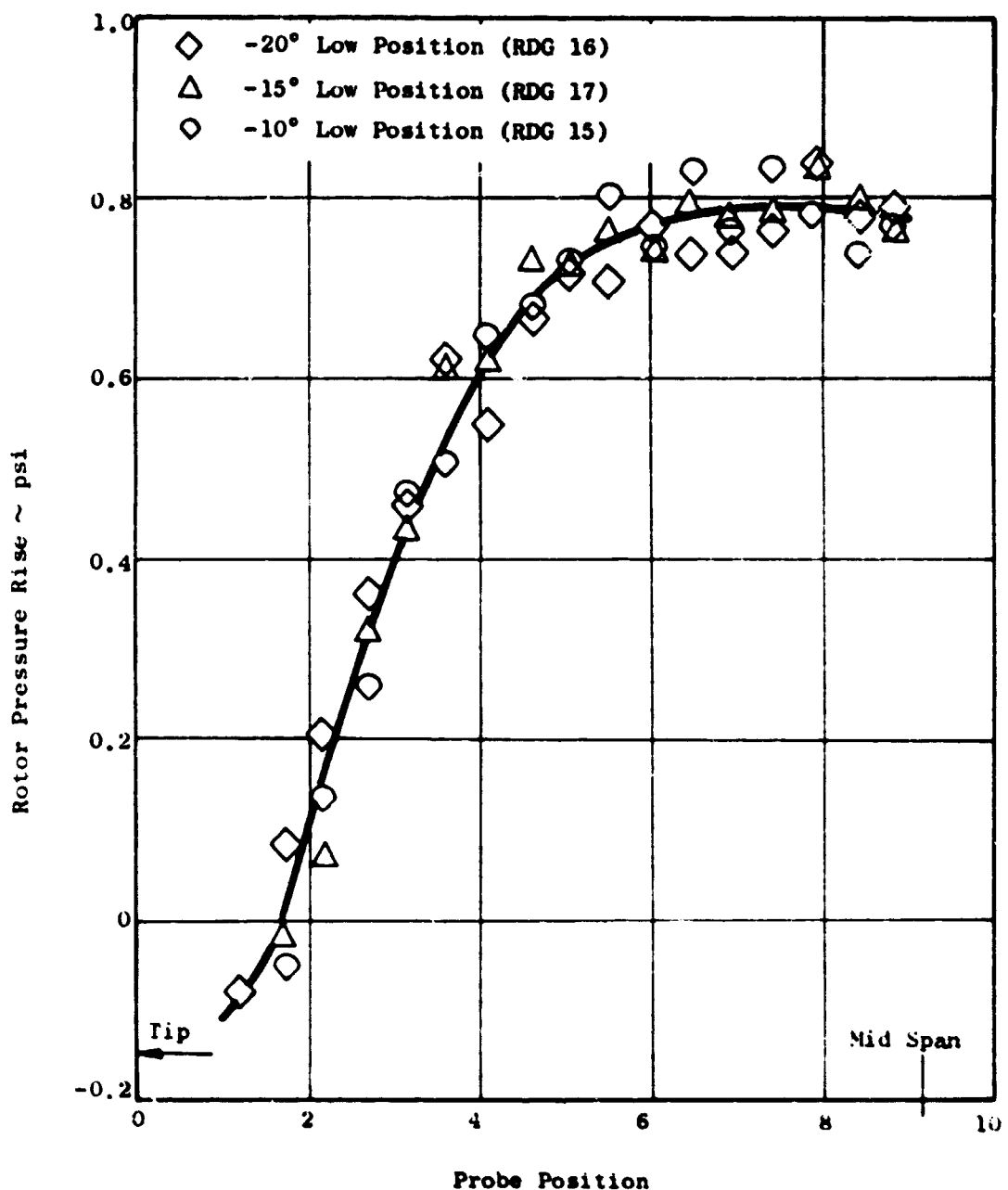


Figure 343 LF-2 Inlet Investigation  
Traverse Data ~ Cold Side

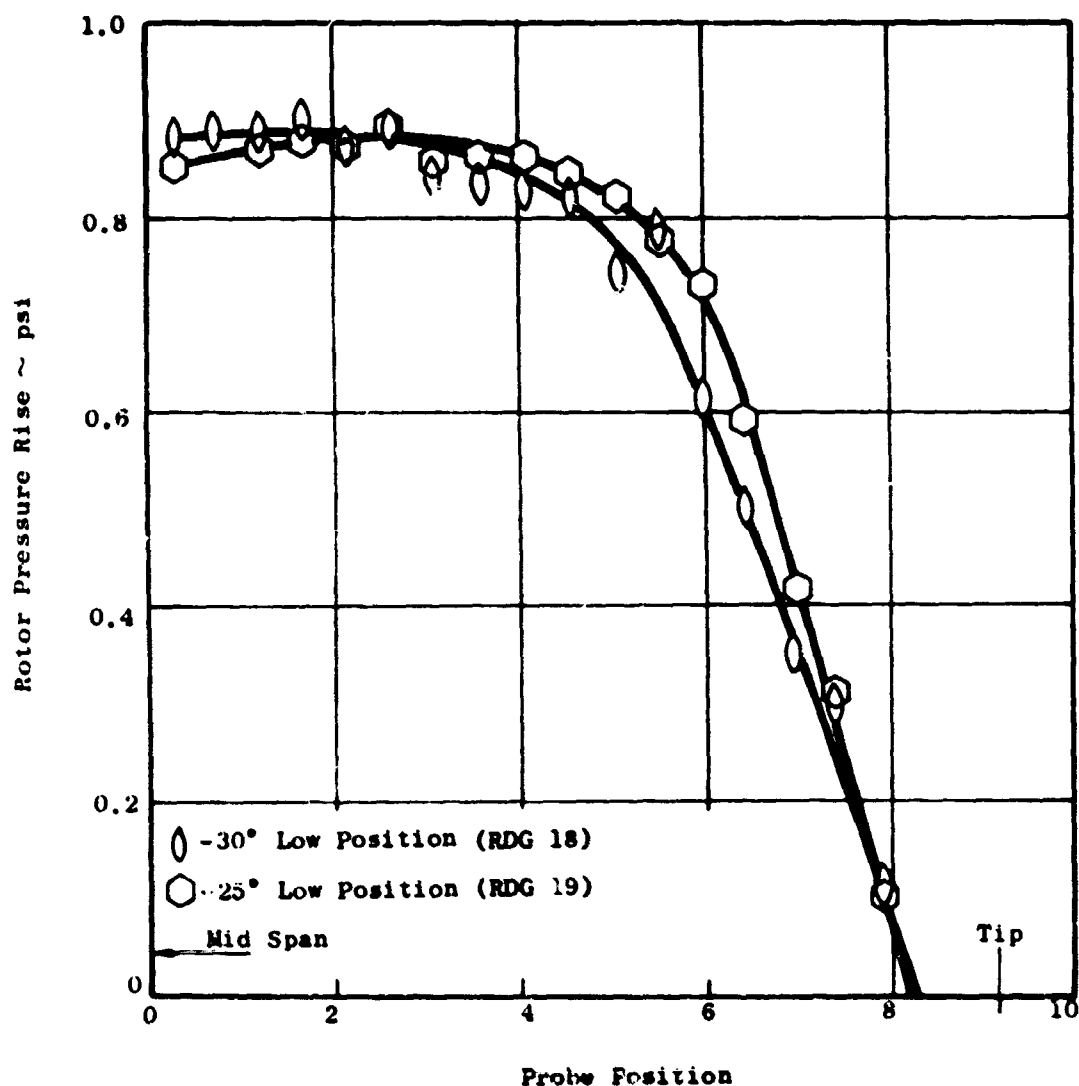


Figure 344 LP-2 Inlet Investigation  
Traverse Data ~ Hot Side

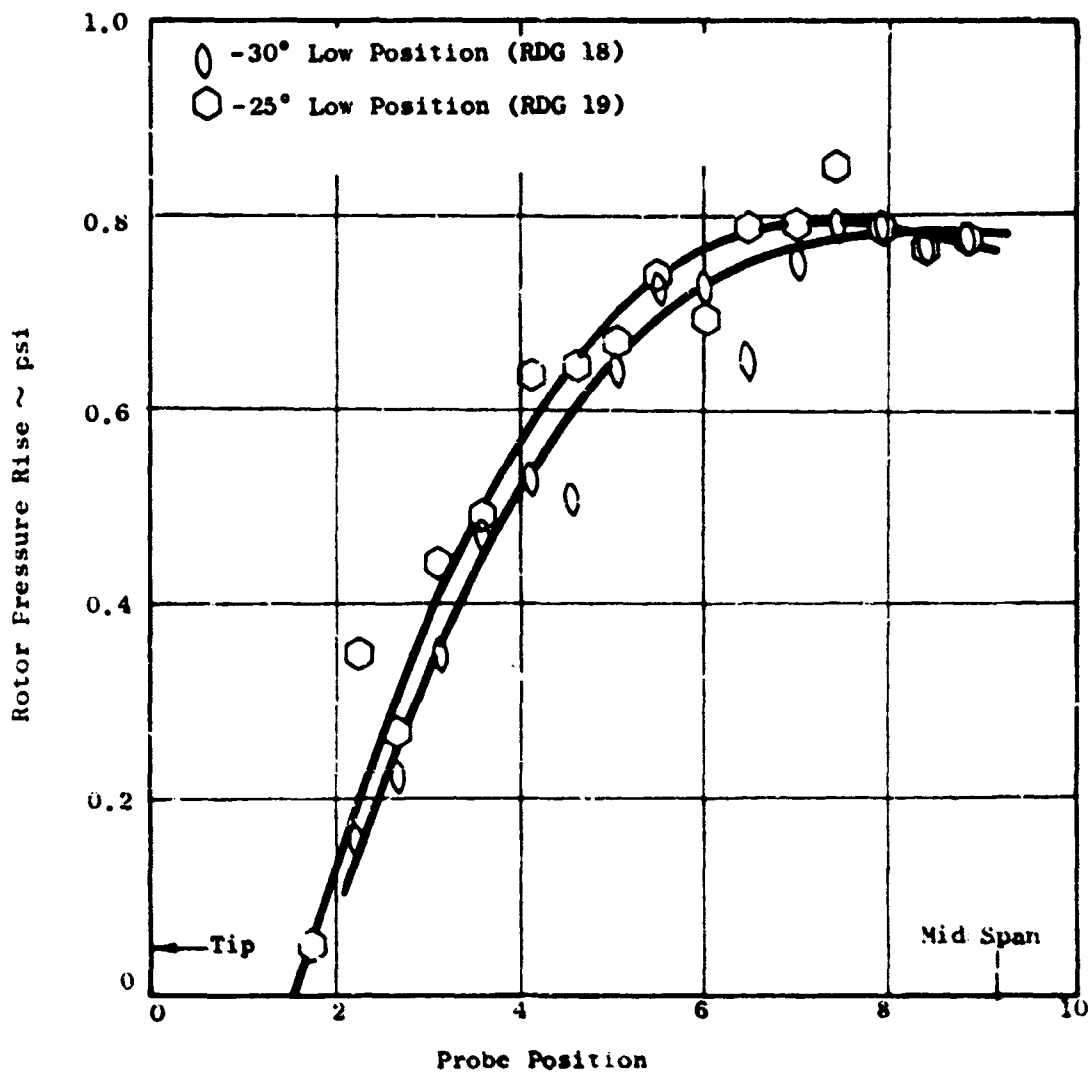


Figure 345 LF-2 Inlet Investigation  
Traverse Data ~ Cold Side

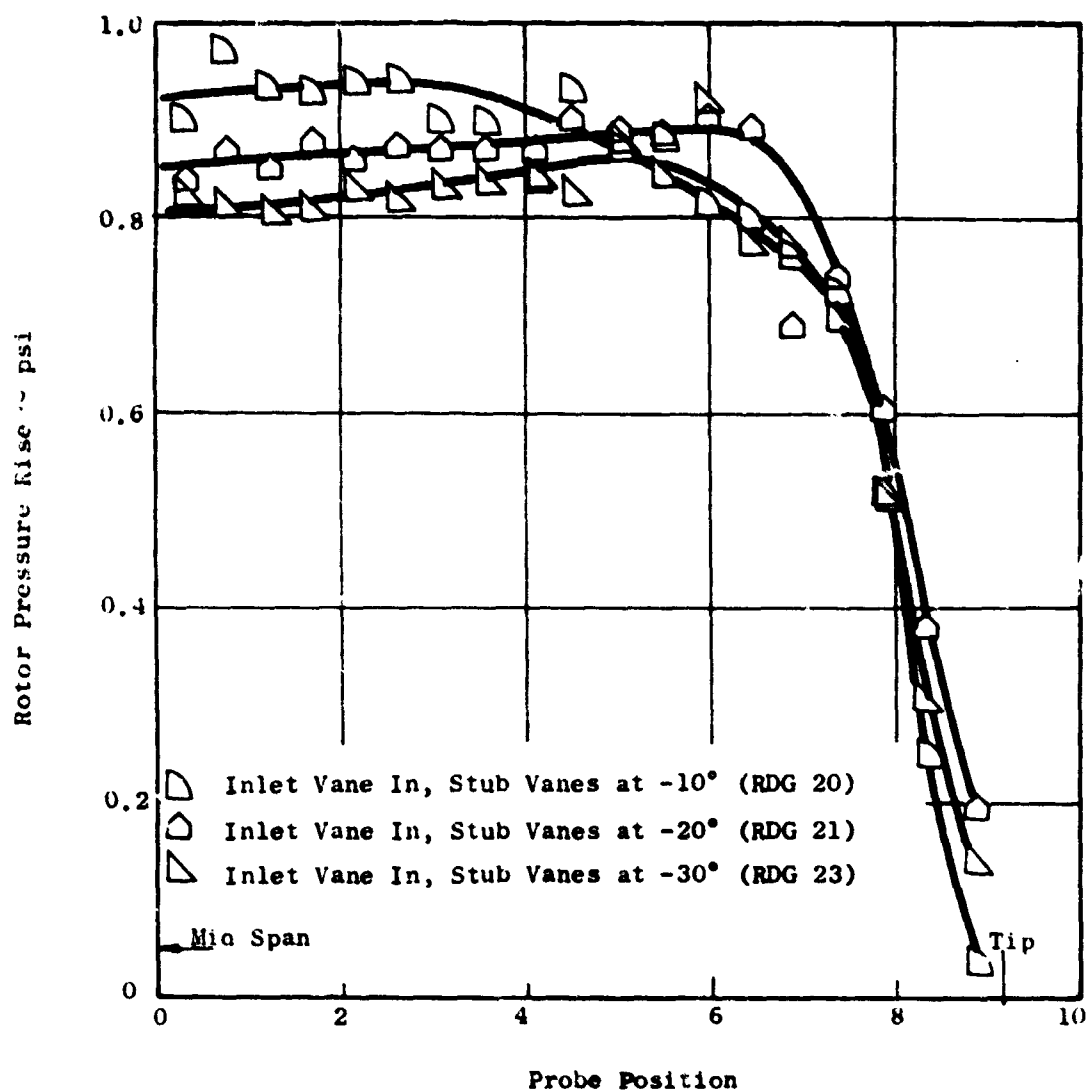


Figure 346 LF-2 Inlet Investigation  
Traverse Data ~ Hot Side

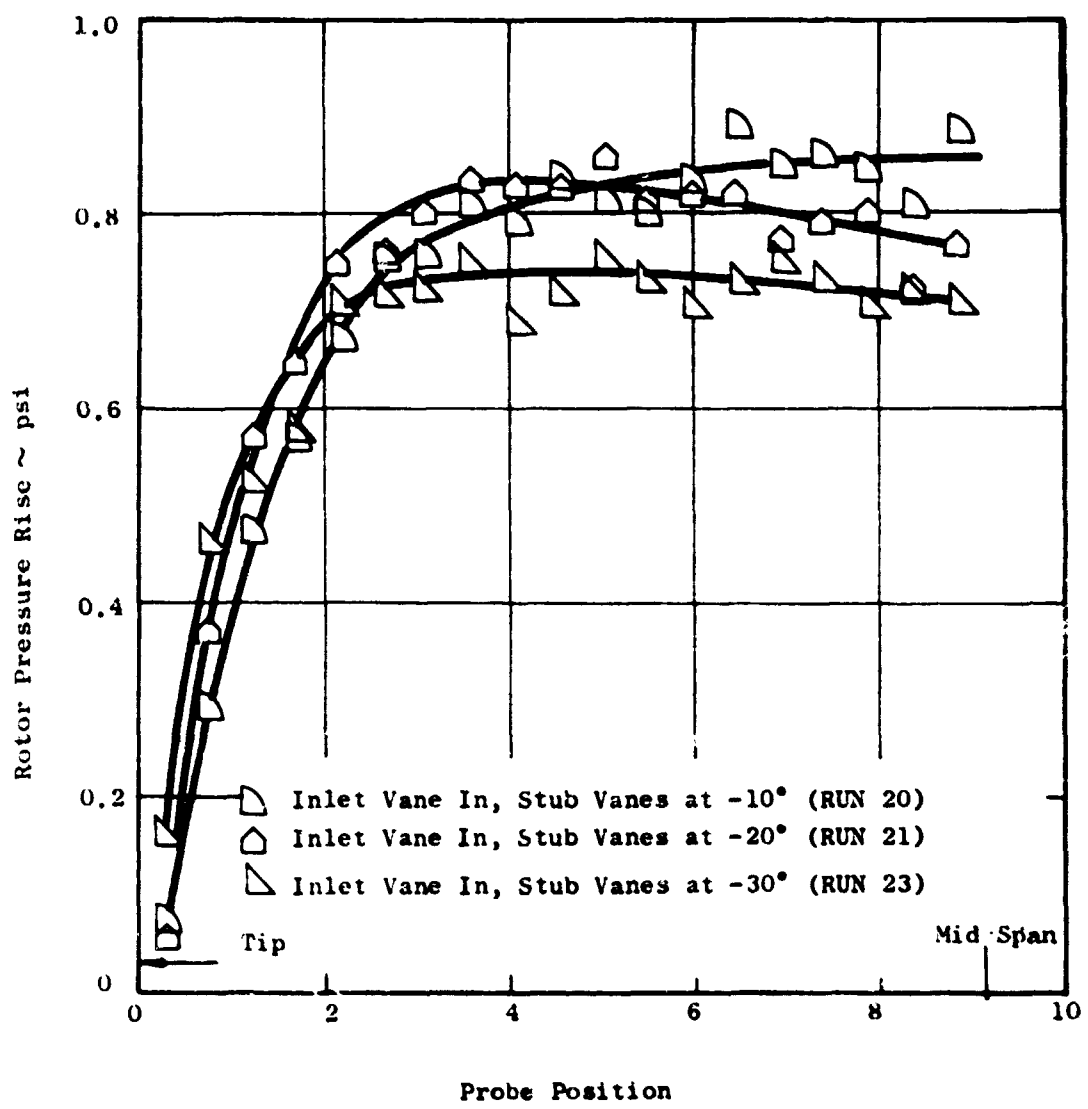


Figure 347 LF-2 Inlet Investigation  
Traverse Data  $\sim$  Cold Side

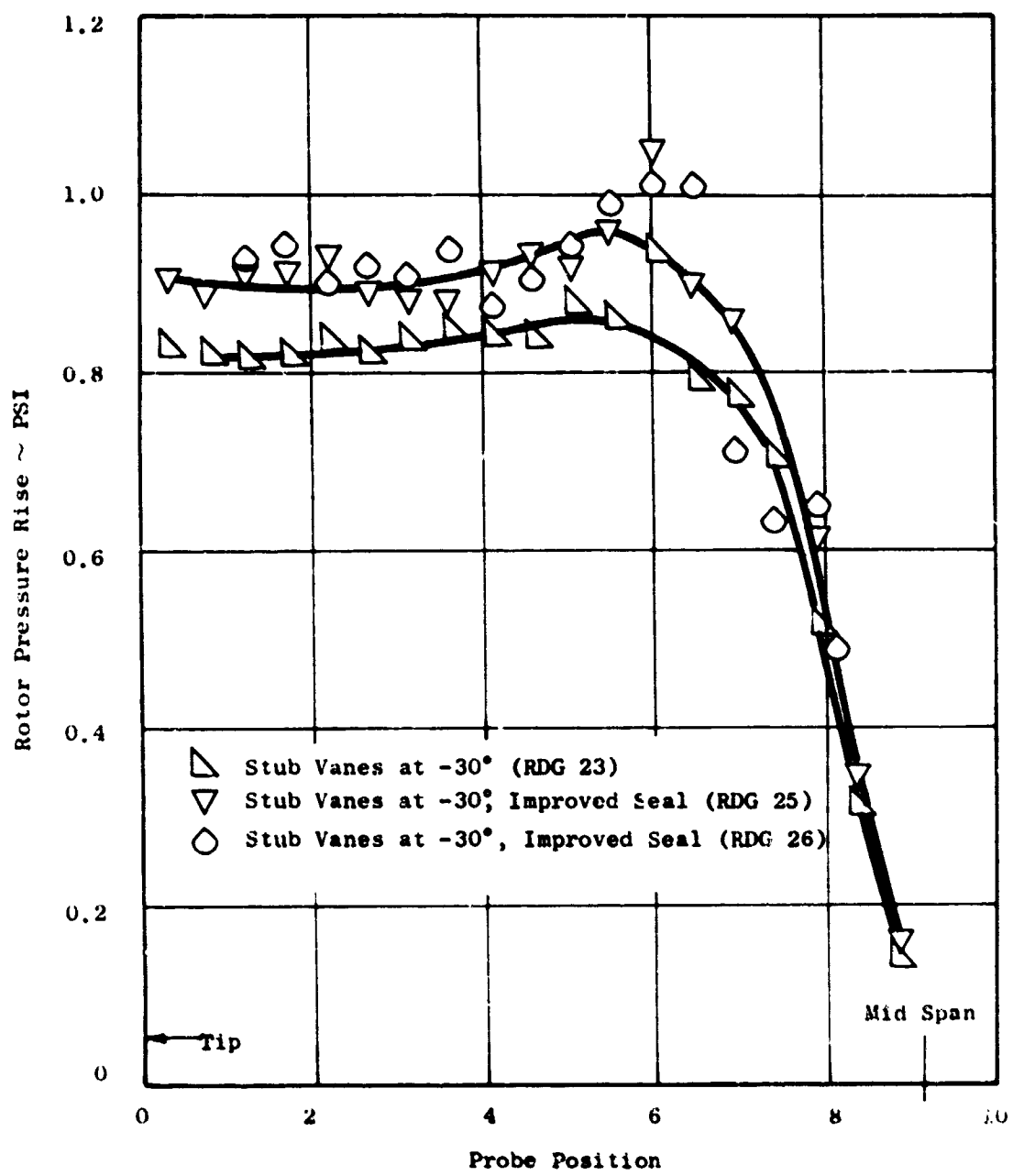


Figure 348 LF2 Inlet Investigation  
Traverse Data ~ Hot Side

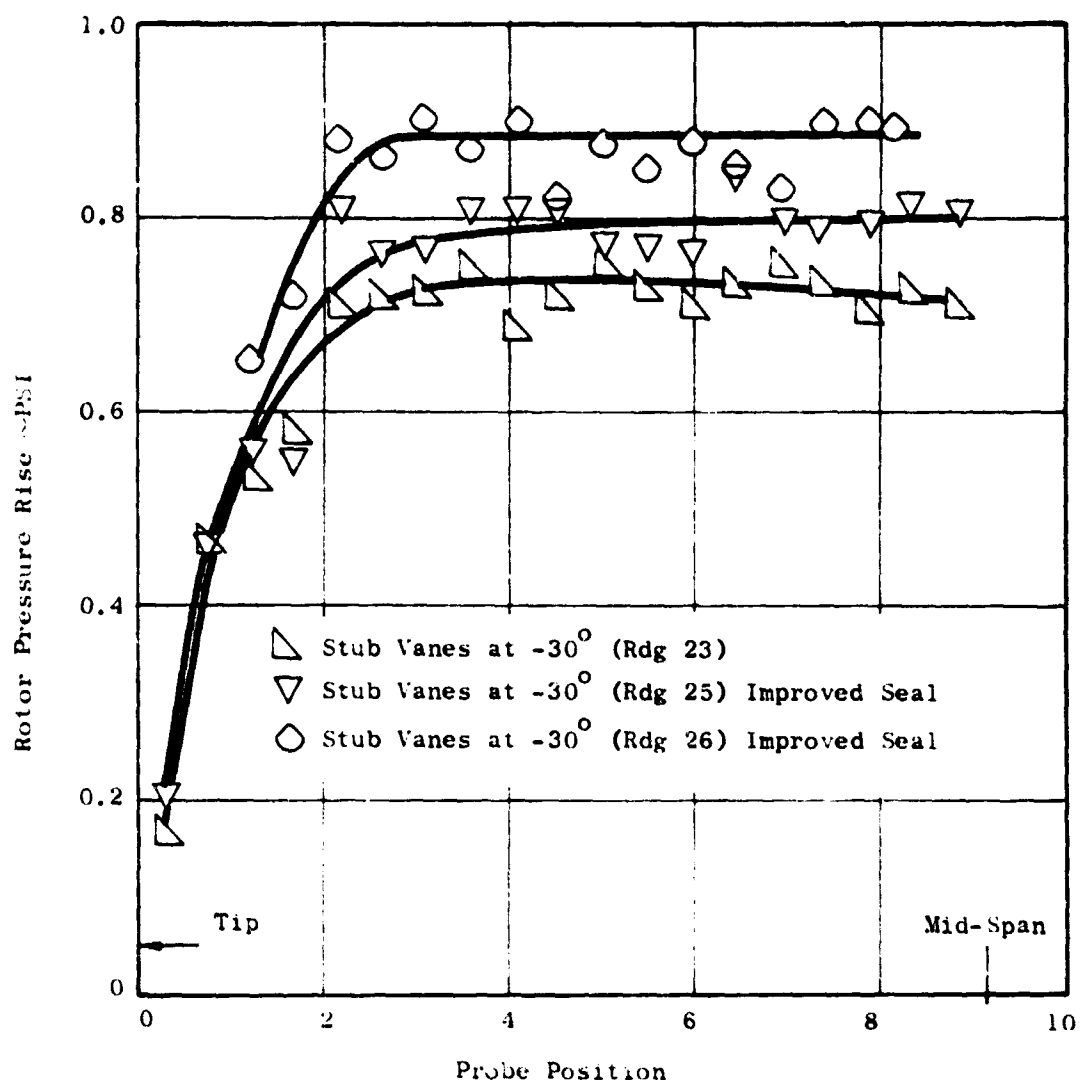


Figure 349 LF2 Inlet Investigation Traverse Data - Cold Side

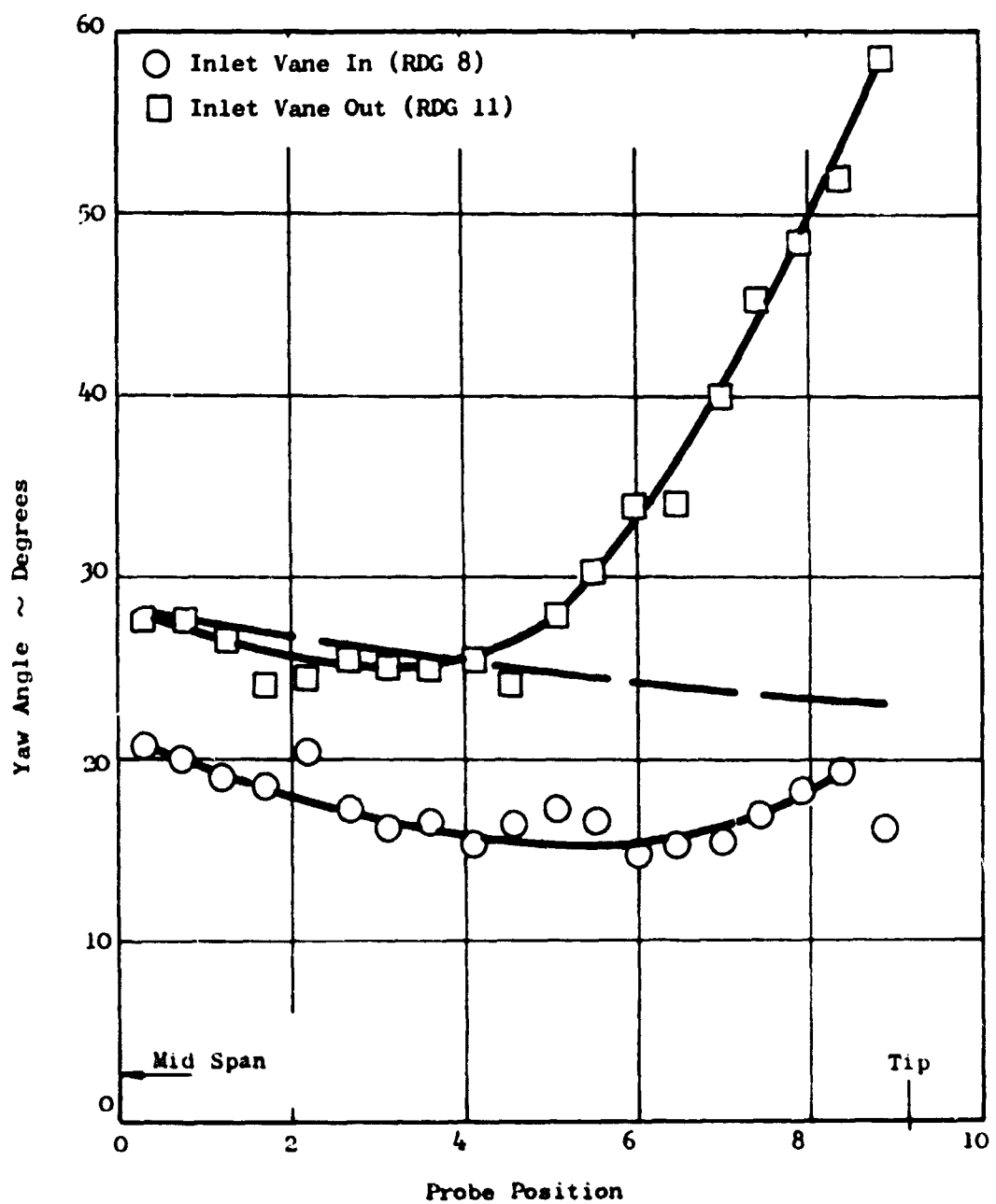


Figure 350 LF2 Inlet Investigation Traverse Data ~ Hot Side

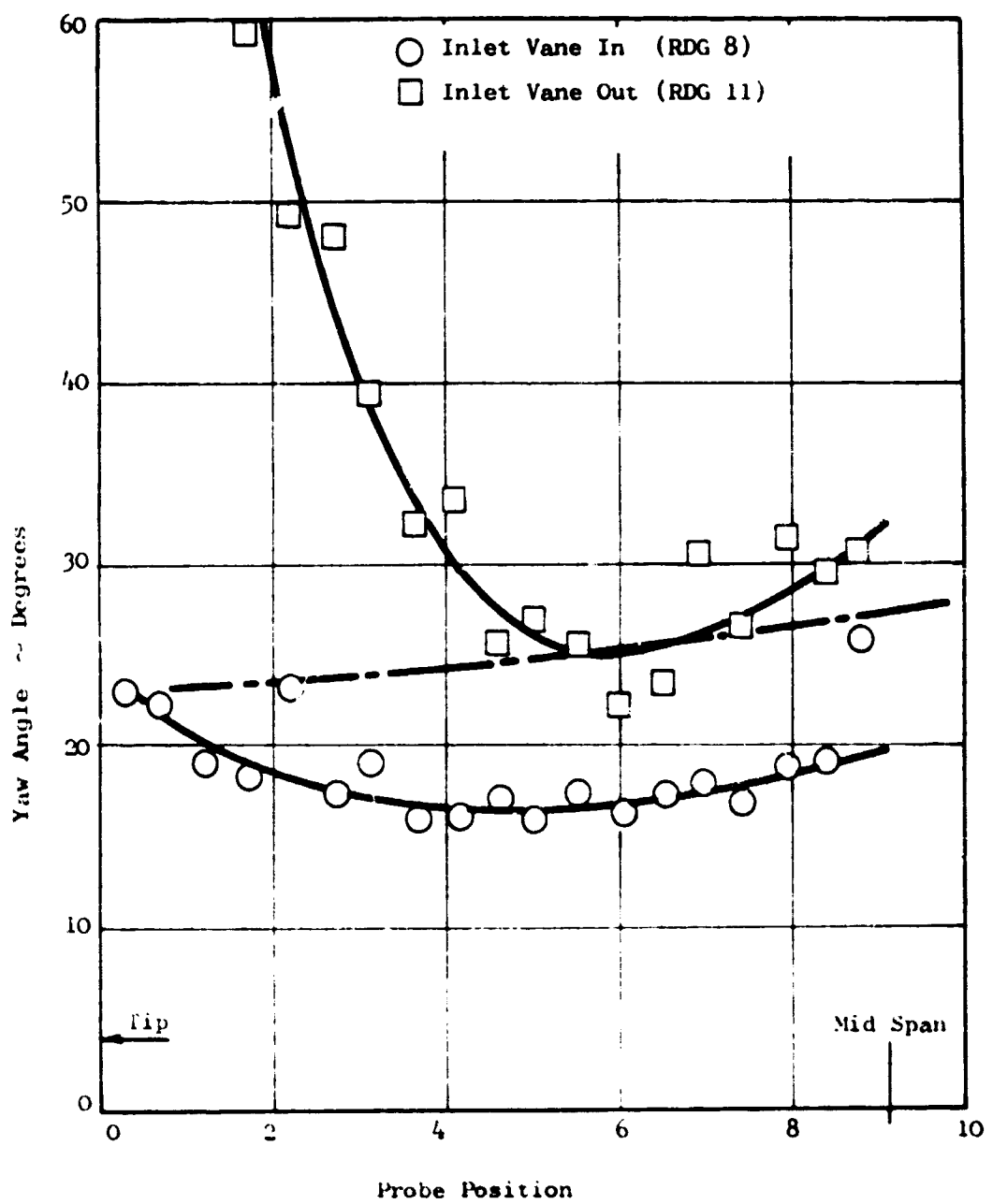


Figure 351 LFG Inlet Investigation Traverse Data -- Cold Side

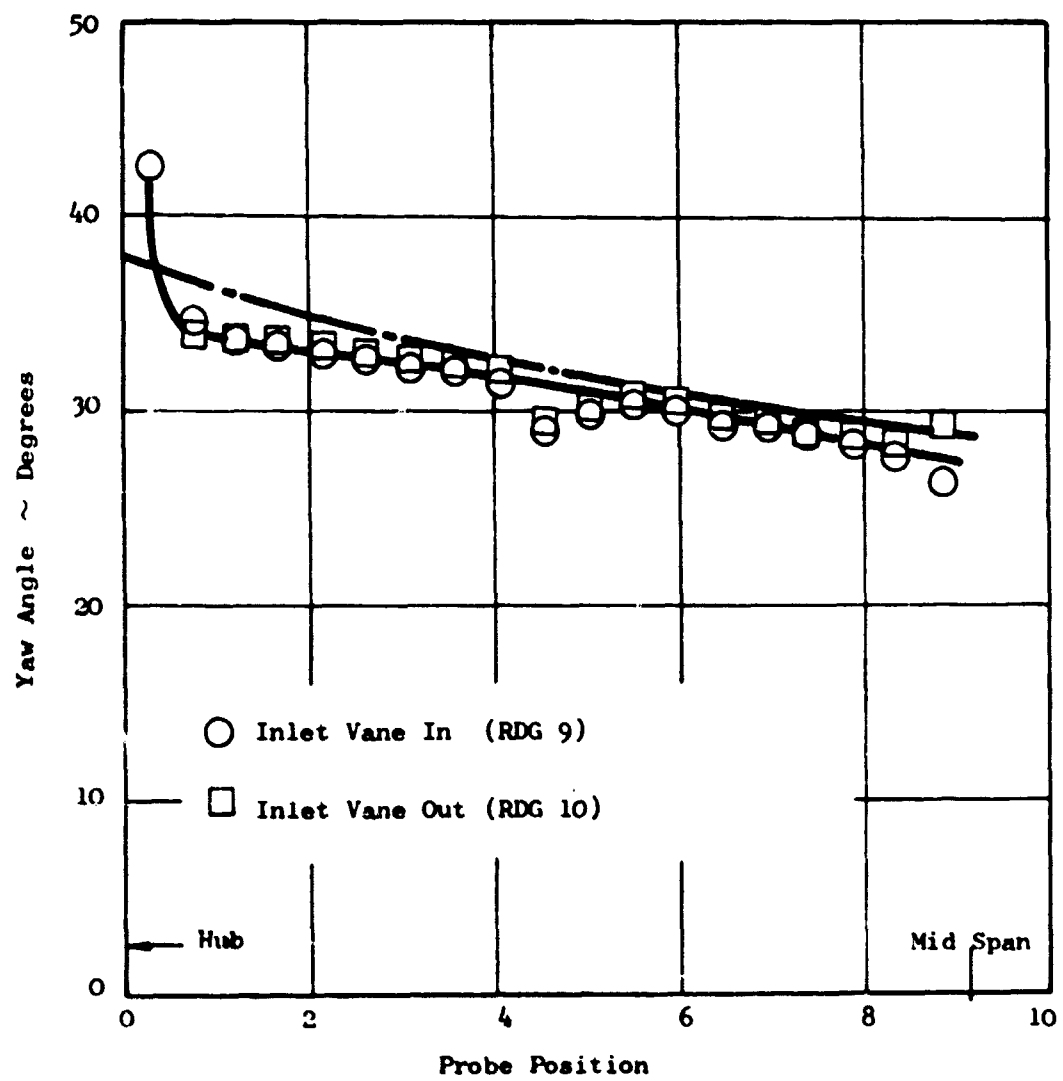


Figure 352 LF2 Inlet Investigation Traverse Data ~ Hot Side

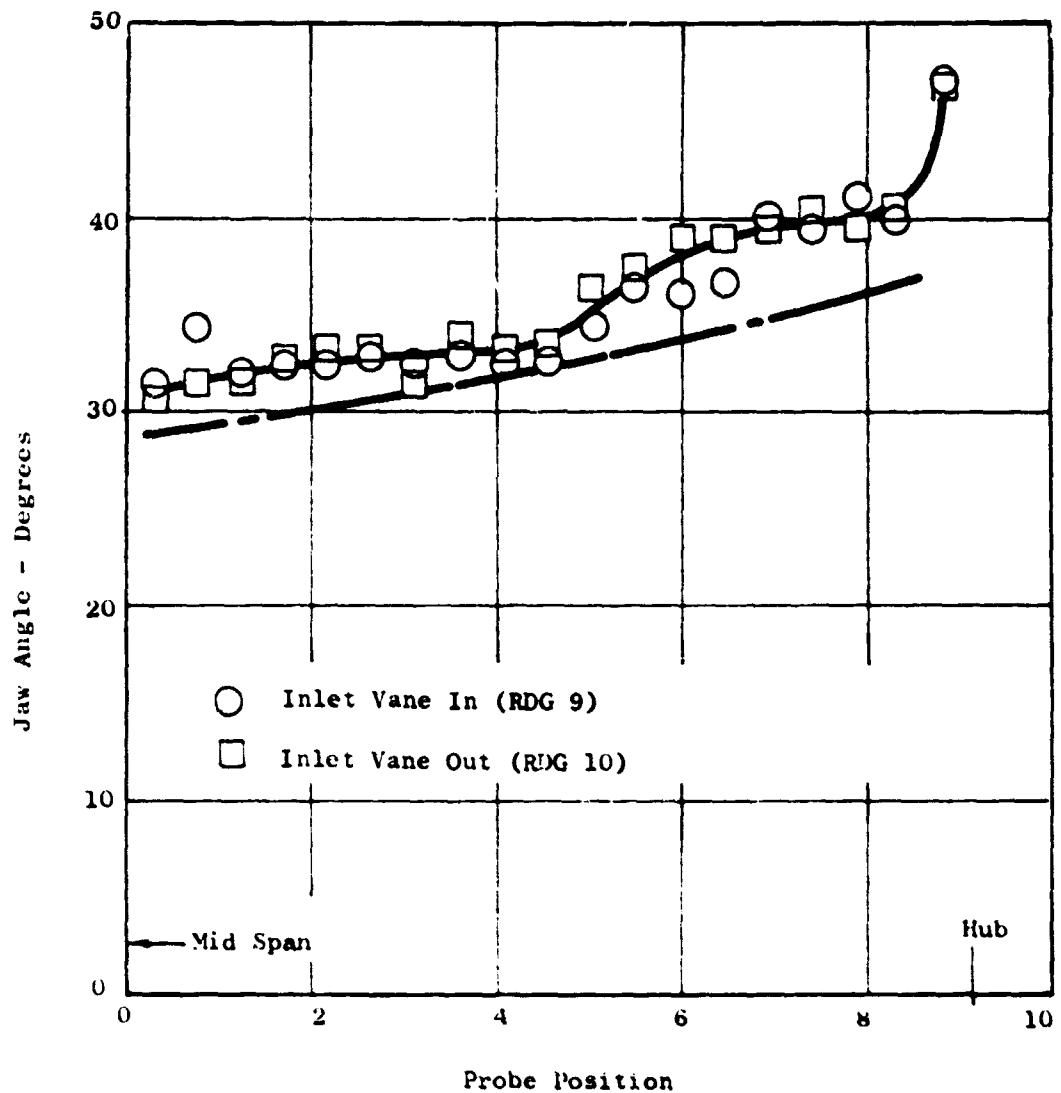


Figure 353 LF-2 Inlet Investigation  
Traverse Data ~ Cold Side

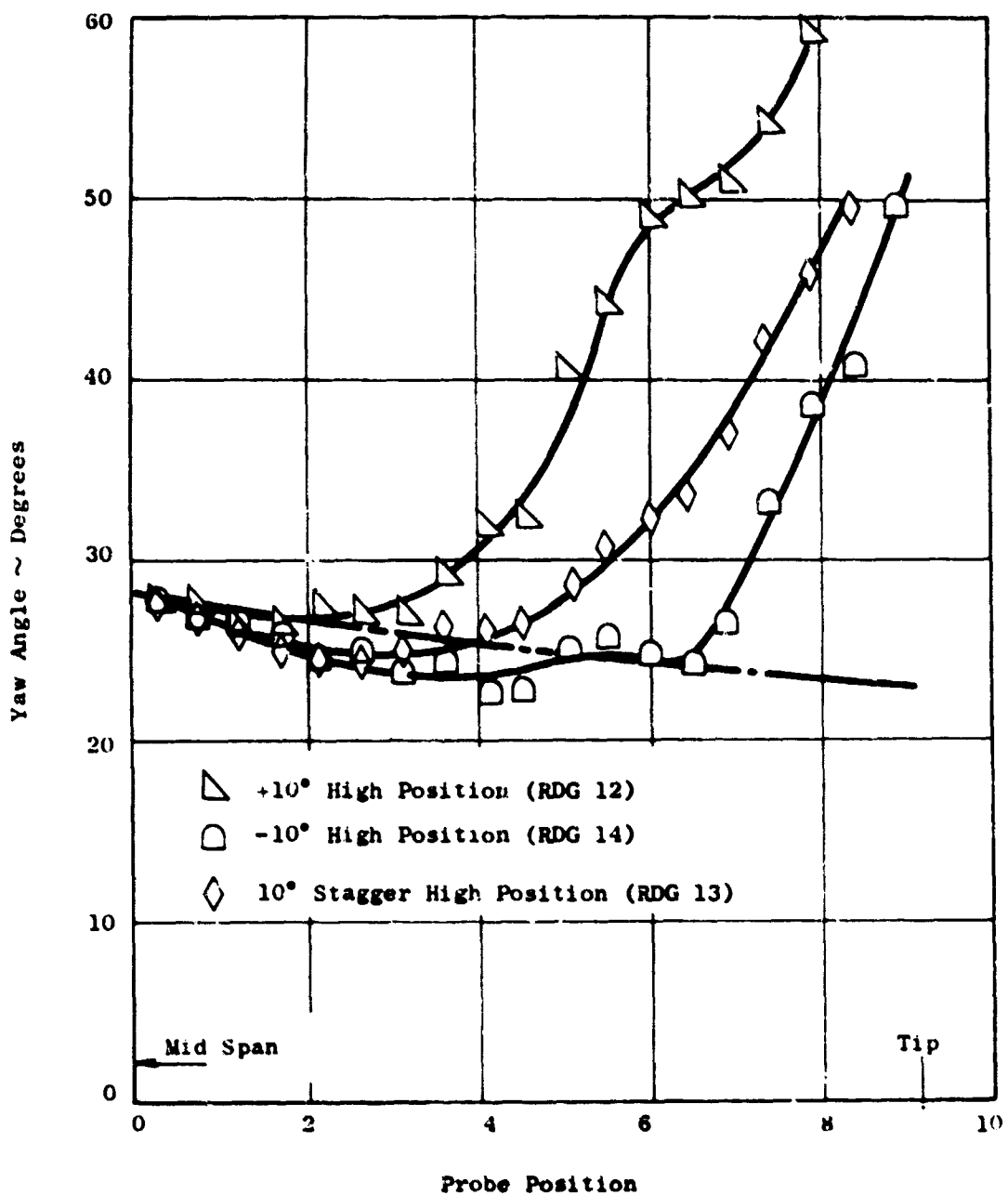


Figure 354 LF-2 Inlet Investigation  
Traverse Data ~ Hot Side

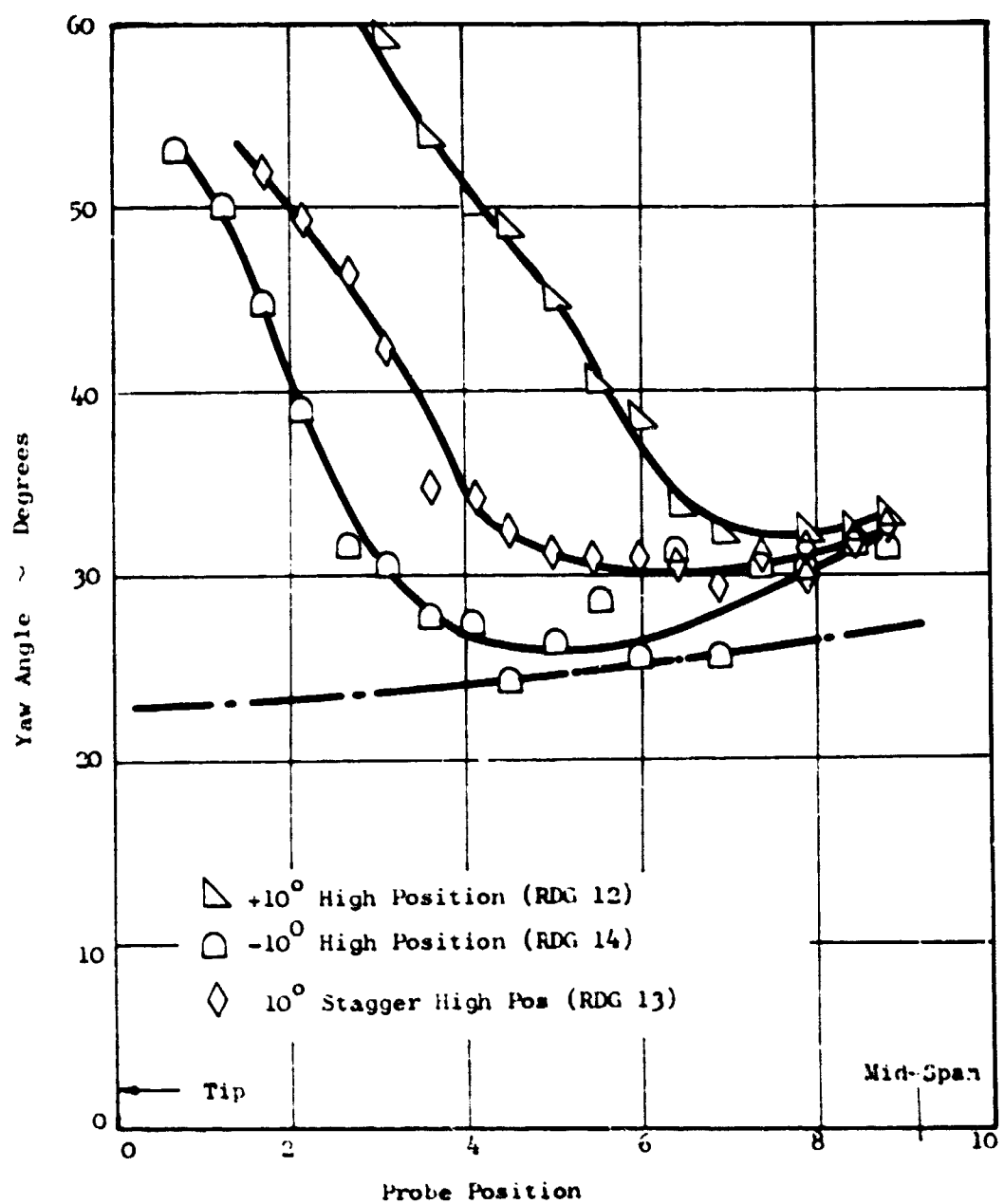


Figure 355 LF2 Inlet Investigation Traverse Data Cold Side

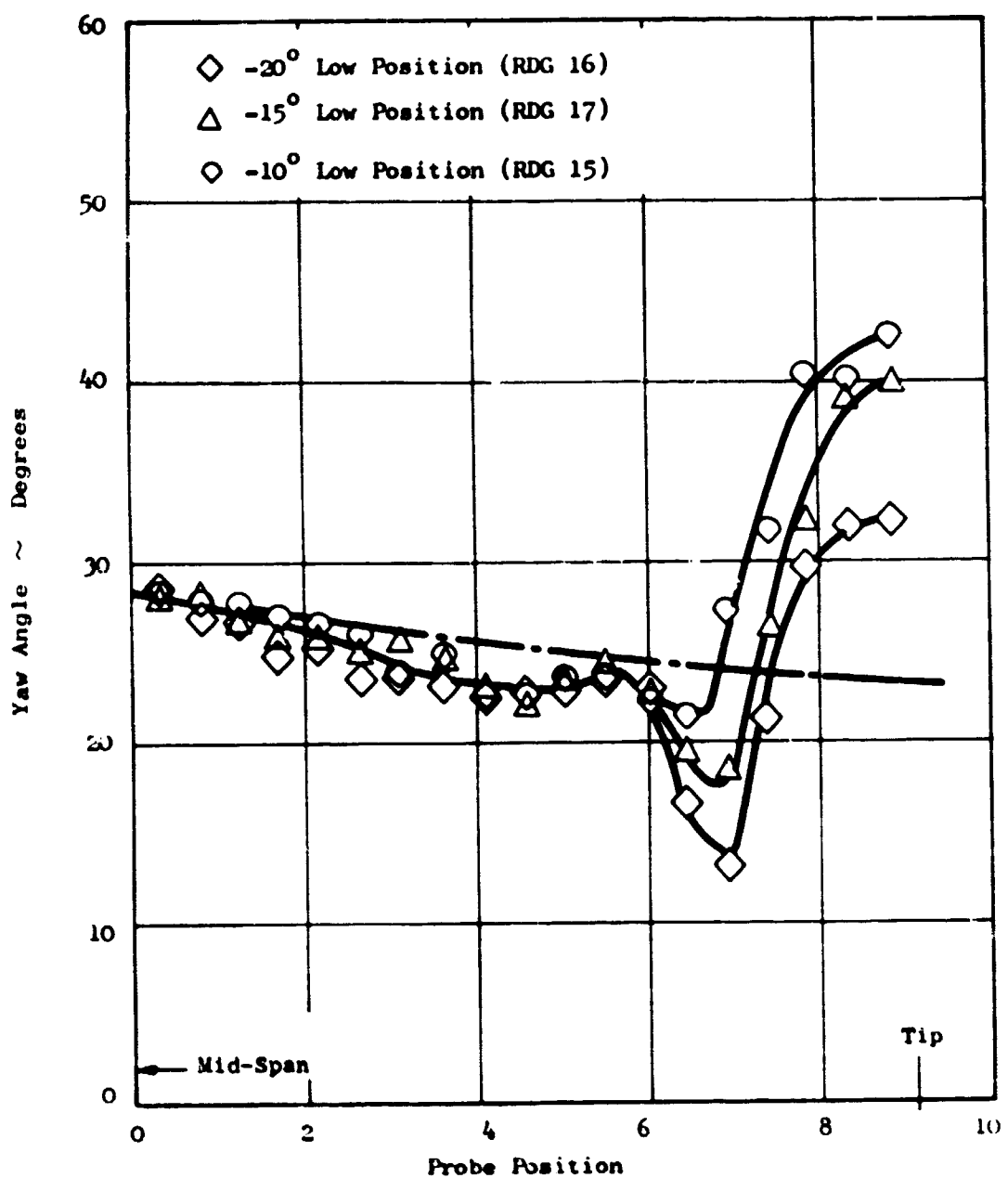


Figure 356 LF2 Inlet Investigation Traverse Data -- Hot Side

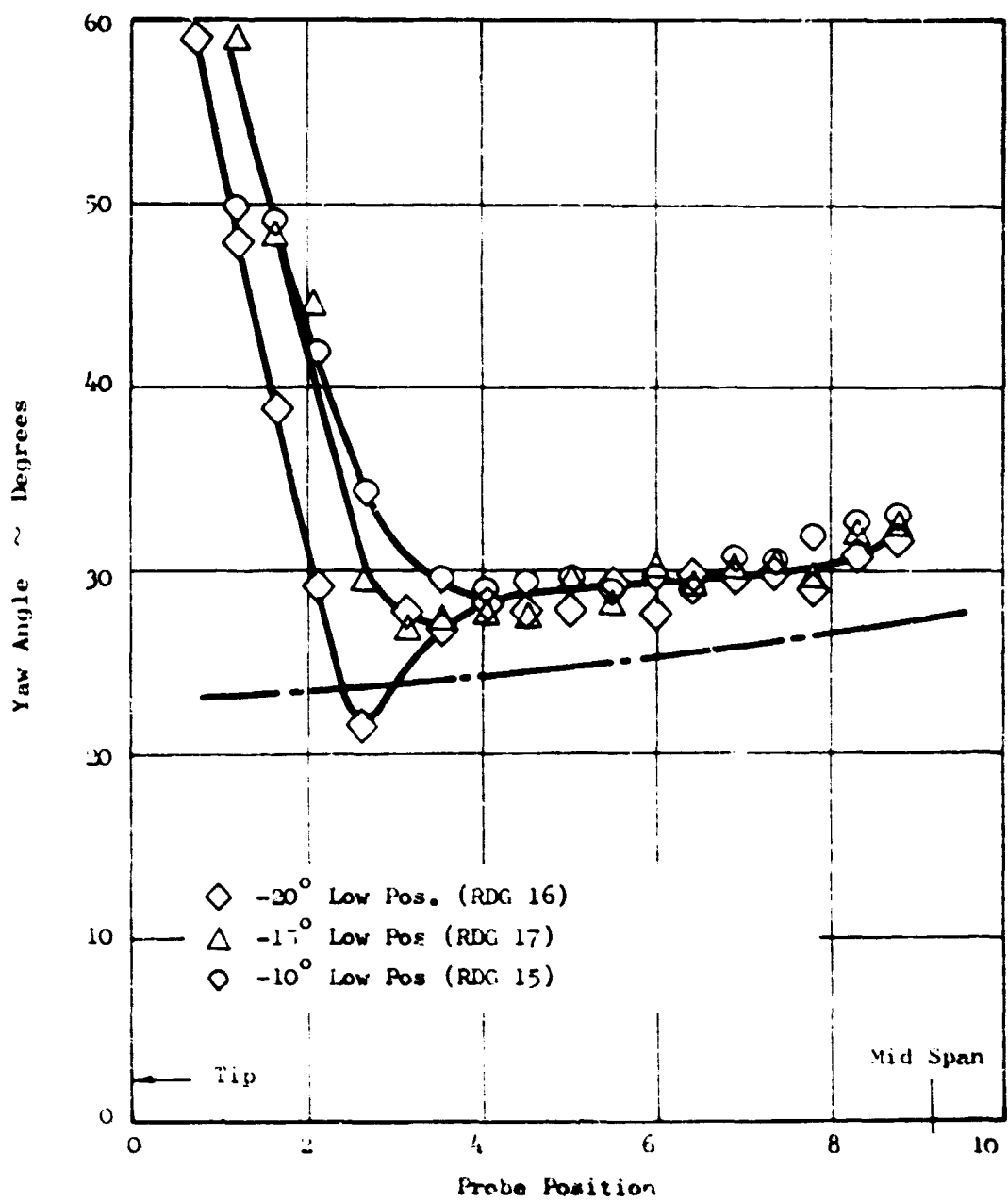


Figure 357 LF2 Inlet Investigation Traverse Data - Cold Side

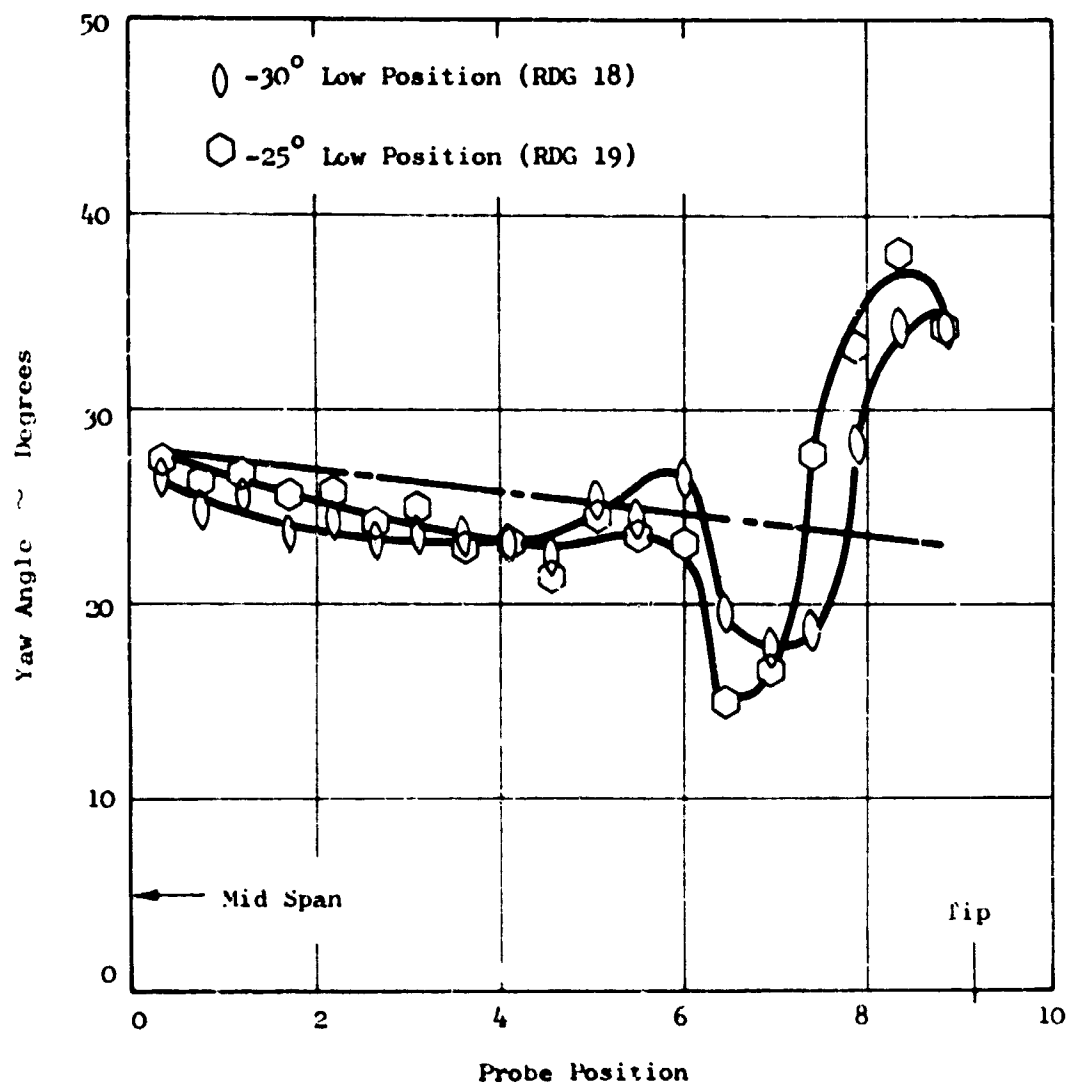


Figure 358 LF2 Inlet Investigation Traverse Data ~ Hot Side

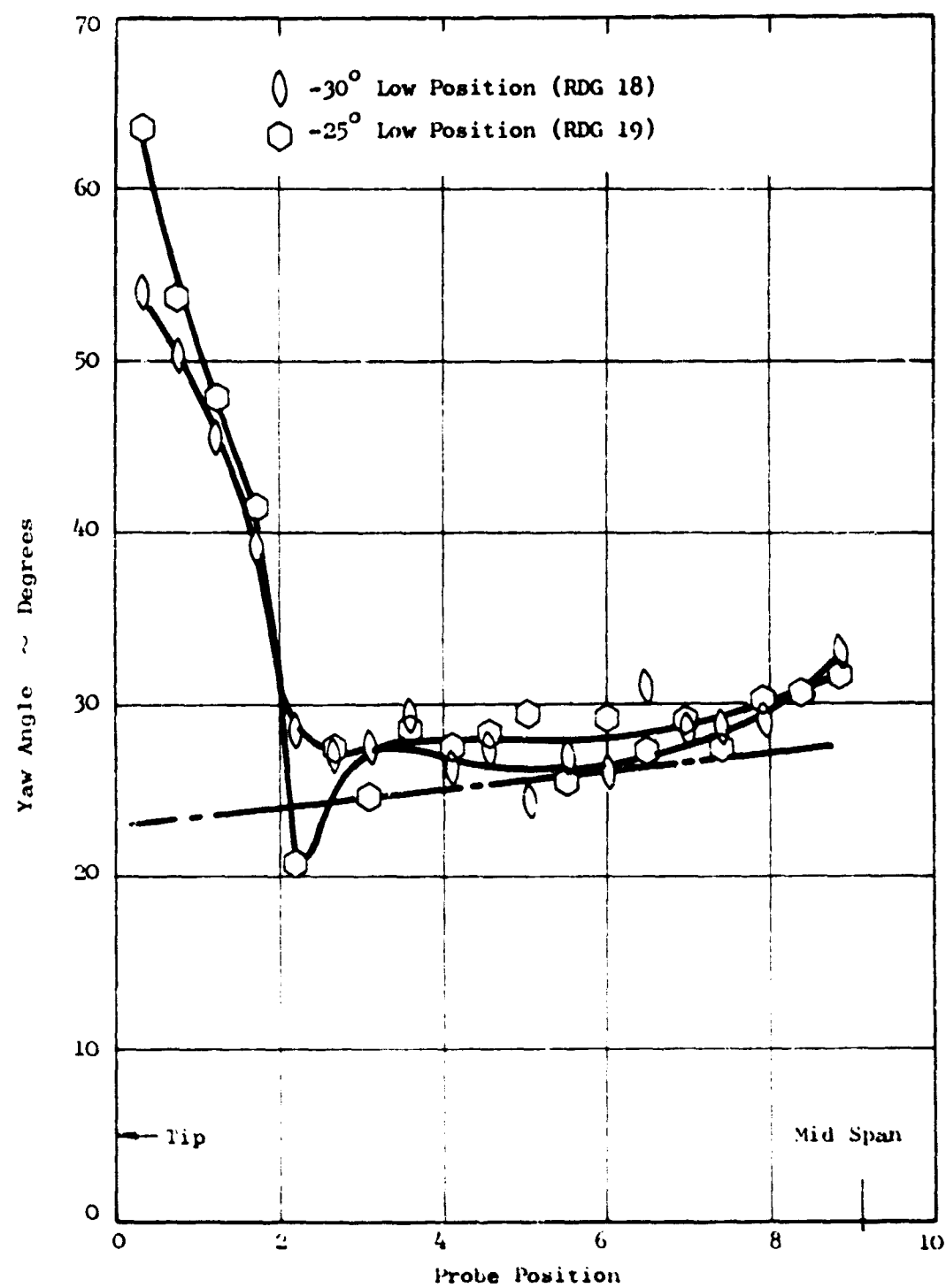


Figure 359 LF2 Inlet Investigation Traverse Data ~ Cold Data

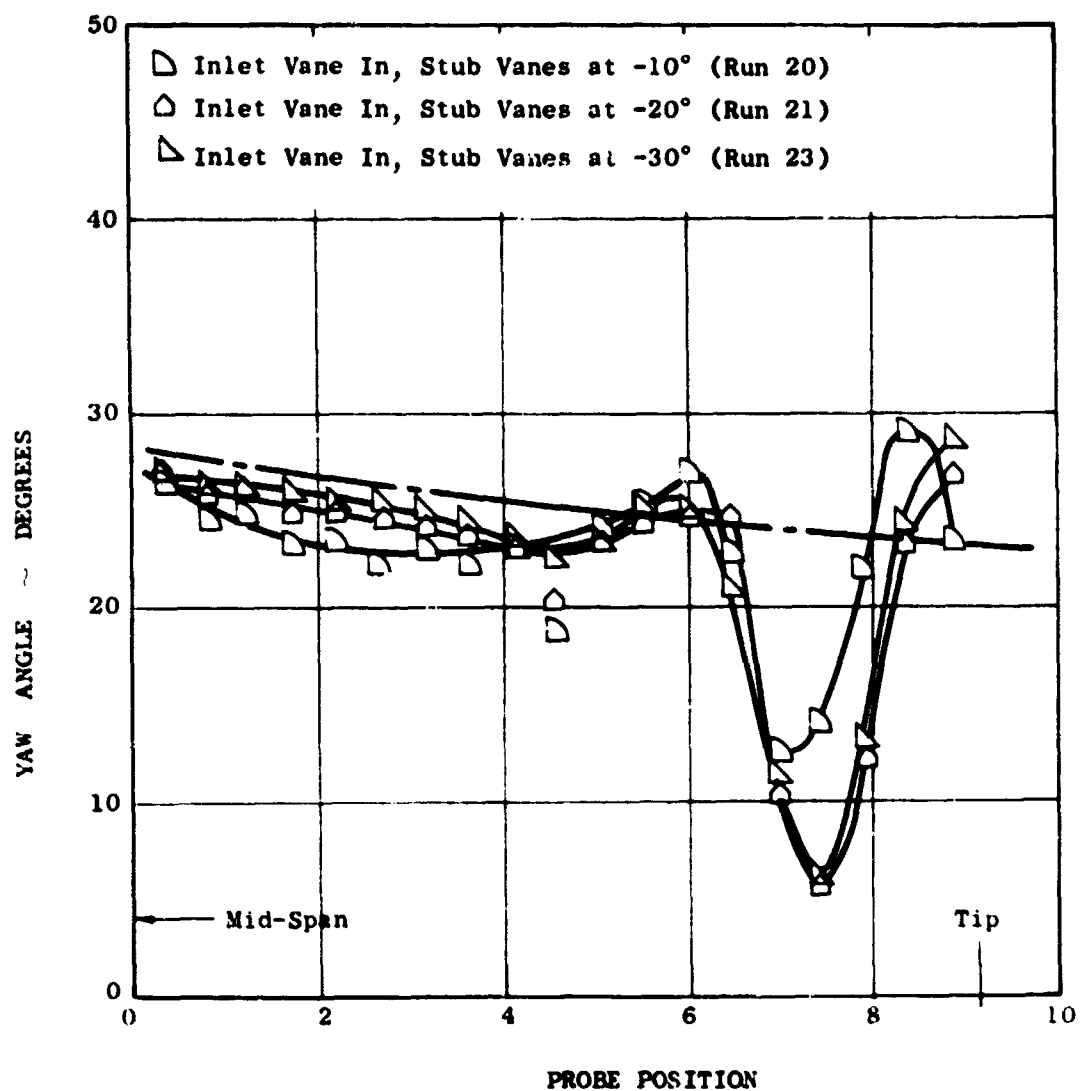


Figure 360      LF2 Inlet Investigation  
Traverse Data ~ Not Side

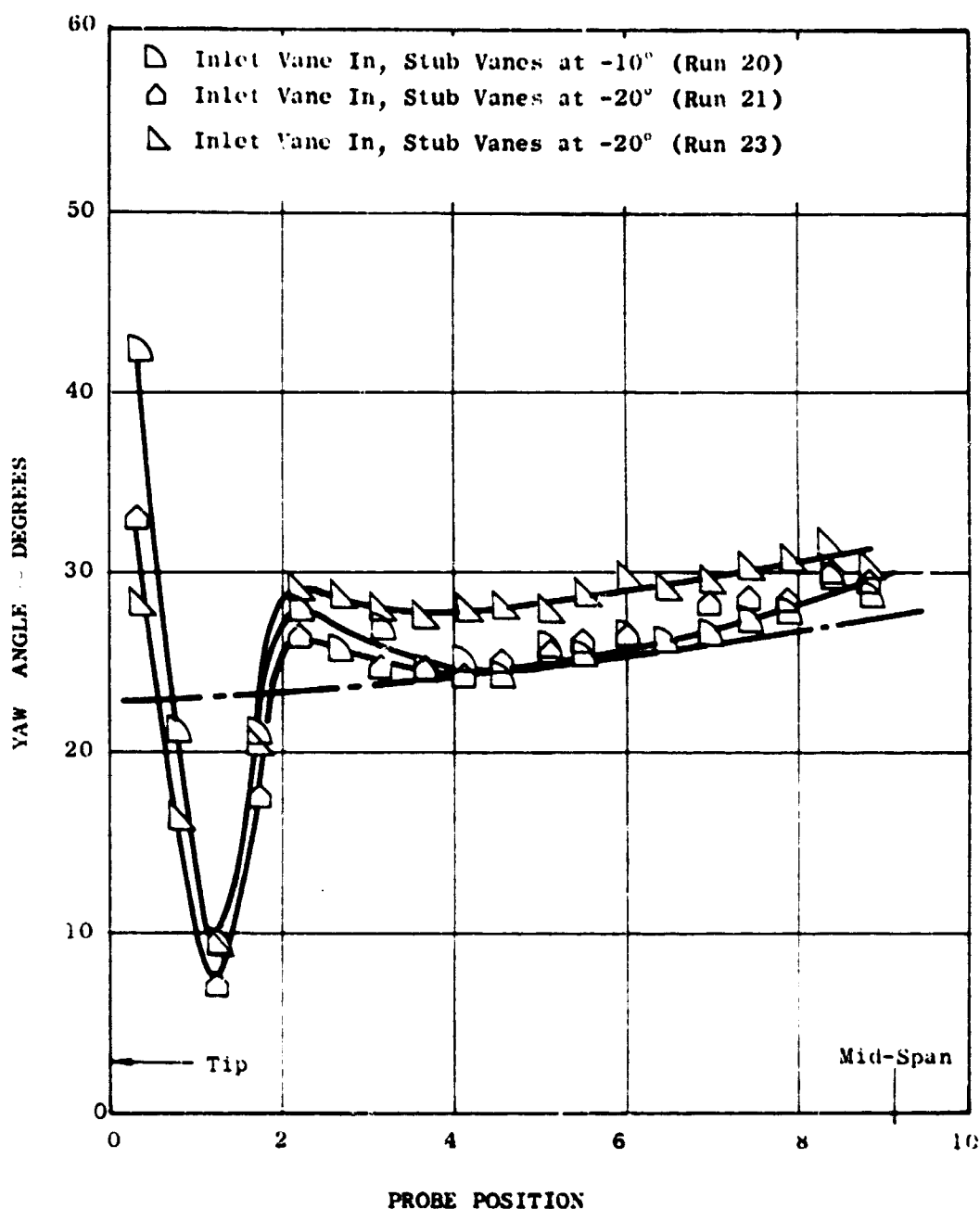


Figure 361 LF2 Inlet Investigation

Traverse Data ~ Cold Side

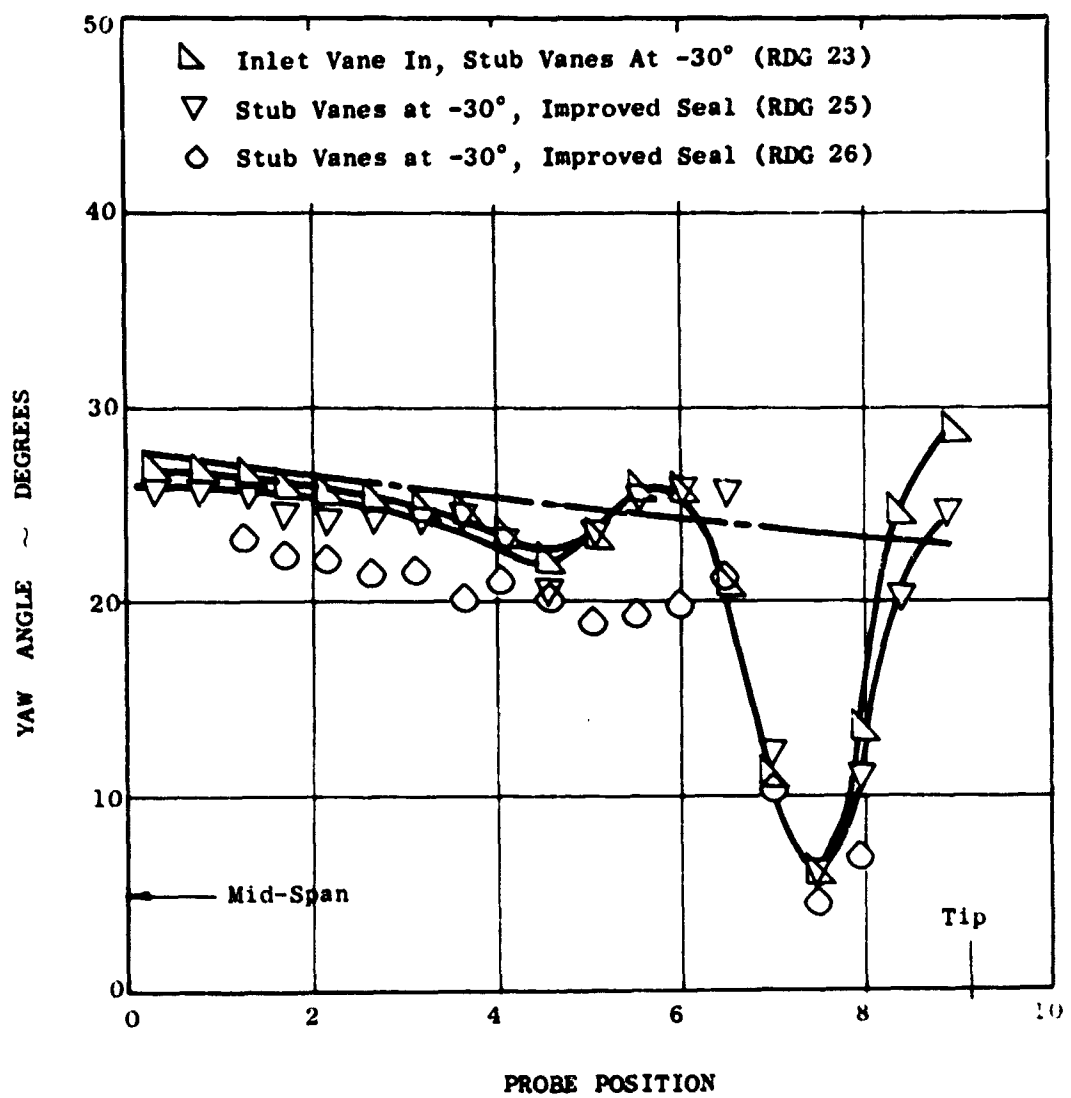


Figure 362 LF2 Inlet Investigation  
Traverse Data ~ Hot Side

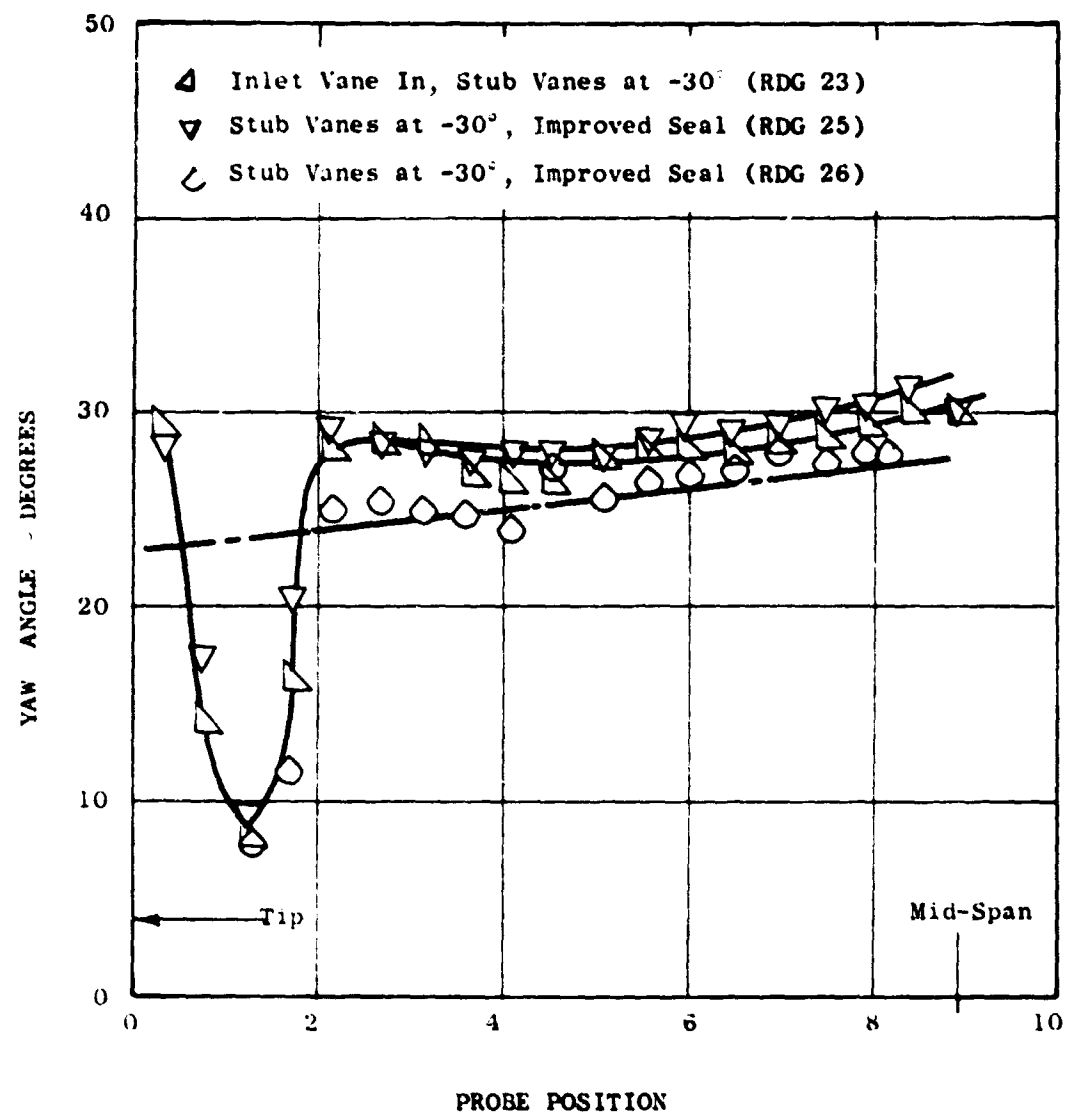


Figure 363 LF2 Inlet Investigation  
Traverse Data - Cold Side

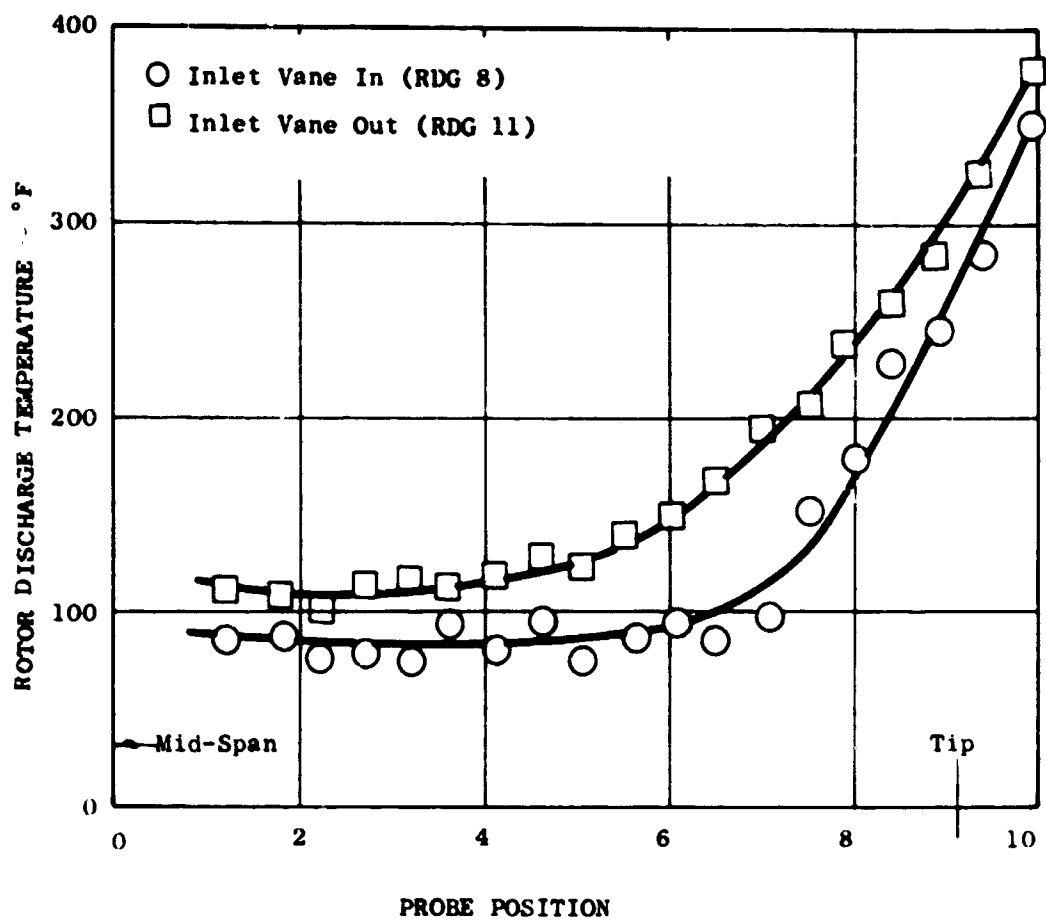


Figure 364 LF2 Inlet Investigation

Traverse Data ~ Hot Side

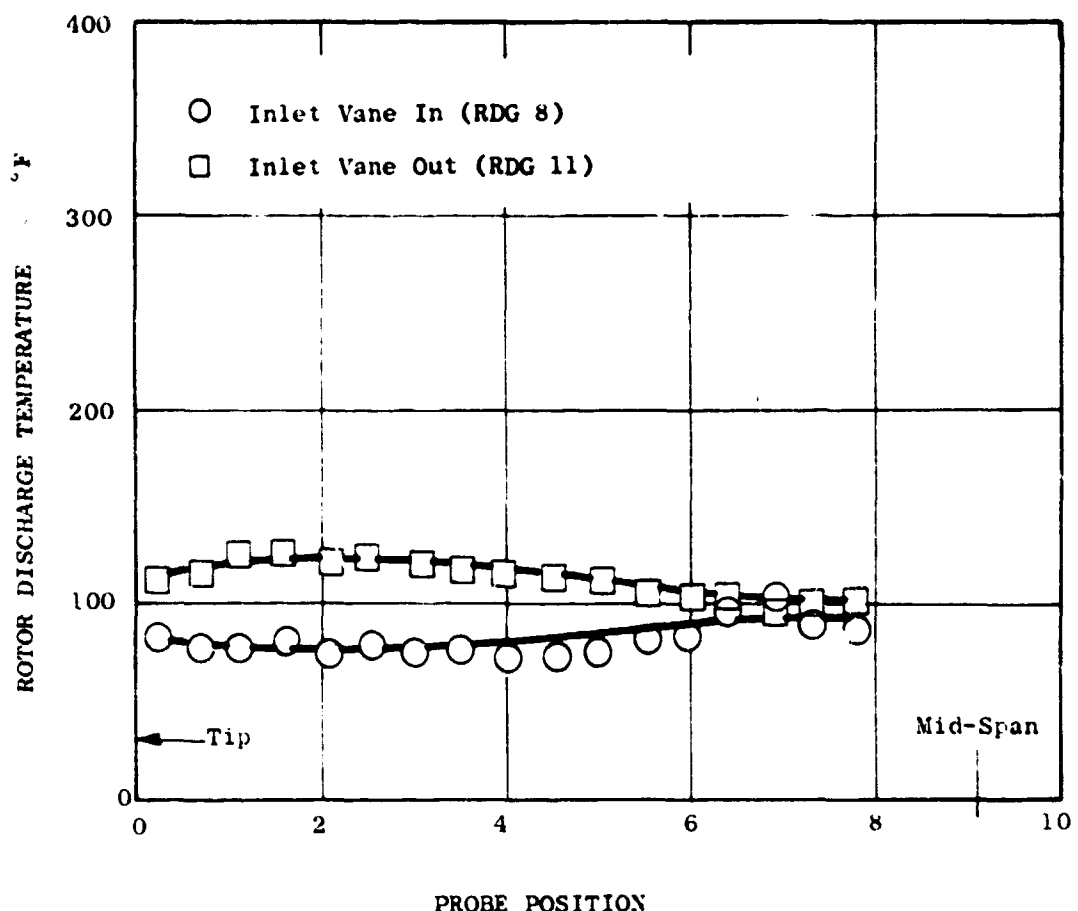


Figure 365 LF2 Inlet Investigation

Traverse Data ~ Cold Side

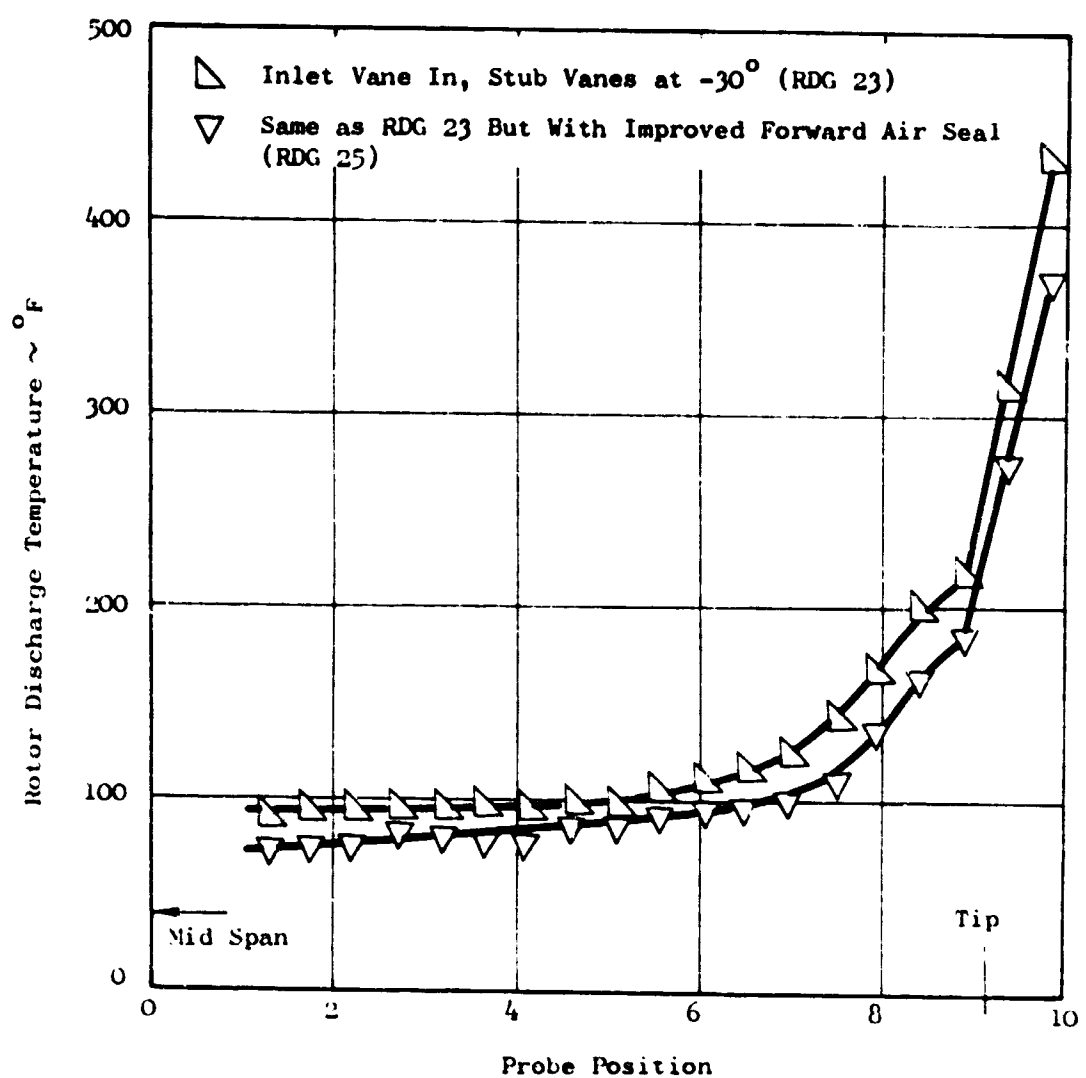


Figure 366 LM2 Inlet Investigation Traverse Data  $\sim$  Hot Side

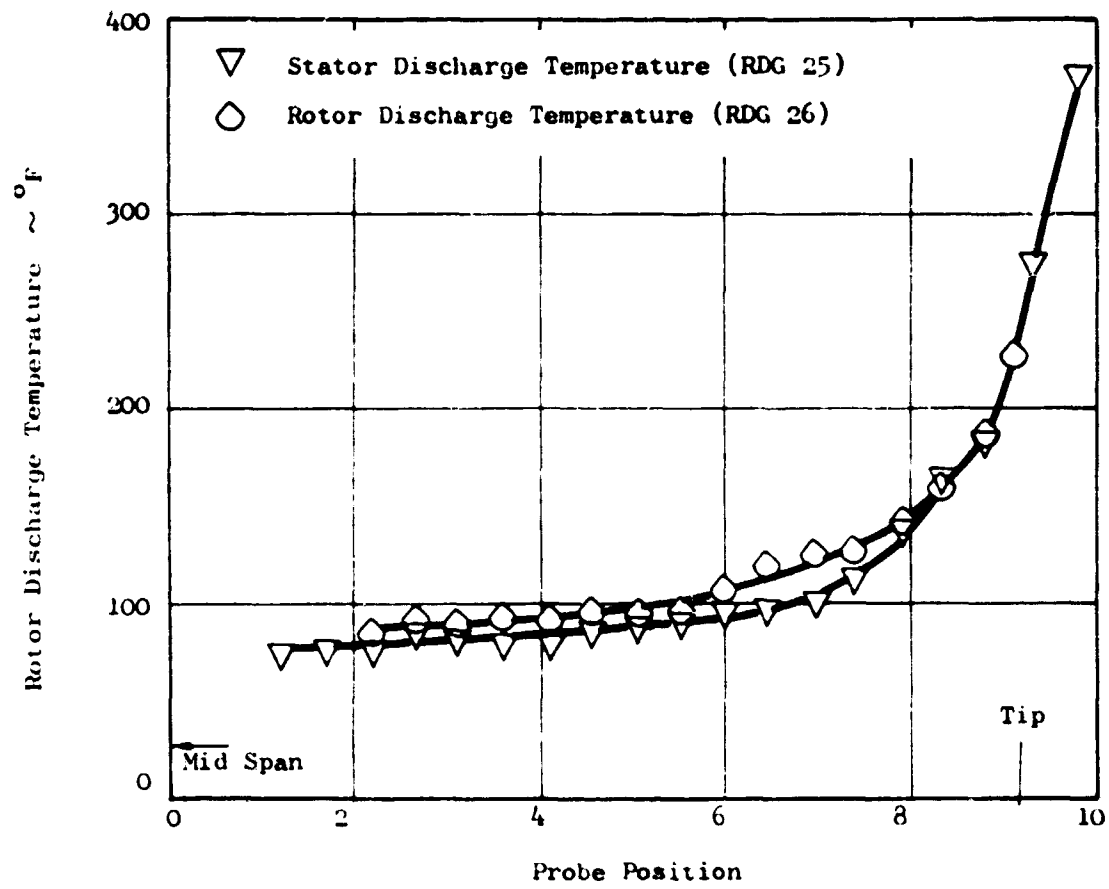


Figure 367 LF2 Inlet Investigation Traverse Data ~ Hot Side

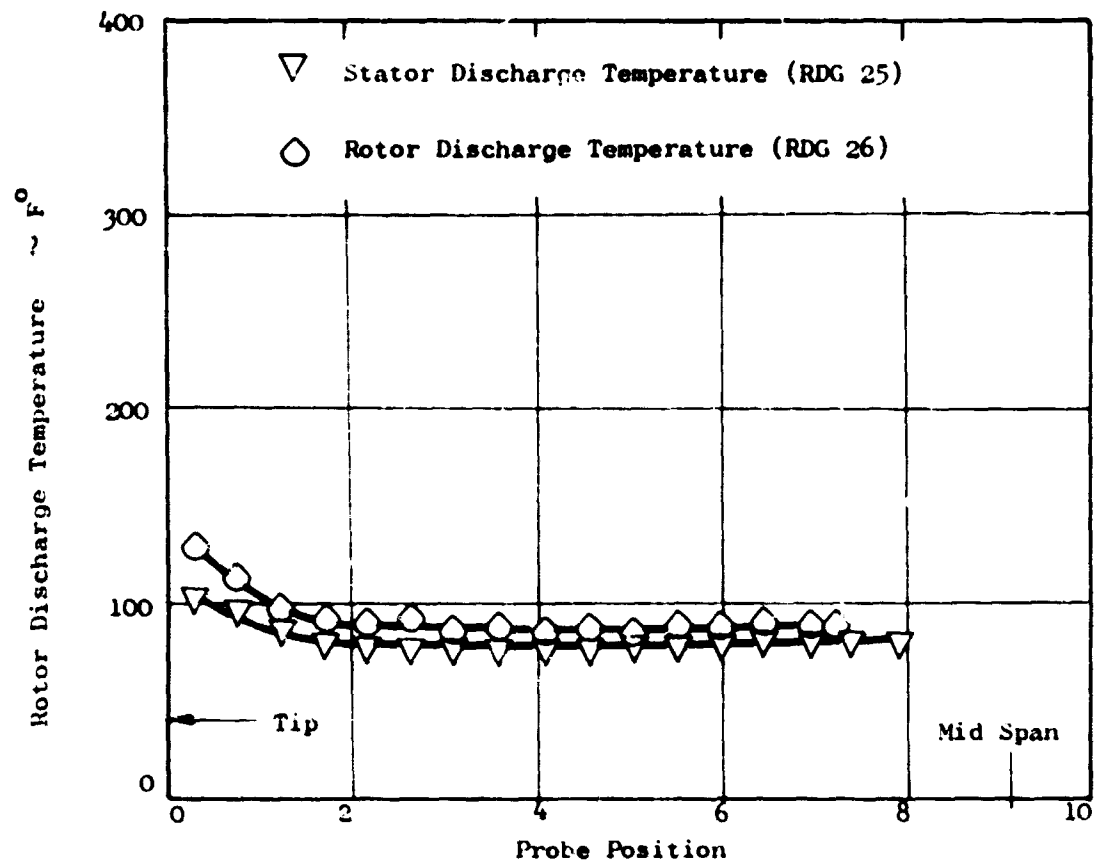


Figure 368 LF2 Inlet Investigation Traverse ~ Cold Side

(U) Yaw angle data, Figures 350 through 353, indicate similar characteristics: no change in the hub region and increasing deviation toward the fan tip. The design values of stator inlet flow angles are represented by the dashed lines in these Figures. There was a yaw angle displacement of 7 degrees existing near the mid-span between the "inlet vane in" and "inlet vane out" configurations (Figures 350 and 351). This resulted from a change in probe installation position. The probe had to be removed and reinstalled after run 8 and after run 10. Data from runs 9, 10 and 11 show good agreement in the region of the mid-span on both hot and cold sides of the fan, indicating a different probe position existing during run 8. Probe position was not changed throughout the remainder of the test so all other probe traverse data are directly comparable.

(U) Rotor discharge temperature traverse data are presented in Figures 364 and 365. These data are primarily of interest in the tip region to measure the extent of the hot gas penetration into the fan stream from the forward air seals. As shown in Figure 364, the inlet vane confines the hot gas penetration to the flow passage between it and the bellmouth. Without the inlet vane, the penetration extends into the fan stream about 5.3 inches from the tip.

Bellmouth vanes in upper position. -

(U) With the inlet vane removed and the 88 bellmouth stub vanes installed in the upper position, a total of three vane setting angles were investigated. The primary purpose of putting the vanes in this position was to determine if the vanes, used as vortex generators by staggering them  $\pm 10$  degrees, could reduce the apparent bellmouth flow separation that exists with no inlet vane installed. In addition to the vortex generator test, the  $+10$  and  $-10$  degree constant-angle settings were investigated to determine if further improvement may be gained in changing the rotor inlet flow angle at the tip.

(U) From Table 55, system lift measurements indicate this vortex generator configuration to be ineffective and to cause an additional 7 percent loss in lift. It was also found that the  $+10$  degree setting resulted in a 13 percent loss in lift, while the  $-10$  degree setting provided a 3 percent improvement in lift.

(U) Fan inlet stream static pressures, Figure 322, indicate the same order of relative performance on the hot side but indicates the cold side may pump slightly more flow with the vortex generator configuration than with the  $-10$  degree vane setting. The rotor inlet static pressure, as indicated by the bellmouth wall statics (element 6) in Figures 330 and 331, is about the same value for the  $10$  degree stagger and  $-10$  degree vane setting configuration.

The -10 degree vane setting produced higher bellmouth surface Mach numbers but a much better inlet recovery as indicated by the boundary layer pressure profiles in Figure 335.

(U) Rotor discharge traverse data are consistent with the system lift measurements. Rotor pressure rise, Figures 340 and 341 indicate that the 10 degree stagger configuration is about equivalent to "inlet vane out" and the -10 degree vane setting does produce some improvement. For the 10 degree stagger setting, yaw angle measurements were about the same as inlet vane out (Figures 354 and 355) while the -10 degree vane setting seems to produce improvement over most of the tip region.

Bellmouth vanes in lower position. -

(U) With the inlet vane removed and the 88 bellmouth vanes installed in the lower position, angle settings of -10, -15, -20, -25, and -30 degrees were investigated. Improvement in performance had already been indicated with a vane setting of -10 degrees in the high position. This series of tests were performed to define the optimum amount of turning and how much improvement could be realized by preturning the flow in a direction opposite to the direction of rotor rotation.

(U) System lift measurements from Table 55 show the optimum turning angle to be near -20 degrees and the maximum improvement in system lift to be 9.8 percent above the "inlet vane out" configuration. This is still considerably less than the 21.4 percent improvement produced by the inlet vane.

(U) Looking at the fan inlet stream static pressures in Figures 323 and 324, increased flow is indicated over most of the span traversed, with the highest flow occurring at the -30 degree vane setting. The cold side appears to have increased flow only near the tip, and doesn't change much with angle setting.

The cold side optimum angle is about -20 degrees.

(U) Rotor pressure rise traverse probe data for all vane settings are shown in Figures 342 through 345. Improvement in rotor pressure rise is seen for all vane setting angles compared to the "inlet vane out" configuration. The hot side shows the greatest improvement, with the optimum angle settings being -20 and -25 degrees. The optimum angle on the cold side is -20 degrees.

(U) Yaw angle measurements, Figures 356 through 359, indicate significant changes within 3 inches of the tip. Again, the hot side showed the greatest improvement over "inlet vane out" and the optimum vane angle setting is -20 degrees on both hot and cold sides.

Bellmouth vanes in lower position, with inlet vane. -

(U) Bellmouth vane angle settings of -10, -20, and -30 degrees were investigated with the inlet vane installed. From Table 55 system lift measurements indicate the optimum turning angle to be -30 degrees with maximum improvement of 26 percent compared to the "inlet vane out" configuration and 3.8 percent compared to the "inlet vane in" configuration. During readings 21 and 22 at the -20 degree vane setting, some difficulty was experienced with one of the load cells and may be the reason for the low indication at this condition.

(U) Rotor pressure rise traverse data are presented in Figures 346 and 347. Increased vane angle seems to depress the rotor pressure rise near the mid-span and increase it towards the fan tip. On both hot and cold side, the -20 degree vane setting would appear to be optimum and all vane settings produce higher rotor pressure rise in the tip region than the "inlet vane in" configuration.

(U) Yaw angle traverse data are shown in Figures 360 and 361. On both hot and cold sides, the largest changes are in the tip region, and the -20 degree vane angle setting appears to produce the lowest angles (the most change). Toward the mid-span, the trend seems to be higher yaw angle with increased vane angle but the changes are small and the measured angles are still relatively close to design.

Improved seals. -

(U) The test configuration for the investigation of improved seals consisted of bellmouth vanes set at -30 degrees and inlet vane in. The seal improvement was provided by application of an industrial adhesive (RTV) to the honeycomb seals. The adhesive layer was about 0.25 inches thick and extended from the top of the seal to the rotor seal lip. After the adhesive was allowed to cure, some of it had to be cut away from the rotor seal lip to permit the rotor to turn. After a short run-in period at idle power setting, the fan rotor turned freely and the adhesive was still intact.

(U) A total of three test runs were made on this configuration. The second and third runs were made to verify the data and to investigate rotor discharge temperature with tube extensions added to the traverse probe temperature elements to insure measurement of rotor discharge characteristics. These temperature elements were below the stators before and could possibly have been influenced by hot gas leakage from the turbine exhaust through the fan aft seal.

(U) System lift measurements in Table 55 did not indicate any appreciable change in performance level due to the improved seals. Inlet stream static profiles (Figure 325 and 326) show higher fan flow with improved seals and this appears to be further verified by the bellmouth static pressure profiles in Figures 332 and 333.

(U) Rotor pressure rise traverse data, Figures 348 and 349 show about the same levels toward the fan tip with some variations in level over the rest of the span. Both readings with improved seals indicate better performance but there is a lot of variation between these two readings particularly on the cold side. Yaw angle, Figures 362 and 363 show similar characteristics, i. e. tip performance is the same and variations in levels are indicated over the rest of the span with the largest difference between the two readings with improved seals.

(U) The changes in rotor discharge temperature traverse data due to the improved seals are shown in Figure 356. Average fan inlet temperature is 16.5°F lower for the run with the improved seals which accounts for the displacement between the two curves in the region from the mid-span to a probe position of 6.5. In the tip region, fan probe positions from 7 to 9.1, the improved seal configuration shows lower rotor discharge temperatures by about 31.5°F. The lower fan inlet temperature accounts for 16.5°F, leaving 15°F to be attributed to lower leakage flow, lower leakage temperature or increased fan flow in the tip region. The engine exhaust gas temperature was about 9°F higher for the improved seal configuration. Fan stream static pressures and bellmouth wall static pressures did indicate an increase in flow, and there was a 47 rpm higher corrected fan speed during the improved seals configuration test. There was also a lower (more negative) static pressure at the fan rotor inlet which produces a higher pressure ratio across the seals tending to pump more leakage flow. The improved seal configuration did produce less hot gas penetration of the fan stream but its net effect is not directly apparent due to the slightly higher fan speed and air flow.

(U) Figures 367 and 368 show the comparison between measuring fan discharge temperature at the original traverse probe location (stator discharge) and at a station as close as practical to the fan rotor discharge. The displacement between readings 25 and 26 from mid-span to the probe position of 5 in Figure 367 is about the difference in fan inlet temperatures. The larger displacement between the probe positions of 5 and 8 could be a result of the flow direction as indicated by a positive pitch angle; if flow is toward the tip, the temperature of a given streamline at rotor discharge correspond to be probe position nearer the tip when measured 3 to 4 inches downstream.

TABLE 55

## MEASURED LIFT AT FAN SPEED OF 1750 RPM

<u>TEST CONFIGURATION</u>	<u>MEASURED LIFT (1750 RPM)</u>
Inlet Vane In, Rdgs 7, 8 & 9	3530
Inlet Vane Out, Rdgs 10 & 11	2907
Stub Vanes in Upper Position	
Vane Setting at +10°, Rdg 12	2530
Vane Setting at 10° Stagger, Rdg 13	2816
Vane Setting at -10°, Rdg 14	3051
Stub Vanes in Lower Position	
Vane Setting at -10°, Rdg 15	3072
-15°, Rdg 17	3111
-20°, Rdg 16	3191
-25°, Rdg 19	3105
-30°, Rdg 18	3062
Stub Vanes in Lower Position With Inlet Vane	
-10°, Rdg 20	3590
-10°, Rdg 21 & 22	3540
-30°, Rdg 23	3663
Stub Vanes in Lower Position at -30° Setting With Inlet Vane and Improved Seal	
Rdg 25	3592
Rdg 26*	3648
Rdg 27*	3650

\*Extension added to traverse probe temperature element.

In the tip region, the temperature lines converge showing that the rotor discharge temperature as measured by the traverse probe produces a very good representation of forward air seal leakage penetration into the fan stream. This verifies that there is no measurable influence from the aft seal.

#### Analysis

(U) Fan performance is indicated by total thrust measurements corrected to standard atmosphere conditions and 1750 rpm. Another indicator that is roughly proportional to thrust is the rotor pressure rise, non-dimensionalized by fan tip speed squared to yield the pressure rise coefficient. Rotor pressure rise is the difference between rotor discharge total pressure and ambient pressure, and includes inlet losses.

#### X353-5 data. -

(U) Figures 369 and 370 presents data from previous tests performed on the X353-5 fan. The test configurations included exit louvers and 6 percent bellmouths. The fan-in-fuselage incorporated a deep inlet duct between the bellmouth and the fan rotor. These comparisons are made at 100 percent speed and show results comparable to the LF2 inlet investigation for the "inlet vane in" and "inlet vane out" configurations. They also show that the fan-in-fuselage and "inlet vane in" performance are about the same level and that the 6 percent bellmouth followed by a deep inlet does not separate at sea level static conditions. The same bellmouth in a fan-in-wing installation separates badly.

(U) It was concluded that the 6 percent bellmouth in the fan-in-wing installation was marginal and required additional turning control or at least leakage air control. The reasoning was as follows: In order to draw flow into the full inlet, very high velocities (in the order of 700 ft./sec) occur on the bellmouth because of the high level of bellmouth suction pressure required to turn the flow. The high velocity air near the bellmouth wall must diffuse to a rotor entrance average velocity of 435 ft/sec. This much diffusion is considered marginal for stable air flow and separation was easily caused by the leakage air entering the fan stream at the lower end of the inlet bellmouth being directed slightly forward and radially inward.

(U) First attempts to solve the problem consisted of adding a baffle fitted near the lower end of the bellmouth to redirect the leakage air into the fan tip region. This appeared to reduce the separated region, but, of course, could not reduce the high bellmouth velocity and so the flow stability was still marginal. A 10 percent improvement in system thrust was obtained.

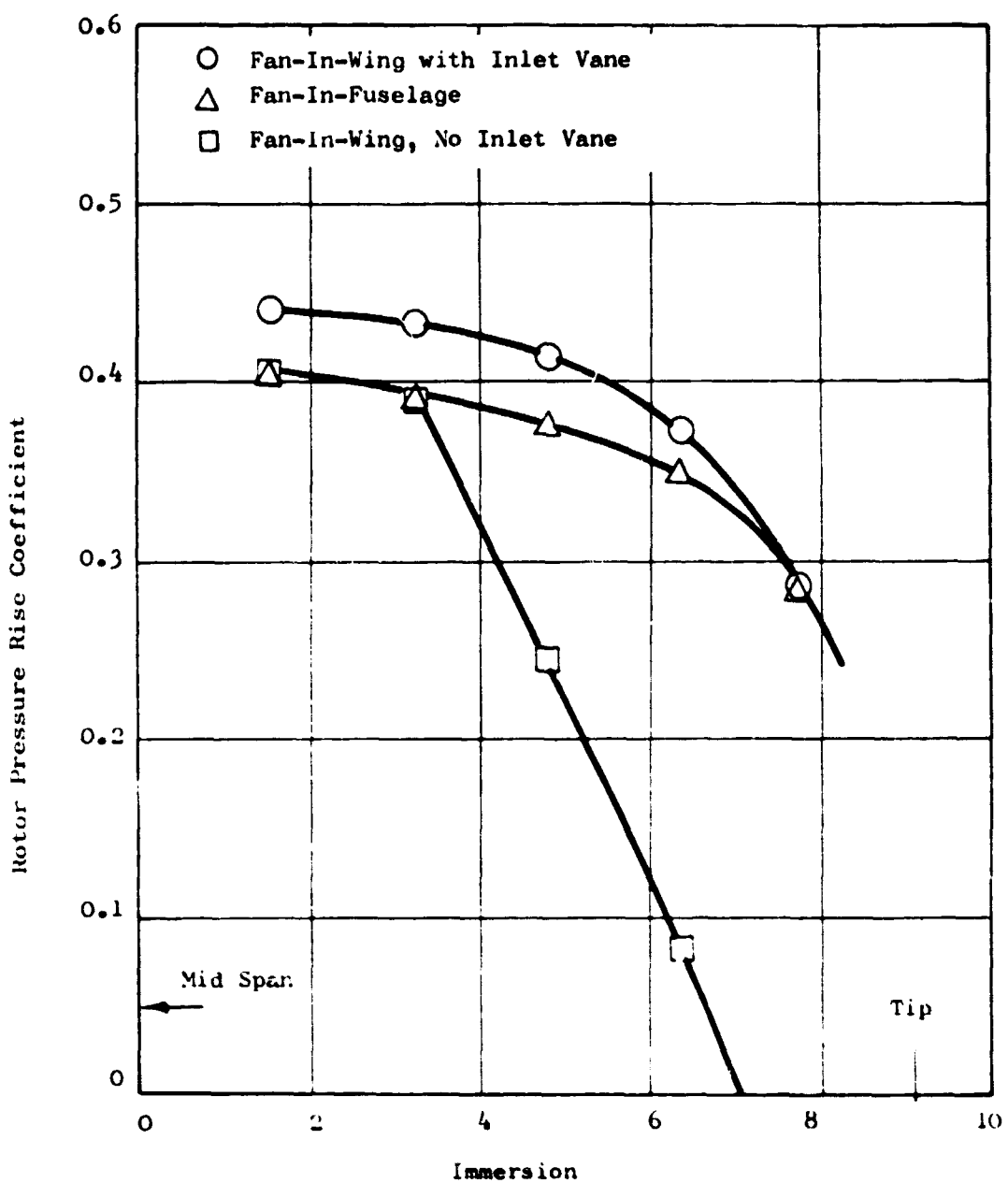


Figure 369 X353-5 Performance Data, Hot Side

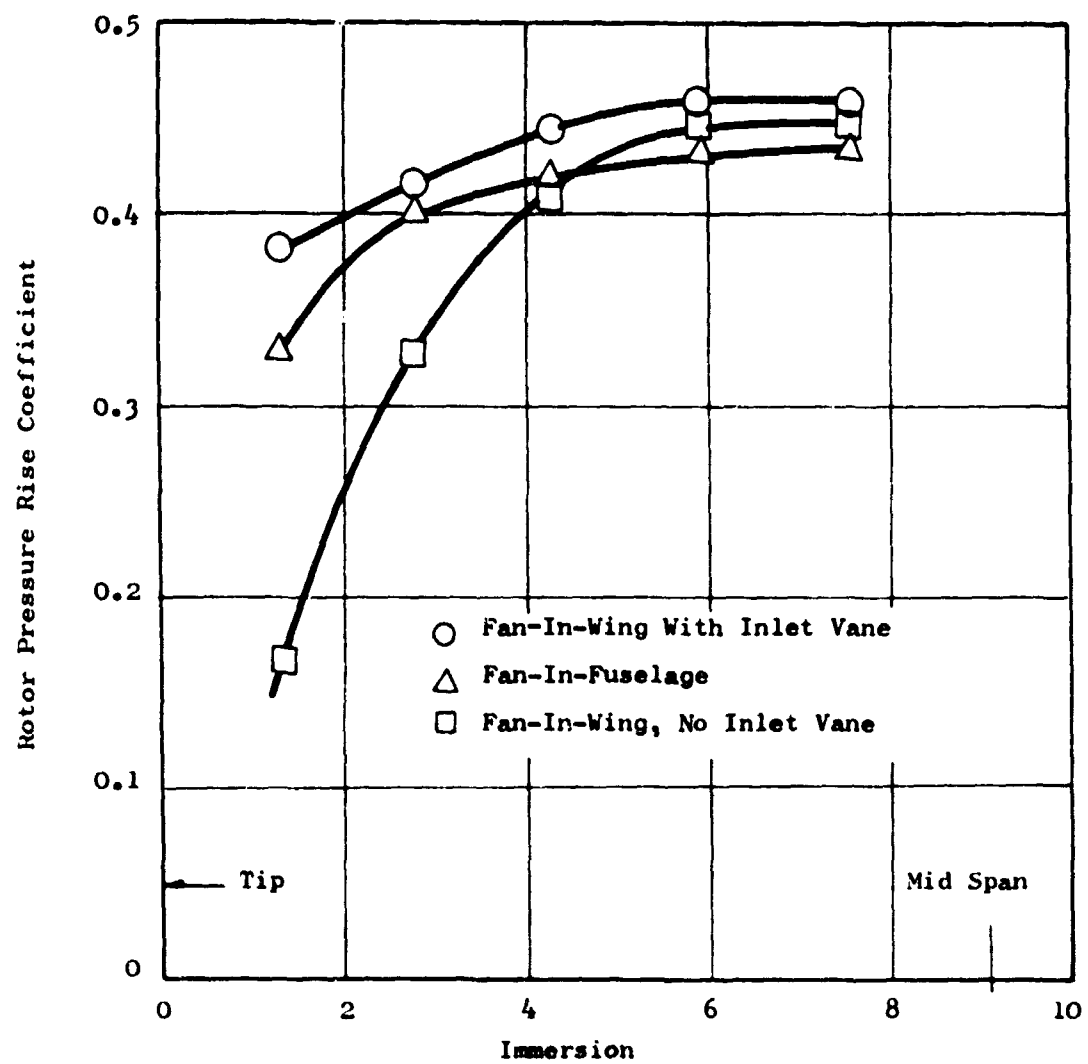


Figure 370 XJ53-5 Performance Data, Cold Side

(U) Adding the inlet vane produced a system thrust improvement of about 25 percent. The vane acts as a lifting surface whose force is directed towards the bellmouth lip relieving the bellmouth lip static pressure and thereby reducing the bellmouth maximum velocity. This device effectively changes the fan rotor inlet velocity distribution in the tip region and makes it more compatible with the values required to match the blade design incidence angles. This improvement was achieved without the aid of a leakage control device; in fact when a baffle was used with the inlet vane installed, a performance loss resulted from the added blockage that is produced.

LF2 data. -

(U) This LF2 inlet investigation explored other means of accomplishing inlet flow stability in an environment very similar to the X353-5. The 6 percent bellmouth was used with the LF2 fan in the same wing installation, but without exit louvers. Performance comparisons were based on 1750 rpm (66%) compared to 100 percent on the X353-5.

(U) For purposes of this study the "inlet vane out" configuration is used to describe base performance. Test data indicate that the fan tip performance is poor, the bellmouth is separated and hot gas penetration extends over five inches into the fan stream in the tip region.

(U) The inlet vane provided a very effective and efficient means of making the fan work properly, producing a net gain in total system lift of 21.4 percent. The installation of the inlet vane prevented the bellmouth from separating, improved the tip performance of the fan and confined hot gas seal leakage to the passage between the vane and the bellmouth. Rotor discharge yaw (stator inlet) angle is near the design value with the inlet vane in.

(U) The bellmouth vanes were installed in the high position at staggered (alternating) + 10 and -10 degree angle settings to act as vortex generators. This was found to be ineffective in reducing bellmouth separation, and produced an additional loss resulting in 3 percent lower system lift.

(U) Using the vanes to preturn the bellmouth flow proved to be more revealing. Preturning the flow in the direction of rotor rotation (unloading the tip) caused a pronounced decrement in performance while turning the flow opposite to the direction of rotation (loading the tip) caused a significant improvement. Placing the vanes in the lower position on the bellmouth (nearer the rotor inlet) proved to be more effective and the range of angle settings from -10 to -30 degrees were investigated.

The maximum improvement in system lift was 9.8 percent at the -20 degree angle setting.

(U) This configuration (bellmouth vanes in lower position) was tested on the theory that bellmouth separation could be avoided if the rotor could be made to pump the high suction pressure required to turn the flow. This was to be accomplished by preturning the flow in the region of the tip to more nearly match the rotor blade design incidence angle. The separation region was reduced but some blockage was provided by the washers and flat discs at the base of the vanes. Rotor pressure rise coefficient was significantly improved and the stator inlet angles (yaw angles) became closer to design in the tip region. Some reduction in hot gas penetration was also noted. The addition of these vane in the inlet must increase inlet losses, and so stable attached bellmouth flow was not attainable.

(U) With the inlet vane installed, bellmouth vane settings of -10, -20, and -30 degrees were investigated. System lift measurement indicated improved performance at all angle settings with the -30 degree angle setting having 26 percent better performance than "inlet vane out" and 3.8 percent better than "inlet vane in" configurations. Even with the added inlet losses of the 88 vanes and the blockage provided by the washers and flat discs at the base of the vanes obstructing the flow, the bellmouth flow did not separate and indicated an even better boundary layer profile on the hot side. The rotor pressure rise coefficient which includes inlet losses also confirms the improved performance. Hot gas penetration remains about the same as it was with "inlet vane in".

(U) The improved seal investigation with the -30 degree vane setting and "inlet vane in" indicated a small improvement in decreasing hot gas penetration but indicated no appreciable change in system lift measurement. An additional run was made to verify that the source of the measured hot gas penetration was the forward air seal.

(U) Other observations noted during the LF2 inlet investigations testing are described below:

1. There are significant variations in rotor pressure rise coefficient between data from the same configuration tested on separate days. This is attributed to differences in prevailing wind conditions. Variations in wind conditions can be seen as a source of traverse data scatter. Measured system lift has been observed to decrease as much as 4 percent at wind velocities of 15 to 20 mph compared to measured lift at 0 to 3 mph at 100 percent fan speed.

2. Performance differences exist between the hot and cold sides of the fan and the performance changes resulting from each test configuration are not necessarily as effective on both sides. The presence of the fuselage wall adjacent to the hot side of the fan acts to some extent like a deep inlet. The air entering this portion of the fan must come in more vertical and therefore does not require the high suction pressure for turning the flow around the short bellmouth. There should then be less tendency to have bellmouth flow separation in this region. However, the hot side is also accompanied by the detrimental effect of hot gas leakage from the forward air seals.
3. The lift fan environment is further complicated to some extent by the varying inlet geometry required to install it in an airfoil-shaped wing making it necessary to have a variable depth inlet. For purposes of this study, instrumentation was located at comparable depth sections on hot and cold sides to eliminate this variable. System lift measurements were used to indicate overall configuration effects.
4. An improvement in the fan tip performance noted from rotor pressure rise coefficient was usually accompanied by a small decrease in pressure rise coefficient in the adjoining region next to the mid-span support ring. This is probably a result of the changes in the inlet flow velocity distribution as the tip region is improved.
5. When the fan tip is working well, reducing the seal leakage has a very small effect on performance. This indicates that nominal amounts of seal leakage can be tolerated with only small performance penalties. At the point where seal leakage induces flow instability or bellmouth separation the performance penalties become very large (in the order of 20 to 25 percent).

#### Conclusions and Recommendations

(U) The following conclusions are derived from the analysis of the presented test data:

1. The inlet vane was a very effective and efficient device to adapt the early lift fan designs to the shallow inlet provided by the fan-in-wing environment.
2. Bellmouth vanes in the vortex generator configuration were ineffective in preventing bellmouth separation.

3. Bellmouth vanes used for flow turning in the tip region demonstrated as much as 10 percent improvement in fan performance. These vanes demonstrated that better fan rotor-to-inlet matching could have been incorporated in this early design. They also demonstrated that this rotor with a modified blade tip geometry could very possibly have worked without an inlet vane.
4. Preturning the flow in the direction of rotor rotation caused a pronounced decrement in performance, while preturning the flow opposite to the direction of rotation caused a significant improvement. Therefore, the fan tip should be designed for high work input, i.e. lower stagger angle and increased camber.
5. Seal leakage can be a major contributing factor to poor tip performance if the inlet design is marginal. If the fan tip is working well, nominal amounts of leakage can be tolerated with very small performance penalties.

(U) The following recommendations are made for application of these results.

1. The LP2 inlet investigation provides data with which current fan aerodynamic design methods and programs can be checked and updated as required. Future fan aerodynamic designs should be fan system designs that provide for compatibility of the inlet bellmouth, the fan rotor, and the stators. The need for an inlet matching device such as an inlet vane or bellmouth turning vanes should be eliminated. This would result in savings in weight and possibly in fan thickness.

#### J79 80-Inch Lift/Cruise Fan Inlet Investigations

##### Introduction

(U) The objectives of the J79 80-Inch Lift/Cruise Fan Inlet Investigation Program are: 1) to investigate the influence of the geometry of the inlet lip on the static performance of lift/cruise fans with special emphasis on low contraction ratio inlets and low frontal area ratio nacelles, and 2) to provide inlet static separation data for use during the design of the L/CP470 inlet and other related programs.

(U) Static inlet performance is very critical for lift/cruise fans because of the requirement for high angle of attack operation during conversion and the incompatibility of suck-in doors. Suck-in doors interfere with the hot gas scroll and their performance would be inferior under cross-flow conditions during thrust vectoring operation.

(U) Previous tests, conducted with a high contraction ratio inlet ( $A_{HL}/A_{TH} = 1.37$ ) in the 40 x 80 foot wind tunnel at NASA-Ames showed good static and transition performance (Reference 9). However, high contraction ratio inlets are incompatible with low frontal area nacelles required for the high subsonic cruise Mach number ( $M_{\infty} = 0.8$ ) design point of the L/CF470. The maximum nacelle diameter for the L/CF470 lift/cruise fan is not any more compromised by the requirement of housing the hot gas ducts in the scroll as in the third generation fans. It is determined by structural requirements and good nacelle design practices (Reference 10).

(U) A literature survey provided the ground rules and the range of the design parameters and several inlets were laid out for the L/CF470 cruise design point. The selected inlets were then scaled to the 80-inch cruise fan throat diameter. These scaled contours provided the basis for the model design and the analytical investigations. Reference 11 is a published report describing the experimental and analytical results of this program.

#### Test Vehicle and Installation

(J) The J79 80-Inch Cruise Fan and engine hardware installed in Test Site No. 3 of the General Electric Peebles Proving Ground was used for all tests. The test installation is shown in Figure 371 before any modification for the inlet investigation program began.

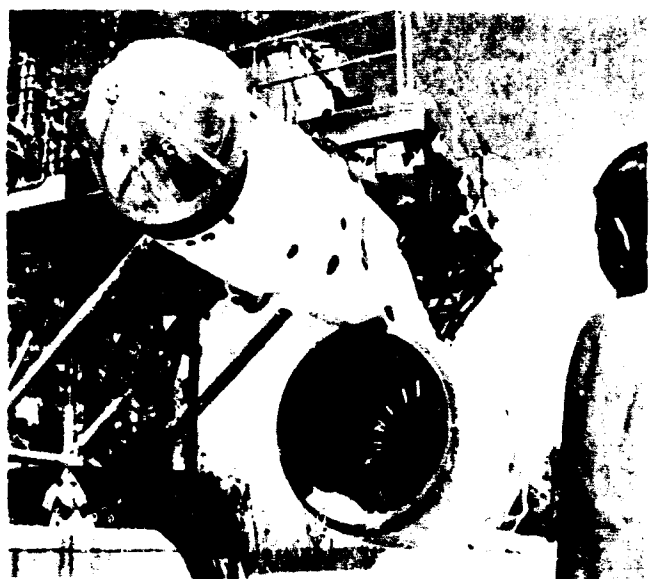
(U) Two new inlet lips were designed and fabricated. These were made to fit over the existing lip and attach to the forward nacelle in the same plane as the original lip. Front and rear views of one of the new lips are shown in Figure 372. After the completion of the design of the inlet lip hardware it became evident that the J79 80-Inch test vehicle would not deliver the required mass flow due to the reduction of the maximum fan speed because of high rotor vibrational stresses. In order to obtain the required mass flow the inlet flow area had to be reduced. This was accomplished by the insertion of a 30-inch diameter centerbody as shown in Figure 373.

#### Instrumentation

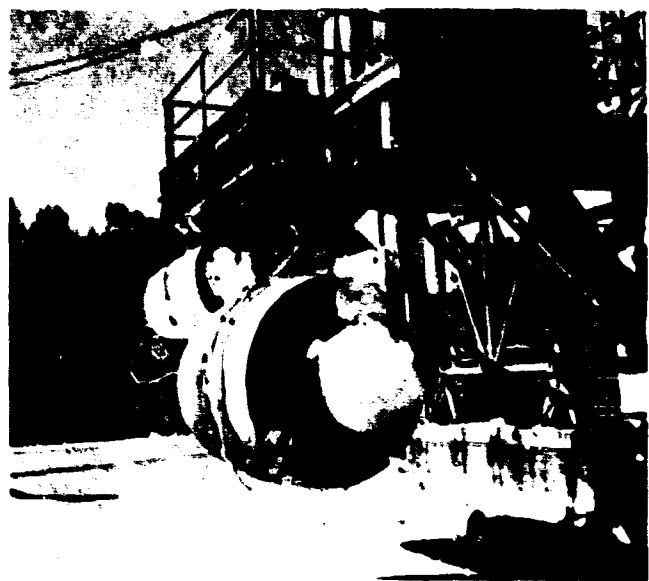
##### Original inlet without centerbody. -

(U) The instrumentation installed in the J79 80-Inch Cruise Fan inlet is shown in Figures 371 and 373.

1. 12 wall static pressure taps with axial spacings as shown in Figure 373 were installed in the inlet nacelle at  $0^\circ$ ,  $90^\circ$  and  $180^\circ$  radial planes.



a. Front View of Fan



b. Aft View of Fan

Figure 371 J79 80-Inch Cruise Fan Test Installation

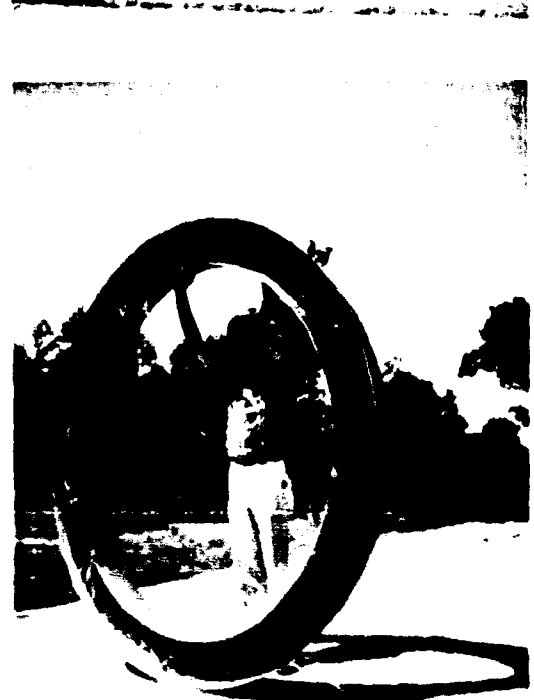


Figure 372 Inlet Lip Models



Figure 373 Lip No. 1 Installed

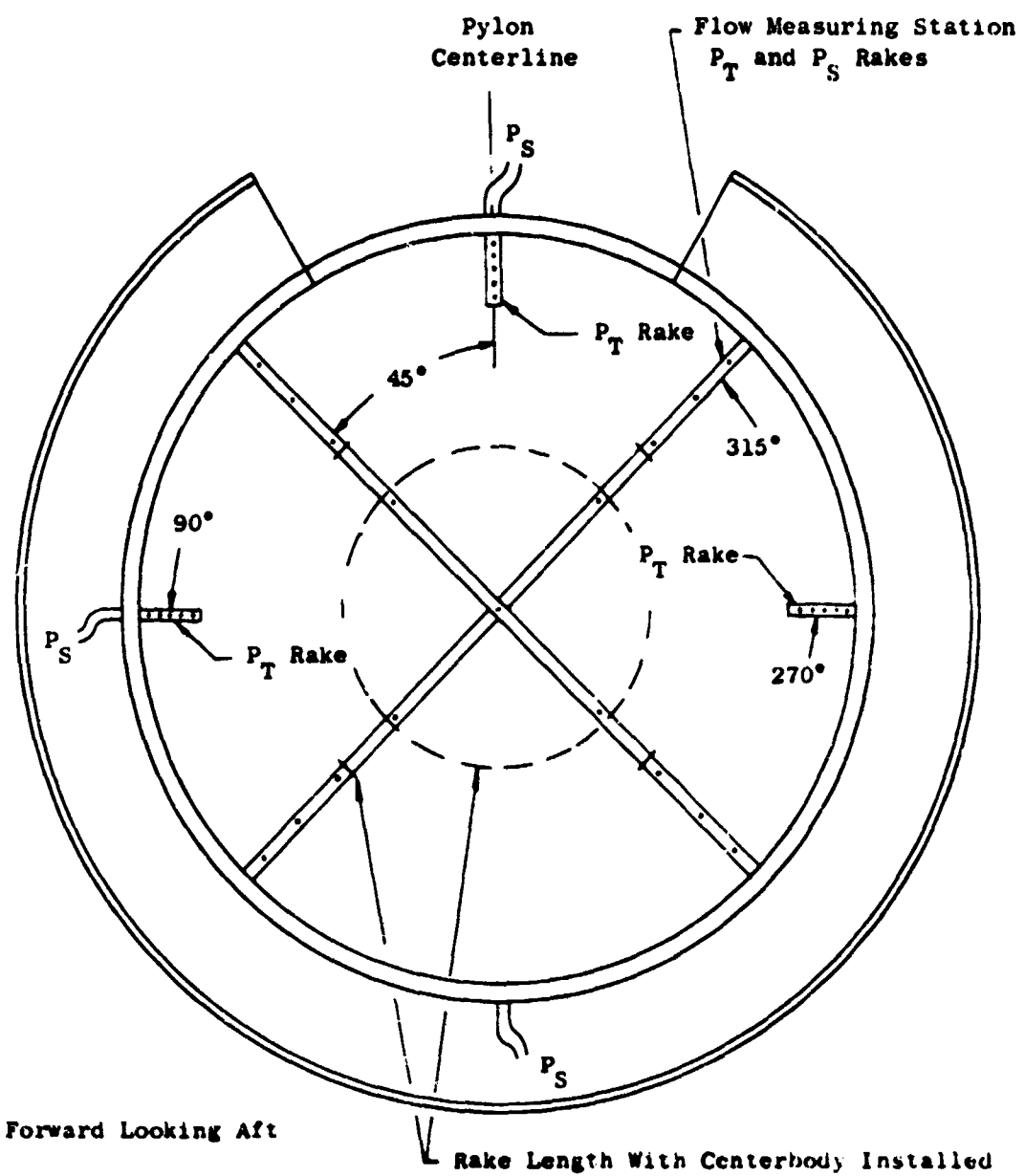


Figure 374 Fan Inlet Instrumentation (Radial Planes).

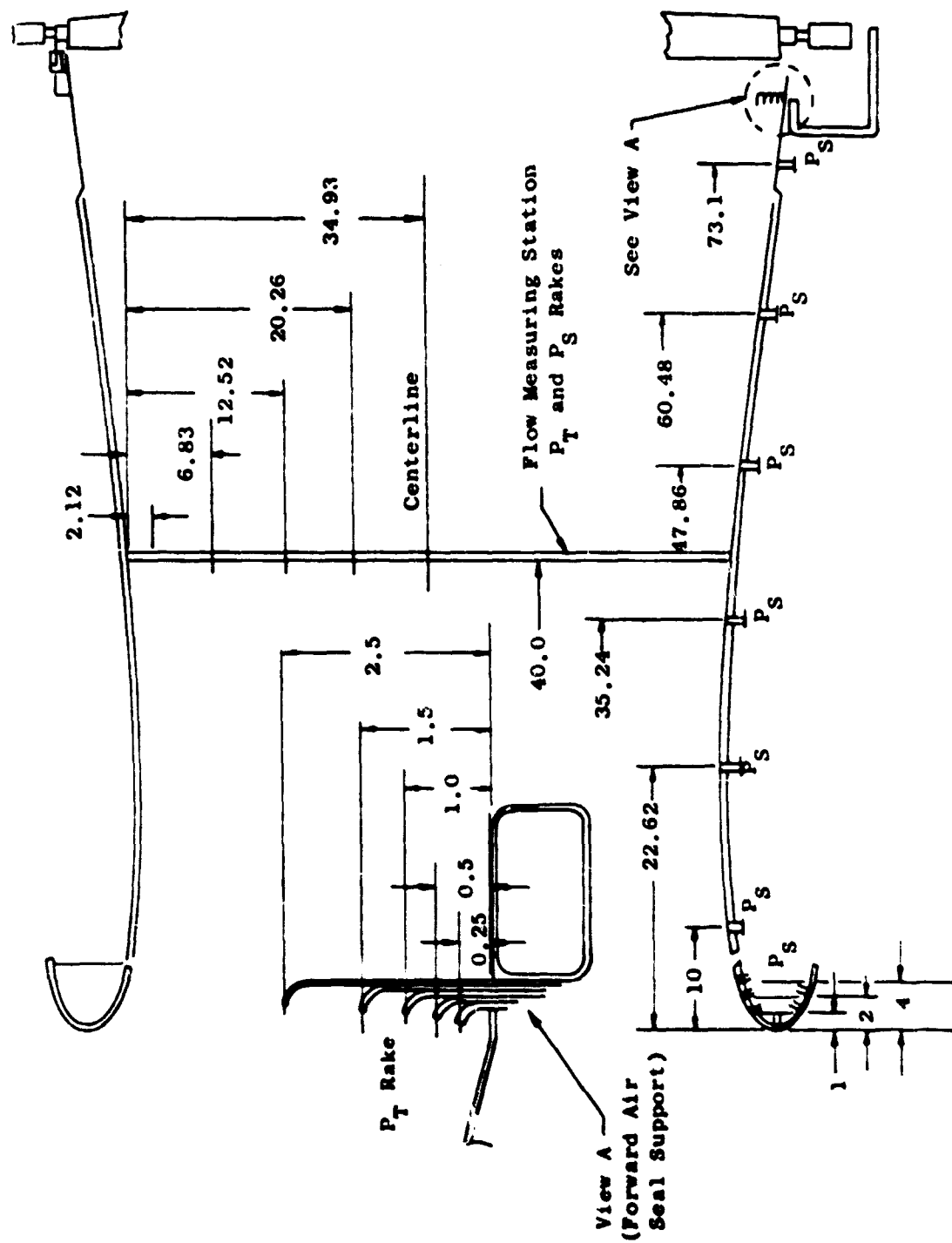


Figure 375 Fan Inlet Instrumentation (Axial Planes)

2. 3 five-element boundary layer total pressure rakes were located on the forward air seal support near the fan rotor inlet at  $0^\circ$ ,  $90^\circ$  and  $270^\circ$  circumferential spacing.
3. 4 total and static pressure rakes were located 40 inches aft of the nacelle leading edge (inlet diameter = 69.9 inches). There were 4 elements per rake plus one center stream element. Element spacing was selected to position them on the centers of 5 equal areas. The rakes are  $90^\circ$  apart with rake 1 at  $45^\circ$  from the fan rear frame pylon.

Original inlet with centerbody. -

(U) The 4 total and static pressure rakes described in (3) above had to be modified for installation of the centerbody. The rakes were cut off, leaving 3 elements per rake as indicated in Figure 374.

Inlet lip models 1 and 2. -

(U) Lip models 1 and 2 (Figures 376 and 377) included 9 surface static pressure elements located in 2 radial planes  $90^\circ$  apart. The lips were installed so that these 2 instrumentation planes were in line with the existing  $90^\circ$  and  $180^\circ$  instrumentation planes in the nacelle.

Inlet Lip Design

(U) The inlet lips were designed for the L/CF470 lift/cruise fan dimensions and then scaled to the J79 80-Inch test vehicle size by the ratio of their throat diameters. The design parameters were selected as follows (Reference Figure 378):

Cruise Mach Number $M_0$	= 0.8
Cruise Altitude, ALT	= 25,000 ft
Engine Power Setting, PS	= Maximum Continuous
Fan Tip Diameter, $D_{FT}$	= 70 in.
Nacelle Maximum Diameter, $D_{MAX}$	= 80 in.
Fan Radius Ratio, $\bar{R}$	= 0.5
Fan Flow at SLS, Takeoff, $w_{10}$	= 785 lb/sec
Fan Flow at Cruise, $w_{10}$	= 455 lb/sec

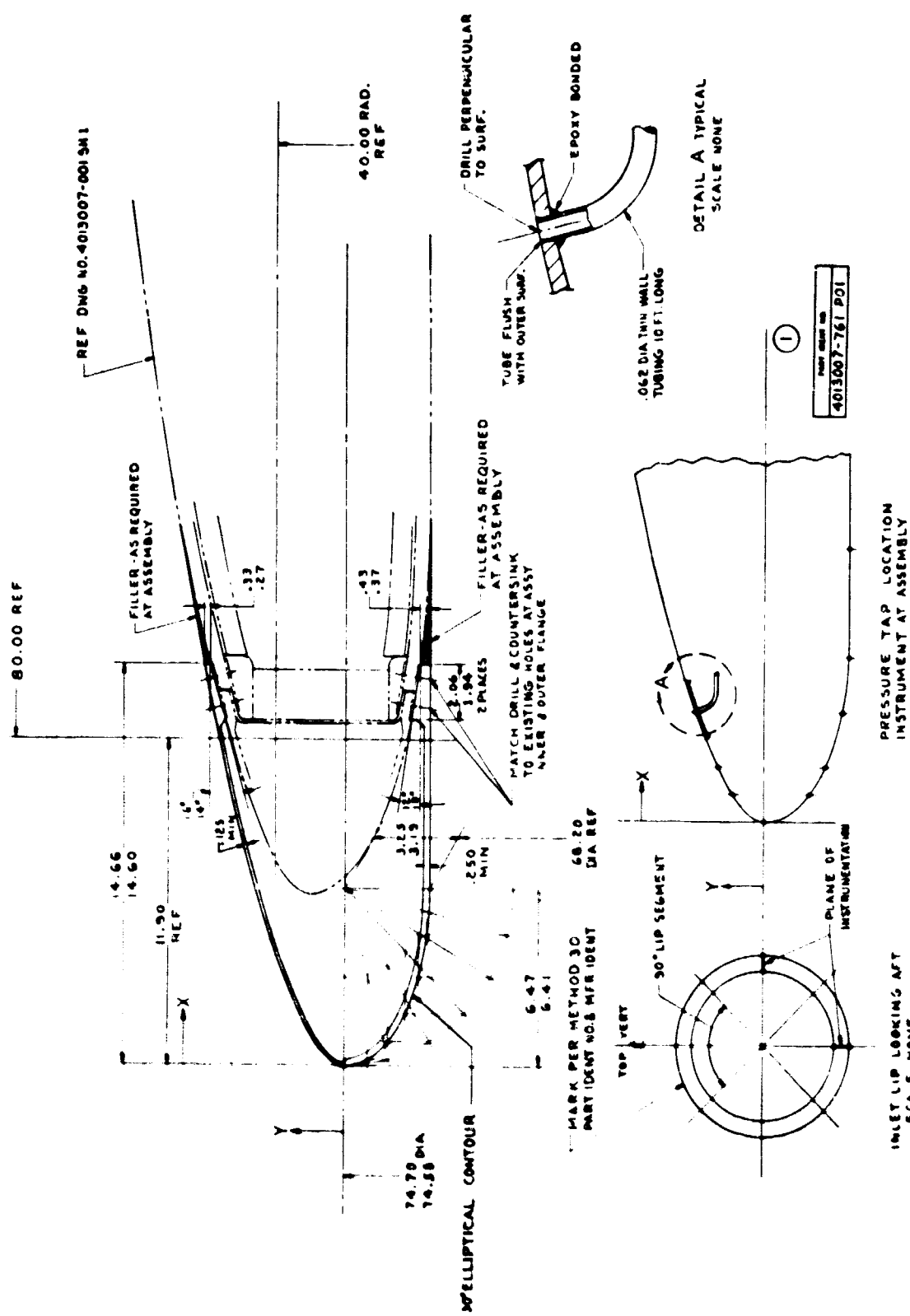


Figure 376 J79-80 Inch Cruise Fan Inlet Investigations - Inlet Lip Model 1

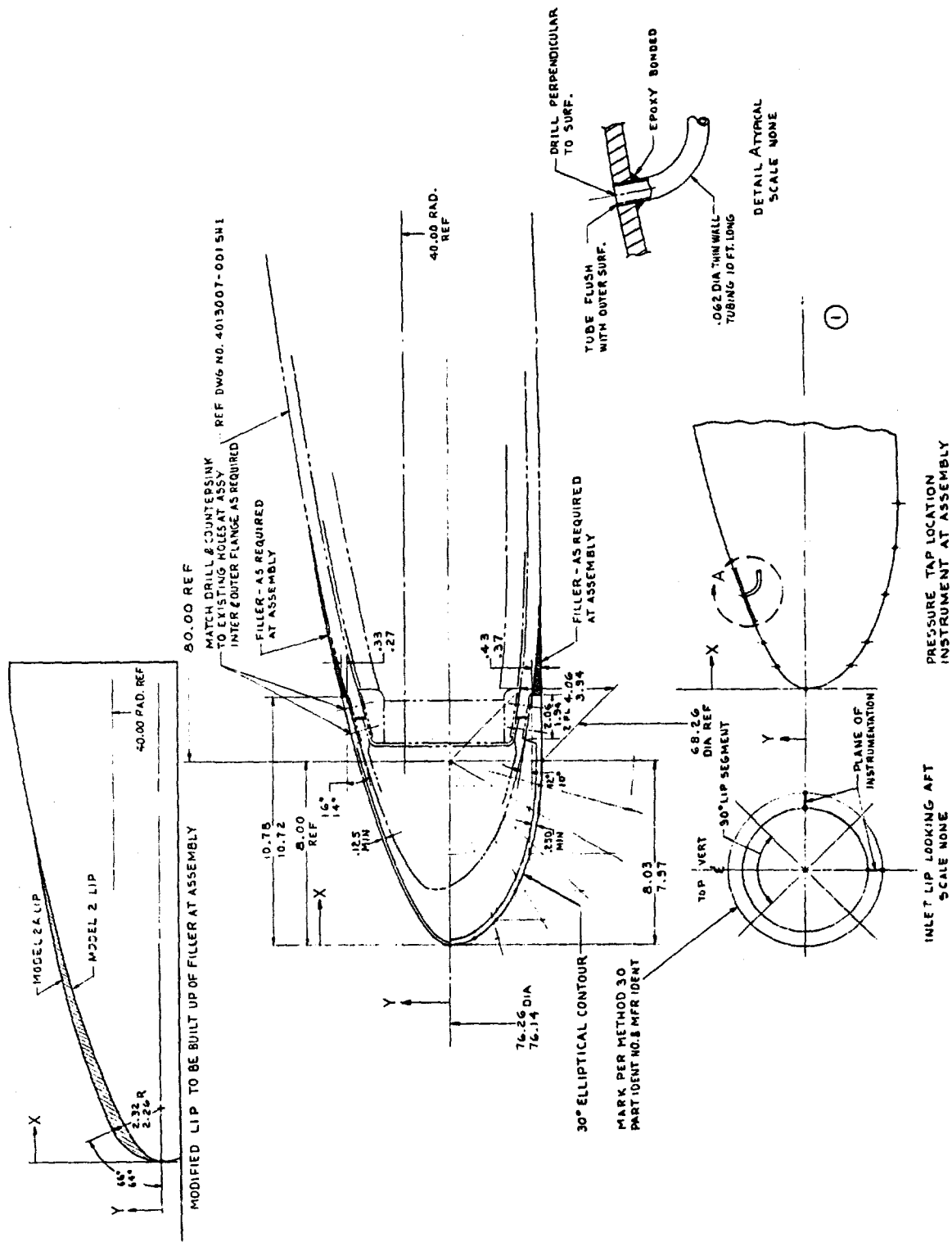
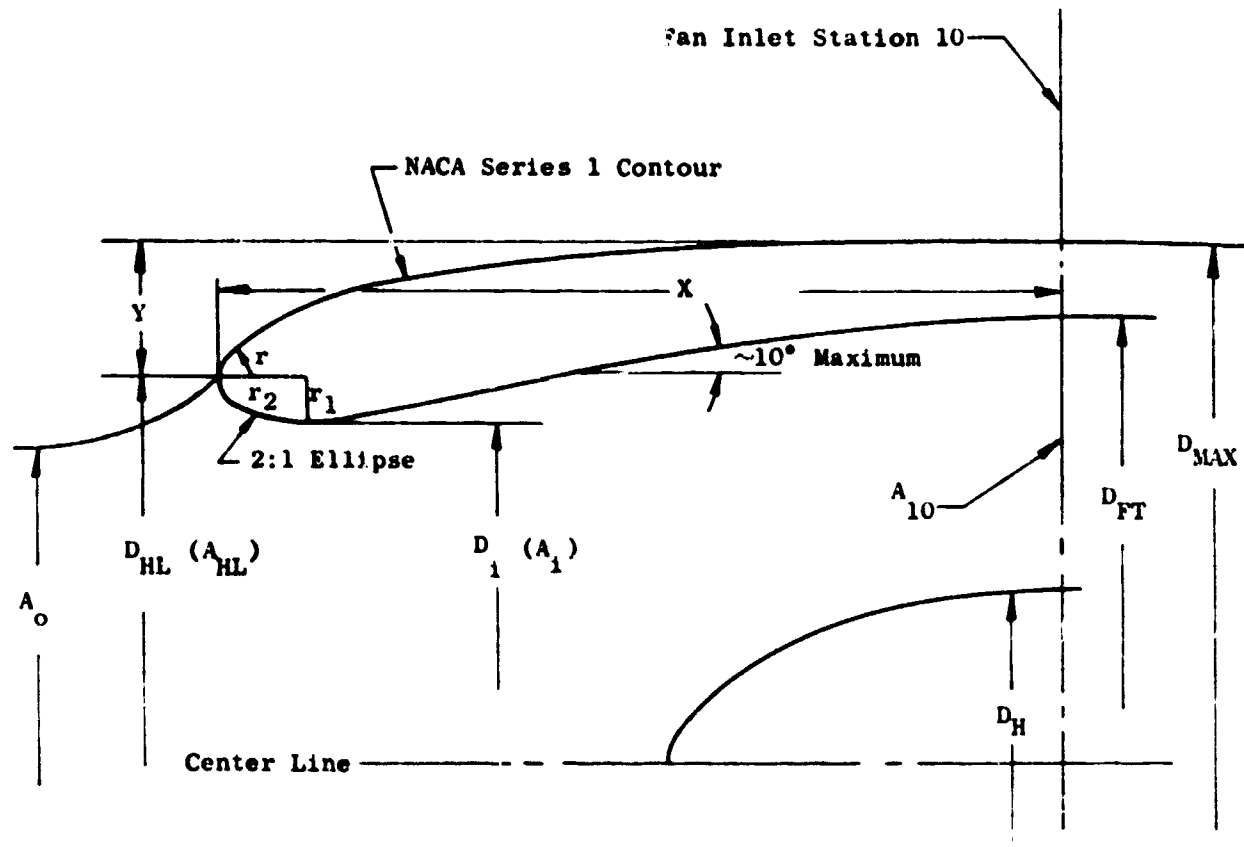


Figure 377 J79, 80 Inch Cruise Fan Inlet Investigations - Inlet Lip Models 2, 2A



Note:

**D** Diameters

**A** Areas

$$A_{10} = (D_{FT}^2 - D_H^2) \frac{\pi}{4}$$

Figure 378 J79 80-Inch Inlet Investigation - Nomenclature

(U) The nacelle contours were designed for the cruise flight condition and then checked for the throat Mach number at the takeoff condition.

(U) Three internal lips were then laid out having contraction ratios of  $A_{HL}/A_{TH}$  = 1.2, 1.25 and 1.3. An ellipse with a major to minor axis ratio of 2 was selected as the internal lip contour. Throat Mach numbers at cruise and takeoff, diffuser area ratios and internal lip roundness parameters were calculated. The results are compared in Table 56. Included in the comparison are the J79 80-Inch inlet parameters which will be designated henceforth as the "original" inlet. Inlet 3 was eliminated because of its high throat Mach number and diffuser area ratio; inlets 1 and 2 were selected for the inlet test.

(U) In order to test the lift/cruise fan inlet lips on the J79 80-Inch Cruise Fan test vehicle it was necessary to scale the inlets by the ratio of the throat diameters. This resulted in the following scale factors:

$$\text{Inlet 1: } 68.2/57.7 = 1.182$$

$$\text{Inlet 2: } 68.2/56.6 = 1.205$$

The scaled inlet lip contours are shown in Figures 376 and 377

(U) Model 2A is a variation to inlet 2 by blunting the outer lip curvature for improving the static performance. Inlet 2A (Figure 377) has an external lip radius to highlight diameter ratio,  $r/D_{HL} = 0.03$  which is 3 times larger than the one of the NACA 1-series contours.

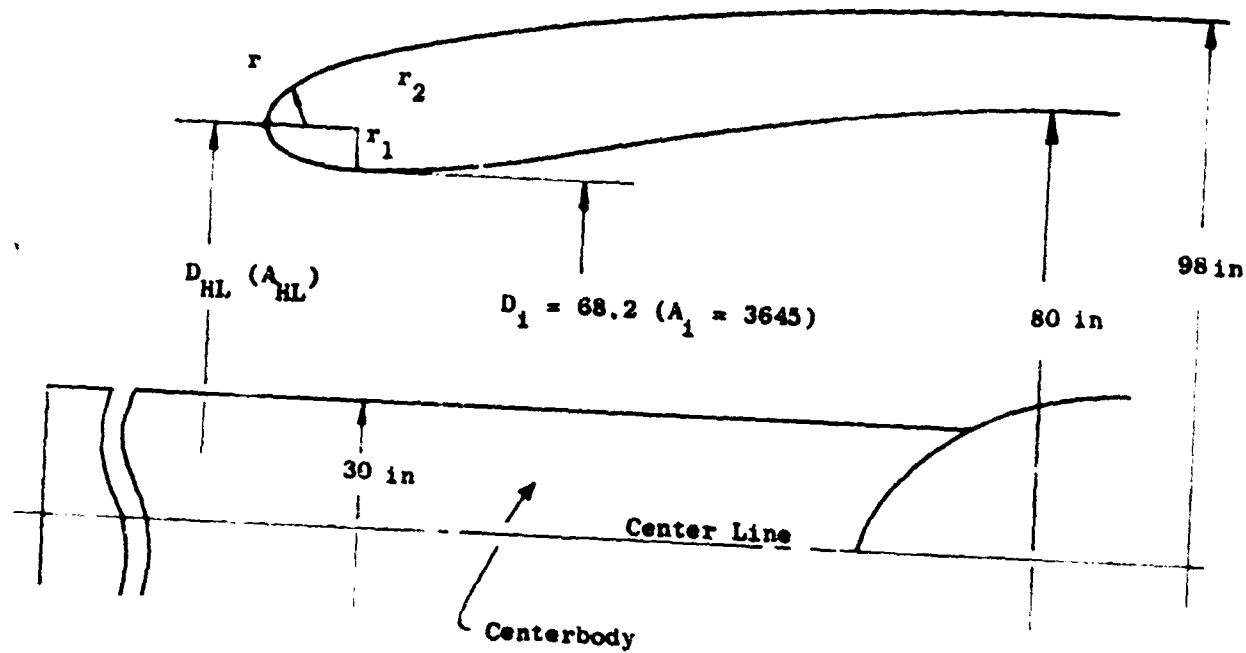
#### Test Procedure and Results

(U) The test hardware was designed for a fan speed of 90% to produce an inlet throat Mach number of 0.75. While the main interest of the test was focused at the inlet design point with a throat Mach number range of 0.55 to 0.75, data was obtained over the whole range of static fan operation. Inlet throat Mach numbers from 0.24 to 0.71 corresponding to fan speeds from 36 to 89 percent were obtained. The test configuration included the original lip, with and without centerbody installed, plus two additional lips (designated No. 1 and No. 2) with centerbody. Also, a lip model designated 2A was planned to be tested, depending on test results from the first 3 configurations. The parameters of the test configurations are summarized in Figure 379. Modification of Lip 2 to Lip 2A and its testing was deleted from the program because of mechanical problems encountered with the J79 80-Inch test vehicle.

TABLE 56  
COMPARISON OF INLET PARAMETERS

Inlet Lip	1	2	2A	3	Original 1)
Contraction Ratio, $A_{HL}/A_{TH}$	1.20	1.25	1.30	1.285	
Diffuser Area Ratio, $A_{10}/A_{TH}$	1.046	1.090	1.132	1.032	
Capture Ratio, $A_0/A_{HL}$ <sup>2)</sup>	0.900	0.937	0.974	0.907	
Inlet Throat Mach Number at Cruise, $(M_{TH})_{CRUISE}$	0.630 <sup>2)</sup>	0.682 <sup>2)</sup>	0.740 <sup>2)</sup>	0.639 <sup>3)</sup>	
Inlet Throat Mach Number at SLS Takeoff, $(M_{TH})_{TO}$	0.641	0.695	0.764	0.620	
Internal Lip Roundness Parameter, $r_1/D_{HL}$	0.0465	0.0550	0.0638	0.0525	
External Lip Radius Ratio, $r/D_{HL}$	0.01	0.01 0.03	0.01	0.01	
Internal Lip Ellipse Axis Ratio, $r_1/r_2$	1/2	1/2	1/2	1/3	

Notes: 1) Original J79 80-Inch Cruise Fan Inlet.  
2) At Cruise Design Point:  $M_0 = 0.8$ , 25,000 Feet.  
3) At Cruise Design Point:  $M_0 = 0.8$ , 36,089 Feet.



No.	<u>Test Configuration</u>	<u><math>A_{HL}/A_1</math></u>	<u><math>r_2/r_1</math></u>	<u><math>r/D_{HL}</math></u>	<u><math>M_1</math> at Takeoff</u>
1	J79 80-Inch	1.285	3	0.01	0.650
2	Lip 1	1.2	2	0.01	0.641
3	Lip 2	1.25	2	0.01	0.695
4	Lip 2A	1.25	2	0.03	0.695

Figure 379 J79 80-Inch Test Configuration Parameters

(U) The test plan is shown in chronological order in Table 57. Data for the J79 80-Inch inlet without centerbody was available from prior testing. Actual test points were taken at 36, 54, 70 and 88 percent fan speeds for mechanical operational and safety reasons. The test run summary, Table 58, includes the inlet investigation testing as well as other configurations completed as part of the previously planned J79 80-Inch Cruise Fan Program. Data from runs 17, 18 and 23 through 26 were used for the inlet test results. The J79 80-Inch Cruise Fan inlet investigation test results are shown in Figures 380 through 388.

#### Data Reduction

(U) From prior analysis of J79 80-Inch Cruise Fan data, a non-uniformity of inlet flow characteristics was noted and was attributed to pylon interference effects on fan performance. Rather than include these effects in the inlet performance analysis, the data reduction was based on measurements in the region of the 90° radial location where the flow characteristics were most uniform and representative. A time-sharing computer program was prepared and used to perform the data reduction.

#### Analysis of Test Data

##### Comparison to analytical calculations. -

(U) An analysis of "low speed" axisymmetric flow at static flight conditions was conducted for the models using the flux plot technique. Potential flow was assumed.

(U) Experimental inlet lip wall pressure distributions are compared to the analytical calculation for lip model No. 1 with centerbody and the original lip without centerbody in Figures 389 and 390. This comparison shows good agreement with regard to the shape of the curves and close agreement with regard to the absolute values of the pressures. The differences between analytical and experimental results increase with mass flow ratio as expected, due to the increase of compressibility and viscosity effects. Because of these effects, the experimental pressures should be higher than the incompressible analytical calculations. Lip No. 1 shows this expected difference, whereas the original lip test data fall slightly below the calculated data. This would indicate that the test data for the original lip without centerbody are low.

##### Effect of centerbody. -

(U) The presence of the centerbody affects the inlet design parameters due to the decrease in flow area. The parameters which are affected by the centerbody are shown in Table 59.

TABLE 57  
INLET TEST PROCEDURE

No.	Configuration	Test Points
1	J79 80-Inch Fan Inlet With Centerbody	7 data points each at approximately the following fan speeds:
2	Lip No. 1 With Centerbody	$\% N_F = 36, 53, 67,$
3	Lip No. 2 With Centerbody	$70, 76, 82,$
4	Lip No. 2A With Centerbody	$85$ and $90$

TABLE 58  
TEST RUN SUMMARY

Run	Date	Readings	Fan Speeds	Configuration
17	6/29/67	62 thru 64	1011 - 2437	Base configuration (aft nacelle modified for increased maximum nozzle area).
18	6/30/67	65 thru 70	1000 - 2600	Same as Run 17.
19	7/31/67	71 thru 75	1006 - 1969	Same as Run 17 with boot inflated for minimum discharge nozzle area.
20	8/ 1/67	76 thru 80	1004 - 2449	Same as Run 17 with boot deflated for maximum nozzle area.
21	8/ 1/67	81 thru 87	1013 - 2472	Same as Run 20 with forward air seal ports covered.
22	8/ 2/67	88 thru 93	999 - 2473	Forward air seal ports uncovered and boot partially inflated for intermediate nozzle area.
23	8/23/67	94 thru 97	986 - 2463	Base configuration with centerbody installed in inlet.
24	8/31/67	98 and 99	1000 - 1500	Lip No. 1 with centerbody installed. Flow splitter installed in nozzle.
25	9/19/67	100 thru 105	1000 - 1910	Same as Run 24 with boot partially inflated for intermediate nozzle area.
	9/19/67	106 thru 112	1000 - 2454	Same as Run 24 with boot deflated for maximum nozzle area.
26	9/26/67	113 thru 118	1011 - 2460	Lip No. 2 with centerbody installed. Maximum nozzle area with flow splitter installed.

TABLE 59  
INLET PARAMETERS WITH CENTERBODY INSTALLED

Inlet Lip	1	2	Original Lip <sup>1)</sup>
Contraction Ratio, $\frac{A_{HL} - A_{CB}}{A_{TH} - A_{CB}}$	1.248	1.306	1.350
Diffuser Area Ratio, $A_{10}/(A_{TH} - A_{CB})$	1.257	1.257	1.257
External Lip Radius to Effective Highlight Diameter Ratio, $r/\sqrt{D_{HL}^2 - D_{CB}^2}$ <sup>2)</sup>	0.011	0.011	0.011
Internal Lip Roundness Parameter, $r_1/\sqrt{D_{HL}^2 - D_{CB}^2}$ <sup>2)</sup>	0.0509	0.0599	0.0570

1) J79 80-Inch Inlet.

2) Effective Highlight Diameter Based on Area,  $(D_{HL})_{Eff} = \sqrt{D_{HL}^2 - D_{CB}^2}$

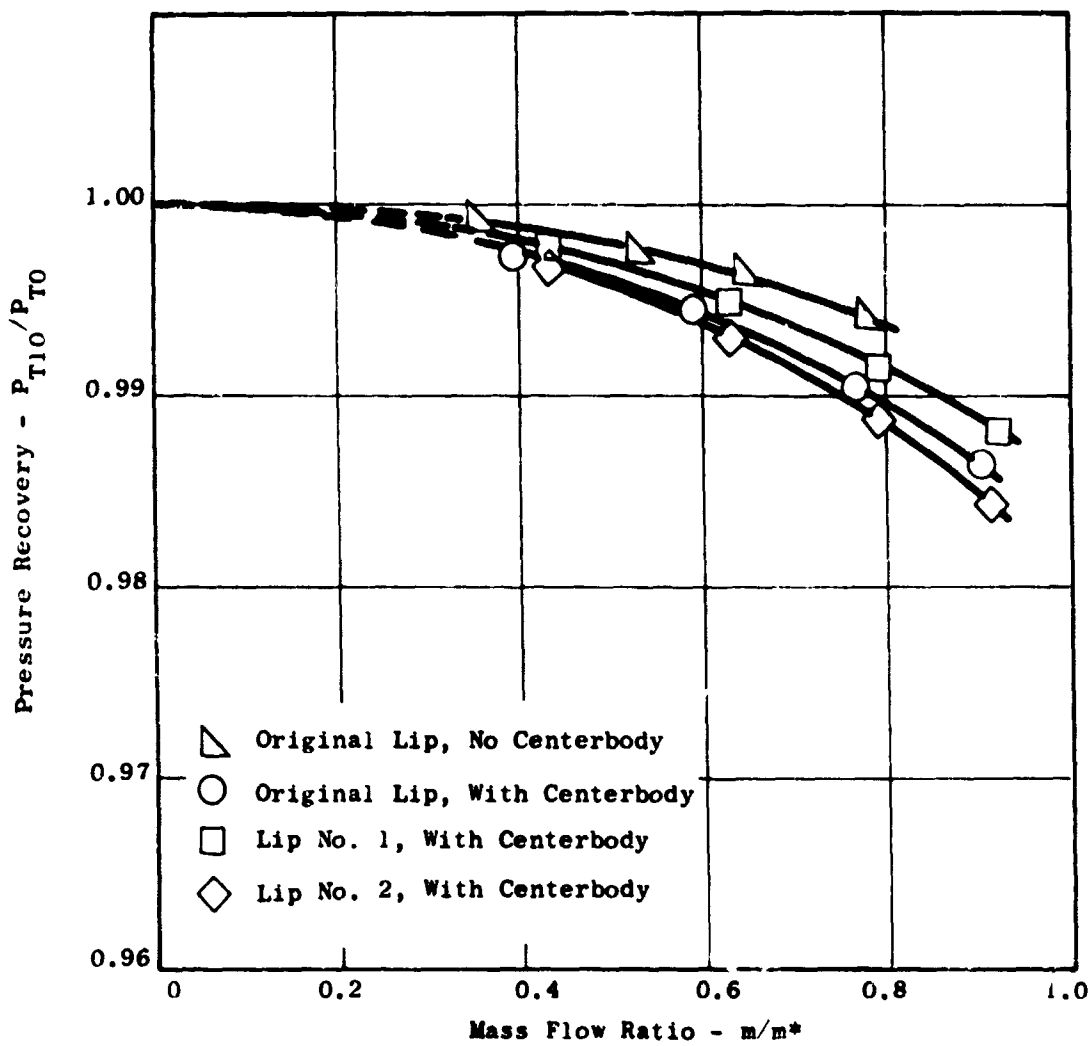


Figure 380 Pressure Recovery Based on Average Loss Coefficient,  
 $90^\circ$  Position, Versus Mass Flow Ratio.

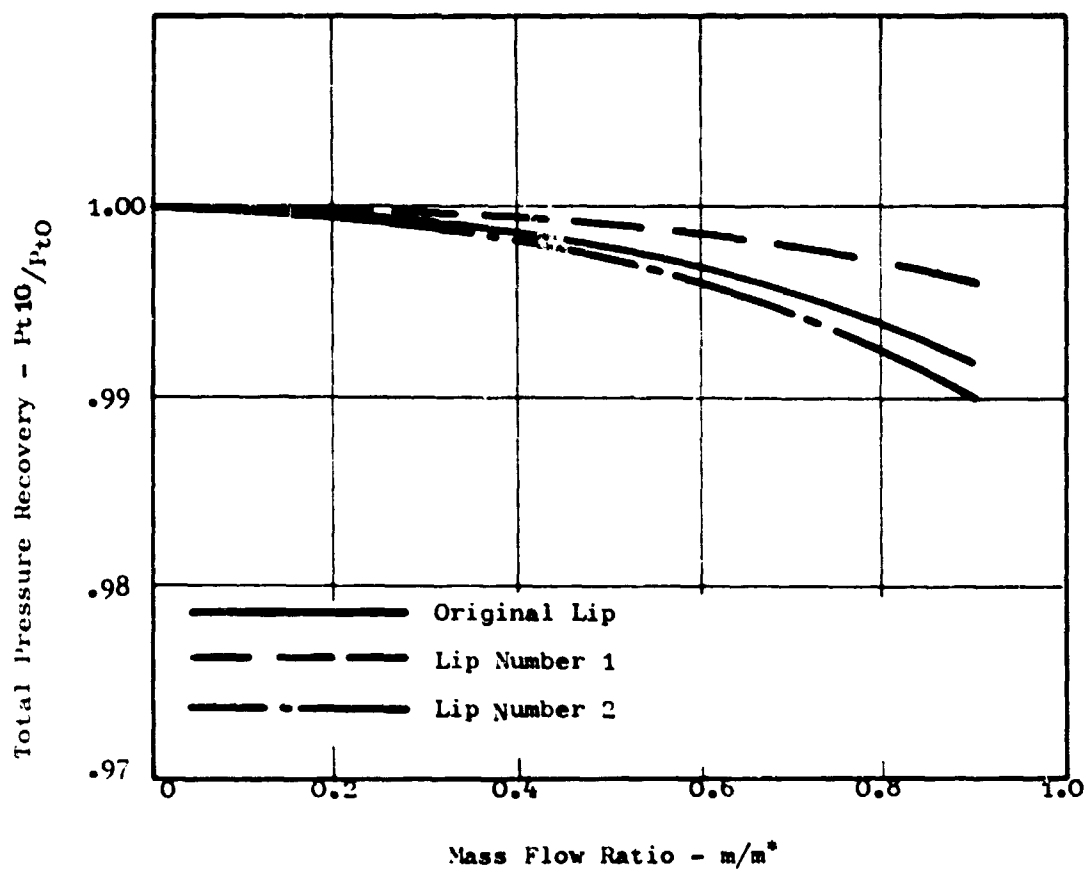


Figure 381 Estimated Pressure Recovery, Without Centerbody,  
Versus Mass Flow Ratio

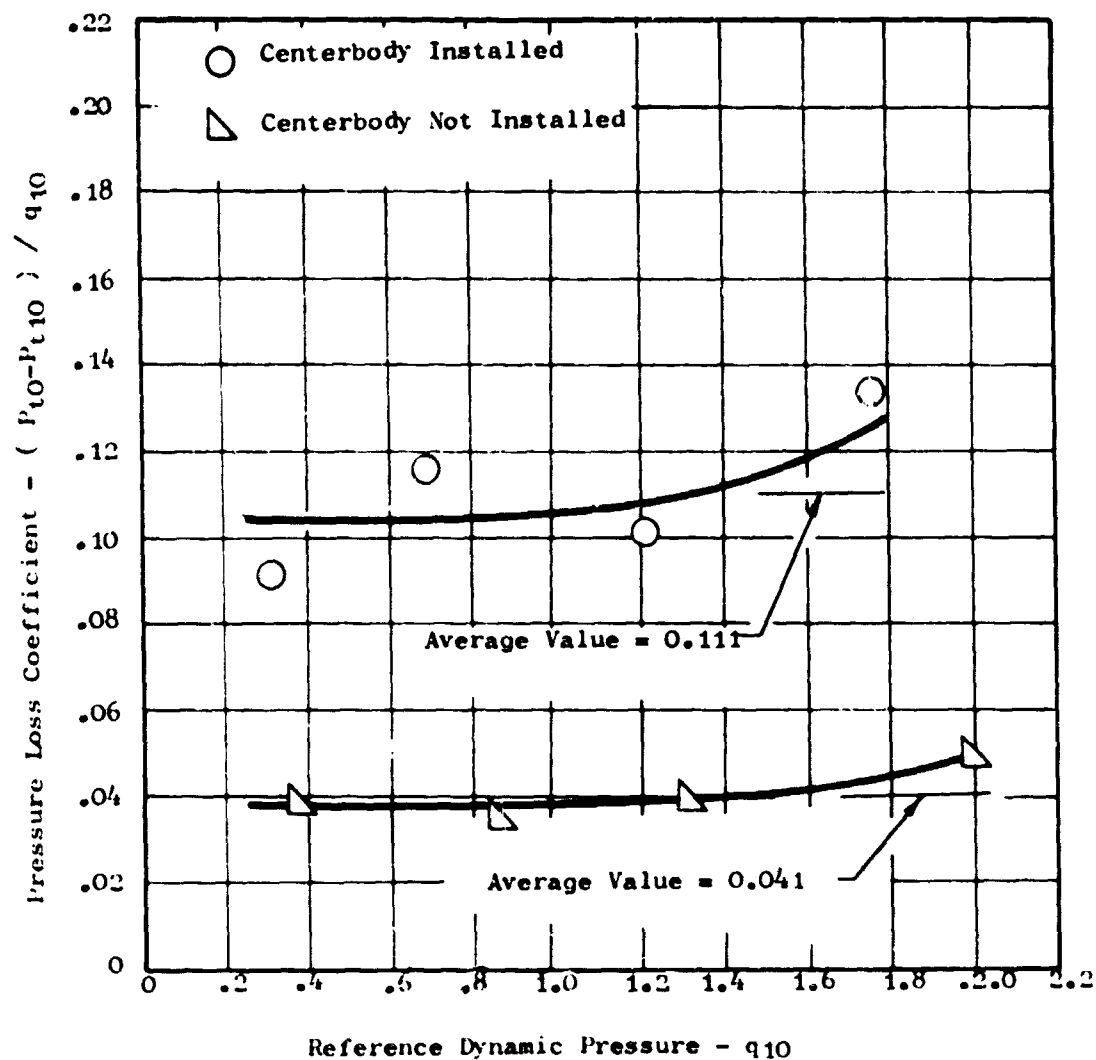


Figure 382 Total Pressure Loss Coefficient, Original Lip,  
at 90° Position, Versus Dynamic Pressure.

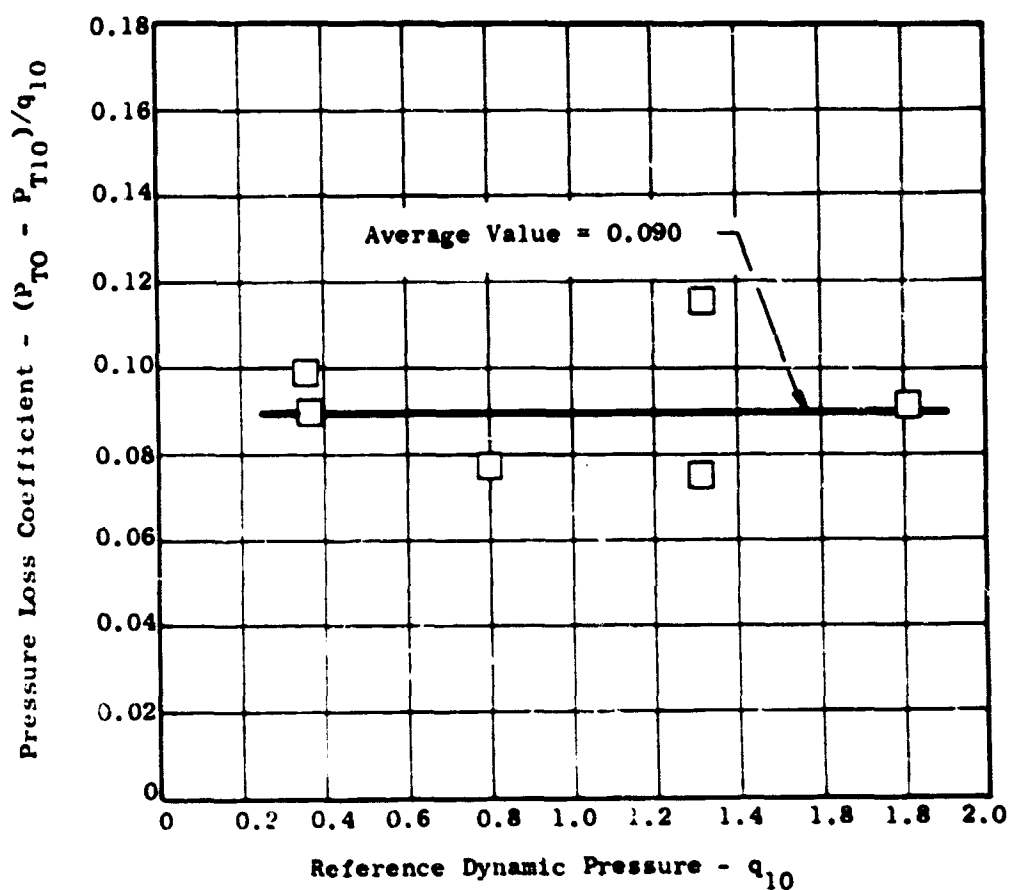


Figure 383 Total Pressure Loss Coefficient, Lip No. 1,  
 $90^\circ$  Position, Versus Dynamic Pressure.

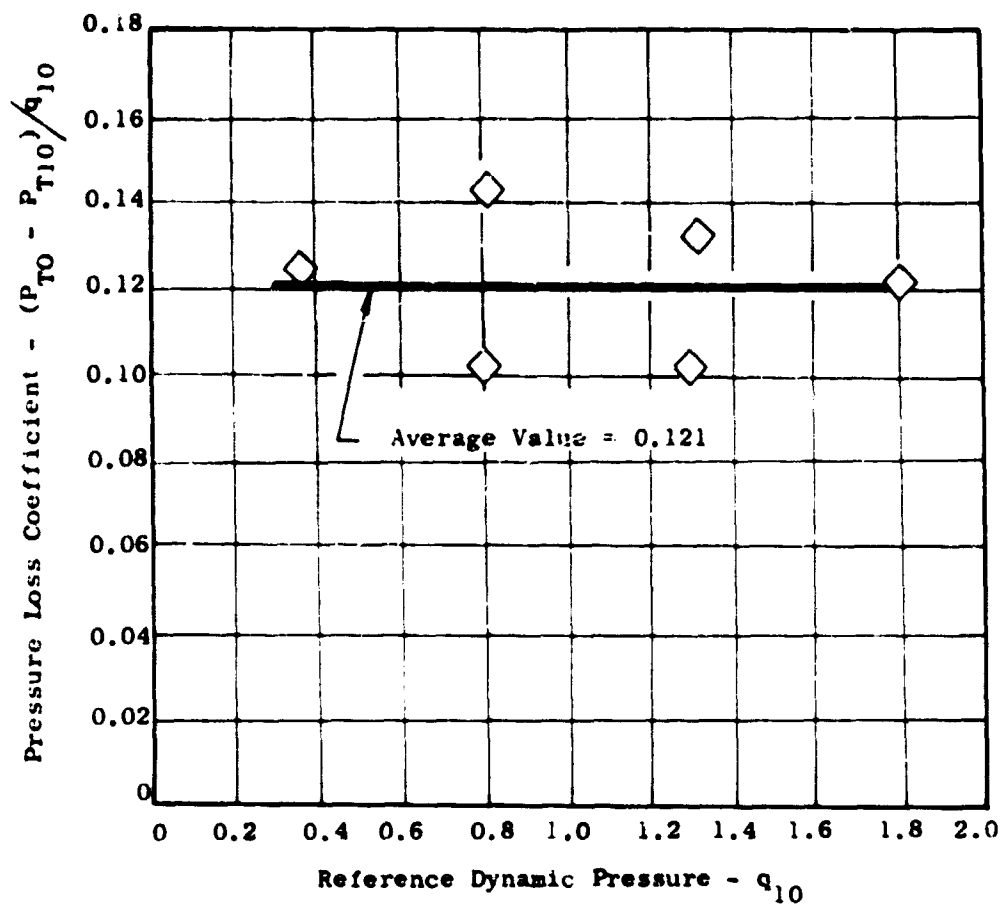


Figure 384 Total Pressure Loss Coefficient, Lip No. 2,  
 $90^\circ$  Position, Versus Dynamic Pressure.

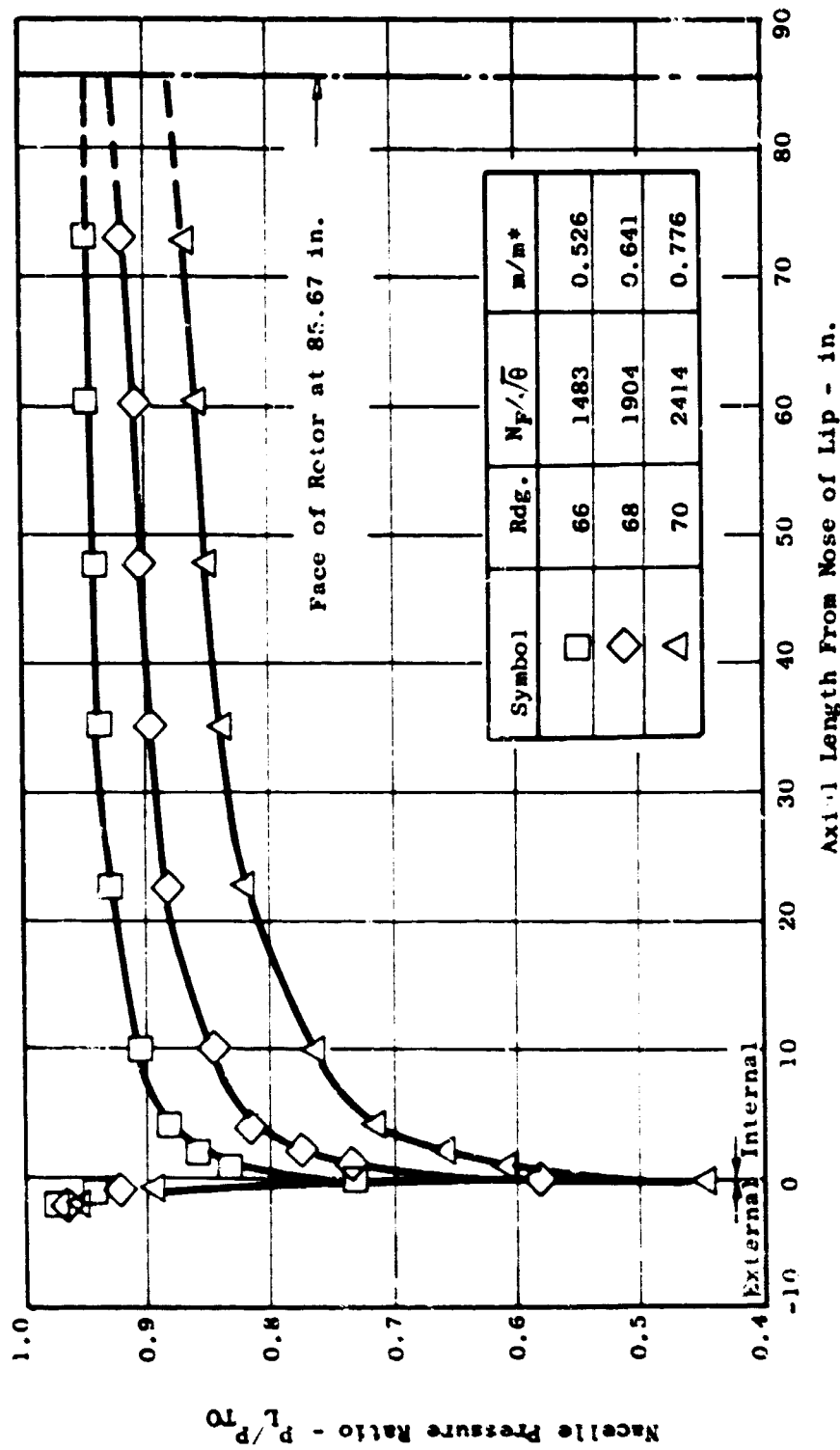


Figure 345 Wall Static Pressure Variation with Axial Length, Original Lip,  $90^\circ$  Position,  
No Centerbody

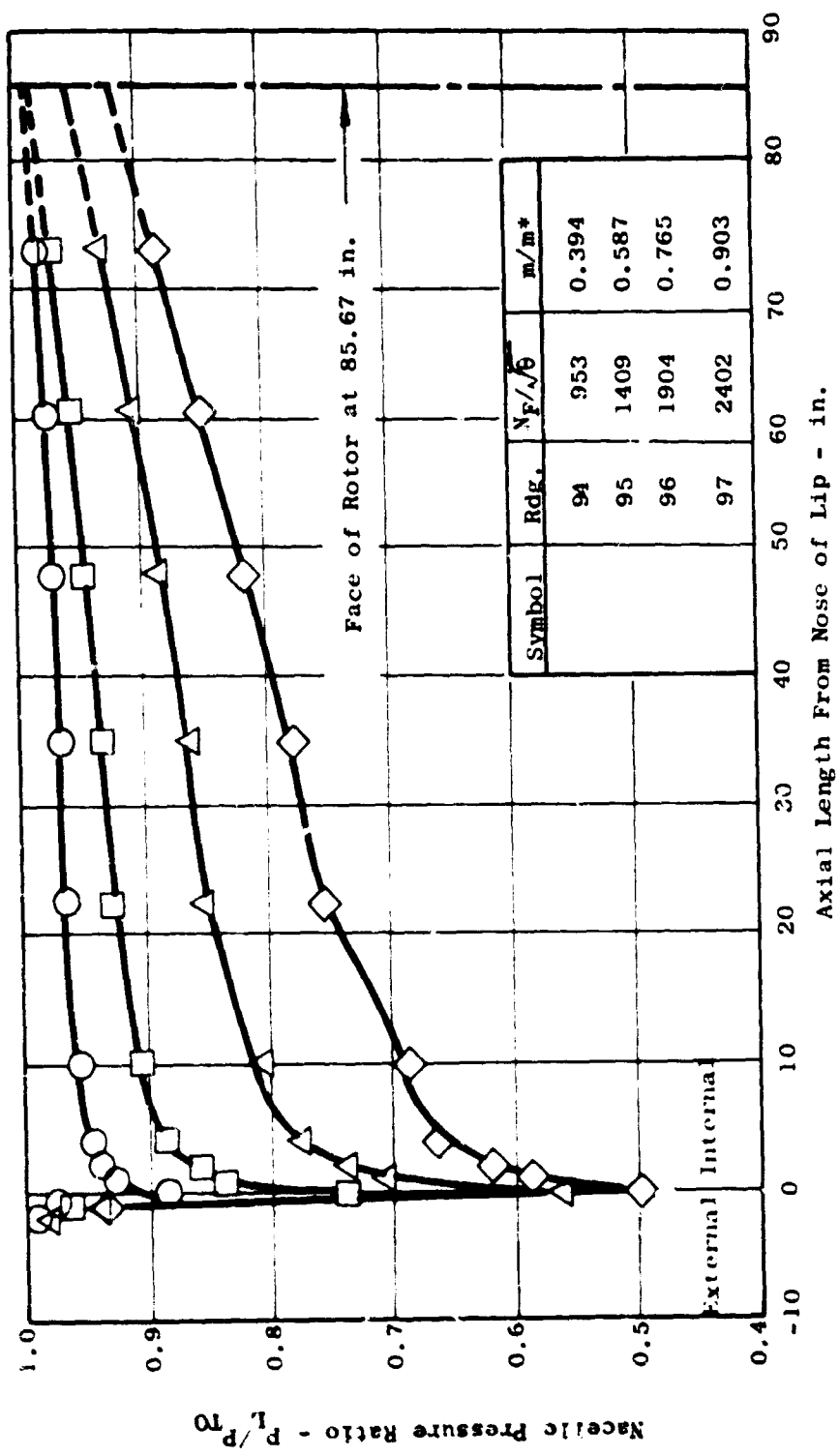


Figure 386 Wall Static Pressure Variation with Axial Length, Original Lip, 90° Position.

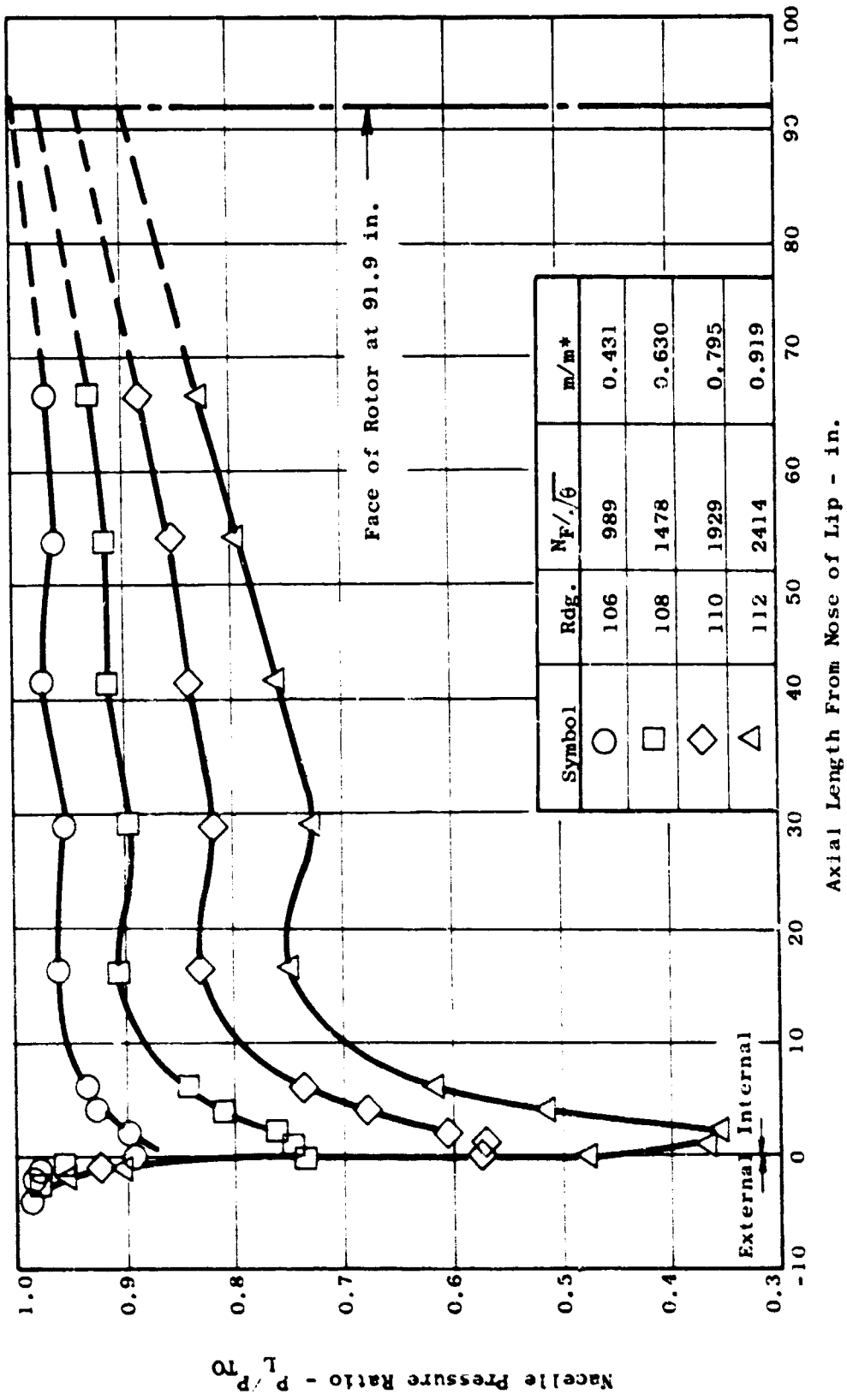


Figure 387 Wall Static Pressure Variation with Axial Length, Lip No. 1, 90° Position.

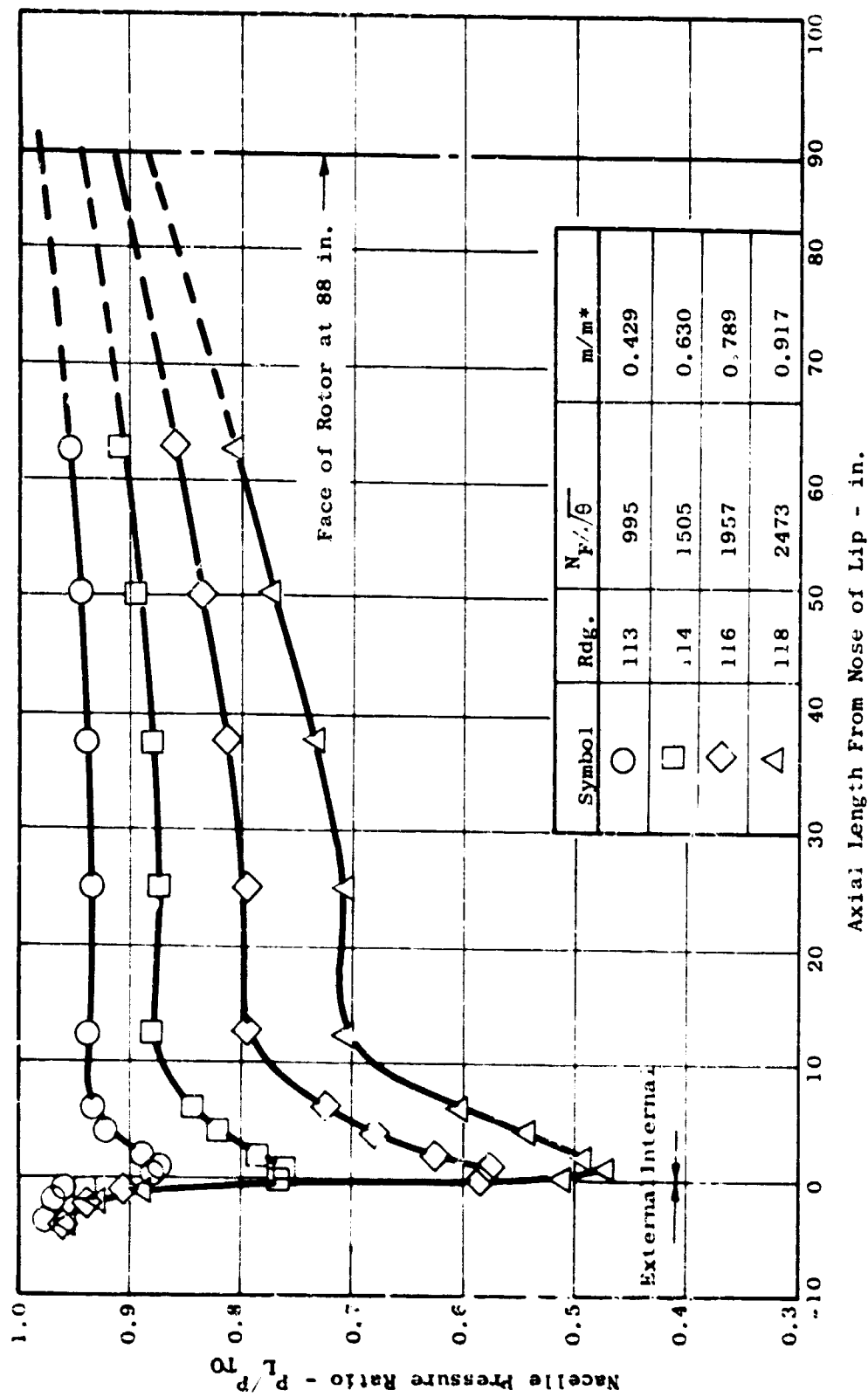


Figure 388 Wall Static Pressure Variation with Axial Length, Lip No. 2, 90° Positive, Versus Length.

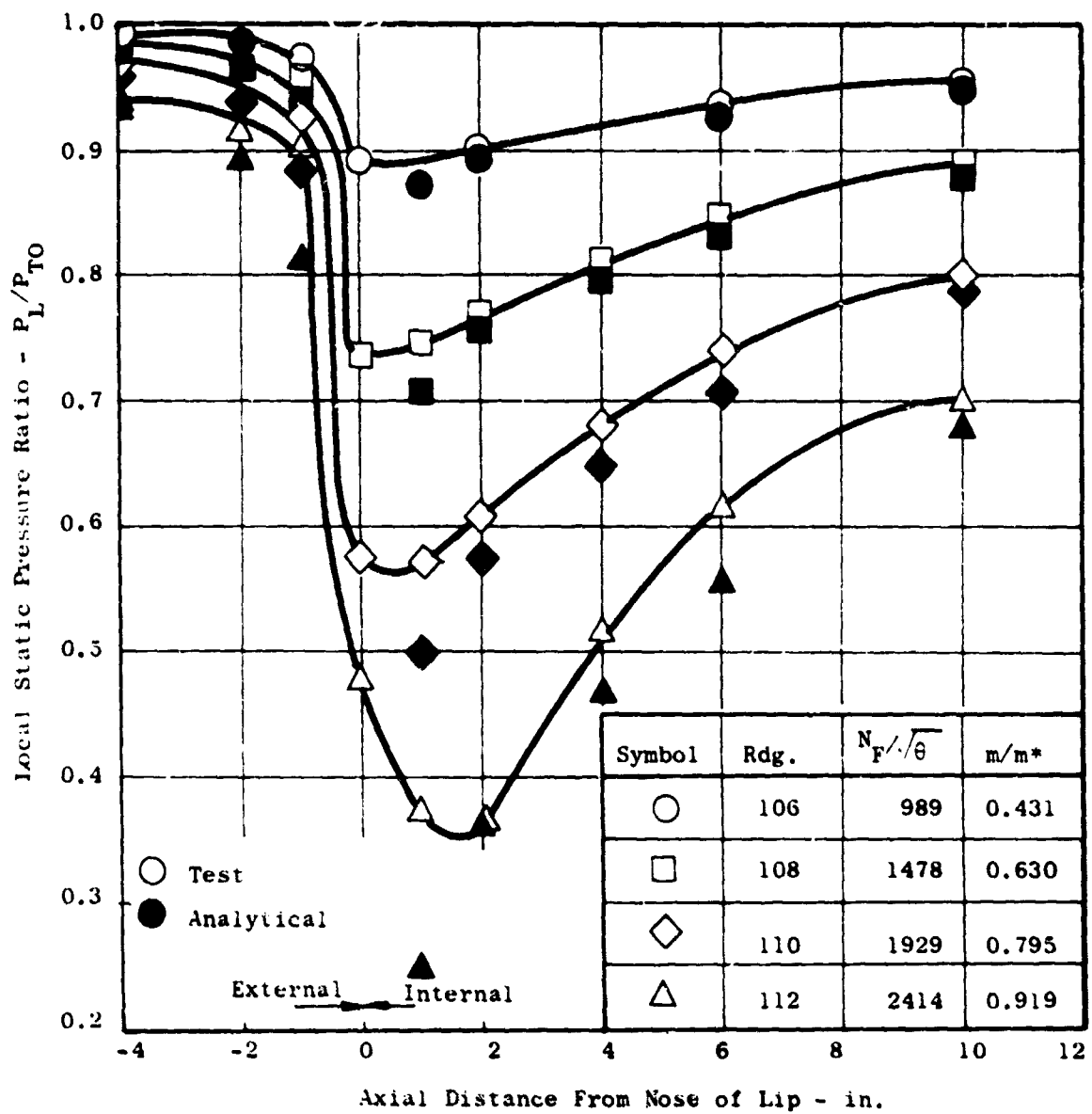


Figure 389 Comparison of Pressure Distribution Versus Length for Lip No. 1 with Centerbody From Test and Analytical Data.

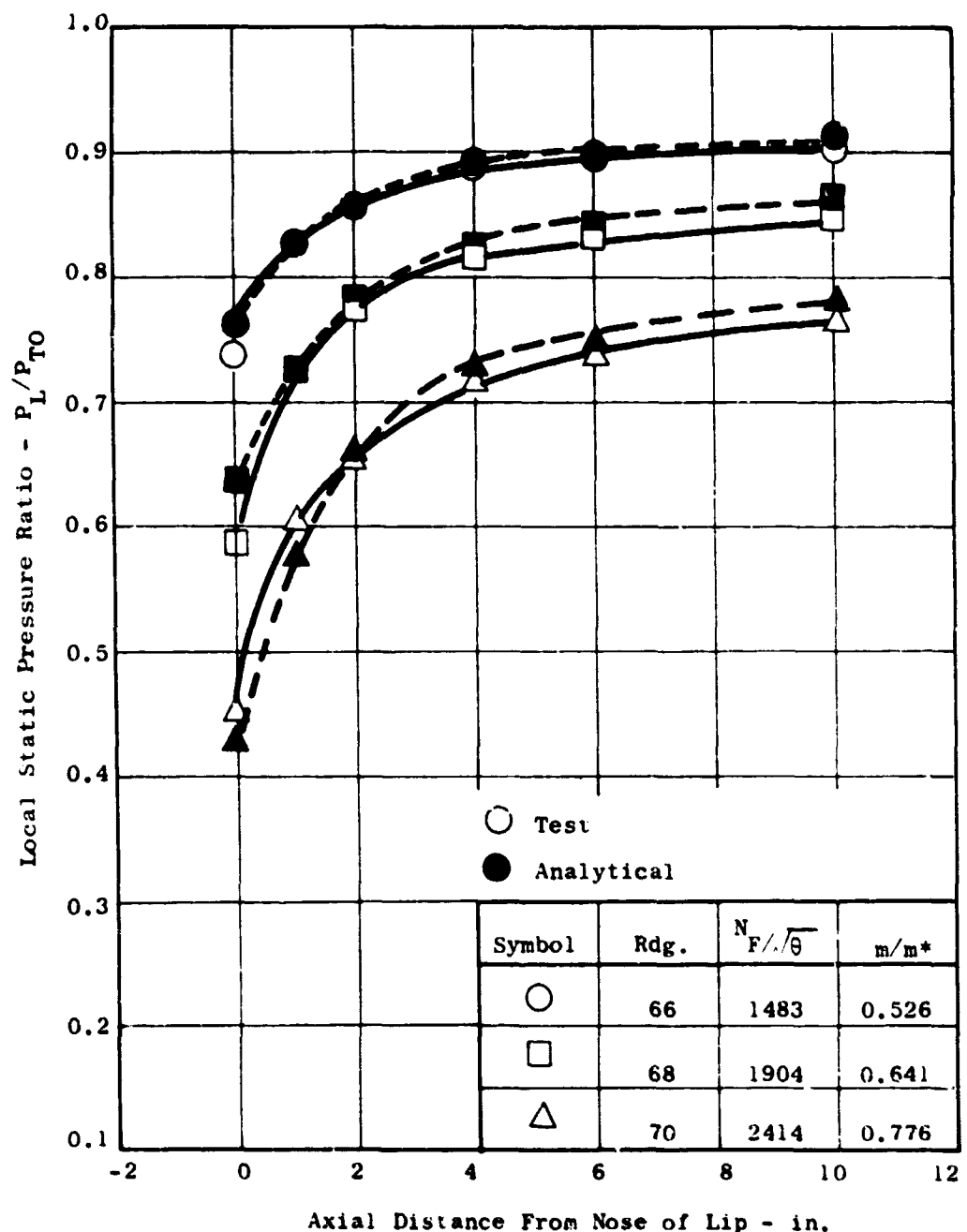


Figure 390 Comparison of Pressure Distributions Versus Length, Original Lip Without Centerbody - Test and Analytical Data.

The effective highlight diameter was based on the flow area, namely  $D_{HL\ eff} = \sqrt{D_{HL}^2 - D_{CB}^2}$ . As can be observed by

comparison of Tables 61 and 58, the insertion of the centerbody increased the contraction ratio by about 4 percent and the diffuser area ratio by about 22 percent. The radius to diameter ratios of the lips was increased by about 10 percent. This effective increase in lip roundness parameter and lip contraction ratio increases the local wall pressures on the lips as shown by the analytical data in Figure 391. The test pressure distribution comparison of the original inlet with and without centerbody (Figure 392) shows the same result. However, when the recovery of the inlet is compared, the improvement in lip wall pressure is over-shadowed by the losses due to the increase in diffuser area ratio and the additional friction losses from the centerbody (Figure 380).

#### Comparison of lip pressure distribution. -

(U) The three test configurations had decreasing highlight to throat area ratios and internal lip roundness parameters in the order of: original lip, lip No. 2 and lip No. 1 as shown in Table 61. It was expected that the performance of the three configurations will be in the same order, namely that the original lip will show the highest local pressures and, therefore, the lowest velocities, followed by lips no. 2 and 1.

(U) The analytically calculated pressure coefficients shown in Figure 393 prove this to be true. Pressure coefficient is defined as  $C_p = (P_L - P_{ref})/q_{ref}$ . Therefore, the higher the negative pressure coefficient, the lower the static local pressure.

(U) Test pressure data for the three configurations with centerbody are shown in Figure 394 for a low and high value of mass flow ratio. These data confirm the analytical results.

#### Comparison of inlet performance. -

(U) Inlet recoveries of the three test configurations are not in line with the analytical and experimental pressure data of the inlet lips. Figures 380 and 381 show inlet performance in the order of: lip No. 1, original lip, and lip No. 2 instead of original lip, lip No. 2 and lip No. 1. It should be pointed out, however, that the maximum spread between the best and the lowest recovery inlet is only about  $\frac{1}{2}$  percent.

(U) From a comparison of the wall pressures versus axial length in Figure 395 and versus area in Figure 396, it can be seen that the pressure distributions in the diffuser are highest for the original J79 80-Inch inlet, followed by model 1 and with lip No. 2 at the lowest.

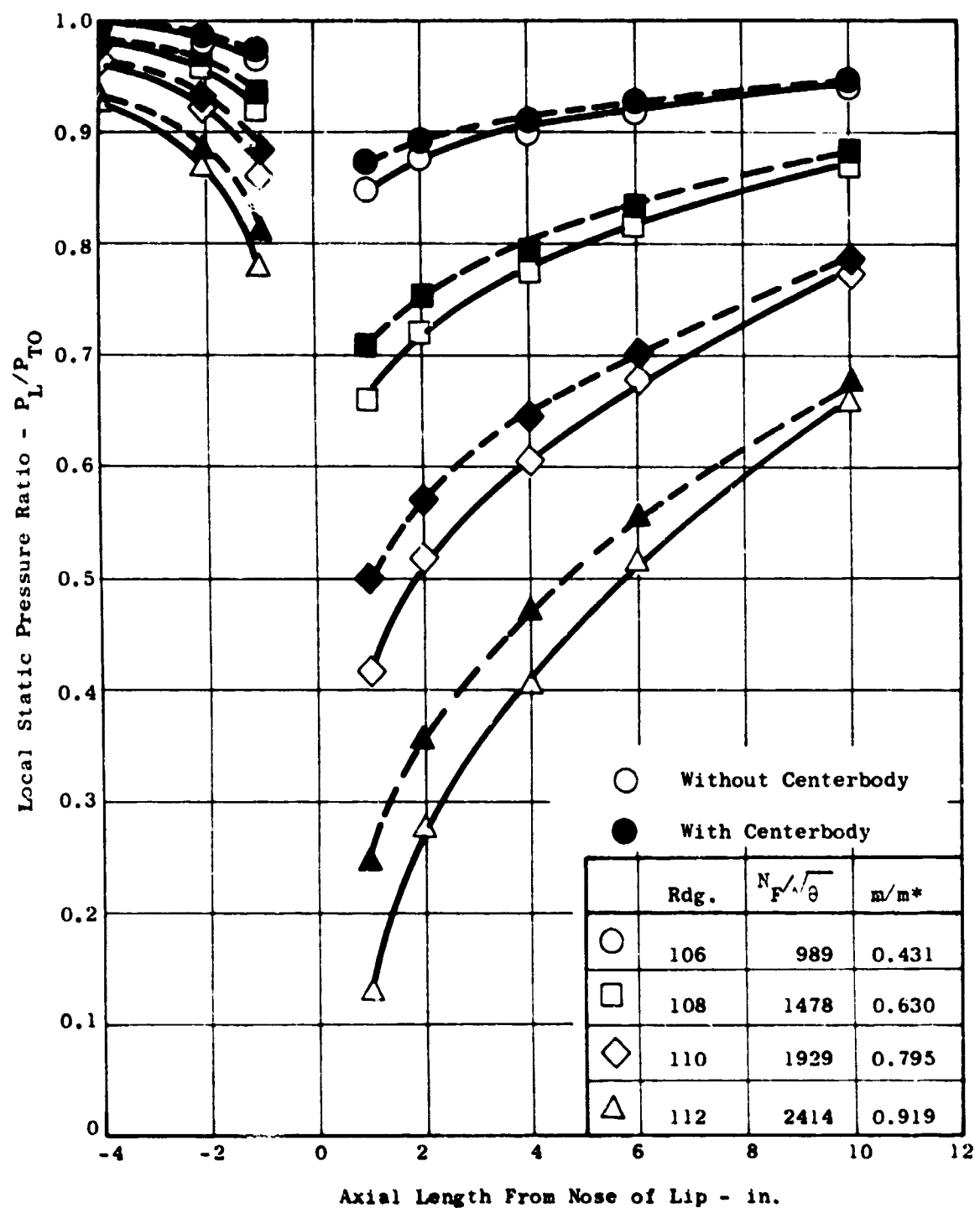


Figure 391 Comparison of Lip Pressure Distribution Versus Length with and Without Centerbody From Analytical Data.

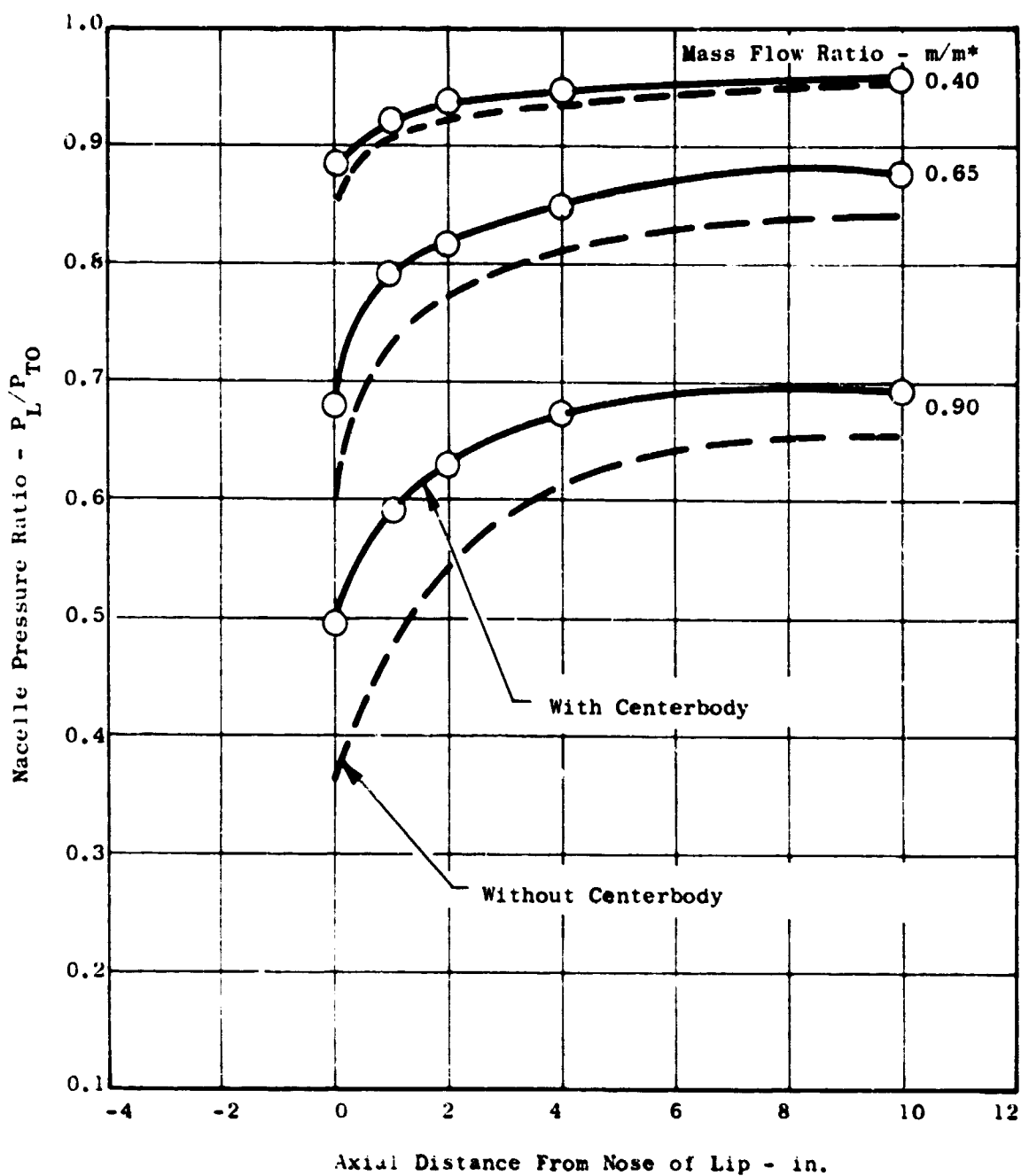


Figure 392 Comparison of Internal Pressure Distribution for Original Lip with and Without Centerbody From Test Data.

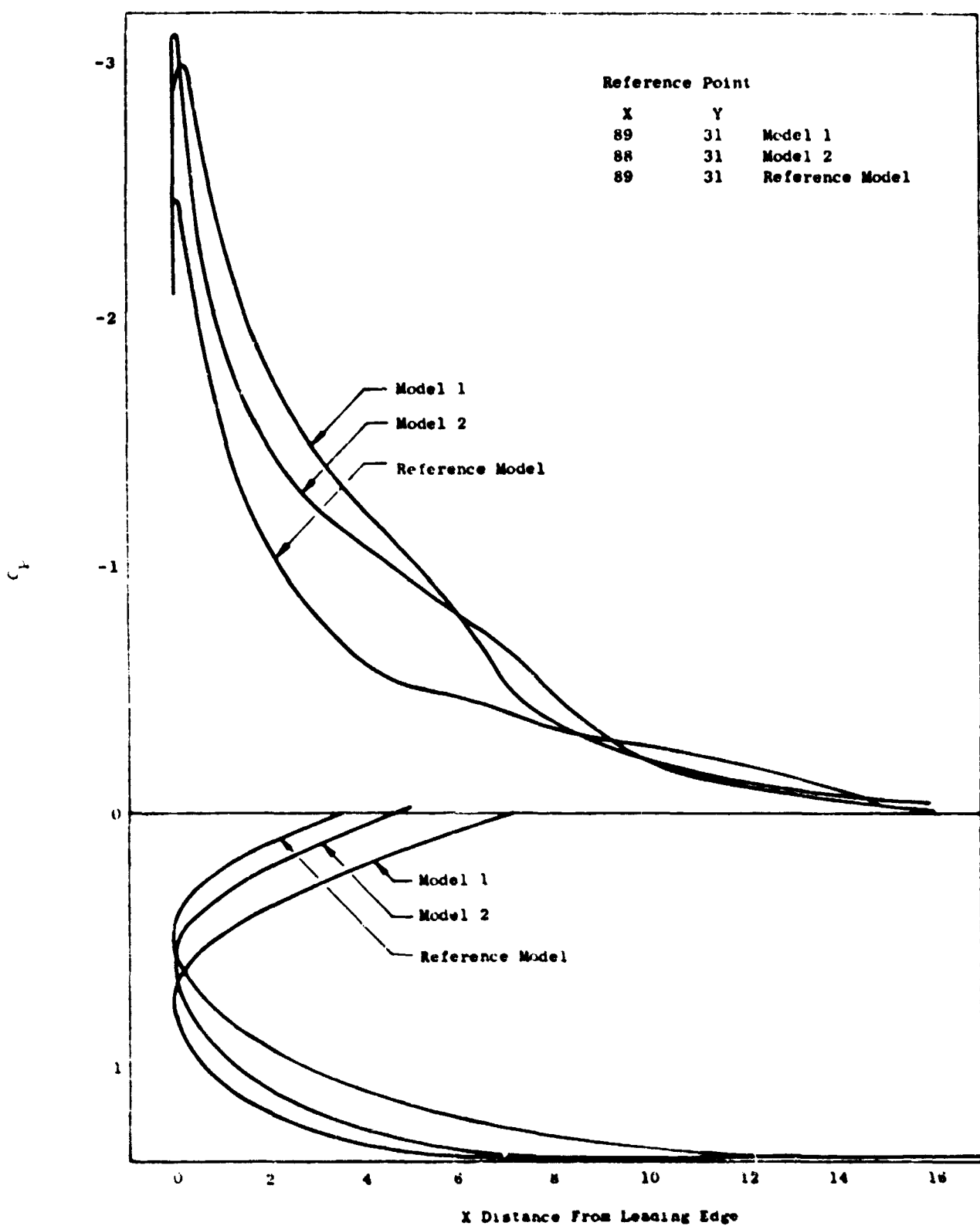


Figure 393 J79 Cruise Fan Nacelle Pressure Coefficient Versus Distance From Leading Edge

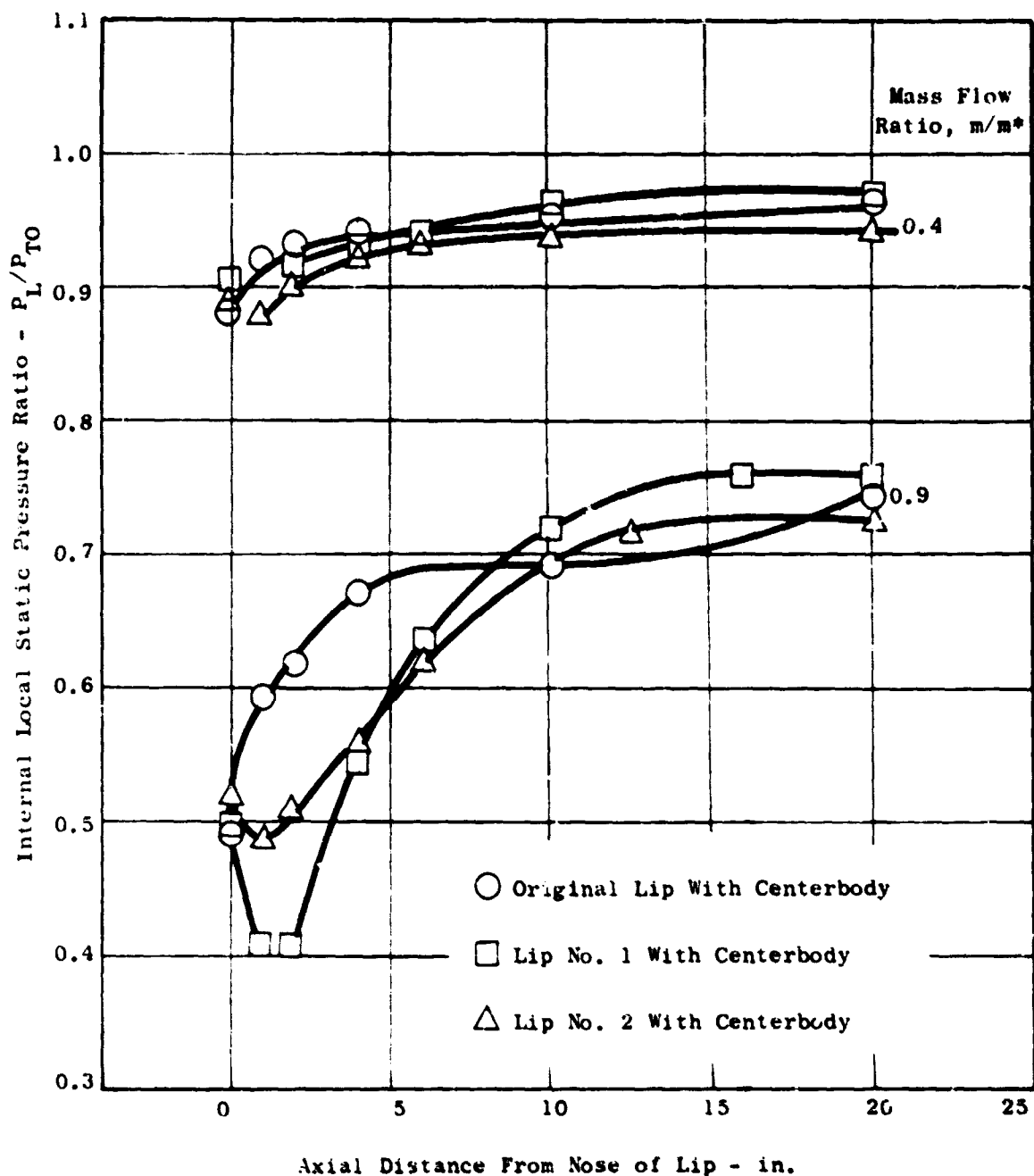


Figure 394 Comparison of Lip Internal Local Pressure Versus Length From Test Data

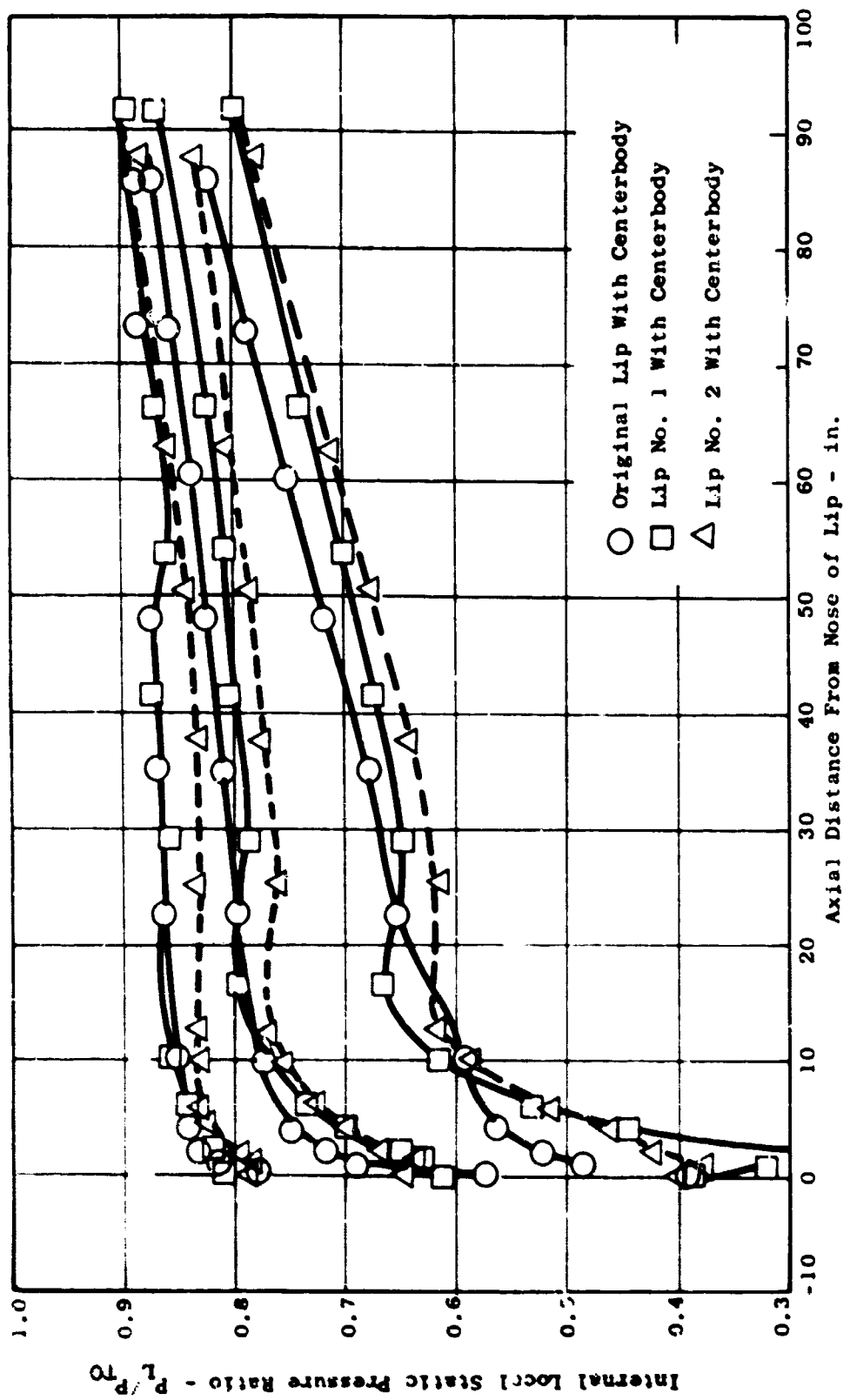


Figure 3:95 Comparison of Internal Pressure Distribution Versus Length

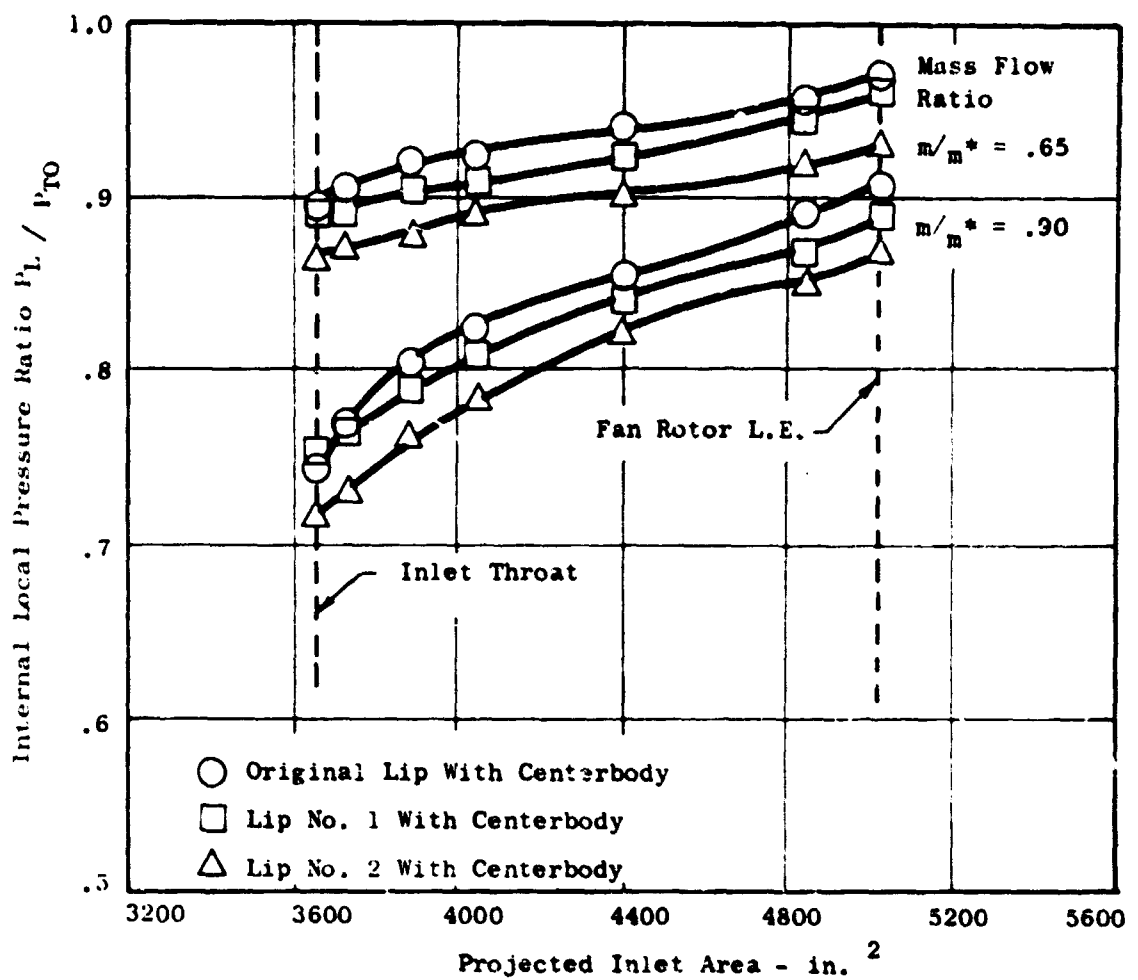


Figure 396 Comparison of Internal Pressure Distribution Versus Projected Inlet Area

This is in contradiction to the expected order of original lip, No. 2 lip and No. 1 lip. A possible explanation for the higher wall pressures for the lip No. 1 configuration in the diffuser could be its especially long constant throat section. The constant area sections vary from 6 inches for the original model to 19 inches for model 1, and model 2 in between with 14 inches (Figure 397). The long constant area sections at the throat have a stabilizing influence on the flow and it is believed that the exceptionally long throat section of the model 1 lip helped to raise the wall pressure level over model 2.

(U) No explanation could be found from the data for the high level of recovery of lip No. 1 which is in contradiction to the test pressure distributions. However, as pointed out before, the spread in recoveries between the three inlets is very small and within the test accuracy. A possible reason for the disagreement could be the accuracy with which it is possible to perform the boundary layer total pressure integration.

#### Comparison to other tests. -

(U) Inlet recovery of the original lip without centerbody is compared to scale model test results of Reference 12 in Figure 398. There is good agreement of the levels of inlet recoveries of the present test with models 2 and 3 of Reference 9. Model 1 of the same data cannot be used for comparison as the flow in this inlet was separated.

#### Conclusions and Recommendations

(U) From the analysis of the presented test data and the analytical calculations, the following is concluded:

1. All three lip models produced high static inlet recoveries ( $T_R = 0.991 - 0.997$  at  $M_{TH} = 0.6$ ). The flow was attached to the inlet wall for all tests. (Reference Figure 380).
2. Test wall pressure distributions for the three lips are in good agreement with predicted analytical pressure distributions. The test pressure data confirm the analytical results that static inlet performance improves with increased internal lip roundness and inlet contraction ratio. (Reference Figures 393 and 394)
3. The insertion of the centerbody increased inlet contraction ratio and lip roundness parameter. The centerbody reduced the local velocities on the inlet lips. (Reference Table 61 and Figures 391 and 392)

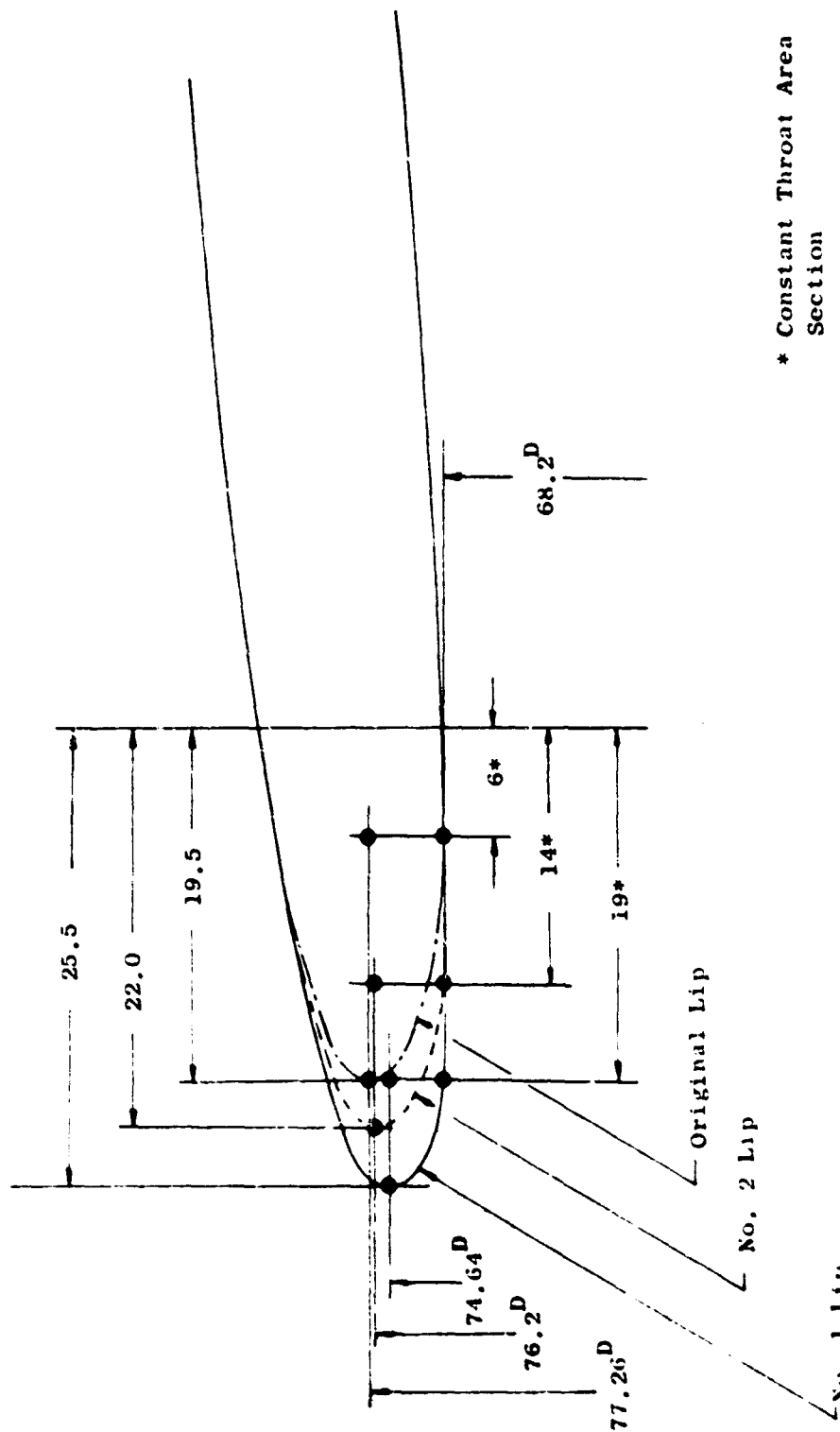


Figure 397 Comparison of Test Configuration Geometry.

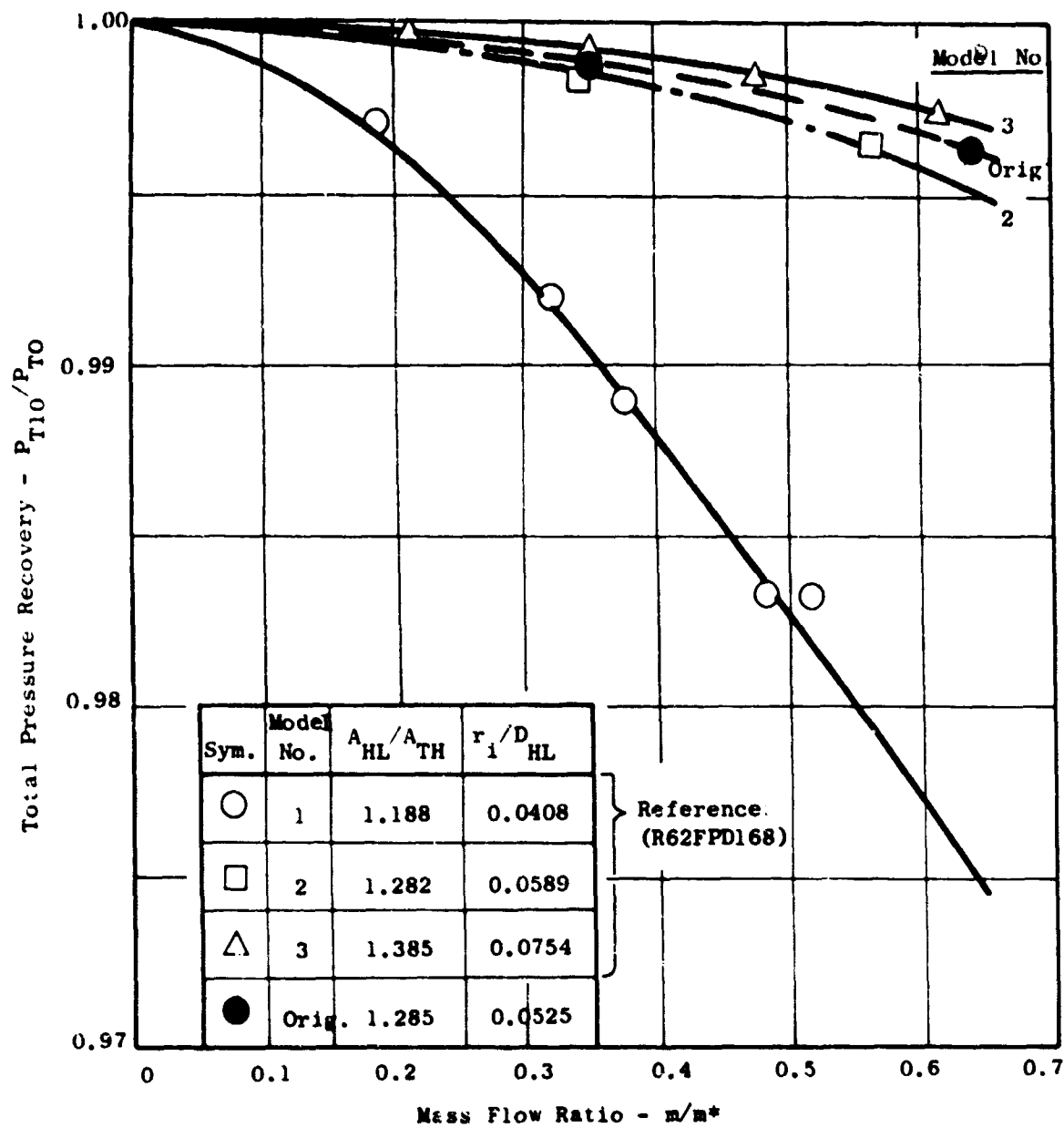


Figure 398 Comparison of Original Inlet Pressure Recovery to Scale Model Test Data - Without Centerbody.

4. Calculated inlet recoveries from test pressure measurements do not agree with the inlet wall pressure distributions. The reason for the disagreement is probably the accuracy with which it is possible to perform the boundary layer total pressure integration. (Reference Figures 380, 381 and 395, 396).
5. Inlet recovery levels are in good agreement with scale model test data. (Reference Figure 398).
6. Incompressible flux plot calculations are a valuable tool for qualitative inlet performance analysis.
7. The predicted static recovery for the L/CF470 inlet at a throat Mach number of 0.6 is  $\frac{\pi}{R} = 0.994$ .

(U) Based on the limited amount of static test data the following recommendations are made for application of these results to the L/CF470 lift/cruise fan inlet and other related programs:

1. Use a low contraction ratio ( $A_{HL}/A_{TH} = 1.2$ ) inlet because it is shorter and lighter, with only slightly lower static performance.
2. Use flux plot calculations for further qualitative evaluation of inlet contour variations.
3. Determine quantitative performance of final inlet configuration from full scale testing.

## SCROLLS

### L/CF470 Scroll Model Test

#### Introduction

(U) This test was intended to verify predicted gas total pressure losses in the cruise fan turbine scroll and to define any design improvements which could improve its performance. Testing was done on a fiberglass scale model using cold air. The scale factor was selected so that both Reynolds number and Mach number would simulate full scale conditions with hot turbine gas.

#### Tests

(U) Figure 399 shows a sketch of the scroll model. Figure 400 is a photograph of the assembled model with the inlet bellmouth and supporting structure attached. Figure 401 is a photograph of the disassembled model. In use, cold air enters the inlet bellmouth from a large 42 inch diameter pipe which serves as a plenum. After flowing through the scroll the air is exhausted into the test cell room through a series of circular rods which serve to simulate the turbine nozzle blockage and distribute the air properly about the scroll circumference. Plexiglass windows were incorporated in several locations in the model so that the flow patterns could be visualized by means of tufts. Other instrumentation was provided to measure inlet total pressure and static pressure in the cylindrical portion of the bellmouth. Total pressure and flow angle measurements were made with a radial traversing probe which could be moved to a number of circumferential locations.

(U) Testing was done with a total to ambient pressure ratio of about 2.3 to insure that choked flow existed at the scroll exit plane between the rods simulating nozzle vanes. Under these conditions the flow Mach number at the scroll inlet was measured to be .31 as opposed to a design value of .30.

(U) The experimentally determined average total pressure loss coefficient was 0.373 based on the average dynamic head at the scroll inlet. This compares very favorably with a predicted total pressure loss of 0.66. Distribution of the pressure loss about the scroll exit annulus is shown in Figure 402 which shows the radial averaged loss coefficient versus angular location about the exit annulus. Radial pressure loss profiles are not shown but were quite flat in all cases except for normal wall boundary layers. These pressure traverses were taken just upstream of the flow restriction bars in the exit annulus so that their loss is not included.

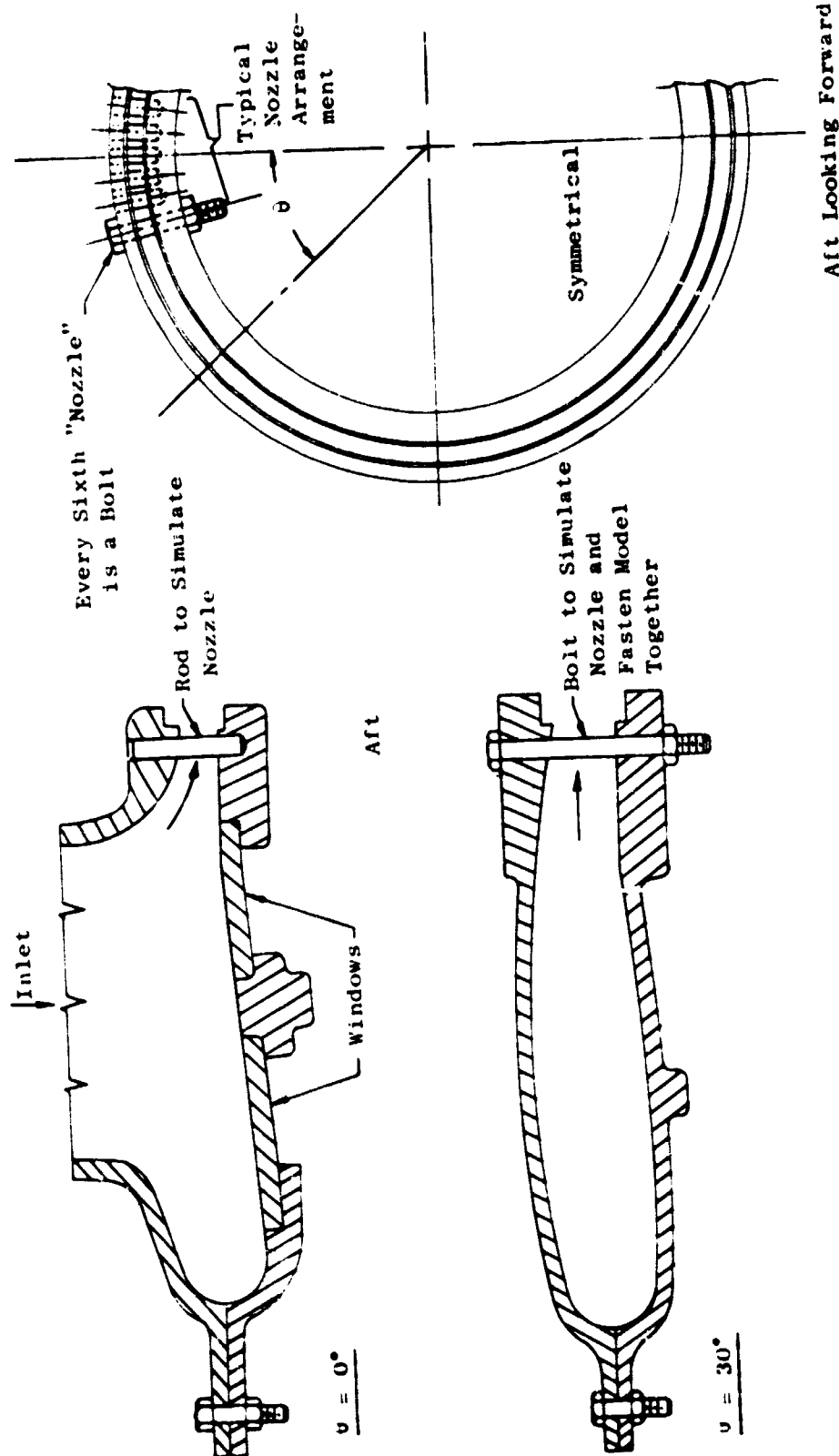
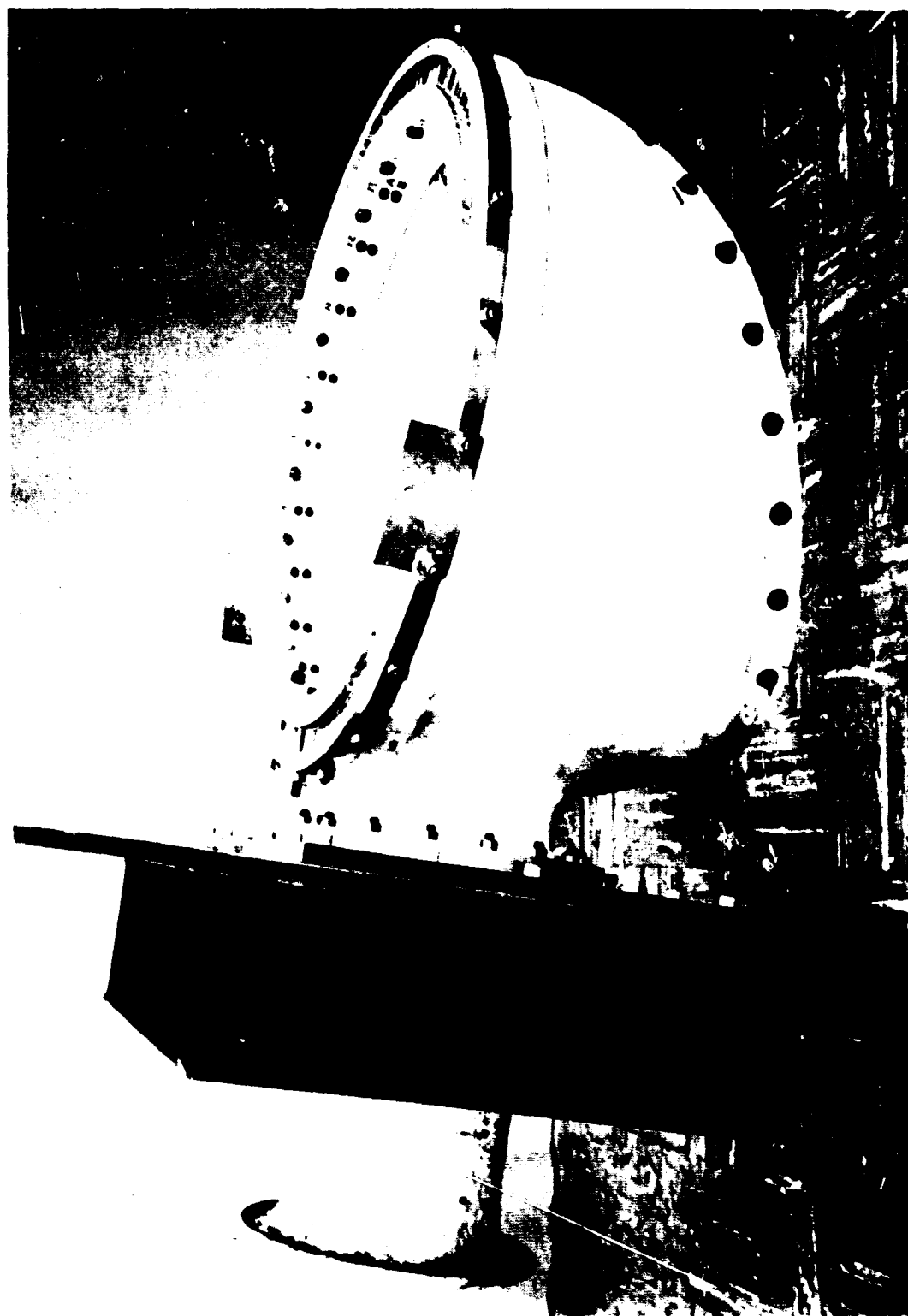


Figure 399 Sketch of Litt/Cruise Scroll Model Showing Cross-Sections at 0 and 30 Degrees From the Centerline that Passes Through the Inlet.

Figure 400 Lift/Cruise Fan Scroll Test Model



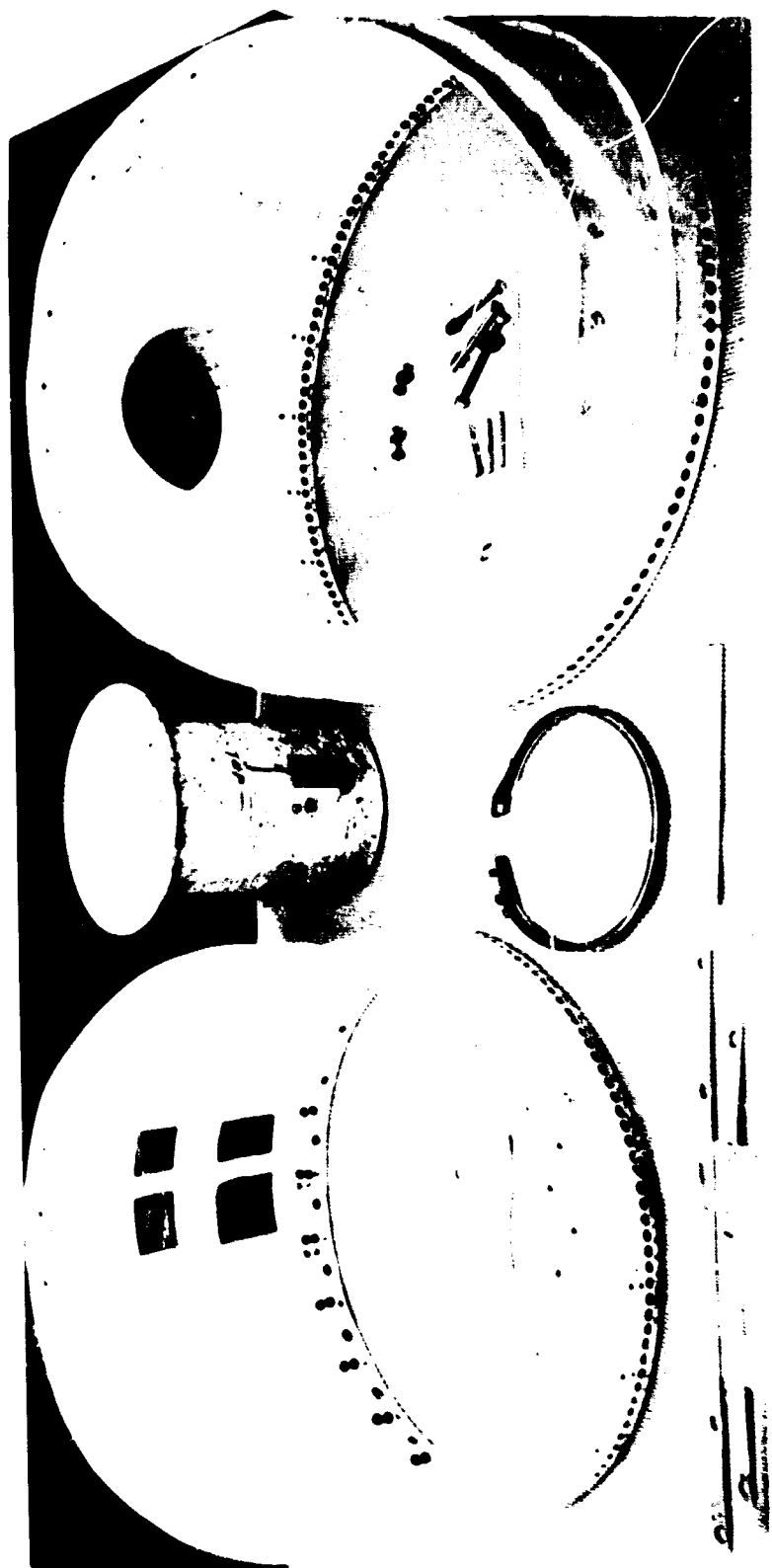


Figure 401 Disassembled List/Cruise Fan Scroll Model

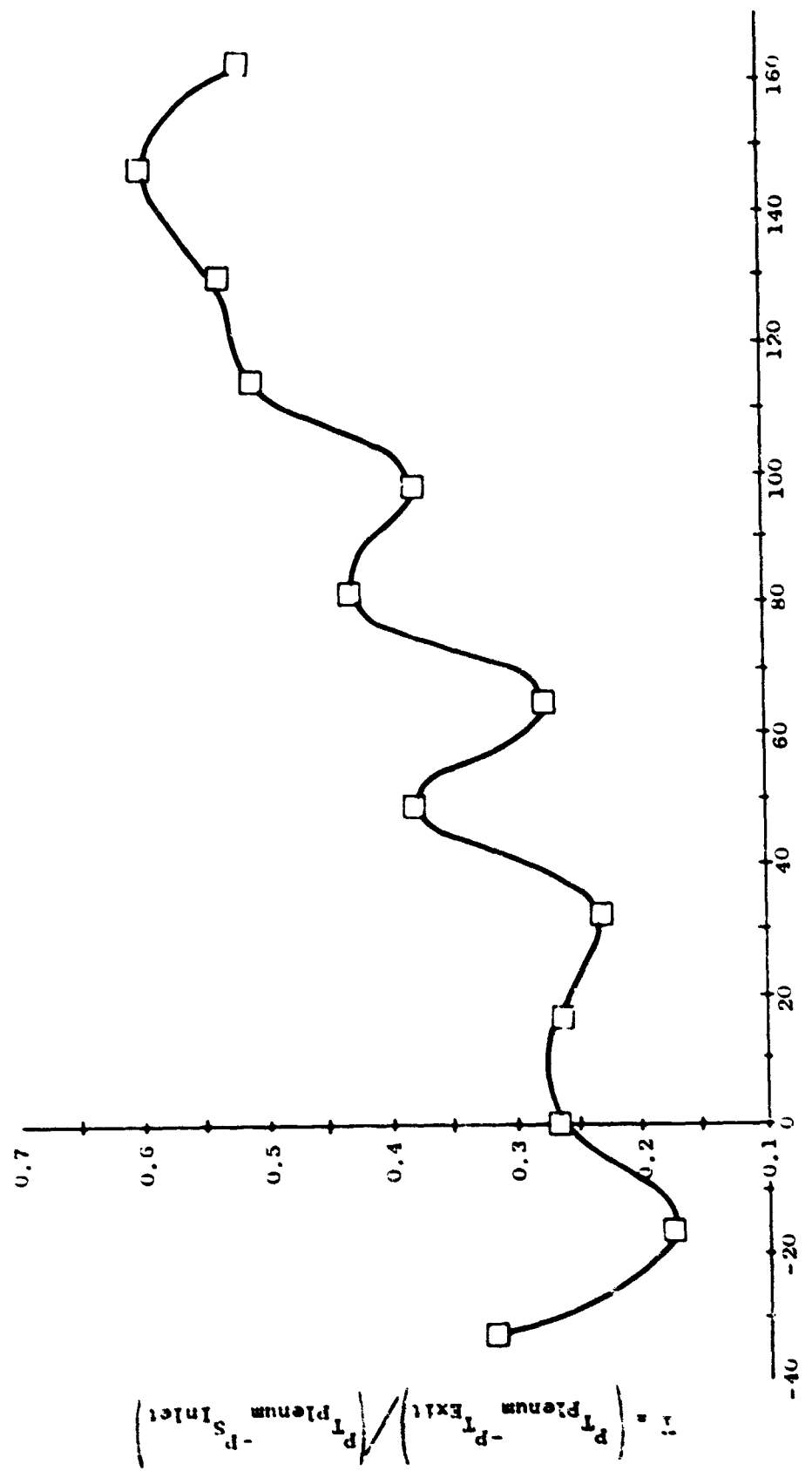


Figure 4i.2 L/CF470 scroll Model Total Pressure Loss Coefficient Versus Angular Location on Annulus

(U) Flow angle distribution about the exit annulus is shown in Figure 403. These angles were also measured upstream of the flow restriction bars and should not have been greatly affected by them. Flow angles varied only slightly in the radial direction except in the boundary layers.

(U) Figures 404, 405 & 406 show photographs of the internal surface of the model and of the flow visualization tufts. Observation of the tufts during running indicated that the flow separated from the scroll inlet fillet radius over the forward quadrant of the inlet. This can also be seen in Figure 404 from the markings left on the model wall by the tufts. The numbers on these photographs indicate angles of the pencil lines drawn to bisect the turf markings.

#### Conclusions and Recommendations

(U) Some improvement in scroll performance might be achieved by inserting a flow splitter just inside the forward inlet radius where some flow separation was observed. On the other hand if it is necessary to use a corrugated liner configuration, as described in the Preliminary Mechanical Design section, additional losses will be incurred. It is recommended then that further testing be done on these configurations if the cruise fan is to be built.

#### LF475 Scroll Model Test

##### Model Design

(U) A fiberglass half model of the LF475 turbine scroll has been designed and is shown in Figure 407. This model will have a bellmouth attached to the inlet and can be tested in the same test facility as the LCF470 scroll model. This model represents only one half of the actual scroll since the other half would be a mirror image of this one and the two halves are aerodynamically separate. One important feature included in the scroll model is the array of structural struts located just upstream of the nozzle vanes in the gooseneck. These struts are expected to be necessary in the full scale scroll and it may be necessary to experimentally determine their optimum orientation angles for minimum total pressure loss. Plexiglass windows are incorporated into the model at several locations to observe flow pattern by means of tufts.

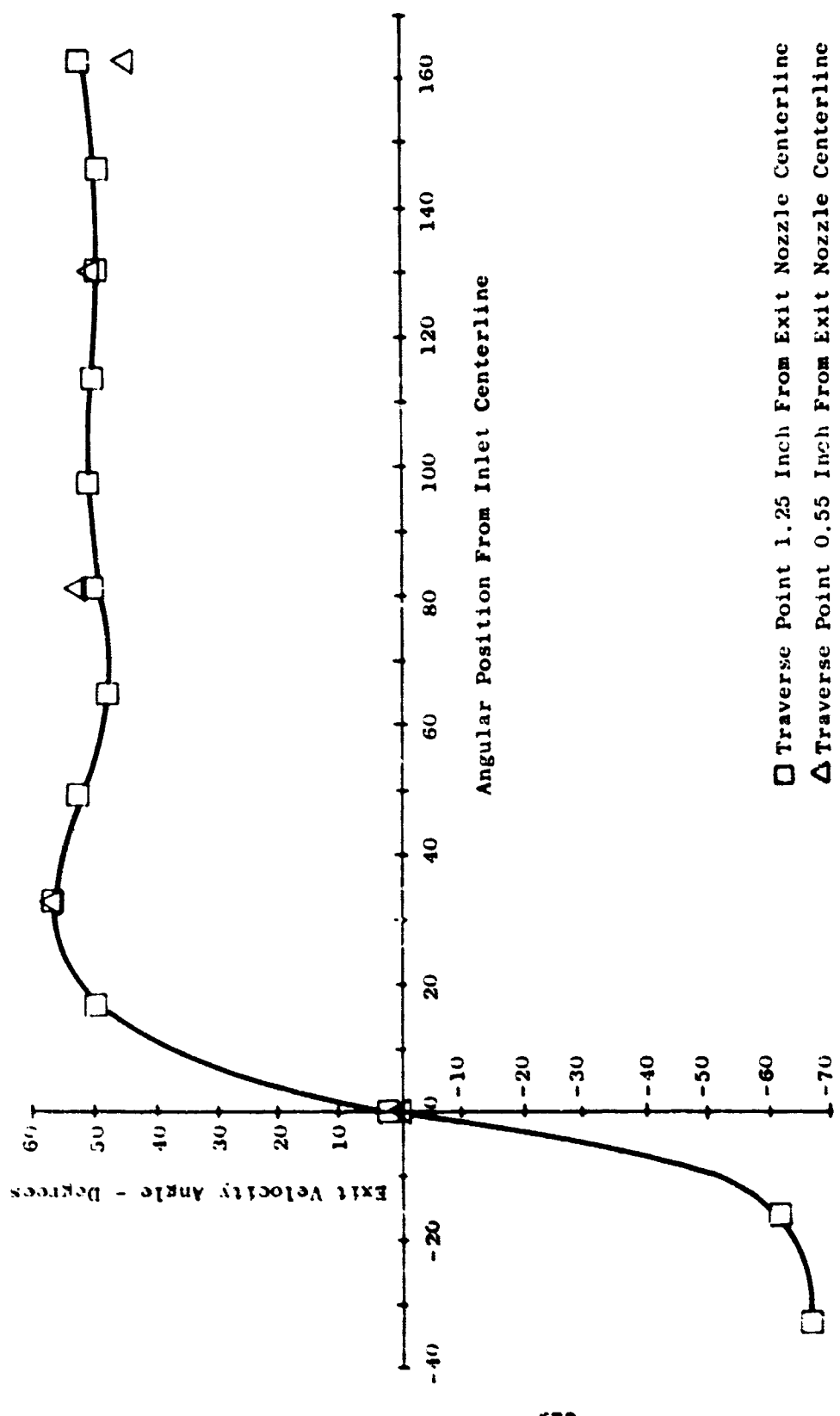
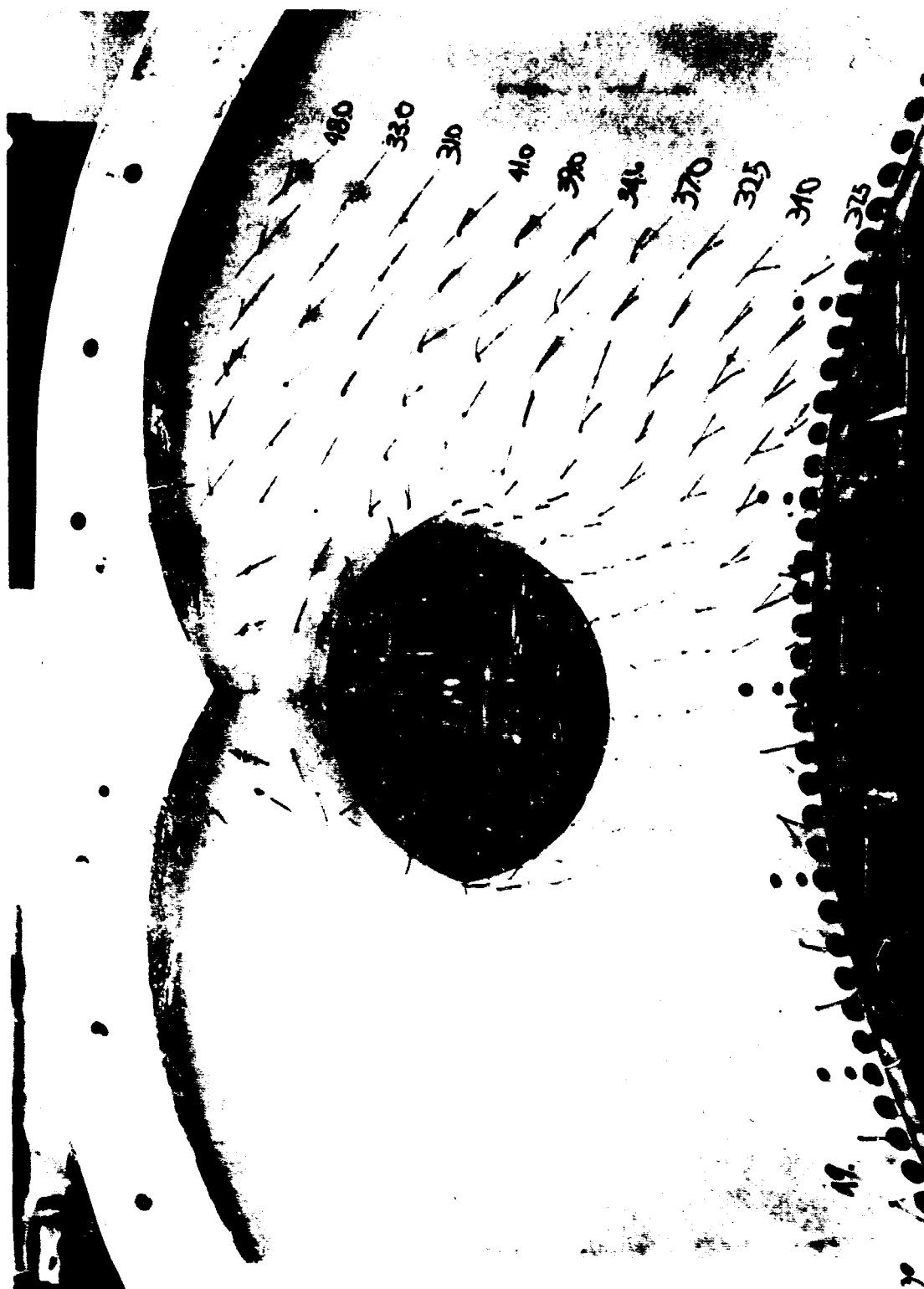


Figure 403 Lift/Cruise Fan scroll scale Model



Picture 404 Lift/Cruise Fan Scroll Model Inlet Region

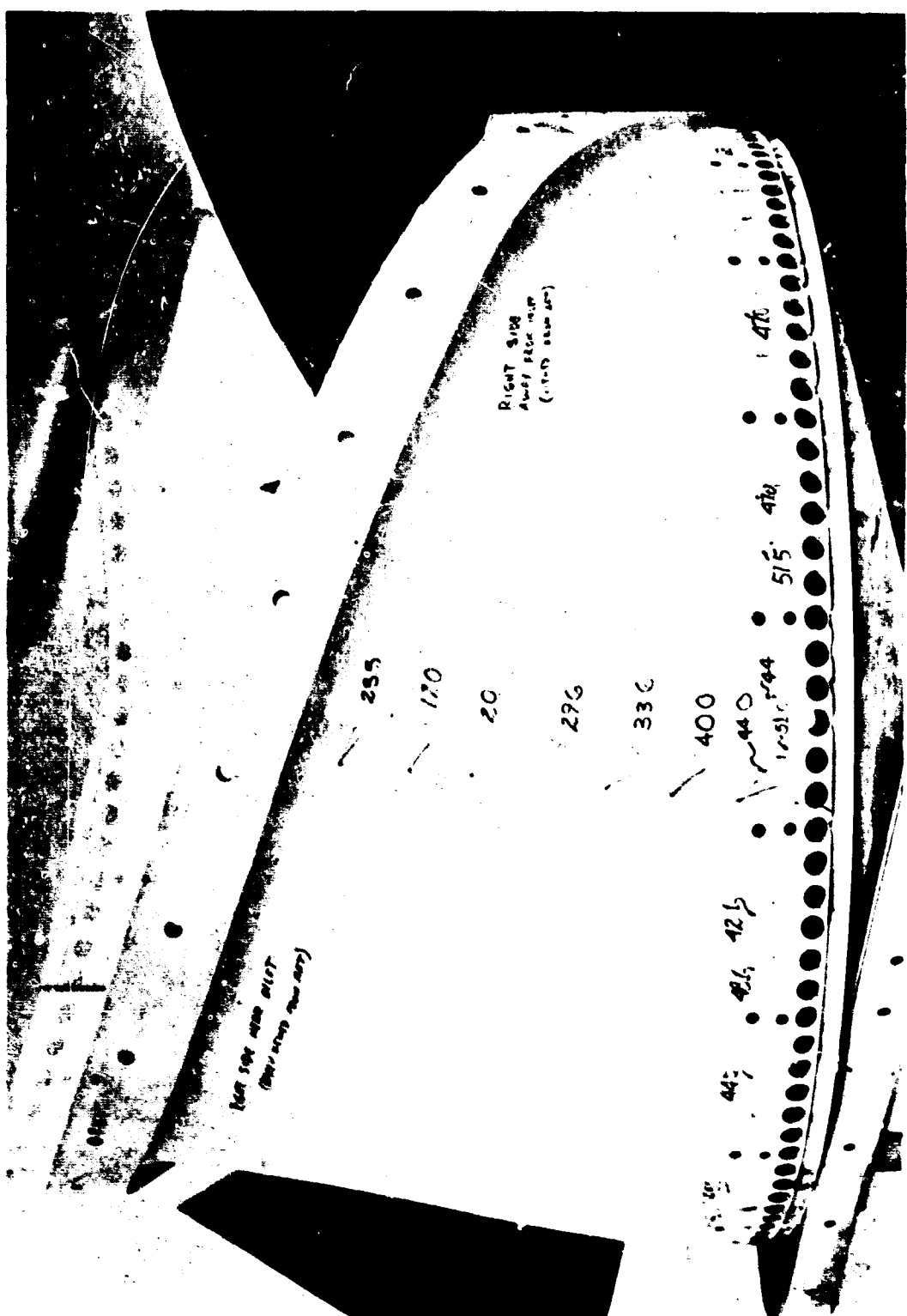


Figure 405 Lift/Cruise Fan Scroll Model Inner Surface 90 Degrees From Inlet

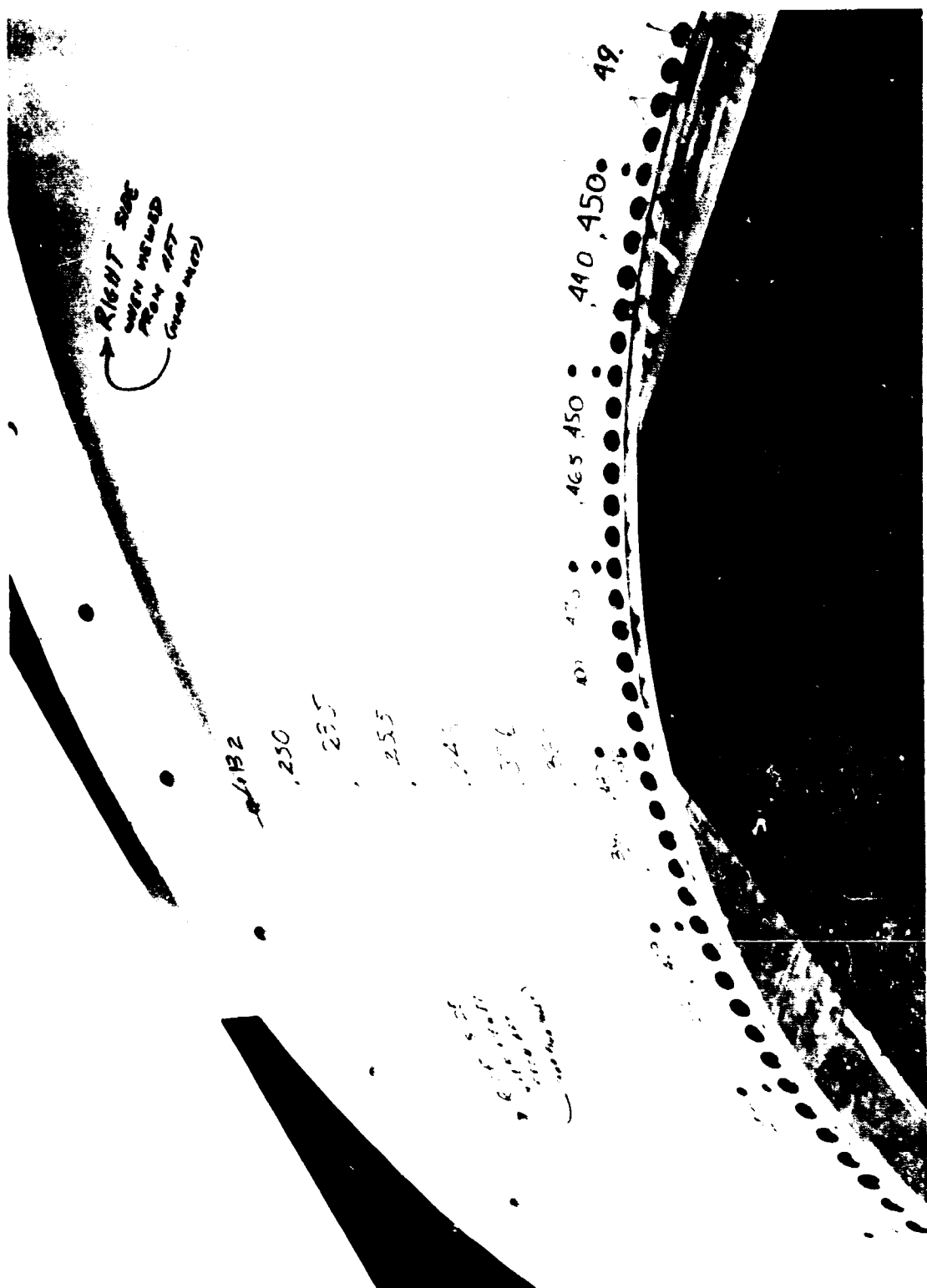


Figure 406 Lift/Cruise Fan Scroll Model Outer Surface 90 Degrees From Inlet

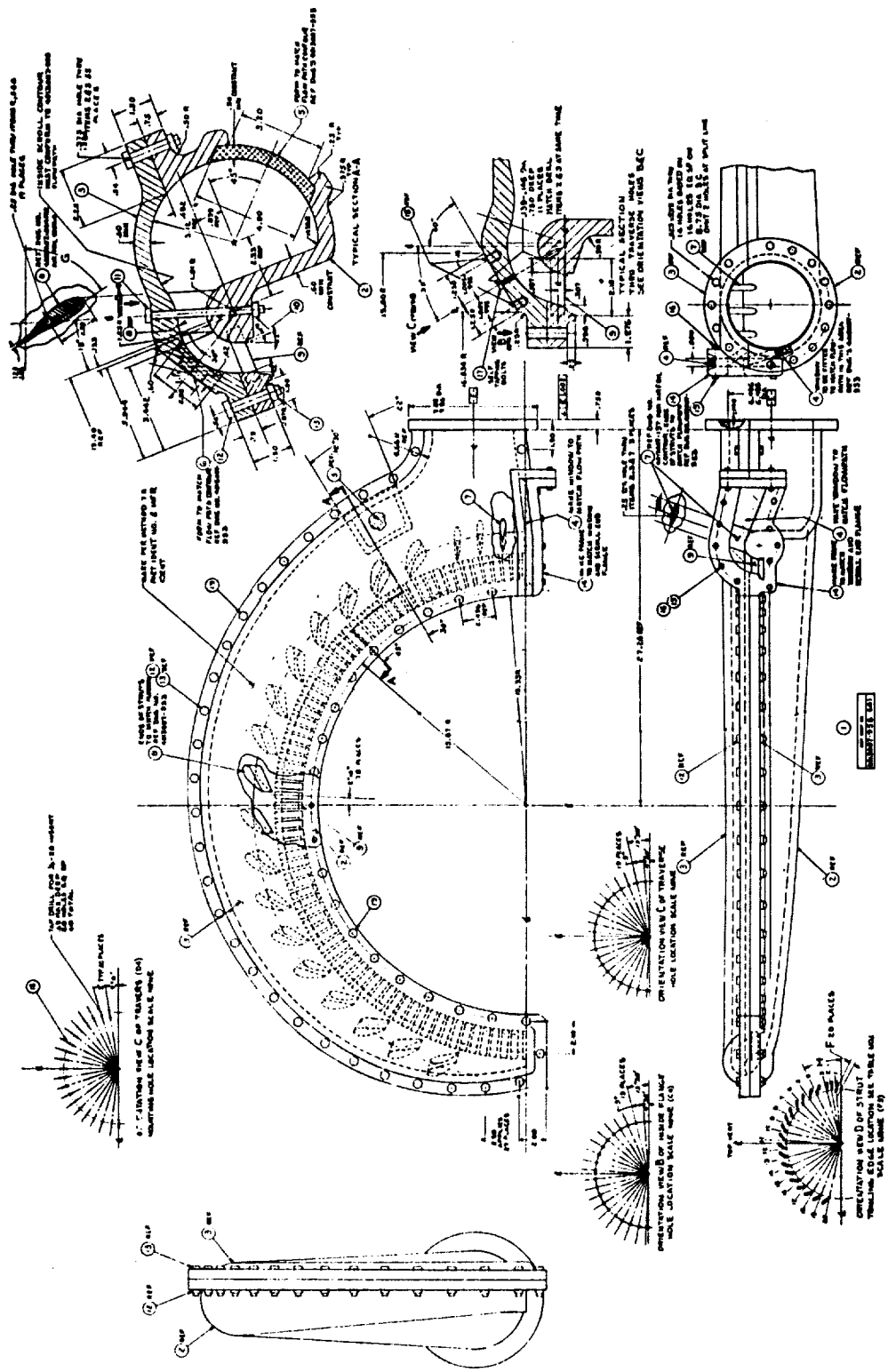


Figure 407 Scroll Model Assembly Lift Fan 475 No. 2

## SEALS AND BEARINGS

### Fan Blade Tip Seal Design

(U) During the early design phases of the advanced fan system, it was assumed that large improvements in fan tip seal performance would be required in order for the fan to achieve objective performance. While conducting numerous related technology programs it immediately became apparent that a simple single tooth honeycomb seal was an effective fan tip seal especially when cost and complexity were considered.

(U) Typical results, primarily obtained during full-scale and scale-model programs have been presented in Section VA

A water table test of inlet configuration was also performed to determine optimum inlet contours for lift-fan systems. The results of this two dimensional program verified that a simple circular arc bellmouth contour as used in previous fan designs is susceptible to separation and is further aggravated when subjected to simulated fan tip seal leakage. Conversely, an elliptical contoured bellmouth proved to be much less prone to separation. Simulated seal leakage also appeared to have no detrimental effect on performance. This result was simply one more factor that led to a simple seal design instead of other more elaborate seal designs intended to reduce or eliminate leakage from the turbine into the fan streams.

(U) The LF2 tests directed towards investigating an improved seal system using a rubbing (zero clearance arrangement) verified that the results concerning simple circular arc inlets is indeed true. The LF2 utilizes a circular arc bellmouth, and even with the rubbing seal, no significant performance improvement was observed. Objective performance of this fan system could only be obtained with the help of an inlet circular vane system.

(U) Conversely, the MF415 fan system has an elliptical contoured bellmouth. For this case, large quantities of leakage air and large seal gaps did not produce any significant deficiency in fan tip performance.

(U) With all of these results tending to indicate one conclusion, the additional information that could have been gained from any two dimensional model program was not required in the selection and design of the fan tip seal system used in the LF475 fan.

### High DN Grease Bearing Test

#### Introduction

(U) Proposed advanced lift fans utilize grease packed bearings. Because the advanced fan demonstrator design objectives required operation beyond state-of-art experience, a program was established to demonstrate high DN greased packed bearing operation. This program would evaluate types of high speed greases, grease seal configurations, greased bearing fatigue life, and effect of bearing geometry upon heat generation.

## Discussion

### Grease survey.-

(U) Recently, grease manufactures have developed new greases for high speed and high temperature application. One of the tests developed for this program was to lubricate a bearing with five (5) grams of grease and run the bearing at 25000 RPM until failure. Failure would occur when the grease was depleted (see Table 60) Texaco Unitemp 500 had the longest time before failure. This was later verified on full scale tests.

### Power loss.-

(U) Power loss (heat generation) has always been difficult to determine for bearings. Power loss of grease lubricated compared to oil lubricated bearings is shown in Figure 408. It can be seen that grease lubrication causes approximately 50% more power loss than oil lubrication. This is primarily due to the higher viscosity of grease compared to oil.

### Grease life..

(U) Endurance testing for this program has been done in the full-scale high DN greased bearing facility. The test bearings in this facility are a 95mm(219 size) ball bearing and a 110mm(1922size) roller bearing (see Figure 409). These grease lubricated test bearings are outer race rotated and are tested at speeds and loads typical of future lift fans such as the LF475.

(U) Two primary objectives of this program were to determine the grease life of a 30 gram charge of grease and to demonstrate adequate grease sealing. The base line grease charge (30 grams) is shown in Figure 410 using the grease seals shown in Figure 411. This seal configuration works well at .6DN, but at higher speeds, grease leakage was evident. In order to eliminate grease leakage, teflon fan rubbing seals were incorporated (see Figure 412) which eliminated grease leakage and increased the grease charge lip at .6DN by 100% (See Figure 412).

## Conclusions and Recommendations

(U) Grease lubrication is a feasible method of lubricating LF475 lift fan rotor bearings. Regrease cycles every 50 - 100 hours should provide adequate lubrication providing the grease retention system is similar to Figure 412. Unitemp 500 seems to be a most adequate grease for present needs.

(U) These areas still need continued investigation:

1. Race way curvature fit effect upon grease flow and heat generation.
2. Outer race rotation power loss data for heat transfer analysis.

TABLE 60  
BEARING FAILURE TESTS

Grease	Hour to failure	Failure Type
Texaco Unitemp 500	197	Cage, Wear, Balls
Dupont Krytox	93	Cage, Wear, Balls
Shell Cyprina 3	85	Cage, Wear
Esso Andox B.R.	40	Cage, Wear, Balls
Texaco Tg 4700	20	Cage, Wear, Balls
Dow Corning Flurcilsilicone	20	Seizure
Luhriplate	20	Seizure

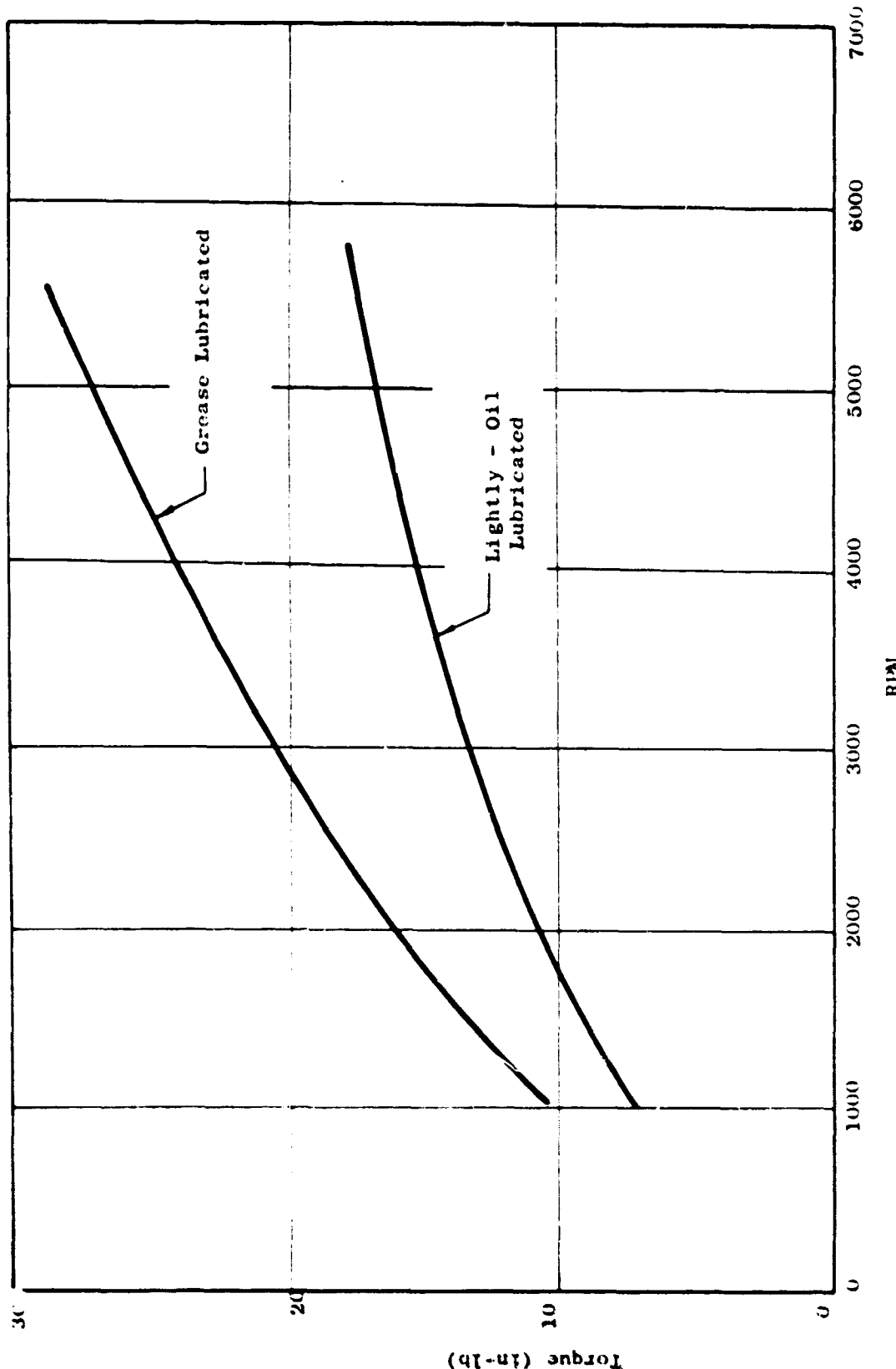


Figure 408 Bearing Power Loss Ref GE TM68-550

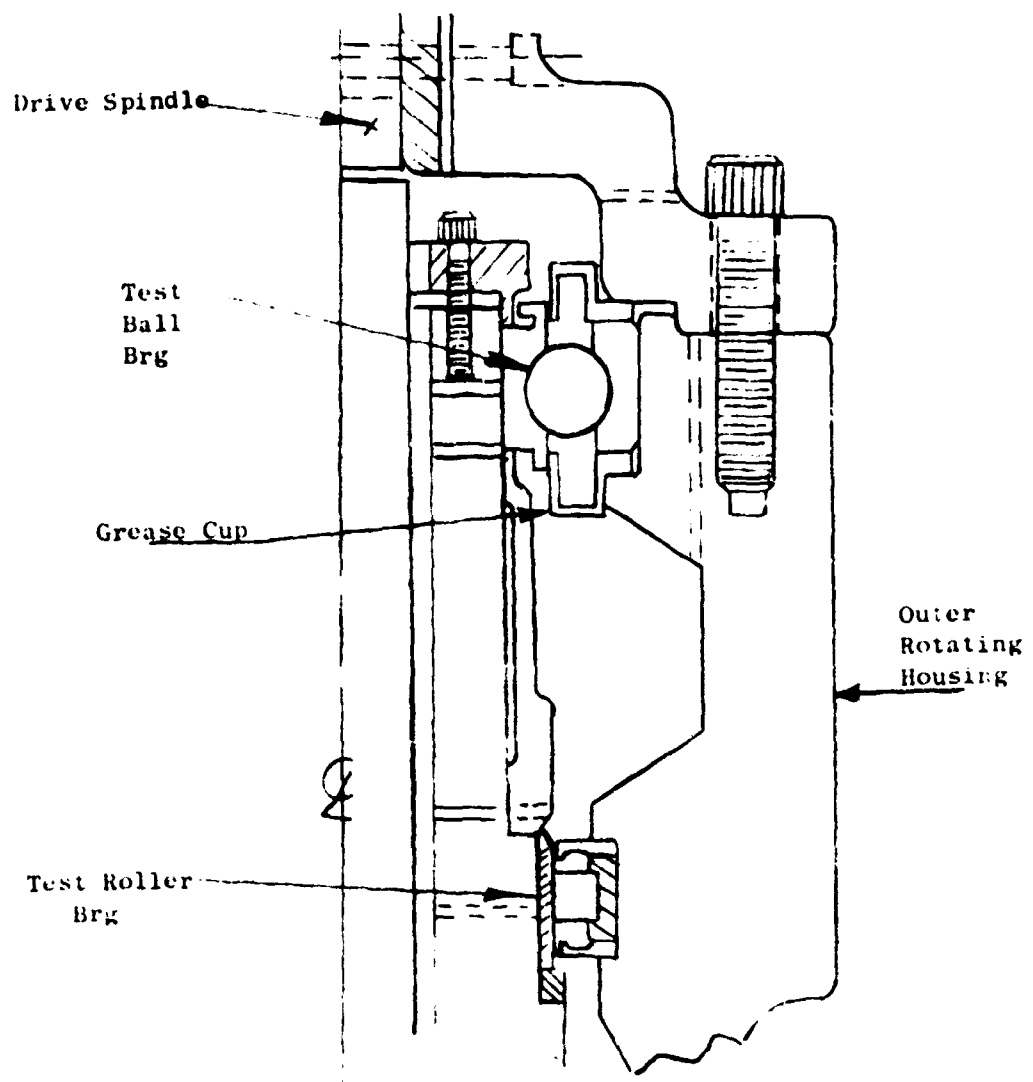


Figure 409 High DN Greased Bearing Facility

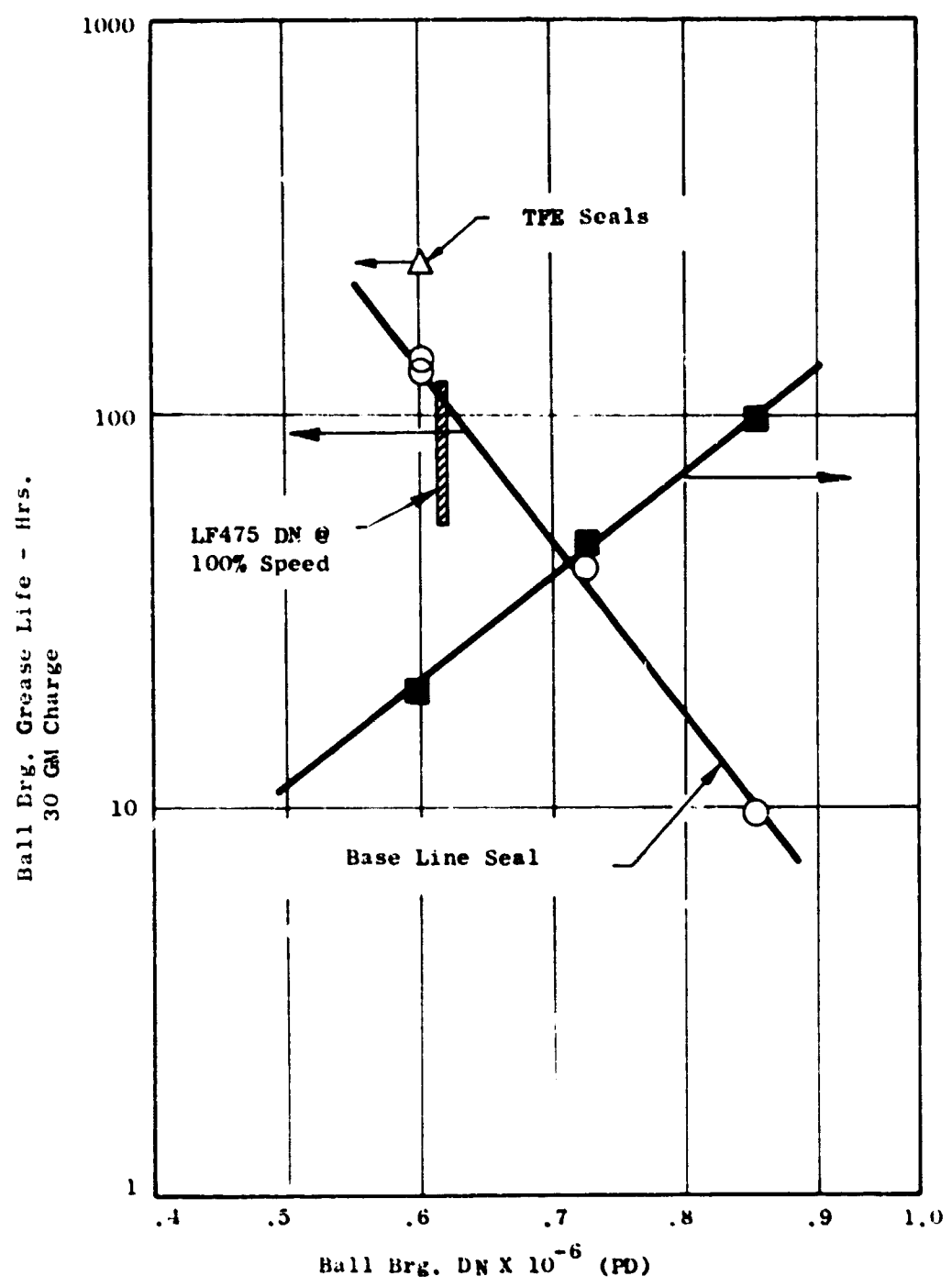


Figure 410 Grease Life and Brg. Temp Versus Brg. Speed

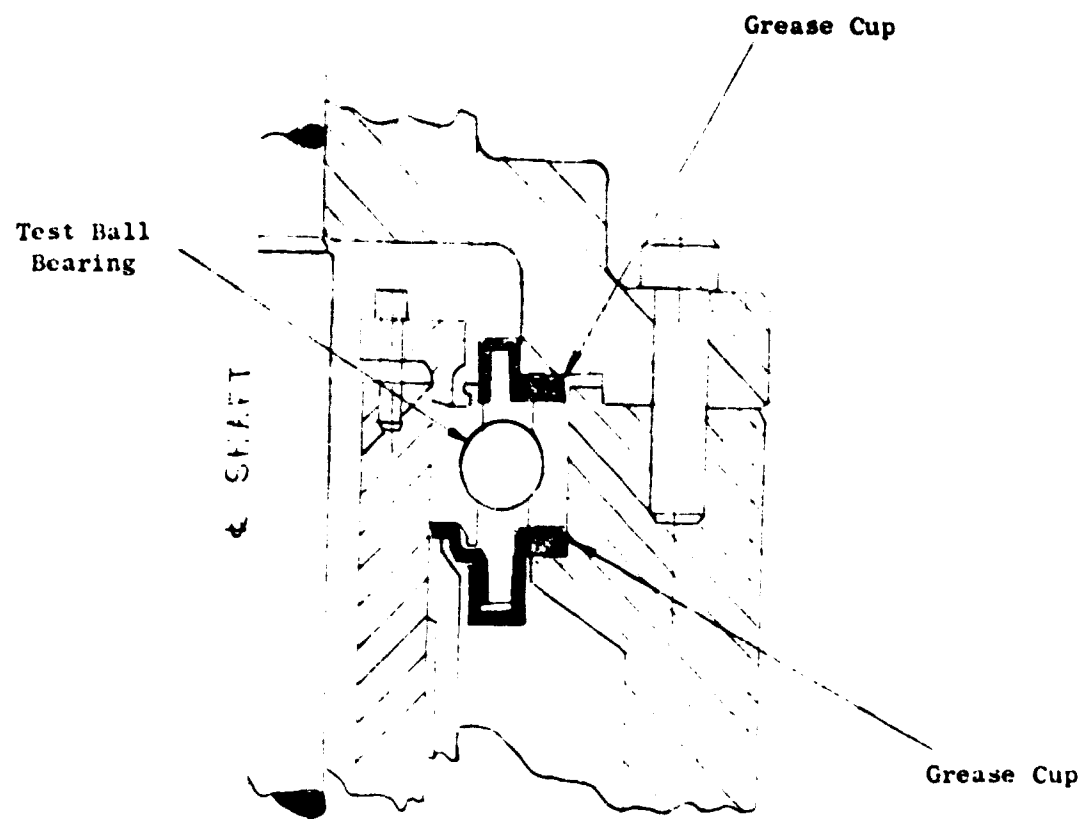


Figure 411 Test Ball Bearings Showing Grease Cups

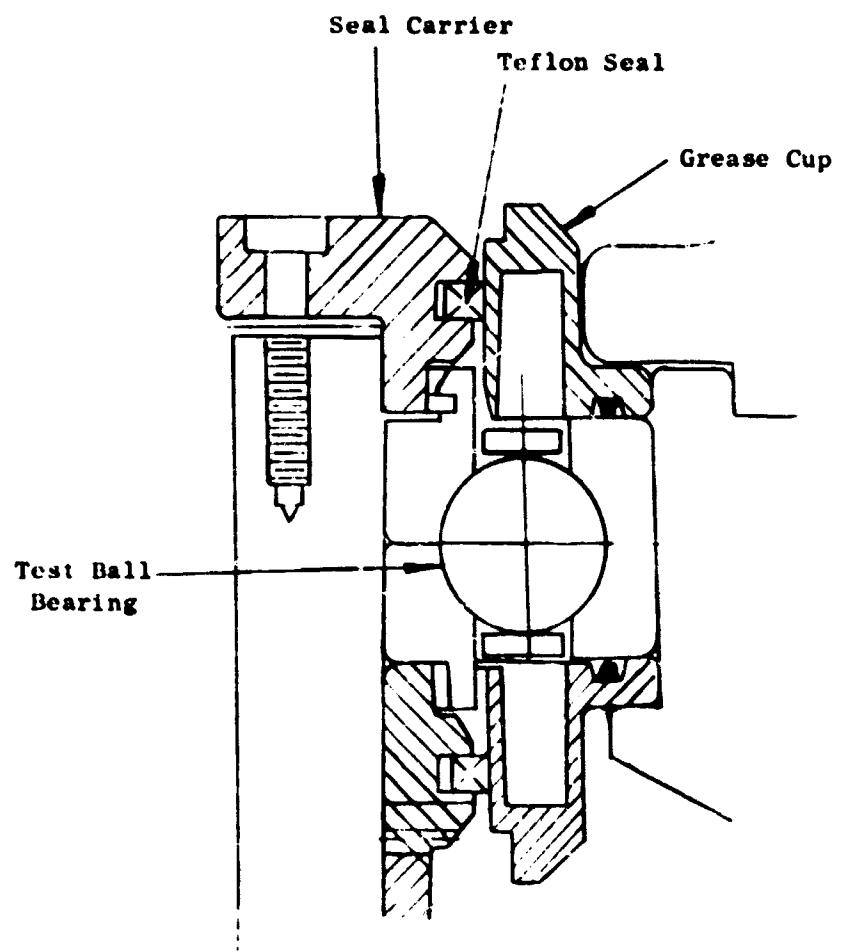


Figure 412 Test Ball Bearing Including Teflon Seal

## THRUST VECTORING

### L/CF470 Lift/Cruise Fan

#### Thrust Reverser Deflector Systems

##### Introduction.-

(U) The incorporation of a tip turbine cruise fan on STOL vehicles requires the capability of thrust reversal to satisfy the general systems requirements during landing. If an augmented flap system is used, further versatility of thrust deflection is required.

(U) Deflection of the engine exhaust up into wing flap systems substantially improves the aircrafts' lift. Deflection downward during ground roll shortens the required take off runway length.

##### Mechanical design comparisons.-

(U) Six methods of aerodynamically obtaining jet deflection of  $\pm 20$  degrees and thrust reversal with the same system were considered.

###### 1. Movable louvers in the exit of a plug nozzle cascade reverser:

This design uses two 140 degree sectors of cascades in the cowl of the existing plug nozzle cruise fan as illustrated in Figure 413, and a set of directional vanes at the exhaust plane. The actuation system, mounted in the plug, is capable of swinging the louver  $\pm 90$  degrees to close off the flow or through any angle between 0 and 90 degrees for thrust deflection. When the vanes are turned 90 degrees a separate hydraulic system is actuated which pulls back the cover doors around the cowl disclosing the reverser cascades.

###### 2. Eyelid deflector with a telescoping target reverser:

The eyelid deflector-reverser system is stowed in the aft end of the thick cowl as shown in Figure 414. For deflection, an actuator mounted in the cowl translates the eyelid aft and simultaneously a separate levered arrangement causes the deflector to rotate down into the exhaust stream.

For reversal the eyelids are again translated aft but, both lever systems are actuated causing both deflectors to rotate down into the exhaust. Further actuation permits the interlocking target reverser to telescope outward closing off the exit plane and reversing the flow.

###### 3. Fantail plug deflector with a cascade reverser:

As shown in Figure 415, deflection is obtained by turning one-half the exhaust with a fan type flap system. The flaps encompass 180 degrees of the plug and are actuated by two hydraulic cylinders located in the plug. Thrust reversal is obtained by actuating 360 degrees of the plug flap system and translating the cowl with a separate cylinder located in the cowl. When the

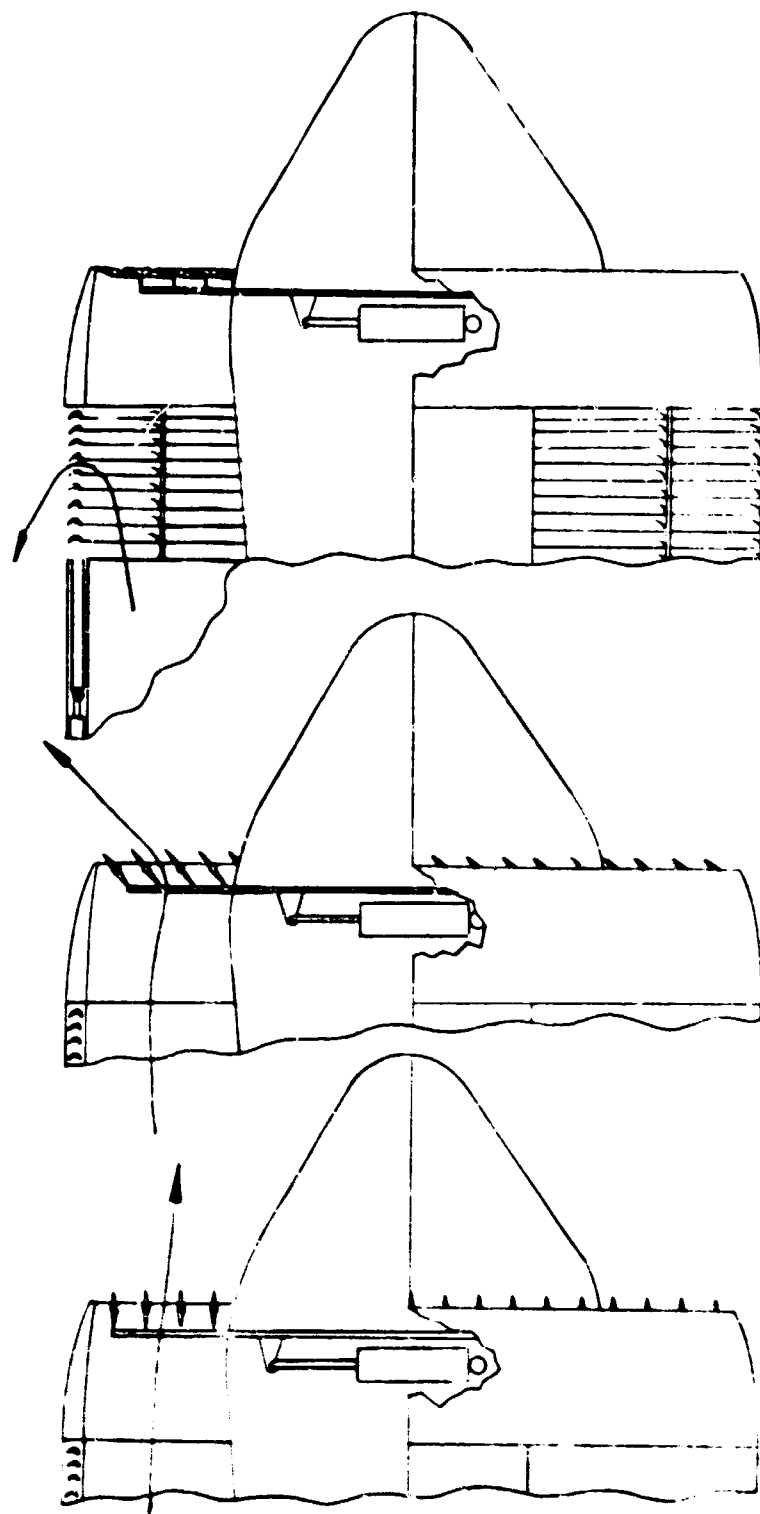


Figure 413 Variable Exit Louvers - Cascade Reverse.

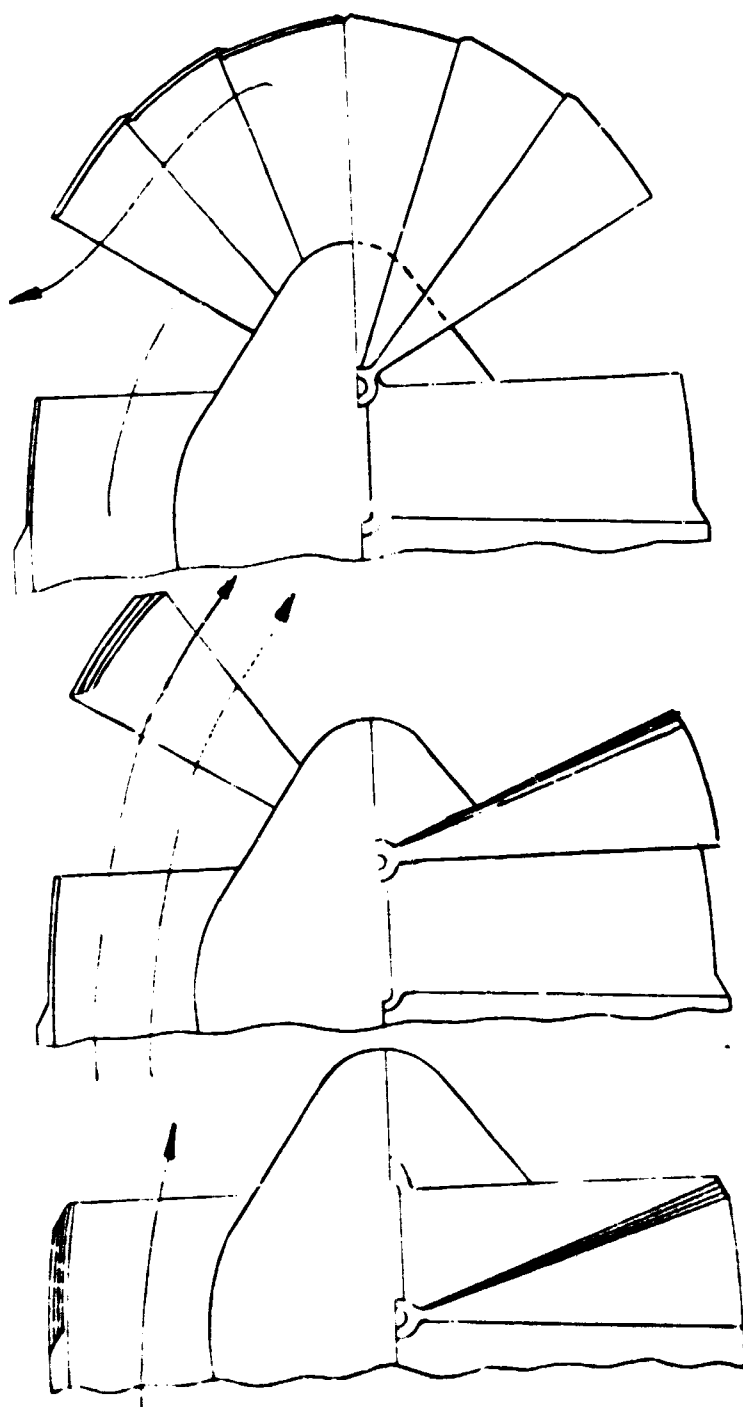


Figure 41: Telescoping Eyelid Deflector - Target Rover

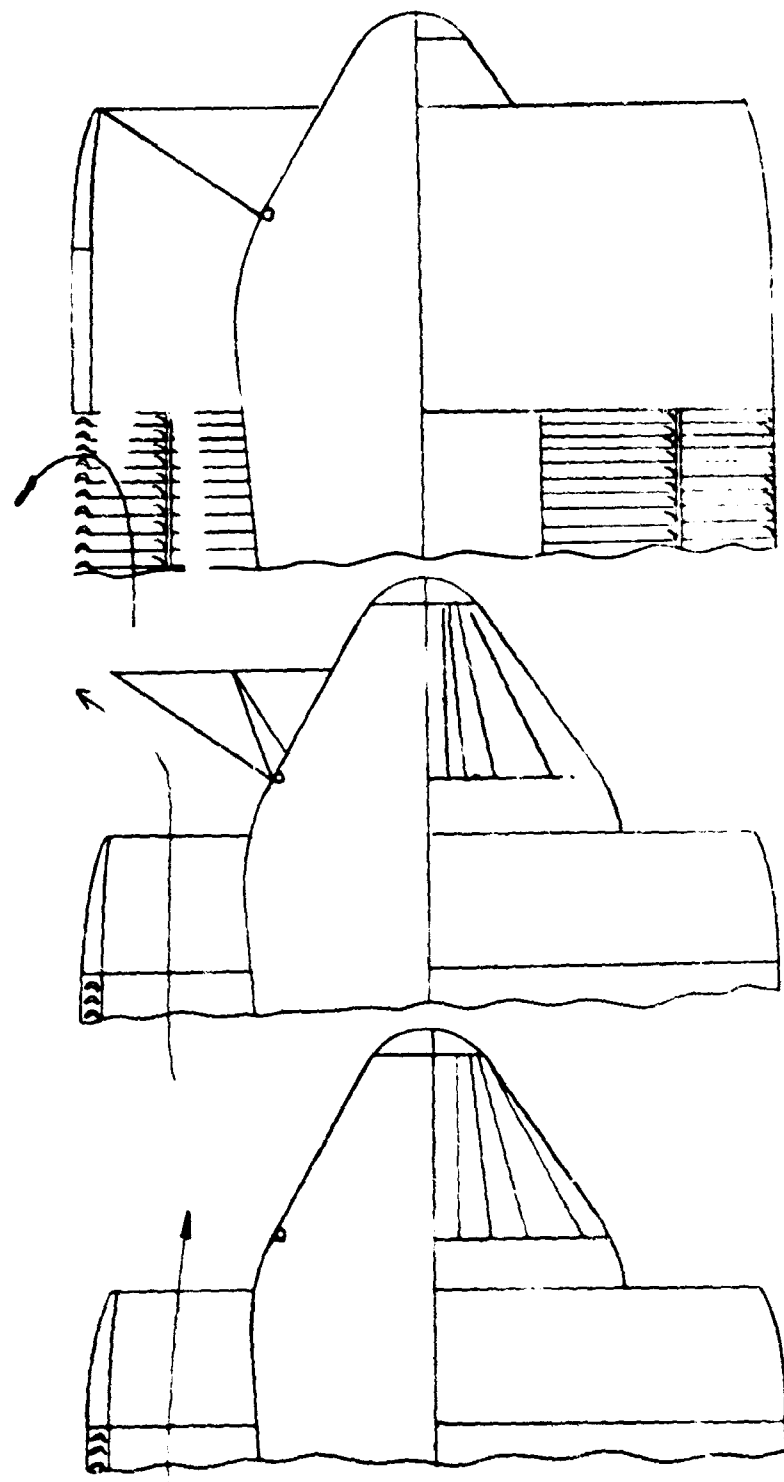


Figure 415 Fanail Plug Deflector - Cascade Reverser

cowl and flaps meet to block off the flow, cascades are completely uncovered.

4. Cowl flap deflector and cascade reverser:

The retractable flap deflector, (Figure 416), consist of two retractable hinged flap sectors having a 180 degree chord angle.

For deflection one set of the finger flaps are extended and turned through the appropriate angle by an actuator located in the plug through a linkage system. For thrust reversal both flap sectors are actuated fully, causing the flaps to meet the plug and simultaneously uncovering the cascade in the cowl.

5. Swiveled conical nozzle-cascade reverser:

The conical nozzle shown in Figure 417 consists of a ball and socket configuration so that the aft end may be rotated for deflection. For thrust reversal, internal blocker doors are swung down and the outer cowl is removed uncovering the cascade system.

6. Conical nozzle with external exit flaps and cascade reversers:

This system shown in Figure 418 is similar to system 4 except the cowl has been extended to give a conical exit and possibly better turning efficiency.

Performance comparisons.-

(U) Aerodynamic performance in deflection reversal and sea level cruise as well as estimates of relative weight increases, dimensional changes and mechanical complexity are summarized in Table 61.

(U) Although systems 5 and 6 gave the best performance they were discarded because of the large penalty in weight and mechanical complexity.

(U) Systems 1 and 4 were eliminated because of the large percentage thrust loss at cruise. Of the remaining two systems, system 3 at first appears to be the most attractive since it has high efficiency in both thrust deflections and thrust reversal.

(U) Although it is true that the net resultant thrust vector is largest in the 20 degree direction for system 3, little of the net exhaust efflux flows at 20 degrees from the horizontal. And since the wing flap system requires both the maximum mass flow and the net thrust to be directed at 20 degrees, system 2 is the most efficient system for deflection. The extremely low thrust reversal efficiency with the small target reverser is, however, unsatisfactory.

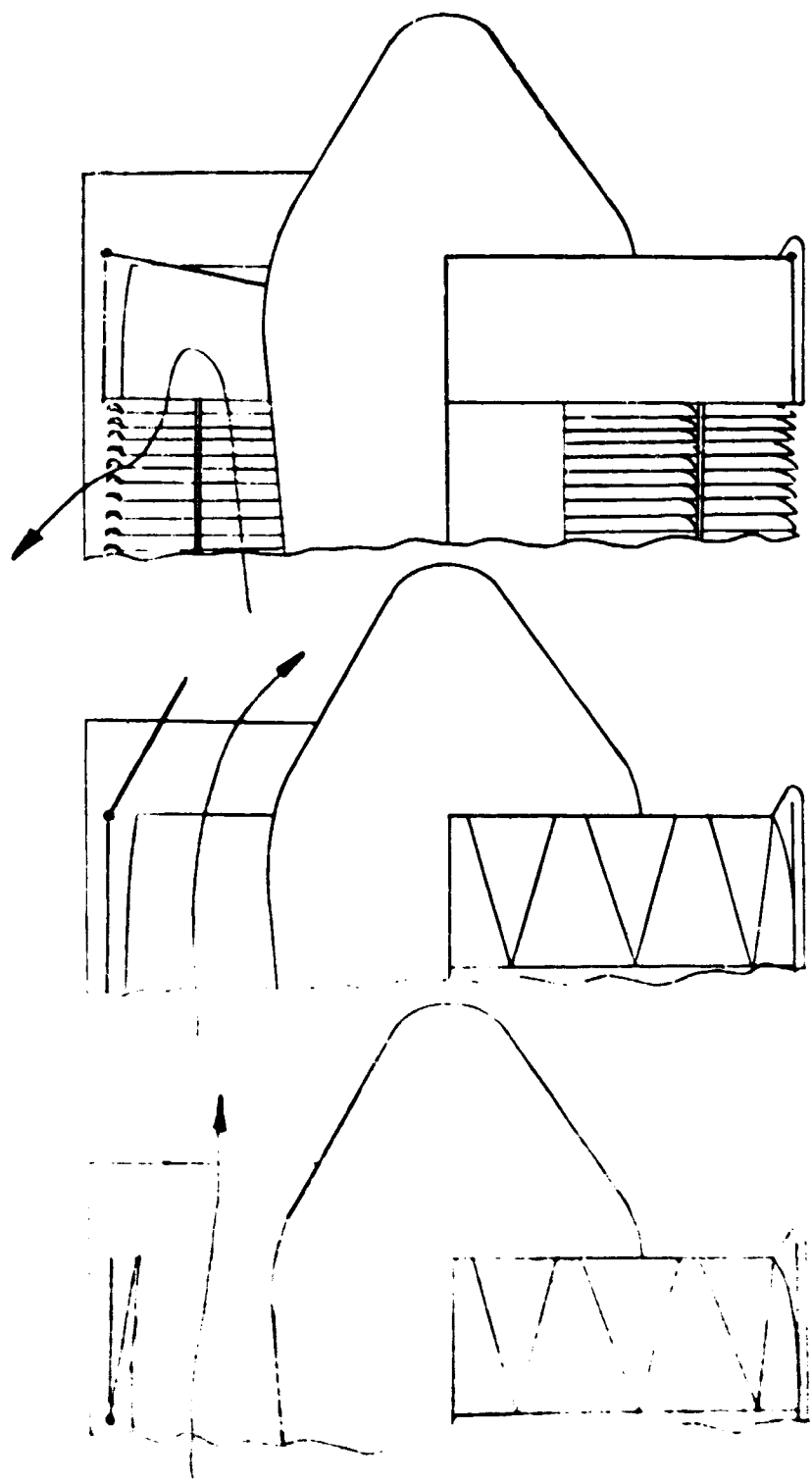


Figure 416 Cowling Flap Deflector - Cascade Reverser

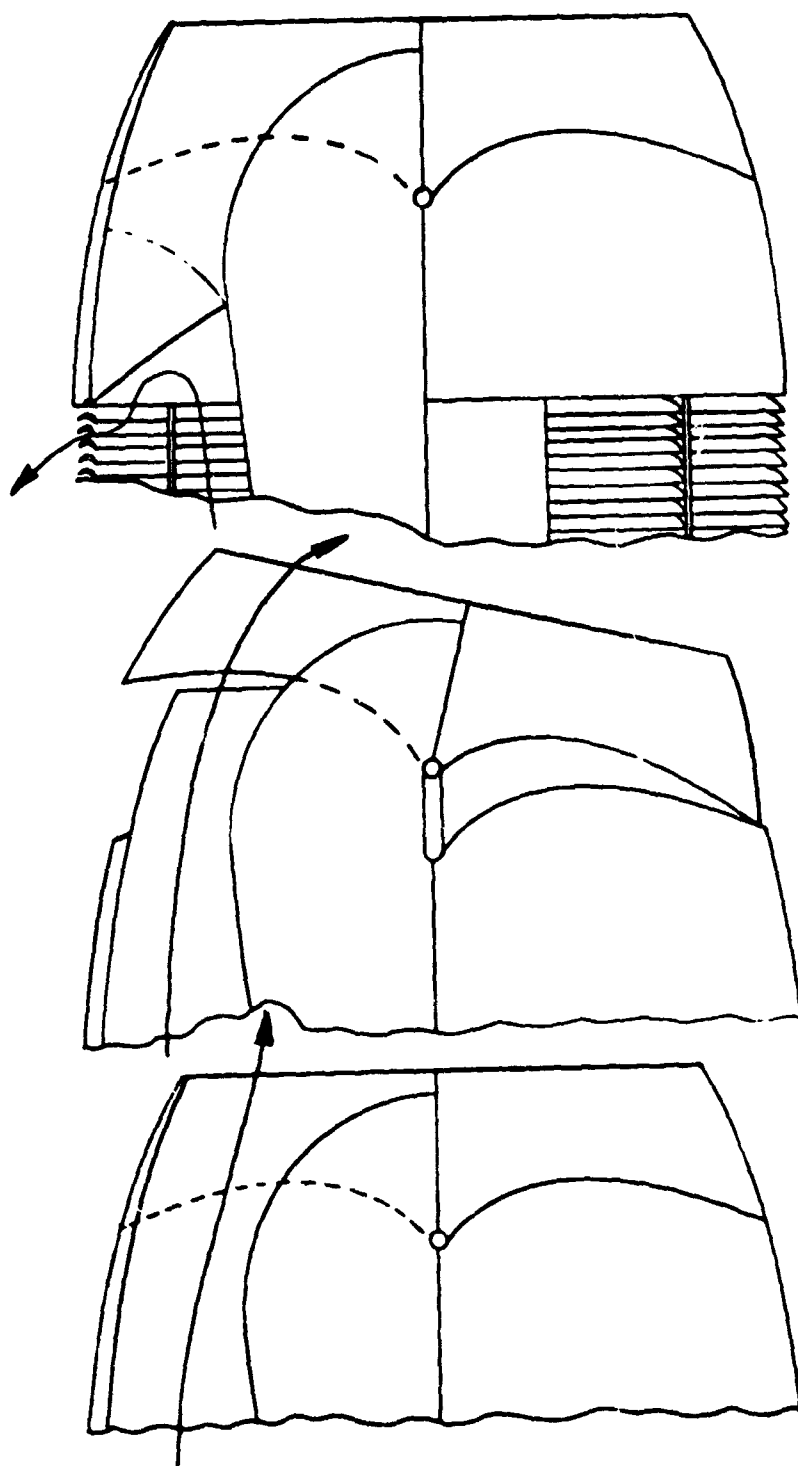


Figure 417 Swivel Conical Nozzle - Cascade Reverser

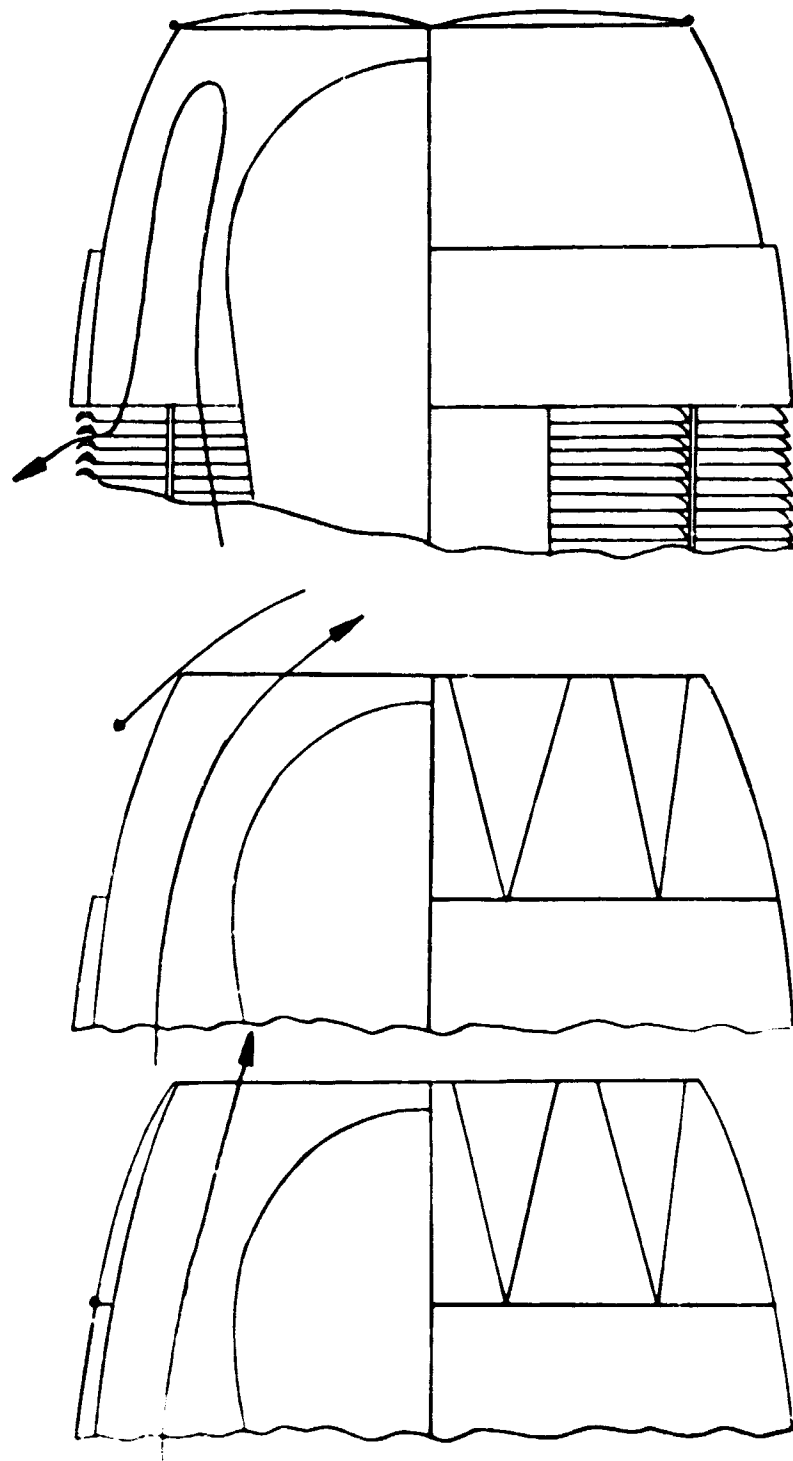


Figure 418 Conical Nozzle with External Exit Flares - Cascade Reverser

TABLE 61

## THRUST DEFLECTOR REVERSER COMPARISONS

SYSTEM	EFFICIENCY % <sub>TR</sub>	EFFICIENCY % <sub>1d</sub>	PHYSICAL DEFLECTION ANGLE TO GIVE 20° DEFLECTION DEGREES	% FG LOSS AT SSL CRUISE	ORDER OF DECREASING WEIGHT	LENGTH INCREASE (INCHES)	ORDER OF MECH. COMP.
1	55	99	18	2.1	4	+11.2	3
2	10	88	25	0	5	0	2
3	55	84	43	0.88	6	+11.2	6
4	55	93.4	24	2.6	3	+11.2	4
693	5	60	100	20	0.3	1*	-10
6	60	93.4	24	2.6	2	-10	5
FINAL DESIGN	55	88	25	0.88	4.5	+11.2	3.5

\* Heaviest

\*\* Least Complex

(U) In analyzing the performance data presented in Table 63 it is important to understand the definitions of the efficiency used in the table. The reverser efficiency,  $\eta_R$ , is the ratio of axial force in thrust reversing to the net gross forward thrust.

(U) The deflection efficiency,  $\eta_d$ , is the ratio of the net resultant thrust vector at the net deflection angle to the effective gross forward thrust. The deflection efficiency was estimated from tests of simular deflectors mounted on conical nozzles. The results of the experiments were measurements of the axial and side force at different deflections and nozzle pressure ratios. This was done by measuring the axial thrust and moments about a line perpendicular to the engine center line. The net thrust deflection angle can then be determined from:

$$\text{deflection angle} = \theta = \text{Arctan} (F_s / F_z)$$

where  $F_s$  = Side force

$F_z$  = Axial force

The net resultant in this direction is the maximum resultant given by:

$$F_d = \sqrt{F_s^2 + F_z^2}$$

The deflection efficiency is then the ratio of this deflected resultant to the effective gross thrust before deflection:

$$\% \eta_d = \frac{F_d}{F_g} \times 100$$

The percent gross thrust loss at static sea level cruise is the decrease in forward thrust performance due to the addition of the thrust reversal-deflection system. These losses occur because of strut drag, turning losses, increased nozzle length and flow leakage.

#### Selected Design

(U) None of the previously studied designs were completely satisfactory. System 2 gave the best thrust and flow deflection for the least cruise loss, weight and mechanical complexity. The cascade thrust reverser used by the other system was far superior to the target reverser proposed in system 2. Two uncoupled systems was then suggested using eyelid deflectors and cascade reversers.

#### Mechanical design description:

(U) The proposed thrust deflector-reverser assemblies for the LCP470 cruise fan include two 180 degree eyelid shroud deflectors,

fixed cascades with translating cowl blocker flaps and two separate hydraulic actuating systems using the same pump.

(U) The deflector is designed for three position use, either deflection up or down and full forward. Figure 419 shows the deflector in full forward and in deflection.

(U) The thrust reverser is designed for two position use, either full open or full reverse thrust operation. Cross section of the reverser in both positions are shown in Figure 420. Since the actuation systems are uncoupled the deflectors may be either stowed or deployed when thrust reversing. A schematic of the system in cruise, deflection and reversing is shown in Figure 421.

(U) Operation of the thrust reverser is initiated by movement of the throttle through the idle position to the reverse position. This energizes the control system and provides hydraulic power to the actuators. The actuators move the translating cowl aft to the reverse thrust position. During translation of the cowl, the linkage mechanism causes the blocker flaps to rotate and block off the fan discharge passage. At the same time, the fixed cascades are uncovered providing the deflected discharge path for the fan exhaust. The control system and reverser are designed to permit application of reverse thrust power after the reverser has actuated to 95% of its fully deployed position.

(U) Thrust deflection is obtained through an independent control system. A signal of deflection up or down provides hydraulic power to the appropriate actuators. The actuators first rotate the deflector then translate it into the exhaust stream.

(U) The deflector eyelids are constructed on  $\frac{1}{2}$  inch steel honeycomb material. The structure is mounted in slots on the outer surface of translating cowl and either pylon splitter or an extended flange on the underside of the engine. The actuating force is provided by a 4-actuator hydraulic system mounted on the translating cowl of the thrust reverser system.

(U) The stationary structure of the fan thrust reverser will be mounted on the engine outer fan stator casing. This structure consists of the main support ring, the actuator support cone, the pylon beam, the pylon cross-structure, the fixed cascade segments, and the cascade inlet fairing. These parts are bolted together for ease of assembly and replacement. When joined, they form a rigid ring structure and a very stable support for the translating parts.

(U) The pylon splitter is bolted to the inner surface of the pylon beams and main support ring, and to the fan exit inner cowl. The fan exit inner cowl is a cage-type structure with removable panels that form the fan exhaust inner surface. The removable panels provide access to the accessories and piping mounted to the gas generator.

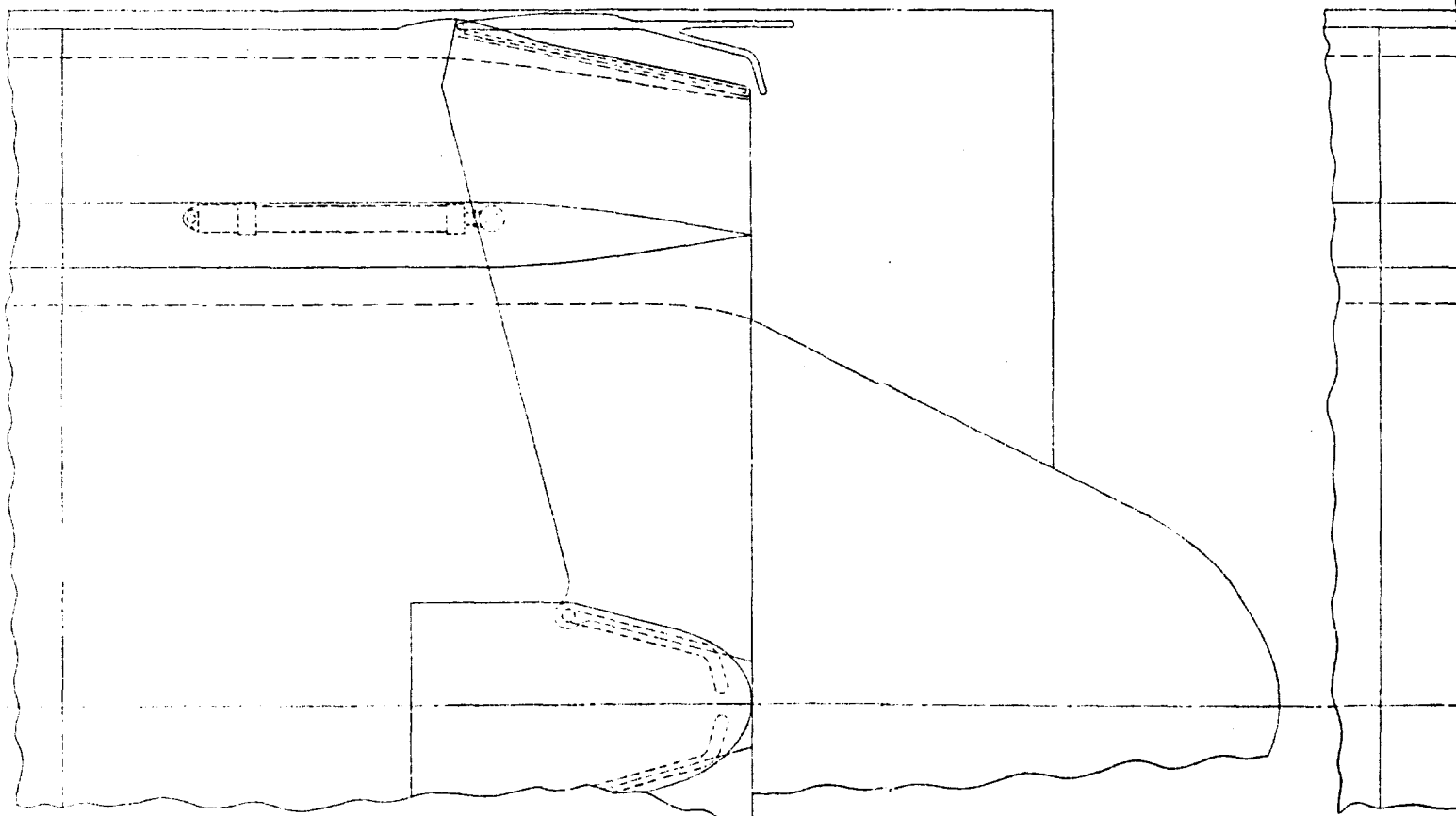
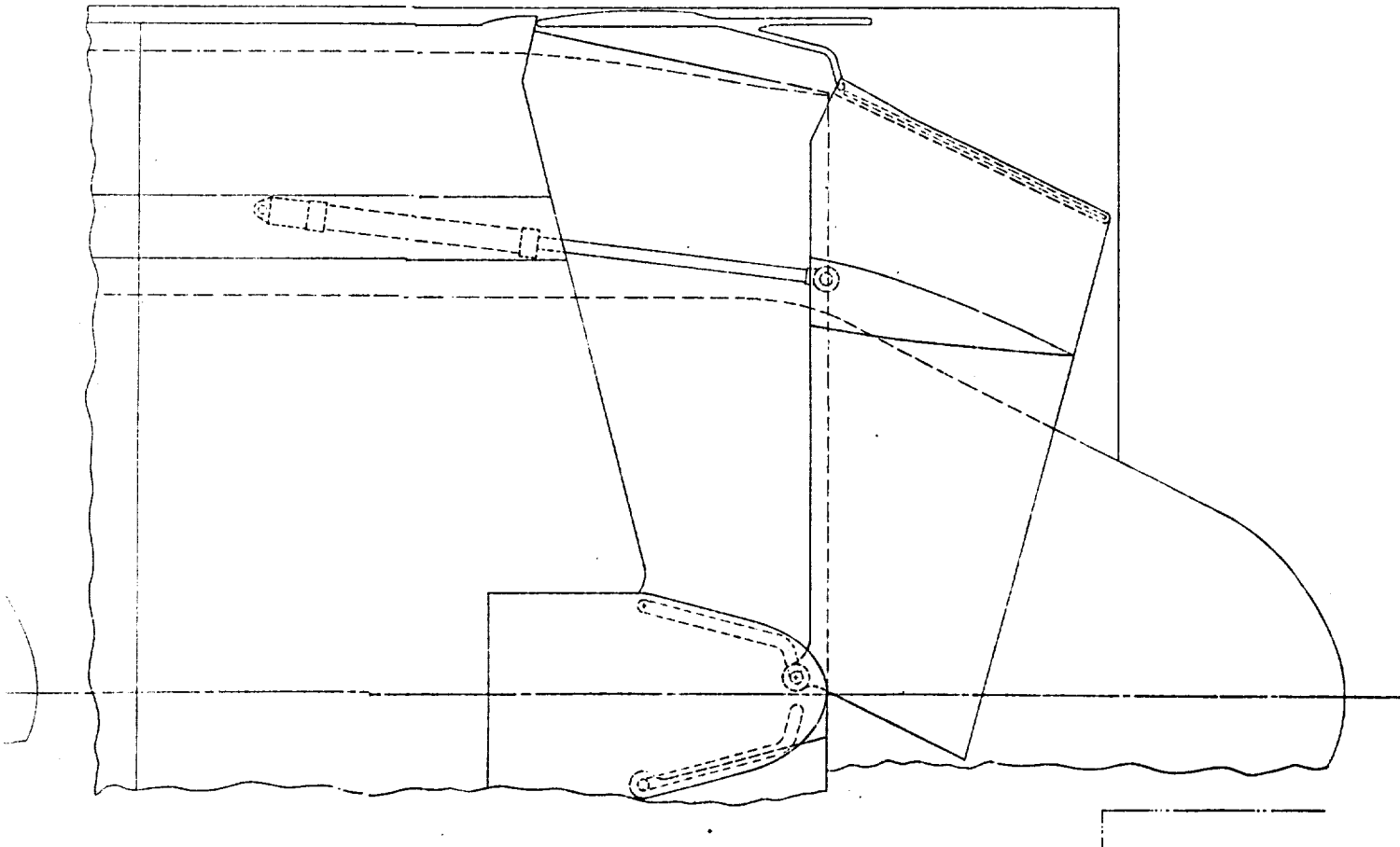


Figure 419 LCF470 Cruise Fan - Th

A.



Cruise Fan - Thrust Deflector

697

B.

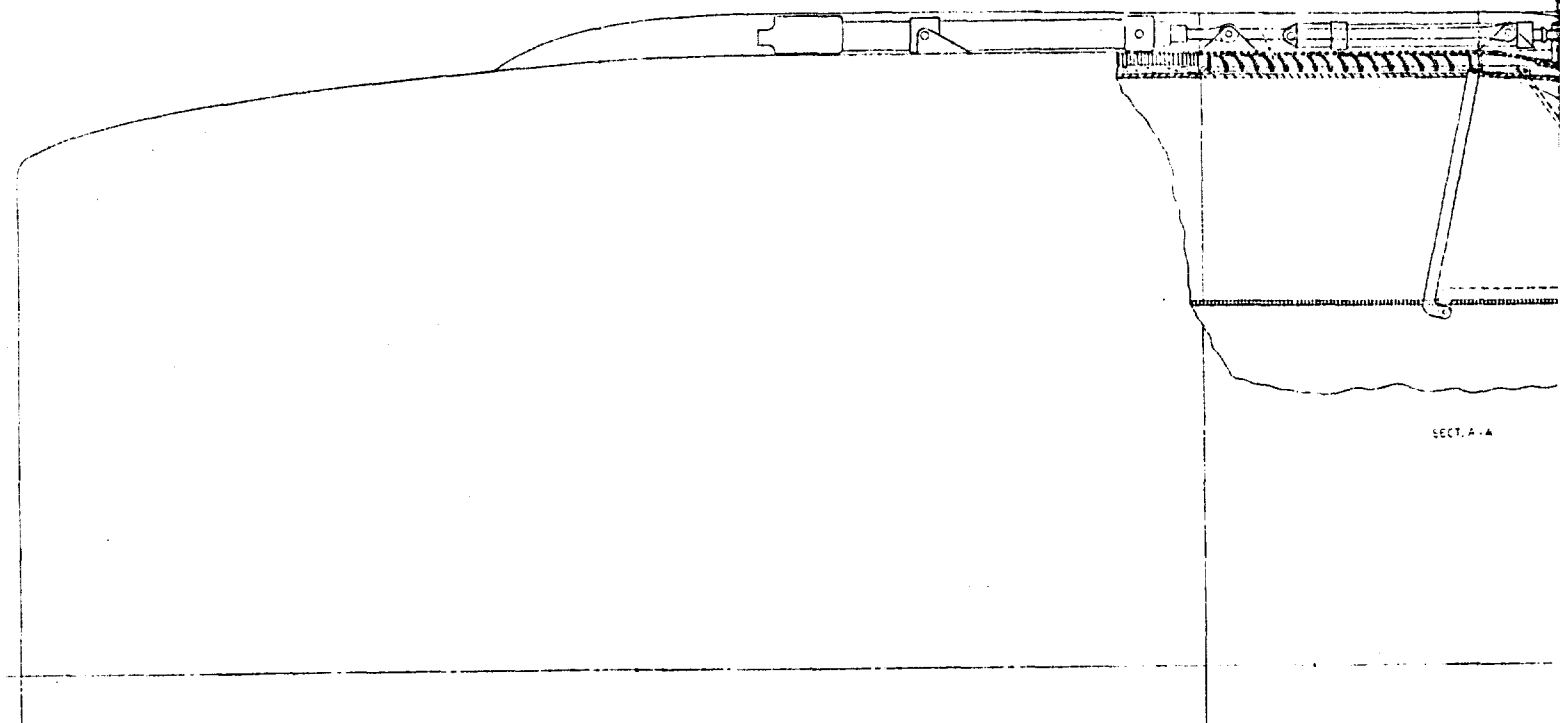
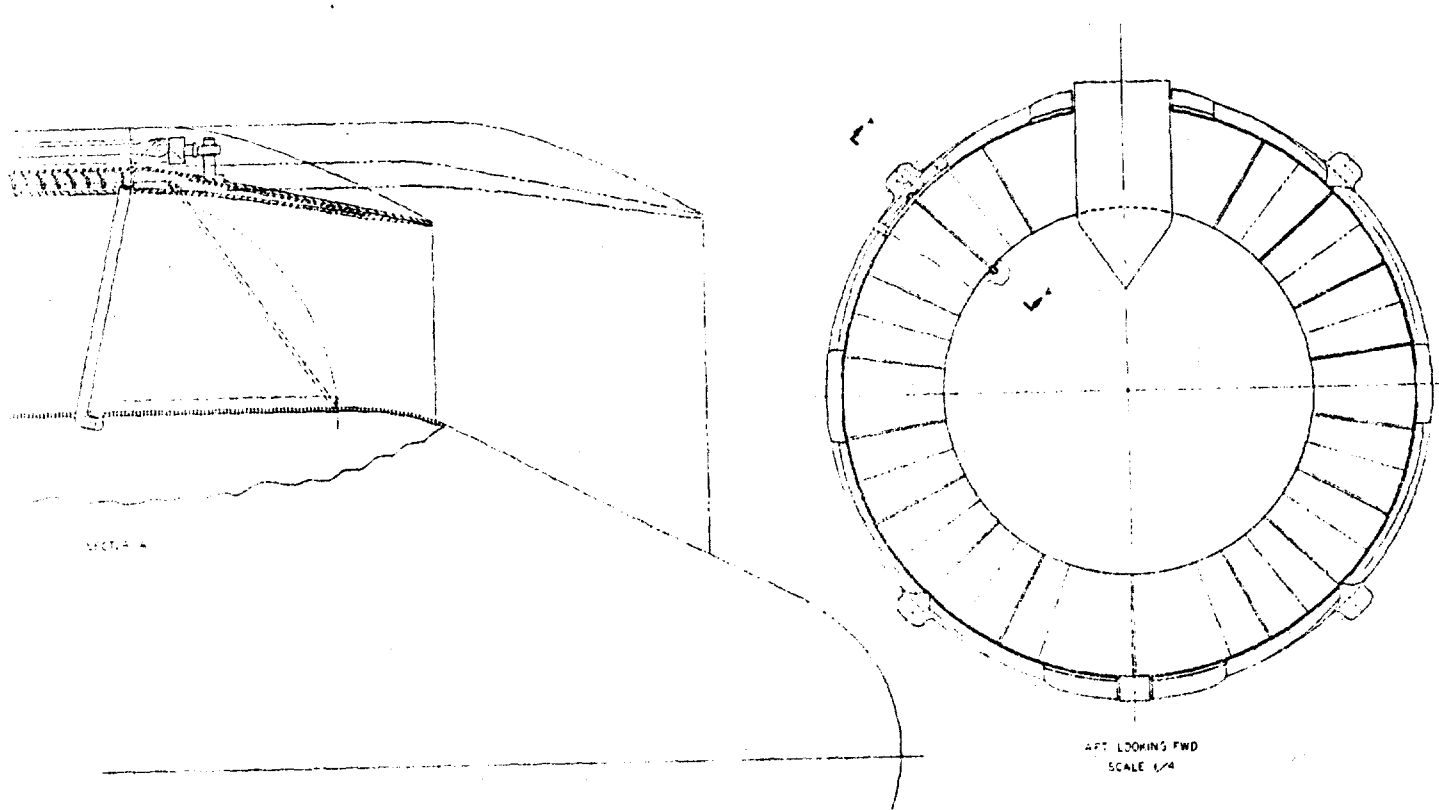


Figure 420 LCF470 Cruise Fan Reverser &

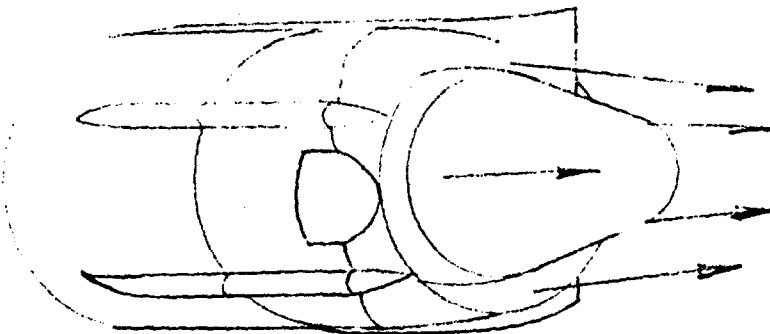
A.



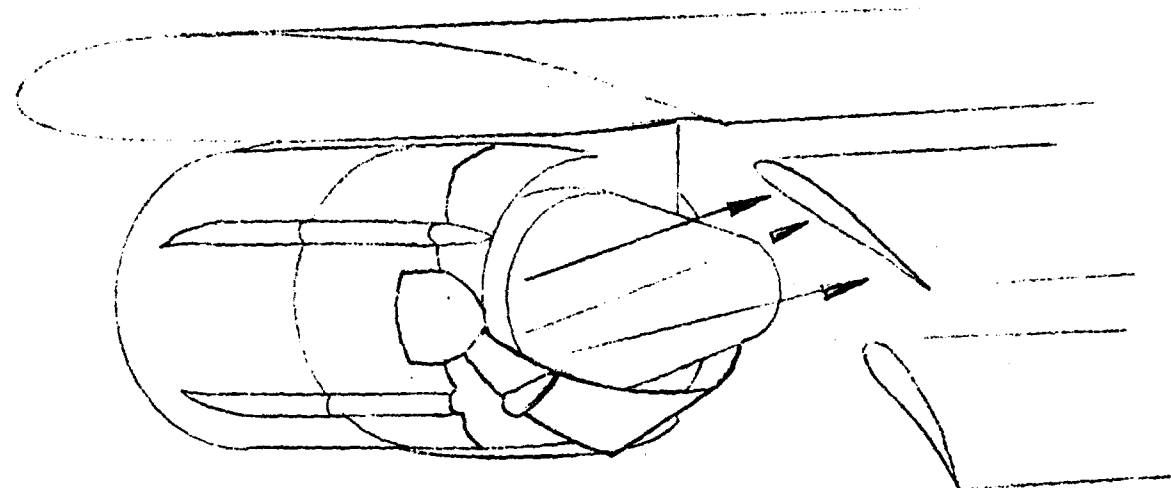
in Reverser & Deflector

699

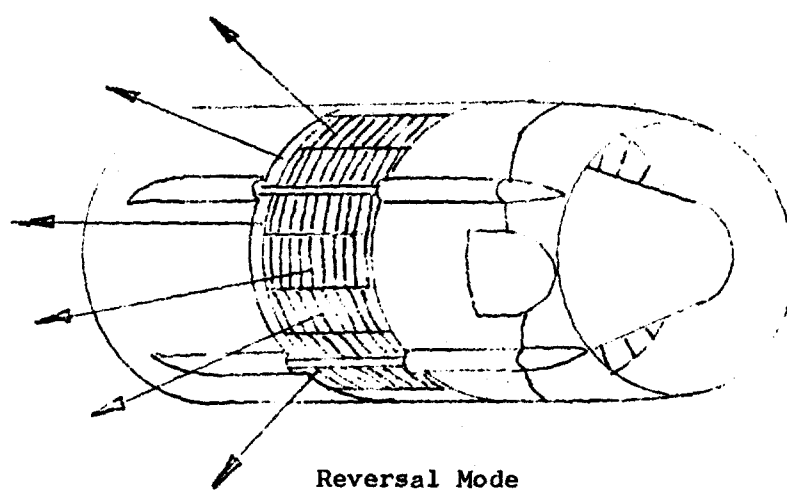
B.



Cruise Mode



Deflection Mode



Reversal Mode

Figure 421 Artist Concept of the Cruise Fan Thrust Deflector - Reverser

(U) The translating structure consists of the outer and inner translating cowl and the blocker flaps. These parts enclose and are supported by the fixed cascade structure as shown in Figure 422. The blocker flaps are attached to the translating cowl by a hinge ring, and nest in cavities in the translating inner cowl. The blocker flaps and the inner surface of the translating cowl are fitted with sound absorbing material to form the outer surface of the fan discharge passage. The blocker flaps are also connected to the fan exit inner cowl by streamlined links across the fan discharge passage. The actuating force is provided by a 4-actuator hydraulic system mounted on the support cone, and connected to the translating outer cowl. A solid film lubricant baked on the surfaces of the cascade support and translating cowl skins would prevent metal rubbing and reduce friction during actuation. The translating cowl is supported by T-shaped sliders at the pylon-cowl split on each side of the pylon. These sliders are keyed into slots in the sides of the pylon beams as shown in Figures 422 and 423, and also have nylon surfaces to reduce friction.

(U) The thrust reverser is mounted to distribute loads between the outer fan casing and the front frame of the core engine. The blocker loads are transmitted to the hinge ring, and through a stop bolted to the hinge ring which is engaged with the flange of the cascade support aft ring, see Figures 420 and 423. These loads are transmitted through the cascade support structure to the main support ring, without being applied to the translating cowl or to the hydraulic actuators. The loads then pass through the main support ring and the support cone to the outer fan casing. The blocker link loads are transmitted to the link housing attached to the fan exit inner cowl. A fixed link, connected to the housing passes this load into the core engine. During the translating cycle, the blocker flap hinge loads are transmitted to the translating cowl and into the actuators. When in the reverse position, the translating cowl is supported radially at the forward end of both the inner and outer sections by the rigid stationary structure, and axially by the aft ring flange of the same structure.

(U) The flap links are spring-loaded at the end of the fan exit inner cowl to eliminate sagging and the possibility of aerodynamically-induced vibration when in the stowed position. Pivot movement is adequate to eliminate manufacturing tolerance effects, thus ensuring good fit of the flaps with the cowl.

(U) The inherent failure mode of the fan reverser is to the committed position. The mechanics of the reverser linkage are such that the loads on the blocker flaps will retain the reverser in the deployed position if actuation capability is lost while in the reverse position and will maintain the blockers in the stowed position during forward thrust operation. Latches are provided however, within the actuators to more securely hold the reverser

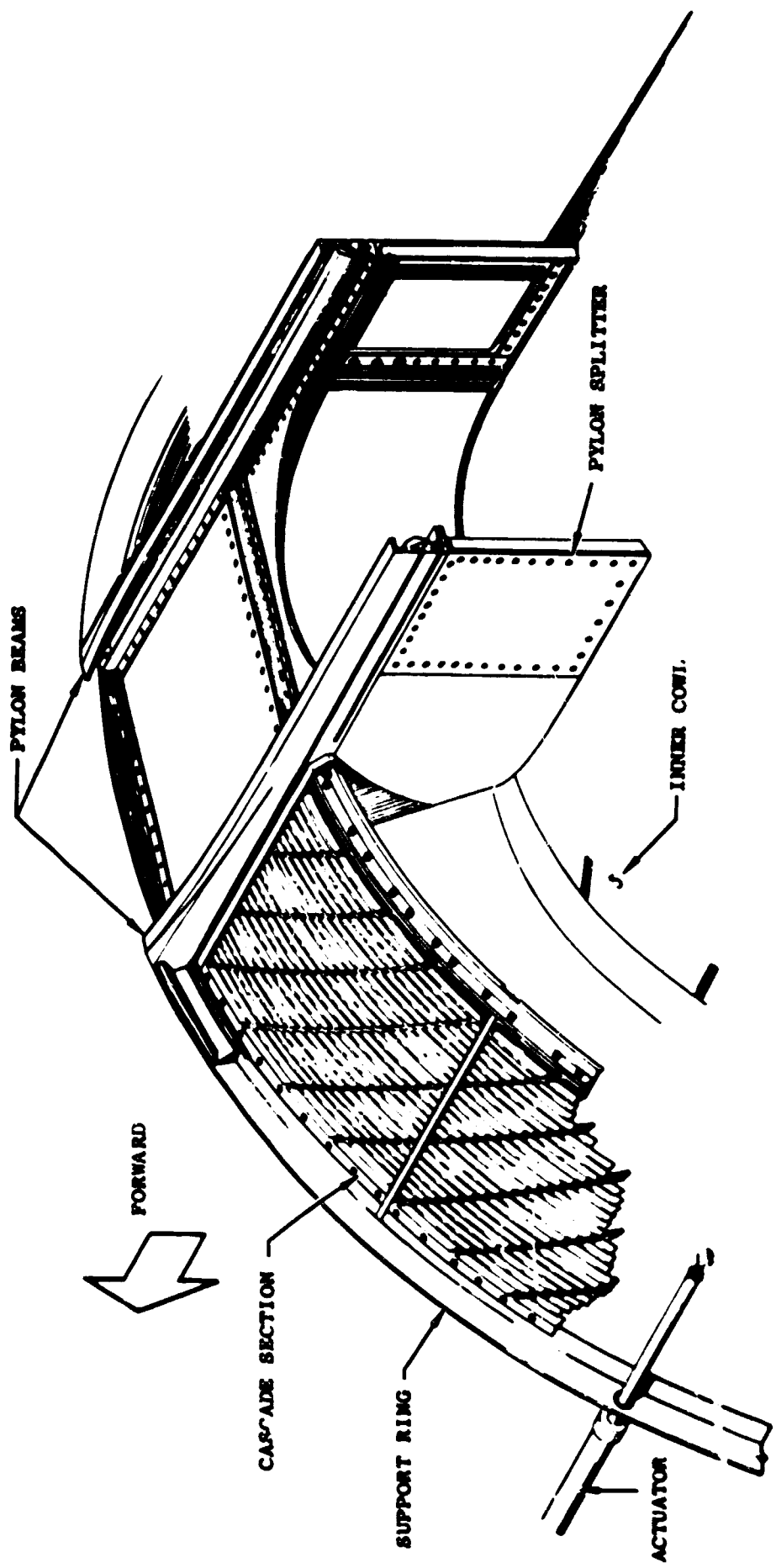


Figure 422 Forward Thrust Position (Translating Cowl Removed)

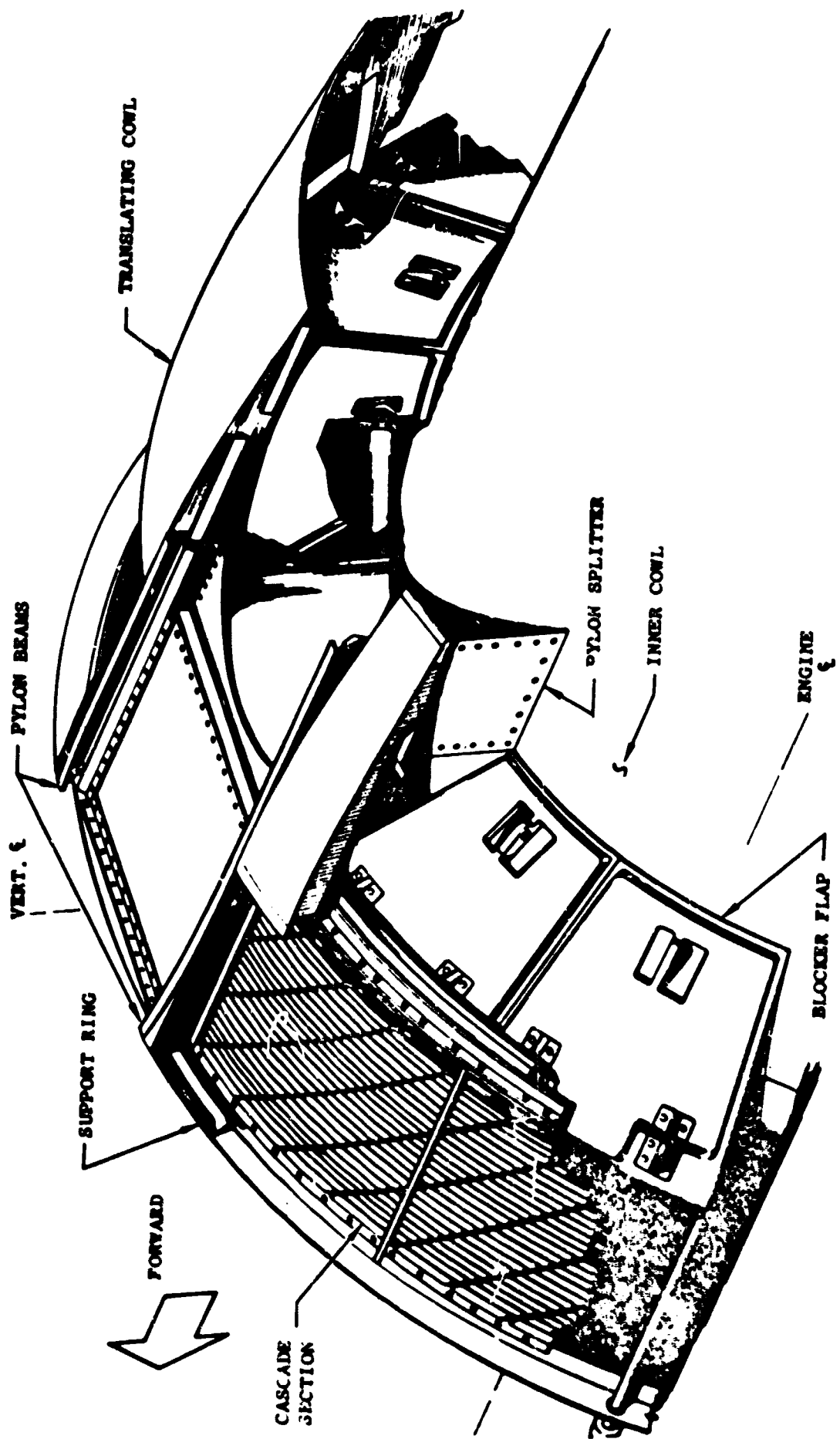


Figure 423 Reverse Thrust Position (Translating Cowl Cut-Away)

in the forward thrust position and to preload the seals for minimum leakage.

(U) All pinned joints in the thrust reverser deflector consist of steel inserts with self lubricating bushings that may be replaced when wear limits are exceeded. Areas of sliding motion requiring low friction surfaces have nylon shoes or similar low friction material sliding on an aluminum surface. All wear shoes are replaceable.

Actuation limits:

(U) Both the thrust reverser and thrust deflector use the same pump system and are capable of actuation within the maximum times listed below:

Reversing or Deflection	1 sec
Stowing	2 sec

Weight and dimensional changes:

(U) The total dry weight of the LCP470 without a reverser or deflector is 1690 pounds. The weight penalties incurred by the addition of a thrust deflector and reverser are 121 pounds and 624 pounds respectively. This 745 pound increase gives a new total engine weight of 2435 pounds.

(U) The addition of the thrust reversal-deflection system increases the cowl length by 23.3 inches to 109.6 inches and the plug length by 11.2 to give a new total engine length of 136.2 inches. The engine's diameter was kept equal to 80 inches except for the small local increases due to the actuator fairings which amount to a 2.6 inch increase.

Performance:

(U) The thrust deflector is estimated to give 88% of the forward gross thrust at a net mass and thrust deflection angle of 20 degrees when the deflectors are inserted in the exhaust stream at 25 degrees.

(U) The thrust reversal system is estimated to produce a minimum gross reverse thrust of 55% of the forward gross thrust. Figure 424 is a plot of percent effectiveness (reverse force/forward gross thrust) versus forward velocity including the estimated small effect of fan reingestion. The effect of reingestion into the gas generator is a function of the engine's location.

(U) The inclusion of the present thrust deflection-reversal system on the LCP470 cruise fan causes a 0.88% loss in forward gross thrust due to flow leakage and strut drag. The increase in drag due to the inclusion of the actuation fairing bumps has not been estimated.

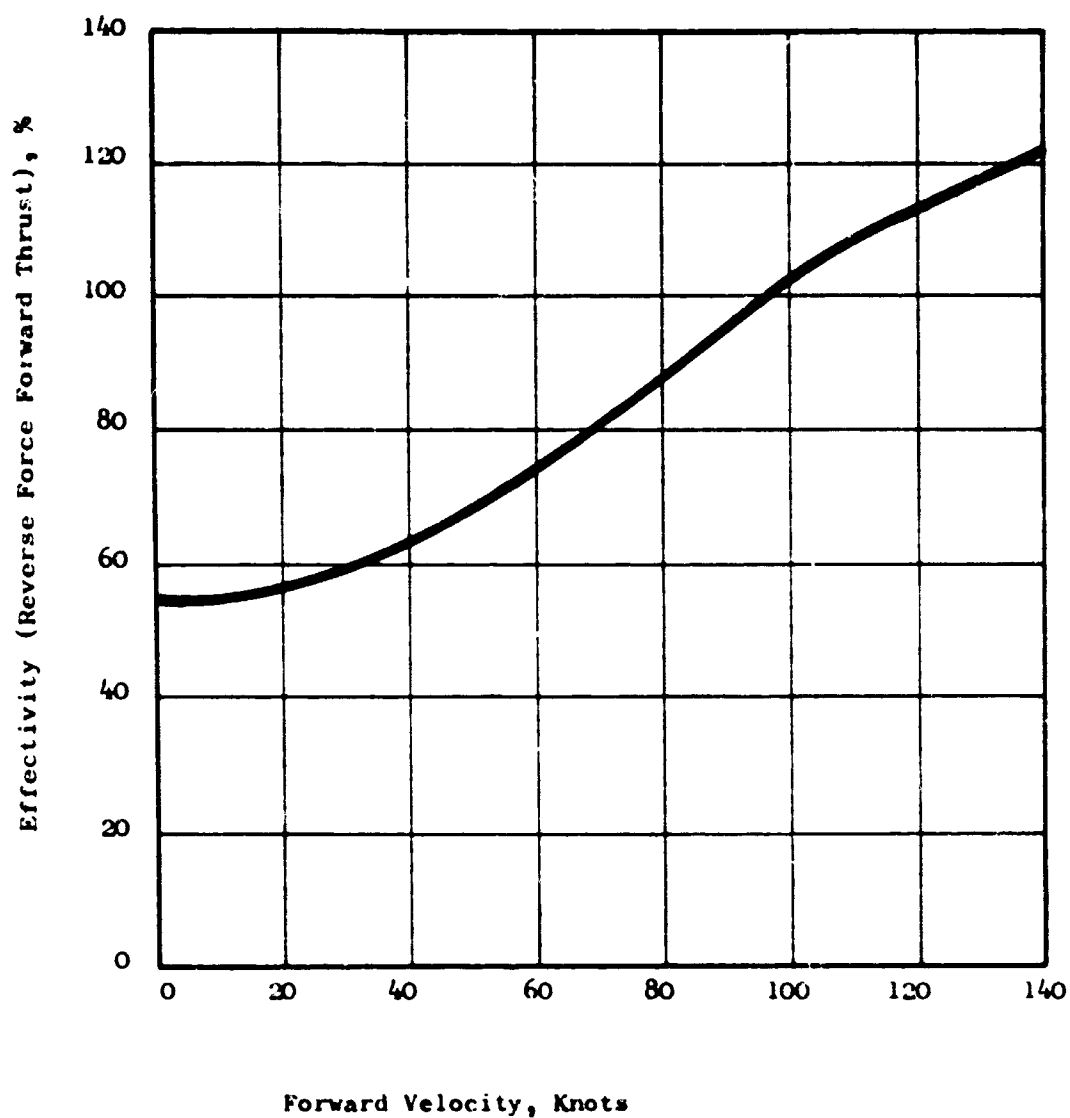


Figure 424 Percent Effectivity Versus Forward Velocity  
Including Fan Ingestion

## Rotating Gas Joint

### Introduction.-

(U) Lift/cruise fan thrust vectoring is most efficiently accomplished when the whole assembly is rotated. A rotating gas joint is required for such a system. Various joint concepts were investigated and are discussed in this study.

(U) A literature search was conducted and 18 reports on rotating seals were identified which were of interest. A bibliography shown in Section VII.

(U) Conceptual studies have been completed and several promising configurations have been identified. Reviews have been held with General Electric lift/cruise engine personnel engaged in rotating seal studies for deflected engine thrust applications, and many useful comments were obtained.

(U) Six joint concepts were identified in the proposal:

1. Helical bearing joint
2. Preloaded face seal joint
3. Piston ring seal joint
4. Tapered joint
5. Labyrinth seal joint
6. Marmont flange joint

A cursory examination reflecting system requirements showed problems and preferences described in the following paragraphs.

(U) The helical bearing joint and the tapered joint require two actuation systems - one for rotation and one for sealing. Weight and complexity would, therefore, be higher than for the single-actuator systems.

(U) The labyrinth seal will not seal tight enough without high friction loads because of wide surface contact.

(U) The Marmont flange joint requires two sets of bearings, which add weight and complexity.

(U) The split ring seal concept showed the most promise and was selected for further study. The preloaded face seal joint and the piston ring seal joint both use split ring seals. A one-stage seal would be adequate if plastic seals could be used, however, the high temperature in this application will require metal ring seals. Friction is a problem with these rubbing seals, therefore, the number of rings should be minimized and the rings should be spring loaded to a predetermined contact pressure.

(U) Consideration is being given to investigation of surface spray coatings, such as tungsten carbide, on the seal rubbing faces and use of solid film lubricants to reduce friction, fretting and wear.

(U) The bearings do not have to be an integral part of the rotating joint - they can be part of the structure which rotates the nacelle. The rotating joint could be tied to this remote bearing set to assure proper rotation. The configuration of the rotating joint then, is a function of the nacelle installations, and could be as simple as a single split ring seal between two flanges. If it is assumed that the bearing set will be part of the rotating joint, then two possible configurations are as shown in Figures 425 and 426. Figure 425 shows a sketch (no scale) of a take-apart design. The double set of fasteners is necessary if it is desired to remove all components at the joint - i.e., to have a complete take-apart design.

(U) Figure 426 shows a sketch (no scale) of a similar joint design, in which cam rollers replace the ball bearings. These rollers are "off the shelf components". This concept is similar to that used in the thrust diverter of the X14 VTOL research aircraft.

#### LF475 Lift Fan

##### Louver Cascade Tests

###### Introduction.-

(U) A test was made on an exit louver cascade for the purpose of obtaining louver performance in the realistic environment of a simulated fan and turbine annulus and with fan pressure ratios up to 1.4. Objectives of the test were:

To determine the back pressure effect of the louvers on the fan as a function of louver angle and fan pressure ratio.

To determine the thrust coefficient and thrust angle at the louver exit as a function of louver angle and fan pressure ratio.

(U) The first objective was met, the second was not.

###### Test.-

(U) The tests were conducted on two fan flowpaths (Figure 427). One set of louvers was used throughout the tests. The first flowpath (diverging exit) was tested at total pressure ratios of 1.3 and 1.4. The second flowpath (cylindrical exit) was tested at total pressure ratios of 1.2, 1.3, 1.4 and 1.45. In the definitions used for the test the "louver angle",  $\alpha_L$  is the design louver exit flow

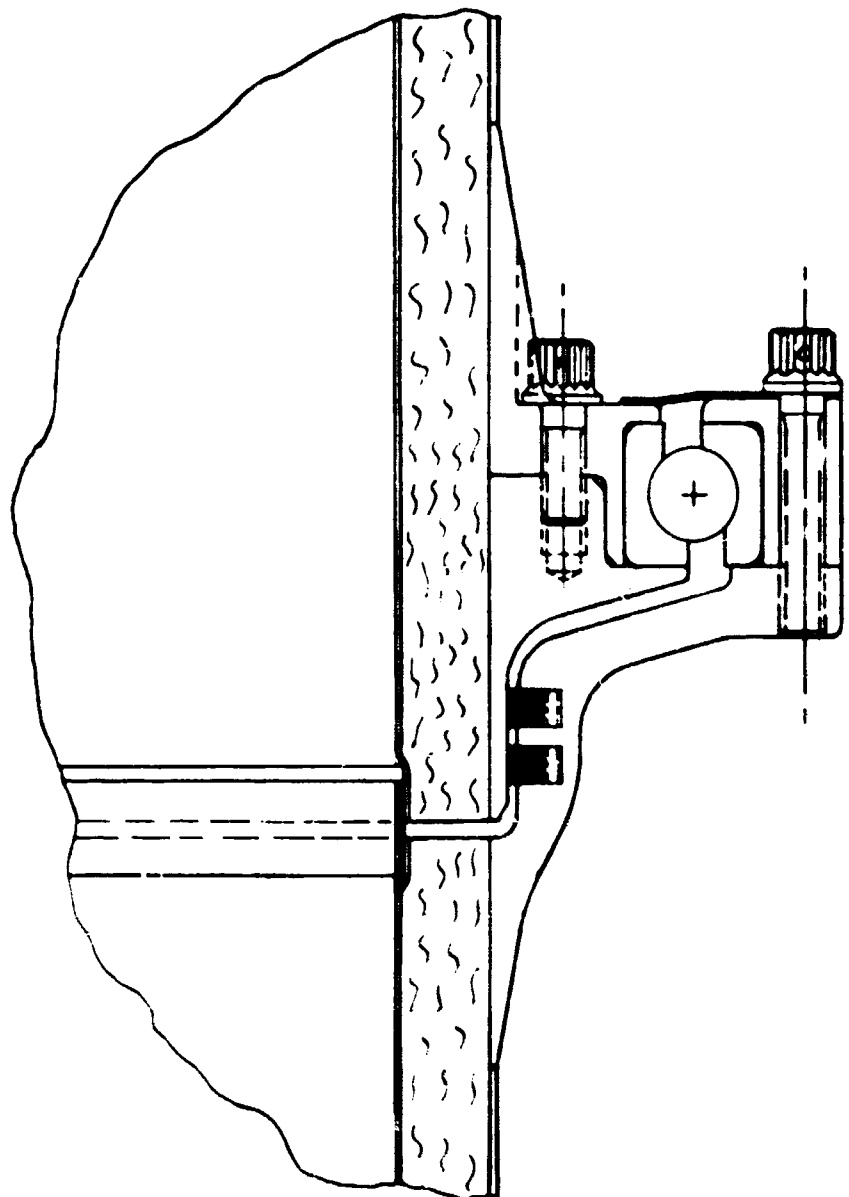


Figure 425 Rotating Nacelle Joint with Ball Bearings

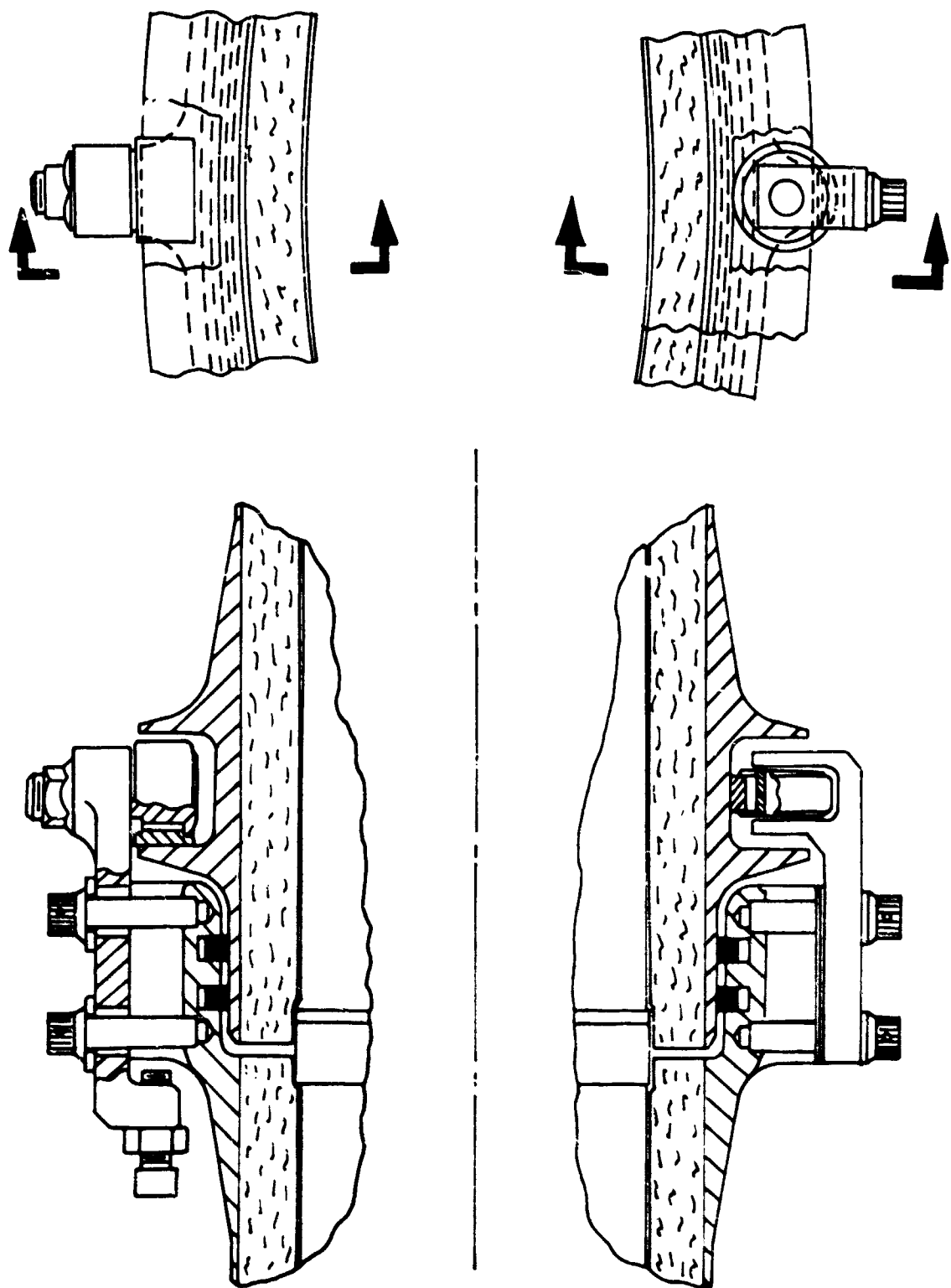


Figure 426 Rotating Nacelle Joint with Cam Rollers

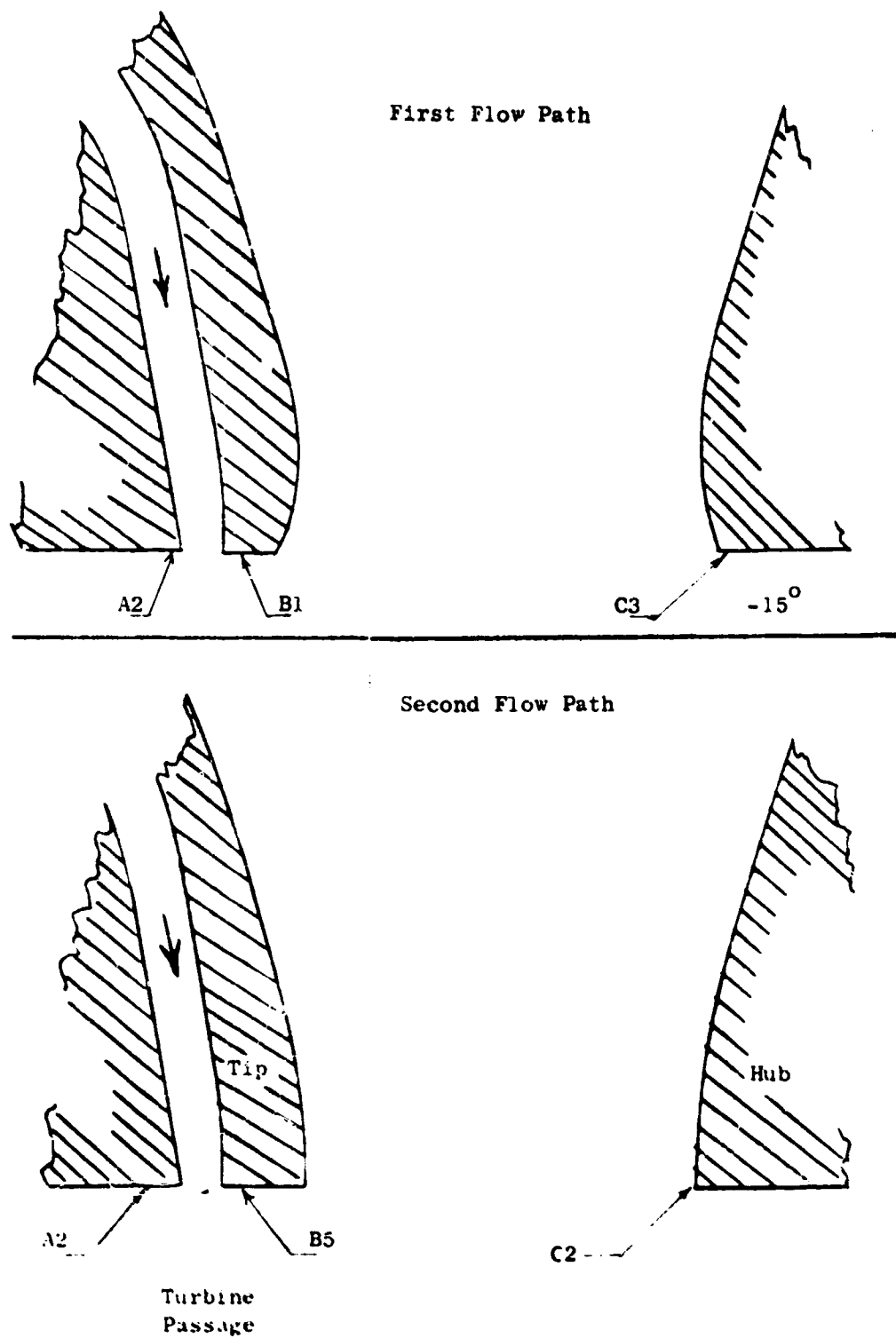


Figure 427 Exits of Flow Paths Tested

angle. Both flowpaths were tested at louver angles of 2°, 20°, 35° and 45°. Due to interference of model and louver linkage  $s_L = 0$  could not be tested.

(U) The total pressure ratios considered are actually averaged values obtained from the pressures measured at the fan passage exit.

Description of model.- (Figure 428)

(U) The test system includes a flow path which is typical of lift fans. This shape was used in an effort to duplicate the static pressure profile expected at a lift fan exit. The simulated turbine passage which surrounds the fan flowpath is passing a flow equal to about 12.5% of the fan flow. The centerbody of the model is held in place by four struts. These struts are also used to support and contain the tubes used for the midstream static pressure instrumentation. The model has the capability for testing many fan and turbine flowpaths by means of exchangeable rings. The rings used for the first set of tests were turbine outer path, A2; combination turbine inner and fan outer, B1; and, fan inner C3. The second configuration consisted of A2, B5 and C2.

Results.-

(U) Exit Static Pressure:

Exit static pressures were measured at 5 radial immersions at four circumferential locations. The resultant static pressure profiles are presented in Figures 429 through 433.

(U) Louver Map:

The form in which the louver map is presented has tended to make the data easily applicable to any fan's performance map. The louver results are plotted (Figure 434) in terms of pressure ratio,  $P_T/P_a$  versus flow coefficient  $W_T/AT$  for each louver angle.

(where A is the fan passage exit area). Both of these parameters used for the map are averages. The flow parameter is a function only of the Mach number at the fan exit. The pressure ratio can be considered a function of the ideal louver exit Mach number. If instead of Mach numbers the data is considered in terms of  $A/A^*$  a simplified inlet to exit area comparison is made. The inlet and exit values of  $A^*$  can be considered equal if the aerodynamic losses in the louvers are assumed confined to the boundary layer displacement thicknesses. Then there is no total pressure loss. Instead, the pressure loss is viewed in terms of effective area reduction. By dividing the exit  $(A/A^*)_{ideal}$  by the inlet  $A/A^*$  this area relationship is immediately seen (Figure 435)

(U) The louver map shown in Figure 434 is primarily based on results from the second flowpath (cylindrical). This data is most

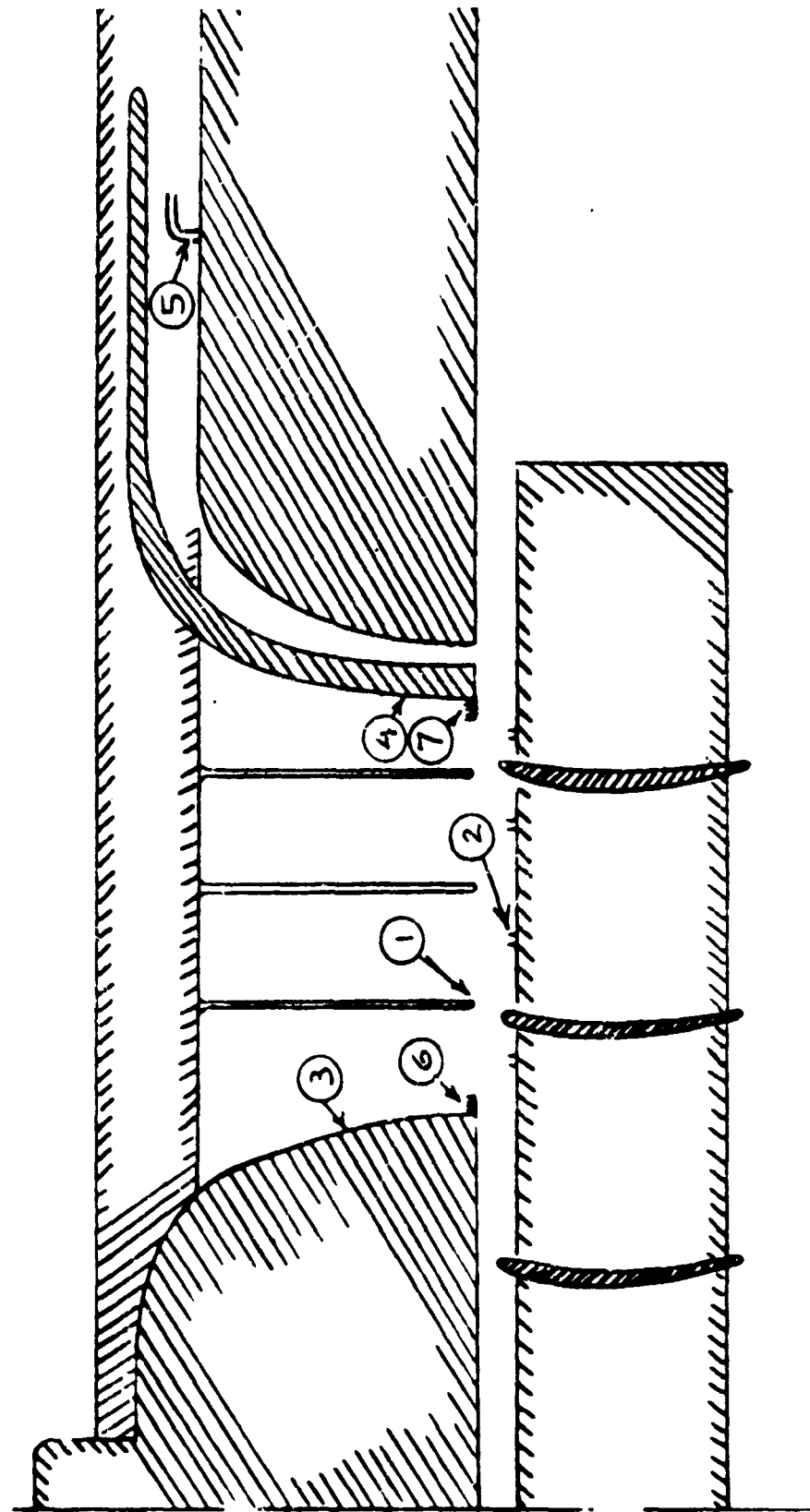


Figure 428 Fixed Instrumentation

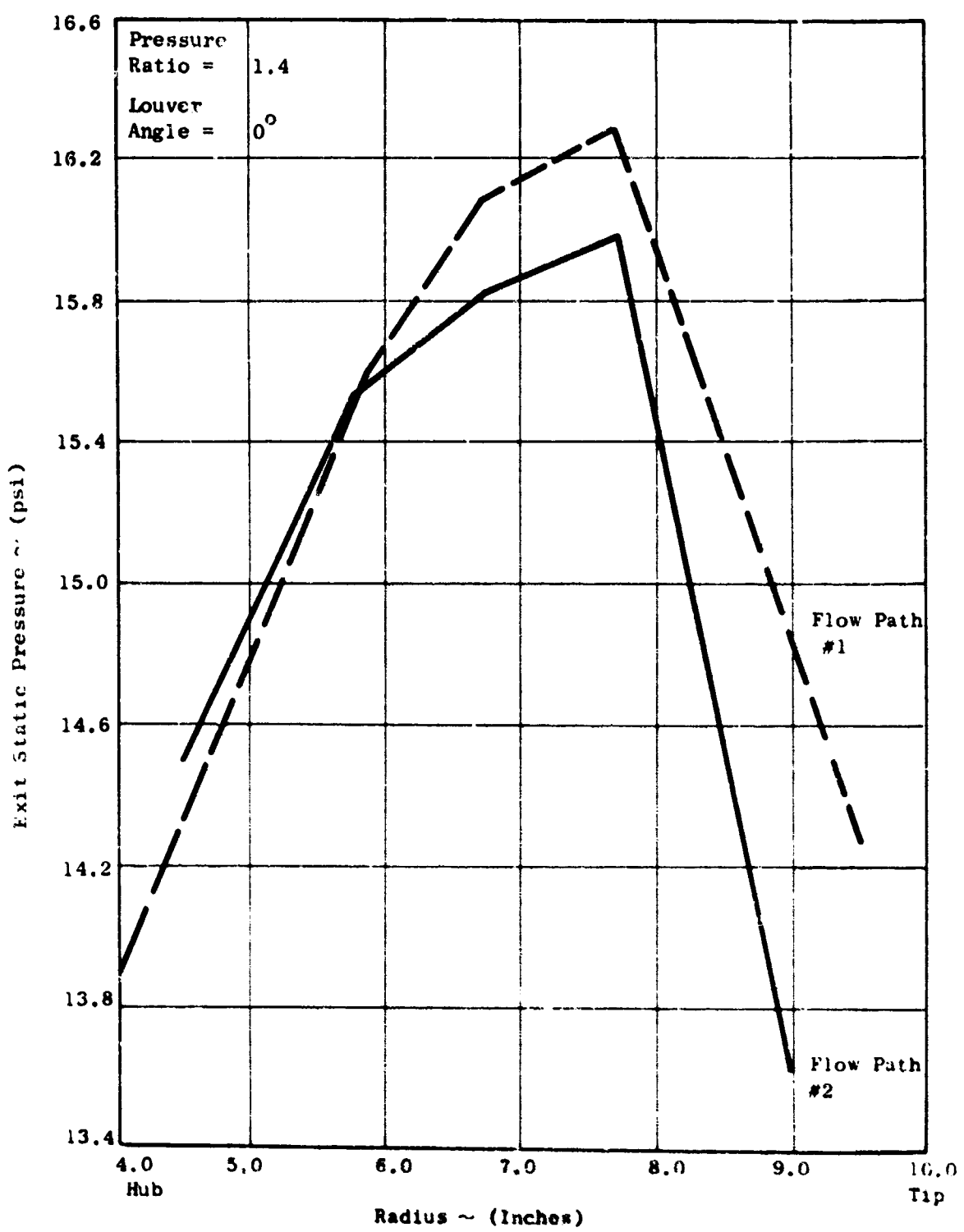


Figure 429 Exit Static Pressure Profiles

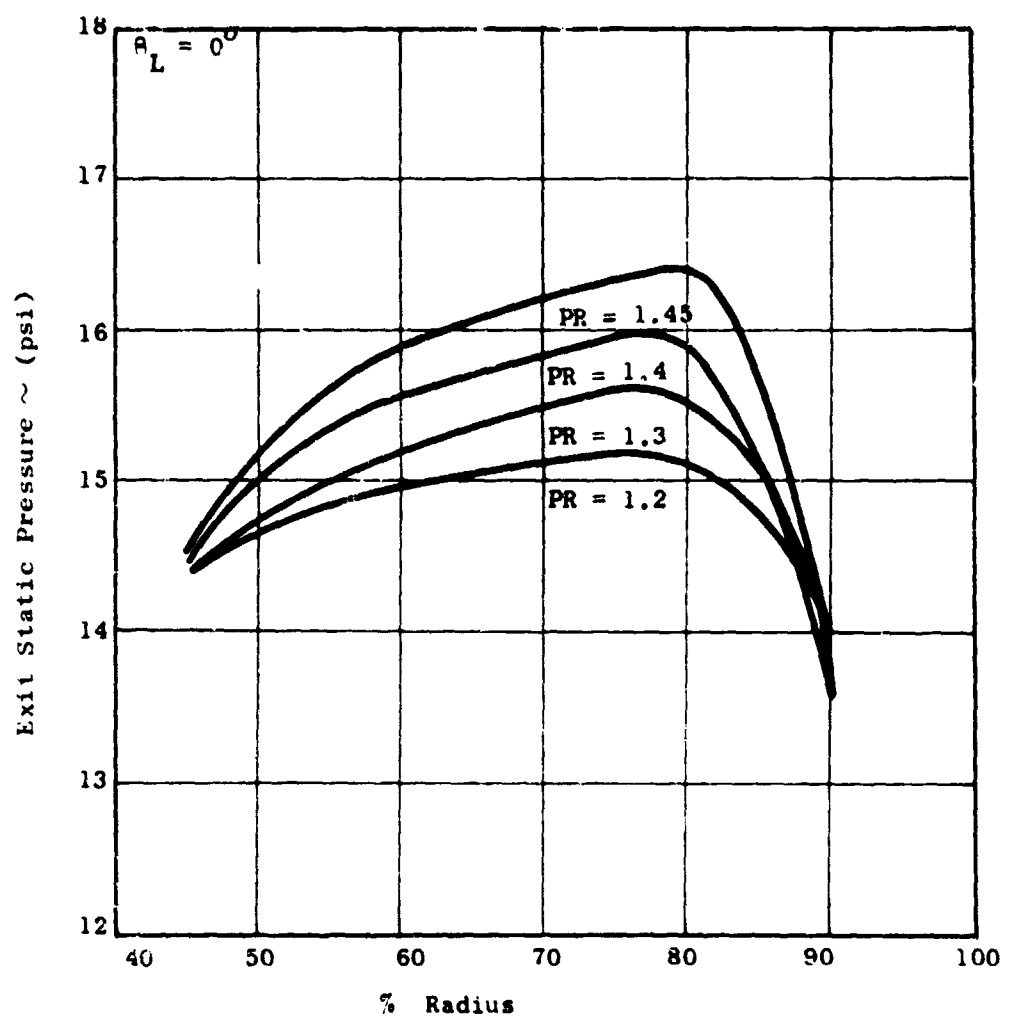


Figure 430 Lift Fan Louver Test Configuration 2

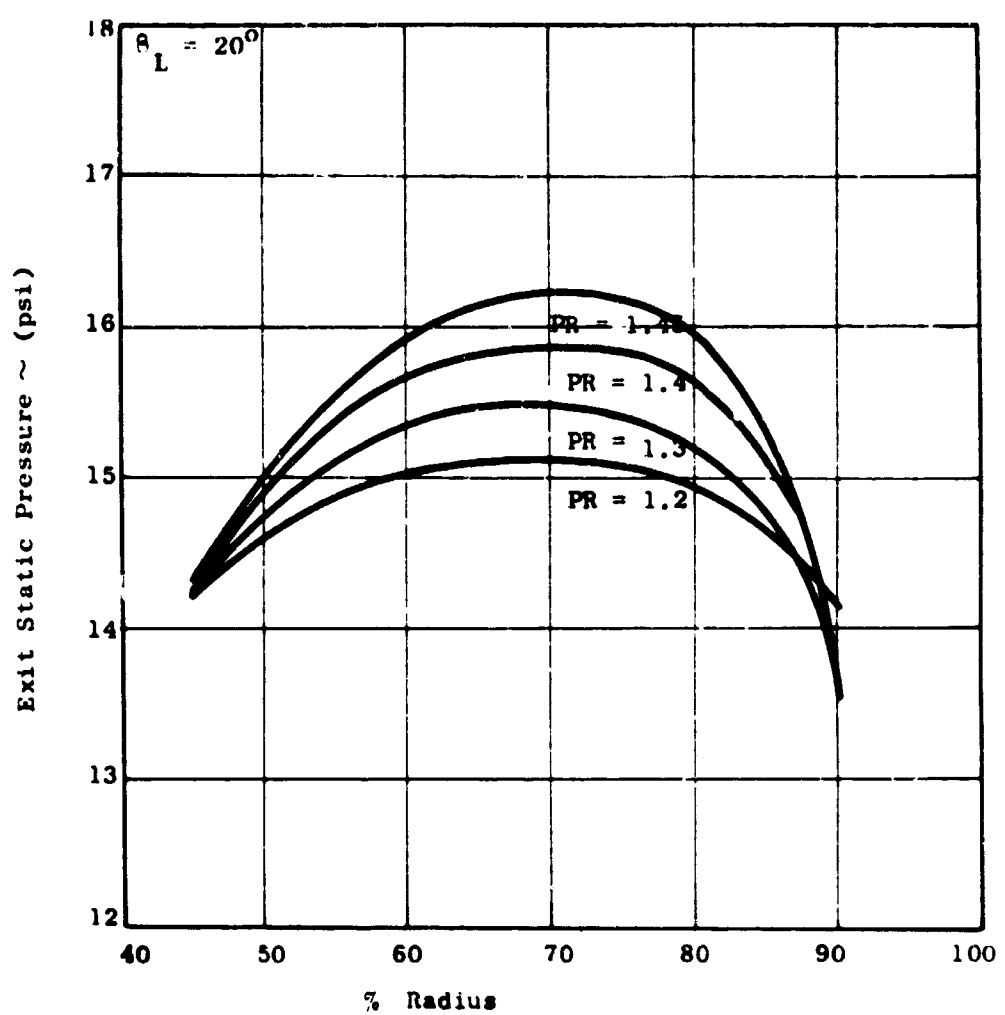


Figure 431 Lift Fan Louver Test Configuration 2

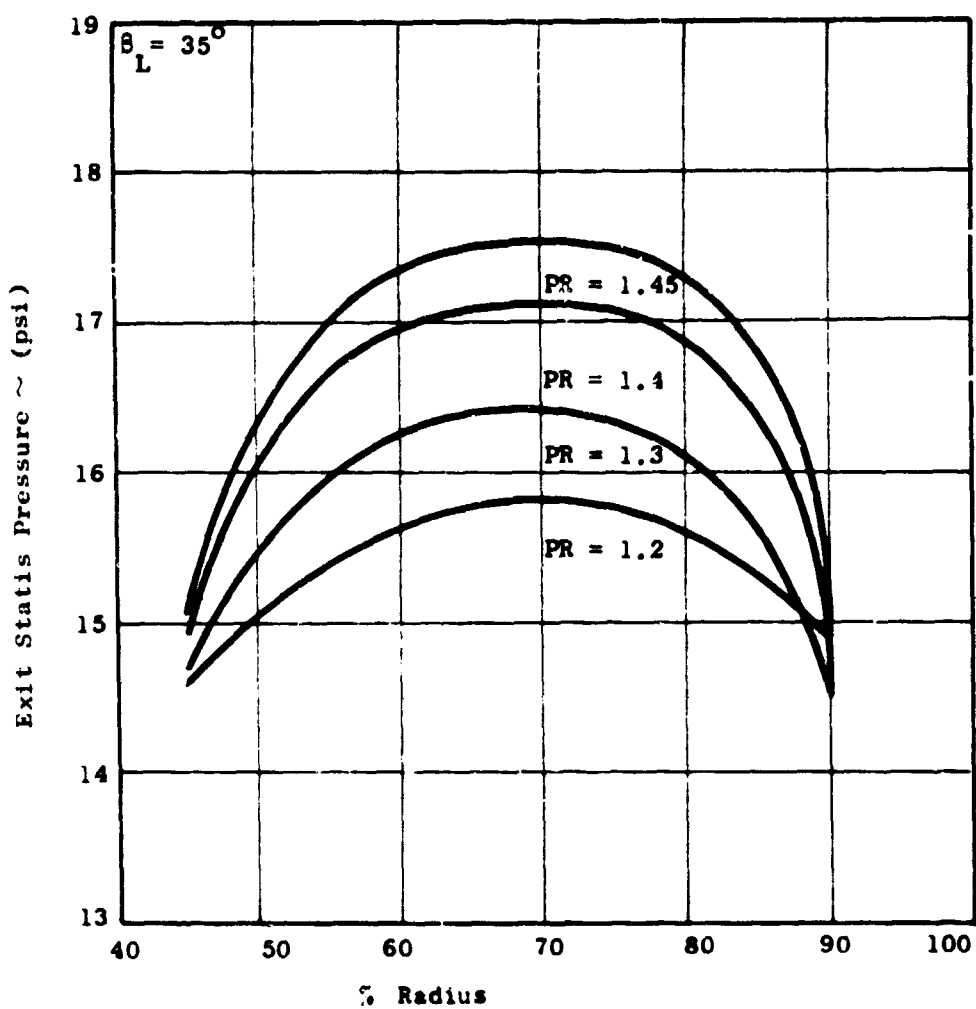


Figure 432 Lift Fan Louver Test Configuration 2

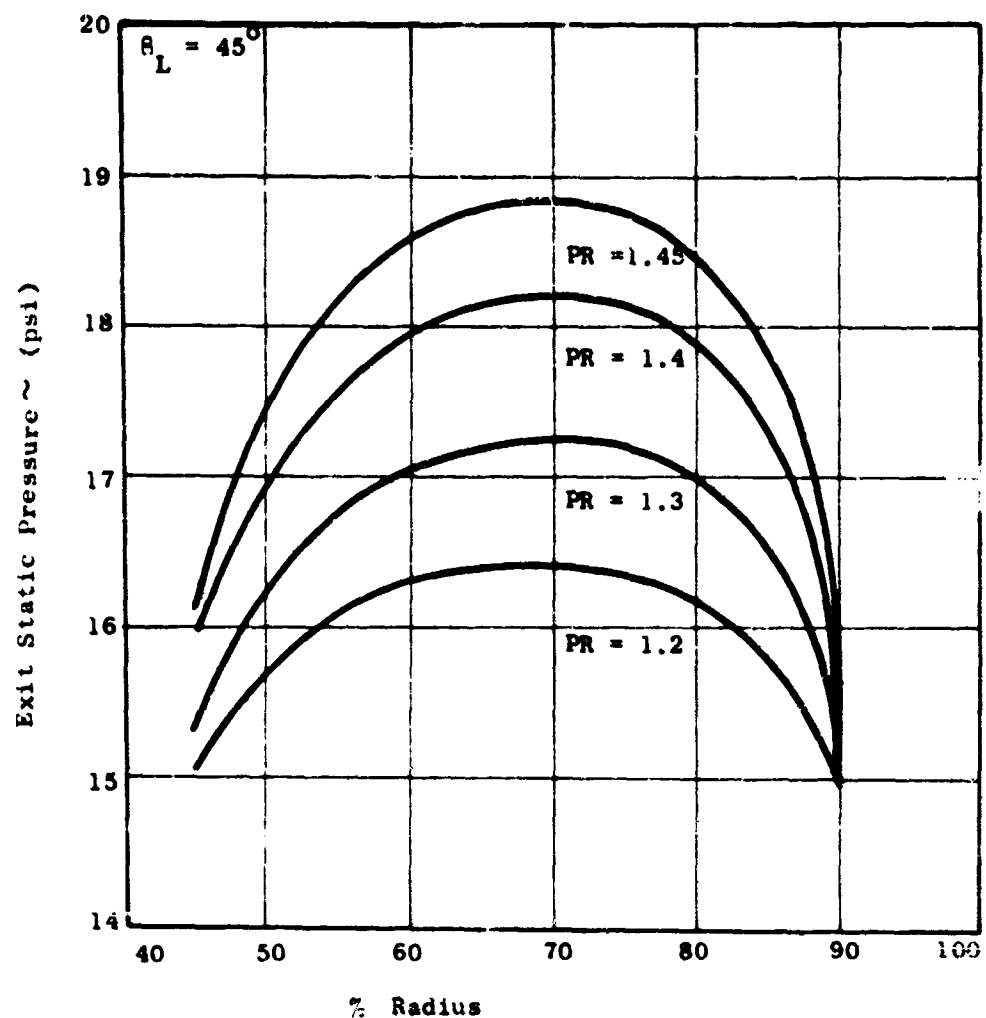


Figure 433 Lift Fan Louver Test Configuration 2

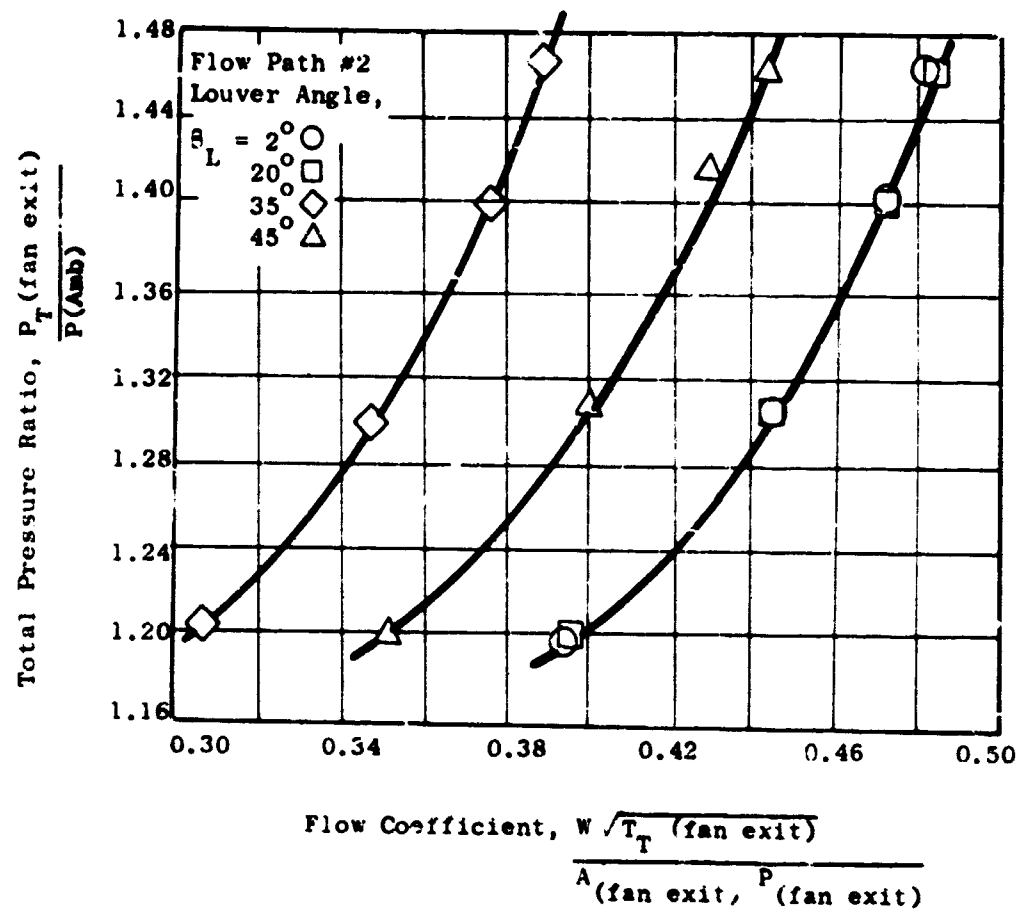


Figure 434 Lift Fan Louver Test

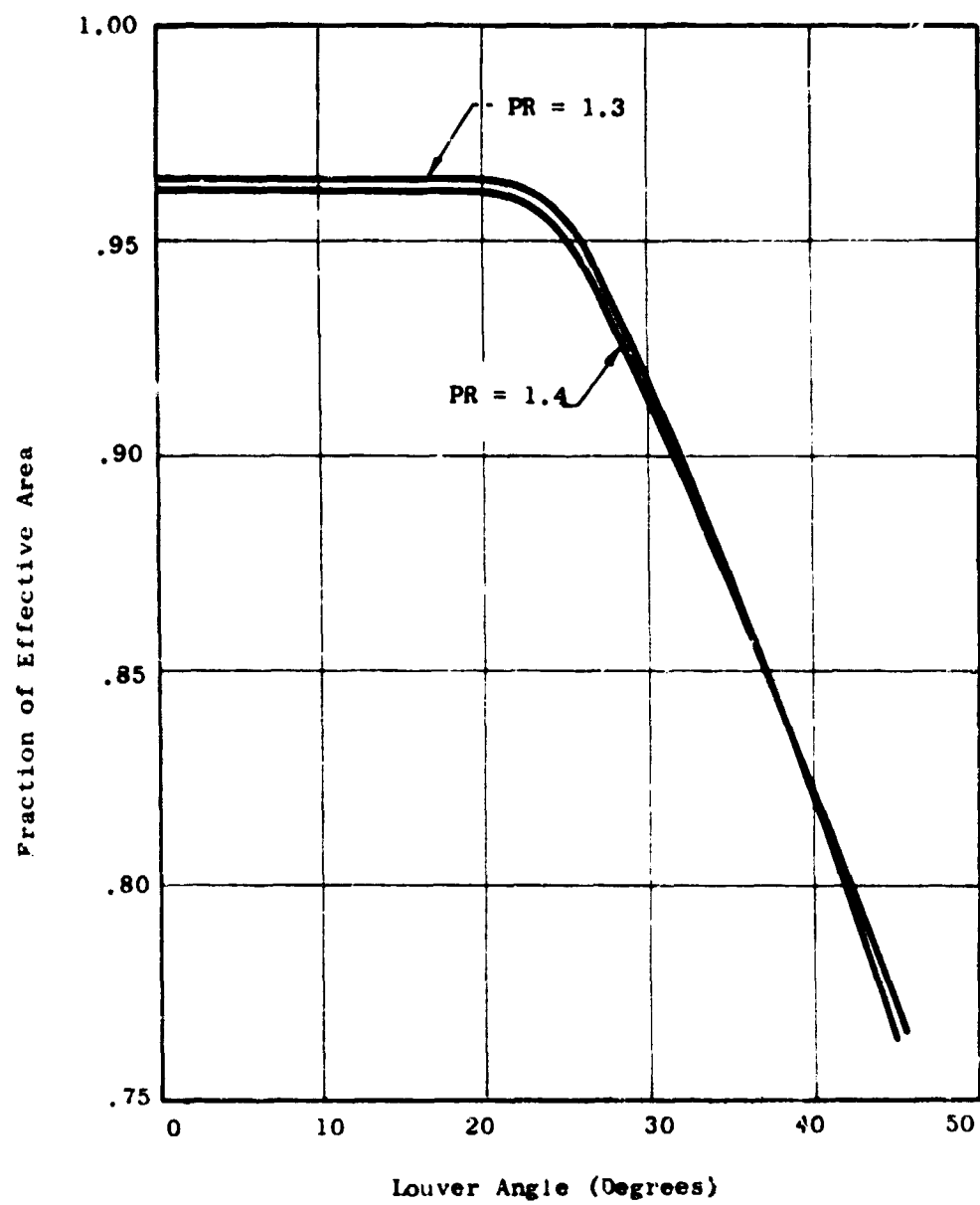


Figure 435 Effective Area Reduction

heavily relied upon because of some lack of information related to the divergence of the flow at the exit of the first path. Furthermore, the results from the first configuration indicate that at a louver angle of 45° there is no significant difference in the throttling effect upon a fan.

(U) Performance Prediction:

The performance prediction for the LF475 fan are represented in Figure 436. The dashed line on this figure is a constant power line. Along this line a fan is absorbing the design point power. Its computation took into account variations of fan weight-flow, total pressure ratio and efficiency. The tip turbine power output was assumed constant. This appears reasonable over the small range of wheel speeds predicted. Furthermore, according to past experience and present test results the turbine is back-pressured by the louvers, considerably less than the fan passage.

(U) The fan performance is presented in terms of total pressure ratio versus fan exit flow parameter. The louver map appears in these same terms; inlet total pressure ratio versus inlet flow parameter (short dashed lines). The performance of the system can be viewed instantly. For a given louver angle, equilibrium between the louver throttling effects and the fan power absorption requirements is shown as an intersection of the appropriate louver curve and the constant power line. At this point the fan exit Mach number equals the louver inlet Mach number. And, the static pressure drop through the louvers is equal to the difference between fan exit static and ambient pressures.

(U) As shown this fan cannot be expected to endure the throttling imposed by this louver configuration at a louver angle of 45°.

(U) Louver performance:

Extensive traverses were made at the louver exit plane in an attempt to measure louver thrust coefficient and resultant thrust angles. However, the flow patterns were so erratic in this area that it was not felt that meaningful results would be obtained from this data and it is recommended that all future louver tests eliminate exit louver traversing for this purpose and instead use a direct measurement of thrust forces and angles.

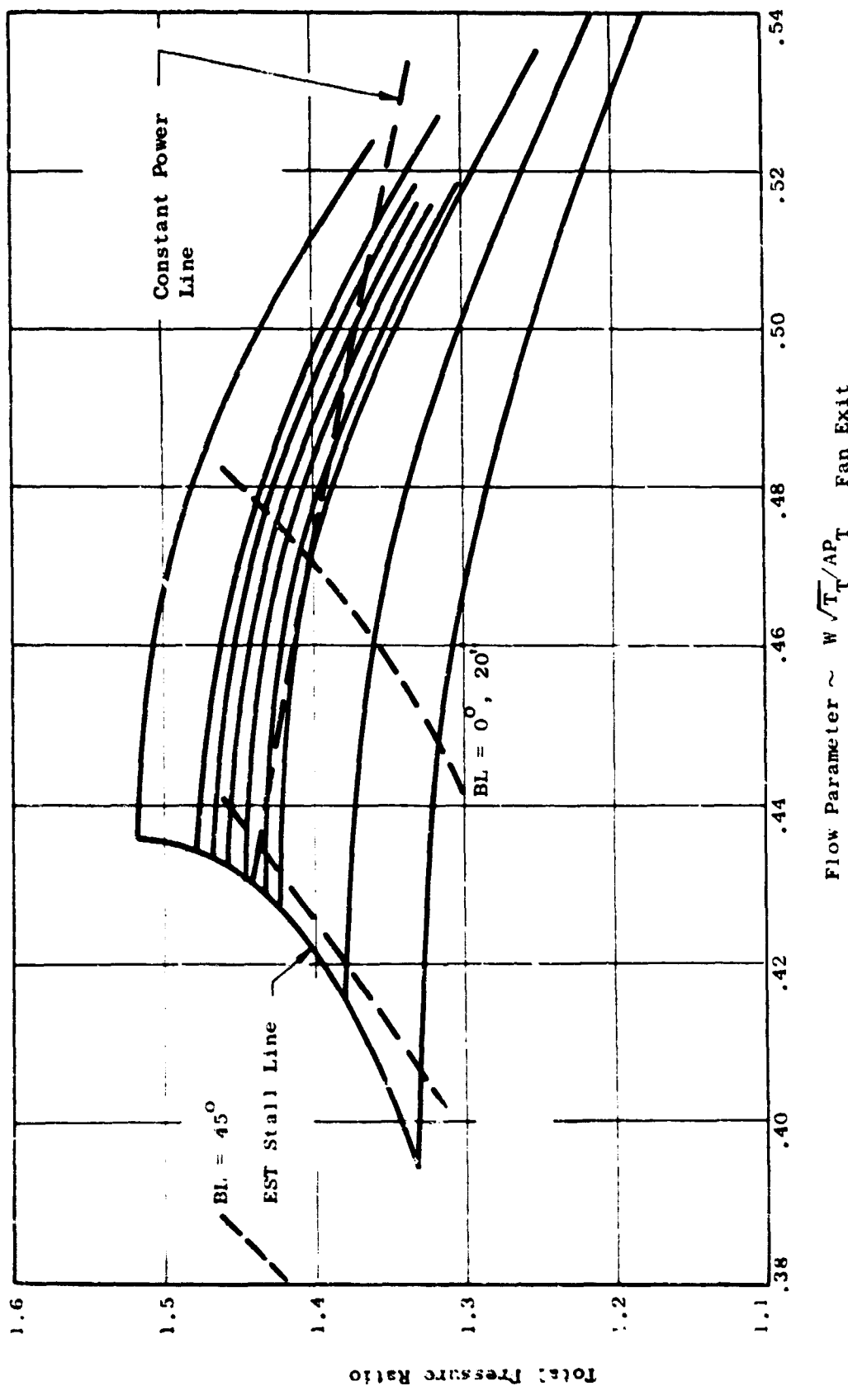


Figure 436 LF475 Louver Induced Migration  
 Flow Parameter  $\sim W \sqrt{T_T / AP_T}$  Fan Exit

## MF415 Louver Tests

### Introduction. -

(U) The louver assembly from the louver cascade test was modified for testing with the MF415 fan. Tests were made with the louver assembly in three positions. First they were tested in the conventional "up close" position. Second, they were dropped one half a louver chord length below the fan exit plane. Third, the whole assembly was tilted at an angle of 22.5 degrees to the fan exit with the aft edge up close and the forward edge dropped down.

### Tests. -

(U) The louvers were mounted on load cells independent from the fan so that the horizontal force on the louvers could be measured. No vertical forces were measured. Figure 437 shows the measured corrected horizontal thrust versus louver angle setting. These thrust values have also been adjusted to a constant corrected fan horsepower. It can be seen that the dropped configuration results in the maximum horizontal thrust load. The 22.5° tilted configuration is second best and the conventional configuration is substantially worse.

(U) Figure 438 compares the total thrust of the dropped and tilted configurations. The total thrust is not a measured value but is an ideal value computed from measured fan flow and pressure ratio. All points have been normalized by the total thrust at 0 louver angle for the dropped configuration. Here we see that the dropped louvers are 2 to 3 percent better than the tilted louvers. It must be pointed out, however that the total thrusts as computed here do not account for either the fan stator losses or the louver losses, either of which could change the above comparison. Also shown on this curve is the normalized total thrust curve for the X353-5 lift fan. This does include stator and louver losses and it can be seen that the total thrust does drop off much more for high positive or negative louver angles.

(U) Figure 439 shows the effect of ground plane height on the total thrust ratios of the dropped louver configuration. Also shown are results from the 26 inch LSSN fan with conventional louvers. It should be noted that Figure 439 is adjustable for constant speed rather than constant horsepower.

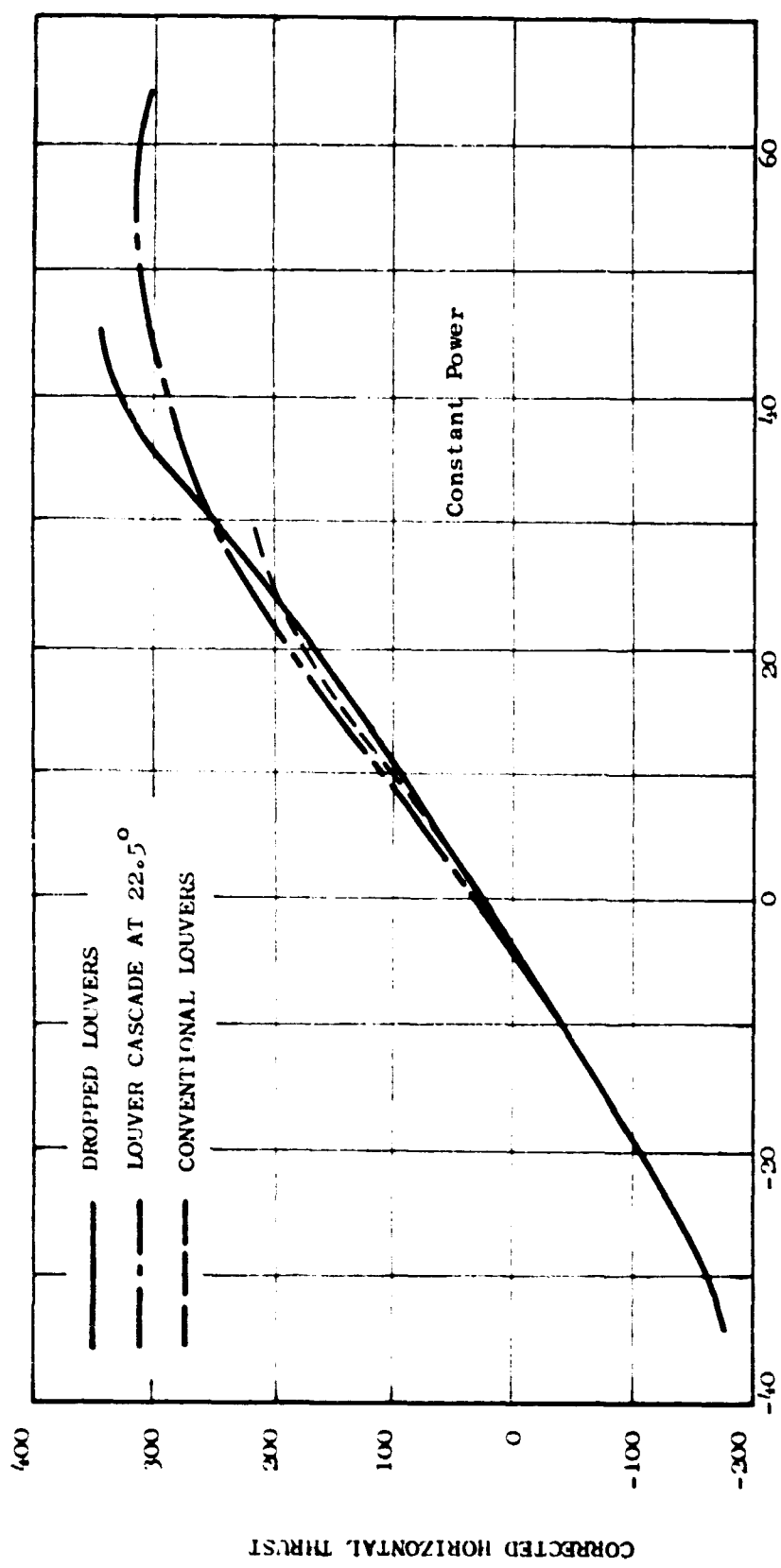


Figure 437 Corrected Horizontal Thrust Versus Louver Angle Setting

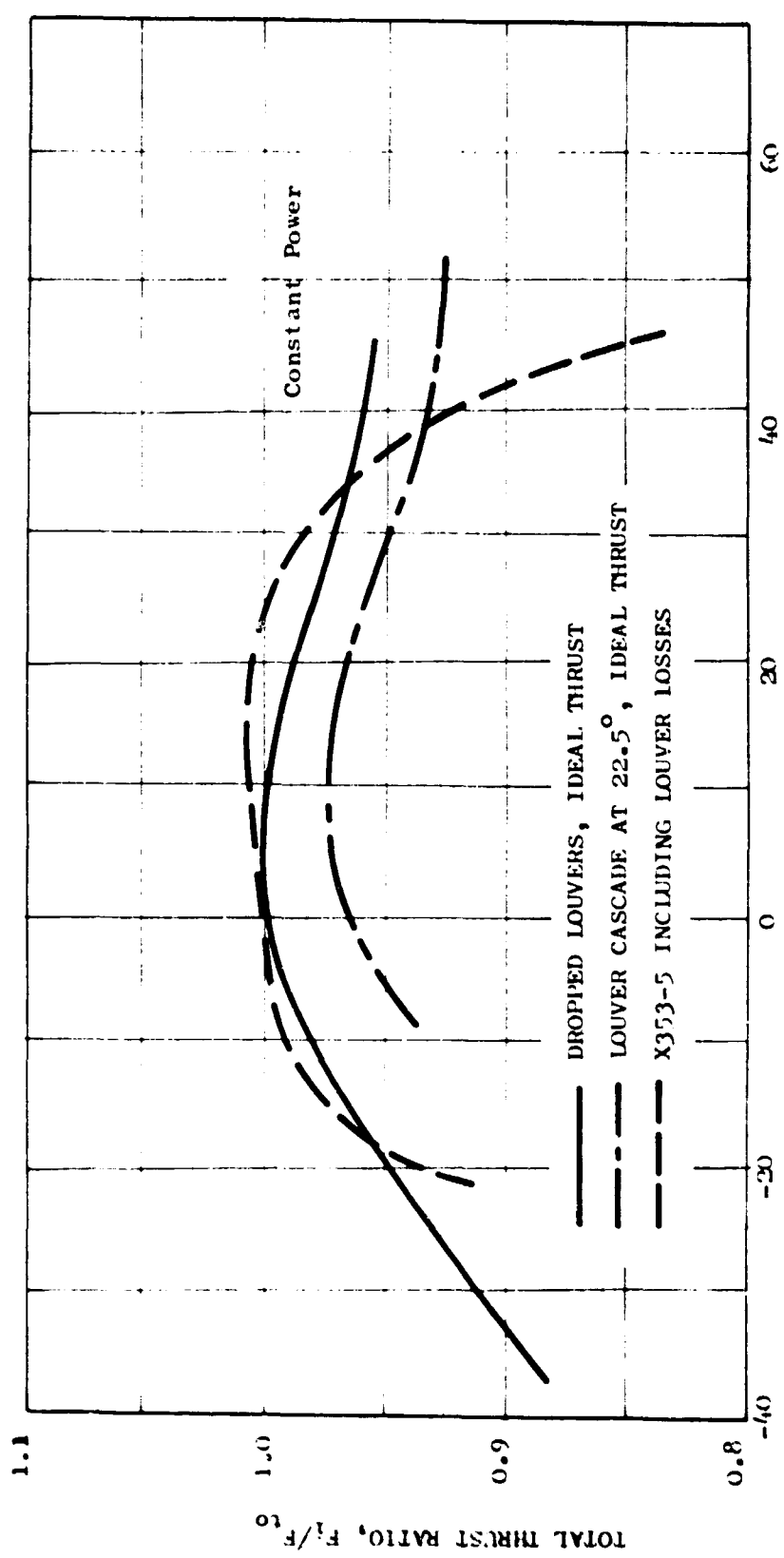


Figure 438 Total Thrust Ratio Versus Louver Angle Setting

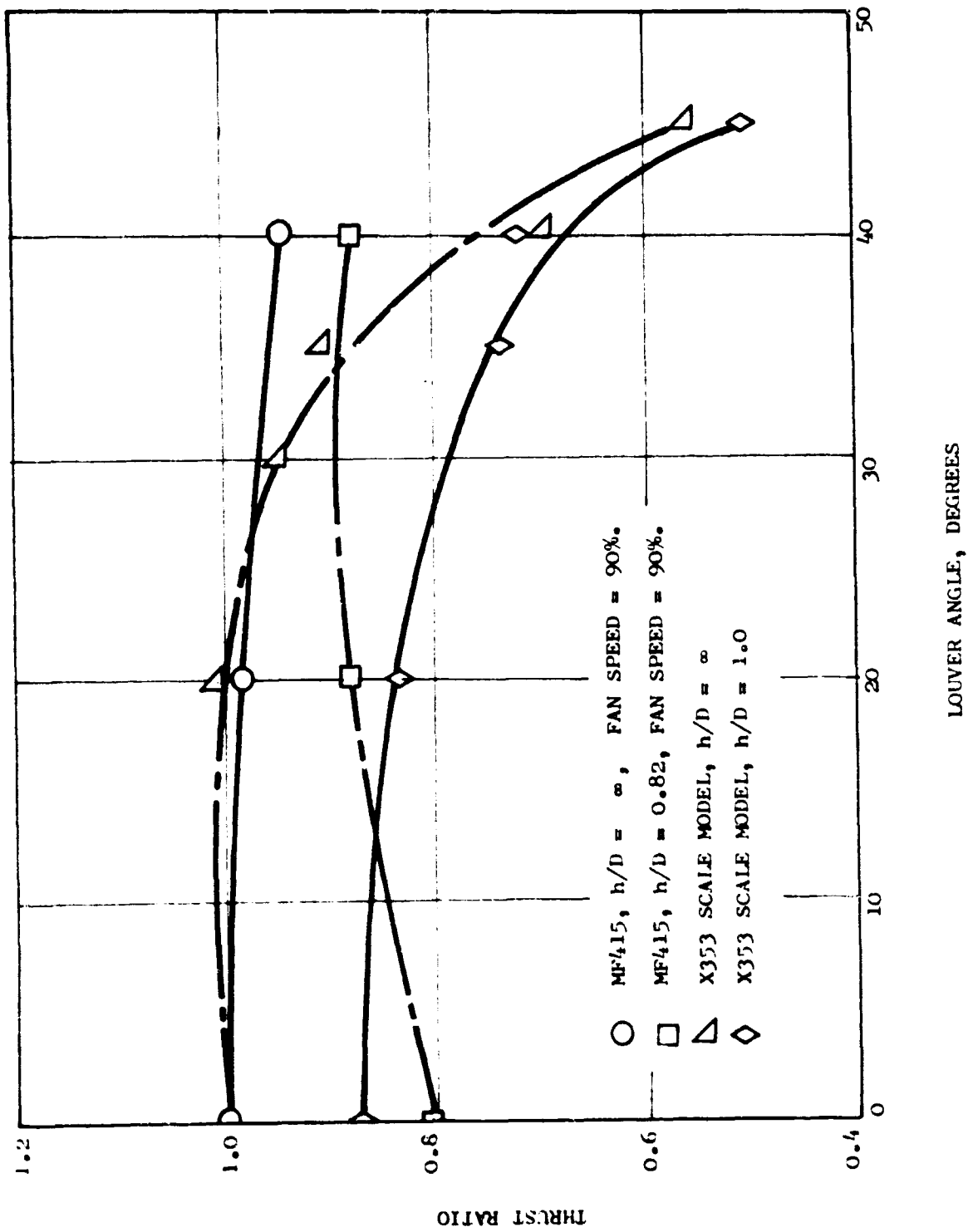


Figure 439 Thrust Ratio Versus Louver Angle

Conclusions & recommendations. -

(U) This data seems to indicate substantial gains in performance by dropping the louvers one half chord length below the fan exit. The tilted configuration also showed some gain. The results cannot be taken as conclusive, however until a better evaluation of actual total thrust is made.

## PNEUMATIC DUCTING

### Ducting Studies

#### Introduction

(U) Advanced lift and lift/cruise fan systems require reliable lightweight ducting for transmitting the hot gas generator exhaust to the fan components. The advanced component technology of the basic gas generators has resulted in higher exhaust gas temperatures and pressures. With this increased gas generator technology, a similar increase in hot gas ducting technology is required. This program had the objective of providing the needed technology for the design of hot gas transmission ducting as well as of the numerous fan components associated with hot gas transmission. The scope of the program to accomplish these objectives included:

The determination of present technology applicable to hot gas ducting for the range of temperatures and pressures anticipated in the advanced gas generators.

The design of selected ducting systems utilizing the results of the technology survey, as well as any possible advanced technology.

The conduction of heat transfer tests utilizing small two-dimensional panels to provide performance information that may be required for any novel ducting design.

The manufacturing and testing of at least two ducting configurations at flow rates, pressures and temperatures representative of the advanced gas generators.

The determination of the vulnerability of hot gas transmission components to potential hazards of operation by demonstrating the performance of the ducting systems under such adverse conditions.

#### Discussion

(U) Surveys of existing technology have led to the definition of some basic ground rules that apply to the design of ducting systems for temperatures in the range of 1600°F. These ground rules are summarized as follows:

Insulation material cannot be used as a load carrying member of the structure. Basically, load carrying capability and the desired insulation property are not compatible. No major development in this area is foreseen.

Materials should maximize the use of existing technology, for

example Rene' 41, L-605, and Hastelloy X. It is desirable that a non-heating material be used to facilitate simple repair by welding. A major breakthrough in material is possible, but the designs should not rely on this future technology.

The ducting systems will be insulated and air cooled, as required, to maintain a maximum external surface temperature of 500°F. This 500°F limit is established by the maximum temperature capability of adjacent aluminum aircraft structure.

Design life at 1600°F will be established by cycle mission requirements. Present design life cycles are between 100 and 1000 hours at temperature.

Ducting minimum material thickness is established by manufacturing and handling requirements, and will range between 0.010 and 0.015 inch.

(U) Three potential ducting systems were identified and carried through the preliminary design phase. A brief description of the three designs is given below.

Single Wall (Figure 440).-

(U) This type of ducting design utilizes the conventional type of design where a single wall is used to provide the pressure vessel and operates at the gas generator exhaust gas temperature. The duct wall thickness is sized to withstand the gas pressure using a design stress established by the plastic creep properties of the material. The material selected for the preliminary design duct wall is Rene' 41. The outer surface of the duct is insulated by a conventional foil enclosed insulating material. John Mansville "Dyna-Quartz" insulation was selected because of its high thermal efficiency (thermal efficiency is a maximum when the product of density and thermal conductivity is a minimum).

Bead Duct (Figure 441).-

(U) The beaded duct type of design makes use of a bellows for the inner liner, providing a structure that exhibits stiffness in the circumferential direction only. The bellows is soft in the axial direction and can withstand considerable axial thermal growth without developing excessive stress levels. The inner liner may be a continuous bellows, or it may be a series of separate closely spaced bellows, the choice being established by the stress levels due to thermal growth.

(U) The outer wall of the duct provides the pressure vessel of the system and will be operating at a temperature considerably below the gas generator exhaust gas temperature because of insulation located between the outer and inner beaded wall duct. The inner wall

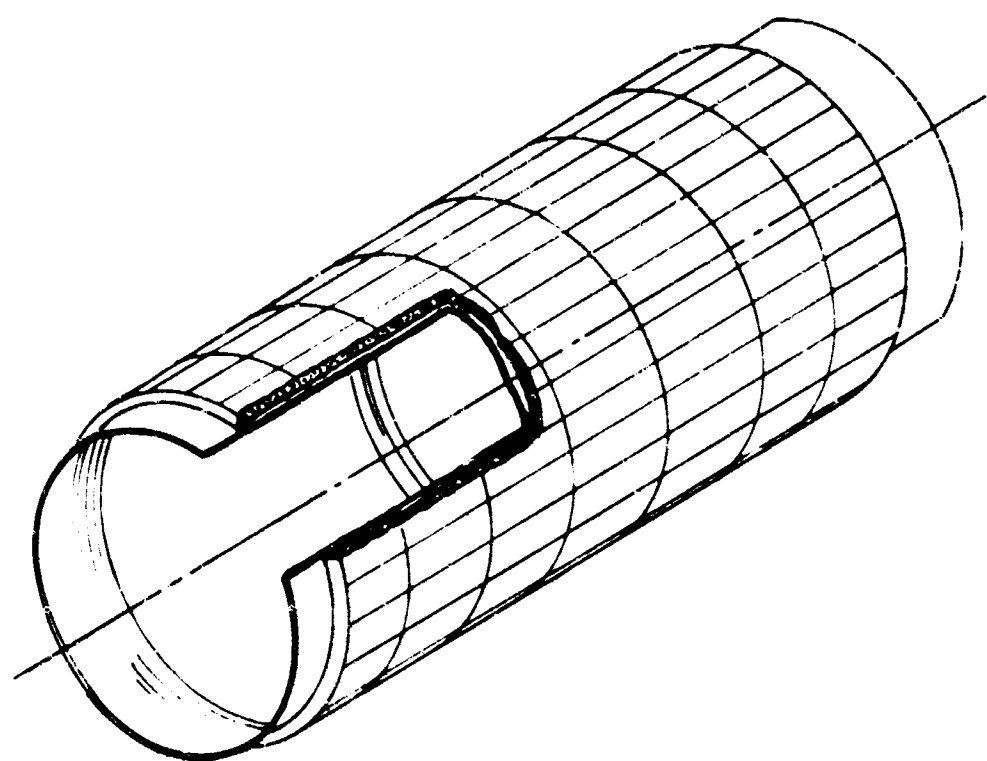


Figure 440 Single Wall Duct

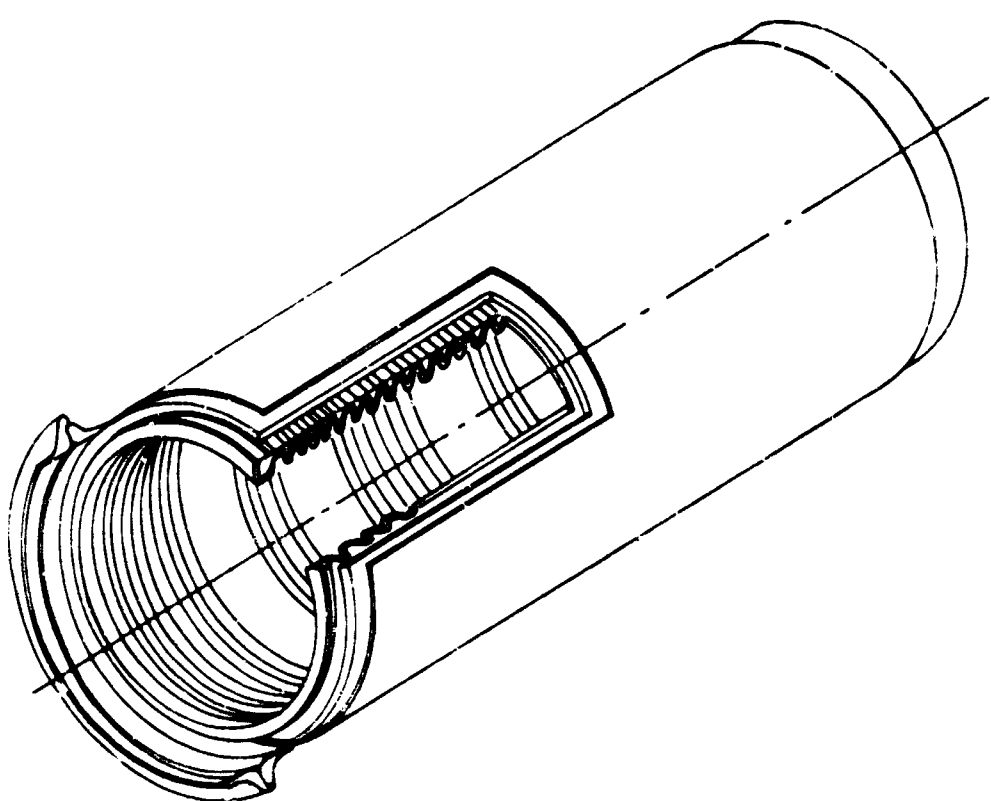


Figure 441 Beaded Ducting

will be vented to equalize the pressure between the inner and outer walls.

#### Insulated Honeycomb (Figure 442).-

(U) This type of ducting system makes use of a novel composite structure to provide the inner liner of the ducting system. The liner is formed by a series of over-lapping panels of insulation filled honeycomb. The panels are loosely attached to the duct outer wall to reduce thermal stresses due to expansion and contraction. The honeycomb system is used as an insulation material as required to reduce the outer duct wall temperature to around 1100°F; this limit is established because of the poor thermal insulating properties of the honeycomb as compared to other conventional insulation. The outer surface of the duct pressure vessel is insulated as required using conventional foil wrapped insulation.

#### Analysis

(U) The following analytical studies were conducted to evaluate pressure loading, cooling requirements and duct vulnerability.

#### Pressure loading on ducting system liners.-

(U) The pressure loading on a ducting system liner is a critical design parameter, particularly an external pressure which could produce liner failure due to buckling. This buckling pressure could occur when the propulsion system is shut down instantaneously. At that time the internal duct pressure rapidly decays to ambient pressure. However, the cavity formed by the inner liner and duct outer wall remains at a somewhat higher pressure and decays more slowly because only a certain amount of vent holes can be provided in the liner.

(U) This transient system was analyzed by writing the general equations of the flow conditions in the duct in a differential form. The equations were then solved by a series of successive incremental steps in order to determine the liner differential pressure. The effect of each variable was investigated and the results are presented in Figures 443 and 444. These figures present the required leakage area (venting),  $A_L$ , as a function of duct Mach number, length of duct and shroud or insulation cavity area. Liner pressure levels of 2.0 and 4.0 pounds per square inch are shown.

#### Cooling air versus insulation trade-off.-

(U) This study was conducted to determine if an optimum ratio of insulation and cooling air existed for a ducting system that resulted in minimum installed system weight. To perform this analysis, the following assumptions were required:

Cooling air would be supplied by a tip turbine driven cooling

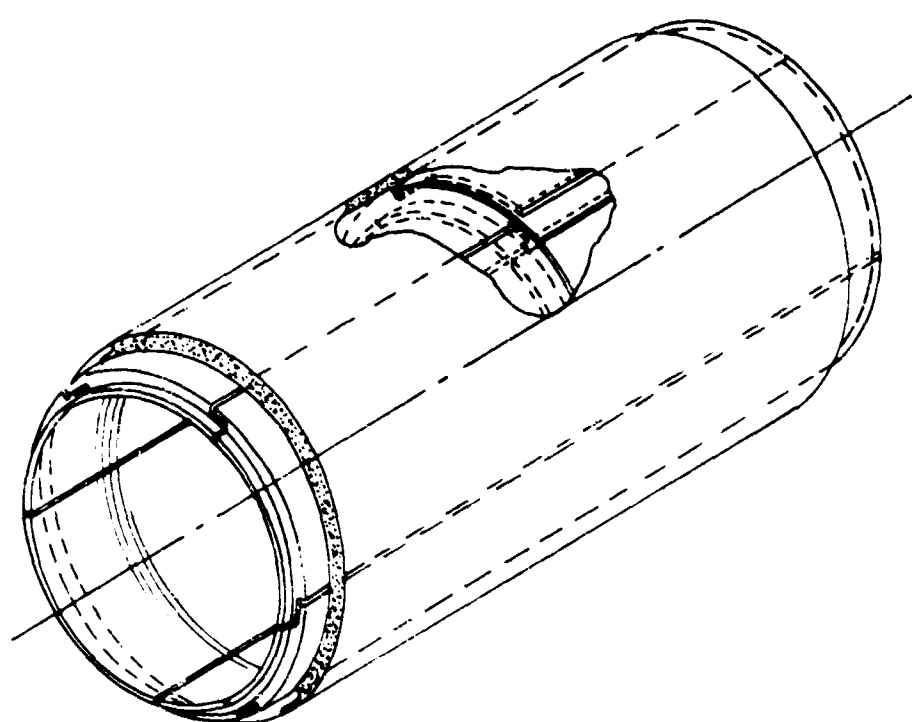


Figure 442 Insulated Honeycomb Ducting

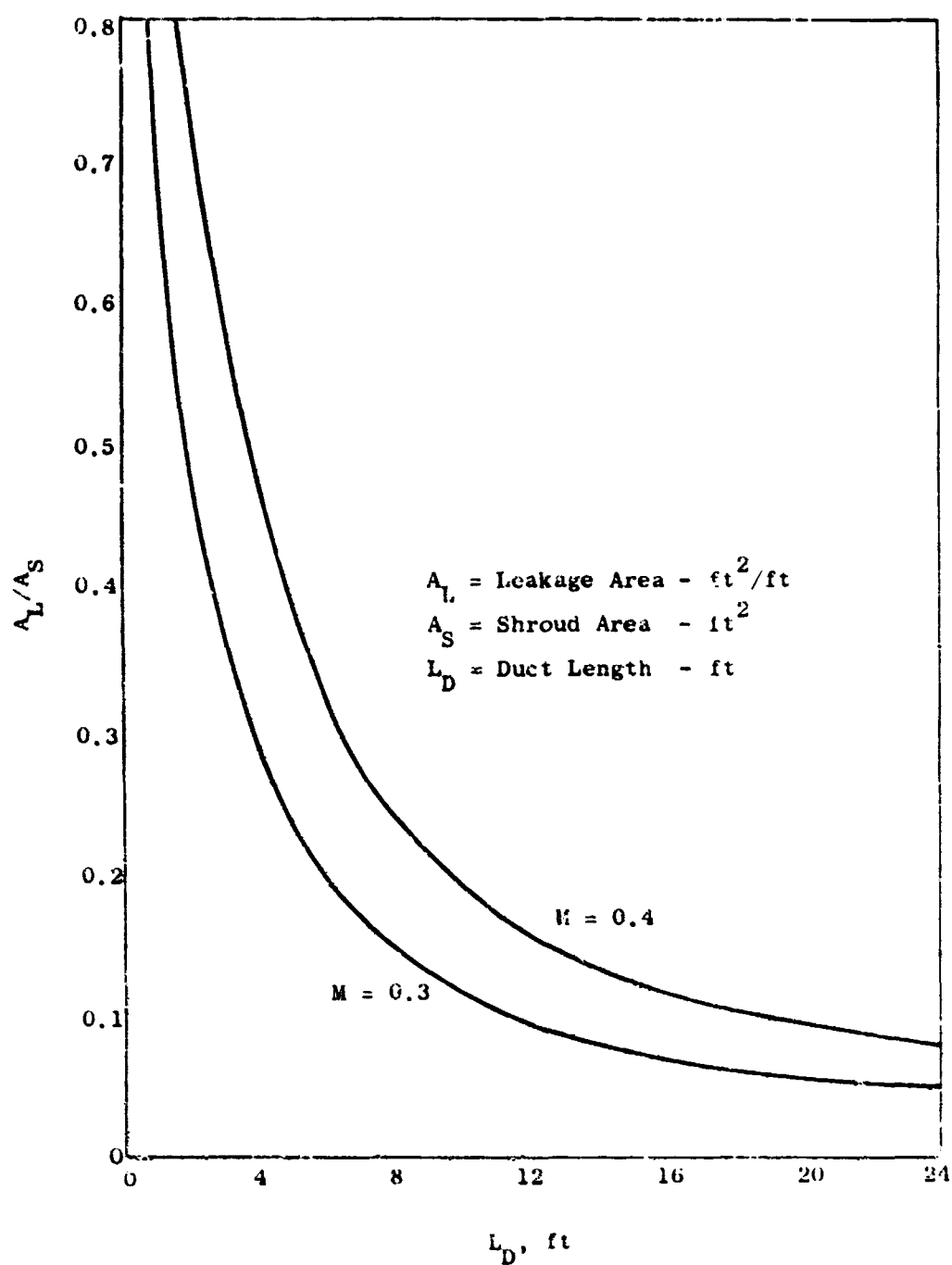


Figure 443 Leakage Area and Shroud Area Versus Duct Length for Maximum  $\Delta P = 2.0$  Pounds Per Square Inch

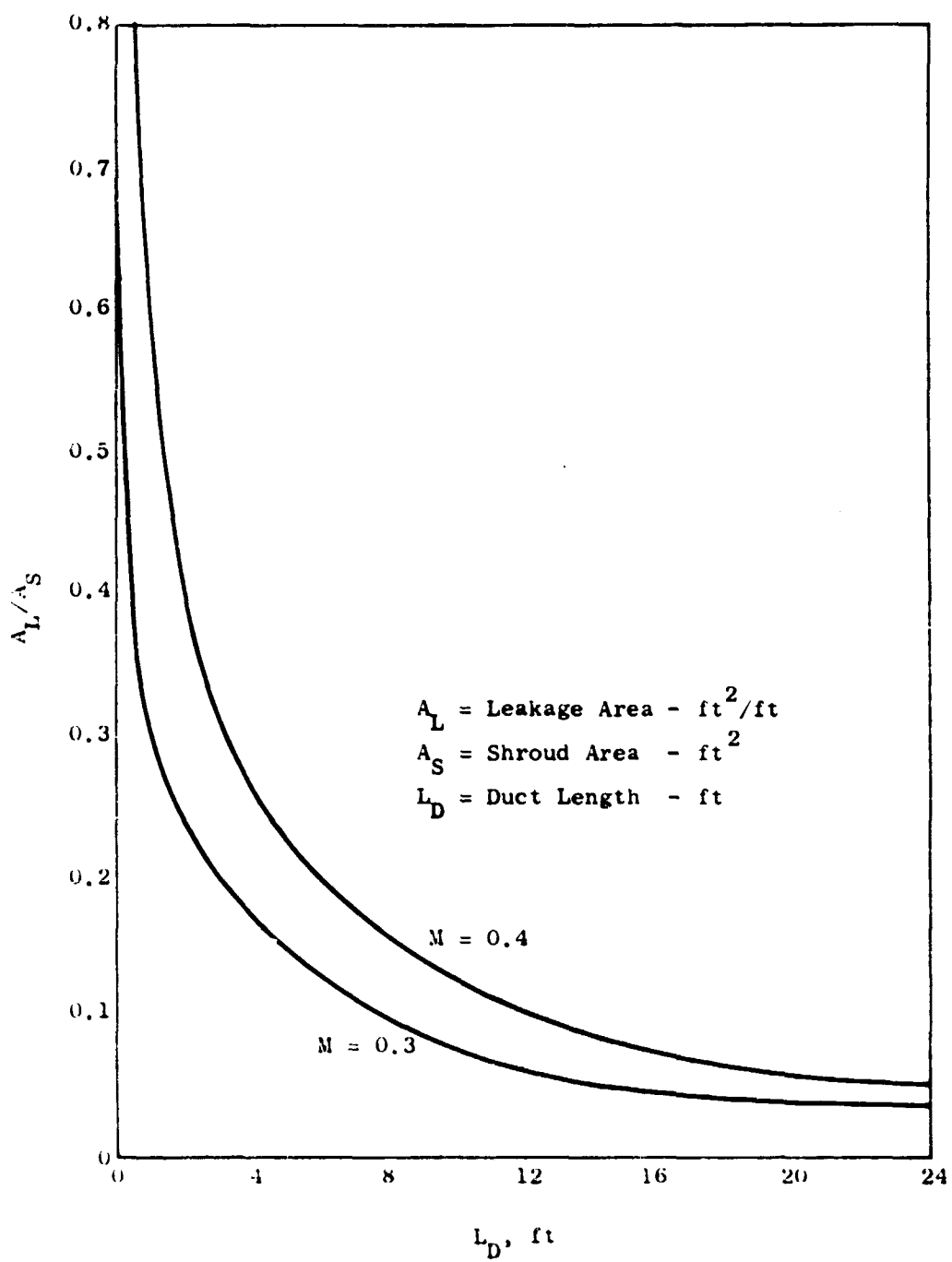


Figure 444 Leakage Area and Shroud Area Versus Duct Length  
for Maximum  $\Delta P = 4.0$  Pounds Per Square Inch

air supply fan of weight comparable to the present control fan technology.

The fan would be driven by gas generator compressor discharge air. The lift loss due to the engine bleed was counted as an added weight for the system.

The weight of the structure required to provide the cooling air flow path was not an added weight to the system.

(U) Using conventional heat transfer analysis and the performance of the cooling system, the optimum cooling flow rate and duct insulation heat transfer coefficient were obtained and are as follows:

$$w_c = \left[ \frac{645 k_i \rho_i A^2}{C_p \ln \frac{T_g - T_{C1}}{T_g - T_{C2}}} \right]^{1/2}$$

$$\frac{k_i}{t_i} = \left[ \frac{645 C_p k_i \rho_i \ln \frac{T_g - T_{C1}}{T_g - T_{C2}}}{T_g - T_{C2}} \right]^{1/2}$$

where

$k_i$  = insulation conductivity

$\rho_i$  = insulation density

$A$  = duct exposed surface area

$T_g$  = core engine temperature

$T_{C1}$  = cooling air inlet temperature

$T_{C2}$  = cooling air discharge temperature

$C_p$  = specific heat of air

$w_c$  = cooling flow rate

$t_i$  = insulation thickness

(U) Using the above relationships for optimum cooling air flow and insulation thickness, a typical system would be as follows:

Insulation: Micro-Quartz with  $\rho_i = 3.0 \text{ lb/ft}^3$ , and  $k_i = 0.061 \text{ BTU/hr/ft/}^{\circ}\text{F}$

Temperature:  $T_g = 1600^{\circ}\text{F}$ ,  $T_{C1} = 60^{\circ}\text{F}$ ,  $T_{C2} = 300^{\circ}\text{F}$

Ducting Area:  $A = 100 \text{ ft}^2$  (approximately 25 linear feet of 15-inch diameter duct)

Cooling Air:  $W_C = 1.5 \text{ lb/sec}$  (optimum)

Insulation Thickness:  $t_i = 0.3 \text{ inch}$

Duct vulnerability.-

(U) An analysis of ducting vulnerability was accomplished by using fracture mechanics to determine the type of failures to be expected in ducting systems with cracks and when punctured. Fracture mechanics is a concept that relates geometry, crack length, material yield strength, and an additional material property called fracture toughness. The following discussion will present methods applicable to the analysis of hot gas ducting using fracture mechanics and some conclusions of duct failure modes.

(U) Two reports presenting test results and data correlations for through-cracked cylinders were obtained. Both reports propose results on explosion of cracked cylinders. The general equation is:

$$\sigma_H = \frac{K_{CN}}{\left[ \pi a_0 + \left( \frac{AK_{CN}}{\sigma_y} \right)^2 \right]^{1/2}}$$

where

$\sigma_H$  = hoop stress for rapid crack growth failure of a through-cracked cylinder

$a_0$  = 1/2 initial crack length

$K_{CN}$  = fracture toughness parameter based on initial crack length before loading, this is a material property (see discussion on next page)

$\sigma_y$  = yield strength of material, 0.2 percent offset

A = an empirical constant

Two definitions of the constant "A" were proposed in the reports as follows:

$$A = \frac{B}{2\pi}$$

$$A = \frac{1}{2\pi} \left[ 1 + C \left( \frac{2a_0}{D} \right) \right]$$

where

B & C = correlation constants

$\frac{2a_0}{D}$  = ratio of crack length to duct diameter

(U) The first report represented tests on aluminum cylinders at room temperature and -423 degrees Fahrenheit. The constant "B" ranged between 0.4 and 0.7. The second report represented tests of both titanium and aluminum cylinders and "C" ranged between 3 and 10. The reason for the variation of the constants was not understood by the authors of both reports. For a conservative analysis approach, the constant "A" should be made a maximum. The level selected for "A" was 0.16. This is equivalent to a value of "B" equal to 1.0 and a value of "C" equal to 10 for a crack length of 1 inch and a duct diameter of 10 inches. The equation for critical hoop stress in the cracked cylinder is then as follows, after rearranging terms and substituting for the constants:

$$\frac{\sigma_H}{\sigma_Y} = 0.564 \left[ \frac{1}{0.16 + a_0 \left( \frac{\sigma_Y}{K_{CN}} \right)^2} \right]^{1/2}$$

(U) This equation is presented graphically in Figure 445. Assuming the above equation is a true representation of the problem, the only remaining unknowns are the basic material properties such as yield strength,  $\sigma_Y$ , and fracture toughness,  $K_{CN}$ .  $K_{CN}$  is the symbol used when fracture toughness is based on initial crack length as measured before applying loads.  $K_C$  is the counterpart symbol that is based on crack length as measured during loading and at the instant of rapid failure of the part.  $K_{CN}$  seems to be used more often because the crack length can be measured by more conventional methods. The yield strength is known for most materials, but the fracture toughness is known for only a relatively few. A detailed testing program would be required to obtain the fracture toughness of all potential materials suitable for ducting. However, certain analysis and test programs presently reported may be used to yield some trends that could be expected. The following is a discussion of the apparent existing technology of fracture toughness of materials.

#### Fracture toughness.-

(U) Fracture toughness of a particular material is not a true invariant. Another report presents a detailed description of general concepts of fracture toughness. The author discusses, in particular, the effects of crack length and material thickness on the fracture

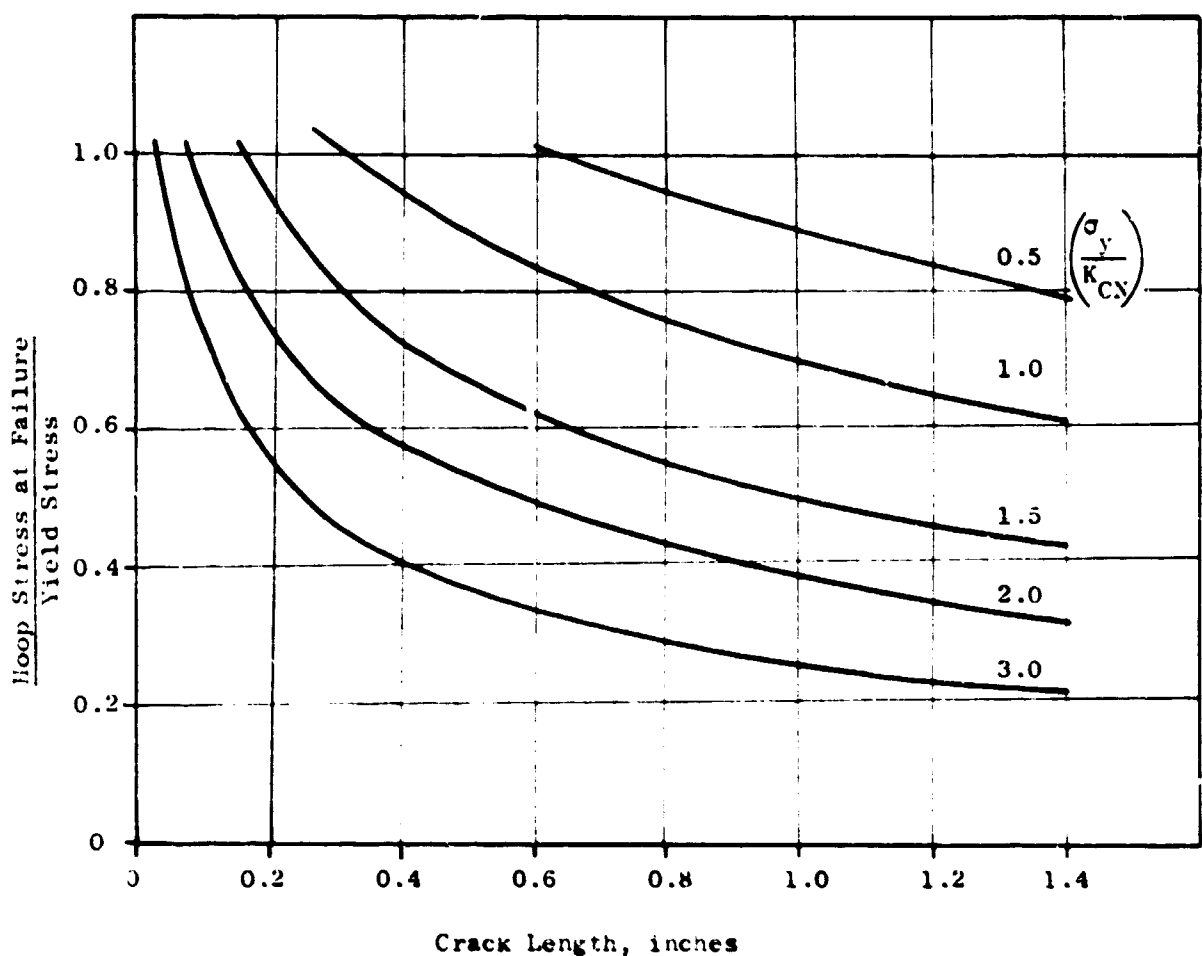
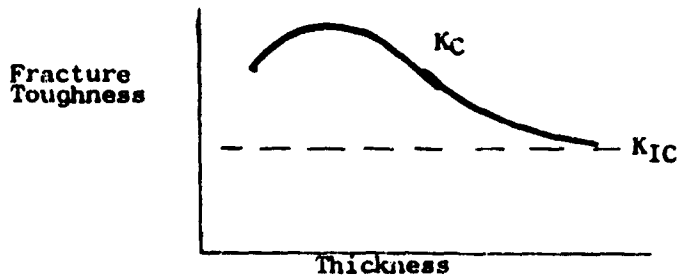


Figure 443 Effects of Crack Size and Fracture Toughness Parameter on Hoop Stress at Failure

toughness of a certain material. It appears that thickness is by far the most significant variable. The curve below shows a typical trend (based on tests of 7075-T6 Al) of fracture toughness with material thickness:



(U) The variation of  $K_c$  with thickness approaches a limiting value of  $K_{IC}$  (I is Roman number I). The significance of  $K_c$  and  $K_{IC}$  is discussed in detail in the fracture toughness report. For this discussion it is sufficient to say that  $K_{IC}$  is the minimum limiting value of fracture toughness except for very thin or foil like material outside the normal useable range.  $K_c$  is greater than  $K_{IC}$ , approaching a maximum at normal sheet stock thickness (0.020-0.200), and must be obtained by testing over a range of material thicknesses. It may, therefore, be concluded that fracture toughness testing could be both time consuming and expensive.

(U) However, several references report the results of measured fracture toughness for sheet material. The measured toughness parameters,  $K_{CN}$ , are summarized in Table 62. This table is presented to indicate general levels of the ratio of yield to fracture toughness only, and will not be used for design purposes.  $K_{CN}$  differs from  $K_c$  in that  $K_{CN}$  is based on initial crack length and  $K_c$  is based on crack length just prior to failure. Crack length at failure is difficult to measure and usually  $K_{CN}$  is used as the material property.

(U) Another report provides an interesting theoretical approach to predicting fracture toughness of materials, based on ordinary tensile properties. This report develops the following equation for  $K_{IC}$ . Note that this is  $K_{IC}$ , the minimum or limit of fracture toughness:

$$K_{IC} = \left[ \frac{2}{3} \cdot \frac{E \cdot \bar{\epsilon} \cdot n^2}{Y} \right]^{1/2}$$

where

$E$  = Young's modulus

TABLE 62  
MEASURED FRACTURE TOUGHNESS OF SHEET MATERIAL

Material	Temp.	Thick	$\sigma_Y$	$K_{CN}$	$\sigma_Y/K_{CN}$
2014-T6Al	-320	0.060	93	34.8	2.6
2014-T6Al	-320	0.060	94.2	48.5	1.9
	RT	0.060	78.1	58.4	1.3
René 41 (Cold Worked & Aged @ 1400°F)	80	0.025	184	210	0.9
	1400	0.025	109	124	0.9
	80	0.050	192	219	0.9
Ti 6-4 (Mill Annealed)	80	0.025	138	115	1.2
	650	0.025	90	123	0.7
	80	0.050	139	125	1.1
Inco 718	80	0.19	156	170	0.9
	650	0.19	144	188	0.8
Ti 6-4	80	0.19	147	125	1.2
	650	0.19	95	137	0.7
Ti 8-1-1	80	0.025	139	123	1.1
	650	0.025	93	115	0.8
	80	0.050	132	145	0.9
Ti 6-6-2	80	0.19	142	140	1.0
	650	0.19	92	138	0.7

$\sigma_y$  = yield strength

$$\frac{\epsilon}{\epsilon_0} = \text{true strain at fracture} = \ln \frac{1}{1-RA}$$

n = strain hardening exponent that may be estimated using:

$$10^n = \frac{0.2\% \text{ yield strength}}{0.02\% \text{ yield strength}}$$

(U) Since the ratio of yield strength to fracture toughness is apparent design criteria for duct systems, then:

$$\frac{\sigma_y}{K_{IC}} = \left[ \frac{3/2}{\frac{\sigma_y}{E\epsilon n^2}} \right]^{1/2}$$

(U) This expression should be a minimum for high failure resistance. Note that reduced yield strength; increased Young's modulus, strain hardening and strain at fracture, all tend to improve relative resistance to fracture. Relative resistance in this case means the probability of failure due to fracture versus general failure due to yielding of the material.

(U) This equation was used to calculate fracture toughness of several common materials and the results are summarized in Table 63. These are minimum values of fracture toughness,  $K_{IC}$ , and are based on only crude estimates of the strain hardening coefficient, n.

#### Conclusions and recommendations.-

(U) Fracture mechanics appear to be a reasonable approach to the prediction of catastrophic duct failures due to the presence of cracks and FOD holes.

(U) The significant parameter for design using fracture mechanics is the ratio of yield strength to fracture toughness,  $\sigma_y/K_{CN}$ . Probability of failure reduces as this ratio becomes smaller. For thin sheet material, probable levels for this ratio are as follows:

Titanium Alloys .....	1.0 to 1.5
Hi-Strength Aluminum Alloys .....	1.0 to 2.0
Heat Treated Steels .....	1.0 to 1.5
Non-Heat Treated Steels .....	0.5 to 1.0

(U) A typical result based on this analysis is as follows: For a duct system with material properties such that  $\sigma_y/K_{CN}$  is 1.0, a hole or crack equal to 1.0 inch in length could be tolerated without

TABLE 63  
CALCULATED FRACTURE TOUGHNESS

Material	Temp.	0.02%	0.2%	E	RA	$\bar{\epsilon}$	$n^{(*)}$	$K_{IC}$	$Y/K_{IC}$
R-41	RT	91	101	31.5	15%	0.16	0.045	26	3.9
	1600	60	65	23.1	12%	0.13	0.035	12	5.2
Hast X	RT	41	53	30.0	35%	0.43	0.114	77	0.7
	1600	22.5	26.5	19.6	40%	0.51	0.071	30	0.9
Ti 6-4	RT	127	135	16.0	42%	0.54	0.027	24	5.6
	600	83	93.5	13.4	57%	0.84	0.052	43	2.2
Inco 625	RT	60	69	29.8	50%	0.69	0.061	59	1.2
	1200	45	51	24.4	42%	0.54	0.053	36	1.4
321 S.S.	RT	34	37	28.4	60%	0.92	0.037	30	1.2
	1200	17.3	20.9	20.5	60%	0.92	0.082	42	0.5
2014-T6Al	-	-	68	10	-	0.37	0.08	35	1.9
2024-T6Al	-	-	50	10	-	0.32	0.16	59	0.8
Ti 6-4	-	-	138	17	-	0.56	0.05	49	2.8
Ti 5-2.5	-	-	170	17	-	0.36	0.06	60	2.8
Inco 718	RT	132.5	165	30.3	35%	0.43	0.095	100	1.7
	1200	121.5	135.5	25.0	35%	0.43	0.062	60	2.3

<sup>(\*)</sup>Strain hardening exponent, n, is only approximate values based on yield strength of materials.

failure at a hoop stress level equal to 70 percent of the material yield strength.

(U) Fracture of ducts appears to be a problem only when the hoop stress levels are above 50 percent of the material strength. This tends to agree with the 2 to 1 safety factors proposed for aircraft ducting. However, this safety factor cannot always be tolerated and still meet weight requirements. This is where selection of materials, based on fracture toughness, may apply. The performance of components that are designed to creep criteria also tend to reduce the probability of catastrophic failure, since they are designed to a stress lower than yield strength.

(U) Depending on the stress levels existing in ducting systems components, it may be desirable to perform some combined fracture toughness and vulnerability testing. This program could include the following:

Measurement of the fracture toughness of the material used in construction of the component.

Build a component with a pre-manufactured crack or hole approximating the maximum anticipated size.

Test this component up to catastrophic failure pressures to verify the analysis and theory

(U) The above analysis and discussion is based on performance of pre-cracked cylinders and ducts. Analysis of instantaneous crack development due to high stress levels requires additional investigation. Preliminary studies of this subject have indicated that it may not substantially differ from the pre-cracked condition.

#### Scroll Duct Liner Design

(U) Due to the importance of the LF475 scroll design and its complete dependency on an adequate cooling system, this program was redirected to specifically provide scroll design information.

(U) Two liner concepts were designed for test evaluation. Identical outer shells, into which variable cooling flows can be admitted, provide the basis for the liner evaluation.

(U) Two basic concepts for holding the liner to the cold structure were designed into the two separate 36-inch long and 8-inch diameter ducts (Figure 446). Duct No. 1 utilizes flexible bellows with overlapping shields attached on the flow side which should eliminate the large pressure losses inherent in a corrugated liner (Figure 447). The flexible Hastelloy X liners are rigidly attached between simulated struts spaced 6 inches apart.

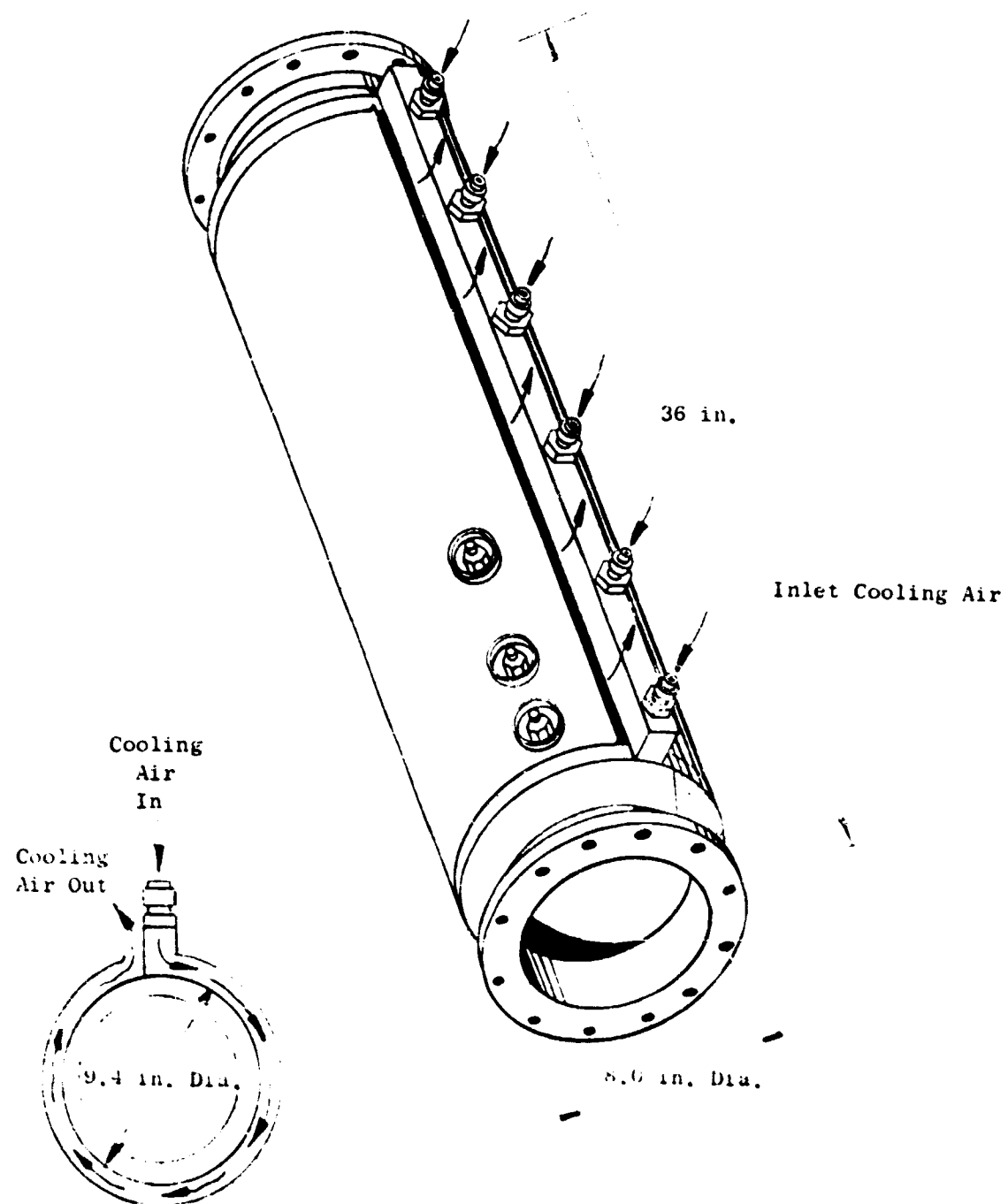


Figure 446 Test Duct Outer Structure

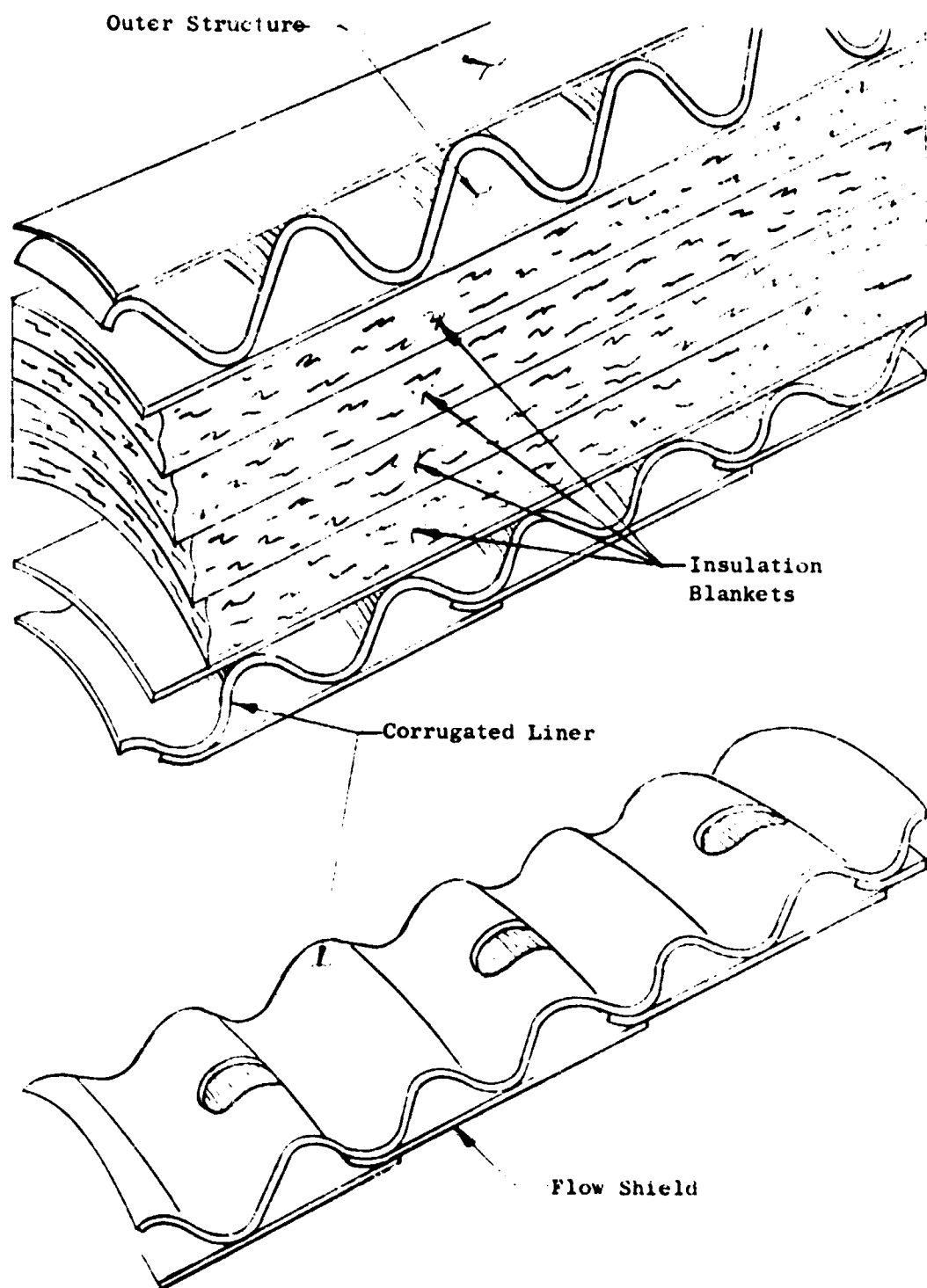


Figure 447 Corrugated Liner

(U) Duct No. 2 employs a series of cylindrically shaped honeycomb liners overlapped in the radial and axial direction and bolted in two places at the tailing edge of each panel. Four panels, when overlapped and bolted to the outer structure, form a cylindrical section. Each honeycomb panel liner is fixed by a bolt on one end, and slotted and held by a bolt at the other end. This arrangement allows unrestrained thermal growth of the panels relative to the fixed bolt.

(U) The same insulation and cooling pattern are in both test ducts. The insulation materials selected for the test ducts are Min-K, Micro Quartz, and Felt Metal. Various combinations of each material will be tried. The insulators separating the bolted attachment between the honeycomb liner and cold outer structure in Duct No. 2 consists of three types of insulating materials: Ceramic, Felt Metal, and Min-K 2000 (see Figure 448)

(U) Micro-quartz insulation is most desirable for this application because of its light weight; approximately 1/3 the weight of Min-K. However, some settling and packing is anticipated due to normal fan vibration and as a precaution, one-half of the blankets will be evaluated using Min-K. The blankets will be fabricated in 1/8 and 1/4-inch thickness with quartz cloth covers stitched one inch apart. Blanket over-lap requirements will also be evaluated.

(U) The advantage of the honeycomb liner is that more is known about this type of liner. An independent research program was conducted by the General Electric Company in 1961, on the application of hot gas ducting in the neighborhood of 2000°F. A successful design was furnished by utilization of a honeycomb liner, bolted rigidly to the structural wall, with insulation encased between the liner and structure.

(U) Another independent research program was conducted by Bell Aerospace in which a heat shield on a Lifting Body had been designed for a temperature of 2000°F. The design incorporated a honeycomb bolted liner to a water cooled structure.

(U) The test cell and test hardware configuration had been finalized (see Figure 449). Scroll Ducts No. 1 and 2 have been delivered for the test and are presently being instrumented.

(U) Premature program termination has prevented flame tunnel heat transfer analysis on this contract. However, testing will be conducted at a later date to evaluate both duct liner designs.

#### Heat Transfer Study

##### Introduction

(U) A test program was conducted to determine the porosity and thermal conductivity of Micro Quartz insulation when subjected to various differential pressures along the insulation. (Figure 449)

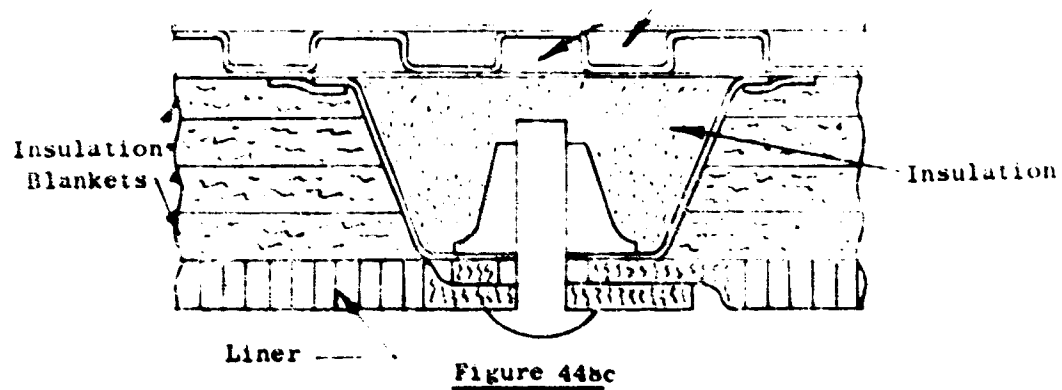
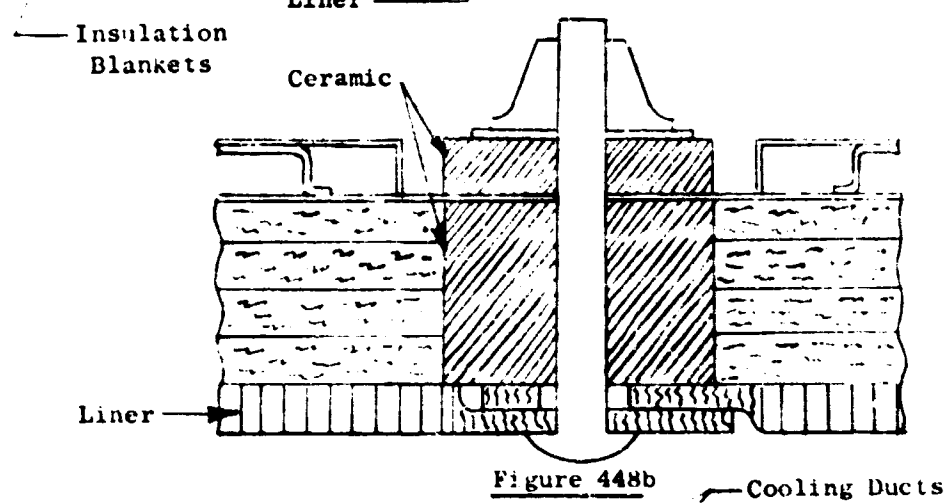
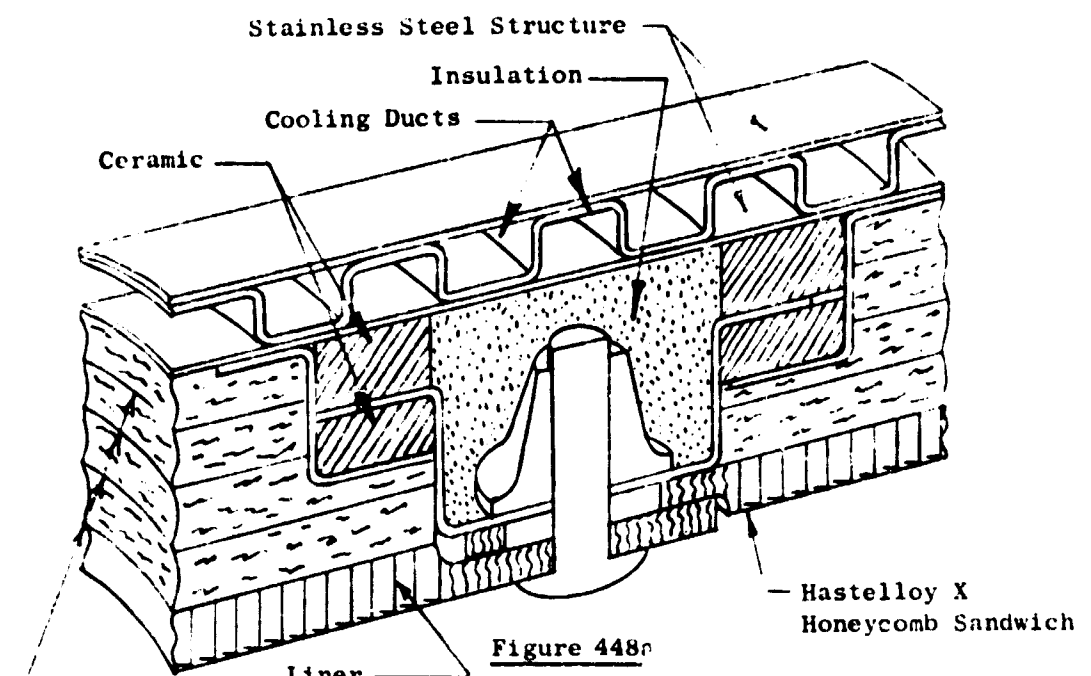


**Figure 448 Bolted Honeycomb Liner**

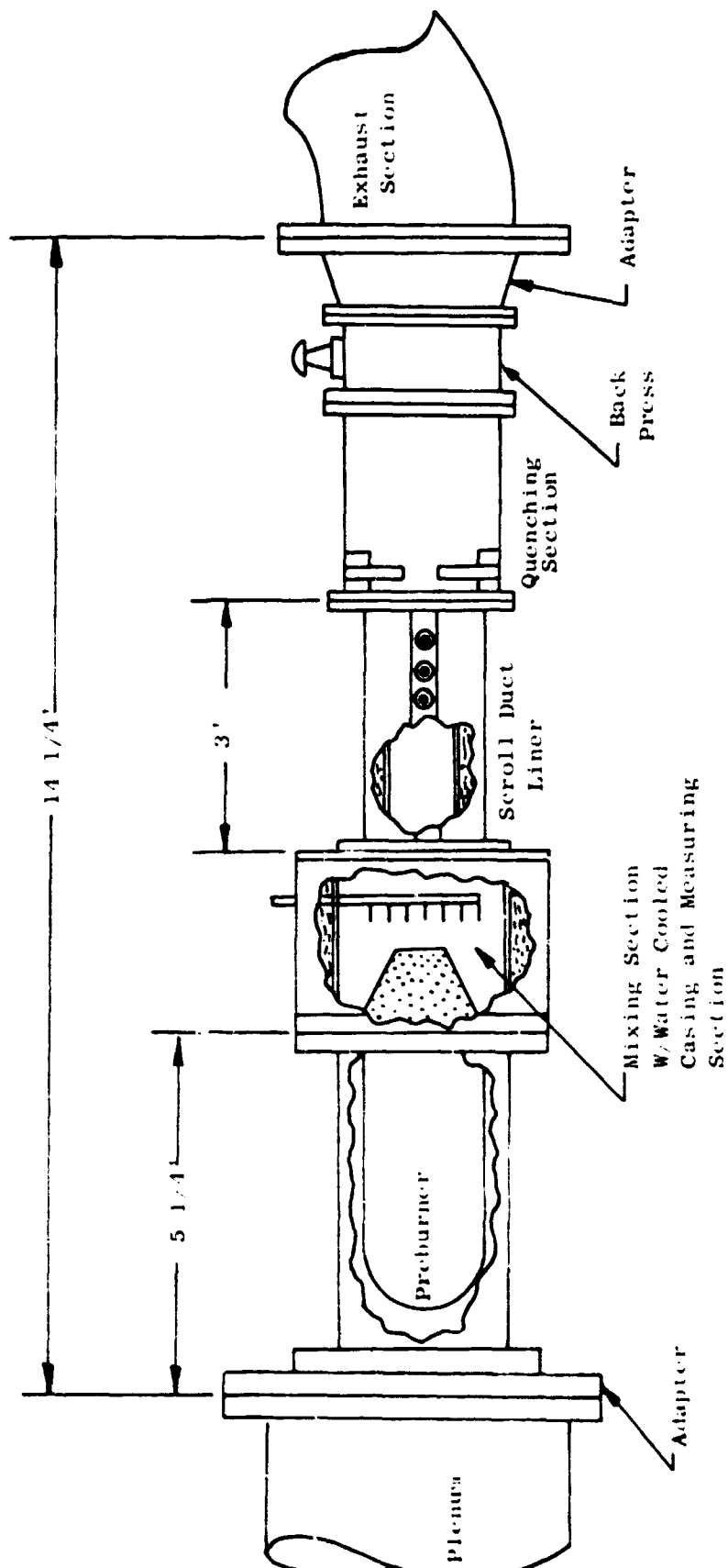


Figure 449 Scroll Duct Liner Test Facility

(U) Johns Mansville "Microquartz" insulation offers the highest heat resistance per pound of material of any applicable high temperature insulating material. It is therefore desirable to use this material for the LF475 scroll and scroll ducting test sections. However, due to the porous and apparently fragile nature of this material it was expected that small pressure gradients within the insulation could adversely affect the high heat resistant properties of the material.

Description

(U) The test duct (Figure 450), consisted of two concentric ducts 1 $\frac{1}{2}$  and 2 inch O.D. between which was sandwiched two layers approximately 1/8 inch thick of 3 pound density "Microquartz" enclosed in quartz cloth backing and stitched in a one inch square pattern as supplied by the Johns Mansville Company.

(U) A 1/4 inch diameter orifice for regulating flow was welded in the center of the inner duct. The space between the two ducts enclosing the insulation was sealed at each end.

(U) Two tests were conducted:

1. Hot air at approximately 500°F was passed through the inner duct. Inner and outer duct wall temperatures were recorded. Using the outer duct wall temperature, the ambient air temperature and the insulation manufacturers thermal conductivity data a convection coefficient between the outer duct wall and the ambient air was established.
2. Holes were then drilled in the inner duct on both sides at the orifice plate. The duct was then reinstalled and the same conditions of inlet flow rate and outside duct wall temperature were established. The required decrease in inner duct wall temperature then established the conductivity of the insulation with the velocity through it. The flow rate within the insulation was established using the calibration of the orifice plate established in part one above.

Results

(U) The results of this test are summarized in Figures 451 and 452 in which the insulation effective conductivity is shown plotted as a function of the pressure gradient causing flow through the insulation and as a function of the actual flow rate within the insulation.

(U) The test results disclosed that the thermal conductivity of the Micro Quartz nearly doubles for a pressure differential of 0.5 psi, which is the maximum  $\Delta P$  anticipated in the scroll. The gas flow through the insulation also depends to a large extent on the

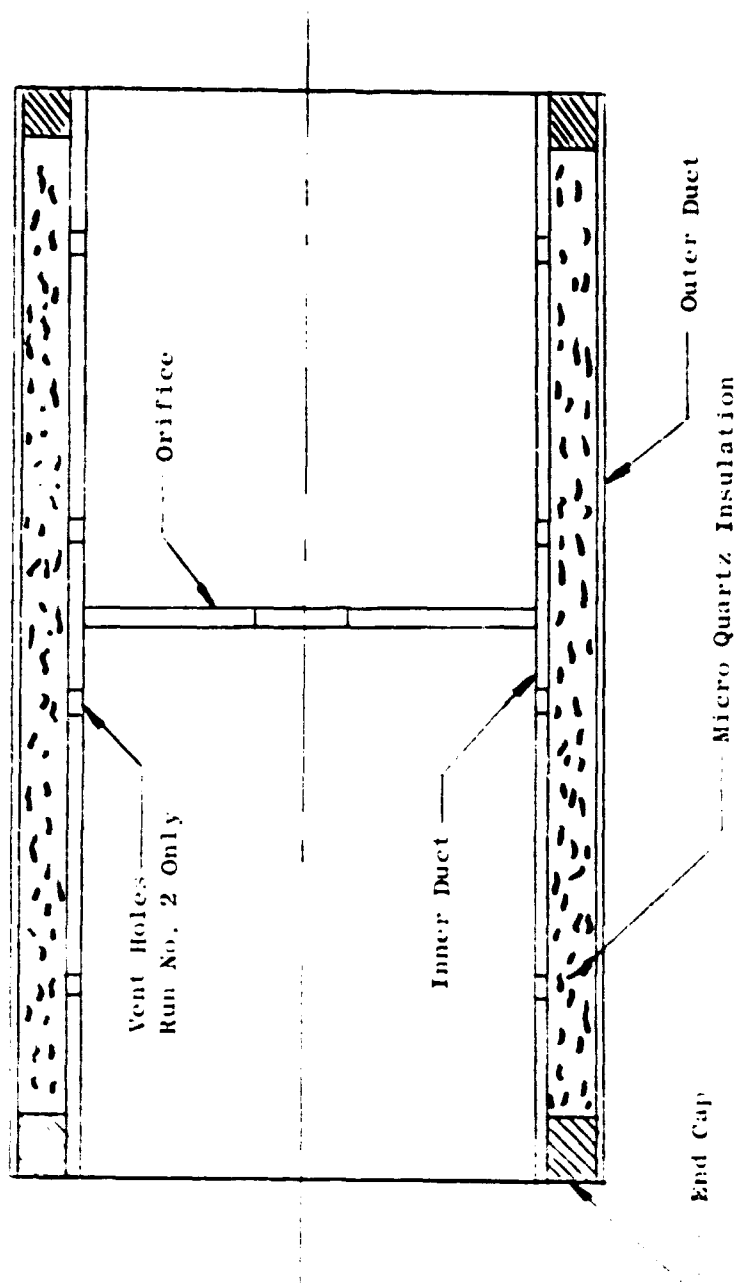


Figure 450 Test Duct

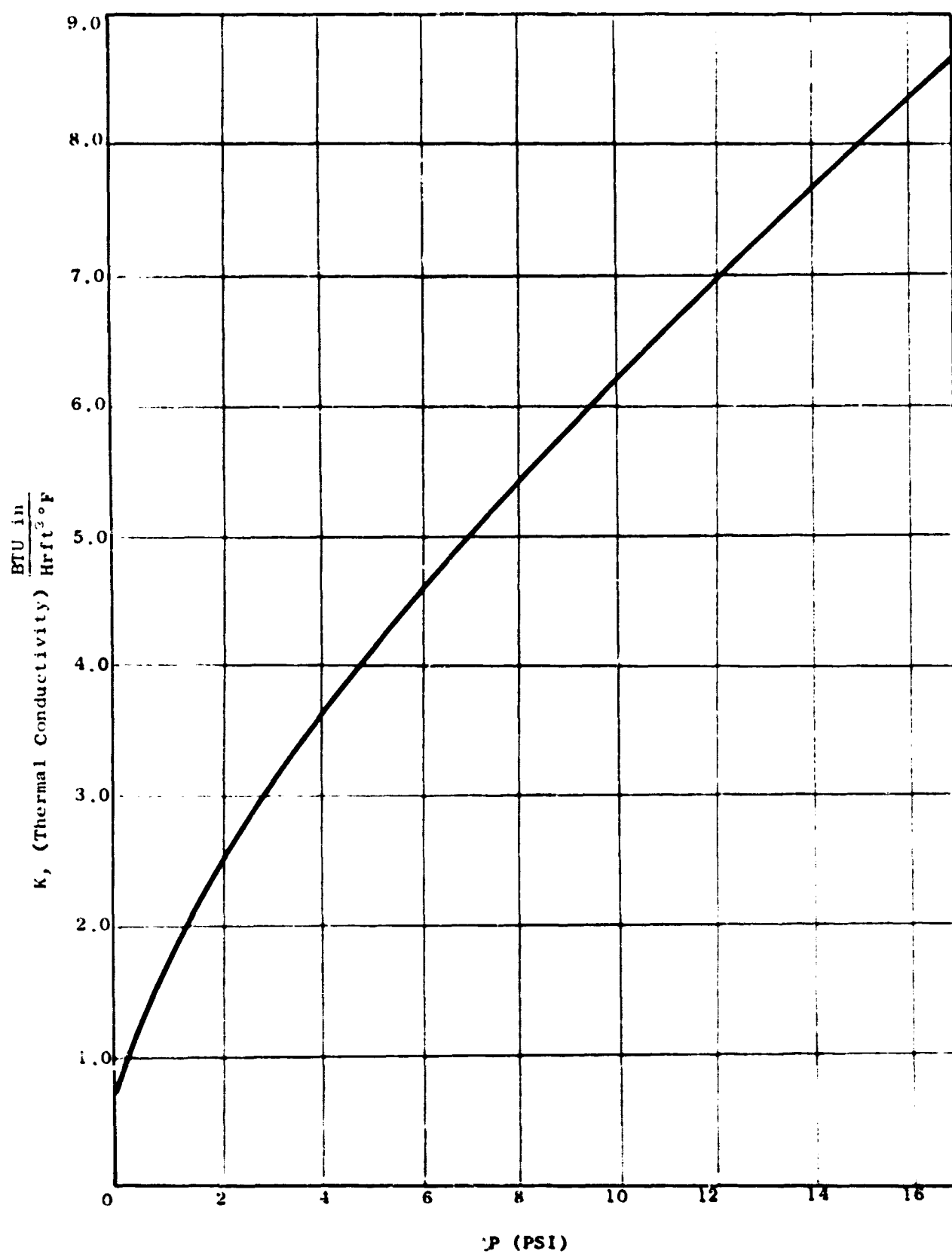


Figure 451 Thermal Conductivity Versus Pressure Gradient

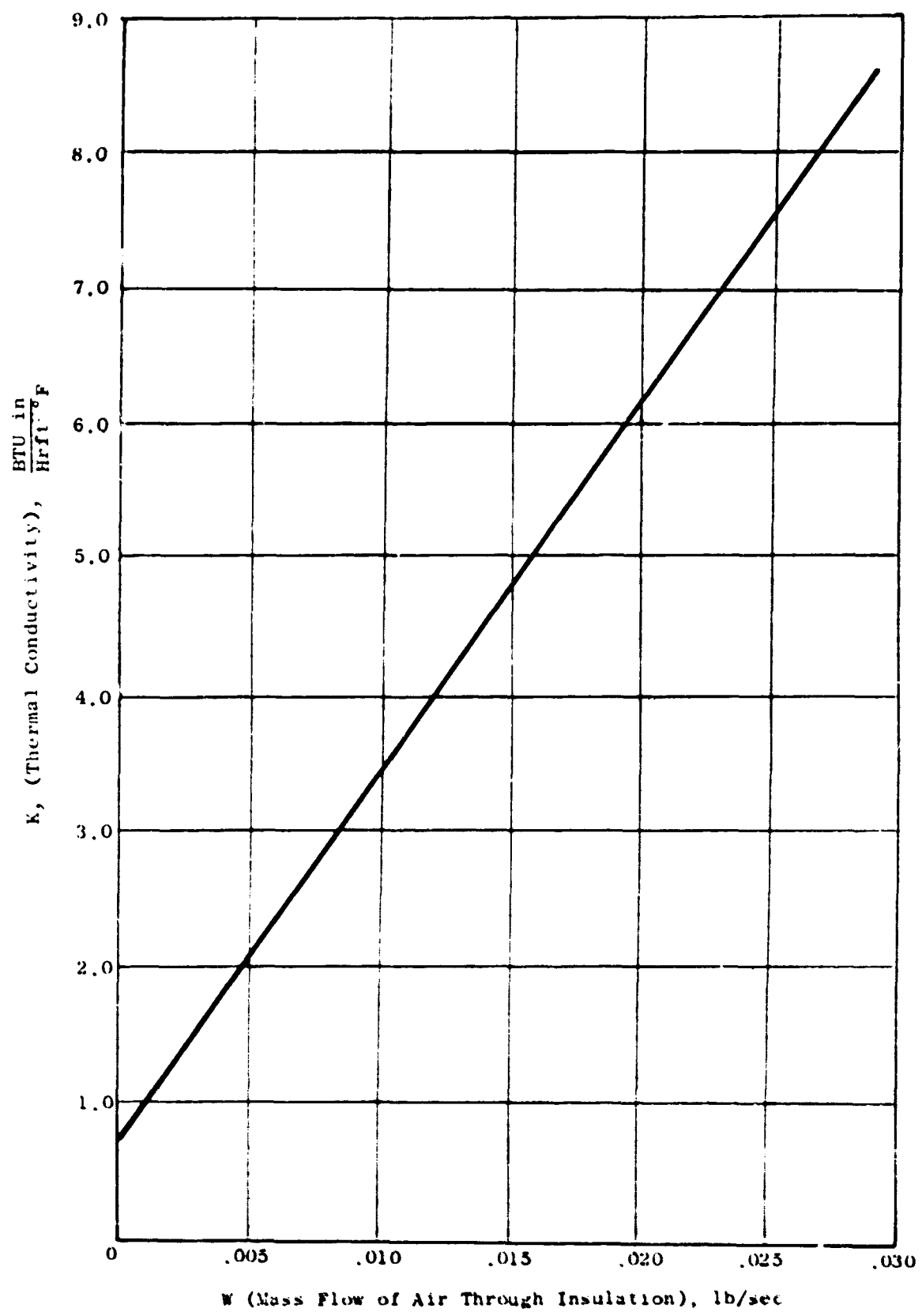


Figure 432 Thermal Conductivity Versus Mass Flow Rate

number and size of holes in the liner, but the test was not protracted to include that parameter.

(U) Although the increase in thermal conductivity of the Micro Quartz doubles for a flow rate induced by a pressure difference of 0.5 psi, this shortcoming, it is felt, is not sufficient to eliminate the lowest density-conductivity material from the selected list of insulation; therefore, additional testing will be made to confirm these results for different liner configurations.

## MATERIAL AND PROCESS TECHNOLOGY

### Introduction

(U) Optimum fan performance is keyed to the proper selection of materials and the manner in which they are applied. To achieve the proper balance between the technological risk inherent in advanced mechanical designs, and the assurance resulting from the use of established construction, several areas of advanced materials and processes were selected for study based on their practicality and the extent of their potential improvement in the overall fan system. These studies were intended to establish feasibility of application and to provide basic metallurgical data for design input. Application of these data to the construction and evaluation of actual designs would require support from supplementary component programs.

(U) Materials and processes selected for study include:

Joining of dissimilar metals by processes which effect a metallurgical bond.

Joining of dissimilar metals by adhesive bonding.

Identification and application of braze alloys and joining processes required to use very thin titanium honeycomb material.

Identification and evaluation of a process to hard surface a beryllium shaft.

Hollow disc fabrication by activated diffusion bonding.

Rene' 41 thin sheet fabricability.

### Titanium - Nickel Joint

#### Introduction

(U) To optimize the weight and performance of the fans, dissimilar metal joining is required in at least three separate locations. One of these locations is the joint between the hollow titanium fan blade and the nickel base alloy used in tip turbine construction. Three different techniques to effect a metallurgical bond at the joint were investigated. These studies encompassed co-extrusion, brazing, and electron beam welding. Basic metallurgical data was developed on joining parameters, effect of heat treat cycles, and mechanical properties.

#### Discussion

(U) For preliminary study of diffusion reactions, coupons of Inconel 718 and Ti 5Al-2.5Sn. were explosively bonded and heat

treated at varying times and temperatures. This work indicated that embrittlement would be a potential problem if thermal exposures above approximately 1000°F were seen by the nickel-titanium interface after joining.

(U) An extrusion technique for joining of dissimilar materials, being developed by Nuclear Metals Division of the Whittaker Corporation, was investigated next. Ti 6Al-4V rods within Inconel 600 hollow cylinders were co-extruded at 1500°F (900% reduction) and machined into tensile specimens (0.175 - 0.200" overlap shear) by gun drilling the rod out of one end and turning the outer cylinder off the other end. Heat treatments and resulting test data are as follows:

Condition	Shear Strength at Temperature		
	Room Temp	800°F	1000°F
As extruded	24,000 psi	31,000 psi	15,600
200 hr at 1000°F	38,500	33,200	-
4 hr at 1300°F	22,800	26,400	-

(U) These results showed promise for a co-extruded transition section between the titanium blade and nickel-base carrier; however, Nuclear Metals could not apply the technique to the required materials (titanium to a super alloy - e.g. - Rene' 41) and shape without an extensive development program. In addition, later work with brazements showed that the shear strengths indicated above were enhanced to an unknown degree by "shrink-fit" compressive stresses set up as a result of the considerable difference in thermal coefficients between the titanium rod and Inconel sleeve.

(U) Attempts to obtain a bi-metal joint by diffusion bonding, using a vanadium interleaf as a diffusion barrier, and by inertia welding (under another program) were not successful. In both instances, the resulting joints were broken by hand. Since those approaches were also not amenable to the required shapes, no further consideration was given to them. For the remainder of the program, efforts were concentrated on brazing and electron beam welding.

(U) The objectives of the brazing investigation were to develop a system meeting the following criteria:

Brazing temperature compatible with Rene' 41 heat treatment and below Ti beta transus.

Sufficient alloy strength and ductility to accommodate stresses set up by differential thermal contraction.

Metallurgical compatibility of braze alloy with parent materials (no intermetallic formation).

(U) Results of all brazing tests are shown in Table 64. Initial tests were made to check the compatibility of two established titanium brazing alloys with a nickel alloy. Using the same pin and sleeve configuration as for the extrusion evaluation, shear strengths of 40,000 psi were obtained with both Ti/15Cu/15Ni and Ti/48Zr/5Be braze alloys. However, when sheet specimens were brazed with Ti/48Zr/5Be, strengths dropped to about 5,000 psi with a single overlap and 9,000 psi average with a double overlap. The shear strength of this alloy in titanium sheet brazements was known (and verified by test in this program) to be at least 30,000 psi. Figure 453 shows the formation of a diffusion zone at the nickel-base alloy surface, which, in conjunction with the low flat tensile shear strengths, indicates metallurgical incompatibility between the selected braze alloy and the nickel alloy.

(U) The next approach was to use a barrier material to prevent interdiffusion of Ti and Ni. By placing thin Cb-1Zr foil between the components, braze alloys could be selected individually for Cb to nickel-base and Cb to titanium alloys. Ti Zr Be was readily shown to be adequate for the titanium to Cb side. Shear strengths of 21-25,000 psi were demonstrated in Ti-Cb-Ti double overlap joints. Because of the fabrication sequence proposed for the actual part, alloys for the Rene' 41/Cb side were limited to those with brazing temperatures below the 1820°F beta transus for Ti-3.1-4V. Of the alloys examined which met this requirement, Nicoro 80 (81.5Au/15.5Cu/3Ni) exhibited the highest shear strength (11,700 and 14,400 psi). Strengths equal to or higher than those of the titanium side can be readily obtained, but only if the component brazing operations are sequenced so that titanium would not be subjected to temperature over 1800°F.

(U) In parallel with the barrier evaluation, other tests were made to select a single alloy which would be compatible with both joint materials.

(U) One method of achieving this was to vapor deposit Cb directly to the titanium. Fansteel San Fernando laboratory supplied two samples for our evaluation. As shown in Figure 454, the bond between the titanium and Cb was questionable, and the application temperature exceeded the beta transformation temperature. A sample was brazed with Nicoro 80, but because of either a bad braze job or a poor Cb bond, the joint had no strength.

(U) Three alloys were identified as capable of providing a reasonably strong joint without a diffusion barrier - 80Au/20Cu, 95 Ag/5Cu, and Silcoro 75(75Au/20Cu/5Ag). The silver-copper alloy was not pursued (although it showed shear strength as high as 38,000 psi) because it was known from past experience to have low resistance to peeling. Of the two gold-base alloys, gold-copper was selected for further development because, although initial data showed large scatter, the alloy showed more potential than did the Silcoro 75. By reducing both the brazing time and

TABLE 64  
RESULTS OF BI-METAL BRAZING TESTS

PART I - PRELIMINARY TESTS

MATERIALS	JOINT TYPE	BRAZE ALLOY	BRAZING TEMP.	SHEAR STRENGTH (KSI)
Ti-Inconel	Pin-Sleeve	TiCuNi	1750°F	40
Ti-Inconel	Pin-Sleeve	TiZrBe	1650°	39.8
Ti-R 41	Single Lap	TiZrBe	1650°	5.2, 4.2, 5.6
Ti-R 41	Double Lap	TiZrBe	1650°	3.8, 10.4, 12.4
Ti-Ti	Double Lap	TiZrBe	1650°	17.9, 28.4
Ti-R 41(Cr Plated)	Double Lap	TiZrBe	1650°	11.0, 12.4
R41-R41	Double Lap	Copper	2050°	24.2, 23.4

PART II - Cb BARRIER TESTS - DOUBLE OVERLAP JOINTS

MATERIALS	BRAZE ALLOYS	BRAZING TEMP. - TIME	SHEAR STRENGTH (KSI)
Ti-Rene' 41	a) Palniro 7 (Cb to R41) b) TiZrBe (Cb to Ti)	a) 1850°F b) 1650°F 1650°	>12.6, 13.3 21.2, 24.8, 22
Ti-Ti	TiZrBe	1800°	2.4
Ti-Ti	Nioro(82Au/18Ni)	1800°	4.7, 6.6, 7.4
R41-R41	TiZrBe	1650°	16.6, 17.3
R41-R41	Copper	2050°	15.4, 15.5
R41-R41	Nioro	1800°	DIDN'T WET
R41-R41	Silcoro75(75Au/20Cu/5Ag)	1650°	11.7, 14.4
R41-R41	Nicoro80(81.5Au/15.5Cu/3Ni)	1750° - 10 min.	
R41-Ti(V.D. Cb)	Nicoro80	1750° - 10 min.	BROKEN BY HAND

TABLE 64 Continued

## PART III - BI-METAL, SINGLE ALLOY TESTS - DOUBLE OVERLAP JOINTS

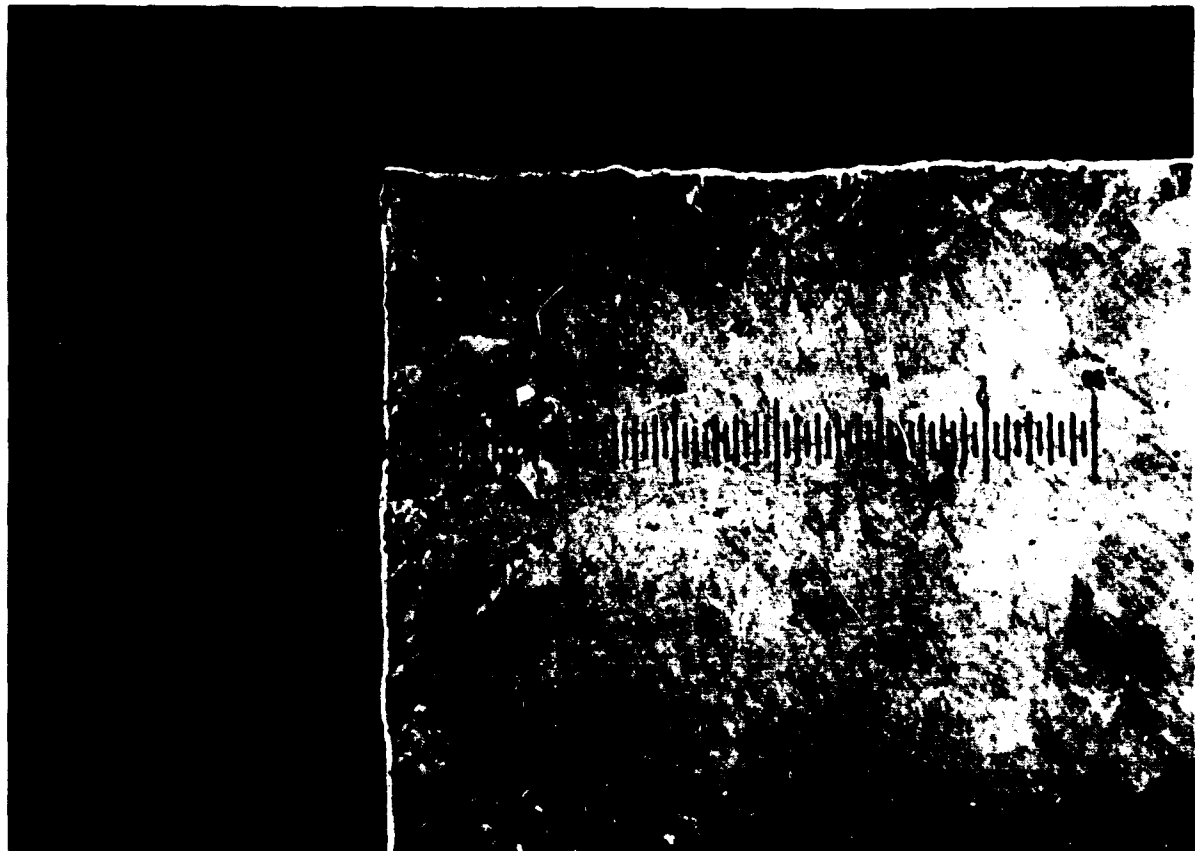
MATERIALS	BRAZE ALLOY	BRAZING TEMP. - TIME	SHEAR STRENGTH
Ti-R11	Nioro	1800°F 5 min.	Broke by hand
Ti-R41	Nioro 80	1750°F 5 min.	Broke by hand
Ti-R41	95Ag/5Cu	1750°F 10 min.	28.3
Ti-R41	95Ag/5Cu	1700°F 3 min.	10.6, 18.4, 20.8
Ti-R41	Silcoro 75	1700°F 1 min.	14.3, 12.8, 15.3
Ti-R41	80Au/20Cu	1750°F 15 min.	9.6, 7
Ti-R41	80Au/20Cu	1750°F 10 min.	18.7
Ti-R41	80Au/20Cu	1750°F 1 min.	15.4, 14.9, 40.25
Ti-R41	80Au/20Cu	1700°F 15 min.	20.1, 24.4, 25.3, 27.1



1500X

P0747

Figure 453 Photomicrograph of Braze Alloy - Ni Base Alloy Interface R41 Brazed to Ti-6Al-4V with Ti-Zr-Be Braze Alloy. Dark Band at Interface is  $Ti_x Ni_y$  Intermetallic. (J-945-R41 Etch, "3%")



100X

94-5-1

Poloroid

**Figure 454** Photomicrograph of Ti-6Al-4V with Approximate 0.0005" of Cb Deposited on Surface by CVD Procedure. Note Lack of Bond, and Transformed Microstructure of Ti-6Al-4V, Indicating the Process was Conducted at Temperatures in Excess of 1825°F. (J-4076)

temperature, consistent acceptable shear strengths ranging from 20,000 to 27,000 psi were obtained.

(U) Fifteen fatigue specimens were manufactured using the 80 Au/20Cu braze alloy in a 30° scarf joint configuration. Five of these have been tested to date in bending-bending fatigue. Runout (10<sup>7</sup> cycles) was achieved at 42,000 psi maximum stress (A ratio = .4).

(U) As backup to the brazing studies, electron beam welding was investigated. Rene' 41 cannot be directly welded to titanium; therefore, the objective of the study was to identify materials suitable for a transition joint between the two alloys. Combinations screened are listed in Table 65. No attempt was made to optimize properties or weldability. One set of welding parameters was investigated for each combination. Materials were welded in the mill-annealed condition and, except where noted, were tested or metallographically examined in the as-welded condition. No single material compatible with both sides of the joint was identified. A composite structure of Ti-6Al-4V to V to AlSi1410 to Rene' 41 exhibited excellent tensile ultimate and yield strengths in the as-welded condition (25,000, psi min UTS, 59,000 min .2YS). However, these values appeared to be drastically reduced by a 1300°F - 1 hour weld stress relief heat treatment. Additional specimens were fabricated and stress relieved at lower temperatures; however, a new vanadium heat with inferior properties was used, and all failures occurred in the vanadium at approximately 40,000 psi ultimate and 30,000 psi yield. These tests will be repeated when suitable vanadium is procured.

#### Conclusions and Recommendations

(U) Extrusion, diffusion bonding, and inertia welding, in their current state of development, are not useable in this program.

(U) Overlap shear strengths above 20,000 psi can be realized with 80 Au/20 Cu braze alloy. Preliminary fatigue test results indicate acceptable combined stress capability in scarf-type joints.

(U) The Cb diffusion barrier concept has the potential for equal or higher strengths than Au/Cu, but poses manufacturing problems in control of fit-up and in process sequencing.

(U) Electron beam welded composite joints exhibit butt tensile strengths in excess of 40,000 psi.

(U) Choice of a final method will hinge on fatigue strength capability of brazed versus welded configurations.

TABLE 65  
Electron Beam Welding Results  
(Butt Welds)

MATERIALS	TEST RESULTS		COMMENTS
	UTS	.2%YS	
R41-Cb	---	---	Weld Cracked
R41-Low C Steel	60.4	---	Good Weld
Cb-Low C Steel	---	---	Broken by hand
Cb-302SS	---	---	Cracked
R41-Mo-.5Ti	---	---	Lack of Penetration
Ti-Mo-.5Ti	---	---	Broken by hand
R41-Ti	---	---	No Joint - Separated in Welder
R41-Mo	---	---	Strong Joint, Microcracks
Ti-Mo	---	---	Best Joint to Ti
R41-V	---	---	Transverse Cracks
Ti-V	---	---	Good weld
R41-321SS	---	---	Good weld
321SS-V	---	---	Strong Joint - Cracks at 30X
Ti-Low C Steel	---	---	Broken by hand
Low C Steel-V	---	---	Good weld
Ti-Hf	---	---	Good weld
R41-Hf	---	---	No weld
410SS-Ti	---	---	Broken by hand
410SS-R41	89.4	---	Failed in Steel
V-410SS	73.6	---	Failed at Joints
R41-Mo-.5Ti	---	---	Broken by hand
Cb-Ti	---	---	Good Weld - No Cracks
321SS-Ti	---	---	Cracked
R41-410SS-V-Ti	65.4	59.0	Good Weld
R41-410SS-V-Ti	84.3	67.2	Good Weld
R41-410SS-V-Ti	86.2	65.0	Good Weld
R41-410SS-V-Ti	35.4	(1)	H.T. 1300°F/2 hrs.
R41-410SS-V-Ti	38.5	(1)	H.T. 1300°F/2 hrs.

(1) FAILED BELOW 0.2 YS

## Adhesive Bonding

### Introduction

(U) Another possible method of joining the fan blade to the turbine sector would be through a suitably designed adhesive bonded joint. The adhesive bonding technology is also required to effect optimized static component design in those areas of the structure where high section modulus construction is required to provide low deflection-light weight parts. Adhesive bonding programs were designed to provide surface preparation procedures, useful joint strengths, and adhesive creep and fatigue data at specified temperature ranges in the fan system. Studies were directed at bonding titanium to nickel base alloys and titanium to beryllium.

### Discussion

(U) The adhesives selected for evaluation were FM34 polyimide glass-supported film and AF31 nitrile-phenolic copolymer unsupported film. Surface preparation procedures for each material of interest were evaluated by tensile testing of single overlap shear specimens. Surface preparation was considered satisfactory when failures were consistently obtained within the adhesive (cohesive failure) as opposed to adhesive failure (at an interface).

(U) As an indication of the strengths attainable with each material, average single overlap shear strengths for each surface preparation selected for the balance of the program are listed:

	Ti 5-2½	Ti 6-2-4-2	Be	Rene' 41
FM34	3,160 psi	3,210 psi	4,130 psi	3,360 psi
AF31	4,290 psi	4,260 psi	3,850 psi	4,910 psi

(U) All additional testing for design data utilized double overlap shear specimens consisting of one leg of Rene' 41 bonded to two Ti 6-2-4-2 legs, and one leg of Be bonded to two legs of Ti 5-2½.

(U) Results of tests on the dissimilar metal combinations, reported in detail in interim reports, are summarized.

#### Tensile Tests (Shear Strength, psi)

	FM 34 Adhesive			AF 31 Adhesive		
	RT	350°F	500°F	RT	350°F	500°F
Ti 5-2½ to Be	3,925	2,670	2,340	5,610	1,500	475
Ti 6-2-4-2 to Rene' 41	3,980	3,180	1,260	5,900	2,760	380

Thirty 8 oz. Salt Spray Test (Shear Strength, psi)			
	FM34 Adhesive	AF31 Adhesive	
	RT	RT	
Ti 6-2-4-2 to Rene' 41	1225	-	5275

#### Temperature - Humidity Exposure

(48 hrs. at 90% humidity, 120°F, plus 24 hrs. at 350°F) 10 cycles			
	RT	RT	
Ti 6-2-4-2 to Rene' 41	2690	6320	

#### Combined Stress Fatigue Tests

(A ratio = 0.9 axial-axial loading, 350°F)

Ti 6-2-4-2 to Rene' 41 FM34  $10^7$  endurance limit  $\approx$  275psi (max.stress)  
 Ti 6-2-4-2 to Rene' 41 AF31  $10^7$  endurance limit  $\approx$  1000psi (max.stress)

(U) Creep tests were run at 350°F using both material combinations and both adhesives. Results were extremely erratic, ranging from negative extension to early stress rupture failures to expected creep values; therefore, no correlation of test results could be obtained.

(U) An adhesive bonded simulated stator vane was torsion tested to determine experimentally the strength of FM34 adhesive and the effect of increasing the overlap width of the bonded joint in a component.

(U) V/STOL Design Engineering chose to approximate the airfoil contour of a typical lift fan stator vane with an elliptical cross section as shown in Figure 455. Each test specimen was 10 inches in length, with the elliptical contour defined by a major axis of 2 inches and a minor axis of .5 inches (Figure 455). The load distribution across the bonded joint is an unknown and by testing specimens with different overlap widths it would be possible to determine the effect of overlap width on the joint load distribution and the strength of the joint itself.

(U) V/STOL Design Engineering performed an analytical investigation of the behavior of thin walled elliptical sections loaded in torsion. The shear strength of the adhesive was approximately 3160 psi; however, since the shear strength of the adhesive is dependent upon surface preparation a range of from 2500 to 4000 psi was considered in the analysis. By assuming a given shear strength for the adhesive, the shear flow in the section can be calculated as well as the torque required to produce this shear flow. Figure 456 contains the analytical results calculated for .25, .275 and .5 inch overlap width specimens.

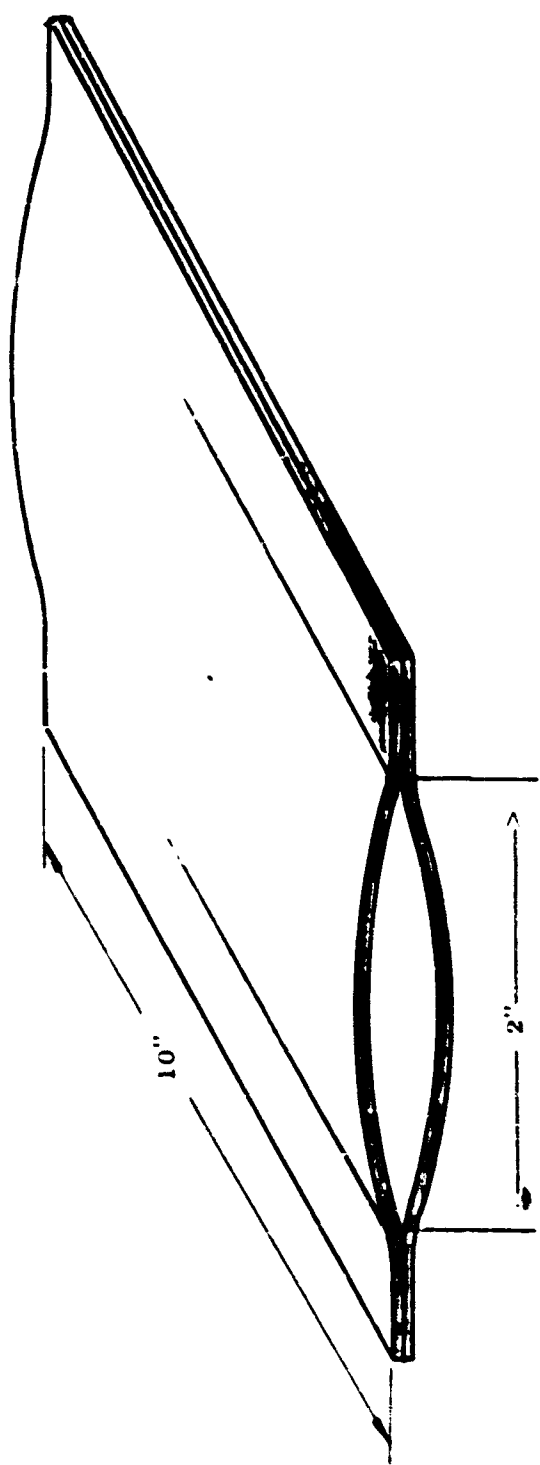


Figure 455. Contour of Test Specimen

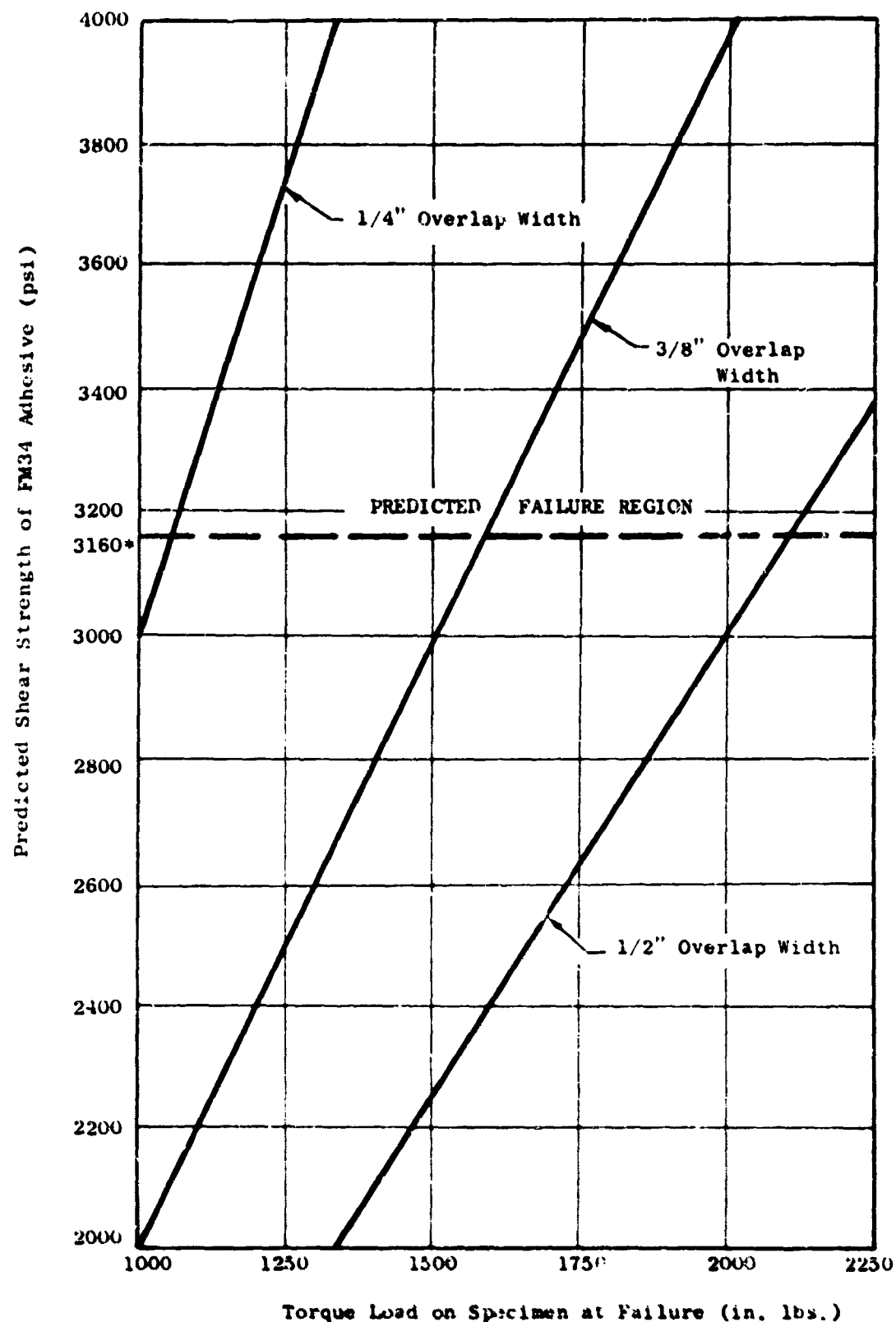


Figure 456. Predicted Shear Strength of Adhesive Versus Failure Torque  
 • Maximum shear strength of FM34 adhesive

(U) Test specimens were made of Ti 5-2½, 0.050" thick, cleaned and bonded using the procedures developed by the laboratory. A 6" by 6" steel plate was bonded to each end for load application.

(U) The test set up, used for evaluation, included a Lebow torque motor with a data track load cell which was used to apply a torque to the test specimens, and a linear pot actuated by the rotation of the Lebow torque motor measured the angle of twist of the test specimen. The torque input from the load cell was calibrated on the horizontal axis of the x-y plotter while the input from the linear pot was calibrated on the vertical axis of the x-y plotter; thus when a torque was applied to the test specimen it was also twisted through an angle and the x-y plotter recorded an approximate linear relationship up to failure.

(U) A three element strain gage was attached midway on the major axis of each specimen; this strain gage was used to provide a means of measuring any bending of the test specimen while being loaded in torsion. If bending did exist, the bonded joints would be subjected to both bending and torsional shear and if this were the case would fail at a lower torque than expected. The strain gage also provided a means of measuring the skin stress from the shear flow generated by torqueing the test specimens.

(U) The failure points of each specimen are shown in Table 66. In the  $\frac{1}{2}$  inch overlap specimens, S/N 2 failed at 800 inch pounds of torque and an angle of twist of  $3.5^\circ$ . This is considered a premature failure since the other  $\frac{1}{2}$  inch specimens failed at approximately 1300 inch pounds. The failure of specimen S/N 2 occurred while the load cell was on hold so that a strain gage reading could be taken, observing the plotter it was noted that the load cell torque was oscillating  $\pm 50$  inch pounds. This oscillation occurred for approximately 3 minutes before the specimen failed.

(U) The 3/8 inch overlap specimens failed over a rather wide range of torque values, minimum being  $\approx 2000$  inch pounds, all bond failures were cohesive and therefore the wide variation in failure torque is most probably due to local inconsistencies in the forming of the titanium along the bonded edge.

(U) In the  $\frac{1}{4}$  inch overlap specimens, one specimen failed while at only 1390 inch pounds, while the other two test specimens failed at approximately 2100 inch pounds torque. The premature failure of S/N 7 was due to a poor adhesive bond. Since S/N 7 was the only test specimen to show an adhesive type failure.

(U) In summary, Figure 457 is a plot of overlap width versus failure torque. Each valid test specimen has been recorded and a curve fitted to an average value of failure torque; the curve represents a linear relationship with a slope of approximately 300 inch pounds/.1 inch increase of overlap width.

TABLE 66  
RESULTS OF ADHESIVE BONDED STATOR VANE TORSION TEST

GROUP 1  $\frac{1}{2}$ " OVERLAP WIDTH

SPECIMEN NUMBER	TORQUE AT FAILURE (INCH - LBS.)	ANGLE OF TWIST AT FAILURE (DEGREES)
S/N 6	2064	8.2
S/N 9	2100	8.0
S/N 7	<u>1390</u>	<u>4.7</u>
Average	2082 <sup>1</sup>	8.1 <sup>1</sup>

GROUP 2  $\frac{3}{8}$ " OVERLAP WIDTH

SPECIMEN NUMBER	TORQUE AT FAILURE (INCH - LBS.)	ANGLE OF TWIST AT FAILURE (DEGREES)
S/N 8	1740	5.0
S/N 4	2027	7.4
S/N 3	<u>1248</u>	<u>4.5</u>
Average	1672	5.6

GROUP 3  $\frac{1}{4}$ " OVERLAP WIDTH

SPECIMEN NUMBER	TORQUE AT FAILURE (INCH - LBS.)	ANGLE OF TWIST AT FAILURE (DEGREES)
S/N 1	1290	4.0
S/N 5	1360	4.0
S/N 2	<u>800</u>	<u>3.5</u>
Average	1325 <sup>2</sup>	4.0 <sup>2</sup>

<sup>1</sup> Specimen S/N 7 not included in average due to adhesive failure of the joint.

<sup>2</sup> Specimen S/N 2 not included in average due to failure during oscillation of load cell.

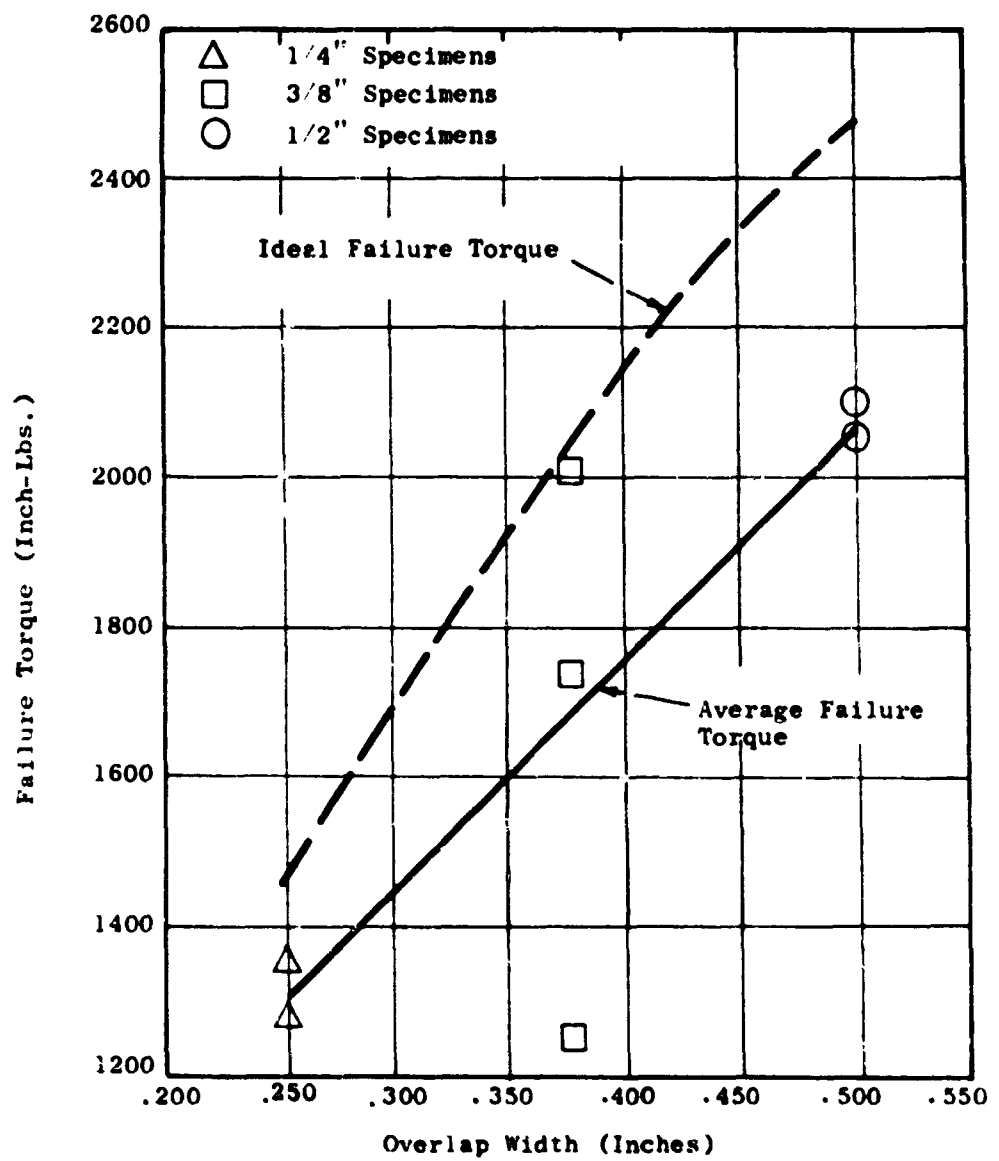


Figure 457. Failure Torque Versus Overlap Width

(U) Table 67 indicates the various strain gage reading for each specimen while under test. Gage (A) measures circumferential strain, Gage (B) measures torsional strain, and Gage (C) measures axial strain. If the test specimen is loaded in pure torsion Gages (A) and (C) should register very little change. The  $\frac{1}{4}$ " overlap width specimens showed almost no circumferential or axial strain as expected; the  $\frac{3}{8}$ " and the  $\frac{1}{2}$ " overlap width specimens did register significant circumferential strain, approximately 340 micro inches/inch, which is equivalent to an average skin stress of 5440 psi.

(U) Thus if the circumferential strain observed in testing the  $\frac{3}{8}$ " and  $\frac{1}{2}$ " overlap width specimens could be eliminated, the failure torque value for these test specimens would increase. The dash line curve in Figure 457 represents ideal failure torque (no circumferential strain) versus overlap width; this curve shows that for larger overlap widths ideal failure torque is considerably more than the experimental average torque would indicate.

(U) Figure 458 is a graph of average adhesive shear strength versus overlap width; the curve shows an adhesive shear strength of 3960 psi for the  $\frac{1}{4}$ " overlap specimens; 3330 psi for the  $\frac{3}{8}$ " overlap specimens; and 3100 psi for  $\frac{1}{2}$ " overlap specimens. Thus the maximum adhesive shear strength occurs at the minimum overlap width.

#### Conclusions and Recommendations

(U) The strut testing procedure left much to be desired, especially with respect to calibration and operation of the x-y plotter; however, the test results should reflect within 10% the true values of torque and angle of twist at failure.

(U) The bonded titanium stator vane torsion test has shown that the FM34 adhesive shear strength is  $\approx$  3100 psi for the  $\frac{1}{2}$ " overlap width specimens. This average shear strength compares closely to the average shear strength of FM34 measured in the development program. Thus the results of the torsion test are consistent with the results of the tensile tests, the difference in average shear strength being on 1.7%.

(U) Figure 457 shows that increasing the joint overlap width is an effective way to increase the strength of an adhesive bonded joint loaded in torsional shear. The basic analytical assumption that the shear load distributes itself effectively across the entire overlap width has been justified by the test results.

(U) Using FM34 adhesive with  $\frac{1}{2}$ " bond overlap width the joint would be capable of taking  $\approx$  3100 psi shear stress, which would be more than required if this concept were to be used in the LF475 Lift Fan. From the LF475 stator vane loads the maximum shear stress developed in an adhesive bonded joint would be 1680 psi shear stress, which is almost 50% less than the average experimental shear strength of FM34 adhesive.

TABLE 67  
STRAIL TESTS  
1/4" OVERLAP WIDTH TEST SPECIMENS

SPECIMEN NUMBER	TORQUE	GAGE (A)	GAGE (B)	GAGE (C)
S/N 1	0	11000	11000	11000
	600	10960	10265	10950
	800	10940	9980	10900
	1300	S P E C I M E N F A I L E D		
S/N 5	0	11000	11000	11000
	600	11030	10270	10945
	800	11030	10000	10890
	1395	S P E C I M E N F A I L E D		
S/N 2	0	11000	11000	11000
	600	10920	10100	10935
	800	S P E C I M E N F A I L E D		

3/8" OVERLAP WIDTH TEST SPECIMENS

SPECIMEN NUMBER	TORQUE	GAGE (A)	GAGE (B)	GAGE (C)
S/N 8	0	11000	11000	11000
	600	11065	10265	10900
	1200	11060	9500	10690
	1740	S P E C I M E N F A I L E D		
S/N 4	0	11060	11000	11000
	600	10945	10275	10950
	1200	10840	9250	10745
	2027	S P E C I M E N F A I L E D		
S/N 3	0	11000	11000	11000
	600	10860	10100	10685
	1200	10840	9240	10430
	1248	S P E C I M E N F A I L E D		

1/2" OVERLAP WIDTH TEST SPECIMENS

SPECIMEN NUMBER	TORQUE	GAGE (A)	GAGE (B)	GAGE (C)
S/N 9	0	11000	11000	11000
	600	11010	10250	10930
	1200	10960	9450	10735
	1800	10870	8270	10340
	2108	S P E C I M E N F A I L E D		
S/N 6	0	11000	11000	11000
	600	11000	10170	10880
	1200	10970	9260	10660
	1800	10900	8170	10250
	2064	S P E C I M E N F A I L E D		
S/N 7	0	11000	11000	11000
	600	10990	10110	10865
	1200	10925	9220	10600
	1390	S P E C I M E N F A I L E D		

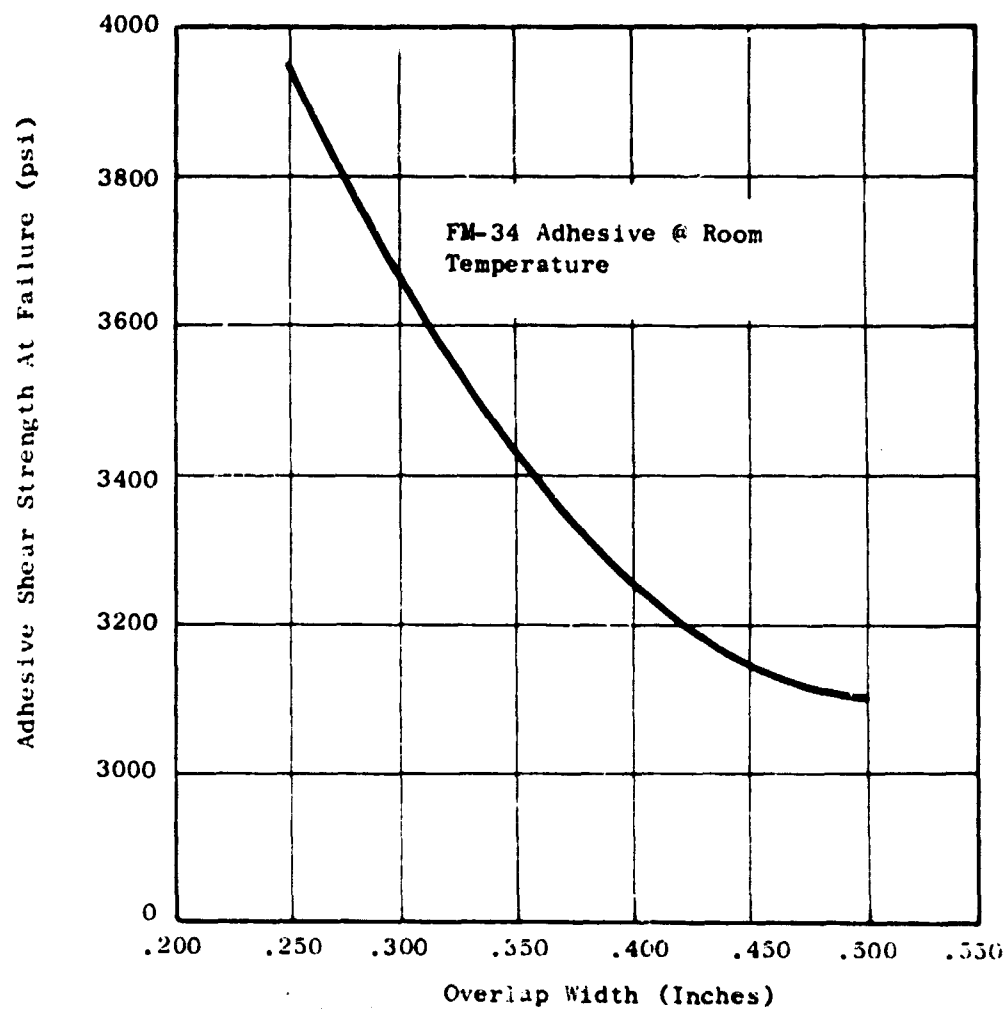


Figure 438. Overlap Width Versus Adhesive Shear Strength

## Activated Diffusion Bonding of Titanium

### Introduction

(U) During the early part of 1967, vendors with known capability for diffusion bonding were surveyed for quotations on a diffusion bonded hollow titanium disc. Because of expected difficulty in maintaining wall thicknesses and cavity location and contour with the high deformations required to affect a diffusion bond, vendors responded with excessively high quotes, and guaranteed only "product of best effort".

(U) Activated diffusion bonding is a relatively new technique for fabrication of titanium alloy parts. Basically the technique is very similar to diffusion bonding except instead of bonding two contamination - free titanium surfaces under heat and high pressure, an interleaf on thin (0.0005") copper foil is introduced which decreases the bonding pressure and deformation required. This decrease is a result of a Cu-Ti eutectic (~76 wt% Cu) which melts at 1625°F. Therefore, a liquid phase is present, at least momentarily, which assures intimate contact across the entire bonding plane. If the specimen is held at elevated temperature (1650-1900°F), the copper diffuses away from the bond into the titanium. Work by Boeing indicated that two hours at approximately 100°F above the beta transus was sufficient for the copper to diffuse to the extent that no point in the original bond area exceeded six percent Cu.

(U) This study was made to determine whether a satisfactory bond could be obtained in Ti 6Al-4V at a temperature below the beta transus, and to ultimately fabricate subscale hollow discs for spin-pit testing.

### Discussion

(U) Bonding cycles and tensile test results are listed in Table 68. The first bonding test was made using copper foil rolled and pickled to .0005 - .0008" thickness. One-inch cubes were bonded in vacuum at 1750°F for two hours under a 15 psi pressure applied by dead weight loading. After bonding, specimens were stress relieved for one hour at 1300°F, ultrasonic inspected and machined into .250 diameter tensile bars. Room tensile strength was degraded slightly by the bonding thermal cycle. Ductility was unaffected.

(U) In attempting to reproduce the results for fatigue testing, bond line failures occurred with reduced ductility (tests 2 and 3). These pieces had shown ultrasonic indications of 10 - 15% at the bond line prior to cut-up. Metallographic examination of good and low ductility bars (Figure 455) indicated

TABLE 68  
BONDING CYCLES AND TENSILE TEST RESULTS

Test Block	Bonding Cycle (Temp. °F)	Time(hr)	Pressure(psi)	Room Temp. Tensile Tests					
				UTS (ksi)	.2YS (ksi)	El %	RA %	Failure location	
1	1750	2	15	124 129	118 120	16 16	41 44	PM	
2	1750	2	15	129 126	120 118	12 5	37 9	PM Bond	
3				131 131	121 120	5 8	6 9	Bond Bond	
3 Recycled	1750	2	0	132	124	11	27	PM	
6 Interior* Edge*	1750	4	15	138 59	131 - 0.4	15 0.4	-	PM Bond	
7 Interior* Edge*	1750	4	15	137 107	129 - 0.8	16 0.8	-	PM Bond	
NONE - (Original Material)				140	130	16	45	-	

\* Average of four tensile tests



Neg. No. P0366      Mount No. H-10833



Neg. No. P0367      Mount No. H-10834



Neg. No. P0368      Mount No. H-10835

Etchant: 94-5-1  
Mag: 100X

Photomicrographs of the One Good Tensile Specimen (A) and Two Which Exhibited Reduced Ductility (B and C).

Note gray phase in zone of failure.

Figure 459.

the problem to be undiffused copper. Remaining material was re-diffused for 2 hours at 1750°F without load. One more tensile test was made, with acceptable results, then the balance of the blocks were machined into fatigue specimens.

(U) Fatigue tests were conducted on a rotating beam machine at 10,000 cycles per minute. The results are shown in Table 69. These data indicate a 10<sup>7</sup> bending-bending endurance limit of 58-60 ksi, which is roughly equivalent to the fatigue strength of wrought Ti 6Al-4V of the same stock thickness.

(U) One other series of tests was run to determine the effect of the edge notch (Figures 460 & 461), and to compare alternate methods of applying the copper interface. Test blocks 6 and 7 were bonded with .0005" of copper foil and copper plating, respectively. Flat tensile specimens .080" thick x 1" wide were machined from each surface of each block, and comparable specimens were machined from the interior of each block, for direct comparison. As seen in Table 70, undiffused copper, plus the inherent notch at the bond edge, caused gross reduction of tensile ductility. Since the electroplated copper gave better results, particularly in strength, this will be used for future work.

#### Conclusions and Recommendations

(U) Activated diffusion bonding is a feasible method of fabricating hollow Ti 6Al-4V lift fan discs.

(U) Sub-scale discs for spin pit testing will be fabricated using this process.

TABLE 69

ROTATING BEAM FATIGUE TESTS  
 Ti-6Al-4V Copper Diffusion Bonded  
 1750°F/2 hours/15 psia + 1750°F/2 hours + 1300°F/1 hour (all vacuum)

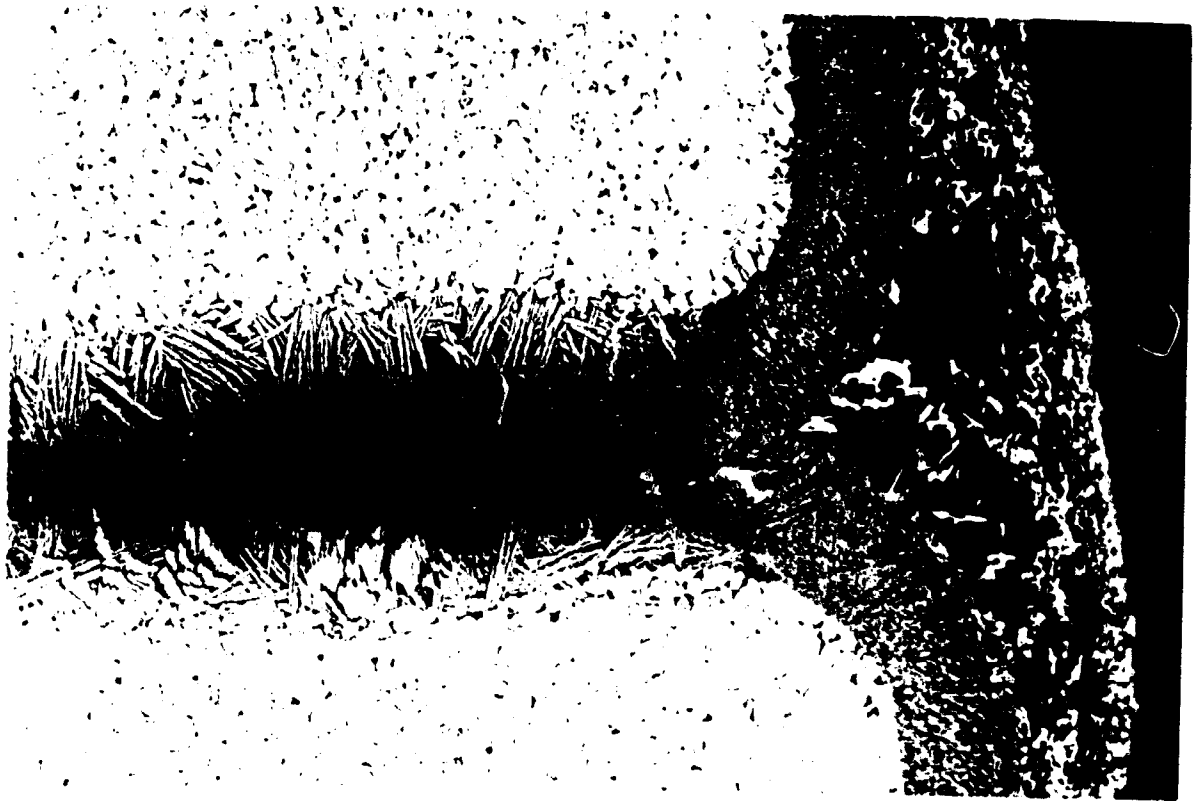
Test Number	Block Number	Stress Level (ksi)	Cycles (10 <sup>3</sup> )	Condition
1	4	60	8,511	Failure
2	4	55	13,316	Runout
3	4	58	74.4(1)	Failure
4	4	58	1,015	Failure
5	4	58	9,365	Failure
6	5	58	23,006	Failure
7	5	60	12,422	Failure
8	5	62	234(1)	Failure
9	4	55	46,050	Runout
10	4	62	31,878	Runout
11	5	64	2,580	Failure
12	4	58	60,000	Runout

(1) Obvious defect in bond.



100X

Figure 460 Copper Plate Edge Effect



100X

Figure 461 Copper Foil Edge Effect

## Titanium Honeycomb Brazing

### Introduction

(U) Brazed titanium honeycomb structures are proposed for use in several areas of the fan designs. Identification of acceptable braze alloys and brazing process technology is mandatory to achieve the lightweight construction proposed for fan static parts such as the scroll, forward nacelle, and stator vanes. Silver-base braze alloys currently being applied do not produce the most desirable, or repeatable, joint strengths. This program was directed toward achieving sound construction with the thin titanium honeycomb material used in the proposed fan parts.

### Discussion

(U) Three titanium base brazing alloys were selected for evaluation:

70% Ti - 15% Cu - 15% Ni

47.5% Ti - 47.5% Zr - 5% Be (6601)

43% Ti - 43% Zr - 2% Be - 12% Ni (6603)

The latter two alloys were selected from the effort conducted by Solar Division of International Harvester, under AF33(615)-3137 entitled, "Development of Joining Processes for Titanium Foils". The Ti-Cu-Ni alloy was developed by General Electric for titanium alloy brazing where service temperatures in excess of 400°F were anticipated.

(U) Flexural bending data was developed for brazed Ti honeycomb panels manufactured by Solar using the two brazing alloys of Solar composition, and for two General Electric Ti honeycomb manufacturing processes. These are: brazed Ti honeycomb using the General Electric brazing alloy Ti Cu Ni, and adhesively bonded Ti honeycomb processed in the General Electric laboratory.

(U) All of these data are shown in the table below:

Alloy Identifi- cation	Braze Alloy or Adhesive	Source	Crushed Core (lb Load) <sup>(1)</sup>	Uncrushed Core (lb load) <sup>(1)</sup>
6601	Ti-Zr-Be	Solar	250	210
6603	Ti-Zr-Ni-Be	Solar	285	260
TiCuNi	Ti-Cu-Ni	GE	240	310
FM34	Adhesive	GE	---	305
FM34	Adhesive	GE	---	290 <sup>(2)</sup>

(1) Breaking load per inch of honeycomb width

(2) Core material - 5052 Aluminum, 0.004 inch core wall thickness.

(U) The cover sheets were Ti-6Al-4V, nominal 0.010-inch; the core material as 0.002-inch Ti-6Al-4V, crimped and welded together to form the roughly hexagonal cell.

(U) Core shear testing was completed for Ti 6Al-4V honeycomb panels, brazed by Solar using two of their own alloys - Ti/Zr/Ni/Be and Ti/Zr/Be - and for panels brazed by General Electric using Ti/Cu/Ni alloy. In each case both crushed and uncrushed 0.002 inch core was utilized. Since flexural bending tests of adhesive bonded titanium and aluminum cores showed promising results, these combinations were also included in the shear testing. The adhesive used was FM34. Aluminum core was 0.004 inch thick type 5052. Test results are summarized below:

Braze Alloy	Crushed 0.002 Inch Core (psi)	Uncrushed 0.002 Inch Core (psi)	5052 Al 0.004 Inch Core (psi)
Ti-Zr-Be	570	605 735	--
Ti-Zr-Ni-Be	730	670	--
Ti-Cu-Ni	563*	630*	--
FM34 Adhesive	--	> 595	550

\* Core Buckled in Shear

#### Conclusions and Recommendations

(U) From the results of shear and flexural bend tests, it must be concluded that there is no clear-cut choice among the three braze alloys evaluated. In the configuration tested, adhesive bonding appears to offer strength equivalent to that of brazed honeycomb, and should be considered, along with aluminum core, for low temperature applications such as stator vanes, for cost and weight advantages.

## Beryllium-Titanium Brazing

### Introduction

(U) The proposed design of the major strut requires a metallurgical joint between the beryllium cap strip and titanium hub casting and between the cap strip and titanium end cap. Very meager published data was available for Be/Ti brazing, and none were available for brazing of the selected alloy (S-350) with its 4% oxide content.

(U) The following investigation was carried out to identify a suitable braze alloy and process, and to determine the shear strength capability of Be-Ti brazements.

### Discussion

(U) After reviewing published data on Be brazing, seven alloys were selected for determination of wetting-flow characteristics in vacuum and argon.

(U) From these tests, three alloys were selected - Al-12% Si, Al-12% Si on Ag-plated Be, and Ag-5% Al. Metallography of these joints is shown in Figures 462-464.

(U) The bare beryllium samples were cleaned in  $HNO_3$  - HF per AEG procedure 4012013-667, "Etching Procedure for Beryllium Forged Parts", and the silver plated beryllium was similarly cleaned prior to plating. Three specimens each were brazed using Al-Si, Al-Si with Ag plated Be, and Ag-Al. Figure 465 shows the brazing fixture used.

(U) The brazing cycle used a 20-minute hold period after which furnace power was killed and the specimen rapidly cooled to 1000°F.

(U) Following the braze cycle all nine specimens were machined per Figure 466, and tensile testing was performed on seven of the nine specimens. Two specimens broke during machining.

(U) The mechanical testing was conducted on double lap joints until one joint failed. At this point, the load was removed and the test reinitiated on the remaining lap joint. The latter data was recorded as "half specimen" data. Half specimen tensile values ranged from 2438 psi to 7867 psi. No consistent results were obtained in the mechanical test program to date, and only one specimen from the Al-Si series using Ag plated Be had double overlap shear strength values of interest to the program.

### Conclusions and Recommendations

(U) A bimetallic braze joint between beryllium S-350 and titanium (6-4) alloy can be fabricated.

Ti



Be (Ag plated - .001)  
Ti  
1250°F ~ 30 min. -  $5 \times 10^{-5}$  Torr  
Al-Si Braze Alloy (71%)  
250X Etched (NaOH-HF)

**Figure 462.** Photomicrographs Be-Ti Braze Section  
("A-C31")



Be  
Ti  
1175°F - 30 min.  
Al-Si Braze Alloy (71B)  
250X Etch.  $(HNO_3-HF)$

**Figure 463.** Photomicrograph Be-Ti Braze Section  
(M-221)

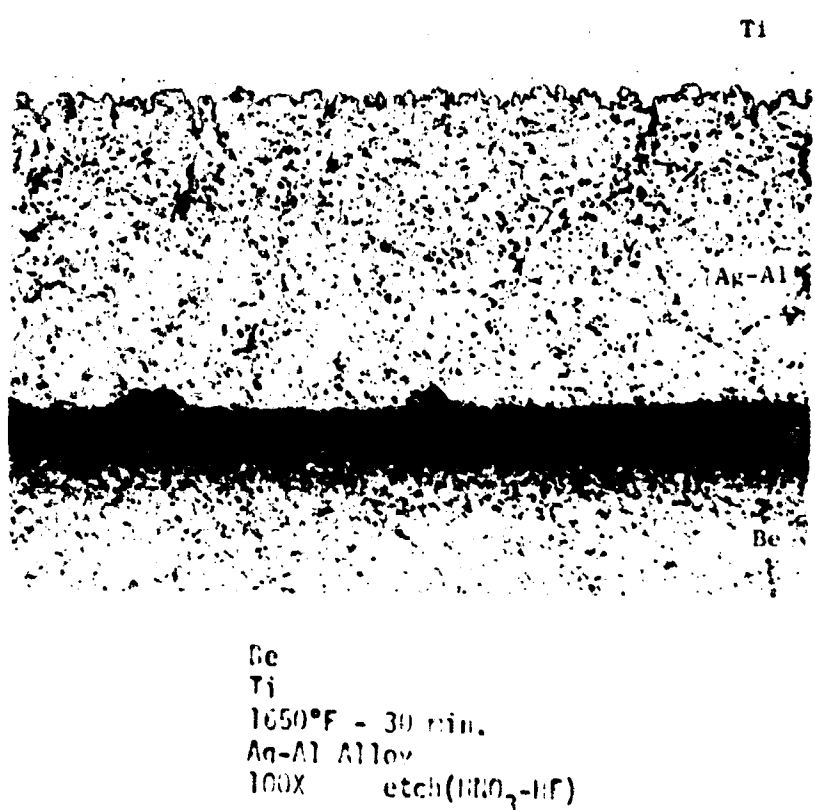


Figure 464. Photomicrograph Be-Ti Braze Section (IA-5250)

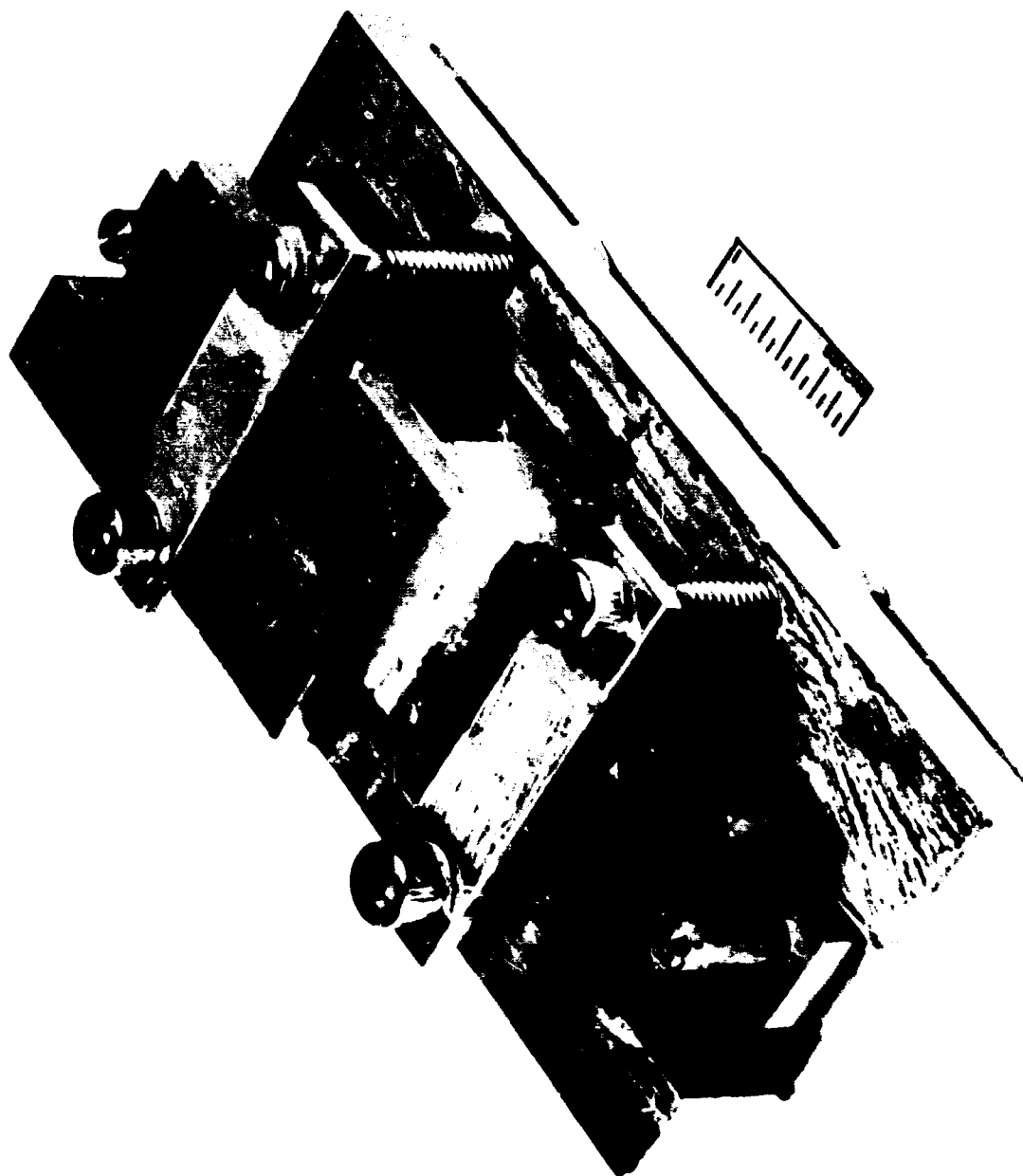


Figure 465 Be-Ti Brazing Fixture (Neg. P68-11-288)



**Figure 466.** Post-Braze Machined Fe-Ti Tensile Specimens

(U) The best strength properties experienced (11,360 psi tensile) were realized with Ag plated beryllium Al-Si braze alloy held at 1200-1225°F for 20 minutes. However, the reproducibility on two other specimens was poor.

(U) The variation in the Be-Ti braze joint mechanical strength is believed to be related to the high BeO content of S-350 Alloy.

(U) In order to fabricate a brazed joint of Beryllium S-350 alloy and titanium (6-4) with reproducible mechanical properties, a more extensive braze development program is required to optimize material and processing parameters. Material variables such as surface oxide content, surface porosity, and the influence of existing cleaning procedures on each of these variables needs to be established.

(U) For the brazing cycle itself, optimum Ag plating thickness (i.e., .001 - .005"), optimum braze foil thickness (.003 - .007"), heating rate, and time at temperature are all variables that can influence braze joint strength. The interrelation between these variables and joint strength must be established before reproducible braze joints of adequate strength can be fabricated.

(U) Contact with Solar Aircraft Company regarding this problem revealed that they have successfully brazed high oxide content beryllium alloy I-400 (no strength values indicated). Solar volunteered to braze AEG design shear specimens for AEG evaluation on the premise that additional larger scale brazing business may develop. No details on the method of brazing were revealed. It is assumed that this information is proprietary. Further investigation into this possibility is recommended.

## Beryllium Hard Surfacing

### Introduction

(U) Beryllium has been proposed as the shaft material; however, forged beryllium is soft (in the range of R<sub>B</sub> 85) and would be subject to fretting and brinelling damage under the inner bearing races. In addition, surfaces could be galled whenever bearings were pulled.

(U) There was available, within the General Electric Company, a fused salt electrolytic process for metal surface coating. Whereas conventional electrolytic processes deposit a plating on a substrate, the "metallidizing" process is described as a diffusion-surface conversion process.

(U) It was proposed, in this program, to form a gall-resistant titanium beryllide coating on beryllium by reversal of existing procedures for berylliding of titanium.

### Discussion

(U) Results reported by AEC indicated that, within the group Y, Hf, Zr and Ti, yttriding was the easiest to accomplish, and titanium the most difficult. It was decided to demonstrate the feasibility of yttriding in initial work at Schenectady R & D Center and then proceed to titanizing in equipment to be set up within AEG, Evendale.

(U) Samples of beryllium were successfully yttrided in a fluoride electrolyte. The desired compound, Y Be<sub>13</sub> was identified by X-ray diffraction analysis of the coating. Hardness was determined to be two to three times that of the beryllium substrate. Thickness was approximately 0.6 mils.

(U) However, the beryllide was not in the form of a diffusion coating, as expected, but was more in the nature of a discrete plating with questionable adherence.

(U) Because of prolonged start-up difficulties in our internal facility, and the availability of more attractive approaches, no further work was performed.

### Conclusions and Recommendations

(U) Design Engineering elected to apply a steel sleeve over the shaft by shrink-fit and/or brazing, eliminating the requirement for a hard coating. This sleeve, in addition to protecting the shaft from damage, eliminates the problems inherent in threading the beryllium shaft, since the spanner nut would thread onto the sleeve.

## Turbine Airfoil Forming

### Introduction

(U) Higher relative velocities associated with high energy gas require thin edged, transonic bucket airfoil design. Also, because of the hotter turbine gas temperature of such high energy drive gas (up from 1200°F to 1600°F), a change in bucket material is required based on allowable stress limits.

(U) The thinner buckets and the change in material to Rene' 41 which does not have the forming ease (allowable bend radius) of formerly used material, means that the manufacturing method used for previous buckets (tubing die-formed into airfoil shape) might not be applicable.

(U) The purpose of this program was to determine whether Rene' 41 could be heat treated to impart sufficient formability to allow a  $\frac{1}{2}$  T bend in 0.010" Rene' 41 sheet.

### Discussion

(U) Material heat treat conditions investigated were: mill annealed; 2050°F solution, air cooled; 1975°F solution, water quench. All samples were initially bent through 120° by forming around a steel punch with a 120° angle and 0.010" nose diameter. A hard rubber plate was used for the female die. The outside diameter was then hand polished and bent through 180° with and without a .005" shim insert to maintain the bend radius. Samples were inspected by fluorescent penetrant after both 120° and 180° bends.

### Conclusions and Recommendations

(U) 180° bends with a 1 T radius could be performed on the mill annealed material.

(U) Heat treatment was not effective as a means of decreasing the bend radius to  $\frac{1}{2}$  T (.005").

(U) Since successful bends would have had slim prospects of surviving the required post-bending heat treatment without strain-age cracking, it is recommended that efforts be directed primarily to fabrication of buckets by brazing.

## Stresskin Louver Evaluation

### Introduction

(U) The X353 fan exit louvers were built in the conventional channel and sheet metal fashion. However, with the higher pressure ratio fans and higher turbine exit temperatures such as were proposed for the LF475 significant weight savings result from a honeycomb-face sheet type structure in which the louver skins are allowed to see a larger percentage of yield strength before compression side buckling occurs. Honeycomb structures in general are more expensive than channel and sheet metal type construction. Construction of a louver from Stresskin eliminates the brazing operation and results in a lighter weight part at lower cost.

### Discussion

(U) Three test sections and one part suitable for installation on the X353 fan configuration as utilized in the XV5-B aircraft were fabricated by Stresskin Products Company. The three sections are identical in airfoil contour to the X353 fan part and differ only in the louver end configuration to facilitate static load testing.

(U) Each test section was tested to failure (whenever a visible buckle had occurred in the test or whenever the test part would accept no more load) in a different manner.

(U) The first test section was loaded to failure in torsion at a load of 4,530 inch pounds corresponding to a stress of 42,000 psi in the airfoil skin. The design point loading for the X353 Fan corresponds to a torsional stress of 1,392 psi.

(U) The second test section was loaded to failure in shear at a load corresponding to a core shear stress of 400 psi. The design point loading for the X353 fan corresponds to a core shear stress of ~ 20 psi.

(U) The third test section was loaded to failure as a short column in compression at a load of 11,750 pounds corresponding to a compressive stress of 46,600 psi.

(U) The design point loading for the X353 fan would produce a compressive stress of 2,410 psi from bending on the airfoil low pressure side.

### Conclusions and Recommendations

(U) While no attempt was made to optimize the design of these parts as is evident from the disparity in design and failure stresses it is estimated that the weight of the existing X353 louver and the Stresskin louver are very close.

(U) It is recommended that the remaining louver be installed on the XV5-B aircraft so that the Stresskin louvers suitability to the vibratory and thermal environments of the actual flight condition be determined.

(U) It is further recommended that this type of louver construction be utilized in any upcoming flight weight designs as the simplicity, cost, and weight effectiveness of this concept appear very good.

## SECTION VI

### CONCLUSIONS & RECOMMENDATIONS

(U) The analysis, preliminary and partial detail design work and the supporting component technology programs performed for the development of the Air Force Advanced LF475 Lift Fan and the L/CF470 Lift/Cruise Fan substantiated the feasibility of the program.

(U) Additional development work is required in the areas of aerodynamic testing of the lift fan scroll and reduced throttling cascades for vectoring as well as in a continuation of the material joining programs and the testing of double wall ducting components.

(U) It is recommended that a program to achieve these objectives be reinstated by the USAF Aero Propulsion Laboratory at the earliest possible date.

## REFERENCES

1. General Electric Company, Advanced Turbotip Lift Fan and Lift/Cruise Fan Demonstrator Program, GE Proposal P66-119, October, 1966, (C).
2. Acheson, W.A., Ganfried, M.S., LF475 Fan Design GE Report TM 68-302, June, 1968, (U).
3. Schaub, W. W., Bassett, R.W., and Cockshutt, E.P., (National Research Council of Canada), An Investigation of the Aerodynamics of Intakes in the Upper Surface of a Wing, GE TIPS Accession No. 110434. (U)
4. Kazin, S.B., LF475 Integrated Strut and Stator Vane Row Study, GE Report (No assigned number) November 13, 1968. (U)
5. Macke, H.J., Analysis of Circular-Arc Dovetails, GE Report R63FPD77, February 1, 1963. (U)
6. Macke, H.J., Revised Analysis of Single-Tang Dovetail Blade Attachments, GE Report R63FPD21, February 1, 1963. (U)
7. Macke, H.J., Notes on Single-Hook Dovetail Analysis Program, GE Report DM65-256, June 1, 1965. (U)
8. Macke, H.J., General Analysis of Dovetail Blade Attachments, GE Report R59FPD611, December 28, 1959. (U)
9. Przedpelski, Z.J., Heikkinen, A.H., and Vacek, L., Aerodynamic Investigation of Low Speed VTOL Transition Characteristics of X353-5B Cruise Fan, GE Report R63FPD426, December, 1963. (U)
10. Nichols, M.R., and Keith, A.L., Jr., Investigation of a Systematic Group of NACA 1-Series Cowlings With and Without Spinners, NACA TR 950, 1949. (U)
11. Fasching, W.A., and Robinett, D.V., J79-80 Inch Lift/Cruise Fan Inlet Investigations, GE Report R68AEG203, March, 1968. (U)
12. King, R.C., Test Results of Three Low Speed Inlet Cowls With NACA 1-Series Centerbody and Outer Profiles and Elliptical Inner Lips, GE Report R62FPD168, April, 1962. (U)

### BIBLIOGRAPHY OF SEALS

P. Bauer, F. Iwatsuki: Analytical Techniques For the Design of Seals For Use In Rocket Propulsion Systems, Volume 2 - Dynamic Seals, RPL TR 65-61V2, May 1965.

R.C. Elwell, A.J. Bialous: Description of Seal Study and of Currently Available Seals, The General Electric Company, 64-GL-65, August 1964.

R.C. Elwell: Studies of Special Topics In Sealing, The General Electric Company, 64-GL-66, August 1964.

R.L. George, R.C. Elwell: Bibliography of Astia Literature on Seals, The General Electric Company, 63-GL-101, July 1963.

R.L. George, R.C. Elwell: Bibliography of Open Literature on Seals, The General Electric Company, 63-GL-102, July 1963.

GE-ATL: Study of Dynamic and Static Seals For Liquid Rocket Engines - Volume 1, Final Report, The General Electric Company, August 1964.

GE-ATL: Study of Dynamic and Static Seals For Liquid Rocket Engines - Volume 2, Final Report, The General Electric Company, August 1964.

GE RDC: Study of Dynamic and Static Seals For Liquid Rocket Engines - Final Report, The General Electric Company, November 1965.

N.A. Kamp: High Temperature Interface Seal Study - SST Phase II-B, The General Electric Company, FPD DM 65-237-3, June 1965.

J. Lee: "Metallic Seals for Extreme Temperature-Pressure Applications", SAE PP 523E, April 1962.

H.T. Libby, W.P. Foster: Fabricated, Abradable, Turbine Seals and Shrouds, The General Electric Company, 61-SE-9, May 1962.

E. Mayer, "Leakage and Wear In Mechanical Seals", Machine Design, Page 106, March 1960.

V.L. Peickii, D.A. Christensen: "How To Choose A Dynamic Seal", Product Engineering, Page 57, March 1961.

L.H. Smith: High Temperature Fluid Seals Engineering Program. Report Number III, The General Electric Company, 59-FL-174, June 1959.

L.H. Smith, High Temperature Fluid Seals Engineering Program Final Report, The General Electric Company, 60-GL-13, June 1960.

J.D. Symons: "Seal Design Parameters and Their Effect On Seal Operating Temperature", ASME PP 66-MD10

H. Tankus, J.B. Stevens: "Axial Mechanical Seals", Machine Design, Page 27 March 1967.

J.H. Thayer: "Construction of Mechanical Seals", Materials Protection, Page 67, March 1966.

Unclassified

Security Classification

DOCUMENT CONTROL DATA - R&D

(Security classification of title, body of abstract and indexing annotation must be entered when the overall report is classified)

1 ORIGINATING ACTIVITY (Corporate entity)	2a REPORT SECURITY CLASSIFICATION
General Electric Company	Unclassified
Aircraft Engine Group	2b GROUP
Cincinnati, Ohio 45215	

3 REPORT TITLE

Air Force Advanced Lift Fan and Lift/Cruise Fan Demonstrator Program

4 DESCRIPTIVE NOTES (Type of report and inclusive dates)

Final Report, Volume II

5 AUTHOR(S) (Last name, first name, middle)

Fasching, Walter A.

6 REPORT DATE	7a TOTAL NO OF PAGES	7b NO OF REPS
February 22, 1969		12

8a CONTRACT OR GRANT NO	8a ORIGINATOR'S REPORT NUMBER(S)
F33657-67-C	

8b PROJECT NO	8b OTHER REPORT NO(S) (Any other numbers that may be assigned to this report)
	R69 AEG 150

10 AVAILABILITY/LIMITATION NOTES	U.S. Government agencies may obtain copies of this report directly from DDC. Other qualified users shall request through: USAF-Air Force Materiel Command
----------------------------------	--------------------------------------------------------------------------------------------------------------------------------------------------------------

11 SUPPLEMENTARY NOTES	12 SPONSORING MILITARY ACTIVITY
	R & TD - SEKNB Wright Patterson AFB, Ohio

13 ABSTRACT
-------------

(U) This report is a technical summary of the preliminary design, component technology development, and partial detail design of an advanced large size remote Turbotip lift fan and a lift/cruise fan for military high sub-sonic V/STOL transport and search/rescue aircraft applications. Volume I covers the preliminary and detail design, Volume II covers the component technology development programs.

DD 1473

Unclassified  
Security Classification

Security Classification		LINK A		LINK B		LINK C	
14. KEY WORDS		ROLE	WT	ROLE	WT	ROLE	WT
<b>INSTRUCTIONS</b>							
<p><b>1. ORIGINATING ACTIVITY:</b> Enter the name and address of the contractor, subcontractor, grantee, Department of Defense activity or other organization (corporate author) issuing the report.</p> <p><b>2a. REPORT SECURITY CLASSIFICATION:</b> Enter the overall security classification of the report. Indicate whether "Restricted Data" is included. Marking is to be in accordance with appropriate security regulations.</p> <p><b>2b. GROUP:</b> Automatic downgrading is specified in DoD Directive 5200.10 and Armed Forces Industrial Manual. Enter the group number. Also, when applicable, show that optional markings have been used for Group 3 and Group 4 as authorized.</p> <p><b>3. REPORT TITLE:</b> Enter the complete report title in all capital letters. Titles in all cases should be unclassified. If a meaningful title cannot be selected without classification, show title classification in all capitals in parentheses immediately following the title.</p> <p><b>4. DESCRIPTIVE NOTES:</b> If appropriate, enter the type of report, e.g., interim, progress, summary, annual, or final. Give the inclusive dates when a specific reporting period is covered.</p> <p><b>5. AUTHOR(S):</b> Enter the name(s) of author(s) as shown on or in the report. Enter last name, first name, middle initial. If military, show rank and branch of service. The name of the principal author is an absolute minimum requirement.</p> <p><b>6. REPORT DATE:</b> Enter the date of the report as day, month, year, or month, year. If more than one date appears on the report, use date of publication.</p> <p><b>7a. TOTAL NUMBER OF PAGES:</b> The total page count should follow normal pagination procedures, i.e., enter the number of pages containing information.</p> <p><b>7b. NUMBER OF REFERENCES:</b> Enter the total number of references cited in the report.</p> <p><b>8a. CONTRACT OR GRANT NUMBER:</b> If appropriate, enter the applicable number of the contract or grant under which the report was written.</p> <p><b>8b. DR. &amp; DR. PROJECT NUMBER:</b> Enter the appropriate military department identification, such as project number, sub-project number, system numbers, task number, etc.</p> <p><b>9a. ORIGINATOR'S REPORT NUMBER(S):</b> Enter the official report number by which the document will be identified and controlled by the originating activity. This number must be unique to that report.</p> <p><b>9b. OTHER REPORT NUMBERS:</b> If the report has been assigned any other report numbers (either by the originator or by the sponsor), also enter this number(s).</p> <p><b>10. AVAILABILITY/LIMITATION NOTICES:</b> Enter any limitations on further dissemination of the report, other than those imposed by security classification, using standard statements such as:</p> <ul style="list-style-type: none"> <li>(1) "Qualified requesters may obtain copies of this report from DDC."</li> <li>(2) "Foreign encumbrance and dissemination of this report by DDC is not authorized."</li> <li>(3) "U. S. Government agencies may obtain copies of this report directly from DDC. Other qualified DDC users shall request through .."</li> <li>(4) "U. S. military agencies may obtain copies of this report directly from DDC. Other qualified users shall request through .."</li> <li>(5) "All distribution of this report is controlled. Qualified DDC users shall request through .."</li> </ul> <p>If the report has been furnished to the Office of Technical Services, Department of Commerce, for sale to the public, indicate this fact and enter the price, if known.</p> <p><b>11. SUPPLEMENTARY NOTES:</b> Use for additional explanatory notes.</p> <p><b>12. SPONSORING MILITARY ACTIVITY:</b> Enter the name of the departmental project office or laboratory sponsoring (paying for) the research and development. Include address.</p> <p><b>13. ABSTRACT:</b> Enter an abstract giving a brief and factual summary of the document indicative of the report, even though it may also appear elsewhere in the body of the technical report. If additional space is required, a continuation sheet shall be attached.</p> <p>It is highly desirable that the abstract of classified reports be unclassified. Each paragraph of the abstract shall end with an indication of the military security classification of the information in the paragraph, represented as (TS), (S), (C), or (U).</p> <p>There is no limitation on the length of the abstract. However, the suggested length is from 150 to 225 words.</p> <p><b>14. KEY WORDS:</b> Key words are technically meaningful terms or short phrases that characterize a report and may be used as index entries for cataloging the report. Key words must be selected so that no security classification is required. Identifiers, such as equipment model designation, code name, military project code name, geographic location, may be used as key words but will be followed by an indication of technical content. The assignment of kinds, rates, and weights is optional.</p>							